micromachines

Special Issue Reprint

Frontiers in Ultra-Precision Machining, Volume II

Edited by
Jiang Guo, Chunjin Wang and Chengwei Kang

mdpi.com/journal/micromachines

MDPI

Frontiers in Ultra-Precision Machining, Volume II

Frontiers in Ultra-Precision Machining, Volume II

Editors

Jiang Guo
Chunjin Wang
Chengwei Kang

MDPI

Basel • Beijing • Wuhan • Barcelona • Belgrade • Novi Sad • Cluj • Manchester

Editors

Jiang Guo
School of Mechanical Engineering
Dalian University of Technology
Dalian
China

Chunjin Wang
Department of Industrial and Systems Engineering (ISE)
The Hong Kong Polytechnic University (PolyU)
Hong Kong
China

Chengwei Kang
School of Mechanical Engineering
Xi'an Jiaotong University
Xi'an
China

Editorial Office

MDPI
St. Alban-Anlage 66
4052 Basel, Switzerland

This is a reprint of articles from the Special Issue published online in the open access journal *Micromachines* (ISSN 2072-666X) (available at: www.mdpi.com/journal/micromachines/special_issues/Ultra_Precision_Machining_Volume_II).

For citation purposes, cite each article independently as indicated on the article page online and as indicated below:

Lastname, A.A.; Lastname, B.B. Article Title. *Journal Name* **Year**, *Volume Number*, Page Range.

ISBN 978-3-7258-1566-1 (Hbk)
ISBN 978-3-7258-1565-4 (PDF)
doi.org/10.3390/books978-3-7258-1565-4

Contents

About the Editors

Jiang Guo

Jiang Guo is a professor at Dalian University of Technology, a doctor of engineering at the University of Tokyo, a recipient of the National Program for the Introduction of Overseas High-Level Talents-Youth Program, a young and outstanding talent under the Liaoning Xingliao Talent Program, and a member of Elsevier's Top 2% of Top Scientists in the World in 2022. Before returning to China, he worked as a researcher at RIKEN in Japan and Singapore Science and Technology Agency (STA). His research interests include precision/ultra-precision machining, optical manufacturing, laser processing, and metal substrate construction and molding. His research achievements have been recognized as 2018 A*STAR Research Highlights, and he has published more than 100 academic papers in renowned international journals in the fields of manufacturing, friction, and optics, and has authorized more than 80 international and national invention patents. He has chaired more than 20 projects, including the Japan Society for the Promotion of Science and Technology (JSPS) Youth Fund, the National Natural Science Foundation of China (NSFC) and the National Key Research and Development Program of China (NKRDP) "Key Scientific Issues of Transformative Technologies". He serves as an editorial board member and young editorial board member of International Journal of Extreme Manufacturing, Advances in Manufacturing, International Journal of Hydromechatronics, etc., as well as a reviewer for more than 80 international journals. He is also a reviewer for more than 80 international journals.

Chunjin Wang

Dr. Chunjin Wang is a Research Assistant Professor in the Department of Industrial and Systems Engineering (ISE) at The Hong Kong Polytechnic University (PolyU). He received his bachelor and PhD degree from Xiamen University in 2010 and 2015, respectively. He joined the State Key Lab of Ultra-precision Machining Technology in ISE at PolyU in 2015 as a postdoctoral fellow and then a research fellow in 2018. His research interests include ultra-precision polishing technology, ultra-precision machining equipment and instrumentation, advanced optics manufacturing and functional surface engineering. He has authored and co-authored more than 70 refereed journal papers, including International Journal of Machine Tools and Manufacture, International Journal of Mechanical Sciences, Applied Surface Science, Robotics and Computer Integrated Manufacturing, etc.

Chengwei Kang

Chengwei Kang, professor of School of Mechanical Engineering, Xi'an Jiaotong University, National Distinguished Young Scholar. He earned his PhD from the prestigious University of Queensland (UQ), located in Australia and ranked 36th globally by U.S. News in 2023. He joined University College Dublin (UCD), Ireland, as a post-doctorral research fellow after receiving his degree in 2016. In 2018, he was promoted to Senior Research Engineer and Lab Supervisor. After receiving the National Distinguished Young Scholar award and Young Talent Support Plan award, Dr. Kang began working as a full-professor at Xi'an Jiaotong University (XJTU) in the year 2022.Professor Kang's research concerns the ultra-precision machining, manufacturing of biomedical implants, manufacturing and post-processing of surface-microstructures. He has published over 30 papers in peer-reviewed journals (over 730 citations with h-index of 13).

micromachines

MDPI

Article

Study of Atmospheric Pressure Plasma Temperature Based on Silicon Carbide Etching

Shaozhen Xu, Julong Yuan *, Jianxing Zhou, Kun Cheng and Hezhong Gan

College of Mechanical Engineering, Zhejiang University of Technology, Hangzhou 310023, China; 2112002412@zjut.edu.cn (S.X.)
* Correspondence: julongyuan2023@126.com

Abstract: In order to further understand the excitation process of inductively coupled plasma (ICP) and improve the etching efficiency of silicon carbide (SiC), the effect of temperature and atmospheric pressure on plasma etching of silicon carbide was investigated. Based on the infrared temperature measurement method, the temperature of the plasma reaction region was measured. The single factor method was used to study the effect of the working gas flow rate and the RF power on the plasma region temperature. Fixed-point processing of SiC wafers analyzes the effect of plasma region temperature on the etching rate. The experimental results showed that the plasma temperature increased with increasing Ar gas until it reached the maximum value at 15 slm and decreased with increasing flow rate; the plasma temperature increased with a CF_4 flow rate from 0 to 45 sccm until the temperature stabilized when the flow rate reached 45 sccm. The higher the RF power, the higher the plasma region's temperature. The higher the plasma region temperature, the faster the etching rate and the more pronounced the effect on the non-linear effect of the removal function. Therefore, it can be determined that for ICP processing-based chemical reactions, the increase in plasma reaction region temperature leads to a faster SiC etching rate. By processing the dwell time in sections, the nonlinear effect caused by the heat accumulation on the component surface is effectively improved.

Keywords: plasma temperature; silicon carbide; plasma etching; removal function

Citation: Xu, S.; Yuan, J.; Zhou, J.; Cheng, K.; Gan, H. Study of Atmospheric Pressure Plasma Temperature Based on Silicon Carbide Etching. *Micromachines* **2023**, *14*, 992. https://doi.org/10.3390/mi14050992

Academic Editors: Jiang Guo, Chengwei Kang and Chunjin Wang

Received: 9 April 2023
Revised: 27 April 2023
Accepted: 29 April 2023
Published: 2 May 2023

1. Introduction

Silicon carbide (SiC), one of the popular third-generation semiconductor materials, has excellent properties, such as a wide bandgap, a high critical breakdown electric field, and high thermal conductivity [1]. It is widely used in 5G communication, aerospace, and semiconductor lighting [2,3]. Due to the covalent bonding between Si and C atoms and the ordered, tightly packed structure, SiC has extremely high hardness (Mohs hardness 9.2) and chemical inertness, which makes SiC a typical hard-to-process material [4,5]. The current SiC ultra-precision machining techniques mainly include electrochemical polishing (ECMP), chemical mechanical polishing (CMP), and magnetorheological processing (MRF). In the above technology, CMP is the only effective means to achieve both surface planarization and global polishing, but the polishing efficiency is generally low. ECMP adds an electric field based on CMP to improve the material removal rate and can process arbitrarily shaped workpieces, but its processing cost is high, and the polishing liquid has the possibility of chemical pollution. MRF has the advantages of a good removal effect and strong controllability. However, the properties of magnetorheological fluid are easily affected by external factors, such as temperature and viscosity; the removal effect is unstable; and the high cost of MRF devices makes it difficult for practical application in industrial fields [6–10]. With the growing demand for processing SiC materials, atmospheric pressure plasma processing methods are gaining more and more attention.

According to the different methods of plasma excitation generation, atmospheric plasma can be divided into inductively coupled plasma (ICP) and capacitively coupled

plasma (CCP) [11,12]. Among the institutions that have conducted plasma research, it is mainly Osaka University in Japan and the Institute of Surface Modification (IOM) in Germany that used CCP to generate plasma. Osaka University adopted various forms of electrodes for different machining requirements, which were named plasma chemical vaporization machining (PCVM) [13]. IOM had inherited the technological advantage of ion beam processing by using a 2.45 GHz microwave plasma power source to generate excited plasma, called plasma jet machining (PJM) [14]. The Lawrence Livermore National Laboratory (LLNL) first proposed reactive atomic plasma (RAP) processing in 1999, which uses ICP to obtain plasma in a high gas pressure environment [15]. However, because the ICP will generate a large amount of joule heat, it is difficult to cool down the plasma inside the generator to ensure the safety of the process. To solve this problem, Cranfield University tried to minimize the negative effects caused by high temperatures during processing and found that improving the temperature by changing the flow rate of the reaction gas had a very limited effect [16]. The scholar Renaud Jourdain built a simulation model and confirmed that the nozzles have a significant cooling effect on the plasma jet [17]. However, the nozzles also bring a certain degree of influence to the process. In the study of RAP processing of ultra-low expansion coefficient glass after adding nozzles and fused silica glass, it was found that the volume removal of material from static fixed-point processing elements was not fully linear but rather had a distinct curvilinear relationship. They tentatively attributed the generation of this phenomenon to nonlinearity due to the effect of temperature on the chemical reactions produced [18]. Different from the above techniques, atmospheric pressure plasma polishing (APPP), proposed by the Harbin Institute of Technology, is characterized by the use of CCP for micro-trimming surface shape and ICP for fast and efficient removal [19].

In addition to the above concerns, during atmospheric plasma excitation, many factors, such as gas flow rate, directly affect the plasma region temperature, which influences the chemical reaction rate during material removal. Some scholars have studied the temperature variation of CCP [20], but the study of plasma region temperature for the ICP excitation process has not been published. Therefore, in this paper, based on the ICP excitation method, the following studies were conducted: firstly, we measured the temperature of the plasma reaction region by infrared thermometry and investigated the influence of the excitation gas Ar flow rate, reaction gas CF_4 flow rate, and RF power magnitude on the plasma region temperature by the single-factor method. Then we studied the influence of plasma region temperature and dwell time on the SiC etching efficiency by using fixed-point etching of SiC material, which laid the foundation for the subsequent study of SiC planarization processing.

2. Materials and Methods

The ICP processing system mainly consists of five subsystems, including the mechanical motion control system, gas supply system, plasma-generating device, RF power supply, and external modules, as shown in Figure 1a.

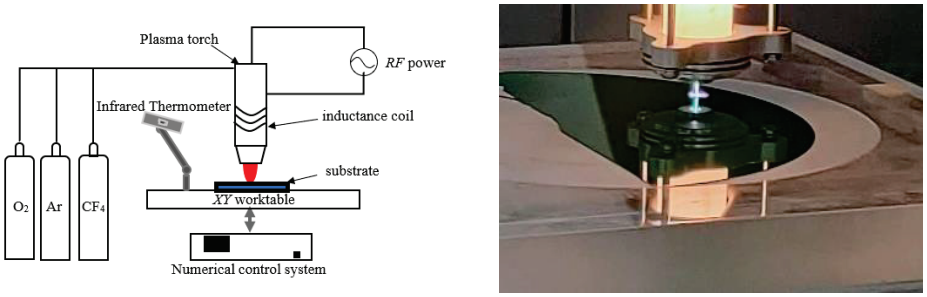

(**a**) (**b**)

Figure 1. ICP processing system. (**a**) schematic diagram; (**b**) physical picture.

The mechanical motion control system includes motion stages (e.g., *X*- and *Y*-axis tables) and a numerical control system that controls the motion of the plasma-generating device. The gas supply system provides two gases: one is the excitation gas, which is the main source of protective plasma and consists mainly of the rare gas Ar; the other is the reaction gas, which is the main source of reactive plasma and consists mainly of F-containing gas (CF_4 or SF_6) and O_2. CF_4 is used in the following experiments as the reaction gas. The external module is an infrared thermometer, which is responsible for measuring the temperature of the plasma reaction area. The outer layer of the plasma generator is connected to an inductive coil, and when the RF power supply is powered up, the tube ionizes the gas under the coupling effect of the electric field and the peripheral coil to produce reactive etching particles F*, which react with the substrate material to convert the solid substrate material into a gaseous compound. The expression of the reaction between F* and SiC material is as follows:

$$SiC + F^* + O \rightarrow SiF_4 \uparrow + CO_2 \uparrow + CO \uparrow \quad (1)$$

In the above equation, SiC is the main material of the substrate; the active particles F* and O are formed by ionization of CF_4 and O_2, respectively; and the products SiF_4, CO_2, and CO are volatile gases. A physical picture of the processing system is shown in Figure 1b.

The atmospheric plasma removal function is similar to conventional ion beam machining in that it has a Gaussian shape. The removal profile cross-section after fixed-point processing, which uses common processing parameters, is shown in Figure 2. The APPP removal profile is generally fitted with a standard Gaussian function with the following expression:

$$R(x) = a * e^{\frac{x^2+y^2}{2\sigma^2}} \quad (2)$$

$$FWHM = 2\sqrt{2\ln 2\sigma} \quad (3)$$

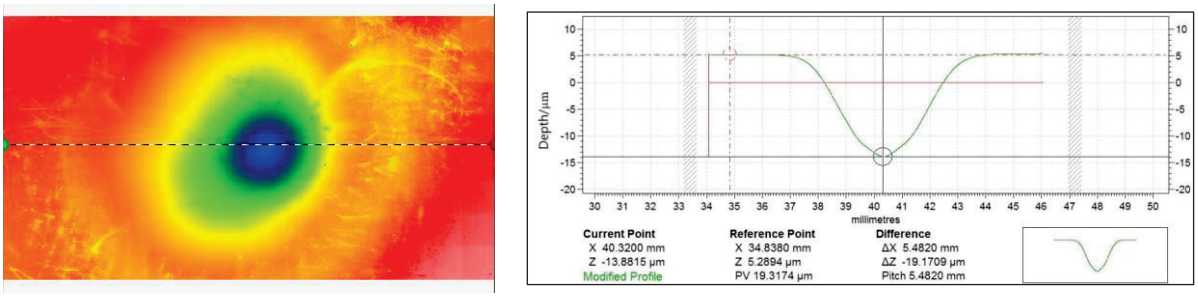

Figure 2. APPP removal contour.

In the above formula, *a* is the removal depth, that is, the peak of the removal function; the peak of the removal function per unit time can also be expressed as the removal rate. FWHM indicates the size of the half-height width of the removal function, that is, the width value in the horizontal direction when the removal depth is half of the peak; σ is the standard deviation of the Gaussian function, determined by the half-height width of the removal function, FWHM, as shown in Equation (3) above.

3. Temperature Measurement Method

The most commonly used methods for plasma region temperature measurement are the spectral intensity method, the probe method, and the infrared thermometry method [21]. The principle of the spectral intensity method is to use a spectrometer to measure the absolute intensity of different spectra emitted by the plasma, combined with an analysis of the spectral emission theory to obtain the plasma's internal temperature. However, since most spectrometers still measure the relative intensity of the emission spectrum rather than

the absolute intensity, experimental spectral thermometry research for measuring atmospheric plasma is not yet complete, and the probe method is not suitable for an atmospheric pressure environment. In contrast, infrared thermometry has many advantages, such as speed, lightness, and safety, which have made the use of infrared thermometry increasingly popular in various fields [22]. Therefore, in this paper, infrared thermometry is chosen to measure the plasma region's temperature. Erroneous use of infrared thermometers may cause significant errors in the measured temperature. Therefore, the temperature measurement experiment follows these specifications: (1) fix the infrared thermometer to keep the measuring distance and the measuring angle constant; (2) select the correct material emissivity; (3) after adjusting the experimental parameters, wait for a certain time to measure after the plasma region temperature is stable. Figure 3 shows the diagram of the infrared thermometer and the infrared radiation of the plasma torch.

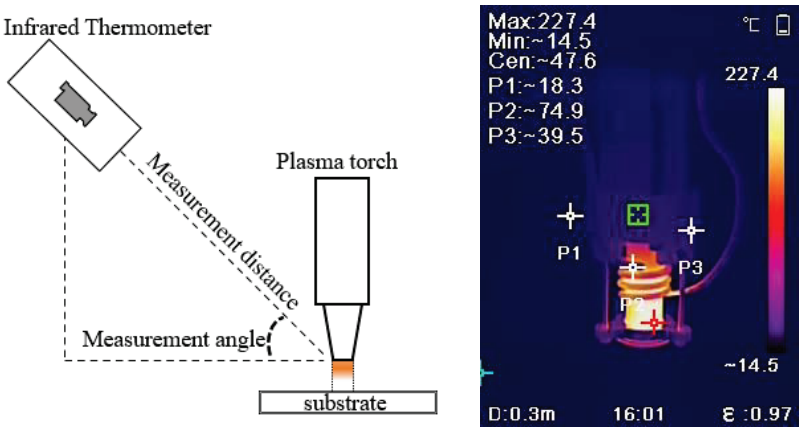

Figure 3. Schematic diagram and effect drawing of the infrared thermometer.

4. Results and Discussion

4.1. Effect of Processing Parameters on Plasma Region Temperature

4.1.1. Effect of Ar Gas Flow Rate

Ar gas, as one of the most common inert gases, does not form stable compounds with other elements at room temperature, so it is mainly used as an excitation gas or protective gas in ICP excitation. After the RF power supply is charged, the Ar molecules are continuously hit by high-energy electrons in the strong electromagnetic field to obtain internal and kinetic energy, and the particles are transformed from the ground state to the high-energy state. This refers to active Ar atoms, which are mixed with high-energy electrons and a variety of ground-state particles in the field to form an electrically neutral Ar plasma. If Ar gas is the main source of plasma generation and its flow rate is too low or too high, the formed plasma flame will be unstable or even extinguished, so the Ar gas flow range is generally around 11–27 slm. This section sets the experimental parameters under different Ar flow rates, as shown in Table 1.

Table 1. Processing parameters under different Ar flow rates.

Parameter	Value
Ar flow rate/slm	10, 12.5, 15, 17.5, 20, 22.5, 25, 27
CF_4 flow rate/sccm	60
O_2 flow rate/sccm	10
Input power/W	500

The experimental results are shown in Figure 4. The plasma region temperature keeps rising when the Ar flow rate is between 10 and 15 slm, then decreases instead of rising as the Ar gas flow rate increases, which is due to the limited ionization capacity of the RF power of 500 W. The ionization capacity is saturated when the Ar gas flow rate reaches

15 slm, at which time there are no more free electrons generated in the electromagnetic field and no more heat can be released. The excess Ar gas is passed through the plasma field in the form of low-energy molecules flowing from the nozzle to the air, which plays the role of heat dissipation, so the temperature of the plasma decreases. Additionally, the molecular form of Ar inhibits the generation of active reaction particles, thus making the etching efficiency decrease. Excess Ar gas also makes the plasma flame formed from the nozzle more elongated, so the shape of the removal profile of the workpiece also changes, and the Ar gas flow rate generally cannot be too low.

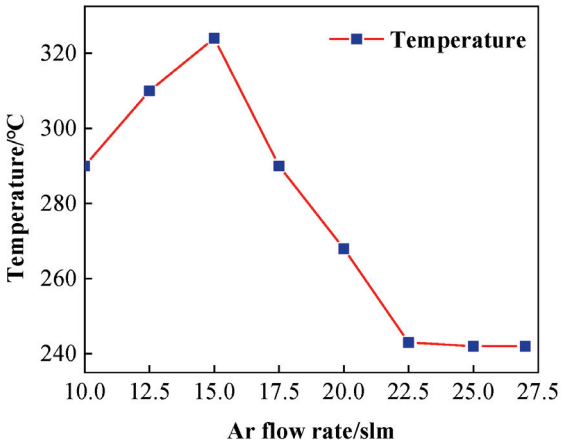

Figure 4. Influence of Ar flow rate on plasma temperature.

4.1.2. Effect of CF_4 Gas Flow Rates

When CF_4 is the reaction gas, the addition of a small amount of O_2 gas serves to enhance the F* etching efficiency and inhibit deposit generation [23,24], and its excitation principle is similar to that of CF_4 gas. Therefore, this paper only focuses on the effect of the CF_4 gas flow rate on the plasma region temperature. After CF_4 is passed into the generator, it undergoes multi-stage decomposition under the influence of the active Ar plasma atmosphere and the internal electromagnetic field. Active F-atoms are generated, and this particle interacts with the substrate surface to achieve removal. Considering the completeness of the experiment and the fact that this section only deals with the effect of the gas flow rate on the plasma region temperature, CF_4 gas flow rates of 0 sccm and 5 sccm were added for comparison, as shown in Table 2.

Table 2. Processing parameters under different CF_4 flow rates.

Parameter	Value
Ar flow rate/slm	19
CF_4 flow rate/sccm	0, 5, 10, 15, 25, 35, 45, 55, 65, 75, 85
O_2 flow rate/sccm	10
Input power/W	500

The plasma region temperature change curve with CF_4 flow is shown in Figure 5. When the CF_4 flow range is around 0–45 sccm, a large number of free electron collisions constantly enter the F atom and get enough energy after being excited by high-energy F ions to lead to a sharp rise in the plasma torch temperature, and at this time the plasma flame at the nozzle will become light green. This is because in the high-energy state, active F atoms are not stable, and a large number of photons are released in the process of returning to the ground state. When the flow rate of CF_4 is greater than 45 sccm, after the RF electric field excitation capacity reaches saturation, the excitation ratio of F atoms in the generator remains unchanged. The excess CF_4 gas flows out in its original form, so the temperature of the plasma torch tube gradually flattens out with the increase in CF_4 gas flow rate and

even slightly decreases. This is the same reason why the temperature drops when the Ar gas flow rate is excessive. However, because the CF_4 gas flow rate increases by only 10 sccm, which is too small compared to the proportion of Ar gas in the tube, the cooling trend of the plasma is less obvious.

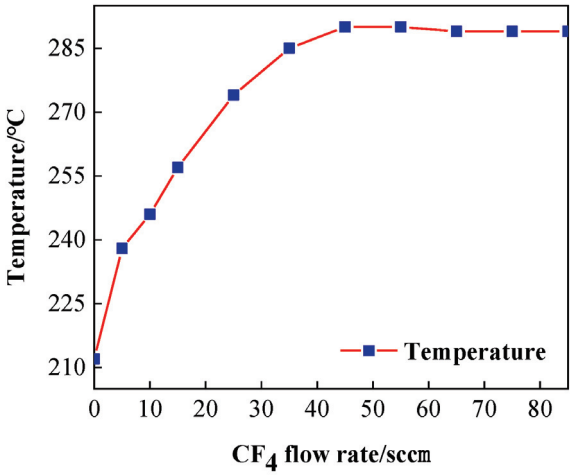

Figure 5. Influence of CF_4 gas flow on plasma temperature.

4.1.3. Effect of RF Power

The RF power supply is the energy input source for the plasma processing system. RF input power indicates the energy input to the plasma torch and is an important parameter of plasma excitation. The size of the RF input power determines whether it can discharge and the size of the discharge intensity. When the electric field strength is greater, the electron concentration increases, a large number of electrons hit the reaction gas, dissociate more active etching particles, and the APPP etching rate increases. Theoretically, the higher the RF input power, the higher the Ar gas excitation intensity, and the temperature will increase [25]. This section sets the parameters under different RF power values, as shown in Table 3, to experimentally prove that the reasonable RF input power range based on this parameter is around 350–700 W. Too high or too low will produce an arc-pulling phenomenon or even quenching.

Table 3. Processing parameters under different RF power values.

Parameter	Value
Ar flow rate/slm	19
CF_4 flow rate/sccm	60
O_2 flow rate/sccm	10
Input power/W	350, 400, 450, 500, 550, 600, 650, 700

Figure 6 shows the change curve of the plasma region temperature at different RF power, the RF power from 350 W to 700 W plasma region temperature steadily increases, which is also in line with the above theory. The acceleration of temperature rise increases when 600 W, so the RF power should be controlled below 600 W in practical processing.

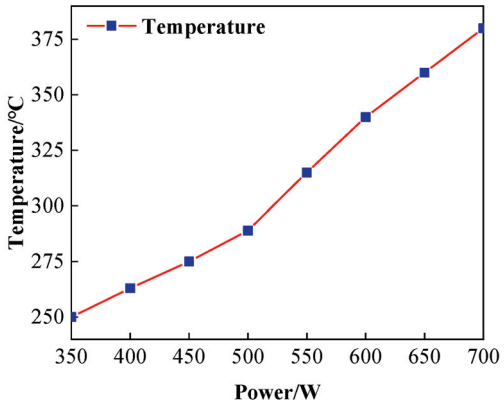

Figure 6. Influence of RF power on plasma temperature.

4.2. Study on the Removal Function of Silicon Carbide by ICP Processing

4.2.1. Effect of Plasma Region Temperature on the Removal Function

Atmospheric plasma processing is not affected by the physical properties of the material, so it can perform efficient and rapid processing of the material, the essence of which is material removal through the chemical reaction between the active particles generated under the active atmosphere of the plasma and the surface of the substrate. Its reaction rate is also in accordance with the Arrhenius formula with the following expressions [26,27]:

$$k = Ae^{-\frac{E_a}{RT}} \tag{4}$$

In the above equation, k is the chemical reaction rate constant; A is the Arrhenius constant; E_a is the reactivity energy, in units (J/mol); T is the absolute temperature, in units K; and R is the molar gas constant, in units (J/mol-K). The etching efficiency of ICP-processed silicon carbide varies with the temperature of the plasma reaction region. In order to study the effect of plasma region temperature on silicon carbide under the same process parameters, in this section, the experimental parameters of the conventional processing were made constant. The processing distance between the nozzle tip and the sample surface was 4 mm, the dwell time was 30 s, the Ar flow rate was 19 slm, the CF_4 flow rate was 60 sccm, the O_2 flow rate was 10 sccm, and the RF power supply power was 500 W. It should be noted that the workpiece must be completely cooled at intervals to prevent thermal accumulation. The experimental results were obtained by preheating to get the plasma reaction area temperatures of 256 °C, 288 °C, and 297 °C for three groups of fixed-point etching, which were recorded as points A, B, and C, respectively.

The profile data of the machined section at three points were measured using a Taylor profiler and imported into Matlab to obtain Figure 7. The peak removal depths were 3.64 μm, 3.93 μm, and 4.47 μm at points A, B, and C, respectively. The increase in longitudinal etching caused the peak removal profile to increase with temperature, indicating that the increase in plasma region temperature promotes the etching rate of the active particles on the SiC material. Hence, the higher the plasma region temperature, the higher the removal depth peak for the same dwell time. Comparing the temperature change, it is found that when the temperature increases from 256 °C to 288 °C, the peak removal depth increases by 0.29 μm, with a ratio of about 0.009 μm/°C to the temperature increment, while from 288 °C to 297 °C, the peak removal depth increases by 0.54 μm/min, with a ratio of about 0.06 μm/°C to the temperature increment. This is much larger than the first two points of difference ratio change, which indicates that the influence of the plasma area temperature on the etching efficiency is more significant with the increase in temperature. Therefore, in the actual processing, it is necessary to ensure the stability of the processing environment while controlling the plasma temperature within a small range to ensure the stability of the plasma removal capacity.

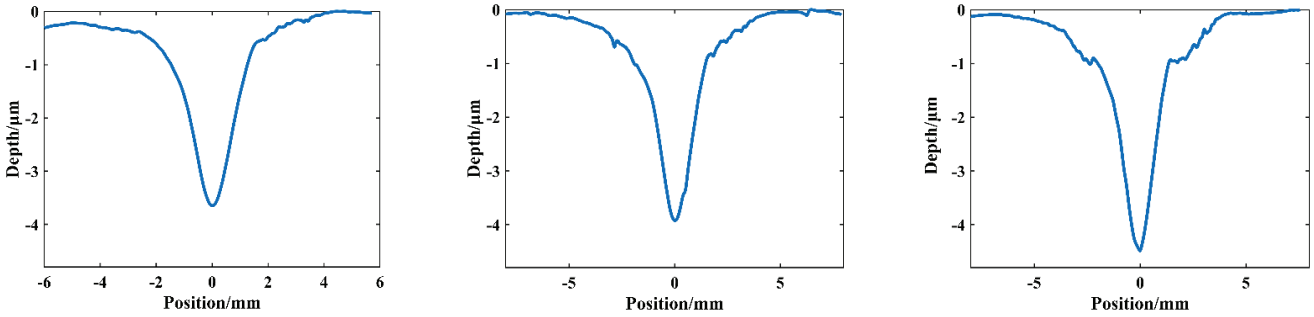

Figure 7. Cross-sectional profile of the removal function at different plasma temperatures: (**a**) point A, 256 °C; (**b**) point B, 288 °C; and (**c**) point C, 297 °C.

4.2.2. Effect of Dwell Time on the Removal Function

In ICP fixed-point or planar processing, the plasma flame equivalent to a fixed-point heat source will continuously conduct heat transfer to the substrate surface to increase its temperature, as shown in Figure 8, so the relationship between the dwell time and etching rate will not be a simple linear fit [28].

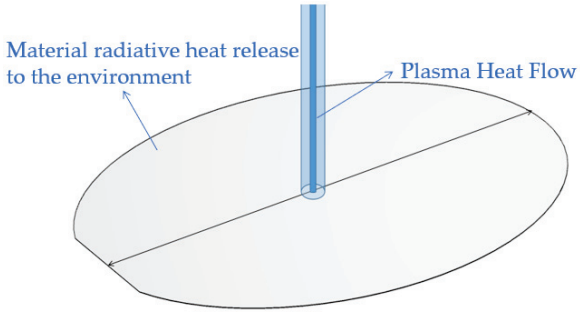

Figure 8. Plasma thermal radiation schematic.

To investigate the effect of heat removal due to increasing dwell time, the dwell time is set in this section, as shown in Table 4, and other parameters are the same as in the previous section. In addition to this, the same five processing points were set without changing other parameters, and their dwell times were divided into 10-s increments, as shown in Table 4. For example, the processing point with a dwell time of 6 × 10 in the table means that the point was processed six times for 10 s each time. Sufficient intervals were made between each processing so that the surface of the SiC wafer processed twice was sufficiently cooled to minimize the temperature accumulation on the wafer surface. To facilitate the distinction between the two types of processing, the processing point with uninterrupted dwell time is recorded as a single processing point, and the interval division is recorded as multiple processing.

Table 4. Experimental parameters with different dwell times.

Processing Method	Dwell Time/s
Single process	10, 20, 30, 40, 50, 60
Multiple process	10 × 1, 10 × 2, 10 × 3, 10 × 4, 10 × 5, 10 × 6

The experimental results are shown in Figure 9. Figure 9a shows the results of single processing, and Figure 9b shows the results of multiple processing. The blue curve in the figure represents a simple linear fit to the removal depths of the first two processes to compare the extent to which the experimentally obtained removal depth curves deviate

from linearity. Theoretically, when the dwell time of a section is constant, then the total dwell time of the same removal amount should be equal. However, when comparing the peak depth of removal curves of single processing and multiple interval processing, it can be found that the greater the dwell time, the greater the deviation from the linear curve of single processing under the same cumulative dwell time of both. This is consistent with the conclusion about the effect of temperature on the depth of removal in the previous section. This indicates that the thermal accumulation on the wafer surface is the reason for the non-linear relationship between the dwell time and etching rate, and the longer the dwell time accumulation, the greater the effect on the instability of the etching rate. Therefore, in the planarization processing, the temperature accumulation on the wafer surface can be reduced by speeding up the process multiple times, and at the same time, the temperature accumulation on the wafer surface can be dissipated as much as possible.

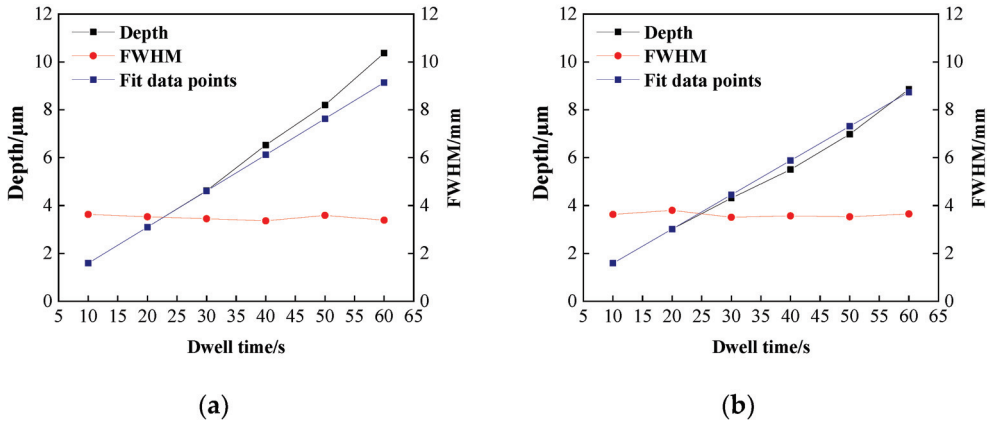

Figure 9. Removal function and dwell time variation curve: (**a**) single processing; (**b**) multiple processing.

5. Conclusions

In this paper, based on ICP processing of SiC material, the temperature variation in atmospheric plasma processing was measured by infrared thermometry, and the influence of the three main processing parameters, Ar, CF_4, and RF power, on the temperature in the plasma region was analyzed by the single-factor method. The following conclusions were drawn in combination with the profilometer measurements:

(1) In atmospheric plasma processing, plasma temperature fluctuations affect the working gas excitation, the decomposition process, and the energy and distribution of active particles on the surface of the components, which further affect the removal stability of the material. Infrared thermometry reveals that the plasma region temperature rises with increasing Ar gas flow rate, reaching a maximum of 325 °C at 15 slm. With the reaction gas CF_4 flow rate in the interval of around 0–45 sccm, the plasma will be continuously exothermic with the ionization of the system's overall temperature increase until the flow rate reaches 45 sccm, at which point the system's ionization capacity reaches saturation after the temperature stabilizes with only a small decline. The size of the RF input power determines the size of the discharge and its intensity. When the RF power is around 350–700 W, the plasma region temperature increases with the increase in RF power.

(2) The higher the plasma region temperature under the same parameters, the faster the etching rate of ICP-etched SiC, and the higher the plasma region temperature, the more easily the removal rate is affected. Additionally, the dwell time has a non-linear relationship with the peak removal depth due to the effect of heat accumulation on the wafer surface.

Author Contributions: Conceptualization, S.X. and J.Y.; Methodology, S.X., J.Y. and J.Z.; software, S.X., J.Y., J.Z., K.C. and H.G.; validation, S.X., J.Y., J.Z., K.C. and H.G.; formal analysis, S.X. and K.C.; investigation, J.Z.; resources, J.Z.; data curation, S.X.; writing-original draft preparation, S.X.; writing-review and editing, J.Z. and J.Z. All authors have read and agreed to the published version of the manuscript.

Funding: This research received no external funding.

Conflicts of Interest: The authors declare no conflict of interest.

References

1. Nguyen, T.K.; Aberoumand, S.; Dao, D.V. Advances in Si and SiC materials for high-performance supercapacitors toward integrated energy storage systems. *Small* **2021**, *17*, 2101775. [CrossRef] [PubMed]
2. Kimoto, T. Material science and device physics in SiC technology for high-voltage power devices. *Jpn. J. Appl. Phys.* **2015**, *54*, 040103. [CrossRef]
3. Pearton, S.J.; Yang, J.C.; Cary, P.H.; Ren, F.; Kim, K.; Marko, J.; Tadjer, M.K.; Mastro, M.A. A review of Ga_2O_3 materials, processing, and devices. *Appl. Phys. Rev.* **2018**, *5*, 011301. [CrossRef]
4. Kovalcikova, A.; Sedlacekb, J.; Lencesb, Z.; Bystrickyb, R.; Duszaa, J.; Sajgalikb, P. Oxidation resistance of SiC ceramics prepared by different processing routes. *J. Eur. Ceram. Soc.* **2016**, *36*, 3783–3973. [CrossRef]
5. Seo, Y.K.; Kim, Y.W.; Nishimura, T.; Seoc, W.S. High-temperature strength of a thermally conductive silicon carbide ceramic sintered with yttria and Scandia. *J. Eur. Ceram. Soc.* **2016**, *36*, 3755–3760. [CrossRef]
6. Luo, Y.G.; Xiong, Q.; Lu, J.B.; Yan, Q.B.; Hu, D. Chemical mechanical polishing exploiting metal electrochemical corrosion of single-crystal SiC. *Mater. Sci. Semicond. Process.* **2022**, *152*, 107067. [CrossRef]
7. Adia, H.; Doi, T.; Takeda, H.; Katakura, H.; Kim, S.W.; Koyama, K.; Yamazakib, T.; Unedab, M. Ultraprecision CMP for sapphire, GaN, and SiC for advanced optoelectronics materials. *Curr. Appl. Phys.* **2012**, *2*, 41–46. [CrossRef]
8. Deng, H.; Hosoya, K.; Imanishi, Y.; Endo, K.; Yanmamura, K. Electro-chemical mechanical polishing of single-crystal SiC using CeO_2, slurry. *Electrochem. Commun.* **2015**, *52*, 5–8. [CrossRef]
9. Alam, Z.; Khan, D.A.; Jha, S. A study on the effect of polishing fluid volume in ball end magnetorheological finishing process. *Mater. Manuf. Process.* **2018**, *33*, 1197–1204. [CrossRef]
10. Liang, H.Z.; Yan, Q.S.; Lu, J.B.; Gao, W.Q. Experiment on Chemical Magnetorheological Finishing of SiC Single Crystal Wafer. *Mater. Sci. Forum* **2016**, *874*, 407–414. [CrossRef]
11. Verma, Y.; Chang, A.K.; Berrett, J.W.; Futtere, K.; Gardopee, G.J.; Kelley, J.; Kyler, T.; Lee, J.; Lyford, N.; Proscia, D.; et al. Rapid damage-free shaping of silicon carbide using reactive atom plasma(RAP) processing. In *SPIE Astronomical Telescopes Instrumentation*; International Society for Optics and Photonics: Washington, DC, USA, 2006.
12. Piechulla, P.; Bauer, J.; Boehm, G.; Paetzelt, H.; Arnold, T. Etch mechanism and temperature regimes of an atmospheric pressure chlorine-based plasma jet process. *Plasma Process Polym* **2016**, *13*, 1128–1135. [CrossRef]
13. Yamamura, K.; Shimada, S. Damage-free Improvement of Thickness Uniformity of Quartz Crystal Wafer by Plasma Chemical Vaporization Machining. *CIRP Ann. Manuf. Technol.* **2008**, *57*, 567–570. [CrossRef]
14. Arnold, T.; Boehm, G.; Eichentopf, I.M. Plasma Jet Machining. *J. Vac. Sci. Technol.* **2010**, *22*, 10–16. [CrossRef]
15. Fiske, P.S.; Verma, Y.; Chang, A.; Lyford, N.; Kelley, J.; Sommer, P.; Li, N.; Pang, K.; Gardopee, G.; Kyler, T.; et al. Reactive atom plasma processing for lightweight SiC mirrors. In *OSA Technical Digest*; Optical Society of America: Rochester, NY, USA, 2006; p. OFMB1.
16. Castelli, M.; Jourdain, R.; Morantz, P.; Shorea, P. Fast figuring of large optics by reactive atom plasma. In Proceedings of the SPIE 8450, Amsterdam, The Netherlands, 15 October 2012; SPIE: Amsterdam, The Netherlands; p. 845034.
17. Yu, N.; Jourdain, R.; Gourma, M.; Shorea, P. Analysis of De-Laval nozzle designs employed for plasma figuring of surfaces. *Int. J. Adv. Manuf. Technol.* **2016**, *87*, 735–745. [CrossRef]
18. Castelli, M.; Jourdain, R.; McMeeking, G.; Morantz, P.; Shore, P.; Proscia, D.; Subrahmanyan, P. Initial strategies for 3D RAP processing of optical surfaces based on a temperature adaptation approach. In Proceedings of the 36th International MATADOR Conference, Manchester, UK, 14–16 July 2010; Springer: London, UK; pp. 569–572.
19. Wang, D.F.; Jin, H.L.; Jin, J.; Bo, W. Research on the Influence of Reactive Gas CF_4/SF_6 upon the Temperature of Atmospheric Pressure Plasma Jet. *Aviat. Precis. Manuf. Technol.* **2011**, *47*, 33–36.
20. Zhao, X.; Jin, H.L.; Li, N.; Jiang, J.; Bo, W. Research on Influence of Plasma Gas He and process Time upon Temperature of Atmospheric Pressure Plasma Jet. *Aviat. Precis. Manuf. Technol.* **2012**, *48*, 8–10.
21. Lin, Q.; Ren, Q.L. Investigation in Radiation Characteristic of Atmospheric Pressure Glow Discharge Plasma in Air. *J. Xiamen Univ. (Nat. Sci.)* **2005**, *44*, 621–624.
22. Shen, X.; Deng, H.; Zhang, X.; Peng, K.; Yamamura, K. Preliminary study on atmospheric-pressure plasma-based chemical dry figuring and finishing of reaction-sintered silicon carbide. *Opt. Eng.* **2016**, *55*, 105102. [CrossRef]
23. Yan, Y.Y.; Chan-Park, M.B.; Yue, C.Y. CF_4 plasma treatment of poly(dimethylsiloxane): Effect of fillers and its application to high-aspec-ratio UV embossing. *Langmuir* **2005**, *21*, 8905–8912. [CrossRef]

24. Wang, D.F. Research on atmospheric pressure plasma processing technology of fused silicon. *J. Shaanxi Univ. Technol. (Nat. Sci. Ed.)* **2013**, *29*, 1–11.
25. Su, X. Design and Study on the Atmospheric Pressure Plasma Jet Torch. Master's Thesis, Harbin Institute of Technology, Harbin, China, 2016.
26. Laidler, K.J. The development of the Arrhenius equation. *J. Chem. Educ.* **1984**, *61*, 494. [CrossRef]
27. Tang, W.J.; Liu, Y.W.; Zhang, H. New approximate formula for Arrhenius temperatureintegral. *Thermochim. Acta* **2003**, *408*, 39–43. [CrossRef]
28. Peng, B.; Dun, A.H.; Wu, L.Z.; Wang, Z.; Xu, X.K. Variable Removal Function in Atmospheric Pressure Plasma Polishing. *Chin. J. Lasers* **2021**, *48*, 2403002.

micromachines

MDPI

Article

An Exploration of the Influence of Abrasive Water Jet Pressure on the Friction Signal Characteristics of Fixed Abrasive Lapping Quartz Glass Based on HHT

Yanling Zheng [1], Zhao Zhang [1], Zhankui Wang [1,2,*], Minghua Pang [1], Lijie Ma [1] and Jianxiu Su [1]

[1] Henan Institute of Science and Technology, Xinxiang 453003, China
[2] Postdoctoral Station, Henan University of Science and Technology, Luoyang 471000, China
* Correspondence: luckywzk@126.com

Abstract: Abrasive water jetting is an effective dressing method for a fixed abrasive pad (FAP) and can improve FAP machining efficiency and the impact of abrasive water jet (AWJ) pressure on the dressing effect; moreover, the machining state of FAP after dressing has not been thoroughly studied. Therefore, in this study, the FAP was dressed by using AWJ under four pressures, and the dressed FAP was subjected to lapping experiments and tribological experiments. Through an analysis of the material removal rate, FAP surface topography, friction coefficient, and friction characteristic signal, the influence of AWJ pressure on the friction characteristic signal in FAP processing was studied. The outcomes show that the impact of the dressing on FAP rises and then falls as the AWJ pressure increases. The best dressing effect was observed when the AWJ pressure was 4 MPa. In addition, the maximum value of the marginal spectrum initially rises and then falls as the AWJ pressure increases. When the AWJ pressure was 4 MPa, the peak value of the marginal spectrum of the FAP that was dressed during processing was the largest.

Keywords: fixed abrasive pad; abrasive water jet; friction; Hilbert marginal spectrum; friction coefficient

Citation: Zheng, Y.; Zhang, Z.; Wang, Z.; Pang, M.; Ma, L.; Su, J. An Exploration of the Influence of Abrasive Water Jet Pressure on the Friction Signal Characteristics of Fixed Abrasive Lapping Quartz Glass Based on HHT. *Micromachines* **2023**, *14*, 891. https://doi.org/10.3390/mi14040891

Academic Editors: Jiang Guo, Chunjin Wang and Chengwei Kang

Received: 29 March 2023
Revised: 17 April 2023
Accepted: 18 April 2023
Published: 21 April 2023

1. Introduction

The fixed abrasive machining technique was first proposed in the 1990s. It can quickly lap flat workpieces and has been extensively used in the machining of parts in aerospace and optical communication industries [1,2]. In contrast to the conventional free abrasive lapping technique, the fixed abrasive lapping technique involves fixing the abrasive on pad and wiping the workpiece surface using the exposed abrasive grains on the pad [3–5]. As the lapping time continues, the surface of the fixed abrasive pad (FAP) experiences abrasive wear and glazing, making the surface of the FAP flat and smooth, which decreases its processing performance. Therefore, the dressing of the FAP surface is required to improve its machinability.

Abrasive water jet (AWJ) technology is a new processing technology. Its principle is that the abrasion strikes the workpiece surface with the high-speed water jet, thus realizing the machining of the workpiece surface [6,7]. It has strong applicability, high flexibility, low damage, and other characteristics, and has been widely used in surface processing, surface finishing, and other fields in recent years [8,9]. Qu et al. [10] used AWJ to perforate shale with different components, thus defining the damage characteristics of AWJ to shale with different components. Lv et al. [11] used ultrasonic-assisted AWJ to polish aluminum nitride as this method can achieve efficient aluminum nitride processing and high surface quality. Che et al. [12] explored the effect of AWJ process parameters on polishing quality. The experimental results showed that ideal polishing results could be obtained by adjusting the process parameters. Zhu et al. [13] used AWJ for precision surface processing of difficult-to-process materials. The results showed that AWJ has great potential in the processing of difficult-to-machine materials. Zhang et al. [14] used an ultrasonic-assisted micro AWJ

processing device to conduct experiments on K9 glass erosion. This technology can realize high efficiency and the high-quality machining of K9 glass using AWJ.

The machinability of an FAP is directly related to the surface state after finishing. Moreover, there is a certain correlation between the surface state of an FAP and the friction signal between its interfaces. Therefore, the machining capability of an FAP can be described by the friction signals between its interfaces. However, friction signals are characterized by instability and nonlinearity, which require appropriate processing and extraction of the characteristic signals. At present, researchers have conducted a lot of research on fault detection and process monitoring. For example, Wada M. et al. [15] investigated the characteristics of the acoustic emission (AE) from frictional wear, observing the correlation between the frictional wear phenomenon and the magnitude of the AE signal, and found that the magnitude of the AE signal was smaller in the wear state and larger in the adhesive wear state. Olalere et al. [16] analyzed the vibration signals in turning machining to classify the working state of the tool and found that the method was more accurate than other models in predicting tool failure by comparison. Pandya et al. [17] used wavelet packets to decompose and extract signals from healthy and faulty bearings and used energy and kurtosis to diagnose bearing faults so that bearing faults could be accurately identified. Liu et al. [18] processed and analyzed the cutting force signal based on the Hilbert–Huang transform (HHT), thus facilitating an accurate monitoring of the tool wear state. Shen et al. [19] monitored the tool state under different working states, which led to the identification of a feature able to characterize the tool worn state that is resistant to interference. Ma et al. [20] monitored the frictional state of bearings under different operating states based on wavelet packets, thus establishing a model for assessing the state of bearings, and the model can accurately identify faults. Chen et al. [21] classified the processing of an FAP based on acoustic emission technique, and the method allows for a better identification of the processing of an FAP for its accurate monitoring. Tyč et al. [22] monitored the process of AWJ cutting hard materials using vibration signals. This method allows for an effective monitoring of the AWJ machining process.

In summary, researchers have conducted a lot of research on AWJ trimming technology and process machining inspection technology, and a lot of results have been achieved. However, no one has studied the effect of AWJ pressure on the FAP dressing effect and machining process by dressing FAP with AWJ. Therefore, this paper uses AWJ with different pressures to dress an FAP surface. Through an analysis of experimental data, the impact of AWJ pressure on the dressing performance of an FAP and the feature signal of friction in a dressed FAP was studied.

2. Materials and Methods

2.1. Experimental Equipment

The AWJ dressing system was selected to dress the FAP in the experiment. The dressing system was designed and built in the laboratory. Figure 1 shows the working principle of the AWJ. In the selection of abrasives, it was considered that too small an abrasive size would cause an insignificant dressing effect that was not obvious, while too large an abrasive size would easily block the nozzle and cause excessive dressing. Therefore, W3.5 white corundum abrasive was chosen, which has the properties of high hardness and high strength. The name standard is based on the China National Standards: W indicates the particle size, and its unit is μm. Therefore, W3.5 means the abrasive with a particle size of 3.5 μm. A ZDHP-30B lapping and polishing machine (Shenyang Maike material processing equipment Co., Ltd, Shenyang, China) was used for the lapping experiments. Figure 2 shows the processing equipment and schematic diagram. An FAP of type W7 was chosen for the lapping experiments, as shown in Figure 3; the preparation process was taken from the literature [23]. Deionized water was chosen as the lapping slurry. The test workpiece was quartz glass. The test piece is quartz glass, which has high chemical stability, good light transmission and low electrical conductivity, and has a Mohs hardness of 7. Tribological experiments were conducted on an MWF-500 tribological wear tester

(Jinan Huaxing Testing Equipment Co., Ltd., Jinan, China). The equipment is shown in Figure 4. Figure 5 shows the experimental process diagram.

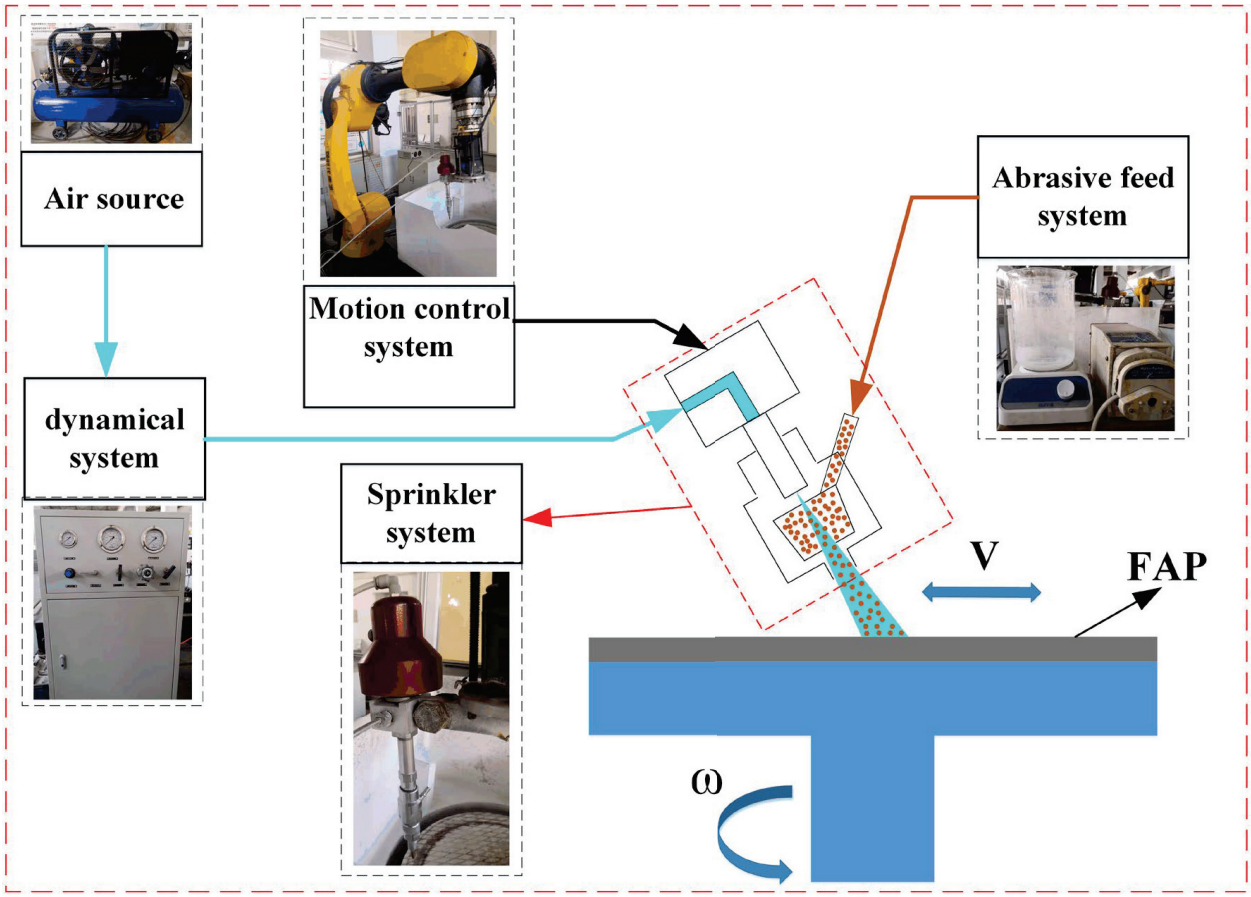

Figure 1. Working principle of AWJ.

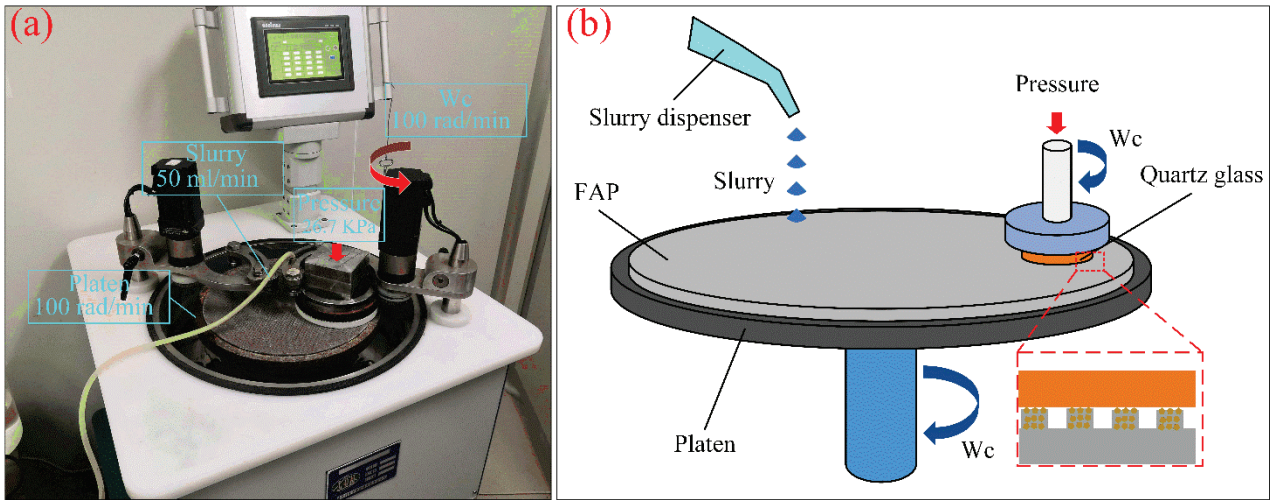

Figure 2. ZDHP-30B lapping and polishing machine and lapping schematic diagram: (**a**) test equipment; (**b**) working principle diagram.

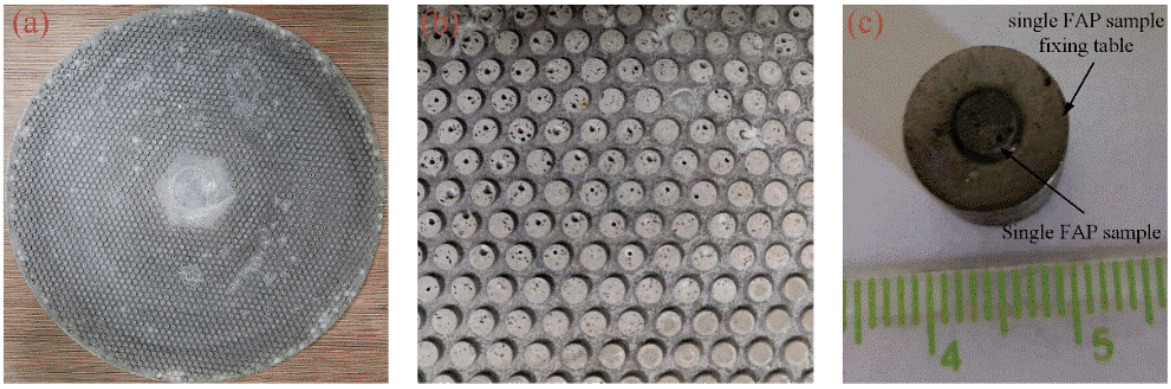

Figure 3. Polishing pad measurement sample: (**a**) FAP; (**b**) FAP local magnification; (**c**) FAP sample.

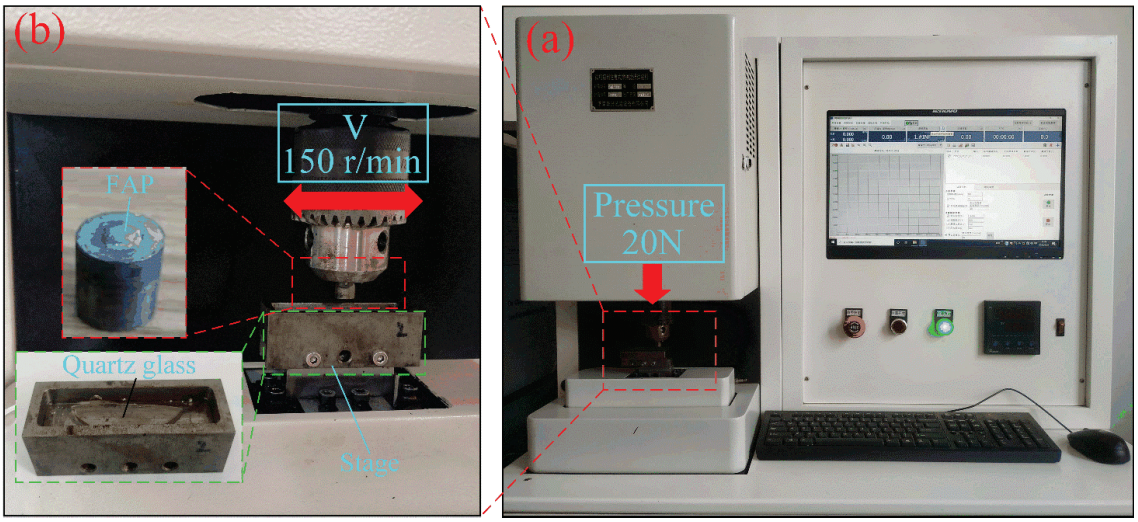

Figure 4. MWF-500 equipment and local amplification: (**a**) equipment working position; (**b**) test equipment.

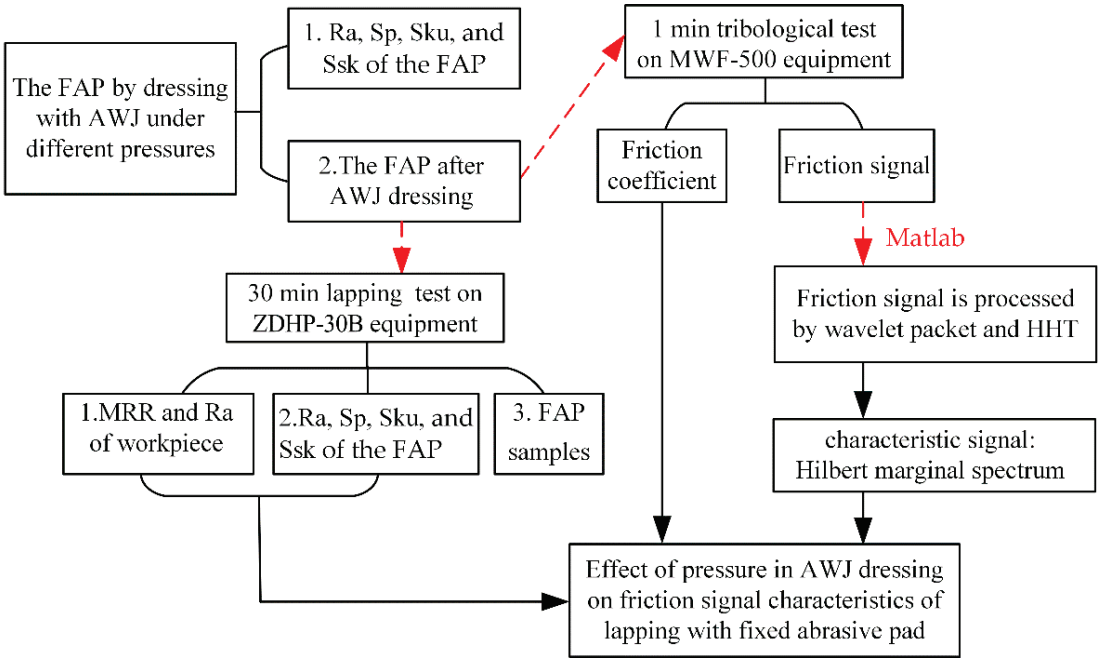

Figure 5. Experimental process diagram.

2.2. Experimental Design

This paper investigates the effect of four AWJ pressures on the frictional signal characteristics of the FAP after dressing. The experimental part consisted of a lapping experiment and a tribological test. Moreover, its tests are carried out three times using a repeatability test to reduce the error. Before the lapping experiment, the AWJ device was used to dress the FAP. Table 1 shows the dressing parameters. Quartz glass lapped the FAP after dressing with AWJ to obtain the arithmetic mean deviation of the roughness profile Ra and material removal rate (MRR) of the workpiece, as well as the surface morphology and Ra of FAP. The tribology test was used to collect the friction signal generated by the FAP sample after dressing with AWJ. The signal processing part mainly processes the friction signal through HHT and obtains the corresponding marginal spectrum peak.

Table 1. Process parameters of AWJ dressing test.

Abrasive Size	Abrasive Flow	Rotational Speed	Traverse Speed	Dress Time	AWJ Pressure
W3.5 (3.5 μm)	100 cm^3/min	110 r/min	2.5 mm/s	5 min	2 MPa, 3 MPa, 4 MPa, 5 MPa

2.3. Feature Selection and Extraction of Friction Signal

Recent studies have shown that the HHT (Hilbert–Huang transform) method, which is commonly used in nonstationary signal processing, has high adaptability and can better represent the variation of the original signal during the analysis and processing [24,25]. Therefore, the Hilbert marginal transform that extracts the friction signal while lapping the process of the FAP can accurately represent the changes of the signal, which is combined with the surface situation of the FAP. The HHT method includes two steps: EMD (Empirical Mode Decomposition) and Hilbert transform [26]. First, EMD is used to decompose the signal to obtain a limited number of the Intrinsic Mode Function (IMF). Then, the Hilbert transform is performed on each feature mode IMF to obtain the Hilbert spectrum. Figure 6 shows the feature extraction process.

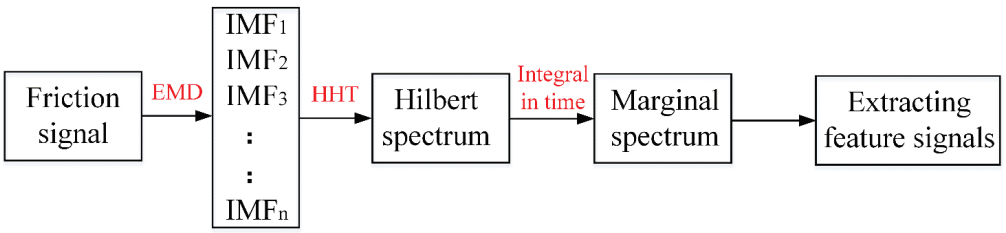

Figure 6. The feature extraction process.

2.4. Measurement and Characterization

2.4.1. Workpiece MRR

After each group of lapping tests, the workpiece samples were placed in an ultrasonic cleaner for 5 min to remove impurities from the surface of the workpiece samples. The ultrasonic cleaned and dried samples were placed in a precision balance (Satorious CP225D) and the sample mass was measured and the MRR was calculated using Equation (1):

$$\mathrm{MRR} = \frac{\Delta \mathbf{m}}{\rho \times \mathbf{s} \times \mathbf{t}} \times 10^7 \quad (1)$$

2.4.2. Workpiece Ra and 3D Morphology

The surface topography and Ra of the workpiece sample after ultrasonic cleaning are measured using a Contour GT-X3/X8 white light interferometer (Bruker, Nano, Inc.,

Berlin, Germany) which has a measurement accuracy of 0.001 nm. To reduce measurement errors, three points are selected uniformly on the surface of the sample for each test.

2.4.3. Surface State and 3D Morphology of FAP

The processed and treated FAP samples were fixed on the stage and a blower was used to remove impurities and dust from the FAP surface. Then, the surface topography was measured using a contour white light interferometer (Contour GT-X3/X8) to obtain the Ra and 3D roughness parameters of FAP: the maximum height of the summit Sp, skewness of the height distribution Ssk, kurtosis of the height distribution Sku, and root mean square deviation of the surface Sq. Based on the existing reports, the Sp represents the height of abrasive grains on the surface of FAP, the Sq can represent the state of surface texture, the Ssk represents the surface symmetry, and the Sku represents the surface height distribution [27]. Therefore, the above roughness parameters are chosen to accurately represent the change in the surface condition of the FAP.

3. Results and Discussion

3.1. Experimental Results

Figure 7 shows the MRR and Ra of the FAP after dressing using AWJ with four pressures. Figure 7 shows that the MRR of the FAP dressed using a 4 MPa pressure AWJ is greater than other AWJ-dressed pressures, while the surface quality obtained by lapping the workpiece with the FAP dressed with a 5 MPa pressure AWJ is the smallest.

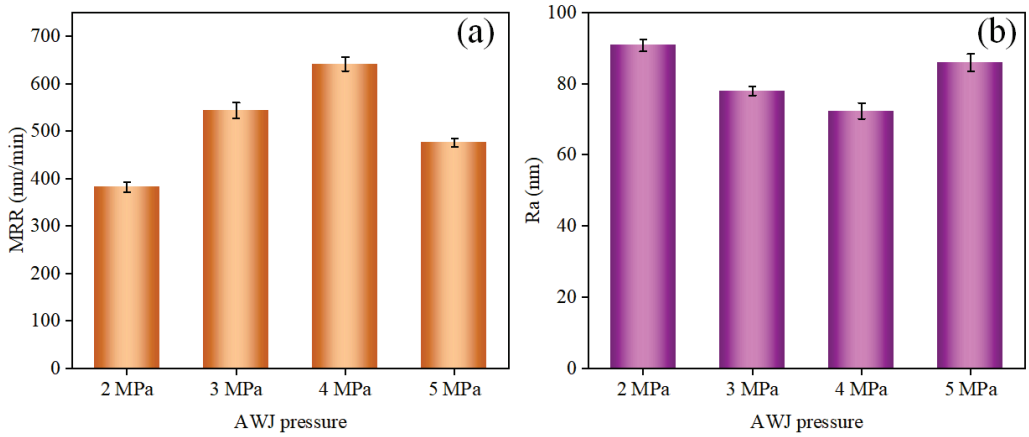

Figure 7. MRR and Ra of the FAP after dressing using AWJ with four pressures: (**a**) MRR, (**b**) Ra.

3.2. Effect of AWJ Pressure on Surface Morphology after FAP Dressing

Figure 8 shows the surface parameters of the FAP after dressing with AWJ under four pressures. Moreover, Figure 9 shows the morphology of the FAP after dressing with four AWJ pressures. It can be seen from Figure 8 that the Sp, Sq, and Ssk of the FAP after lapping are the smallest, while Sku is the largest. With an increase in AWJ pressure, Sp, Sq, and Ssk increase firstly and then decrease, whereas Sku decreases firstly and then increases. This is due to the small number and low height of the abrasive grains exposed on the FAP surface. Most of the substrate is exposed to the surface, which is relatively smooth, and the Ra is the smallest. The AWJ pressure is 2 MPa, and it does not provide enough energy for the abrasive to remove the protruding matrix and worn abrasive grains from the FAP surface while dressing. The exposed height of the abrasive grains on the surface is small, and the phenomenon of high local concentration is not well improved. Therefore, Sp, Sq, and Ssk are small, while Sku is large. With an increase in the pressure of the AWJ, the abrasive sprayed by the nozzle can obtain greater kinetic energy. The abrasive can effectively remove the surface matrix and worn abrasive grains. It also improves the local height concentration and exposes more fresh abrasive grains on the surface of the FAP. When the AWJ pressure is 4 MPa, its Sp, Sq, and Ssk are the largest, whereas Sku is the

smallest, which shows that, when the pressure is 4 MPa, the AWJ has the best dressing performance for the FAP, in which the exposed height of the surface abrasive grains is the largest and its Ra is the largest. When the AWJ pressure is 5 MPa, due to the rapid flow rate in the mixing chamber, some abrasive grains will be broken, which will affect the dressing effect of the AWJ on the abrasive pad; therefore, Sp, Sq, and Ssk decrease and Sku increases.

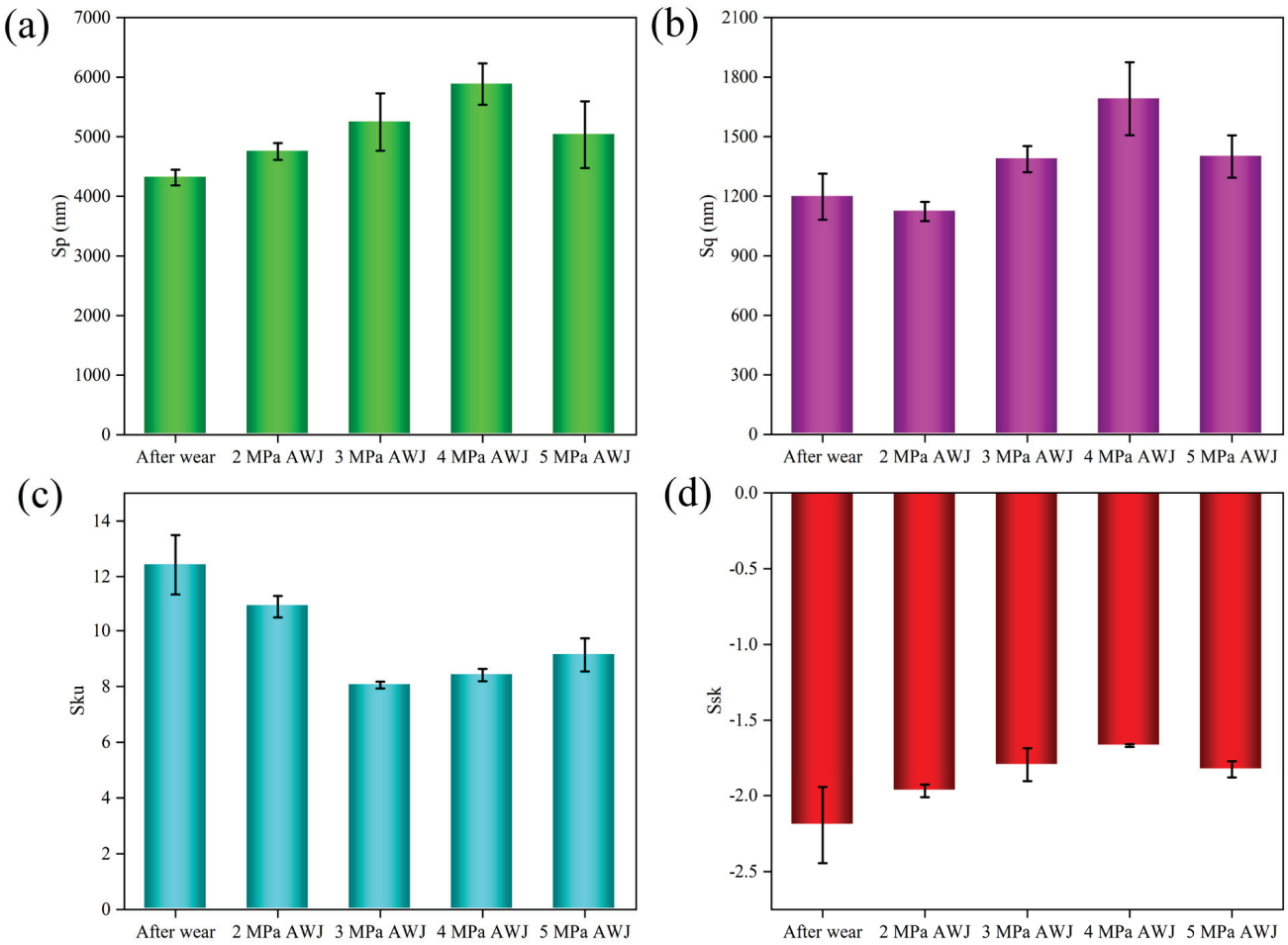

Figure 8. Surface parameters of FAP after dressing with AWJ under four pressures: (**a**) Sp; (**b**) Sq; (**c**) Sku; (**d**) Ssk.

3.3. Effect of AWJ with Four Pressures on Machining Performance of FAP and Surface Morphology of Workpiece

Figure 10 shows the workpiece morphology of FAP lapping with AWJ dressing under four pressures. Figure 11 shows the Ra of FAP and workpiece after dressing with AWJ under four pressures. Figure 11 shows that the Ra of the FAP rises and then falls with an increase in AWJ pressure, while the Ra of the workpiece firstly decreases and then increases with a rise in AWJ pressure. This is because, when the AWJ pressure is 2 MPa, the AWJ cannot effectively improve the surface state of the FAP. The local higher matrix or abrasive grains contact and scratch the workpiece. The abrasive grains cut into the surface deeply, and the scratch caused by scratching is deep. The Ra of the workpiece is the largest, and the Ra of the FAP is small. With an increase in AWJ pressure, the kinetic energy obtained by abrasive increases, which can effectively improve the surface state of the FAP. When the AWJ pressure is 4 MPa, the exposed height of the abrasive grains increases, and the greater the Ra of FAP, the better the machining performance. During the lapping process, more abrasive grains make contact with the workpiece. The abrasive grains are subjected to small and uniform forces, resulting in small scratches caused by

scraping and the good surface quality of the workpiece (Figure 9). When the AWJ pressure is 5 MPa, the dressing performance of the abrasive will be affected in the mixing room. The effect of the phenomenon of local height concentration on the surface of the FAP leads to a large and uneven force on abrasive grains in the machining process, which contributes to the scratches caused by abrasive grains scratching the workpiece becoming deeper, and the workpiece's surface quality worsens as a result. Therefore, when the AWJ pressure is 4 MPa, the FAP machining performance and workpiece surface quality are the best after dressing.

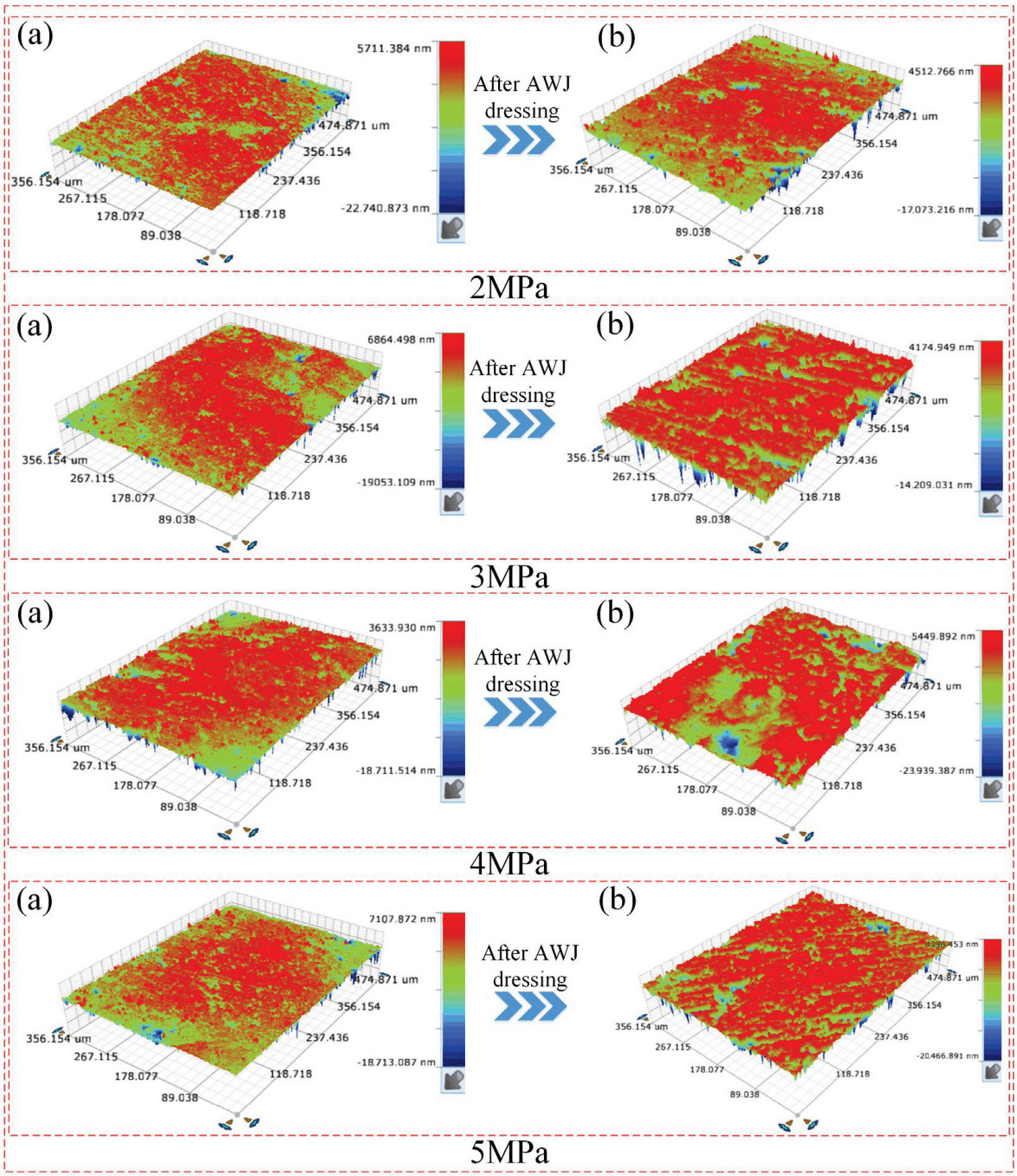

Figure 9. Morphology of FAP before and after dressing with AWJ under four pressures: (**a**) after lapping; (**b**) after AWJ dressing.

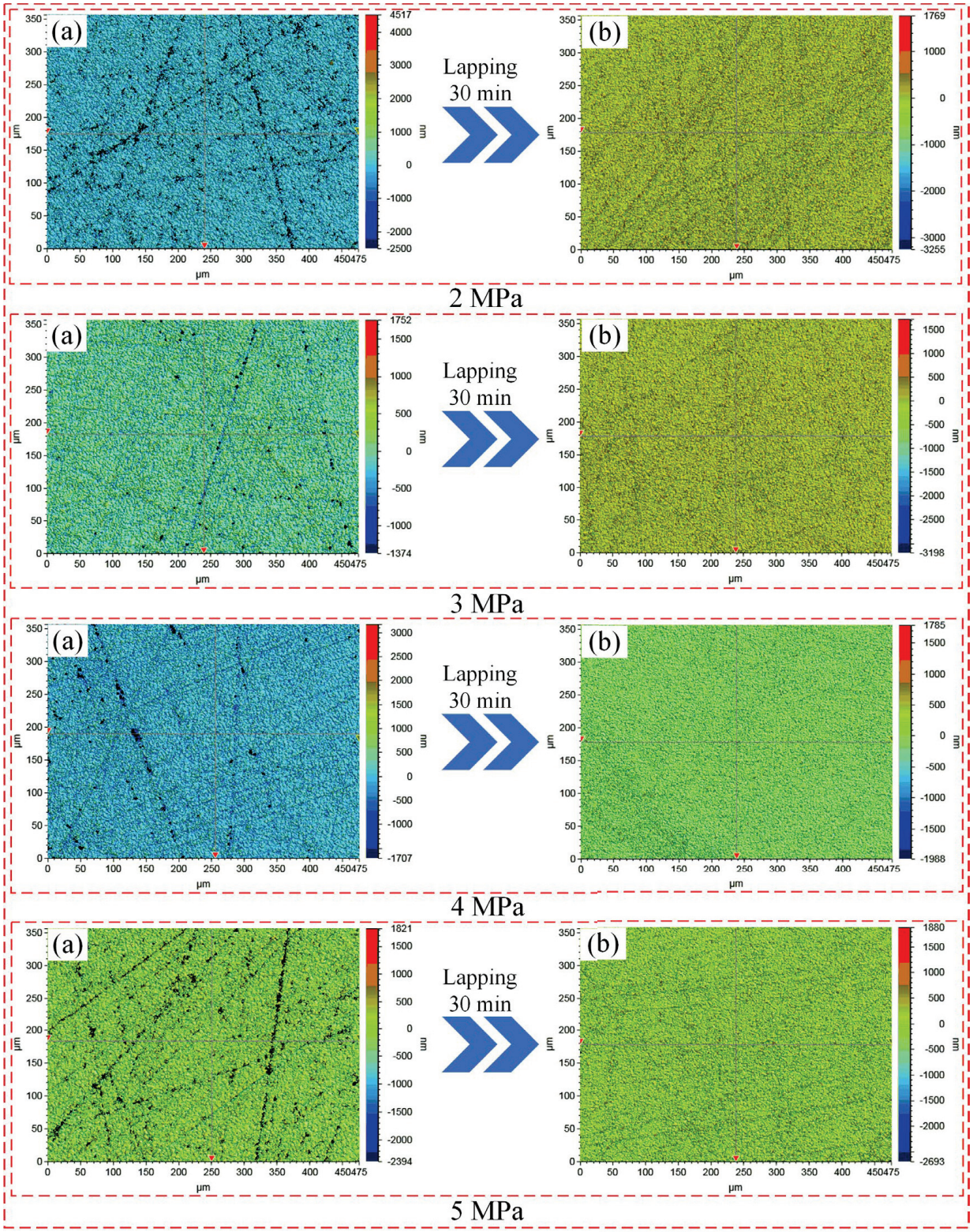

Figure 10. Workpiece morphology of FAP lapping with AWJ dressing under four pressures: (**a**) before lapping; (**b**) after lapping.

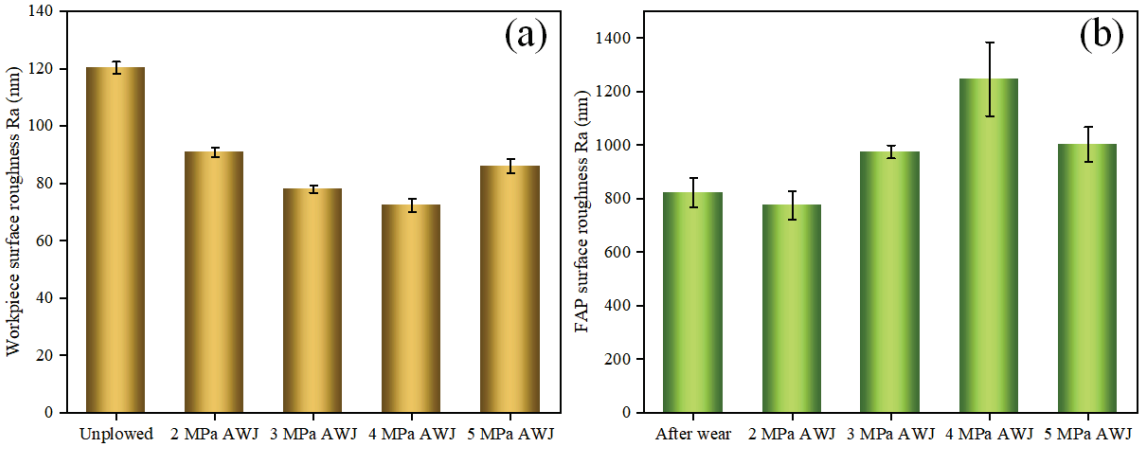

Figure 11. Ra of FAP and workpiece after dressing with AWJ under four pressures: (**a**) Ra of workpiece; (**b**) Ra of FAP.

3.4. The Influence of AWJ Pressure on Friction Coefficient of FAP

The friction coefficient has a certain relationship with the wear degree and micro cutting performance of FAP surface abrasive grains [28]. Therefore, the coefficient of the friction collected can indirectly represent the surface state and machinability of the FAP after four AWJ dressing pressures. Figure 12 shows that the coefficient of the friction of the FAP dressed using AWJ at four pressures. From Figure 12b, the coefficient of friction first rises and then falls with an increase in AWJ pressure. When the AWJ pressure is 4 MPa, the coefficient of the friction of the FAP during machining is the largest; however, when the AWJ pressure is 2 MPa, the coefficient of the friction of the FAP during machining is the smallest. This is because the AWJ with 4 MPa pressure has the best dressing effect on the FAP. The matrix and worn abrasive grains on the surface of the FAP can be effectively removed during the dressing process, which greatly enhances the machinability of the FAP. More abrasive grains on the surface of the FAP contact and scratch the workpiece to maximize the friction coefficient. The AWJ under a 2 MPa pressure has the worst dressing performance on the FAP, as this leads to an ineffective removal of the matrix and abrasive grains from the FAP surface during dressing, making its plus performance poor. The FAP surface has better matrix contact and scrapes the workpiece, thus minimizing the coefficient of friction during machining.

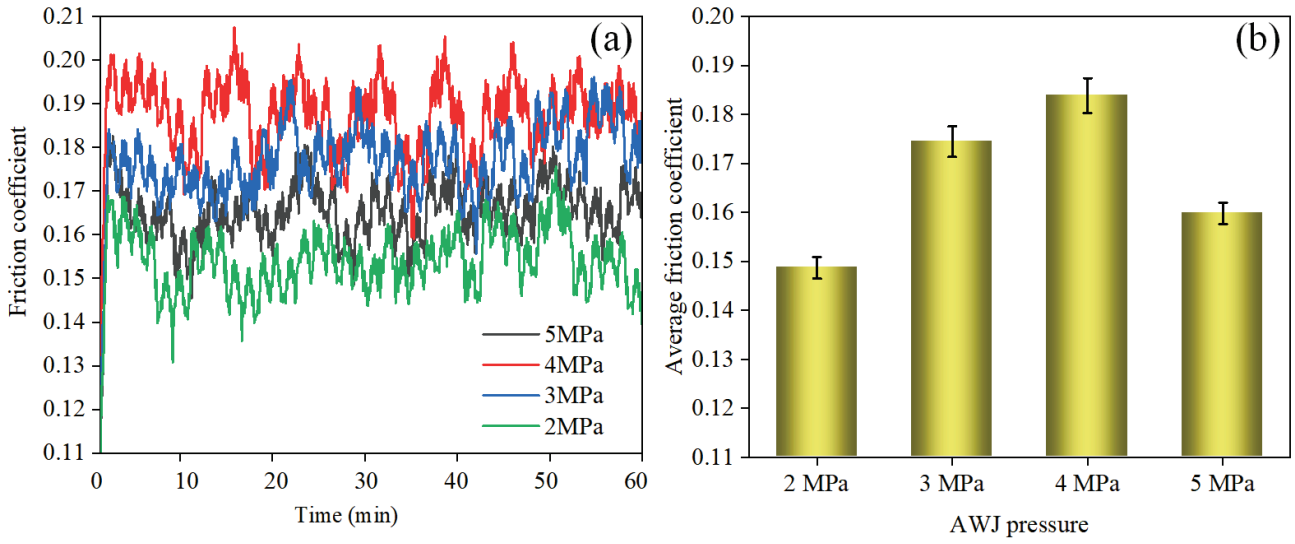

Figure 12. Friction coefficient for AWJ-dressed FAP at four pressures: (**a**) friction coefficient; (**b**) average friction coefficient.

3.5. Effect of AWJ with Different Pressure on Friction Characteristic Signal of FAP

The friction signal is processed using MATLAB software. A marginal spectrum of the FAP after dressing with four AWJ pressure was obtained. Figure 13 shows that the maximum value of the marginal spectrum is mainly around 4.7 Hz and that it is related to the cutting ability of the FAP [29]. Therefore, the processability of the FAP after dressing with AWJ under four pressures can be reflected by the maximum value of the marginal spectrum.

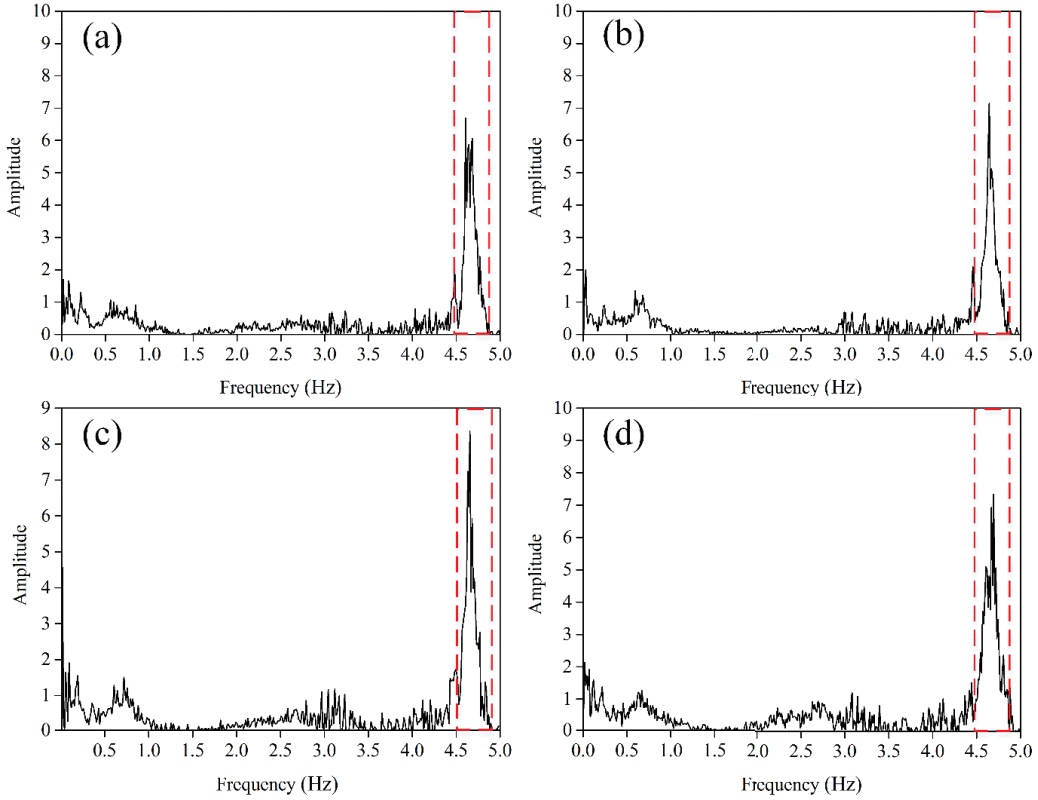

Figure 13. Marginal spectrum maximum value of FAP after dressing with AWJ under four pressures: (**a**) 2 MPa; (**b**) 3 MPa; (**c**) 4 MPa; (**d**) 5 MPa.

Figure 14 shows the relationship between the maximum value of the edge spectrum and the AWJ pressure, and its value first rises and then falls as the AWJ pressure increases. This is because the surface state of the FAP is not effectively improved at AWJ pressures of 2 MPa; moreover, because the worn particles and protruding matrix on the FAP surface are not effectively removed, the matrix mainly scrapes the workpiece to produce its frictional characteristic signal. Therefore, the edge spectrum peak is minimal. The surface state of the FAP was effectively improved when the AWJ pressure was 4 MPa. Abrasive grains and the excess matrix worn on the FAP surface can be effectively removed. The abrasive grains mainly contact and scrape the workpiece to achieve material removal. Therefore, the edge spectrum peak energy is the maximum. AWJ pressure is 5 MPa, and the dressing performance of the abrasive on the FAP is affected. The abrasive particles and excess matrix on the FAP surface cannot be effectively removed, and there is more of the matrix on the FAP surface. The more of the matrix that touches the workpiece during machining, the more the peak marginal spectral value decreases.

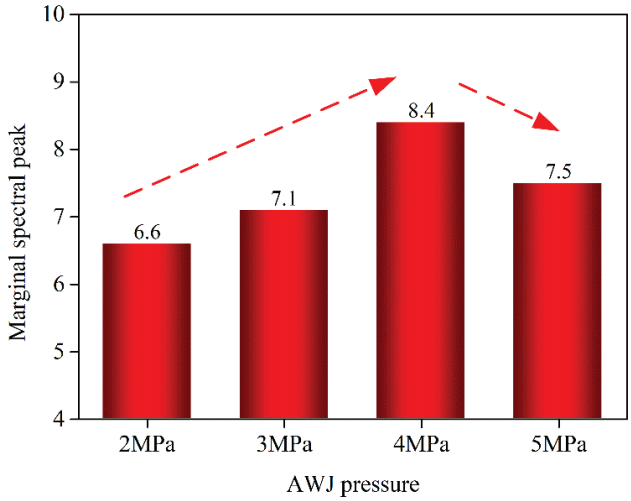

Figure 14. The relationship between the maximum value of the marginal spectrum and the AWJ pressure.

3.6. Discussion

In AWJ dressing, the pressure of the AWJ is an essential factor in the machinability of the FAP after dressing. Figure 14 shows a schematic diagram of the AWJ dressing. Figure 15a shows that, after the abrasive and water are mixed in the mixing room, the mixture is sprayed through the nozzle. The interaction between abrasive and water removes the matrix and abrasive from the FAP surface and enhances its machinability. When the pressure of AWJ is 2 MPa, the abrasive and water are not fully mixed in the mixing room, and the kinetic energy of the abrasive and water ejected from the nozzle is small. It is difficult to remove the matrix and worn abrasive grains from the FAP surface, and the dressing performance is poor. As the pressure of AWJ increases, the abrasive and water can be fully mixed. When the AWJ pressure is 4 MPa, the kinetic energy of the abrasive and water ejected from the nozzle is large. As shown in Figure 15b, it can effectively remove the matrix and abrasive grains of wear from the FAP surface, improve the local high concentration of the surface, and possess a good dressing effect. As shown in Figure 15c, when the pressure of AWJ is 5 MPa, it will accelerate the flow of abrasive in the mixing room, so that more abrasive will be broken in the mixing room and thus more broken abrasive will be ejected from the nozzle, which will eventually lead to a decrease in the removal of the matrix and abrasive grains on the surface of the FAP.

Regarding the FAP surface, by dressing with AWJ, the excess matrix and worn abrasive grains on the FAP surface are removed, and more fresh abrasive grains are exposed. When the AWJ pressure is 2 MPa, the AWJ is not effective in dressing the FAP surface, the abrasive grains on the FAP surface cannot be effectively removed, and its machining capability cannot be effectively enhanced. There is still a significant amount of worn abrasive grains in contact with the workpiece and scraping it. At this time, the marginal spectral peak value generated by abrasive grains scratching the workpiece is the smallest (Figure 16b). When the AWJ pressure is 4 MPa, the worn abrasive grains and the redundant matrix on the FAP surface can be effectively removed, and the FAP surface after AWJ dressing has more fresh and sharp abrasive grains. Fresh abrasive grains can be easily cut to the workpiece. The large removal thickness of the workpiece makes its MRR large (Figure 8a). When fresh abrasive scratch and cut the workpiece, a significant amount of debris is generated. Under the influence of the flow of the lapping slurry, the debris will form eddy currents between the FAP and the workpiece, and the abrasive grains will scratch the workpiece and matrix off the FAP under the drive of the eddy currents [30]. The shedding of worn particles and the appearance of fresh abrasive grains are promoted to achieve the self-repair of the FAP [31]. Therefore, the maximum value of the marginal spectrum is the largest (Figure 16c). When the AWJ pressure is 5 MPa, the dressing performance of the AWJ

decreases, the removal rate of worn abrasive grains and the exposure rate of fresh abrasive grains during lapping slows down, and the amount of fresh abrasive grains scraping the workpiece decreases. As a result, the maximum value of the marginal spectrum is reduced.

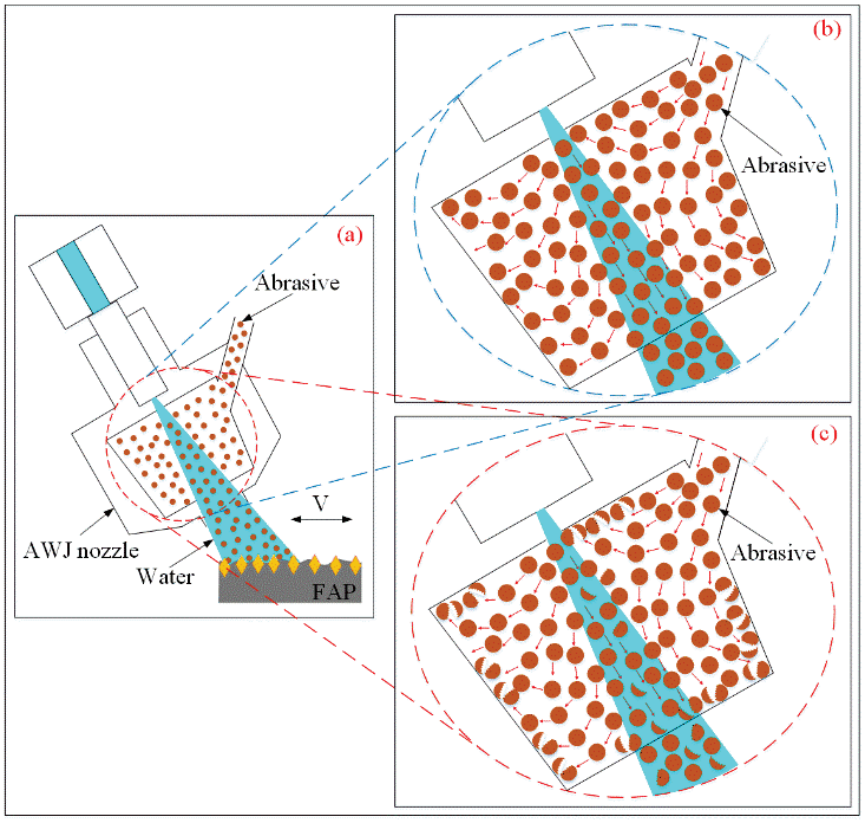

Figure 15. Schematic diagram of AWJ dressing the FAP: (**a**) schematic diagram of AWJ dressing; (**b**) 4 MPa AWJ dressing diagram; (**c**) 5 MPa AWJ dressing diagram.

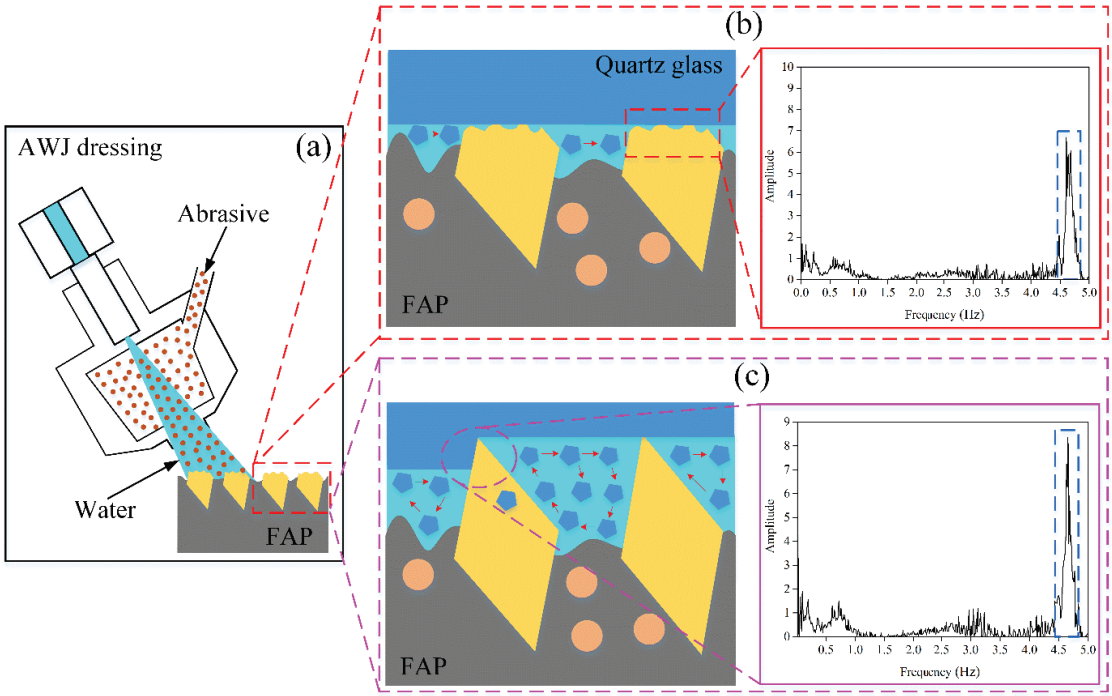

Figure 16. Lapping mechanism of FAP: (**a**) schematic diagram of AWJ dressing; (**b**) 2 MPa; (**c**) 4 MPa.

4. Conclusions

In the present work, dressing tests of the FAP were conducted using a self-designed AWJ system, and separate lapping tests and tribological tests of the dressed FAP were conducted. The influence of jet pressure on the FAP morphology, workpiece morphology, MRR, and frictional characteristic signals was discussed, and the mechanism of the influence was analyzed. The results are as follows:

An AWJ-dressed FAP can effectively improve its machining performance, and the AWJ pressure greatly impacts the dressing effect. The Ra of the FAP firstly rises and then falls with the AWJ pressure. When the AWJ pressure is 4 MPa, the dressing effect of the AWJ is the best, the machining performance of the FAP is the best, and the maximum MRR can reach 632.76 nm/min.

The AWJ pressure has an impact on the friction coefficient of the dressed FAP. The friction coefficient increases firstly and then decreases with an increase in AWJ pressure. When the FAP was dressed with 4 MPa AWJ, the micro-cutting capability of the FAP surface abrasive grains was the strongest and the friction coefficient was the largest, up to 0.184.

The maximum value of the marginal spectrum can be used to detect the micro cutting capability of FAP surface abrasive grains, and the AWJ pressure has a certain influence on the maximum value of the marginal spectrum generated during the processing of the dressed FAP. The value first rises and then falls as the AWJ pressure increases. When the AWJ pressure is 4 MPa, the value is at its largest.

Author Contributions: Conceptualization, Y.Z. and Z.W.; methodology, Z.Z.; software, Z.Z.; validation, Z.Z., Y.Z. and M.P.; formal analysis, Z.Z.; investigation, L.M.; resources, J.S.; data curation, Z.Z.; writing—original draft preparation, Y.Z.; writing—review and editing, Z.Z.; visualization, Y.Z.; supervision, Y.Z.; project administration, J.S.; funding acquisition, Z.W. All authors have read and agreed to the published version of the manuscript.

Funding: This research was funded by [The National Natural Science Foundation of China, Project funded by China Postdoctoral Science Foundation, Science and Technology Plan Projects of Henan province] grant number [U1804142, 2020M672220, 212102210062], and the APC was funded by [The National Natural Science Foundation of China, Project funded by China Postdoctoral Science Foundation, Science and Technology Plan Projects of Henan province].

Conflicts of Interest: The authors declare that they have no known competing financial interest or personal relationships that could have appeared to influence the work reported in this paper.

References

1. Subramanin, R.S.; Appat, R.M. A Model of Chemical Mechanical Planarization of Patterned Wafers with Fixed Abrasives. *Electrochem. Solid-State Lett.* **2001**, *4*, 12. [CrossRef]
2. Fletcher, T.D.; Gobena, F.T.; Romero, V.D. Diamond fixed abrasive lapping of brittle substrates. *Ind. Diam. Rev.* **2004**, *65*, 5. [CrossRef]
3. Cho, B.J.; Kim, H.M.; Manivannan, R.; Moon, D.J.; Park, J.G. On the mechanism of material removal by fixed abrasive lapping of various glass substrates. *Wear* **2013**, *302*, 1334–1339. [CrossRef]
4. Demirci, I.; Mezghani, S.; Mkaddem, A.; Mansori, M.E. Effects of abrasive tools on surface finishing under brittle-ductile grinding regimes when manufacturing glass. *J. Mater. Process. Technol.* **2010**, *210*, 466–473. [CrossRef]
5. Gacliardi, J.J.; Kim, D.; Sokol, J.J.; Zazzera, L.A.; RomeroO, V.D.; Atkinson, M.R.; Nabulsi, F.; Zhang, H. A case for 2-body material removal in prime led sapphire substrate lapping and polishing. *J. Manuf. Process.* **2013**, *15*, 348–354. [CrossRef]
6. Melentiev, R.; Fang, F.Z. Recent advances and challenges of abrasive jet machining. *CIRP J. Manuf. Sci. Technol.* **2018**, *22*, 1–20. [CrossRef]
7. Hu, Y.; Chen, J.D.; Dai, Q.W.; Huang, W.; Wang, X.L. Recent Advances and Status of Abrasive Jet Machining Technology. *Surf. Technol.* **2022**, *51*, 1–23. [CrossRef]
8. Liu, X.C.; Liang, Z.W.; Wen, G.L.; Yuan, X.F. Waterjet machining and research developments: A review. *Int. J. Adv. Manuf. Technol.* **2019**, *102*, 1257–1335. [CrossRef]
9. Yao, P.; Wang, W.; Huang, C.Z.; Wang, J.; Zhu, H.T.; Zhang, Z.Y. High Efficiency Abrasive Waterjet Dressing of Diamond Grinding Wheel. *Adv. Mater. Res.* **2014**, *1017*, 243–248. [CrossRef]
10. Qu, H.; Tang, S.M.; Sheng, M.; Liu, Z.H.; Wang, R.; Hu, Y.H. Experimental investigation of the damage characteristics and breaking process of shale by abrasive waterjet impact. *J. Pet. Sci. Eng.* **2022**, *211*, 110165. [CrossRef]

11. Lv, Z.; Huang, C.Z.; Zhu, H.T.; Yao, P. A research on ultrasonic-assisted abrasive waterjet polishing of hard-brittle materials. *Int. J. Adv. Manuf. Technol.* **2015**, *78*, 1361–1369. [CrossRef]
12. Che, C.L.; Huang, C.Z.; Wang, J.; Zhu, H.T. Study of Abrasive Water Jet Polishing Technology. *Key Eng. Mater.* **2011**, *487*, 327–331. [CrossRef]
13. Zhu, H.T.; Huang, C.Z.; Wang, J.; Li, Q.L.; Che, C.L. Experimental study on abrasive waterjet polishing for hard–brittle materials. *Int. J. Mach. Tools Manuf.* **2009**, *49*, 569–578. [CrossRef]
14. Zhang, X.; Qin, S.K.; Qi, H.; Viboon, T. Experimental Study on Erosion Processing of K9 Glass Using Ultrasonic-assisted Micro-abrasive Water Jet. *Surf. Technol.* **2021**, *50*, 346–353. [CrossRef]
15. Wada, M.; Mizuno, M. Study on friction and wear utilizing acoustic emission. relation between friction and wear mode and acoustic emission signals. *J. Jpn. Soc. Precis. Eng.* **1989**, *55*, 673–678. [CrossRef]
16. Olalere, I.O.; Olanrewaju, O.A. Tool and Workpiece State Classification Using Empirical Mode Decomposition (EMD) with Hilbert–Huang Transform (HHT) of Vibration Signals and Machine Learning Models. *Appl. Sci.* **2023**, *13*, 2248. [CrossRef]
17. Pandya, D.H.; Upadhyay, S.H.; Harsha, S.P. Fault diagnosis of rolling element bearing by using multinomial logistic regression and wavelet packet transform. *Soft Comput.* **2014**, *18*, 255–266. [CrossRef]
18. Liu, Q.Z.; Guo, Q.; Lin, Z.C.; Shen, B. A new method of real-time monitoring of cutting tool status bases on HHT. *Int. J. Abras. Technol.* **2020**, *9*, 276–285. [CrossRef]
19. Shen, B.; Gui, Y.; Chen, B.; Lin, Z.C.; Liu, Q.; Liu, Q.Z. Application of spindle power signals in tool state monitoring based on HHT algorithm. *Int. J. Adv. Manuf. Technol.* **2020**, *106*, 1385–1395. [CrossRef]
20. Li, G.B.; Ren, Z.Y.; Wang, H.Z.; Wei, H.Z. Characteristics Extraction of Friction Vibration Signal Using Harmonic Wavelet Packet Transforms. *Tribology* **2011**, *31*, 452–456.
21. Chen, J.P.; Li, J.; Peng, Y.N.; Wang, Z.K.; Sun, T.; Zhu, Y.W. In-situ manifestation of lapping mechanisms by rapid intelligent pattern recognition analysis (RIPRA) of acoustic emission via a point density fuzzy C-means (PD-FCM) method. *J. Manuf. Process.* **2022**, *79*, 924–933. [CrossRef]
22. Tyč, M.; Hlaváčová, I.M.; Barták, P. Analyses of Vibration Signals Generated in W. Nr. 1.0038 Steel during Abrasive Water Jet Cutting Aimed to Process Control. *Materials* **2022**, *15*, 345. [CrossRef]
23. Wang, Z.K.; Niu, F.L.; Zhu, Y.W.; Wang, J.B. Comparison of lapping performance between fixed agglomerated diamond pad and fixed single crystal diamond pad. *Wear* **2019**, *432–433*, 202963. [CrossRef]
24. Zhou, Y.H.; Xie, S.Y.; Xie, Q.; Zhou, H.M. Holes drilling quality consistency analysis based on the fusion of marginal spectrum characteristics. *J. Vib. Shock* **2015**, *34*, 40–45. [CrossRef]
25. Li, H.; Zhang, Y.P.; Zheng, H.Q. Hilbert-Huang transform and marginal spectrum for detection and diagnosis of localized defects in roller bearings. *J. Mech. Sci. Technol.* **2009**, *23*, 291–301. [CrossRef]
26. Zhao, X.Y.; He, Y.; Liu, Z.H.; Tong, L. Method for extracting Raman spectra characteristic variables of biological sample based on Hilbert–Huang transform. *J. Raman Spectrosc.* **2020**, *51*, 1019–1028. [CrossRef]
27. Zhang, Z.; Yao, P.; Zhang, Z.; Xue, D.; Wang, C.; Huang, C.; Zhu, H. A novel technique for dressing metal-bonded diamond grinding wheel with abrasive waterjet and touch truing. *Int. J. Adv. Manuf. Technol.* **2017**, *93*, 3063–3073. [CrossRef]
28. Wang, Z.; Niu, F.; Wang, Z.; Li, J.; Zhu, Y. Friction and wear characteristics of agglomerated diamond abrasives and lapping performance of fixed agglomerated diamond pads. *Wear* **2021**, *470–471*, 203598. [CrossRef]
29. Wang, Z.K.; Zhang, Z.; Wang, S.W.; Pang, M.H.; Ma, L.J.; Su, J.X. Study on Wavelet Packet Energy Characteristics on Friction Signal of Lapping with the Fixed Abrasive Pad. *Micromachines* **2022**, *13*, 981. [CrossRef]
30. Zhou, P.; Guo DMKang, R.K.; Jin, Z.J. Numerical Simulation of Micro Two-phase flow in Multilevel Rough Gap. *J. Mech. Eng.* **2011**, *47*, 83–88. [CrossRef]
31. Wang, Z.K.; Pang, M.H.; Liang, M.C.; Wang, J.B.; Ma, L.J.; Liu, H.X.; Su, J.X. Effect of material structure on spinel machinability in its fixed abrasive lapping. *J. Manuf. Process.* **2021**, *68*, 141–153. [CrossRef]

micromachines

MDPI

Article

Simulation and Experimental Study of Laser Processing NdFeB Microarray Structure

Yong Zhao [1], Shuo Wang [1], Wenhui Yu [2], Pengyu Long [1], Jinlong Zhang [1], Wentao Tian [2], Fei Gao [1], Zhuji Jin [1], Hongyu Zheng [2], Chunjin Wang [3] and Jiang Guo [1,*]

[1] State Key Laboratory of High-Performance Precision Manufacturing, Dalian University of Technology, Dalian 116024, China
[2] Centre for Advanced Laser Manufacturing (CALM), School of Mechanical Engineering, Shandong University of Technology, Zibo 255000, China
[3] State Key Laboratory of Ultra-Precision Machining Technology, Department of Industrial and Systems Engineering, The Hong Kong Polytechnic University, Hong Kong, China
* Correspondence: guojiang@dlut.edu.cn

Abstract: NdFeB materials are widely used in the manufacturing of micro-linear motor sliders due to their excellent permanent magnetic properties. However, there are many challenges in processing the slider with micro-structures on the surface, such as complicated steps and low efficiency. Laser processing is expected to solve these problems, but few studies have been reported. Therefore, simulation and experiment studies in this area are of great significance. In this study, a two-dimensional simulation model of laser-processed NdFeB material was established. Based on the overall effects of surface tension, recoil pressure, and gravity, the temperature field distribution and morphological characteristics with laser processing were analyzed. The flow evolution in the melt pool was discussed, and the mechanism of microstructure formation was revealed. In addition, the effect of laser scanning speed and average power on machining morphology was investigated. The results show that at an average power of 8 W and a scanning speed of 100 mm/s, the simulated ablation depth is 43 μm, which is consistent with the experimental results. During the machining process, the molten material accumulated on the inner wall and the outlet of the crater after sputtering and refluxing, forming a V-shaped pit. The ablation depth decreases with the increment of the scanning speed, while the depth and length of the melt pool, along with the height of the recast layer, increase with the average power.

Keywords: NdFeB; laser processing; simulation; microstructure formation mechanism; melt pool flow evolution

Citation: Zhao, Y.; Wang, S.; Yu, W.; Long, P.; Zhang, J.; Tian, W.; Gao, F.; Jin, Z.; Zheng, H.; Wang, C.; et al. Simulation and Experimental Study of Laser Processing NdFeB Microarray Structure. *Micromachines* **2023**, *14*, 808. https://doi.org/10.3390/mi14040808

Academic Editors: Jie Yin and Nam-Trung Nguyen

Received: 1 March 2023
Revised: 19 March 2023
Accepted: 30 March 2023
Published: 31 March 2023

1. Introduction

Micro-linear motors are widely used in microrobots, smartphones, and medical applications. The relative motion between the slider with the microarray structure and the stator with the embedded micro-coil is generated by the Lorentz force, which drives the micro-linear motor to produce linear micro-movements. NdFeB materials are used in the manufacturing of sliders for micro-linear motors because of their excellent permanent magnetic properties. Currently, micro-cutting and micro-milling technologies are used to manufacture micro-array structures on the surface of NdFeB, which are then used to produce the sliders required for micro-linear motors. In addition, micro-electro-mechanical systems (MEMS) technology is also used in the manufacture of sliders. Zhi et al. [1] bonded NdFeB sheets to a silicon substrate and cut it into a long strip pattern at 100 μm intervals by using a cutting saw. Furthermore, Wang et al. [2] fabricated a chessboard microarray structure with a pitch of 1.2 mm and a length and width of 810 μm on the surface of a NdFeB sheet by lithography and wet etching. These reported processing methods can process regular arrays with hundreds of microns scale and misaligned arrays with the

millimeter scale. With the miniaturization of micro-linear motors, it is desired to develop the efficient processing technologies that can manufacture smaller-scale arrays on NdFeB sheets. The micro-cutting and micro-milling technologies can process regular arrays of 100 μm, but it is difficult to fabricate misaligned arrays of the same scale. Moreover, the processing efficiency is low. Although MEMS can fabricate misaligned array structures, it is cumbersome and inefficient, so it is not suitable for processing deeper structures.

Laser processing technology [3,4] is widely used in preparing the functional surface and treating artificial bone due to its controllability and high efficiency. Li et al. [5] used picosecond pulsed lasers to generate precise mesh structures on pure titanium surfaces to improve their surface wettability and biocompatibility. Melo-Fonseca et al. [6] fabricated pyramidal-shaped microscale columns on metallic biomaterials, thereby improving the interaction between bone and implant. Zhao et al. [7] investigated the feasibility of preparing a bionic superhydrophobic stainless steel surface by laser precision engineering to achieve dynamic control of targeted superhydrophobicity and water transport. The above applications demonstrate the potential of laser processing technology to process microscale array structures on NdFeB surfaces. Currently, there are few studies on the laser processing of NdFeB materials. Numerical simulations can greatly reduce the number of experiments and facilitate the investigation of the material removal mechanism during laser processing. In terms of simulation, Lim et al. [8] investigated the effect of processing parameters on the ablation depth and morphology during nanosecond pulsed laser processing of copper and aluminum by finite element simulations. Berenyi et al. [9] investigated the heat effect induced during the laser processing of copper materials by building a three-dimensional finite element model. Zhang et al. [10] carried out finite element modeling of the nanosecond pulsed laser processing of stainless steel, and the moving boundary conditions were considered. Considering the solid–liquid phase transition and the removal of the materials due to liquid evaporation is significant in simulating the material removal process. The surface tension caused by the flow field and the Marangoni effect caused by the tension gradient also have a large impact on the simulation of the laser processing process. Ding et al. [11] considered the Marangoni effect as the main driving force for fluid flow from the top center region of the melt pool to the outside of the rim in selective laser melting (SLM) modeling. Similarly, Yuan et al. [12] suggested that in SLM, the Marangoni effect plays a key role in enhancing convective heat transfer and changing the melt pool geometry. In addition to the Marangoni effect, the center of the molten pool is mainly subject to recoil pressure, which drives surface profile changes. Cho et al. [13] investigated the molten pool dynamics of laser welding and concluded that molten metal flow is mainly driven by surface tension and that the buoyancy drive in the bulk forces cannot be neglected. The energy of the nanosecond pulsed laser is high; the recoil pressure is the main driving force for the formation of the crater profile. Yuan et al. [14] carried out simulations and experiments on the melt pool state during SLM and found that the effect of recoil pressure was more significant when the scanning speed became lower. Material loss due to evaporation during laser processing should not be ignored either. Zhang et al. [15] considered the recoil pressure and mass loss due to material evaporation in the model and investigated the effect of laser energy and pulse width on the morphology and quality of the processed micro-hole. Therefore, it is necessary to consider the effect of fluid flow and recoil pressure when simulating the effect of laser processing parameters on the processed morphology. There are two main methods for describing the melt pool surface: the surface tracing method, represented by the level set method, and the free deformation method, represented by the deformation geometry method. Zhu et al. [16] developed both deformation geometry and level set models and demonstrated through comparison that both methods were suitable for laser processing melt pool simulation, while the deformation geometry method was more accurate and efficient. The level set method has a unique advantage in modeling the two-phase flow direction, while the deformation geometry method is preferred as the gas–liquid phase change is not considered.

In this study, the COMSOL finite element analysis software was used to couple the physical fields of heat transfer and fluid flow, and a 2D simulation model of laser processing of NdFeB materials was established. The model considers heat conduction, heat convection, and evaporation heat loss, as well as the effects of surface tension, recoil pressure, and gravity on the fluid. The ablation rate was added for evaporation removal by introducing the Hertz–Knudsen equation via the deformation geometry method. The temperature field distribution, morphological characteristics, and the flow field velocity of the melt pool were analyzed. In addition, the effects of laser scanning speed and average power on processing quality were simulated. The accuracy of the model was verified by conducting experiments with a nanosecond laser using the same parameters as in the simulation for microarray processing. Based on this research, the heavy laser processing experiment will be replaced by simulations, and then the processing parameters can be inverted according to the simulation results. This can greatly reduce the number of experiments and help to obtain the preferred processing parameters.

2. Numerical Simulation Modeling

The COMSOL Multiphysics simulation software has complete finite element simulation capabilities and has significant advantages in multiphysics field coupling. It was chosen to simulate the process of laser processing of NdFeB and the material removal mechanism. The physical fields of heat transfer, fluid flow, and deformation geometry were coupled in this study. The physical parameters of the required NdFeB material are shown in Table 1, and the following assumptions were made to simplify the model.

1. The laser has a Gaussian profile. The ablation process is stable, and the reflection of the laser beam on the surface of the crater is neglected.
2. Solid metals are considered very viscous fluids, and molten metals are incompressible non-Newtonian fluids under laminar flow.
3. Effects such as the shielding effect of the plasma are ignored.

Table 1. Physical parameters of NdFeB material.

Property	Symbol	Value	Unit
Melting temperature	T_m	1811.2	K
Vaporizing temperature	T_v	3135.2	K
Ambient temperature	T_a	293.15	K
Solid phase density	ρ_s	7500	kg/m^3
Liquid phase density	ρ_l	6500	kg/m^3
Specific heat of solid phase	C_{ps}	440	J/(kg·K)
Specific heat of liquid phase	C_{pl}	551	J/(kg·K)
Solid phase thermal conductivity	k_s	9	W/(m·K)
Liquid phase thermal conductivity	k_l	7	W/(m·K)
Latent heat of fusion	L_m	2.466×10^5	J/kg
Latent heat of vaporization	L_v	6.071×10^6	J/kg
Coefficient of heat transfer	h_1	15	$W/(m^2 \cdot K)$
Temperature transition interval of melting	ΔT	50	K
Dynamic viscosity of liquid phase	μ_l	8×10^{-3}	Pa·s
The surface tension of the pure metal	γ	1.84	N/m
Surface tension temperature coefficient	A_γ	-5×10^4	N/(m·K)
Mushy zone constant	A_m	10^6	$kg/m^3 \cdot s$

2.1. Heat Transfer Modeling

According to the assumptions, the laser source is a Gaussian surface heat source. The pulse function $p(t)$ was set, which in turn set the pulse width, frequency, and period of the

laser. With respect to the direction x, the laser energy density function $Q(x,t)$ at time t can be expressed as Equation (1):

$$Q(x,t) = (\frac{2P}{\pi r^2})exp(-\frac{2(x-v_0t)^2}{r^2}) \tag{1}$$

where P is the power of the laser, r is the laser spot diameter, and v_0 is the spot travel speed.

At this point, the heat flux q_0 at the input boundary can be expressed as Equation (2):

$$q_0 = a \cdot Q(x,t) \cdot p(t) \tag{2}$$

where a is the absorption rate of the material at the laser wavelength. To find the exact absorption rate parameter, the law of variation with temperature was considered, as shown in Equation (3) [17]:

$$a(T) = \sqrt{\frac{4\pi c\varepsilon_0[1+\alpha(T-T_a)]}{\lambda\sigma_0}} \tag{3}$$

where ε_0 is the permittivity of vacuum, α is the resistance coefficient of the target as a function of temperature, λ is the wavelength of the laser beam, c is the velocity of light, and σ_0 is the target conductance at the initial temperature T_a.

When the laser acted on the surface of the material, the material absorbed energy and heated up rapidly, and a phase transition occurred, which follows the equation of energy conservation, as shown in Equation (4):

$$\rho C_p(\frac{\partial T}{\partial t}+\mathbf{u}\cdot\nabla T) - \nabla\cdot(k\nabla T) = q_0 \tag{4}$$

where ρ is the liquid phase density, C_p is the specific heat, $\mathbf{u}$ is the fluid flow rate, and k is the thermal conductivity.

The materials undergo phase transitions, including melting, evaporation, and sublimation, during laser processing. This process will absorb or release a lot of latent heat so that the temperature at the phase transition point is constant, and the latent heat of phase transition needs to be considered. The equivalent heat capacity method allows the treatment of the latent heat energy as an equivalent heat capacity, where the heat capacity changes considerably in the interval near the phase transition point, and the area enclosed by the heat capacity vs. temperature graph is the latent heat of phase transition [18]. As shown in Equation (5),

$$C_p = C_{p0} + \delta_m L_m + \frac{L_m}{T_m}H'\left((T-T_m),\Delta T\right) + \delta_v L_v + \frac{L_v}{T_v}H'\left((T-T_v),\Delta T\right) \tag{5}$$

where δ_m and δ_v are temperature smoothing functions for the phase transition interval, with expressions as shown in Equations (6) and (7), respectively:

$$\delta_m = \frac{\exp[-\frac{(T-T_m)^2}{\Delta T^2}]}{\Delta T\sqrt{\pi}} \tag{6}$$

$$\delta_v = \frac{\exp[-\frac{(T-T_v)^2}{\Delta T^2}]}{\Delta T\sqrt{\pi}} \tag{7}$$

L_m and L_v denote the latent heat of melting and the latent heat of vaporization, respectively, T_m and T_v denote the melting temperature and vaporization temperature, H' is the Heasivide function, and ΔT is the phase transition half interval temperature.

2.2. Heat Transfer Boundary Condition

The nanosecond pulsed laser processing also involves convective heat transfer, radiative heat transfer, and evaporative heat loss. The above heat losses were considered at the processing surface boundary, as shown in Equation (8):

$$-k\nabla T = h_1(T - T_a) + \varepsilon\sigma(T^4 - T_a^4) + q_v \tag{8}$$

where h_1 is the heat transfer coefficient, ε is the emissivity, σ is the Stefan–Boltzmann constant, and q_v is the evaporative heat loss; the specific expression is shown in Equation (9) [19].

$$q_v = \dot{m}L_v \tag{9}$$

$$\dot{m} = (1 - \beta)\sqrt{\frac{M_{mol}}{2\pi R_0 T}}P_0 \exp(\frac{L_v M_{mol}}{R_0}(\frac{1}{T_v} - \frac{1}{T})) \tag{10}$$

$$P_a(T) = P_0 \cdot \exp(\frac{M_{mol}L_v}{R_0}(\frac{1}{T_v} - \frac{1}{T})) \tag{11}$$

where $\dot{m}$ is the evaporation rate, M_{mol} is the molar mass of the metal, $P_a(T)$ represents the saturation vapor pressure, β is the diffusion coefficient, R_0 is the universal gas constant, and P_0 is the atmospheric pressure.

2.3. Solid–Liquid Interface Treatment

The liquid phase fraction θ was required to treat each parameter as a temperature-dependent segmental function bounded by the solid–liquid phase temperature line, as shown in Equation (12).

$$\theta = \begin{cases} 0 & , T < T_m - \Delta T \\ \frac{T-(T_m-\Delta T)}{2\Delta T} & , T_m - \Delta T < T < T_m + \Delta T \\ 1 & , T > T_m - \Delta T \end{cases} \tag{12}$$

At the same time, the phase transition will lead to a change in the physical parameters of the material. Therefore, the transition parameters need to be smoothed in the transition zone of the solid–liquid interface. The density, thermal conductivity, and kinetic viscosity of the transition zone are expressed in Equations (13)–(15), respectively.

$$\rho = (1 - \theta)\rho_s + \theta\rho_l \tag{13}$$

$$k = (1 - \theta)k_s + \theta k_l \tag{14}$$

$$\mu = (1 - \theta)\mu_s + \theta\mu_l \tag{15}$$

where ρ_s and ρ_l denote the density of solids and liquids, respectively, k_s and k_l denote the thermal conductivity of solid phase and liquid phase, respectively, μ_s and μ_l are dynamic viscosity of solid phase and liquid phase, respectively.

According to the Carman–Koseny formula [20], a force term was introduced to absorb the loss of momentum in the solid material, as shown in Equation (16).

$$F_D = \frac{A_m(1 - \theta)^2}{\theta^3 + \xi}u \tag{16}$$

where A_m is the Carman–Koseny coefficient. The solid material has a large viscous drag, and a larger value needs to be set. In addition, to avoid a zero denominator, a very small amount ξ should be added.

2.4. Flow Modelling

The NdFeB material is melted to form a molten pool, and the flow of molten metal in the pool is controlled by the conservation of momentum equation, with the expression shown in Equation (17) [21].

$$\rho\frac{\partial u}{\partial t} + \rho u \cdot \nabla \mathbf{u} = \nabla(\mu(\nabla \mathbf{u} + (\nabla \mathbf{u})^2 - pI)) + \rho g - \beta_1(T - T_a)\rho g - F_D \tag{17}$$

where ρg and $\beta_1(T - T_a)\rho g$ represent the forces of gravity and buoyancy, respectively.

The molten material flowing in the melt pool is subjected to recoil pressure and surface tension, which drive the formation of craters. The recoil pressure was generated by the material evaporation in the opposite direction of evaporation, resulting in driving the liquid materials outwards, as shown in Equation (18) [22]:

$$P_r = \begin{cases} P_0 & , T_a \le T < T_v \\ \frac{1+\beta}{2} P_a(T) & , T \ge T_v \end{cases} \tag{18}$$

Surface tension acts on the surface of molten materials to cause liquid flow, which is also known as Marangoni convection. It is caused by a surface tension gradient due to a free surface temperature gradient, which drives the penetration and expansion of the melt pool. In the central region of the Gaussian surface heat source, where the temperature is highest and the surface tension is lowest, the fluid flows from the center to the edge of the melt pool. The surface tension depended on the material and the temperature, as shown in Equation (19) [23]:

$$\gamma = \gamma_m - A_\gamma(T - T_m) - R_g T \Gamma_s \ln(1 + k_i a_i e^{\frac{\Delta H_0}{R_g T}}) \tag{19}$$

where γ is the coefficient of surface tension between the molten metal and air, and A_γ represents the temperature coefficient of surface tension. The third term in Equation (19) is insignificant and can be neglected to simplify the model.

2.5. Ablation Deformation Modelling and Meshing

The ablation removal process was simulated by the deformation geometry method. The movement of the upper boundary finite element mesh was controlled by the ablation velocity based on the fluid flow rate and the Hertz–Knudsen equation, which was calculated by the hyperplastic smoothing method. The movement velocity of the mesh is shown in Equation (20).

$$s = u + v - \frac{\dot{m}}{\rho} \tag{20}$$

where u and v represent the lateral and longitudinal flow velocities, respectively.

The 2D finite element geometry model was generated and shown in Figure 1. The vertical red arrows represent the laser beam loading direction and the horizontal red arrow indicates the laser spot travel direction. The laser beam was initially at the home position and oriented along the positive direction of the *X*-axis. Partitioning was carried out via a free triangular mesh. To improve the model accuracy, the mesh density of the upper boundary was increased. Furthermore, an automatic re-meshing function was used to avoid mesh inversion distortion during the simulation calculations.

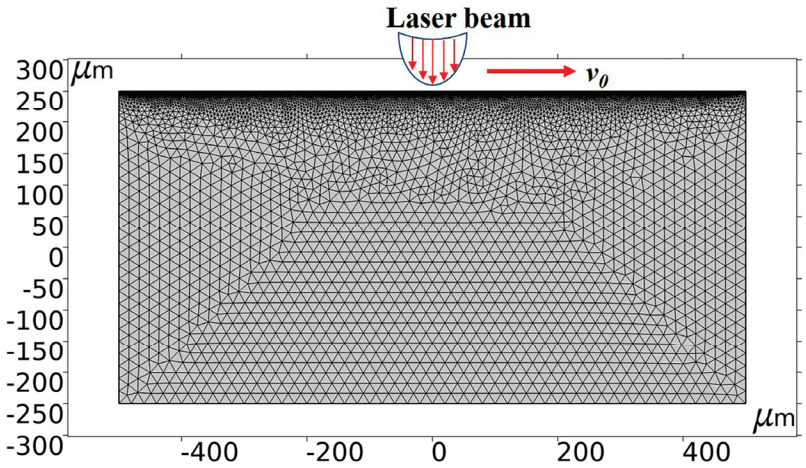

Figure 1. Mesh division image.

3. Simulation and Experiment Procedures

For the analysis of the processing morphology, temperature field distribution, and flow fields velocity in the simulation, the average power of the nanosecond pulsed laser was set at 8 W, the pulse width at 40 ns, the frequency at 150 kHz, and the scanning speed at 100 mm/s. Due to the complexity of the model calculation, the variation over 15 pulse cycles was simulated. In this study, the laser processing parameters were determined by the simulation results and the laser parameters adjustment range of the laser processing machine. To investigate the effect of laser scanning speed and average power on the processing results, the laser processing parameters selected for the simulation are shown in Table 2; other parameters were kept constant.

Table 2. Laser processing parameters used for simulations.

Groups	Average Power	Scanning Speed
1	8	100, 500, 1000
2	5, 8, 13	100

The schematic and dimension of the NdFeB microarray structure are shown in Figure 2. The experiments were carried out to verify the accuracy of the model by a UV nanosecond laser. The laser processing parameters used for experiments were consistent with those used in the simulation. After the experiment, the processed microstructures were observed with an ultra-deep field microscope (VHX-600E, Osaka, Japan). In addition, a ZYGO 3D profiler (Zygo 9000, Middlefield, CT, USA) was employed to measure the microstructure and the ablation depth.

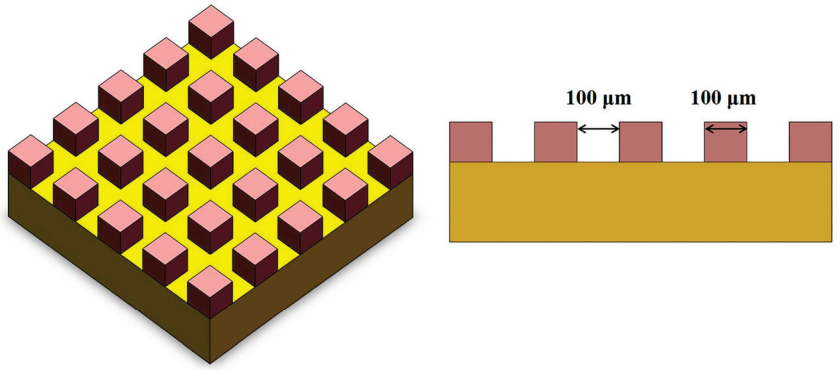

Figure 2. Schematic and dimension of the microarray structure.

4. Results and Discussion

4.1. Temperature Field and Flow Fields Analysis

Figure 3 shows the formation of the crater and the distribution of the temperature field during the simulation. The NdFeB starts to undergo phase change phenomena such as liquefaction and vaporization under the action of the laser pulse heat source; the material is removed by ablation, the depth and width increase with the increment of laser action time, and a crater is formed under the action of recoil pressure, surface tension, etc., finally causing the molten material to build up at the edges. The figure shows that the temperature at the bottom of the crater was the highest and spread around and inwards to form a heat-affected region. The morphology was roughly symmetrical due to the short travel distance of the laser spot within 15 pulses at a travel speed of 100 mm/s. Due to the nature of the Gaussian distribution of the laser heat source, the crater continues to get deeper as the number of cycles increases, as shown in Figure 3a–d, generating a roughly V-shaped morphology. The phenomenon of material accumulation can be reflected by the dimension of the upper boundary. Comparing the boundaries set in Figure 1, the original height before the simulation was 250 μm. After the laser ablation simulation, the molten material gradually stacked on both sides of the crater, which increased the height to approximately 255 μm, as shown in Figure 3d. The stacking height of the material is about 5 μm.

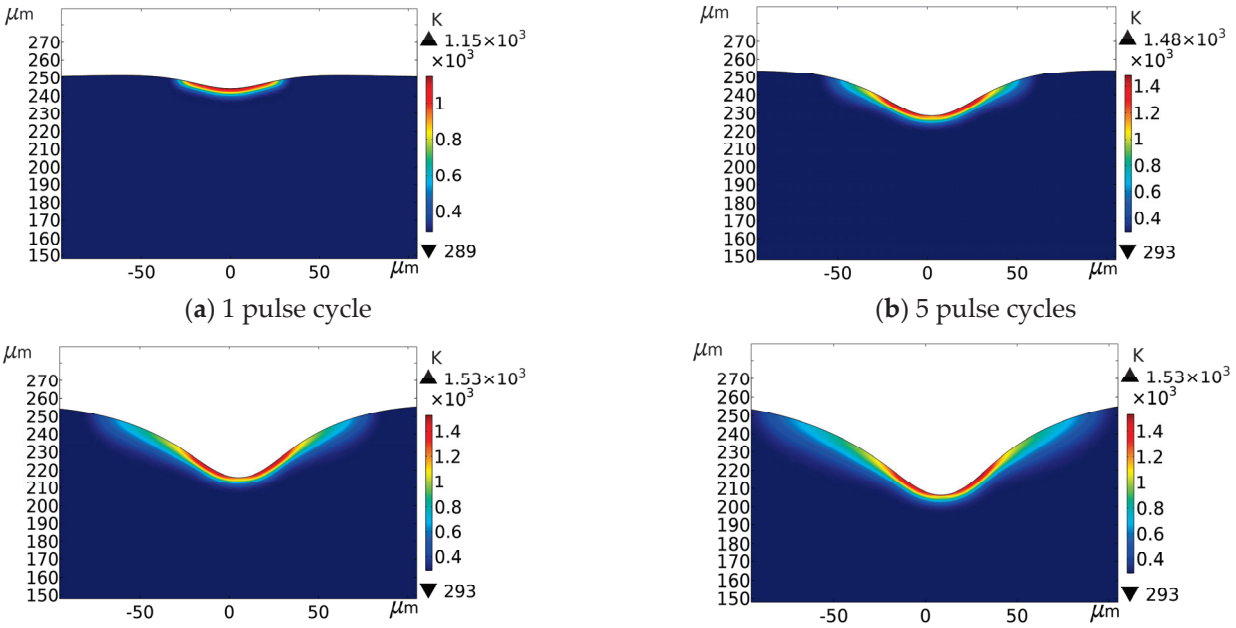

(**a**) 1 pulse cycle (**b**) 5 pulse cycles

(**c**) 10 pulse cycles (**d**) 15 pulse cycles

Figure 3. Microstructure morphology and temperature field distribution at different pulse cycles (Average power = 8 W, pulse width = 40 ns, frequency = 150 kHz, scanning speed = 100 mm/s).

Figure 4a shows the experimental surface morphology of NdFeB with laser processing; the material was stacked at the edge of the columnar array structure. Figure 4c shows the change in section depth at the black line in Figure 4b. As can be seen from the figure, the processed groove has a large taper, and the average depth at the bottom is about 50 μm, while the depth of the simulation result is about 43 μm. In the simulation, due to the limited number of pulses, the scanning distance of the laser beam is short, at a scanning speed of 100 mm/s, and the local heating is insufficient, while the actual processing is multi-pulse and long distance. In addition, the processing experiment is also influenced by multiple factors, so there exists a few micrometers error in depth. Overall, the experiment and simulation results have better consistency in terms of morphology and depth.

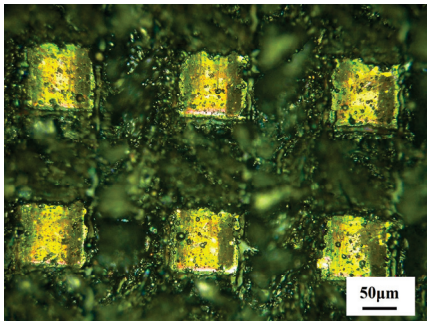

(**a**) Surface morphology

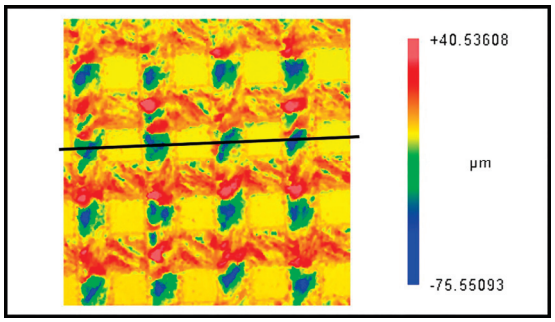

(**b**) Depth distribution of morphology

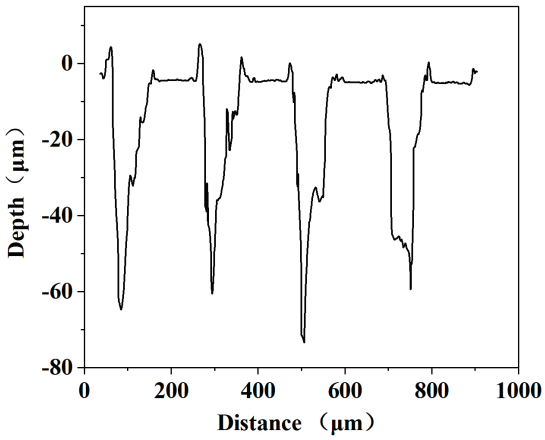

(**c**) Section depth at the black line

Figure 4. Experimental results of laser processing (Average power = 8 W, pulse width = 40 ns, frequency = 150 kHz, scanning speed = 100 mm/s).

In order to describe the temperature change, the maximum temperature curve was calculated by using a probe to trace the entire process. Figure 5a shows the maximum temperature change and the ablation depth for a single pulse. As can be seen from the figure, the maximum temperature rose rapidly during the pulse duration, and the maximum temperature reached over 4000 K. In this process, the material melting and vaporization occurred. After the process was over, the temperature dropped rapidly and then tended to flatten until the end of the cycle. The change in the ablation depth first increased rapidly, then tended to flatten, and finally showed a slight decrease. The reason of the above phenomenon is that the melting, evaporation, and sublimation of the material occur when the temperature rises sharply. As a result, the material starts to eliminate. When the temperature was below the melting temperature, the molten metal flowed back due to gravity. A recast layer at the bottom of the crater was formed, making the ablation depth drop back. Figure 5b shows the curve of the maximum temperature value within five pulse cycles; it can be seen that the maximum temperature tends to be the same within each cycle, and the minimum temperature gradually rises, which was caused by the heat affected after laser processing.

Figure 6 shows the flow field velocity of the melt pool for 15 pulse cycles. The red arrow in the figure indicates the flow direction, the length of the arrow is proportional to the flow velocity, and the density of the arrow indicates the flow intensity of the flow field. In Figure 6, it can be seen that the direction of flow velocity at the crater bottom was vertically upwards, and the direction of flow velocity at the edge of the crater was approximately the normal direction along the sidewall. The reason is that the crater bottom is the central area of the Gaussian heat source. Under the Marangoni effect, the spontaneous metal liquid flow will occur from the bottom of the high-temperature crater towards the low-temperature sidewalls and the edges of the back. The recoil pressure can then induce a jet of low-viscosity metallic liquid which will split into small droplets during flight to

minimize surface tension. This creates the entire spattering process [24]. Figure 7a further demonstrates the ejection phenomenon during processing: the spherical particles deposited near the processed microstructure, as indicated by the white arrows. In contrast, because the temperature on both sides was lower than the vaporization temperature, the molten material flowed roughly along the normal direction of the crater sidewall under the role of the surface tension of the liquid surface and gravity. Eventually, all the molten material solidified, and a recast layer was formed on the inner wall and top of the crater, resulting in morphology as stimulated. As shown by the arrow in Figure 7b, the accumulation morphology formed on the top of the crater when the flowing molten material solidified. The experiment morphology in Figure 7 is consistent with the simulation results in Figure 6. This proves the correctness of the simulation.

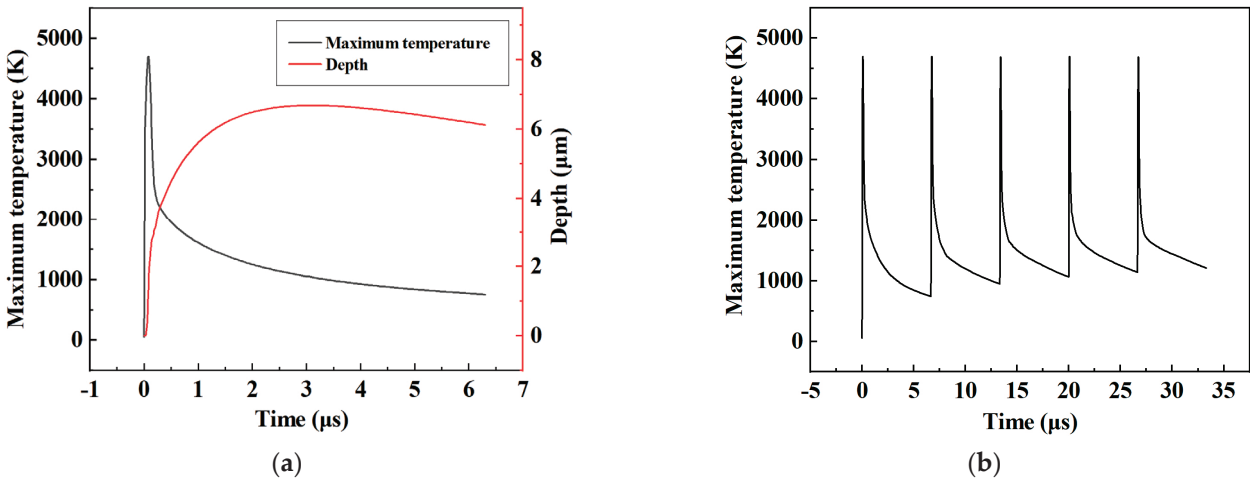

Figure 5. Maximum temperature and ablation depth variation. (**a**) Maximum temperature and ablation depth variation in single pulse cycle. (**b**) Maximum temperature variation in five pulse cycles.

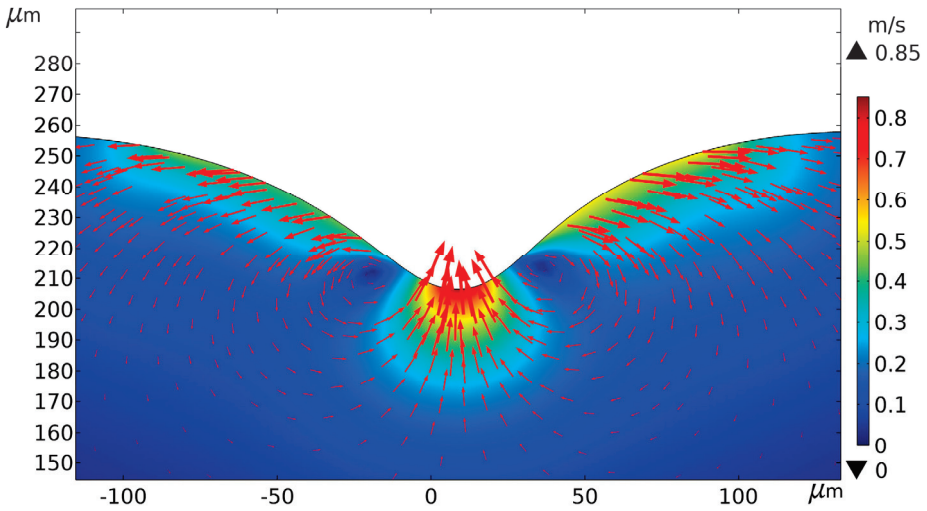

Figure 6. Flow field velocity of the melt pool. (Average power = 8 W, pulse width = 40 ns, frequency = 150 kHz, scanning speed = 100 mm/s).

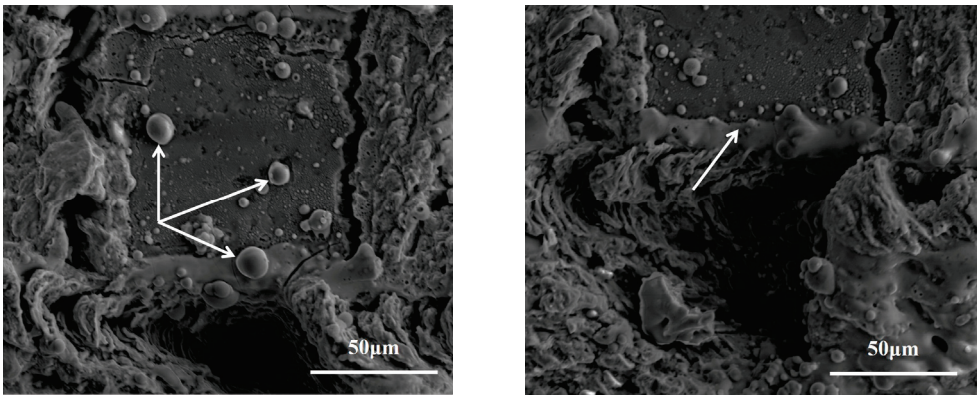

(**a**) Spherical particles deposited near the processed microstructure

(**b**) Accumulation morphology formed on the top of the crater

Figure 7. SEM morphology of microstructure after laser processing. (Average power = 8 W, pulse width = 40 ns, frequency = 150 kHz, scanning speed = 100 mm/s).

4.2. Effect of Laser Scanning Speed on the Processing Morphology

The laser scanning speed is an important parameter that affects the processing morphology of the crater. Different laser scanning speeds can produce different spot overlap rates. The spot overlap rate will become small while the scanning speed gets faster. The theoretical overlap rate η between adjacent laser spots can be expressed as Equation (21).

$$\eta = \left(1 - \frac{v_0}{2fr}\right) \times 100\% \tag{21}$$

where f is the laser pulse frequency, v_0 is the laser scanning speed, and r is the spot radius.

The scanning speeds chosen for simulation and experiment were 100 mm/s, 500 mm/s, and 1000 mm/s, respectively, and the spot overlap rates were 96.7%, 83.3%, and 66.7%, respectively. Other laser parameters were kept constant. As the spot scanning speed increased, the linear energy input of the material decreased because the laser-material interaction time decreased. Figures 3d and 6 show the simulation results of temperature field distribution and flow field velocity when the scanning speed is 100 mm/s. Combined with the simulation results in Figure 8, it can be seen that within the 15 pulse cycles, as the scanning speed became faster, the length of the processing area increased, the ablation depth became shallower, and the heat-affected area decreased accordingly. When the scanning speed increased, the maximum flow rate increased, but the flow intensity of the overall area was weakened. The reason of this phenomenon is that, when it was at a larger scanning speed, the residence time of the laser spot at the unit area was short, and the heat-affected zone was small, which made the ablation depth small and flow intensity weak. When the scanning speed was large, the processed area of the crater was farther away from the laser spot, and the flow field velocity became weaker. Moreover, the impact of the recoil pressure on the melt pool was also weakened, so the melt pool flow was relatively gentle, and the ablation depth was reduced, which was conducive to the escape of bubbles from the melt pool. In contrast, the flow field on the right side of the crater was more intense.

Figure 9 shows the experimental results of laser processing at different scanning speeds; the parameters used for the experiment were kept consistent with the parameters for the simulation. As can be seen from the figure, the height of the accumulation on both sides of the crater decreased, and the depth of the crater decreased significantly when the scanning speed increased. The comparison results of laser ablation depth between the experiment and simulation are shown in Figure 10, where the simulated results show good agreement with the experimental results. In addition, the variation of the flow velocity under different laser scanning speeds is also shown in Figure 10.

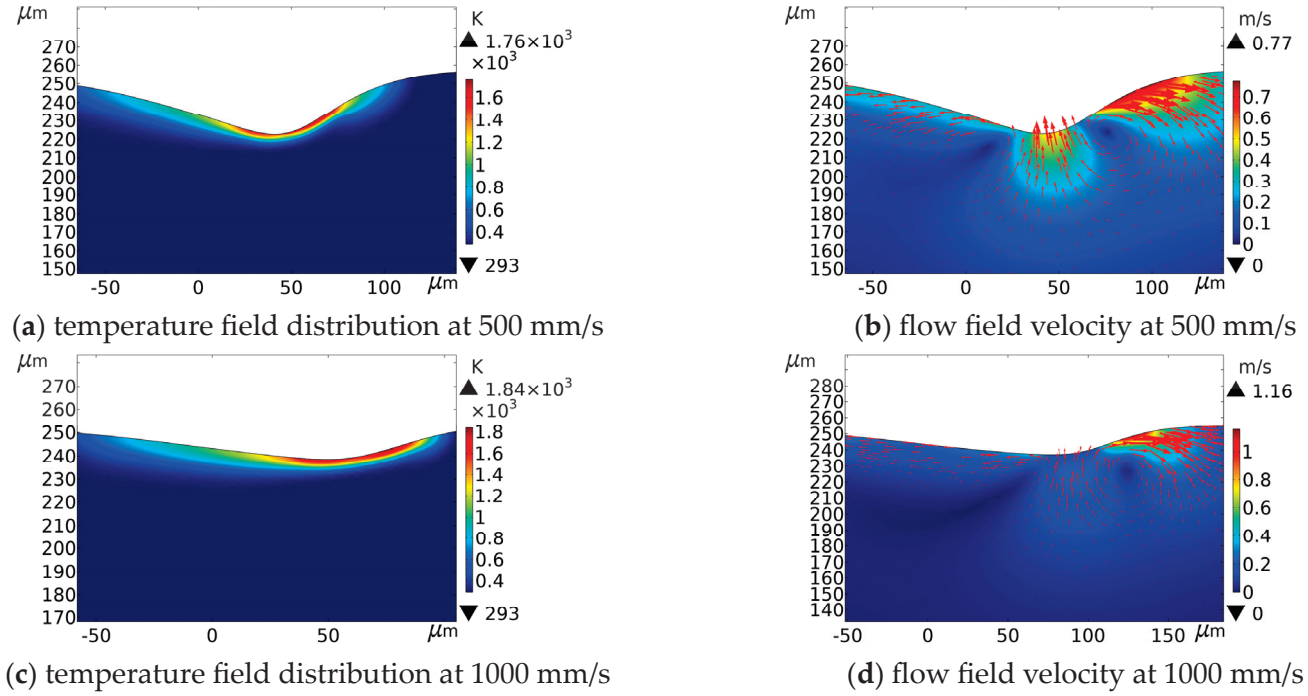

(**a**) temperature field distribution at 500 mm/s

(**b**) flow field velocity at 500 mm/s

(**c**) temperature field distribution at 1000 mm/s

(**d**) flow field velocity at 1000 mm/s

Figure 8. Temperature field distribution and flow field velocity at different scanning speeds (Average power = 8 W, pulse width = 40 ns, frequency = 150 kHz).

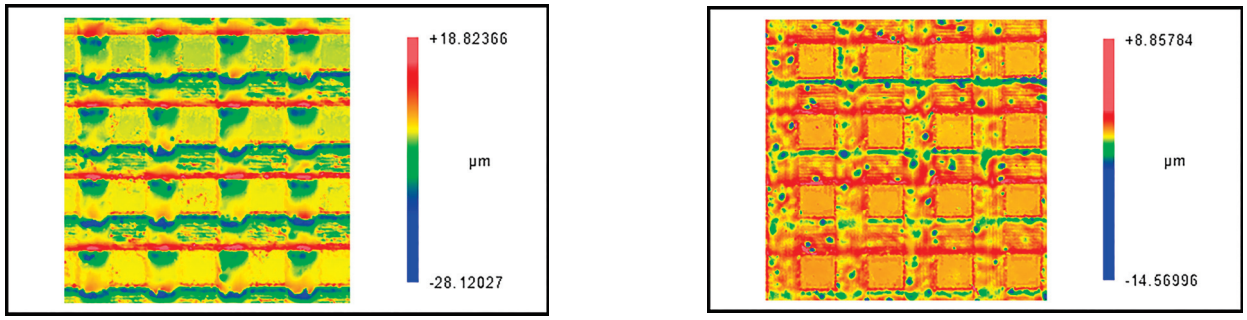

(**a**) 500 mm/s

(**b**) 1000 mm/s

Figure 9. Experimental results of laser processing at different scanning speeds (Average power = 8 W, pulse width = 40 ns, frequency = 150 kHz).

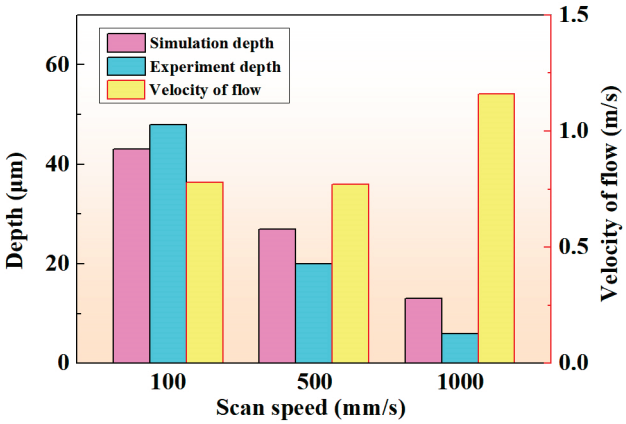

Figure 10. The comparison results of laser ablation depth and the variation of the flow velocity at different scanning speeds.

4.3. Effect of Average Power on the Processing Morphology

The effect of laser processing on crater morphology was simulated when the average powers were 5 W, 8 W, and 13 W. Figures 3d and 6 show the simulation results of temperature field distribution and flow field velocity under the average power of 8 W, respectively. The simulation results of temperature field distribution and flow field velocity under the average power of 5 W and 13 W are shown in Figure 11.

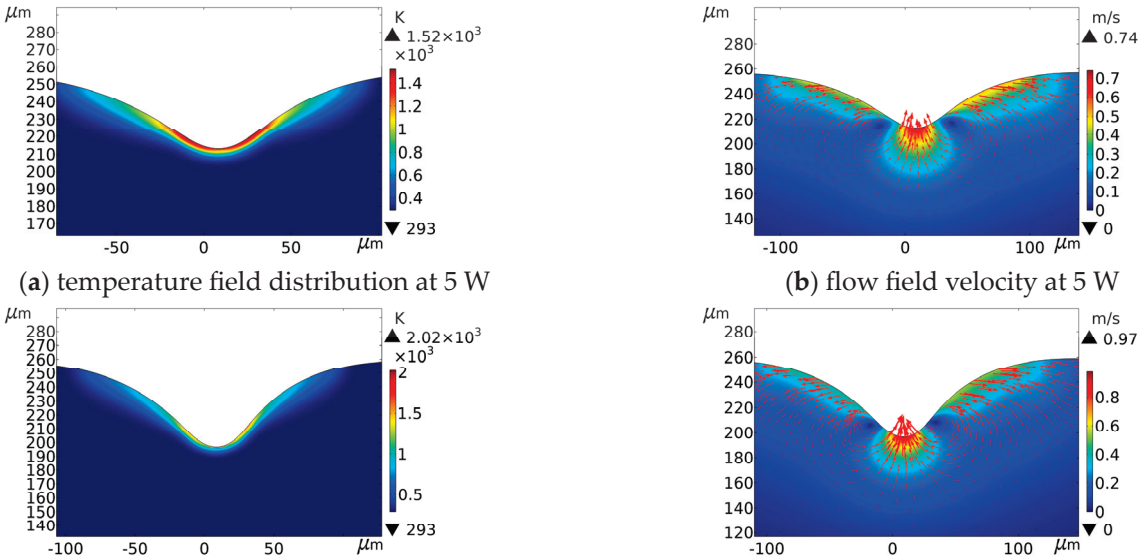

(**a**) temperature field distribution at 5 W

(**b**) flow field velocity at 5 W

(**c**) temperature field distribution at 13 W

(**d**) flow field velocity at 13 W

Figure 11. Temperature field distribution and flow field velocity at different average powers (Pulse width = 40 ns, frequency = 150 kHz, scanning speed = 100 mm/s).

The results show that as the average power increased, the depth of the crater gradually increased. At the same time, the melt pool flow rate became faster, and the flow state became more intense. Moreover, the height of accumulation around the crater increased. This is because more laser energy was irradiated on the substrate surface when the average power density became higher, which increased the temperature and drove the movement of the flow field, and the evaporation of the molten material became intense. As a result, more vapor was formed, and the intensive vapor movement created a stronger recoil pressure on the molten pool, causing more molten metal to stack around the crater. Figure 12 further supports the above conclusion. In a pulse cycle, the maximum temperature becomes higher, but the drop becomes smoother when the average power increases.

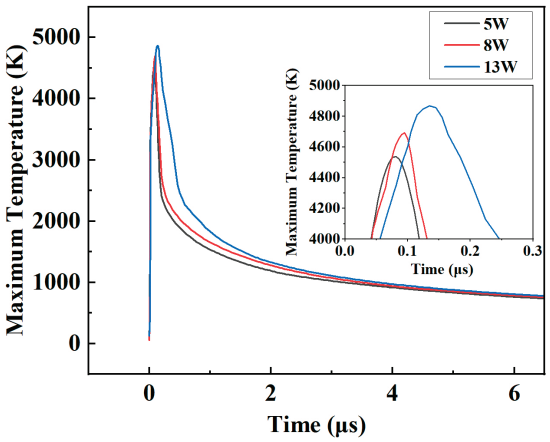

Figure 12. Maximum temperatures at different average power.

The experimental results are shown in Figure 13; the laser processing parameters were the same as the parameters of the simulation. The experimental results show a consistent trend with the simulation results. The ablation depth increased as the average laser power increased, and the molten material stacked more and more around the column structure. The comparison between the simulation and experimental results is shown in Figure 14. Although the variation of the experiment and simulation ablation depths shows a consistent trend, the experimental ablation depth was much smaller than that of the simulation when the average power was 5 W. This can be attributed to the surface treatment of the NdFeB material, which makes it difficult for the energy to break through the surface layer, resulting in a small ablation depth obtained in the experiment. The larger average power fabricates deeper microstructures, but the shape retention of the microstructures gets worse. As shown in Figure 13b, the ablation depth was deeper at 13 W, but the material accumulation at the edge of the columnar structure was serious. Therefore, it is necessary to balance the relationship between the ablation depth and morphology, or improve the shape retention capability by other auxiliary methods.

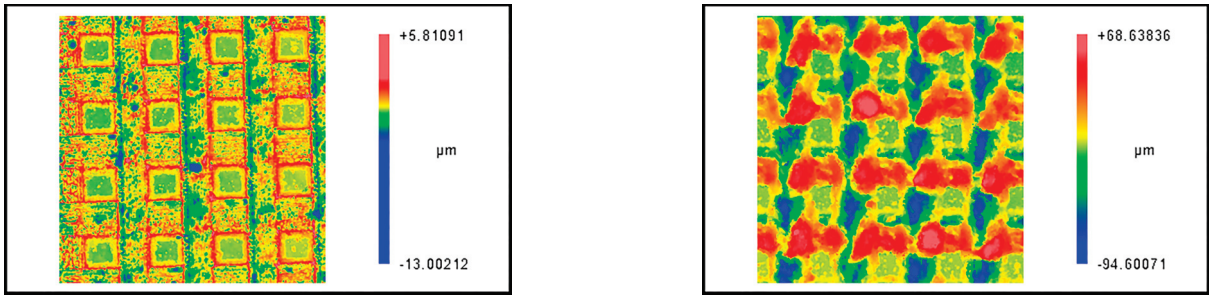

(**a**) 5 W (**b**) 13 W

Figure 13. Experimental results of laser processing at different average powers (Pulse width = 40 ns, frequency = 150 kHz, scanning speed = 100 mm/s).

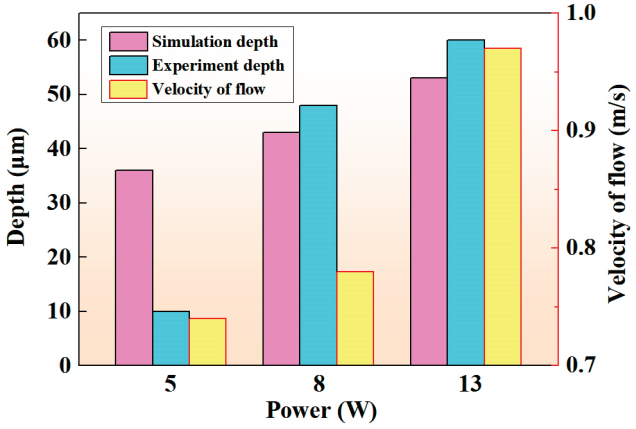

Figure 14. The comparison results of laser ablation depth and the variation of the flow velocity at different average power.

5. Conclusions

In this study, a two-dimensional simulation model of laser processing of NdFeB material was established. The temperature field distribution, microstructure morphology, and flow field velocity of the melt pool after laser processing were analyzed through simulation and experiment. The influence trends of the scanning speed and average power of laser processing on the machining morphology of microstructure were investigated. The main conclusions can be drawn as follows:

(1) A simulation model for laser processing of NdFeB materials was developed, and its accuracy was verified. Under the laser processing parameters of the average power of

8 W, pulse width of 40 ns, frequency of 150 kHz, and scanning speed of 100 mm/s, the simulation cross-section morphology showed a V-shaped profile with a crater depth of about 43 μm, which is in good agreement with the experimental results;

(2) The flow evolution of the melt pool and the formation mechanism of the microstructure in the laser processing NdFeB materials were revealed. The molten material was ejected outwards under recoil pressure, and the molten materials flowed normally to the side walls of the crater by the role of surface tension and gravity. After the temperature decreased, the molten material solidified, and a recast layer was formed at the inner wall and top of the crater, which eventually formed the processing morphology;

(3) The effect of laser scanning speed and average power on the processing morphology was investigated. When the scanning speed increased, the processing area length increased, but the ablation depth became shallow. The fluid flow intensity decreased, especially on the left side of the crater, and the melt pool flow was gentler. When the average power increased, the flow field velocity in the melt pool was more intense, and the ablation depth gradually increased.

In the future, the influence of external fields such as the electric field and the magnetic field on the processing effect in laser processing of NdFeB materials will be studied, and reveal the internal mechanism.

Author Contributions: Conceptualization, Y.Z. and S.W.; methodology, Y.Z.; software, S.W.; validation, Y.Z., S.W. and W.Y.; investigation, Y.Z.; resources, P.L.; data curation, J.Z.; writing—original draft preparation, S.W.; writing—review and editing, Y.Z. and C.W.; visualization, W.T.; supervision, Z.J. and H.Z.; project administration, F.G.; funding acquisition, J.G. All authors have read and agreed to the published version of the manuscript.

Funding: This work was supported by the National Key Research and Development Program (No. 2018YFA0702900) and the National Natural Science Foundation of China (No. 51975096).

Data Availability Statement: Data are available within the article.

Acknowledgments: The authors thank Xu Zhu for providing language help.

Conflicts of Interest: The authors declare no conflict of interest.

References

1. Zhi, C.; Qu, M.; Wang, Y.; Li, Y.; Xie, J.; Feng, W.; Tang, B. Fabrication and characterization of micro electromagnetic linear actuators. *J. Micromechan. Microeng.* **2020**, *30*, 125011. [CrossRef]
2. Wang, Y.; Zhi, C.; Tang, B.; Yang, K.; Xie, J.; Xu, W.; Li, H.; Wang, X. A micro electromagnetic actuator with high force density. *Sens. Actuator A Phys.* **2021**, *331*, 112771. [CrossRef]
3. Feng, Z.; Zhao, H.; Tan, C.; Zhu, B.; Xia, F.; Wang, Q.; Chen, B.; Song, X. Effect of laser texturing on the surface characteristics and bonding property of 30 CrMnSiA steel adhesive joints. *J. Manuf. Process.* **2019**, *47*, 219–228. [CrossRef]
4. Ijaola, A.O.; Bamidele, E.A.; Akisin, C.J.; Bello, I.T.; Oyatobo, A.T.; Abdulkareem, A.; Farayibi, P.K.; Asmatulu, E. Wettability transition for laser textured surfaces: A comprehensive review. *Surfaces Interfaces* **2020**, *21*, 100802. [CrossRef]
5. Li, H.; Wang, X.; Zhang, J.; Wang, B.; Breisch, M.; Hartmaier, A.; Rostotskyi, I.; Voznyy, V.; Liu, Y. Experimental investigation of laser surface texturing and related biocompatibility of pure titanium. *Int. I Adv. Manuf. Technol.* **2022**, *119*, 5993–6005. [CrossRef]
6. Melo-Fonseca, F.; Guimarães, B.; Gasik, M.; Silva, F.S.; Miranda, G. Experimental analysis and predictive modelling of Ti6Al4V laser surface texturing for biomedical applications. *Surf. Interfaces* **2022**, *35*, 102466. [CrossRef]
7. Zhao, Y.; Su, Y.; Hou, X.; Hong, M. Directional sliding of water: Biomimetic snake scale surfaces. *Opto-Electron.* **2021**, *4*, 210008. [CrossRef]
8. Lim, H.S.; Yoo, J. FEM based simulation of the pulsed laser ablation process in nanosecond fields. *J. Mech. Sci. Technol.* **2011**, *25*, 1811–1816. [CrossRef]
9. Berenyi, R.; Szaffner, D. *FEM Based 3D Simulation of Nanosecond UV Laser Ablation*; ISSE: Eger, Hungary, 2015; pp. 385–389.
10. Zhang, J.; Zhao, L.; Rosenkranz, A.; Song, C.; Yan, Y.; Sun, T. Nanosecond pulsed laser ablation of silicon-finite element simulation and experimental validation. *J. Micromechanics Microeng.* **2019**, *29*, 75009. [CrossRef]
11. Ding, X.; Wang, L.; Wang, S. Comparison study of numerical analysis for heat transfer and fluid flow under two different laser scan pattern during selective laser melting. *Optik* **2016**, *127*, 10898–10907. [CrossRef]
12. Yuan, P.; Gu, D. Molten pool behaviour and its physical mechanism during selective laser melting of TiC/AlSi10Mg nanocomposites: Simulation and experiments. *J. Phys. D* **2015**, *48*, 35303–35316. [CrossRef]

13. Cho, W.; Na, S.; Thomy, C.; Vollertsen, F. Numerical simulation of molten pool dynamics in high power disk laser welding. *J. Mater. Process. Technol.* **2012**, *212*, 262–275. [CrossRef]
14. Yuan, W.; Chen, H.; Cheng, T.; Wei, Q. Effects of laser scanning speeds on different states of the molten pool during selective laser melting: Simulation and experiment. *Mater. Des.* **2020**, *189*, 108542. [CrossRef]
15. Zhang, Y.; Shen, Z.; Ni, X. Modeling and simulation on long pulse laser drilling processing. *Int. J. Heat Mass Transf.* **2014**, *73*, 429–437. [CrossRef]
16. Zhu, D.; Zhang, P.; Tian, Z.; Chen, C.; Hua, X.; Xu, S.; Xie, X. Numerical Study on the Evolution Mechanism of the Crater under a Millisecond Laser. *Appl. Sci.* **2020**, *10*, 9054. [CrossRef]
17. Vasantgadkar, N.A.; Bhandarkar, U.V.; Joshi, S.S. A finite element model to predict the ablation depth in pulsed laser ablation. *Thin Solid Films* **2010**, *519*, 1421–1430. [CrossRef]
18. Vora, H.D.; Santhanakrishnan, S.; Harimkar, S.P.; Boetcher, S.K.S.; Dahotre, N.B. Evolution of surface topography in one-dimensional laser machining of structural alumina. *J. Eur. Ceram. Soc.* **2012**, *32*, 4205–4218. [CrossRef]
19. Courtois, M.; Carin, M.; Masson, P.L.; Gaied, S.; Balabane, M. A new approach to compute multi-reflections of laser beam in a keyhole for heat transfer and fluid flow modelling in laser welding. *J. Phys. D* **2013**, *46*, 505305–505314. [CrossRef]
20. Lu, J.; Zhang, Y.Z.; Ni, X.W. Modeling of dynamic process in the laser-off period during laser drilling. *Chin. Opt. Lett.* **2015**, *13*, 62–65. [CrossRef]
21. Desmaison, O.; Bellet, M.; Guillemot, G. A level set approach for the simulation of the multipass hybrid laser/GMA welding process. *Comput. Mater. Sci.* **2014**, *91*, 240–250. [CrossRef]
22. Sharma, S.; Mandal, V.; Ramakrishna, S.A.; Ramkumar, J. Numerical simulation of melt pool oscillations and protuberance in pulsed laser micro melting of SS304 for surface texturing applications. *J. Manuf. Process.* **2019**, *39*, 282–294. [CrossRef]
23. Sahoo, P.; Debroy, T.; Mcnallan, M.J. Surface tension of binary metal—Surface active solute systems under conditions relevant to welding metallurgy. *Met. Mater. Trans. B* **1988**, *19*, 483–491. [CrossRef]
24. Li, Z.; Li, H.; Yin, J.; Li, Y.; Nie, Z.; Li, X.; You, D.; Guan, K.; Duan, W.; Cao, L.; et al. A review of spatter in laser powder bed fusion additive manufacturing: In situ detection, generation, effects, and countermeasures. *Micromachines* **2022**, *13*, 1366. [CrossRef] [PubMed]

micromachines

MDPI

Article

Modeling and Compensation of Positioning Error in Micromanipulation

Miao Hao [1], Bin Yang [2,*], Changhai Ru [3], Chunfeng Yue [4], Zongjie Huang [4], Rongan Zhai [5], Yu Sun [6], Yong Wang [3,*] and Changsheng Dai [7]

1 School of Mechanical and Electrical Engineering, Soochow University, Suzhou 215137, China
2 The Reproductive Medicine Centre, The First Affiliated Hospital of Suzhou University, Suzhou 215031, China
3 School of Electronic and Information Engineering, Suzhou University of Science and Technology, Suzhou 215009, China
4 Suzhou Boundless Medical Technology Co., Ltd., Suzhou 215163, China
5 School of Mechatronic Engineering and Automation, Shanghai University, Shanghai 200444, China
6 Department of Mechanical and Industrial Engineering, University of Toronto, Toronto, ON M5S 3G8, Canada
7 School of Mechanical Engineering, Dalian University of Technology, Dalian 116081, China; daichangsheng@gmail.com
* Correspondence: ybdz@163.com (B.Y.); wangyong@mail.usts.edu.cn (Y.W.)

Abstract: In order to improve the positioning accuracy of the micromanipulation system, a comprehensive error model is first established to take into account the microscope nonlinear imaging distortion, camera installation error, and the mechanical displacement error of the motorized stage. A novel error compensation method is then proposed with distortion compensation coefficients obtained by the Levenberg–Marquardt optimization algorithm combined with the deduced nonlinear imaging model. The compensation coefficients for camera installation error and mechanical displacement error are derived from the rigid-body translation technique and image stitching algorithm. To validate the error compensation model, single shot and cumulative error tests were designed. The experimental results show that after the error compensation, the displacement errors were controlled within 0.25 μm when moving in a single direction and within 0.02 μm per 1000 μm when moving in multiple directions.

Keywords: micromanipulation platform; systematic error; image stitching; error compensation model

Citation: Hao, M.; Yang, B.; Ru, C.; Yue, C.; Huang, Z.; Zhai, R.; Sun, Y.; Wang, Y.; Dai, C. Modeling and Compensation of Positioning Error in Micromanipulation. *Micromachines* **2023**, *14*, 779. https://doi.org/10.3390/mi14040779

Academic Editors: Nam-Trung Nguyen and Jiang Guo

Received: 20 February 2023
Revised: 18 March 2023
Accepted: 18 March 2023
Published: 30 March 2023

1. Introduction

With the rapid development of modern biomedical technology, micromanipulation techniques have obtained widespread application, including nucleus transfer, microinjection, microdissection, embryo transfer, etc. However, accurate positioning plays a vital role in the micromanipulation [1–3]. Micro positioning technology uses image processing algorithms to visually locate the cells and microorganisms, converts image coordinates into object coordinates, and sends the converted coordinate information to the end effector for corresponding micro positioning [4]. Therefore, it is of great significance to study the systematic errors and compensation methods of microscopic vision systems. In order to improve the precision of micro-positioning, digital image correlation (DIC) is usually used to compensate the coordinate conversion error between the vision module of the micro-operating system and the end-effector [5–10]. For example, Lee [11] proposed a vision based high precision self-calibration method by the use of a designed chess board for converting the position relationship between the end-effector and the camera without operator intervention in the calibration process. At high magnifications, however, the optical microscope imaging cannot strictly meet the pinhole imaging model due to lens distortion, which will deteriorate the measurement of DIC [12–14]. Normally, the rigid-body translation technique is used for eliminating the distortion of the microscope camera [15–19].

Koide [20] describes a conversion technique based on reprojection error minimization by directly taking images of the calibration pattern. Malti [21] optimized the distortion parameters, the camera intrinsics and the hand–eye transform with epipolar constraints. Although the above method can effectively solve the camera distortion problem, it ignores the mechanical errors arising from the installation error of the camera and the mechanical displacement error. It can be seen that neither the rigid body translation method nor the DIC method can eliminate camera distortion errors and mechanical errors at the same time. In addition, in the current research, there is no comprehensive method to compensate these errors simultaneously.

The research object of this paper is a micromanipulation system based on machine vision, in which the camera and micromanipulation platform are the key components of positioning. In order to improve the positioning accuracy, not only the camera distortion error must be considered, but also the analysis and calculation of mechanical errors such as camera installation error and the mechanical displacement error of the micromanipulation platform. However, these are rarely discussed together in former works. Therefore, this paper proposes a novel error compensation model that unites the camera distortion errors compensation and the mechanical error compensation. The influences and derivation of the above errors are studied first. Then, a novel error compensation model is established to comprehensively take into account the microscope nonlinear imaging distortion, camera installation error, and the mechanical displacement error. Finally, to validate the error compensation model, single shot error tests and cumulative error tests were designed. The experimental results show that the proposed method is not only easy to implement, but also leads to accurate positioning.

2. System Overview

As shown in Figure 1, the micromanipulation system consists of a camera (scA1300-32 gm, Basler, Inc., Lubeck, Germany) which captures at 30 Hz in real time, a standard inverted microscope (Nikon Ti, Nikon, Inc., Tokyo, Japan), and a micromanipulation platform with a motorized X-Y stage (travel range of 75 mm along both axis, MLS-1740, Micro-Nano Automation Institute Co., Ltd., Suzhou City, China).

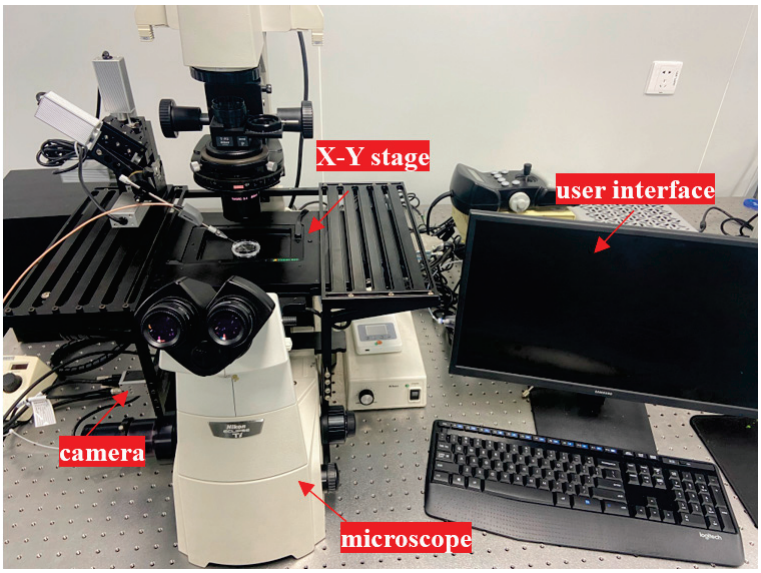

Figure 1. The hardware system of the micromanipulation system.

3. Derivation of System Errors

As the operating time of the micromanipulation system increases, the cumulative error of the system has a great impact on the accuracy of the micropositioning, and even leads to its failure. As shown in Figure 2, when the motorized stage is moved from point A to point

C, due to the system errors, the actual displacement path of the platform deviates from the predetermined displacement path.

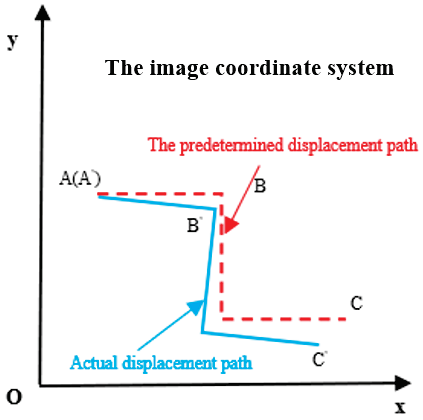

Figure 2. Deviation of displacement path caused by system error. The predetermined displacement path is moved from point A to point C via point B, while the actual displacement path of the platform is moved from point A′ to point C′ via B′ which deviates from the predetermined displacement path due to the system errors.

3.1. Image Model Error

The microscope imaging model will affect the positioning accuracy. At present, the commonly used imaging models are pinhole models or parallel projection models. However, the basic assumption of these imaging models is linearity, and the lens group of a microscope is susceptible to handling, shaking and other factors, causing distortion and non-linearity. Image distortion is caused by the manufacturing and assembly errors of the optical system, which will lead to the transform error while transforming between image coordinate and physical coordinate during micromanipulation [22]. In this paper, the microscope is equipped with a standard camera interface for installing a camera. There is a dedicated optical path inside the microscope for imaging, as shown in Figure 3a, which presents the composition diagram of the vision system. For a micro-vision system equipped with an infinity-corrected optical path, its basic geometric imaging model can be simplified as shown in Figure 3b.

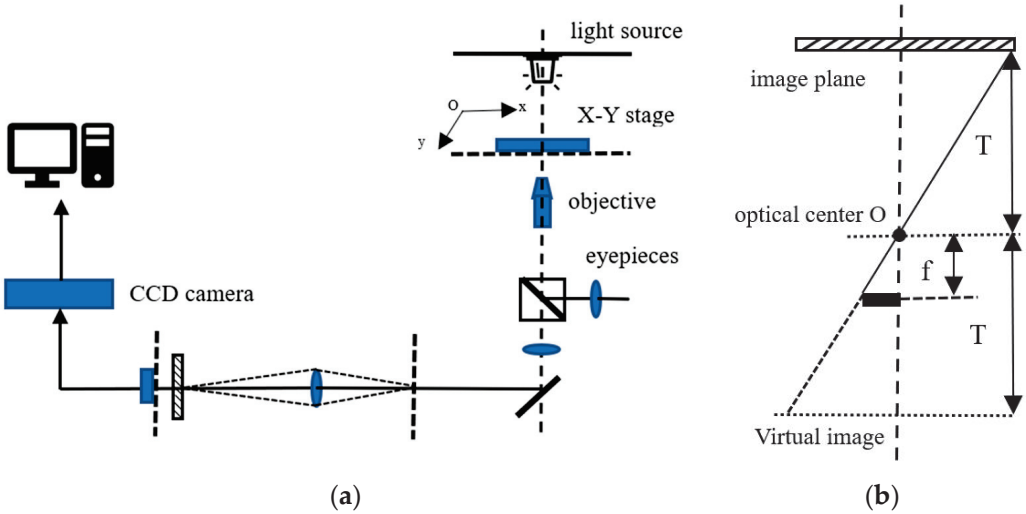

Figure 3. The vision system and simplified imaging model of the micromanipulation system. (**a**) The diagram of the vision system, (**b**) The simplified imaging model. T is the working distance of the microscope and f is the focal length of the objective lens.

Assume that there is a point in the physical coordinate system whose coordinate is $P = (X, Y, 0)^T$, and after microscope imaging, its corresponding coordinate in the image coordinate system is $p = (u, v)^T$. If the image distortion is ignored, the relationship between P and p is obtained according to the geometric principle of 2D photography:

$$\lambda \widetilde{p} = H\widetilde{P} = A[R_{12}t]\widetilde{P} \tag{1}$$

where λ represents any scale factor.

H represents the homography matrix of the imaging model.

$\widetilde{p}$ and $\widetilde{P}$ represent the homogeneous coordinates in the physical coordinate system and image coordinate system without considering the Z component, respectively.

A represents the internal parameter matrix $A = \begin{bmatrix} f_x & 0 & u_0 \\ 0 & f_y & v_0 \\ 0 & 0 & 1 \end{bmatrix}$.

R_{12} represents the first two columns of the 3×3 external parameter rotation matrix R. $R = [R_{12}r_3] = [r_1r_2r_3]$.

t represents the translation vector in the external parameter matrix. $t = [t_1t_2t_3]$.

Assuming that L and l represent a pair of lines in the physical coordinate system and image coordinate system, respectively. According to the contravariant property of point-line mapping, the relationship between its homogeneous coordinates can be expressed as:

$$\lambda \widetilde{l} = H^{-1}\widetilde{L} \tag{2}$$

However, due to the existence of lens distortion, the linear model in Equations (1) and (2) does not apply. The relationship between theoretical projection coordinates $p(\widetilde{u}, \widetilde{v})$ and actual projection coordinates $p'(u, v)$ in the image coordinate system is non -linear, which can be described as:

$$\begin{bmatrix} \widetilde{u} \\ \widetilde{v} \end{bmatrix} = \begin{bmatrix} u + k(u - u_0)\left[(u - u_0)^2 + (v - v_0)^2\right] \\ v + k(v - v_0)\left[(u - u_0)^2 + (v - v_0)^2\right] \end{bmatrix} \tag{3}$$

where k is a second-order distortion factor.

The nonlinear imaging model formula can be obtained as:

$$\lambda \begin{bmatrix} u + k(u - u_0)\left[(u - u_0)^2 + (v - v_0)^2\right] \\ v + k(v - v_0)\left[(u - u_0)^2 + (v - v_0)^2\right] \end{bmatrix} = H\widetilde{P} \tag{4}$$

The translation vector $\hat{t}$ in Equation (1) needs to be further corrected. The expression of the actual microscope magnification M and the actual translation vector $\hat{t}$ is obtained below:

$$\begin{cases} M = \frac{M_u + M_v}{2} = \frac{f_x * L_u + f_y * L_v}{2\lambda} \\ \hat{t} = L_u t = L_v t \end{cases} \tag{5}$$

where M_u and M_v represent the magnification of the microscope along the u axis and the v axis, respectively.

L_u and L_v represent the physical side lengths of the camera pixel unit along the u axis and the v axis, respectively.

The transformation matrix caused by the lens distortion is:

$$T_D = M'R\hat{t} \tag{6}$$

where M' is the ratio of the actual magnification and the theoretical amplification multiple.

3.2. Camera Installation Error

The camera of the micromanipulation system is fixed to the microscope through a screw connection. However, this mechanical fixing method, whether it is a thread or other high-precision connection methods, inevitably has a certain deflection angle which is expressed as a clear deviation between the image coordinate system and the physical coordinate system, as shown in Figure 4, after being highly magnified by the microscope.

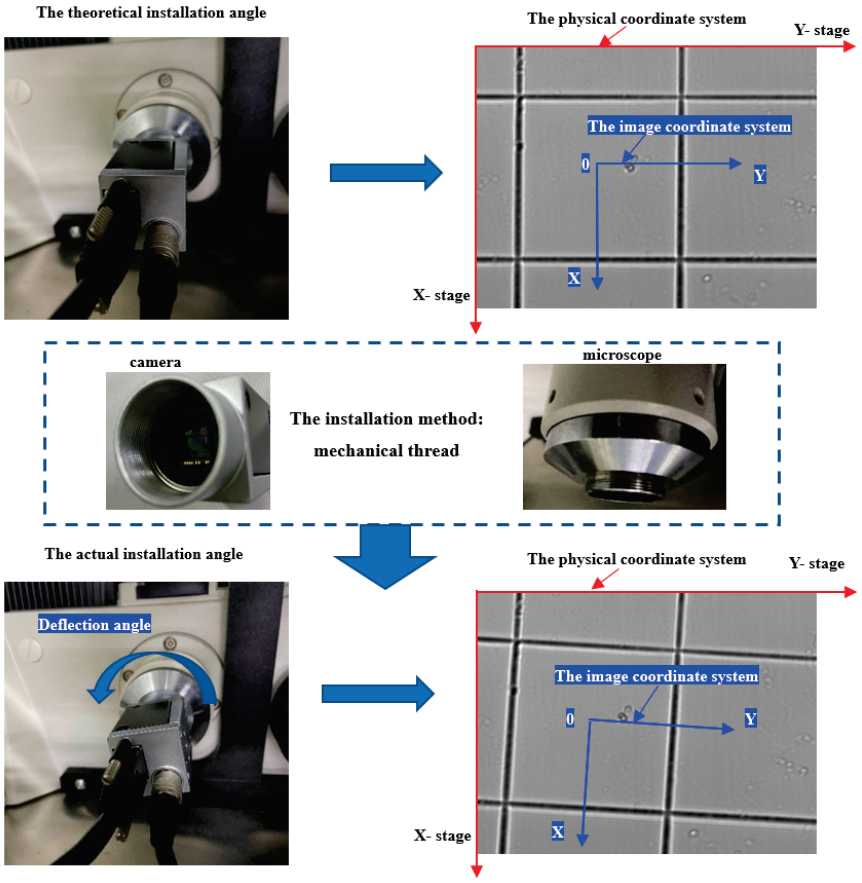

Figure 4. Deviation of the image coordinate caused by camera deflection angle. The camera is connected with the microscope by mechanical threaded. This installation method is easy to produce a deflection angle which is expressed as a clear deviation between the image coordinate system and the physical coordinate system.

The coordinate transformation caused by the deflection of the camera can be written as:

$$T_R = \begin{bmatrix} 1 & \varepsilon_y & 0 \\ \varepsilon_x & 1 & 0 \\ 0 & 0 & 1 \end{bmatrix} \tag{7}$$

where ε_x and ε_y are the conversion factors about rotation deflection angles around the X-axis and Y-axis of the physical coordinate system, respectively.

3.3. Mechanical Displacement Error

The X-Y stage of the micromanipulation system generates the displacement error due to the mechanical drive, which will accumulate with the increase of the displacement. So the

mechanical displacement error of the system needs to be compensated. The homogeneous transformation matrix of coordinates can be written as:

$$T_M = \begin{bmatrix} \Delta_x \\ \Delta_y \\ 1 \end{bmatrix} \tag{8}$$

where Δ_x and Δ_y are the mechanical displacement errors of X-direction and Y-direction, respectively.

4. Establishment of Error Compensation Model

It can be seen from the last section that the error of the micromanipulation platform is mainly composed of three parts: the image distortion error, the deflection angle error between the image coordinate system and the physical coordinate system, and the mechanical displacement error. So, the compensation for the systematic error mainly compensates for these three parts.

4.1. The Compensation Principles

A. The compensation principle of the image distortion error

This article calculates the image distortion error with the standard ruler shown in Figure 5. The parameters required for image distortion error models are obtained through image processing. Image distortion error compensation is mainly implemented through the four steps: automation center line extraction, distortion correction based on linear projection characteristics, estimation of the homography matrix, and the complete solution of internal and external parameters. The specific process and implementation method are shown in Figure 5.

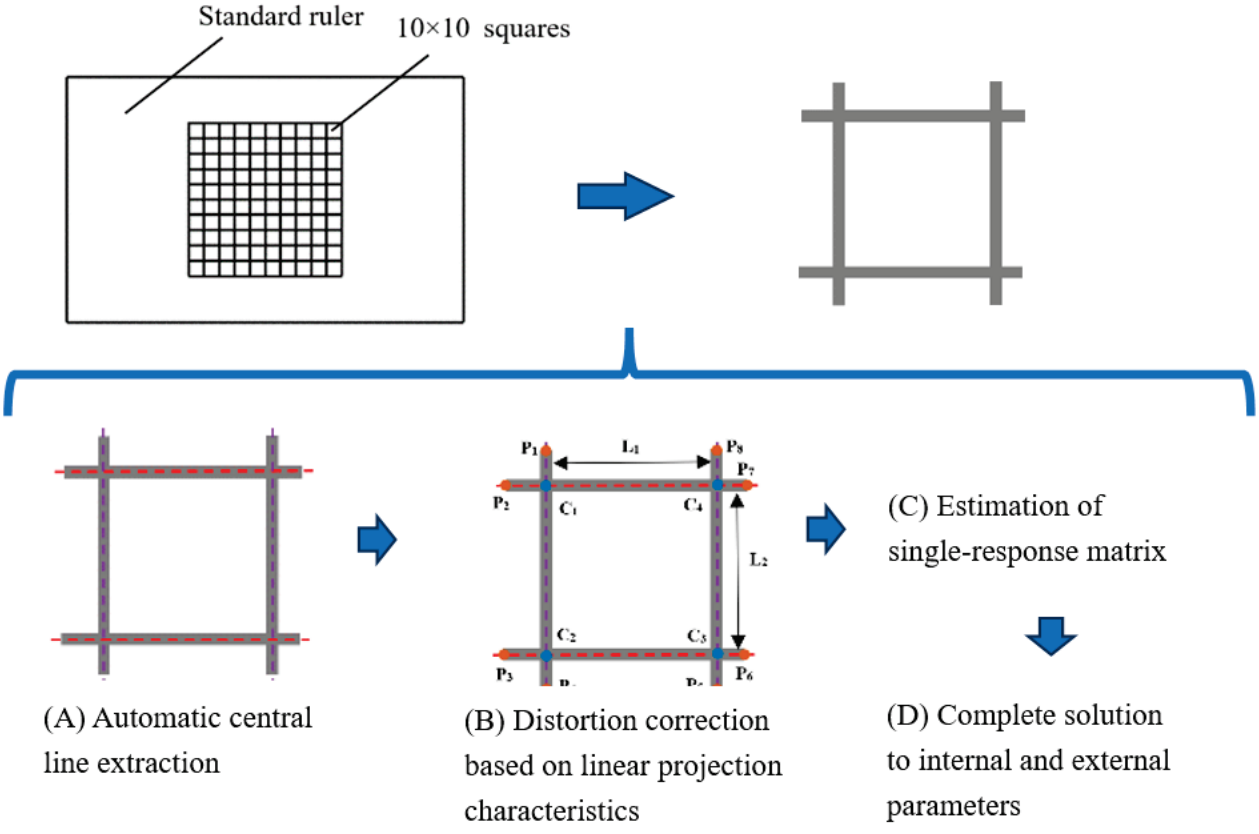

Figure 5. The process of image distortion error.

Image distortion can cause the lines of projection not to be straight. Therefore, the problem of parameter solving in the deformed projection model is the problem of non-

linear optimization. If there are n straight lines in the physical coordinate system, after the digital camera imaging, the central line is discrete to several discrete points. The distorted coordinates $(\hat{u}_i^j, \hat{v}_i^j)^{\mathrm{T}}$ are mapped through the distortion model Equation (3) to obtain the corresponding theoretical point coordinates. Then, the following nonlinear optimization objective function can be established:

$$\begin{aligned} F(k, u_0, v_0, \alpha_1, \alpha_2, \ldots\ldots \alpha_n, \varphi_1, \varphi_2, \ldots\ldots \gamma_n) \\ = min \sum_{i=1}^{n} \sum_{j=1}^{m_i} \left(\hat{u}_i^j \cos \alpha_i + \hat{v}_i^j \sin \alpha_i + \varphi_i \right)^2 \end{aligned} \tag{9}$$

where $\begin{cases} \hat{u}_i^j = u_i^j + k(u_i^j - u_0){r_d}^2 \\ \hat{v}_i^j = v_i^j + k(v_i^j - v_0){r_d}^2 \end{cases}$

m_i represents the number of discrete points on the theoretical center line.

$(u_i^j, v_i^j)^T$ and $(\hat{u}_i^j, \hat{v}_i^j)^T$ represent the theoretical coordinate of the i-th point on the j-th point of the theoretical center line, respectively.

α_i and φ_i represent the tilt angle and interception of the i-th theoretical center line, respectively.

According to the target function in Equation (9) and the central line coordinates extracted from the previous step, the distortion coefficient K, main point coordinate $(U_0, V_0)^T$, and the tilt angle α_i and interception φ_i can be obtained through the Levenberg–Marquardt optimization algorithm.

Since the entire projection is a 2D projection, the homography matrix H is a 3×3 matrix. For the intersection line pattern, through the above steps, 4 pairs of parallel straight lines and 4 pairs of intersecting dots can be obtained through the above steps. Thus, the complete estimation of the homography matrix is further achieved. Assume that $(P_i \rightarrow p_i)$ and $(L_i \rightarrow l_i)$ are the point pairs of the line pairs after distortions. Then, from the Equations (1) and (2), the following can be obtained:

$$\begin{cases} P_i \times Hp_i = 0 \\ l_i \times HL_i = 0 \end{cases} \tag{10}$$

By means of a singular value decomposition matrix, the homologous matrix H can be obtained, and $f_x, f_y, (u_0, v_0), k, M, R, t$ can be further obtained through matrix decomposition.

B. The compensation principle of the deflection error between image coordinate system and physical coordinate system

The deflection angle error between the image coordinate system and the physical coordinate system is primarily caused by the installation error of the camera. For the calculation of the deflection angle between the image coordinate system and the physical coordinate system, a series of frames that the previous frame and the after frame has an 1/2 width's (while displacing along X-direction of the stage) or height's (while displacing along Y-direction of the stage) overlap are obtained by using the standard rule shown in Figure 5. Take X-direction displacement as an example: two adjacent frames with partially overlapping images as shown in Figure 6a are selected and processed by the computer for image stitching. In the process, the SIFT algorithm [23] is used for image feature extraction, the RANSAC algorithm [24] is applied for image feature matching to eliminate outliers, and key matching points are put into use for image stitching. Finally, the displacement errors dy and dx can be calculated using the stitched image as shown in Figure 6b. Then, the deflection angle error θ between the image coordinate system and the physical coordinate system is obtained, i.e., θ of the camera installation is written as

$$\theta = arctan \frac{dy}{dx} \tag{11}$$

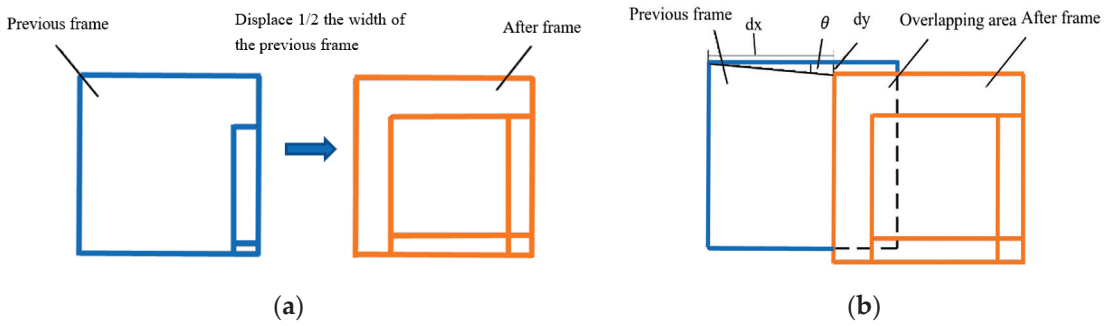

Figure 6. Image stitching schematic diagram. (**a**) Two adjacent images, (**b**) Image stitching.

C. The compensation principle of the mechanical displacement error

In a certain displacement direction, the difference between the theoretical and the actual displacement value of the platform is the displacement error in this direction after the compensation of the deflection angle error. Thus, the platform was moved several times in a fixed step along the positive and negative directions of the X-direction and the Y-direction, respectively, and the corresponding images were captured by the camera after each displacement. After that, the image stitching algorithm mentioned in Section 4.1B can be used to obtain the average displacement error of the platform along the X-direction and Y-direction which can be represented by Δx_+, Δx_-, Δy_+ and Δy_-, respectively.

Taking the X-direction as an example, a schematic diagram of mechanical displacement error calculation is shown in Figure 7 after the deflection angle error is compensated. Then, the calculation formula of Δx_+ is written as

$$\begin{aligned} \Delta x_+ &= \frac{1}{n}\left((\Delta x_+)_{12} + (\Delta x_+)_{23} + \cdots (\Delta x_+)_{(n-1)n} + (\Delta x_+)_{n(n+1)}\right) \\ &= \frac{1}{n}\sum_{i=1}^{n}(\Delta x_+)_{i(i+1)} \end{aligned} \tag{12}$$

where $(\Delta x_+)_{12}$ is the displacement error value obtained after image stitching of the first image and the second image in the positive direction of X-direction; $(\Delta x_+)_{23}$ is the displacement error value of the second and third images. Similarly, $(\Delta x_+)_{n(n+1)}$ is the displacement error value of the nth and nth $+ 1$ images.

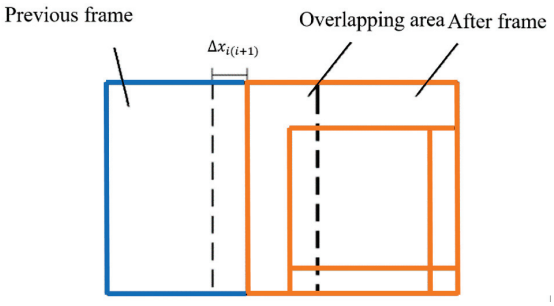

Figure 7. Schematic diagram of mechanical displacement error calculation.

Based on the axisymmetric principle, $\Delta x_-, \Delta y_+$ and Δy_- have similar calculation principles to Δx_+.

When the platform moves in a non-axial direction, the displacement error of the system is combined by the X-direction and Y-direction systematic errors. For example, as shown in Figure 8, when displacing from point O to point A in the physical coordinate system, the mechanical displacement error consists of Δx_+ and Δy_+. While it is in other quadrants, the corresponding mechanical displacement errors distribution is also shown in Figure 8.

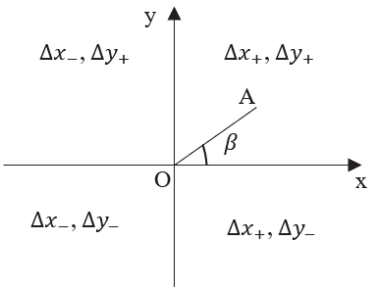

Figure 8. The distribution of mechanical displacement error.

Thus, the formula for calculating the compensation coefficient of mechanical displacement error is modeled as:

$$\begin{aligned} \mu &= \begin{bmatrix} 1+\Delta x_+ & 1+\Delta y_+ \\ 1+\Delta x_- & 1+\Delta y_+ \\ 1+\Delta x_- & 1+\Delta y_- \\ 1+\Delta x_+ & 1+\Delta y_- \end{bmatrix} \begin{bmatrix} cos\beta \\ sin\beta \end{bmatrix} \\ &= \begin{bmatrix} (1+\Delta x_+)cos\beta_1 + (1+\Delta y_+)sin\beta_1 \\ (1+\Delta x_-)cos\beta_2 + (1+\Delta y_+)sin\beta_2 \\ (1+\Delta x_-)cos\beta_3 + (1+\Delta y_-)sin\beta_3 \\ (1+\Delta x_+)cos\beta_4 + (1+\Delta y_-)sin\beta_4 \end{bmatrix} \end{aligned} \tag{13}$$

where μ is the mechanical error compensation coefficient of the micromanipulation platform. β is the positive deviation angle between the displacement direction and the X-direction. β_1 belongs to First quadrant, β_2 belongs to Second quadrant, β_3 belongs to Third quadrant, β_4 belongs to Fourth quadrant.

4.2. Error Compensation Model

Combined with Equations (6)–(8), the error transformation matrix can be obtained:

$$T = M' \begin{bmatrix} 1 & \varepsilon_y & \Delta_x \\ \varepsilon_x & 1 & \Delta_y \\ 0 & 0 & 1 \end{bmatrix} R\hat{t} \tag{14}$$

To compensate the system errors, an error compensation model needs to be established. As shown in Figure 9, when the stage is expected to move from point $A(X_0, Y_0)$ to point $B(X_1, Y_1)$, due to the system error, the stage actually moves to point $B'(X_1', Y_1')$. This can be expressed as

$$\overline{S} = T\overline{S'} \tag{15}$$

where $\overline{S}$ and $\overline{S'}$ are the vectors of expected displacement and actual displacement, respectively.

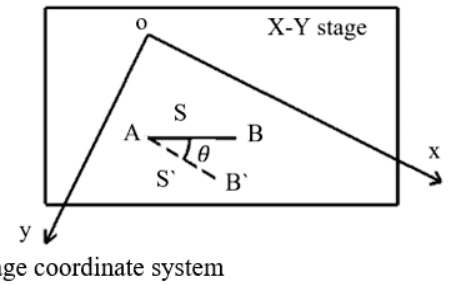

Figure 9. Schematic diagram of expected displacement and actual displacement. The expected vector displacement $\overline{S}$ is from point A to point B, but the actual displacement becomes vector $\overline{S'}$ that is from point A to point B'. The deflection angle between the expected displacement and actual displacement is θ.

Further,

$$\begin{cases} X_1 = X_0 + M'\delta_x s\cos\theta \\ Y_1 = Y_0 + M'\delta_y s\sin\theta \end{cases} \tag{16}$$

where δ_x and δ_y are the first and second lines of $R\hat{f}$, which represent the compensation coefficient of the image distortion of the X-direction and the Y-direction, respectively. s is the magnitude of S'.

Since the mechanical error of X-Y stage is positively linearly correlated with the moving distance, the error compensation model is as follows:

$$\begin{cases} X_1 = X_0 + M'\delta_x \mu * s\cos\theta \\ Y_1 = Y_0 + M'\delta_y \mu * s\sin\theta \end{cases} \tag{17}$$

It can be seen from Equation (17) that the establishment of the error model is mainly related to the five compensation coefficients M', δ_x, δ_y, μ and θ.

5. Experimental Results and Discussion

5.1. Calibration of Error Compensation Model

In order to determine the error compensation formula, an experiment was designed in this paper. A high-precision scale, the center of which consists of 20 × 20 squares with a side length of 50 μm, was selected as the standard ruler, and the image resolution was set as 1200 × 900. When the image samples were collected, the X-Y stage was used to adjust the step length under a 20× objective so that there is an overlap of 1/2 between adjacent images. A total of 40 images were taken according to the stepping method shown in Figure 10.

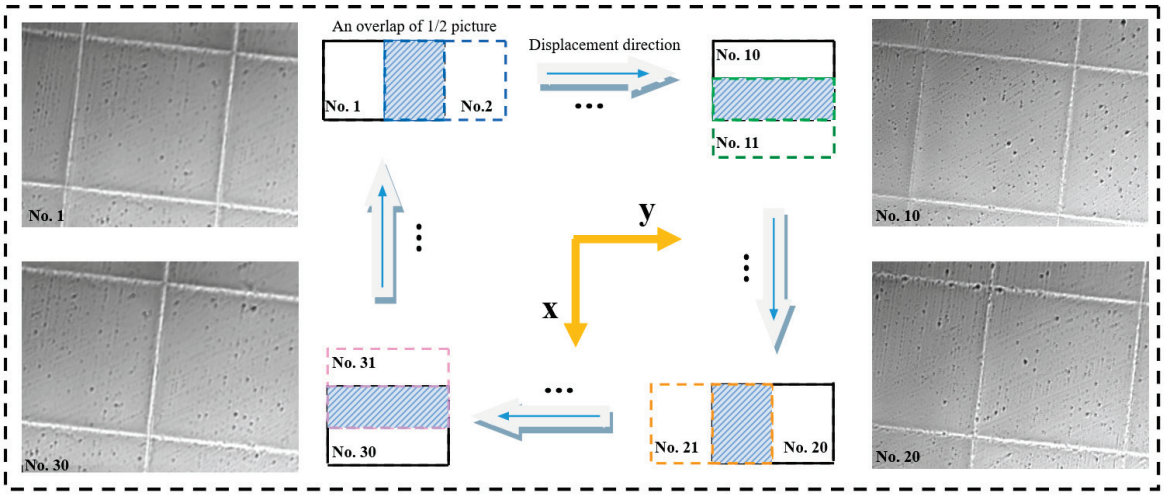

Figure 10. Image acquisition method. A total of 40 pictures were collected over multiple displacements by using the X-Y stage with a step size of half the width of the image (when it is displaced along the X-direction) or half the height (when it is displaced along the Y-direction). No.1 represents the first picture. No.2 represents the second picture, and so on.

The error compensation coefficients of image distortion are obtained through the algorithm of Section 4.1A. The results are shown in Table 1.

Among the 40 images, 10 groups of pairwise adjacent images were randomly selected for image stitching to obtain the error compensation coefficient of the deflection error between image coordinate system and platform coordinate system. Image stitching was performed on adjacent images. The effect diagram of this when moving in the X-direction is shown in Figure 11a, and when moving in the Y-direction is shown in Figure 11b. Thus, the deflection angle error compensation coefficient θ is obtained. The results are shown in Table 2.

Table 1. Results of error compensation coefficient M, δ_x δ_y.

Parameters	Theoretical Values	Actual Values
f_x (pixel/μm)	1	0.993
f_y (pixel/μm)	1	0.992
(u_0, v_0) (pixel)	(600.0,450.0)	(600.3,450.2)
k $(\text{pixel})^{-2}$	0	0.0122
M	20	19.843
R	$\begin{bmatrix} 1.000 & 0 & 0 \\ 0 & 1.000 & 0 \\ 0 & 0 & 1.000 \end{bmatrix}$	$\begin{bmatrix} 0.999 & -0.045 & 0.021 \\ 0.02 & 1.000 & 0.013 \\ -0.014 & -0.05 & 0.999 \end{bmatrix}$
t	$\begin{bmatrix} 0 & 0 & 0 \end{bmatrix}^T$	$\begin{bmatrix} -2.5 & -2.7 & 0.2 \end{bmatrix}^T$
M'	1	0.9922
δ_x	0	−2.3718
δ_y	0	−2.7474

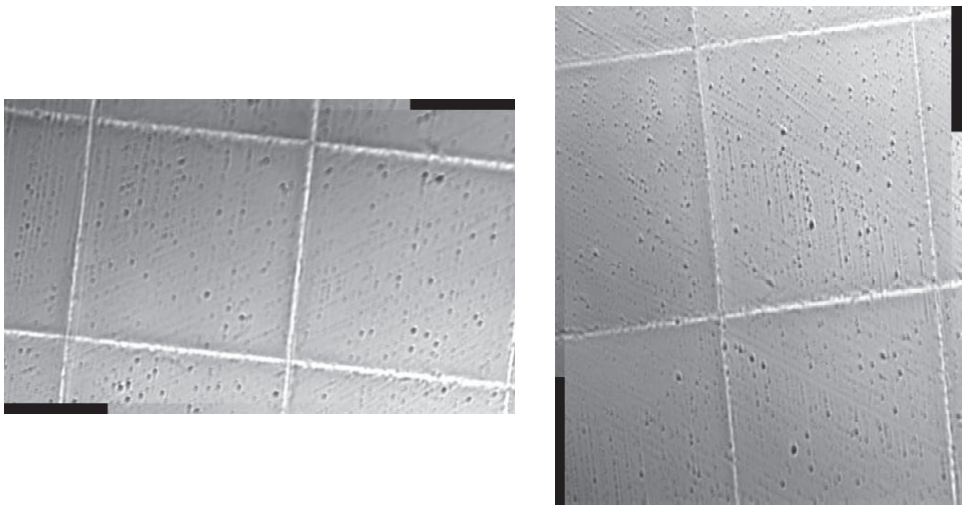

(**a**) (**b**)

Figure 11. Effect diagram of image stitching. (**a**) X-direction, (**b**) Y-direction.

Table 2. Results of error compensation coefficient θ.

Groups	Result of Error Compensation Coefficient θ		
	dy (pix)	dx (pix)	θ
1	−30	304	−5.636
2	−29	306	−5.414
3	−30	308	−5.563
4	−31	308	−5.747
5	−29	303	−5.467
6	−30	307	−5.581
7	−30	306	−5.599
8	−31	308	−5.747
9	−29	305	−5.431
10	−30	306	−5.599
average	-	-	−5.578

The mechanical displacement error obtained by image stitching is shown in Table 3.

Table 3. Results of Δx_+, Δx_-, Δy_+ and Δy_-.

Groups	Δx_+ (pix)	Δx_- (pix)	Δy_+ (pix)	Δy_- (pix)
1	−3	−4	−6	−4
2	−7	−6	−6	−5
3	−6	−8	−6	−5
4	−5	−8	−5	−7
5	−5	−6	−5	−6
6	−4	−5	−7	−5
7	−3	−7	−5	−4
8	−6	−5	−6	−5
9	−7	−4	−5	−6
10	−6	−5	−6	−5
average	−5.2	−5.8	−5.7	−5.2

Thus, the compensation coefficient of mechanical displacement error can be obtained.

$$\mu = -\begin{bmatrix} 4.2cos\beta_1 + 4.7sin\beta_1 \\ 4.8cos\beta_2 + 4.7sin\beta_2 \\ 4.8cos\beta_3 + 4.2sin\beta_3 \\ 4.2cos\beta_4 + 4.2sin\beta_4 \end{bmatrix} \tag{18}$$

According to Equations (17), the error compensation formula of the micromanipulation platform is further obtained as follows:

$$\begin{cases} X_1 = X_0 - 2.341 * \begin{bmatrix} 4.2cos\beta_1 + 4.7sin\beta_1 \\ 4.8cos\beta_2 + 4.7sin\beta_2 \\ 4.8cos\beta_3 + 4.2sin\beta_3 \\ 4.2cos\beta_4 + 4.2sin\beta_4 \end{bmatrix} * s) \\ Y_1 = Y_0 - 0.264 * \begin{bmatrix} 4.2cos\beta_1 + 4.7sin\beta_1 \\ 4.8cos\beta_2 + 4.7sin\beta_2 \\ 4.8cos\beta_3 + 4.2sin\beta_3 \\ 4.2cos\beta_4 + 4.2sin\beta_4 \end{bmatrix} * s) \end{cases} \tag{19}$$

5.2. Single Shot Error Test

In order to further measure the accuracy of the error compensation formula of the micromanipulation platform, the single shot error test was performed in this paper, and the center of the image was set as the origin. The test was started by clicking the mouse to randomly select points of interest other than the origin. Then, the relative distance size between the selected point of interest and the origin in the image coordinate system was calculated, and the corresponding step command was transferred to the microoperation platform, so that the point of interest displaces to the origin. Finally, the position error between the point of interest after displacing and the origin can be calculated as the single shot error, which is also the error value of the algorithm after compensation. The single shot error test interface is shown in Figure 12.

Based on the above-mentioned single shot error test rule, 50 groups of tests before and after the error compensation were carried out, respectively. The results for the absolute values of the difference in X-direction and Y-direction between the point of interest after displacing and the target position (the origin of the coordinate system in the diagram) are plotted in the coordinate system shown in each figure of Figure 13.

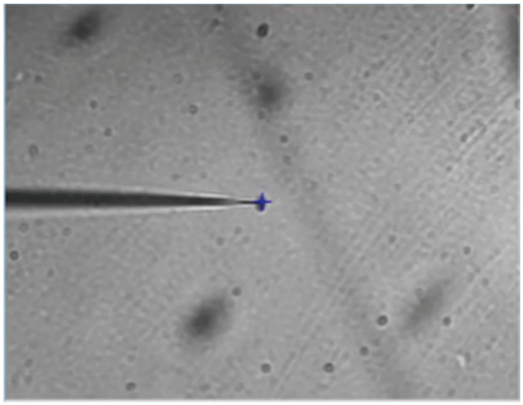

Figure 12. Single shot error test interface.

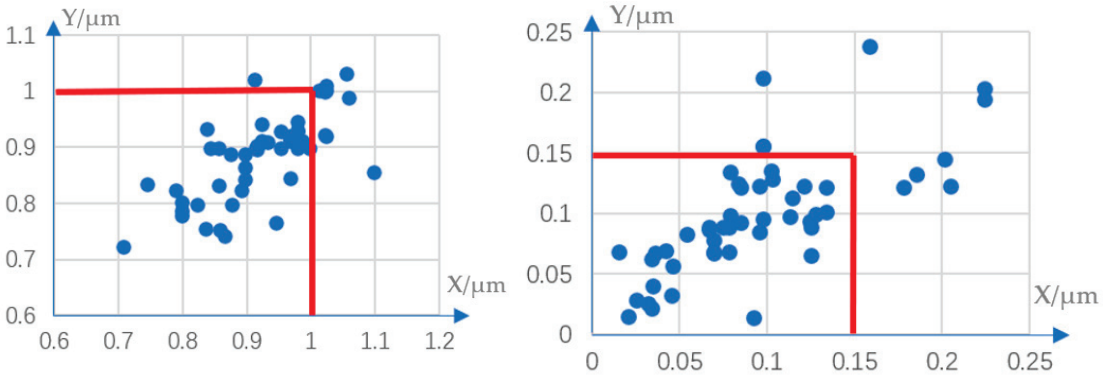

(**a**) (**b**)

Figure 13. Single shot error before and after compensation. (**a**) before, (**b**) after.

The comparison of the test results shows that the errors of the single shot error test before compensation are all above 0.7 μm, and some even as high as 1 μm. But after compensation, the error of the single shot error test is basically within 0.2 μm, the coverage rate is 82%, the maximum error is within 0.25 μm, and the errors are all within the acceptable range of biological operations.

5.3. Cumulative Error Test

The experimental analysis using the single shot error test has proved that the systematic error of the micromanipulation platform can be basically eliminated by the method in this paper. However, the single shot error test is only a test and analysis of the error compensation effect in a single displacement direction, which cannot reflect the cumulative error after multiple displacements. Therefore, in order to further measure the cumulative errors after the error compensation of the micromanipulation system, the following experiments were designed for analysis. First, image sample collection was carried out through the visual module using the image acquisition method shown in Figure 11. By adopting this method, if there is no systematic error, the first image and the last image of each group should line up over each other exactly in theory. Therefore, the image stitching error between the first and last image can be calculated as the cumulative error value.

According to the above methods, 50 groups of image samples before and after error compensation were collected. The classification of the 50 groups of experiments is shown in Table 4.

Table 4. Classification of the experiments.

Classification	Groups	The Step Length (μm)	Total Number of Images in a Group	Number of Displacement Images in One Direction	Total Step Length in One Direction (μm)
1	1–10	600	5	2	1800
2	11–20	600	9	3	2400
3	21–30	600	13	4	3000
4	31–40	600	17	5	3600
5	41–50	600	21	6	4200

According to the image stitching error of samples, the cumulative error distribution diagram was obtained as shown in Figure 14. Before compensation, the displacement error in the X-direction of the 50 groups was basically in the range of 1~1.4 μm, and which in the Y-direction was −2.9~−4.8 μm. After the error compensation, the displacement error in the X-direction of the 50 groups of samples was reduced to 0.01~0.06 μm, and that in the Y-direction was reduced to −0.02~−0.07 μm. In addition, through five kinds of experiments, it can be seen that as the total step length in each direction increased, the cumulative error in both the X-direction and the Y-direction also increased. However, before compensation, the overall X-direction error difference between classification 5 and classification 1 shown in Table 4 is about 0.4 μm, and the Y-direction error difference is about 1.9 μm. In comparison, the compensated X-direction error difference can be controlled within 0.05 μm, and the Y-direction can be controlled within 0.07 μm. For every 1000 μm of platform displacement, the cumulative error increases within 0.02 μm. It can be seen that through the error compensation, the cumulative error of the micromanipulation platform has been significantly reduced, so that its error value can meet the basic accuracy requirements of the micromanipulation.

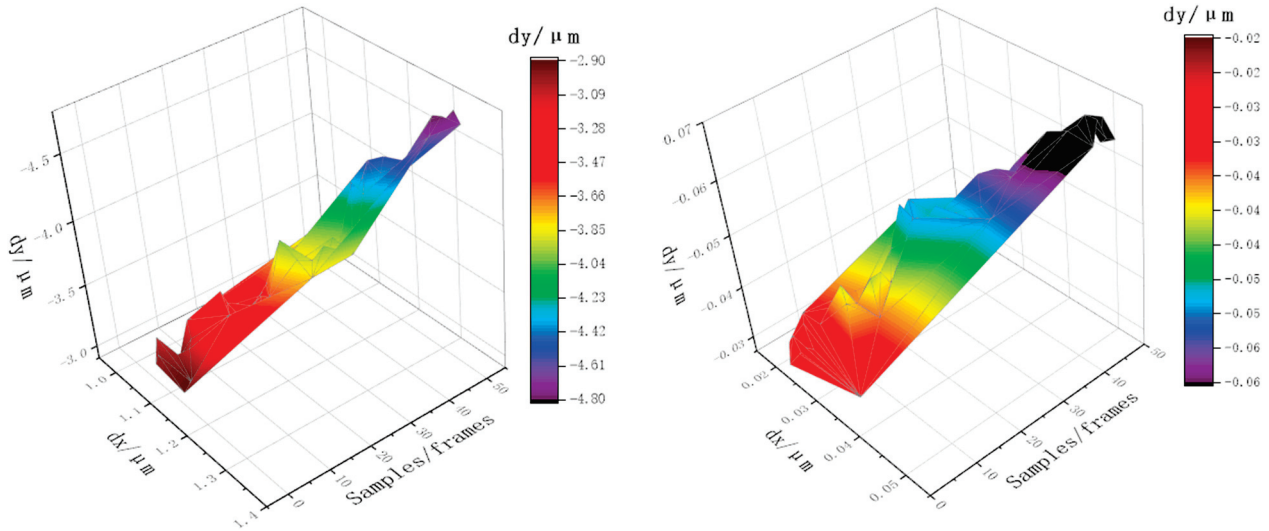

(**a**) (**b**)

Figure 14. Cumulative errors before and after compensation. (**a**) before, (**b**) after.

6. Conclusions

To reduce positioning errors in micromanipulation, modeling and compensation principles were proposed to deal with the error caused by the non-linear imaging distortion and mechanical errors such as camera installation error and the mechanical displacement error of the micromanipulation platform. The influences and derivation of those errors are analyzed first. Then, a novel and comprehensive error compensation model is established based on the compensation principle of each error. The distortion error compensation coef-

ficients were obtained by the Levenberg–Marquardt optimization algorithm combined with the deduced nonlinear imaging model. The mechanical error compensation coefficients were derived from the rigid-body translation technique and image stitching algorithm. Finally, to validate the error compensation model, single shot and cumulative error tests were designed. The experimental results show that the positioning accuracy of the micromanipulation system has been significantly improved. The systematic error of a single displacement can be controlled within 0.25 μm, while the cumulative displacement is controlled within 0.02 μm per 1000 μm, which basically meets the positioning requirements of cell microorganisms.

Author Contributions: Conceptualization, M.H.; software, M.H.; investigation, C.Y. and R.Z.; resources, Y.W.; writing—original draft preparation, M.H.; writing—review and editing, B.Y., Y.S. and C.D.; supervision, C.R. and Z.H. All authors have read and agreed to the published version of the manuscript.

Funding: This research was funded by the National Natural Science Foundation of China grant number 62273247, the Natural Science Foundation of the Jiangsu Higher Education Institutions of China grant number 20KJA460008.

Data Availability Statement: Not applicable.

Conflicts of Interest: The authors declare no conflict of interest.

References

1. Sariola, V.; Jääskeläinen, M.; Zhou, Q. Hybrid Microassembly Combining Robotics and Water Droplet Self-Alignment. *IEEE Trans. Robot.* **2010**, *26*, 965–977. [CrossRef]
2. Rodríguez, J.A.M. Microscope self-calibration based on micro laser line imaging and soft computing algorithms. *Opt. Lasers Eng.* **2018**, *105*, 75–85. [CrossRef]
3. Gorpas, D.S.; Politopoulos, K.; Yova, D. Development of a computer vision binocular system for non-contact small animal model skin cancer tumour imaging. In Proceedings of the SPIE Diffuse Optical Imaging of Tissue, Munich, Germany, 12–17 June 2007; pp. 6629–6656.
4. Su, L.; Zhang, H.; Wei, H.; Zhang, Z.; Yu, Y.; Si, G.; Zhang, X. Macro-to-micro positioning and auto focusing for fully automated single cell microinjection. *Microsyst. Technol.* **2021**, *27*, 11–21. [CrossRef]
5. Wang, Y.Z.; Geng, B.L.; Long, C. Contour extraction of a laser stripe located on a microscope image from a stereo light microscope. *Microsc. Res. Tech.* **2019**, *82*, 260–271. [CrossRef]
6. Wu, H.; Zhang, X.M.; Gan, J.Q.; Li, H.; Ge, P. Displacement measurement system for inverters using computer micro-vision. *Opt. Lasers Eng.* **2016**, *81*, 113–118. [CrossRef]
7. Sha, X.P.; Li, W.C.; Lv, X.Y.; Lv, J.T.; Li, Z.Q. Research on auto-focusing technology for micro vision system. *Optik* **2017**, *142*, 226–233. [CrossRef]
8. Tsai, R. A versatile camera calibration technique for high-accuracy 3D machine vision metrology using off-the-shelf TV cameras and lenses. *IEEE J. Robot Autom.* **1987**, *3*, 323–344. [CrossRef]
9. Korpelainen, V.; Seppä, J.; Lassila, A. Design and characterization of MIKES metrological atomic force microscope. *Precis. Eng.* **2010**, *34*, 735–744. [CrossRef]
10. Steger, C. A comprehensive and Versatile Camera Model for Cameras with Tilt Lenses. *Int. J. Comput. Vis.* **2017**, *123*, 121–159. [CrossRef]
11. Lee, K.H.; Kim, H.S.; Lee, S.J.; Choo, S.W.; Lee, S.M.; Nam, K.T. High precision hand-eye self-calibration for industrial robots. In Proceedings of the 2018 International Conference on Electronics, Information, and Communication (ICEIC), Honolulu, HI, USA, 24–27 January 2018.
12. Maraghechi, S.; Hoefnagels, J.P.; Peerlings, R.H.; Rokoš, O.; Geers, M.G. Correction of scanning electron microscope imaging artifacts in a novel digital image correlation framework. *Exp. Mech.* **2019**, *59*, 489–516. [CrossRef]
13. Lapshin, R. Drift-insensitive distributed calibration of probe microscope scanner in nanometer range: Real mode. *Appl. Surf. Sci.* **2019**, *470*, 1122–1129. [CrossRef]
14. Yothers, M.; Browder, A.; Bumm, A. Real-space post-processing correction of thermal drift and piezoelectric actuator nonlinearities in scanning tunneling microscope images. *Rev. Sci. Instrum.* **2017**, *88*, 013708. [CrossRef]
15. Liu, X.; Li, Z.; Zhong, K.; Chao, Y.; Miraldo, P.; Shi, Y. Generic distortion model for metrology under optical microscopes. *Opt. Laser Eng.* **2018**, *103*, 119–126. [CrossRef]
16. Yoneyama, S.; Kitagawa, A.; Kitamura, K.; Kikuta, H. In-plane displacement measurement using digital image correlation with lens distortion correction. *JSME Int.* **2006**, *49*, 458–467. [CrossRef]

17. Yoneyama, S.; Kikuta, H.; Kitagawa, A.; Kitamura, K. Lens distortion correction for digital image correlation by measuring rigid body displacement. *Opt. Eng.* **2006**, *45*, 023602. [CrossRef]
18. Pan, B.; Yu, L.; Wu, D.; Tang, L. Systematic errors in two-dimensional digital image correlation due to lens distortion. *Opt. Laser Eng.* **2013**, *51*, 140–147. [CrossRef]
19. Tiwari, V.; Sutton, M.A.; McNeill, S.R. Assessment of high speed imaging systems for 2D and 3D deformation measurements: Methodology development and validation. *Exp. Mech.* **2007**, *47*, 561–579. [CrossRef]
20. Koide, K.; Menegatti, E. General hand-eye calibration based on reprojection error minimization. *IEEE Robot. Autom. Lett.* **2019**, *4*, 1021–1028. [CrossRef]
21. Malti, A. Hand–eye calibration with epipolar constraints: Application to endoscopy. *Robot. Auton. Syst.* **2013**, *61*, 161–169. [CrossRef]
22. Hartley, R.; Kang, S.B. Parameter-free radial distortion correction with center of distortion estimation. *IEEE Trans. Pattern Anal. Mach. Intell.* **2007**, *29*, 1309–1321. [CrossRef]
23. Lowe, D.G. Distinctive image features from scale-invariant keypoints. *Int. J. Comput. Vis.* **2004**, *60*, 91–110. [CrossRef]
24. Fischler, M.A.; Bolles, R.C. Random sample consensus: A paradigm for model fitting with applications to image analysis and automated cartography. *Commun. ACM* **1981**, *24*, 381–395. [CrossRef]

micromachines

MDPI

Article

Process Chain for Ultra-Precision and High-Efficiency Manufacturing of Large-Aperture Silicon Carbide Aspheric Mirrors

Bo Zhong [1], Wei Wu [2], Jian Wang [1], Lian Zhou [1], Jing Hou [1], Baojian Ji [1], Wenhui Deng [1], Qiancai Wei [1], Chunjin Wang [2] and Qiao Xu [1,*]

[1] Laser Fusion Research Center, China Academy of Engineering Physics, Mianyang 621900, China; zhongbo_foerc@163.com (B.Z.)
[2] State Key Laboratory of Ultra-Precision Machining Technology, Department of Industrial and Systems Engineering, The Hong Kong Polytechnic University, Hung Hom, Hong Kong 999077, China
* Correspondence: xuq_rclf@163.com

Abstract: A large-aperture silicon carbide (SiC) aspheric mirror has the advantages of being light weight and having a high specific stiffness, which is the key component of a space optical system. However, SiC has the characteristics of high hardness and multi-component, which makes it difficult to realize efficient, high-precision, and low-defect processing. To solve this problem, a novel process chain combining ultra-precision shaping based on parallel grinding, rapid polishing with central fluid supply, and magnetorheological finishing (MRF) is proposed in this paper. The key technologies include the passivation and life prediction of the wheel in SiC ultra-precision grinding (UPG), the generation and suppression mechanism of pit defects on the SiC surface, deterministic and ultra-smooth polishing by MRF, and compensation interference detection of the high-order aspheric surface by a computer-generated hologram (CGH). The verification experiment was conducted on a Ø460 mm SiC aspheric mirror, whose initial surface shape error was 4.15 μm in peak-to-valley (PV) and a root-mean-square roughness (Rq) of 44.56 nm. After conducting the proposed process chain, a surface error of RMS 7.42 nm and a Rq of 0.33 nm were successfully obtained. Moreover, the whole processing cycle is only about 216 h, which sheds light on the mass production of large-aperture silicon carbide aspheric mirrors.

Keywords: silicon carbide; aspheric mirror; ultra-precision shaping; deterministic polishing; precision testing

Citation: Zhong, B.; Wu, W.; Wang, J.; Zhou, L.; Hou, J.; Ji, B.; Deng, W.; Wei, Q.; Wang, C.; Xu, Q. Process Chain for Ultra-Precision and High-Efficiency Manufacturing of Large-Aperture Silicon Carbide Aspheric Mirrors. *Micromachines* **2023**, *14*, 737. https://doi.org/10.3390/mi14040737

Academic Editor: Seung-bok Choi

Received: 14 March 2023
Revised: 21 March 2023
Accepted: 22 March 2023
Published: 27 March 2023

1. Introduction

With the continuous development of space science and technology, the performance of space optical systems has gradually improved, which has put forward increasingly strict requirements on the working band, imaging resolution, thermal stability, and system weight of optical systems, thereby promoting the development of optical systems in the large aperture, reflection, and lightweight directions [1,2]. Silicon carbide (SiC) material has the characteristics of low density, high modulus, high specific stiffness, high dimensional stability, and good thermal properties and has become the preferred material for the new generation of space reflectors [3]. Currently, large aperture silicon carbide (SiC) aspheric mirrors have been used in space optical remote sensing detection systems, high-resolution ground observation systems, space telescopes, and other space optical systems such as the SPICA infrared astronomical telescope [4], the ASTRO-F astronomical telescope [5], and the JWST space telescope [6].

However, due to its high hardness and complex composition compared to traditional optical glass, SiC material is difficult to process with high efficiency, precision, and an ultra-smooth surface [7]. In particular, the machining of large, lightweight, and aspherical SiC

mirrors is still a major challenge in the field of optical manufacturing, which involves high difficulty and long cycle times. In recent decades, extensive research has been conducted on SiC mirror optical processing worldwide, accumulating a wealth of experience and achieving some results. An American SSG company developed the ALI optical subsystem for NASA, with both its primary mirror and tertiary mirror being coated silicon RB-SiC reflecting mirrors. The surface form accuracy of the main mirror was as high as 0.035 λ (λ = 632.8 nm), and the surface roughness RMS was 1–1.5 nm [8]. SiC reflective mirrors prepared by the reaction sintering method developed by SSG [9] in the United States were applied to space telescopes such as the Miniature Infrared Camera and Spectrometer (MICAS) and the Advanced Land Imager (ALI), both of which are important parts of NASA's NMPDS-1 (New Millennium Program Deep Space-1) project. The PV value of the SiC reflective mirror was 0.7 λ and the RMS was 0.13 λ (λ = 632.8 nm). Litton Itek and HDOS (Hughes Danbury Optical Systems) in the United States have used reaction-sintered SiC material to produce lightweight mirrors. Breidenthal et al. from Litton Itek [10] used reaction-sintering to produce a SiC mirror with dimensions of 1125 mm × 825 mm. The surface shape accuracy after polishing was λ/20, and the surface roughness was 3 nm. ASTRIUM used ion beam figuring (IBF) technology to process SiC mirrors, and the upper-level reflecting mirror of the SOFIA telescope is an aspherical SiC mirror with an open back structure, with a diameter of 352 mm and a thickness of 40 mm. The surface shape accuracy after IBF is 39 nm RMS [11]. The S.I. Vavilov State Optical Institute in Russia developed a SiC-Si biphasic material called Sicar using the RB method. The institute used Sicar to manufacture honeycomb-structured mirrors with a diameter of 170 mm and closed-back mirrors with dimensions of 308 mm × 210 mm. The RMS surface accuracy achieved for these mirrors is between ±0.02 λ and ±0.04 λ [12]. Hang [13] employed a coupled process of CCOS and MRF techniques to modify the surface of an off-axis aspherical SiC mirror with a diameter of 540 mm. After 33 h of polishing, the modified layer improved the surface accuracy while also controlling the mid-to-high-frequency errors, resulting in a final PV value of 0.486 λ and an RMS of 0.018 λ. Wang et al. [14] conducted milling, grinding, rough polishing, and precision polishing on an octagonal off-axis silicon carbide aspheric surface with a dimension of 600 mm × 270 mm, whose RMS value is better than 1/50 λ. Zhang et al. [15] used precision milling technology to process a 900 mm × 660 mm off-axis SiC aspheric mirror, with a surface shape accuracy PV of 18.8 μm and a RMS 3.5 μm after processing. Zhang et al. [16] combined computer numerical control polishing, flexible chemical mechanical polishing, and IBF to process a 600 mm × 200 mm modified carbonized silicon flat mirror for a space camera. The RMS surface accuracy achieved was 0.014 λ (λ = 632.8 nm), and the surface roughness was 0.71 nm. Zhang et al. [17] employed computer-controlled optical surface processing (CCOS) technology to fabricate a 650 mm × 200 mm SiC mirror, achieving a higher polishing efficiency with CeO_2 polishing agent and the best optical surface using a SiO_2 polishing agent. The surface accuracy of the modified aspherical SiC mirror was 0.016 λ (RMS), and the surface roughness was 0.85 nm (RMS). Song et al. [18] improved the processing stability by optimizing the grinding tool, and after four rounds of about 40 h of processing (634 mm × 560 mm), SiC was off-axis spherical with a machining error of 239 λ that was improved to 115.32 λ. Zhang et al. [19] recently reported the strategies for the fabrication of the world's largest SiC aspheric mirror, with a size of Ø4.03 m. Extremely high surface accuracy of this mirror was obtained after the whole fabrication process, whose final surface figure error and roughness were 15.2 nm RMS and 0.8 nm RMS, respectively. While the production efficiency is still not high enough, which can take several months.

As mentioned above, processing methods based on advanced optical manufacturing technologies such as MRF and IBF have greatly improved the manufacturing accuracy of large-aperture silicon carbide optical components, and the ultimate manufacturing accuracy can reach the nanometer level. However, research on ultra-precision shaping and high-efficiency polishing of large-aperture silicon carbide aspherical mirrors is still limited, and the overall manufacturing efficiency is still relatively low. Currently, the entire process

of manufacturing large-aperture silicon carbide aspherical mirrors is still imperfect, for example, because of the low efficiency and precision of shaping [15,18], the low efficiency and insufficient stability of polishing [20,21], the tendency for the silicon carbide substrate to form concave pit defects [22,23], and the tendency for comet-like defects to form on the modified silicon surface [24], resulting in a low overall manufacturing efficiency (the manufacturing cycle of large-aperture silicon carbide aspherical mirrors can be several months or more) and an inability to meet the increasing demand for rapidly deploying space optical systems. This paper proposes an efficient manufacturing process chain combining ultra-precision grinding, rapid polishing, central fluid supply, and magnetorheological finishing (MRF), aiming at the high-precision and batch manufacturing requirements of large-aperture silicon carbide aspheric mirrors in space optical systems, and it has been experimentally proven to be effective in improving the manufacturing accuracy and efficiency of large-aperture silicon carbide aspheric mirrors.

2. Ultra-Precision Manufacturing Technology for Large Aperture Silicon Carbide Aspheric Mirrors

To meet the demand for batch manufacturing of aspherical surfaces, the research team proposed a strong laser-based ultra-precision manufacturing process with "ultra-precision and determinism" as its core [25]. After years of research and exploration, a relatively mature aspherical surface processing process has been developed, including aspherical surface grinding, and shaping, rapid polishing, and precision polishing stages. In the ultra-precision grinding and shaping stage, micro-level surface accuracy is directly obtained through parallel grinding technology while controlling defects. In the rapid polishing stage, high-efficiency polishing technology is used to remove grinding ripples and defects, quickly correct the surface shape to meet the requirements of precision polishing, and suppress processing defects. In the precision polishing stage, high-deterministic technology is used to correct the surface accuracy to nanometer-level accuracy, with surface roughness reaching sub-nanometer accuracy. The characteristics of this process route are based on the ideas of accuracy decomposition and efficiency matching. By combining ultra-precision shaping technology with various deterministic sub-aperture polishing technologies, the advantages of unit technology are fully utilized to achieve quantifiable control over the entire process in terms of accuracy, efficiency, and defects.

As a typical aspherical component, large-aperture silicon carbide aspheric mirrors are also applicable to the main process route mentioned above. However, the technical scheme needs to be optimized according to the characteristics of silicon carbide aspheric mirrors, such as hard materials and lightweight structures. In order to obtain the designed optical function, the asphericity of silicon carbide mirrors is generally large, and a structurally unstable layer is formed on the surface of the mirror blank during sintering, resulting in a large amount of material removal. Therefore, the most efficient way is to use ultra-precision grinding to remove the surface layer of the mirror blank and directly obtain a micrometer-level aspherical shape, which will greatly reduce the processing margin in the subsequent polishing stage. Aspherical grinding and shaping are necessary processing methods for the efficient manufacturing of silicon carbide mirrors, with the main focus on the blunting problem of the grinding wheel for hard materials. Due to the high hardness of silicon carbide materials, traditional polishing methods have low removal efficiency. Therefore, a small tool based on CNC polishing technology and bonded abrasives is proposed to quickly remove grinding ripples and defects. In addition, RB-SiC is a multiphase structure, and the traditional high-speed and high-pressure processing method can easily cause "pitting" defects due to thermal effects at the processing interface. Therefore, a small tool CNC polishing technology based on center-supplying liquid is proposed to suppress the thermal effects at the processing interface and thus suppress the defects on the silicon carbide substrate. In the final precision polishing stage, the modified silicon layer is the target of processing. The silicon surface layer is prone to comet-like defects, and a magnetorheological polishing technology with low stress and high determinism is used

for precise shaping. The ultra-precision manufacturing process for large-aperture silicon carbide aspheric mirrors is shown in Figure 1.

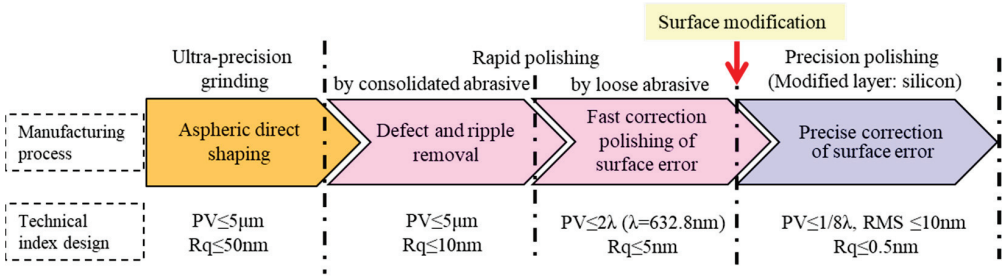

Figure 1. Design of an ultra-precision manufacturing process for large-aperture silicon carbide aspheric mirrors.

3. Key Technologies for Ultra-Precision Manufacturing of Large-Aperture Aspheric Silicon Carbide Mirrors

3.1. Ultra-Precision Grinding Wheel Blunting and Life Prediction

The Mohs hardness of silicon carbide material exceeds 9. During the grinding process of large-aperture silicon carbide mirrors, diamond grinding wheels are prone to wear and dullness [26], resulting in a sharp increase in grinding force, affecting the shaping accuracy of the component, and reducing the surface quality. To achieve ultra-precision shaping and processing of large-aperture aspherical silicon carbide components, it is necessary to clarify the wear failure mechanism of the diamond grinding wheel during the grinding process, establish the evolution law of grinding wheel wear, and quantitatively predict the service life of the grinding wheel.

(a) Wear and failure mechanisms of a silicon carbide grinding wheel.

Through experiments using arc-profiled diamond abrasive wheels for grinding silicon carbide materials, it was found that the silicon carbide material was removed through brittle fracture under the action of diamond abrasives. The surface morphology of the worn diamond abrasive wheel is shown in Figure 2. It can be seen that during the interaction between the diamond abrasives and the silicon carbide material, the micro-wear form of the wheel mainly exhibits abrasive wear. With the intensification of wear, the individual abrasive particles experience an increased reactive force from the component, gradually leading to the phenomenon of abrasive particle fracture and detachment. During the aspherical machining process using an arc-profiled grinding wheel along parallel machining tracks, since the component contact point with the grinding wheel surface is tangent to the point of processing, the entire arc-profiled grinding wheel section is involved in the grinding process and exhibits uniform wear, as shown in Figure 3, which depicts the macroscopic wear morphology of the silicon carbide grinding wheel. It can be seen that only slight changes in geometric dimensions occur in the wear area. Through experiments, it was found that the wear failure mechanism of the silicon carbide grinding wheel is mainly due to the micro-wear of the diamond abrasive grains. As the exposed edges of the abrasive particles become dulled, the grinding force increases, affecting both the surface roughness and the depth of crack defects on the component surface. It can also lead to significant elastic deformation of the lightweight silicon carbide component and affect the final processing accuracy.

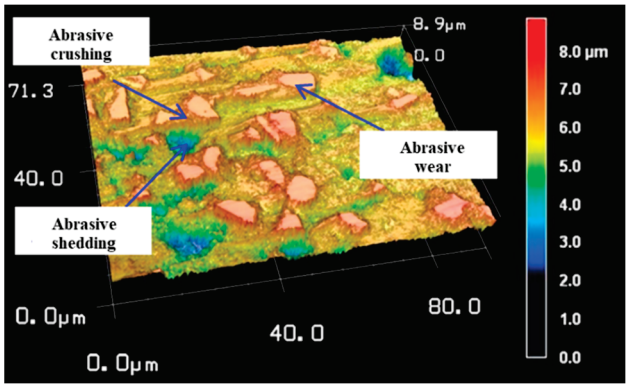

Figure 2. Microscopic wear of a silicon carbide grinding wheel.

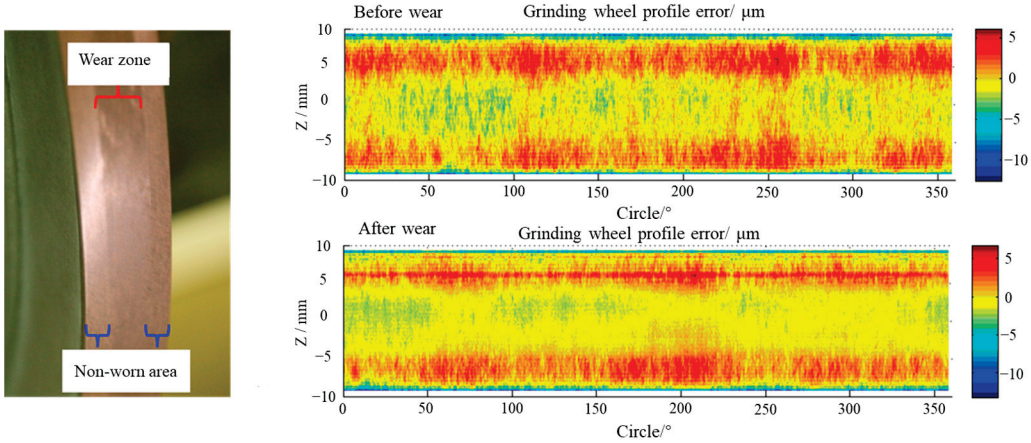

Figure 3. Macroscopic wear morphology of a silicon carbide grinding wheel.

(b) Wear pattern and life prediction of silicon carbide grinding wheels.

Grinding force is the key factor that affects the shaping accuracy and quality of SiC aspheric mirrors with lightweight structures. The grinding force is related to the abrasive wear characteristics of the grinding wheel and the working time (i.e., the degree of grinding wheel wear). Working time under fixed process conditions can also be equivalent to cumulative material removal. Therefore, there are two core process requirements for the high-precision forming and processing of large-aperture SiC mirrors. One is to improve the wear resistance of the grinding wheel, and the other is to clarify the cumulative removal amount within the wheel life and complete the machining within the service life of the wheel. In response to the above requirements, a diamond grinding wheel wear experiment was conducted in which common processing parameters were selected, namely the grinding wheel linear speed of 30 m/s, the feed speed of 5000 mm/min, and the grinding depth of 10 μm per time. The parameters of the diamond grinding wheel are 400 mm in diameter, 20 mm in width, and 8–12 μm in grain size. The electrolytic parameters of the grinding wheel are DC 24 V, current 2 A, and electrolytic time 30 min. Under the same process parameters, metal-bonded diamond grinding wheels with and without electrolytic sharpening were used to process silicon carbide components, and the grinding forces at different cumulative removal volumes of silicon carbide materials were measured simultaneously, as shown in Figure 4. From the experimental results, it can be seen that as the cumulative volume of material removal increases, the grinding force gradually increases, and the grinding wheel wear gradually intensifies. For the diamond grinding wheel that has undergone electrolytic sharpening, the microprotrusions of the diamond abrasive particles are effective, and the abrasive particle sharpness is high. The grinding force at the same cumulative volume of material removal is significantly smaller than that of the grinding wheel without electrolytic sharpening, and the growth rate is also significantly

lower than that of the electrolytic wheel. After the arc-shaped diamond grinding wheel is dressed, further electrolytic sharpening is performed to selectively remove the metal binder on the surface of the grinding wheel and expose the diamond abrasive particles. This can greatly improve the processing performance of the grinding wheel and reduce the grinding force. Using the grinding force fitting model obtained from the experiment and the cumulative volume of material removal as the quantified evaluation index of grinding wheel wear, the grinding force of the same type of diamond grinding wheel at different machining stages under the same grinding parameters can be accurately predicted.

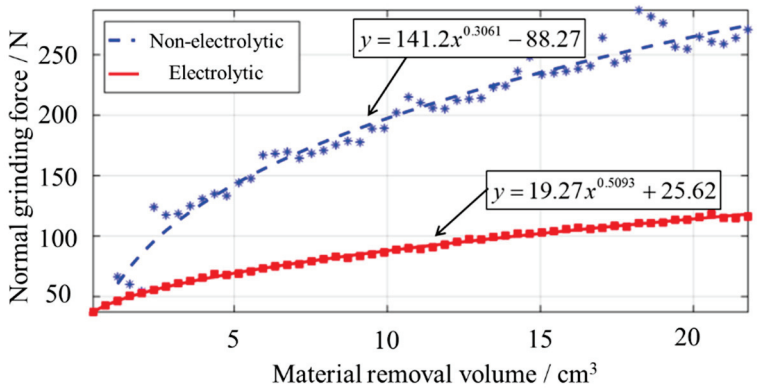

Figure 4. Evolution of grinding force during grinding of silicon carbide material.

This text describes the experiment and processing of aspherical silicon carbide mirrors for lightweight structures, combined with non-contact displacement sensors to measure the force deformation at different positions on the surface of the component. The experiment found that when a normal force of 70 N is applied at the central position of the lightweight hole of the silicon carbide mirror, the deformation at that position has reached about 1μm, which has already affected the processing accuracy of the component. Therefore, to ensure the processing accuracy of the component, it is necessary to ensure that the normal grinding force during the entire grinding process does not exceed 70 N. Based on the evolution law of the silicon carbide material grinding wheel wear in Figure 4, on the one hand, an electrolytically trimmed diamond grinding wheel is selected for grinding, and on the other hand, the cumulative volume of material removed is controlled not to exceed 5.13 cm^3 as the criteria for grinding wheel life. The above research shows that electrolytic grinding wheels have stronger wear resistance, which can inhibit the rapid increase in grinding force, thereby ensuring the micron-level shaping accuracy of large-aperture SiC aspherical surfaces during long-term processing (within the lifetime of the electrolytic grinding wheel).

3.2. Low-Defect Rapid Polishing

(a) Efficiency of center-feed rapid polishing

In order to improve the efficiency of aspherical polishing, a more stable polishing mechanism was designed in the early stages to significantly increase the rotational speed and polishing pressure of the polishing tool (the rotational speed was increased from 200 rpm to 3000 rpm, and the pressure was increased from 20 N to 120 N) to improve efficiency. However, experiments found that increasing the process parameters did not result in efficiency improvements consistent with the theory. It was speculated that in the high-speed and high-pressure machining process, it was difficult for the polishing liquid to enter the bottom of the polishing tool, resulting in fewer polishing particles participating in the grinding and polishing, which affected the polishing efficiency. In addition, because it was difficult for the polishing liquid to enter the central area of the bottom of the tool, the heat generated by the friction between the tool and the component could not be taken away, increasing the temperature in the central area of the bottom of the tool, accelerating tool wear, and further affecting the stability of material removal. To address these issues, a

center-feed CNC polishing device was introduced [27], as shown in Figure 5. The device includes a public rotation motor, a hollow cylinder, a hydraulic display gauge, and an internally fed polishing tool. The upper end of the hollow rotating shaft in the cylinder is connected to the polishing liquid injection pipe through a rotating slip ring. When the hollow rotating shaft rotates at high speed, the polishing liquid injection pipe does not rotate. The lower end of the hollow rotating shaft is connected to the hollow polishing disc. The public rotation motor drives the polishing disc to move in a planetary motion. The polishing liquid enters the polishing contact area through the injection pipe, the hollow shaft, and the hollow polishing disc, which is conducive to updating the polishing liquid and taking away the machining heat.

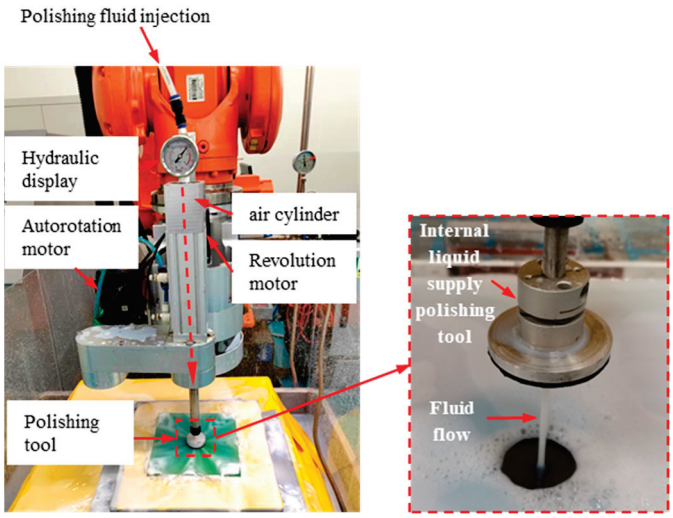

Figure 5. Center liquid supply small tool polishing device.

To obtain different removal characteristics, the polishing disc mold layer uses sintered abrasive, polyurethane, and asphalt, as shown in Figure 6. The above three polishing molds with central supply polishing tools were used for spot experiments on silicon carbide test substrates. Other experimental parameters remained the same, with a tool diameter of Ø50 mm, a diamond abrasive particle size of 3 μm, a solution concentration of 1%, a polishing pressure of 45 N, a tool speed of 1000 rpm, and a processing time of 10 s. After the experiment, the polished spot was collected using a flat interferometer, and the volume removal efficiency was calculated as shown in Figure 7.

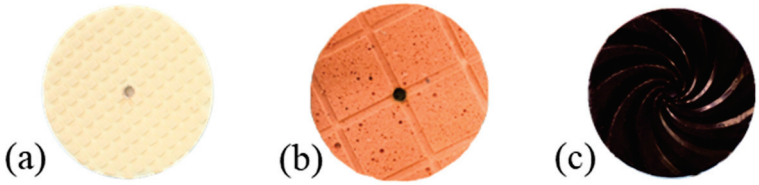

Figure 6. Three types of polishing tools. (**a**) Consolidated abrasive; (**b**) polyurethane; (**c**) asphalt.

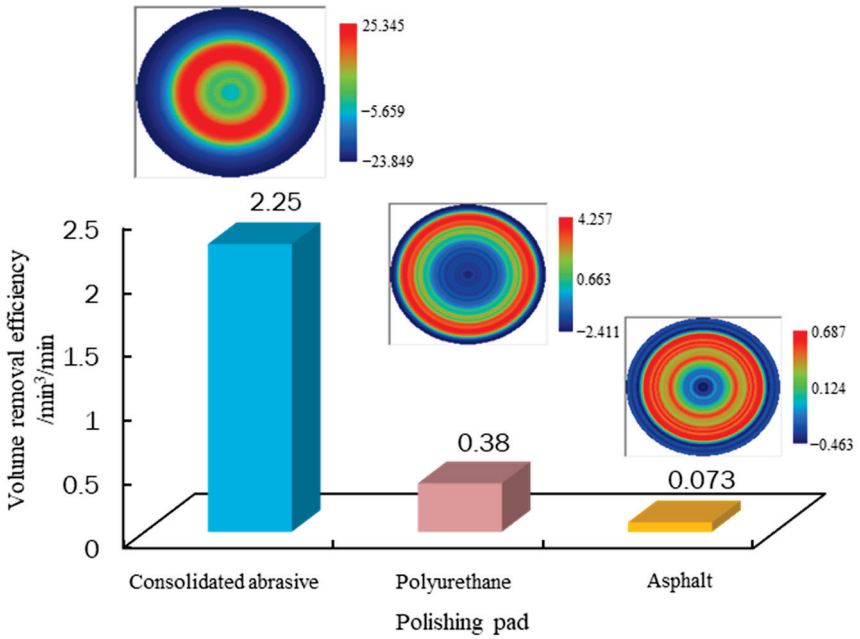

Figure 7. Comparison of the removal efficiency of different polishing tools.

According to Figure 7, the volume removal rates of the three polishing models, namely sintered abrasive, polyurethane, and asphalt, are 2.25 mm^3/min, 0.38 mm^3/min, and 0.073 mm^3/min, respectively. It can be seen that the sintered abrasive has the highest removal efficiency in processing SiC materials, which is six times that of polyurethane and thirty times that of asphalt. To meet the process requirements of "efficient removal of grinding defects and ripples", "rapid shape correction", and "quick improvement of smoothness" in the rapid polishing stage, a consolidated abrasive tool is used to quickly remove ripples and defects, a polyurethane tool is used for rapid shape correction and the removal of primary knife marks; and an asphalt tool is used for further improving the surface roughness. Based on the processing characteristics of three-layer materials, a combination of polishing tools with different layer materials can fully meet the requirements of the rapid polishing stage, while the consolidated abrasive tool greatly improves processing efficiency.

(b) Generation and suppression mechanism of "pit" defects in SiC

In the traditional high-speed and high-pressure rapid polishing process of SiC components, it was found that the surface of SiC components is prone to "white spot" defects, which can expand during subsequent processing, affecting processing accuracy and surface quality. To solve this problem, a comprehensive orthogonal comparison experiment of rapid polishing of SiC components was conducted under internal and external fluid supply conditions. Two different fluid supply methods were used in the experiment: internal and external fluid supply, with the remaining parameters including a tool diameter of Ø50 mm, the diamond abrasive particle size of 3 μm, a solution concentration of 1%, air pressure parameters of 0.15, 0.2, and 0.25 MPa, and rotational speed parameters of 500, 1000, and 1500 rpm. In the experiment, an infrared imaging camera was used to detect the temperature of the polishing area. After the experiment, the defect density of the components under different parameters was statistically analyzed, the surface defect characteristics of the components were observed under a microscope, and the surface roughness of the components was detected using a white light interferometer. The experimental results are shown in Figures 8–10.

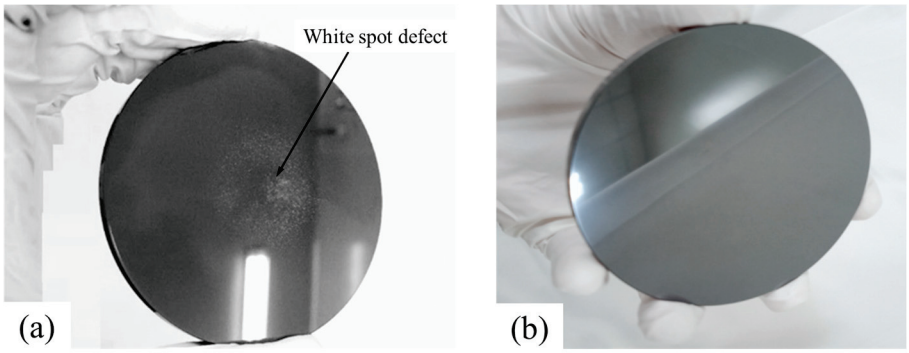

Figure 8. Comparison chart of surface quality with different liquid supply methods. (**a**) External liquid supply; (**b**) internal liquid supply.

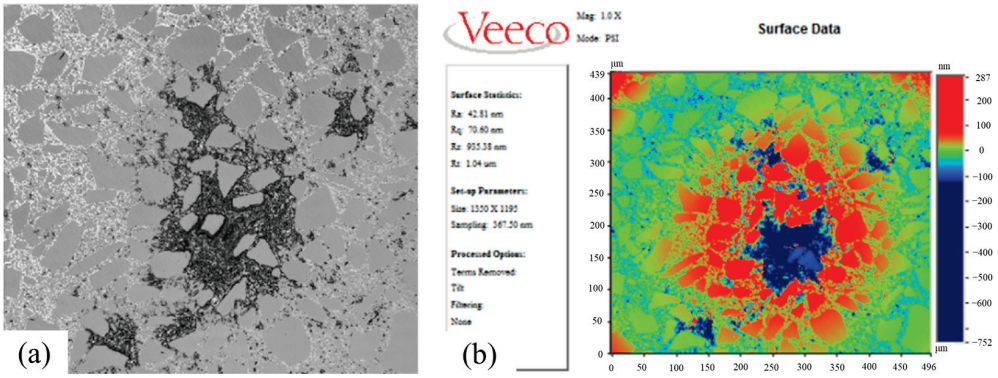

Figure 9. Microscopic imaging of the surface of externally supplied machining components. (**a**) Micrograph; (**b**) roughness.

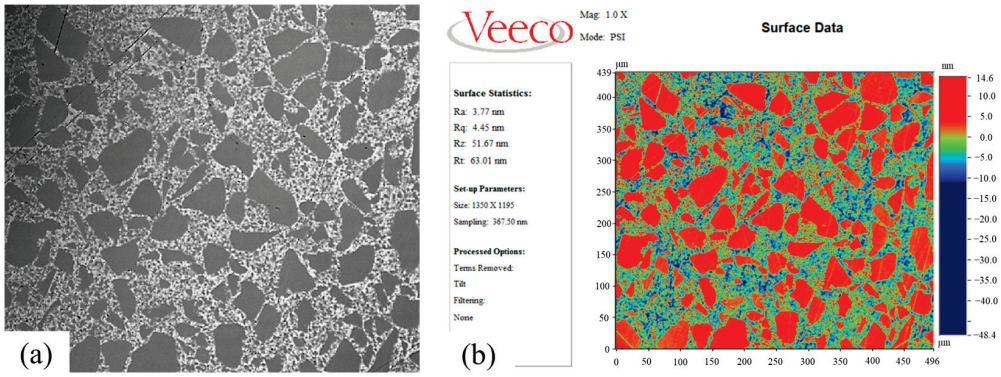

Figure 10. Microscopic imaging of the surface of internally supplied machining components. (**a**) Micrograph; (**b**) roughness.

The experimental results showed that the surface defects of SiC under external fluid supply conditions were related to the process parameters, with higher rotational speeds and air pressures resulting in higher defect densities on the surface of SiC. However, under central fluid supply conditions, there were no surface defects on SiC under all process parameters. It was therefore clear that a central fluid supply can greatly suppress SiC processing defects. Figure 8 shows a comparison of surface quality under different fluid supply methods, where there are "white spot" defects in the center of the component under external fluid supply conditions but no defects on the surface of the component under internal fluid supply conditions.

Figures 9 and 10 are microscopic images of the surface of SiC components processed using two different liquid supply methods, internal and external. RB-SiC is composed

of silicon carbide particles and a binder (silicon), and when the surface is defect-free, the silicon carbide and binder are randomly distributed, as shown in Figure 10a. When defects appear on the surface of the silicon carbide, they exhibit a "binder erosion" characteristic, as shown in Figure 9a. Furthermore, comparing the surface roughness of the silicon carbide, it is found that the "white spots" defects are "pits", which significantly increase the roughness (Rq 70.6 nm), as shown in Figure 9b, whereas the normal area without defects has excellent roughness results (Rq 4.45 nm), as shown in Figure 10b.

From Figure 11, it can be seen that under external liquid supply conditions, there is a significant amount of machining heat at the contact interface between the tool and the component (a temperature of 24.6 °C), and the temperature at the contact center may be even higher. Under internal liquid supply conditions, there is no significant temperature rise at the contact interface between the tool and the component, and the machining area is forcibly cooled by the low-temperature polishing liquid (temperature of 16.8 °C). This indicates that under high-speed and high-pressure conditions, it is difficult to polish the center region using the external liquid supply method since the heat generated during machining cannot be effectively removed. In contrast, with an internal liquid supply, the polishing liquid is updated promptly, and the polishing heat can be carried away.

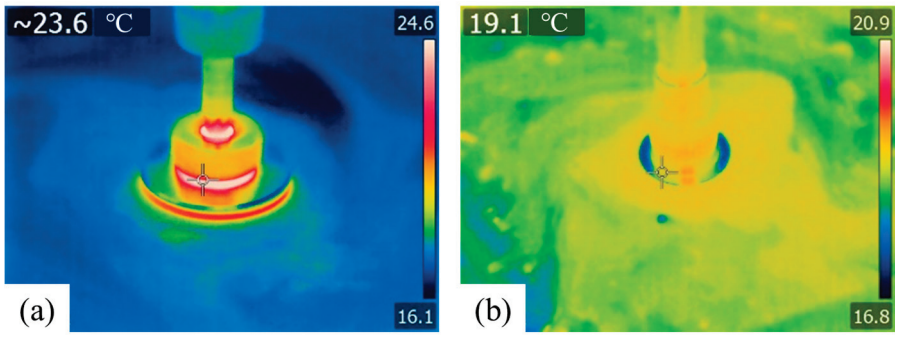

Figure 11. Thermal imaging of machining with different liquid supply methods. (**a**) External liquid supply; (**b**) internal liquid supply.

In summary, the temperature rise in the machining area is the primary cause of surface defects on SiC, and it has been demonstrated that center supply polishing can significantly suppress machining heat, thereby achieving defect-free and excellent surface roughness.

3.3. Magnetorheological Precision Polishing and Ultra-Smooth Surfaces

The magnetorheological polishing process has high determinism, manifested in the fact that different sizes and highly stable flexible polishing spots can be obtained by selecting process parameters, making it feasible to use magnetorheological polishing to process high-precision silicon layer mirrors. In the precision polishing stage, different sizes of polishing spots can be obtained by controlling the process parameters of the magnetorheological polishing process, including immersion depth and polishing fluid flow rate, to achieve high-precision matching with different frequency band errors on the surface of the component and to accurately correct the surface shape of the component. Figures 12 and 13 show real photos and results of magnetorheological polishing.

After completing the precision polishing, the surface shape of the component has reached the required accuracy, but the surface roughness is still insufficient. The processed mirror then enters the next process, which is ultra-smooth machining using magneto-rheological finishing (MRF). By optimizing the MRF process parameters, the processing force acting on the component can be reduced, and the surface smoothness can be improved. Aiming to achieve low-force machining, a simulation analysis was conducted to control the contact pressure between the component and the polishing spot by using a controlled variables approach for immersion depth, rotational speed, and water content, which are commonly used process parameters. The immersion depth typically ranges from 0.2 mm

to 0.4 mm, and the rotational speed ranges from 80 rpm to 100 rpm. The water content that affects the viscosity of the polishing fluid is usually controlled within the range of 13–17%, and water content values of 13%, 15%, and 17% were selected for the simulation calculation within the controllable range. The influence curve of different process parameters (i.e., immersion depth, rotation speed, water content) on contact pressure are shown in Figure 14.

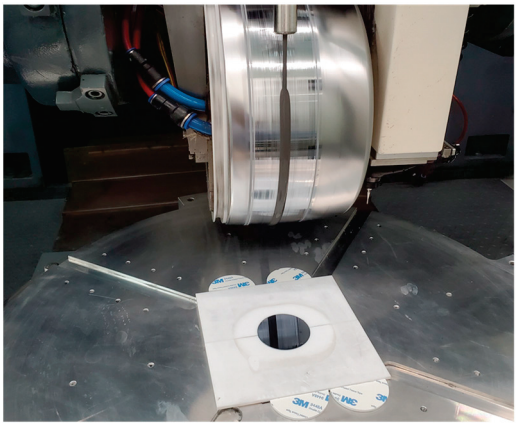

Figure 12. Experimental photo of magnetorheological polishing.

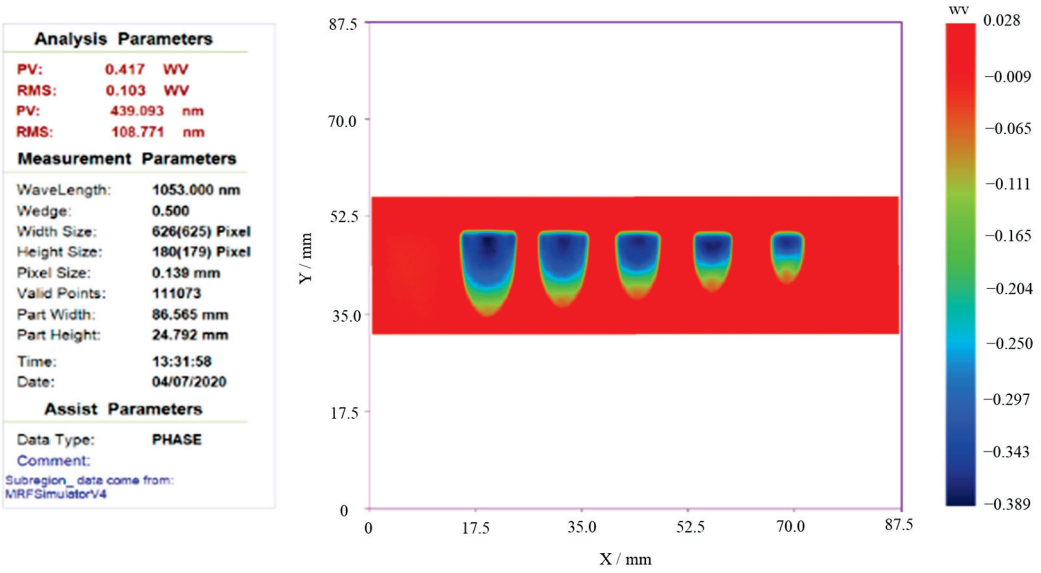

Figure 13. MRF spots with different scales.

As shown in the above figure, to obtain a smaller contact pressure during the polishing process, it is necessary to select a lower rotational speed and immersion depth, as well as a higher water content within the controllable range. Meanwhile, changing the particle size of the polishing fluid can reduce the impact force of the fluid on the element and improve the surface quality of the element. In the process, a polishing fluid with a particle size of 50 nm is used for ultra-smooth polishing of element surfaces, which achieves rapid convergence of surface roughness while avoiding damage to the well-polished surface shape.

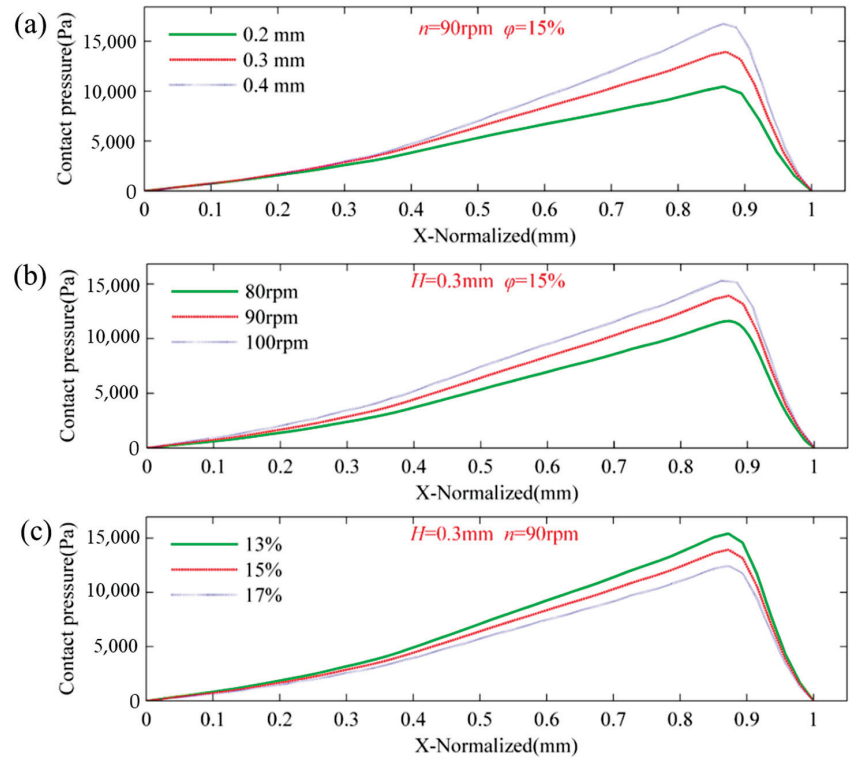

Figure 14. The influence curve of different process parameters on contact pressure. (**a**) Immersion depth; (**b**) rotation speed; (**c**) water content.

3.4. Compensation of High-Order Surface in Interferometric Measurement Using CGH

To meet the high-precision testing requirements of silicon carbide aspherical mirrors, a diffraction compensation method was used to complete the compensation design of a Ø460 mm silicon carbide aspherical element. The equation of Ø460 mm silicon carbide aspheric surface is shown in Formula 1. In this formula, $c = -1/R_0$, the vertex radius R_0 is 5378.6 mm and the cone coefficient k is 6.963. α_i is the high-order aspheric coefficient; $\alpha_1 = 0$, $\alpha_2 = 3.737 \times 10^{-11}$, and $\alpha_3 = 4.226 \times 10^{-17}$.

$$z(x,y) = \frac{c(x^2+y^2)}{1+\sqrt{1-(1+k)c^2(x^2+y^2)}} + \sum_{i=1}^{n} \alpha_i (x^2+y^2)^i \quad (1)$$

Considering the characteristics of the element, such as its long focal length and lack of off-axis, a defocused carrier frequency method was used to design the computer-generated hologram (CGH) for shape measurement, and the phase parameters of the compensating element were optimized based on a circular symmetrical diffraction surface. The ideal design wavefront was obtained with a design wavefront PV of 0.0003 λ (λ = 632.8 nm), as shown in Figure 15.

The basic design and area distribution of the compensation plate are shown in Figure 16. The size of the element substrate is Ø100 mm × 10 mm, with an etching ratio of 1:1 and etching depths of 484 nm for level 1 and 152 nm for level 3. A certain ring area is reserved at the edge for mechanical clamping. The central region is the main compensation area for transmissive diffraction (radius 0–35 mm), mainly used for compensating the asphericity of the test element, with a design minimum period of ~14.18 μm. The edge annular area (radius 35–45 mm) is designed for level 3 reflection diffraction; considering the low diffraction efficiency, a high reflectivity film is deposited, and the minimum etching period is ~8.64 μm.

Microscopic inspection equipment combined with precision translation stages was used to evaluate the etching distortion error. Samples were taken at intervals along the horizontal and vertical radii and compared to the corresponding theoretical linewidth data

from software simulations. The etching error of the component was then evaluated using a multi-region etch line error analysis. A binary phase-type CGH was used in the design, and the etching step depth was measured using an optical profiler. The etching step depth error was statistically analyzed by continuous sampling at 3 mm intervals. Due to the use of a first-order phase-type diffraction design, the influence of etching aspect ratio error on wavefront error can be neglected. According to the current level of etching technology, other errors such as mask encoding errors and amplitude errors caused by etching are also negligible. The overall fabrication accuracy of the diffraction compensating plate meets the design requirements.

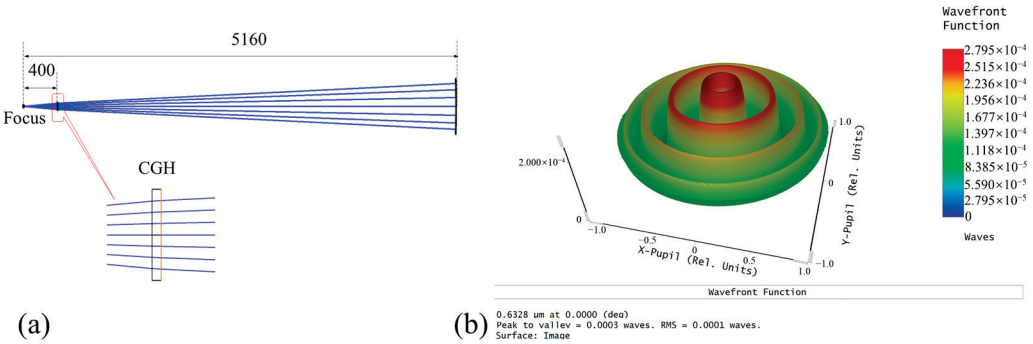

Figure 15. Design of the inspection optical path. (**a**) CGH compensator; (**b**) design wavefront.

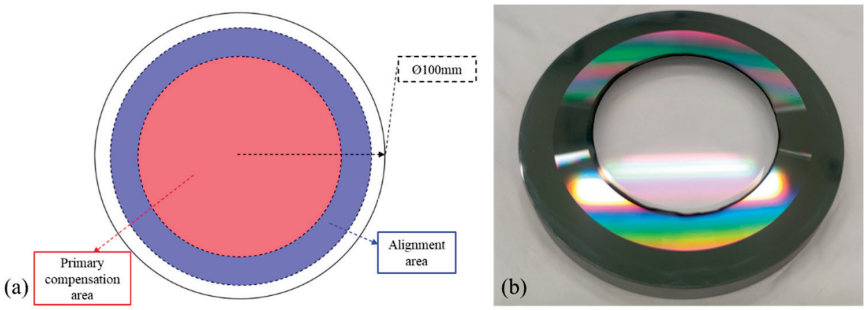

Figure 16. Design and fabrication of CGH compensation. (**a**) CGH design; (**b**) compensator.

Based on a computational holographic plate, a detection optical path for compensating the surface shape of a large-aperture SiC reflective mirror element was built. Using the CGH ring to assist in adjusting the region, the focus of the detection optical path and the precise alignment between the compensating element were realized, which ensured the high-precision adjustment of the detection optical path and the high-precision surface shape detection of the element, as shown in Figure 17.

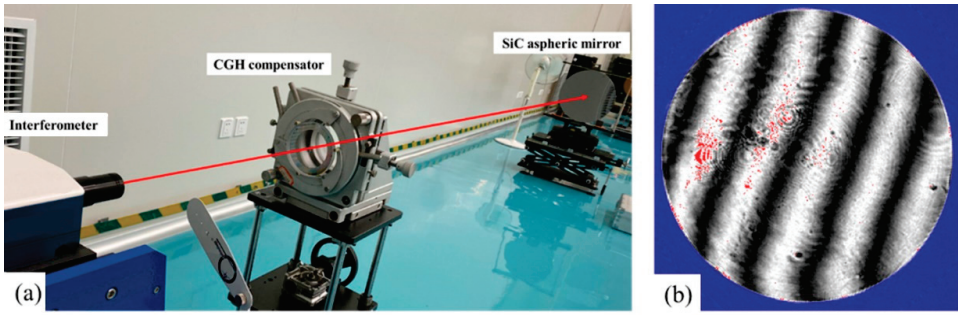

Figure 17. Optical path and interference fringe. (**a**) The optical path of measurement; (**b**) fringe.

4. Verification of the Process Chain on a Ø460 SiC Aspheric Mirror

Based on the above technical scheme and key technologies, the entire process of ultra-precision machining and inspection was carried out for a Ø460 mm carbonized silicon aspheric reflector.

4.1. Ultra-Precision Grinding

According to the technical process, the Ø460 mm SiC aspherical mirror was the first ultra-precision part ground using an aspherical parallel grinding technique on an ultra-precision grinding machine. The diamond grinding wheel with a controlled arc section profile was used to strictly follow the aspherical shape, and the wheel was moved in a raster envelope motion along the surface of the component. The trajectory of different contact points on the outer circular contour surface of the wheel formed an aspherical envelope surface on the workpiece, completing the entire aspherical surface shaping process, as shown in Figure 18. In the shaping process, a non-contact in situ detection method was combined to control the non-contact displacement sensor to move along the surface of the component according to the aspherical shape and obtain the aspherical contour error. The three-dimensional surface shape error of the aspherical surface was determined by data postprocessing for deterministic compensation grinding. After 32 h of grinding, the final surface shape of the component converged on a PV of 4.15 μm, as shown in Figure 19. After grinding, the surface roughness of the aspherical surface was measured using a roughness tester, and the result was 44.56 nm, as shown in Figure 20.

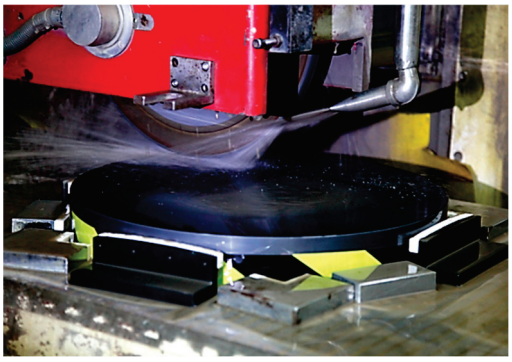

Figure 18. Photos of the ultra-precision grinding process.

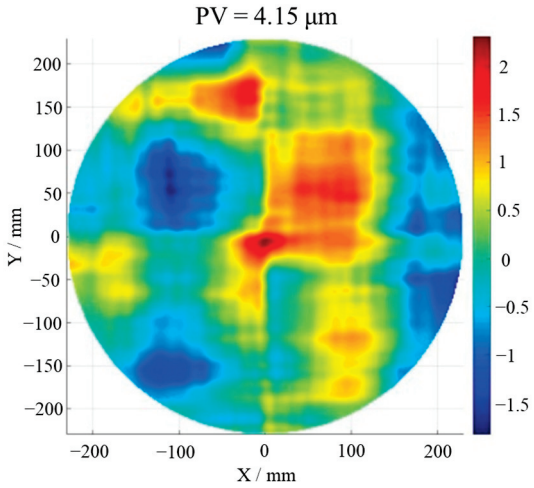

Figure 19. Figure of SiC aspheric mirror after grinding.

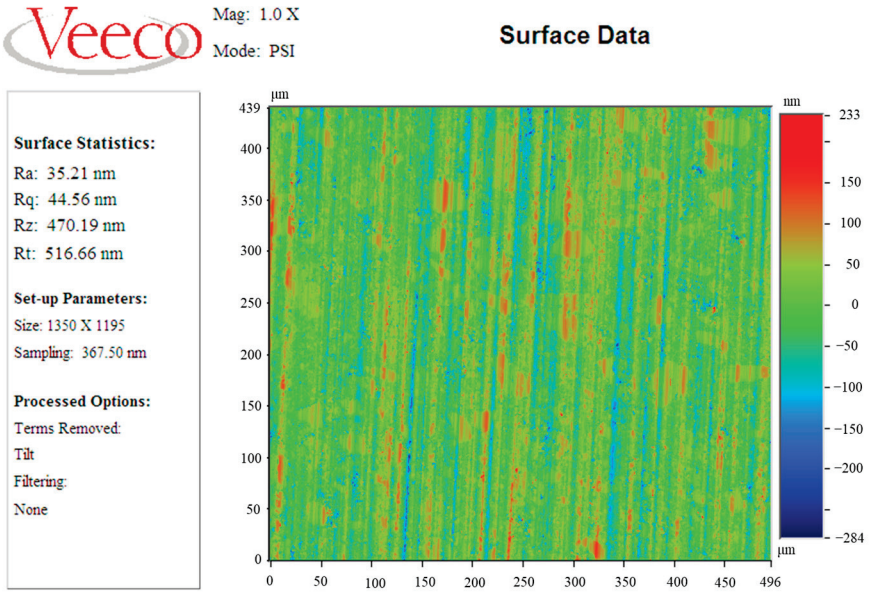

Figure 20. Roughness of SiC aspheric mirror after grinding.

4.2. Center-Supply Fluid Rapid Polishing

After non-axisymmetric grinding, a combination of fixed abrasive and loose abrasive tools based on robot-centered fluid supply technology was used for shape-preserving rapid polishing of the ultra-precision ground non-axisymmetric component, removing surface defects and ripples from the grinding process, removing depths greater than 10 µm, and then quickly shaping to the precision polishing entrance accuracy. First, a 4 µm fixed abrasive polishing disk was used to quickly remove grinding ripples, followed by a 3µm loose abrasive diamond slurry and asphalt disk to further smooth residual ripples from the previous step, resulting in a surface that can be entered into interferometric testing. Next, a 3 µm loose abrasive diamond slurry and polyurethane disk were used to shape the surface. The process of robot-centered fluid supply for small tool rapid polishing is shown in Figure 21.

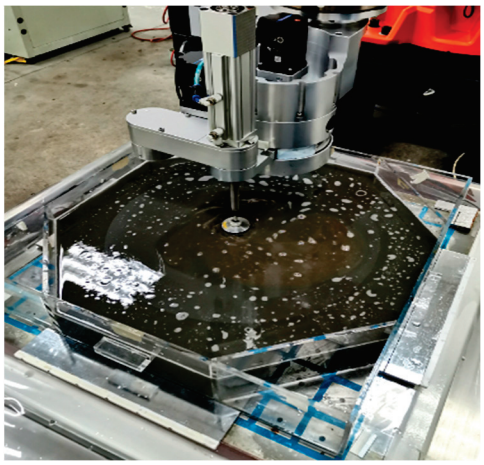

Figure 21. Photos of the rapid polishing process with center fluid supply.

During the polishing process, a high-order surface mirror CGH compensation interferometric detection optical path (as shown in Figure 17) was constructed using a spherical interferometer and a CGH compensator for aspherical surface shape detection, which guided subsequent surface shape correction. After approximately 160 h of rapid polishing with a center supply liquid tool, the surface shape error was significantly improved, with a

PV of 1.78 λ and an Rq surface roughness of 3.91 nm for the aspherical mirror, as shown in Figures 22 and 23.

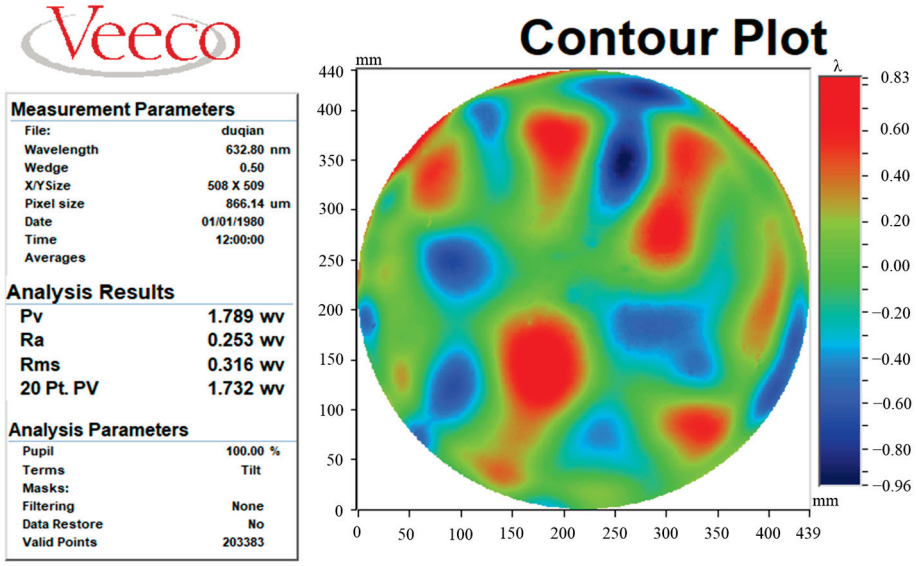

Figure 22. Surface form error of the SiC aspheric mirror after CCOS.

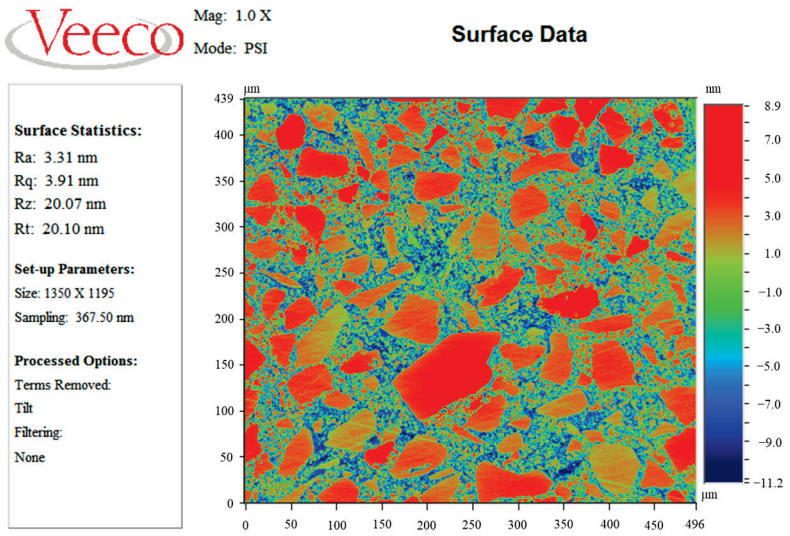

Figure 23. Roughness of the SiC aspheric mirror after CCOS.

4.3. Deterministic and Ultra-Smooth Polishing by MRF

After the rapid polishing, the surface of the element was modified by silicon plating with a thickness of about 15 μm, and the surface shape was kept unchanged. Then, the magneto-rheological polishing technology was used for aspherical element shape correction and ultra-smooth polishing, as shown in Figure 24. Based on the basic research of magneto-rheological processing of silicon materials, the magneto-rheological removal function control and ultra-smooth surface polishing technologies were adopted. After three cycles of about 24 h of magnetorheological finishing, the high-precision and high-quality processing of the silicon-plated surface of the Φ460 mm aspherical reflector was achieved. The surface shape was PV 82.16 nm, RMS 7.42 nm, and roughness Rq 0.33 nm, as shown in Figure 25. The experimental results indicate that magneto-rheological polishing not only has a strong surface shape correction ability but also can achieve ultra-smooth polishing of silicon surfaces, thus realizing high-precision and ultra-smooth precision polishing of SiC aspheric mirrors.

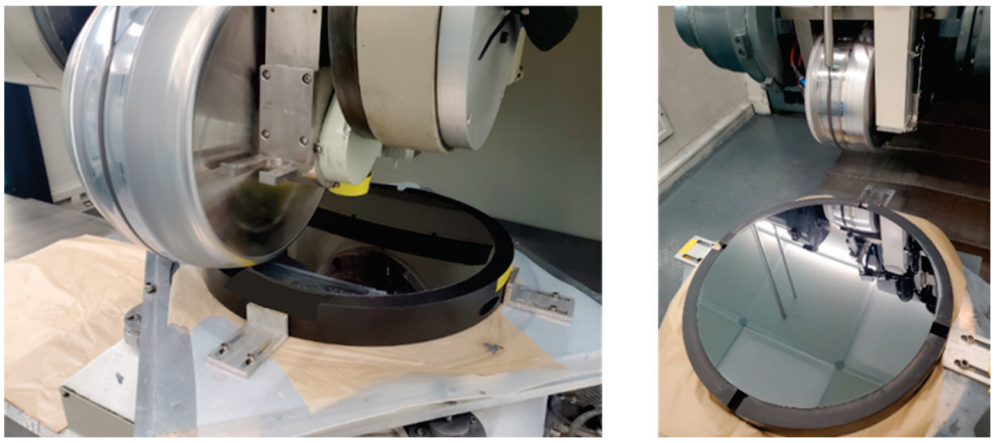

Figure 24. Photographs of the MRF process.

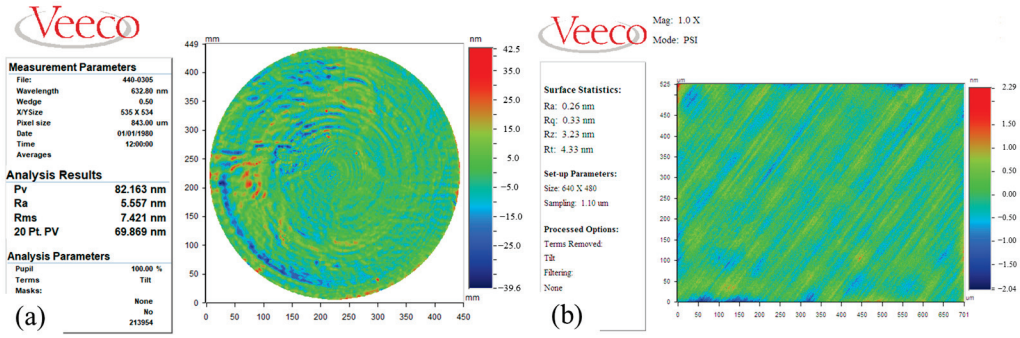

Figure 25. Result of the SiC aspheric mirror after MRF. (**a**) Wavefront; (**b**) surface roughness.

5. Conclusions

This paper proposes an efficient manufacturing process chain for silicon carbide aspheric mirrors that combines ultra-precision grinding, rapid polishing, central fluid supply, and magnetorheological finishing (MRF). This process chain was validated on a Ø460 silicon carbide aspherical mirror with an initial surface shape error for PV of 4.15 μm and a roughness of Rq of 44.56 nm. The surface error of RMS 7.42 nm and roughness Rq of 0.33 nm were successfully obtained, with a total manufacturing cycle of only 216 h, which indicates the feasibility of the proposed process chain for the high-precision and high-efficiency manufacturing of the large-aperture SiC aspheric mirrors. The manufacturing cycle of the proposed process chain would be an effective method for the mass production of large-aperture SiC aspheric mirrors used in space optical remote sensing detection systems, high-resolution ground observation systems, space telescopes, etc. In addition, to further improve the fabrication efficiency of SiC mirrors, manufacturing techniques such as laser-assistance [28,29] and vibration-assistance [30,31] may be integrated into current process chains in the future.

Author Contributions: Conceptualization, B.Z., Q.X. and J.W.; methodology, B.Z. and W.W.; validation, B.Z., J.W. and J.H.; formal analysis, B.Z.; investigation, B.Z., W.W., C.W., L.Z., J.H., B.J., W.D. and Q.W.; resources, J.W. and Q.X.; writing—original draft preparation, B.Z. and W.W.; writing—review and editing, C.W. and J.W.; project administration, B.Z. and Q.X.; funding acquisition, B.Z. and C.W. All authors have read and agreed to the published version of the manuscript.

Funding: This research was funded by the Youth Talent Fund of the Laser Fusion Research Center, the China Academy of Engineering Physics, grant number RCSPD4-2020-3, and the Research and Innovation Office of the Hong Kong Polytechnic University (Project code: BBXL), and "The APC was funded by Youth Talent Fund of Laser Fusion Research Center, the China Academy of Engineering Physics, grant number RCSPD4-2020-3".

Data Availability Statement: Not applicable.

Acknowledgments: We wish to acknowledge the financial support from the Youth Science Association of the Laser Fusion Research Center, CAEP, and the technical support in polishing devices from Tianjin University.

Conflicts of Interest: The authors declare no conflict of interest.

References

1. Pilbratt, G.; Riedinger, J.; Passvogel, T.; Crone, G.; Doyle, D.; Gageur, U.; Heras, A.; Jewell, C.; Metcalfe, L.; Ott, S. Herschel Space Observatory-An ESA facility for far-infrared and submillimetre astronomy. *Astron. Astrophys.* **2010**, *518*, L1. [CrossRef]
2. Antoine, P.; Fruit, M. SiC telescope demonstrator (mirrors and structure): Optomechanical performances. In Proceedings of the Design and Engineering of Optical Systems II, Berlin, Germany, 25–27 May 1999; pp. 418–429.
3. Ealey, M.A.; Weaver, G.Q. Developmental history and trends for reaction-bonded silicon carbide mirrors. In Proceedings of the Advanced Materials for Optical and Precision Structures, Denver, Colorado, 8 August 1996; pp. 66–72.
4. Kaneda, H.; Nakagawa, T.; Enya, K.; Tange, Y.; Imai, T.; Katayama, H.; Suganuma, M.; Naitoh, M.; Maruyama, K.; Onaka, T. Optical testing activities for the SPICA telescope. In Proceedings of the Space Telescopes and Instrumentation 2010: Optical, Infrared, and Millimeter Wave, San Diego, CA, USA, 27 June–2 July 2010; pp. 283–289.
5. Shibai, H. AKARI (ASTRO-F): Flight performance and preliminary results. *Adv. Space Res.* **2007**, *40*, 595–599. [CrossRef]
6. Rodolfo, J. Polishing, coating, and integration of SiC mirrors for space telescopes. In *Advanced Optical and Mechanical Technologies in Telescopes and Instrumentation*; SPIE Press: Bellingham, DC, USA, 2008; pp. 125–132.
7. Beaucamp, A.; Simon, P.; Charlton, P.; King, C.; Matsubara, A.; Wegener, K. Brittle-ductile transition in shape adaptive grinding (SAG) of SiC aspheric optics. *Int. J. Mach. Tools Manuf.* **2017**, *115*, 29–37. [CrossRef]
8. Anapol, M.I.; Hadfield, P. SiC lightweight telescopes for advanced space applications: 1 mirror technology. In Proceedings of the Surveillance Technologies II, Orlando, FL, USA, 21–23 April 1992; pp. 281–295.
9. Robichaud, J.; Guregian, J.J.; Schwalm, M. SiC optics for Earth observing applications. In Proceedings of the Earth Observing Systems VIII, San Diego, CA, USA, 3–6 August 2003; pp. 53–62.
10. Breidenthal, R.S.; Galat-Skey, R.; Geany, J.J. Optical surfacing of one-meter-class reaction bonded silicon carbide. In Proceedings of the Silicon Carbide Materials for Optics and Precision Structures, San Diego, CA, USA, 12–13 July 1995; pp. 248–253.
11. Magida, M.B.; Paquin, R.A.; Richmond, J.J. Dimensional stability of bare and coated reaction-bonded silicon carbide. In Proceedings of the Dimensional Stability, San Diego, CA, USA, 12–13 July 1990; pp. 60–68.
12. Robb, P.N.; Huff, L.W.; Forney, P.B.; Petrovsky, G.T.; Ljubarsky, S.V.; Khimitch, Y.P. Interferometric measurements of silicon carbide mirrors at liquid helium temperature. In Proceedings of the Silicon Carbide Materials for Optics and Precision Structures, San Diego, CA, USA, 12–13 July 1995; pp. 196–200.
13. Hang, D. Research on Key Technology of High Efficiency and High precision Manufacturing of Space Large Scale SiC Aspheric Mirrors. Ph.D. Thesis, National University of Defense Technology, China, Changsha, 2018.
14. Wang, X.K. Fabrication and testing of an of T-axis aspheric surface with abnormal shape. *Infrared Laser Eng.* **2014**, *43*, 2959–2963.
15. Zhang, Z.Y.; Li, R.G.; Zheng, L.G.; Zhang, X.J. Precision grinding technology for the off-axis aspherical silicon carbide mirror blank. *J. Mech. Eng.* **2013**, *49*, 39–45. [CrossRef]
16. Feng, Z. Combined type polishing of silicon modification layer on silicon carbide mirror for space camera. *Chin. J. Lasers* **2013**, *40*, 0716001. [CrossRef]
17. Zhang, F.; Xu, L.; Fan, D.; Gao, J.; Zhang, X. Fabrication of surface modification aspheric SiC mirror. *Opt. Precis. Eng.* **2008**, *16*, 2479–2484.
18. Song, C.; Lu, Y.; Peng, Y. Grinding tool optimization in computer controlled grinding of SiC aspheric mirror. In Proceedings of the International Symposium on Optoelectronic Technology and Application 2014: Imaging Spectroscopy, Telescopes and Large Optics, Beijing, China, 13–15 May 2014; pp. 437–443.
19. Zhang, X.; Hu, H.; Wang, X.; Luo, X.; Zhang, G.; Zhao, W.; Wang, X.; Liu, Z.; Xiong, L.; Qi, E. Challenges and strategies in high-accuracy manufacturing of the world's largest SiC aspheric mirror. *Light Sci. Appl.* **2022**, *11*, 310. [CrossRef] [PubMed]
20. Tam, H.Y.; Cheng, H.; Wang, Y. Removal rate and surface roughness in the lapping and polishing of RB-SiC optical components. *J. Mater. Process. Technol.* **2007**, *192*, 276–280. [CrossRef]
21. Wang, X.; Zhang, X. Theoretical study on removal rate and surface roughness in grinding a RB-SiC mirror with a fixed abrasive. *Appl. Opt.* **2009**, *48*, 904–910. [CrossRef] [PubMed]
22. Nguyen, T.; Liu, D.; Thongkaew, K.; Li, H.; Qi, H.; Wang, J. The wear mechanisms of reaction bonded silicon carbide under abrasive polishing and slurry jet impact conditions. *Wear* **2018**, *410*, 156–164. [CrossRef]
23. Deng, H.; Liu, N.; Endo, K.; Yamamura, K. Atomic-scale finishing of carbon face of single crystal SiC by combination of thermal oxidation pretreatment and slurry polishing. *Appl. Surf. Sci.* **2018**, *434*, 40–48. [CrossRef]
24. Du, H.; Song, C.; Li, S. Study on surface roughness of modified silicon carbide mirrors polished by magnetorheological finishing. In Proceedings of the IOP Conference Series: Materials Science and Engineering, Kuala Lumpur, Malaysia, 13–14 August 2018.
25. Fei, F.; Xi, X.; Qiao, X.; Jian, W.; Bo, Z.; Ruiqing, X.; Xiangyang, L.; Xianhua, C.; Shengfei, W.; Jing, H. Progress on ultra precision manufacturing technology of large-aperture high-power laser optics. *Opto-Electron. Eng.* **2020**, *47*, 200135.

26. Yao, W.; Zhang, Y.M.; Han, J.C. Machining characteristics and removal mechanisms of reaction bonded silicon carbide. In Proceedings of the 2nd International Symposium on Advanced Optical Manufacturing and Testing Technologies: Advanced Optical Manufacturing Technologies, Xi'an, China, 9 June 2006; pp. 216–221.
27. Lin, B.; Jiang, X.M.; Cao, Z.C.; Huang, T. Development and theoretical analysis of novel center-inlet computer-controlled polishing process for high-efficiency polishing of optical surfaces. *Robot. Comput.-Integr. Manuf.* **2019**, *59*, 1–12. [CrossRef]
28. Shahinian, H.; Zhong, Y.; Turnbul, L.R.; Bodlapati, C.; Navare, J.; Mohammadi, H. Single point diamond turning of CVC SiC using the Micro-LAM process. In Proceedings of the 36th Annual Meeting of the American Society for Precision Engineering, Minneapolis, MN, USA, 1–5 November 2021; pp. 125–129.
29. You, K.; Fang, F.; Yan, G. Surface generation of tungsten carbide in laser-assisted diamond turning. *Int. J. Mach. Tools Manuf.* **2021**, *168*, 103770. [CrossRef]
30. Zhang, X.; Yang, L.; Wang, Y.; Lin, B.; Dong, Y.; Shi, C. Mechanism study on ultrasonic vibration assisted face grinding of hard and brittle materials. *J. Manuf. Process.* **2020**, *50*, 520–527. [CrossRef]
31. Yang, Z.; Zhu, L.; Zhang, G.; Ni, C.; Lin, B. Review of ultrasonic vibration-assisted machining in advanced materials. *Int. J. Mach. Tools Manuf.* **2020**, *156*, 103594. [CrossRef]

micromachines

MDPI

Article

Molecular Dynamics Simulation Study on the Influence of the Abrasive Flow Process on the Cutting of Iron-Carbon Alloys (α-Fe)

Junye Li [1], Zhenguo Zhao [1], Junwei Li [2], Fujun Xiao [2], Rongxian Qiu [2,*], Hongcai Xie [1] and Wenqing Meng [1]

[1] Ministry of Education Key Laboratory for Cross-Scale Micro and Nano Manufacturing, Changchun University of Science and Technology, Changchun 130022, China
[2] School of Mechanical Engineering, Nanjing University of Science and Technology, Nanjing 210094, China
* Correspondence: 18436096522@163.com; +86-136-44302-228

Abstract: The plastic deformation behavior and microstructural changes in workpieces during ultra-precision machining have piqued the interest of many researchers. In this study, a molecular dynamics simulation of nano-cutting iron-carbon alloy (α-Fe) is established to investigate the effects of the fluid medium and cutting angle on workpiece temperature, friction coefficient, workpiece surface morphology, and dislocation evolution by constructing a molecular model of $C_{12}H_{26}$ as a fluid medium in the liquid phase using an innovative combined atomic approach. It is demonstrated that the presence of the fluid phase reduces the machining temperature and the friction coefficient. The cutting angle has a significant impact on the formation of the workpiece's surface profile and the manner in which the workpiece's atoms are displaced. When the cutting angle is 0°, 5°, or 10°, the workpiece's surface morphology flows to both sides in a 45° direction, and the height of atomic accumulation on the workpiece surface gradually decreases while the area of displacement changes increases. The depth of cut increases as the cutting angle increases, causing greater material damage, and the presence of a fluid medium reduces this behavior. A dislocation reaction network is formed by the presence of more single and double-branched structures within the workpiece during the cutting process. The presence of a fluid medium during large-angle cutting reduces the number of dislocations and the total dislocation length. The total length of dislocations inside the workpiece is shorter for small angles of cutting, but the effect of the fluid medium is not very pronounced. Therefore, small cutting angles and the presence of fluid media reduce the formation of defective structures within the workpiece and ensure the machining quality.

Keywords: molecular dynamics; nano-cutting; fluid medium; cutting angle

Citation: Li, J.; Zhao, Z.; Li, J.; Xiao, F.; Qiu, R.; Xie, H.; Meng, W. Molecular Dynamics Simulation Study on the Influence of the Abrasive Flow Process on the Cutting of Iron-Carbon Alloys (α-Fe). *Micromachines* **2023**, *14*, 703. https://doi.org/10.3390/mi14030703

Academic Editor: Jiang Guo

Received: 28 February 2023
Revised: 16 March 2023
Accepted: 17 March 2023
Published: 22 March 2023

1. Introduction

Steel is one of the most commonly used materials in industry and has become an essential component in people's daily lives. The mechanical properties and applications of steel are determined by the Fe-C system, which is the foundation of steel. With the continuous development of industries such as aerospace technology, transportation, medical devices, automotive manufacturing and electrical engineering, manufactured steel parts are increasingly used in a wide range of applications. In particular, iron-based materials such as α-Fe are important for applications requiring high strength and good ductility structures in a variety of industries. Researchers are constantly investigating the precision and ultra-precision machining of materials in order to improve the performance of workpieces. The workpiece being machined will be accurate to the micron or even nanometer level during this process [1,2]. In practice, material removal may be limited to the workpiece's surface, only a few layers of atoms or several atoms. However, such material processing or removal phenomena are difficult to describe in the macroscopic manner. Therefore, it

seems necessary to study the behavior and mechanism of material deformation during the cutting process from the nanoscale.

Molecular dynamics (MD) is a popular atomic-scale research tool. Many scholars have recognized the scientific validity of MD because the generation and movement of dislocations during cutting processes can be studied using atomic dynamics simulations. In recent years, the use of molecular dynamics simulations to study the material processes occurring during machining has received great attention, and parameters such as machining surface [3], machining tool shape [4] and machining direction [5] have been widely discussed. Huan Liu et al. proposed an analytical model to predict the chip thickness and ploughing width of a FCC crystal in nanofabrication under an arbitrary crystal orientation, concluding that the crystal orientation determines the chip conversion between removal and ploughing, while the chip thickness and ploughing width can be predicted [6]. Yue et al. used the MD method to investigate a new nanostructured diamond abrasive for the mechanical polishing of single crystal silicon. The analysis showed that the structured abrasive leads to lower polishing forces and thinner subsurface damage layers in silicon polishing [7]. Ma et al. used MD simulations to investigated the crystal structure evolution and phase transition of single-crystal germanium materials during multiple cuts. A clear understanding of the brittle fracture, ductile plasticity and structural changes in single-crystal germanium materials was obtained at the atomic scale [8].

Many researchers are interested in the crystal orientation of BCC iron, using MD methods to simulate the effects of different crystal orientations on cutting, tensile behavior [9], impact phase transformation [10], nanoindentation and nano-scratching processes [11]. Li Xiang et al. found that, at the same defect concentration, different types of point defects cause different degrees of α-Fe lattice distortion and thus different ease of plastic deformation [12]. Wei wei et al. studied the effect of surface lithium atoms on the plastic deformation and yield stress of ferrite by suppressing the phase transition [13]. K Alhafez and Urbassek investigated the effect of different front angle tools on single crystal iron nanocutting using MD simulations [14]. Zamzamian et al. studied the mobility of 1/2 <1 1 1> {0 −1 1} edge dislocations in low carbon α-Fe [15]. Jiao et al. studied the effect of carbon on the deformation mechanism of iron–carbon alloys [16]. However, most of the research environments used in molecular dynamics to study the cutting characteristics of α-Fe are mostly in a vacuum, with a few exceptions in aqueous environments. This essay investigates the role of the liquid phase ($C_{12}H_{26}$) during abrasive flow cutting in a novel way, comparing it to liquid-free machining, and simulates the effect of the liquid phase on aspects such as abrasive grain motion and workpiece surface morphology changes at the microscopic atomic scale.

This study uses MD simulations to model SiC particles cutting iron–carbon alloy (α-Fe) workpieces in a liquid medium. The effects of the presence or absence of a fluid medium ($C_{12}H_{26}$) and cutting angle on the workpiece temperature, friction coefficient, workpiece surface morphology formation and workpiece atomic displacement mode during abrasive flow machining are investigated. This essay provides insight into the microscopic machining state and material removal phenomena in the presence of a fluid medium, which is of great academic significance and application value.

2. Materials and Methods

2.1. Model Building

A molecular dynamics model of SiC particles cutting Fe-C alloys at room temperature was developed in this study to investigate the micro-cutting interaction between the abrasive particles and the workpiece at the atomic scale. In addition, two models were created, one with and one without a fluid medium, to investigate the effect of the fluid medium on the nano-cutting process. It is known that Fe maintains a body-centered cubic (BCC) structure at room temperature with a lattice constant of a = 2.867 Å. The overall dimensions of the simulation model are 11.452 nm × 17.178 nm × 8.589 nm (114.52 Å × 171.78 Å × 85.89 Å), with a total of 147,773 atoms, and the x, y, and z axes correspond to the crystal directions

[100], [010], and [001]. We construct BCC Fe single crystal workpieces with a Newtonian layer, a thermostatic layer and a boundary layer for cutting, transfer, and stabilization. Furthermore, carbon atoms are randomly inserted into the Newtonian layer's octahedral interstitial positions, allowing the carbon to reach its maximum solubility [17]. In this study, β-SiC abrasives with a sphalerite structure were used, which is widely preferred by technical processors due to its low price and polishing effect, comparable to that of diamond. SiC for cutting has a radius of 25 Å and a grain atomic number of 6287. To avoid initial interaction between the abrasive and the workpiece, the distance between the abrasive and the workpiece was set to 10 Å and the center of the abrasive was set flush with the workpiece surface. To simplify the model, the Moltemplate software was used to create a repetitive unit of $C_{12}H_{26}$ molecules as the fluid medium with a liquid phase molecular number of 62,064. The TraPPE-UA [18] force field was chosen to describe the intermolecular interactions of the fluid, and the joint atomic model was used to treat the CH_3 and CH_2 groups as a single interaction point to improve computational efficiency, while the hydrogen atoms in the CH_3 and CH_2 groups were only represented in the mass [19]. Figure 1 depicts the molecular dynamics model of Fe-C alloys cutting by SiC particles with and without a liquid medium at room temperature. The difference between the two models is only the relevant liquid medium setting. The specific model parameters are shown in Table 1.

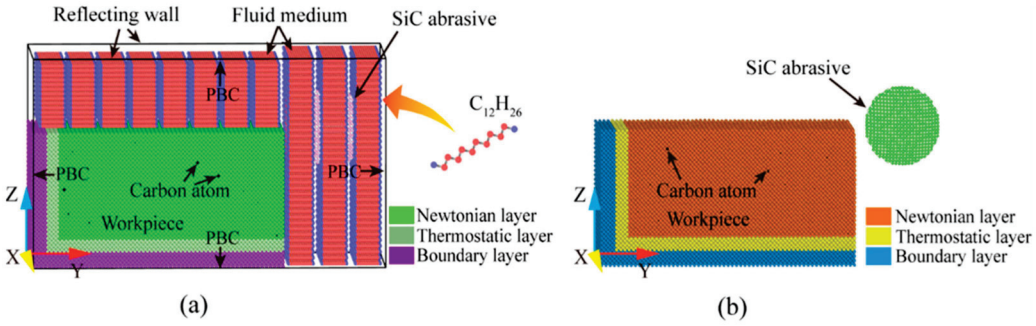

Figure 1. MD simulation system. (**a**) Wet cutting; and (**b**) dry cutting.

Table 1. Model parameters.

Parameters	Values
Workpiece	Iron–carbon alloy
Lattice structure	BCC
Workpiece orientation	[100], [010], [001]
Workpiece size	114.52 Å × 171.78 Å × 85.89 Å
Abrasive particle	SiC
Radius of abrasive particle	25 Å
Atomic number of workpiece	147,773
Atomic number of abrasive particle	6287
Molecular number of fluid medium	62,064

2.2. Interatomic Potentials

In the simulation process, the potential function is related to the accuracy of the simulation, and the selection of the potential function is a very important part of the simulation process. The Modified Embedded Atom Method (MEAM) potential is an extension of the original EAM function, which can be well-applied to metals and alloys with BCC structures. In this study, the MEAM potential developed by Liyanage et al. is used to study the interaction between atoms in the FeC alloy workpiece, which can well-

reproduce the gap energy of C atoms in the octahedral gap of BCC Fe [20]. In the MEAM potential function, the total energy E of the atomic system can be given by Equation (1):

$$E = \sum_i \left\{ F_i\left(\bar{\rho}_i\right) + \frac{1}{2}\sum_{i \neq j} \varnothing_{ij}\left(r_{ij}\right) \right\} \quad (1)$$

where F is the embedded energy as a function of the atomic electrical density ρ. ∅ is a pair of potential interactions, which is the sum of all neighbors j of atom i within the cut off distance r.

The Morse potential function can be effectively applied to the deformation of cubic metals [21]. Therefore, we use the Morse potential function to describe the interaction between the Fe-C alloy workpiece and the SiC abrasive. In the Morse potential function, the potential energy φ_{ij} of two atoms i and j with a distance of r_{ij} is given by Equation (2):

$$\varphi\left(r_{ij}\right) = D\left[e^{-2\alpha(r_{ij}-r_0)} - 2e^{-\alpha(r_{ij}-r_0)}\right] \quad (2)$$

where D is the binding energy coefficient, α is the gradient coefficient of the potential energy curve and r_0 is the equilibrium distance between the two atoms.

The Lennard–Jones (L-J) potential function is usually used for the simulation of the liquid environment [19]. In this study, the micro-cutting process in an organic medium is simulated, and the potential function is selected to describe the interaction involving organic molecules. The potential energy U_{L-J} is given by Equation (3):

$$U_{L-J}(r) = 4\varepsilon\left[\left(\frac{\sigma}{r}\right)^{12} - \left(\frac{\sigma}{r}\right)^{6}\right] \quad (3)$$

where σ is the equilibrium distance between atoms when the interaction potential is 0. ε is the depth of the potential well, which reflects the strength of the mutual attraction between two atoms at a distance of r.

2.3. Simulation Environment

The MD simulation of the cutting process is divided into a chilling phase and a machining phase. In particular, the relaxation phase is used to bring the initial simulated system to a steady state. In this study, the energy minimization process was carried out using the conjugate gradient method, and the equilibrium constraint of 100 fs was applied to the system in a Nose–Hoover heat bath during the relaxation phase to keep the temperature at 293 K. After the relaxation, the system remains intact without any collapse. Figure 2 depicts the model section of the system after relaxation.

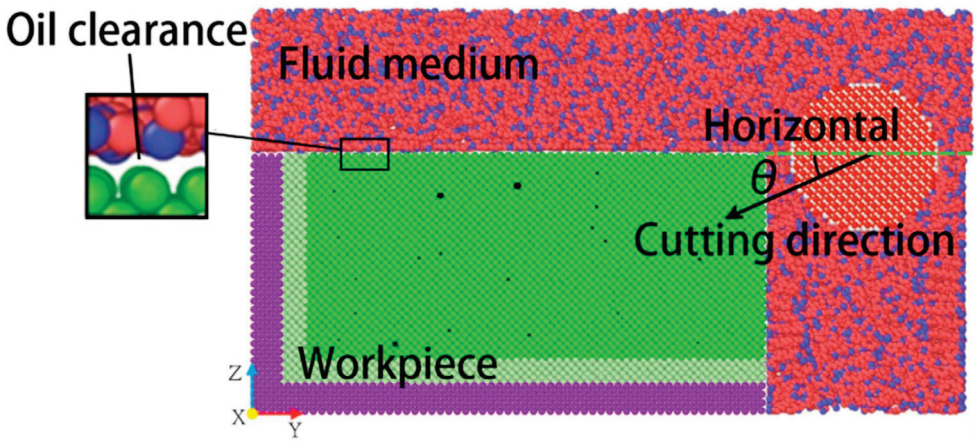

Figure 2. Longitudinal-sectional view of the system model after relaxation.

After relaxation, a stable oil clearance exists between the liquid phase molecules and the workpiece. The fluid molecules have strong self-diffusion and fill the whole free space above and on the right of the workpiece. As can be seen from the figure, the workpiece is wrapped in fluid molecules to form a dense oil film. In the simulated processing stage of abrasive flow, the abrasive grain is set as a rigid body. According to the previous research and calculation of abrasive flow processing, the motion of the abrasive grain is set to 50 m/s according to the actual processing speed, and the depth of cut is 1.25 nm. The cutting is performed along the *y*-axis with cutting angles of 0°, 5°, and 10° to the workpiece. The cutting distance is 11 nm, the cutting crystal direction is (001) [0–10], and the integral step is 1 fs. During machining, the temperature and energy in the system change continuously as the simulation proceeds, but the volume basically does not change. Therefore, the NVE system is used to balance the simulation system. In the process of solid–liquid two-phase abrasive flow, aviation kerosene or hydraulic oil are usually used as the fluid phase of the liquid phase. The fluid medium in this study is aviation kerosene. Aviation kerosene is a mixture of large molecule hydrocarbon complex hydrocarbons with a complex composition, and $C_{12}H_{26}$ is an important component of aviation kerosene, so it is used as a cooling fluid ($C_{12}H_{26}$ is a colorless liquid with a melting point −9.6 °C, boiling point 216.3 °C, flash point 71 °C, density 0.753 g/cm^3, vapor pressure 0.133 kPa/47.8 °C, is insoluble in water, and has good heat dissipation). The Periodic Boundary Conditions (PBC) are set along the X and Y direction for the entire system. Fixed boundary conditions along the Z direction and the reflective wall technique are used to keep the density and pressure of the fluid phase constant. The fluid medium appears to play a larger role in wet and dry cutting with abrasive flow [22]. Therefore, this study explores the effect of the existence of the fluid phase on machining by comparing wet and dry cutting. The initial simulation conditions are similar to the environmental model without the liquid phase. The difference between the two simulations is in the liquid phase environment setting.

In this study, the Large-scale Atomic/Molecular Massively Parallel Simulator (LAMMPS) [23] code is used for MD simulation of SiC abrasive cutting Fe-C alloy. The dislocation extraction algorithm (DXA) [24] is used to identify lattice dislocations, which allows us to determine their Burgers vectors. We used the free software Open Visualization Tool (OVITO) [25] for visualization. In addition, the elastic constants of α-Fe using this EAM potential were $C_{22} = 212.84$ GPa, $C_{13} = 143.23$ GPa, $C_{66} = 118.18$ GPa. These values were very close to the elastic constants $C_{22} = 219$ GPa, $C_{13} = 146$ GPa, $C_{66} = 123$ GPa. Additionally, we calculated by density functional theory (DFT) for the iron–carbon alloy [26]. The above two tests show that the EAM potential function can correctly express the physical properties of α-Fe.

3. Results and Discussion

3.1. Analysis of Liquid Phase Flow State and Effect

3.1.1. Analysis of Fluid Medium Flow State

In the machining process, the fluid medium plays an important role. After relaxation, the workpiece, the abrasive particle and the fluid medium all remain in a stable state. When the abrasive particles move in the machining direction, the fluid molecules also flow around the abrasive particle and the workpiece. Given the size of the simulation cell and the simulated process time, the influence of the fluid on the process must be rated as high. Therefore, in order to study the movement of the fluid medium during the machining process, the instantaneous motion distribution of the fluid medium at different cutting angles at a machining distance of 80 Å was selected for this study. The transient motion of the fluid medium during cutting is shown in Figure 3.

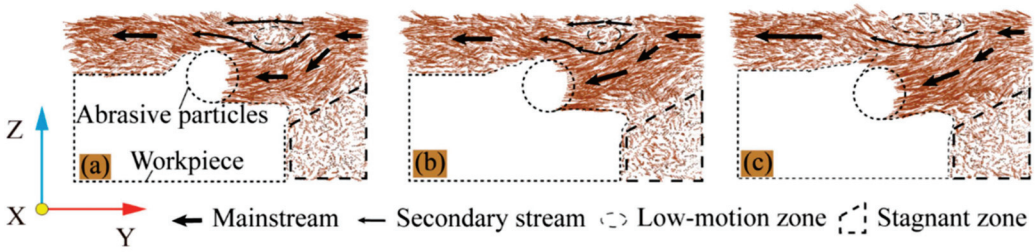

Figure 3. The instantaneous movement distributions of the fluid medium at a cutting distance of 80 Å. (**a**) θ = 0°; (**b**) θ = 5°; and (**c**) θ = 10°.

As can be seen from Figure 3, the fluid medium movement in the abrasive flow is primarily driven by the abrasive particles. The movement in the path through which the abrasive particles pass is the dominant flow, the other mainstream is the flow of fluid molecules attached to the unprocessed surface of the workpiece. The fluid is attached around the workpiece and the abrasive particles. The fluid constantly exchanges heat with the workpiece at all times, which can remove some of the cutting heat generated by the machining. This flow can reduce the increase in workpiece temperature caused by partial processing and reduce the tool wear. The secondary flow and low motion zone, which is primarily above the abrasive particle, is caused by the fact that the movement of the abrasive particle is insufficient to drive the fluid there in a directional flow. Because of the workpiece obstruction and less interference, a stagnant flow zone forms on the right side of the workpiece. As a result, some of the fluid remains inside the workpiece during the machining process, causing losses. As the cutting angle increases, the flow of fluid molecules penetrates deeper into the workpiece with the abrasive grain. To achieve lubrication, the fluid medium surrounding the abrasive particle can reduce friction between the abrasive particle and the machined surface as well as friction between the abrasive particle and the chips. The increase of the cutting angle has a greater influence on the movement direction of the mainstream in the part that moves with the abrasive particle, but has less influence on the flow state of fluid molecules in other areas.

3.1.2. Effect of Fluid Medium on Workpiece Temperature

Cutting heat is produced during the machining process, which is one of the most important physical phenomena in machining. The majority of the energy consumed during machining is converted into heat, except for a very small proportion of the energy used to form new machined surfaces and new lattice deformations. Therefore, we could say that all of the energy consumed during machining is converted into heat. The large amount of cutting heat makes the workpiece temperature rise, which will directly affect the performance of the workpiece material, workpiece processing accuracy, and the quality of the machined surface. At the same time, The temperature also has an effect on the reaction between the dislocations and dislocation rings within the BCC Fe. Relative to dry cutting, the presence of a fluid medium reduces the internal temperature of the workpiece by dissipating heat. The temperature change in the Newtonian layer of the workpiece was recorded for both cases with and without fluid molecules to better characterize the cooling effect of the fluid phase on the workpiece. The workpiece temperature variation with and without fluid media at different cutting angles is shown in Figure 4.

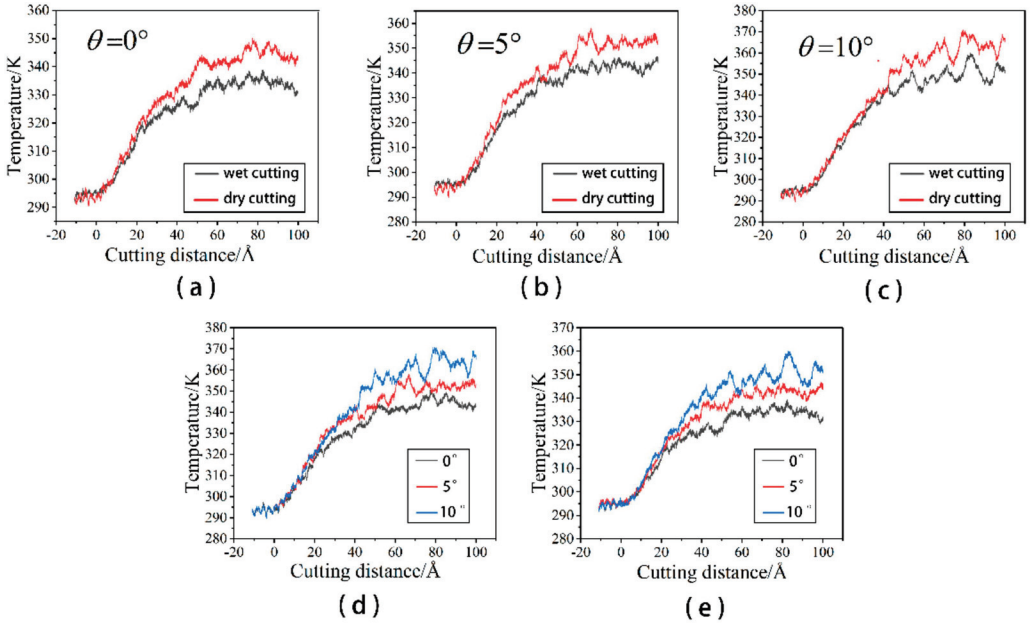

Figure 4. The temperature change of the workpiece. (**a**) θ = 0°; (**b**) θ = 5°; (**c**) θ = 10°; (**d**) workpiece temperature change during dry cutting; and (**e**) workpiece temperature change during wet cutting.

When the cutting angle is 0°, the cutting distance at which the abrasive particle starts to act on the workpiece is set to 0 Å. As can be seen from Figure 4a–c, the presence of the fluid medium has a positive effect on the heat dissipation of the workpiece during the machining process at different chip angles. At the beginning of the machining process, the abrasive grains are only in contact with the workpiece. Because the number of chips produced and the number of lattice transformations are low, the workpiece temperature rises more slowly. At this point, the liquid phase's cooling effect is not visible. On the contrary, due to the friction between the abrasive grain and the fluid medium, the temperature of the fluid medium increases and is transferred to the workpiece. Therefore, in the initial stage of cutting, the cutting process with the fluid media workpiece temperature is higher than the workpiece temperature during dry cutting. The temperature of Newtonian layer atoms rises rapidly as the cutting distance increases. On the one hand, this is partly due to the extrusion of the workpiece atoms by the abrasive particles and the disruption of the chemical bonds between the workpiece atoms. On the other hand, as the lattice strain energy stored is released, some of the released energy is converted into heat. All of this contributes to the workpiece's temperature rapidly rising. The workpiece is severely damaged at this point, and the contact area between the liquid phase and the workpiece expands. The cutting heat in the workpiece and chips is transferred through a large number of liquid phase molecules, which slows down the temperature rise of the workpiece. As can be seen from Figure 4d,e, the temperature of the workpiece increases with increasing cutting angle during wet cutting and dry cutting. This is due to the fact that the large cutting angle increases the degree of workpiece destruction and more atoms release heat. The cut reaches stability in the later stages of cutting, and the number of atoms destroyed and lattice transitions is relatively constant, so the workpiece temperature gradually remains constant. When comparing the work-piece temperature during the stable cutting period, the presence of a fluid medium can reduce the work-piece temperature by approximately 10 K. According to previous research, the presence of cutting fluid in the mechanical cutting process can better reduce the cutting temperature of the conclusion [27,28]. This study is an important resource for explaining the reasons under a microscopic perspective.

3.1.3. Effect of Fluid Medium on Friction Coefficient

During the cutting process, the abrasive particle will rub against the chips or the machined surface, thus impeding the movement of the abrasive particle. The presence of the liquid phase mitigates this effect. In order to characterize the lubrication effect of the presence of the liquid phase on the machining process, we calculate the change of the friction coefficient during the machining process. For the machining with a cutting angle of 0°, the friction coefficient is defined as the ratio between the tangential force and normal force [29]. For the angular cutting in this study, the friction coefficient will be given by Equation (4):

$$\mu = \frac{F_t}{F_n} = \frac{F_y \cos\theta + F_z \sin\theta}{F_z \cos\theta - F_y \sin\theta} \quad (4)$$

The variation of the friction coefficient at different cutting angles is shown in Figure 5.

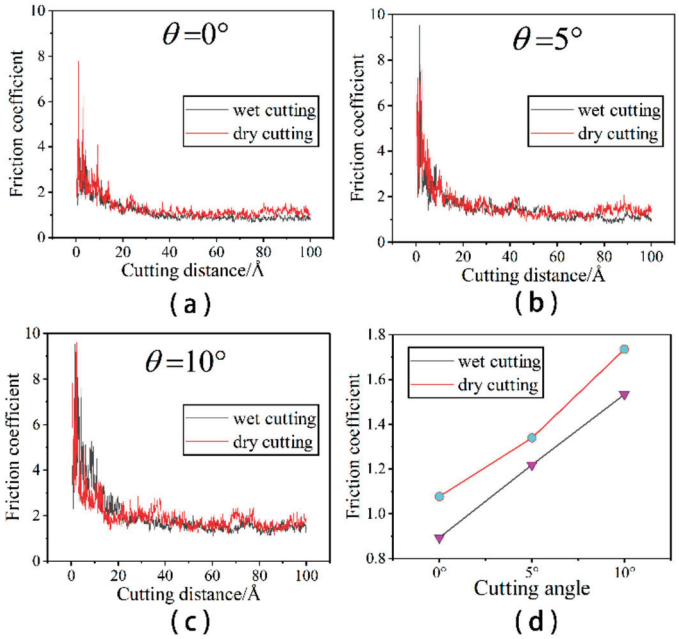

Figure 5. The change of friction coefficient. (**a**) θ = 0°; (**b**) θ = 5°; (**c**) θ = 10°; and (**d**) comparison of friction coefficient during wet and dry cutting at various cutting angles.

As can be seen from Figure 5a–c, the friction coefficient without a liquid phase is slightly higher than that with a liquid phase at the same cutting angle. In the early stages of cutting, when the abrasive grain first contacts the workpiece, a large tangential force is required to displace some of the workpiece atoms in the front of the abrasive particle and build up to produce the chips and measured flow. The resulting machined surface is small at this point, as is the normal force required to form the machined surface. As a result, tangential and normal forces increase in different ways during the preliminary cutting process. In addition, the coefficient of friction fluctuates considerably in the early stages of cutting due to the vibrations caused by the continuous collision between the abrasive grains and the workpiece. The larger friction coefficient ensures that the abrasive grains overcome the interaction forces between the atoms of the workpiece and begin to have a damage the workpiece. As the cut proceeds, the chip formation pattern enters a steady state. The variation of the tangential and normal forces smooths out, as does the value of the friction coefficient. In order to see more visually the effect of the presence of the fluid medium and the cutting angle on the machining, we calculated the mean values of the coefficient of friction after a 2.5 nm cutting distance, as shown in Figure 5d. Figure 5d shows that the presence of the fluid medium reduces the friction coefficient, which reduces the frictional resistance and energy loss. This is also consistent with previous research,

which concluded that cutting forces and frictional wear are better reduced when a cutting fluid is present [30,31]. This essay provides a more detailed explanation of the causes of this. The coefficient of friction increases with the increasing cutting angle. Larger cutting angles cause more increased friction between the abrasive grain and the workpiece, resulting in higher cutting forces and friction coefficients. This study examines the changing state of cutting forces under wet cutting conditions at microscopic angles to further investigate the relationship between cutting forces and cutting angles. At the microscopic scale, the cutting force is the force between the particle atoms and the workpiece atoms. It is the cutting force of the Si and C atoms in silicon carbide particles on the Fe and C atoms in the workpiece. The cutting force between the particle atoms and the workpiece atoms indirectly reflects the micro-cutting action of the abrasive particles and the material removal process, and it is an important physical parameter in the micro-cutting process, as illustrated in Figure 6.

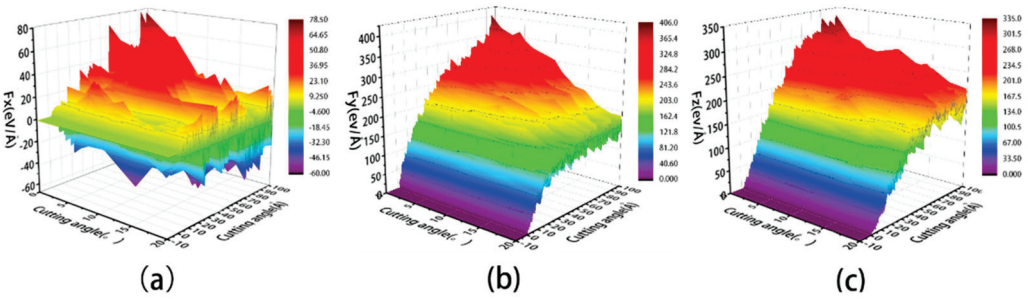

Figure 6. Variation of cutting force with cutting distance. (**a**) Fx; (**b**) Fy; and (**c**) Fz.

As can be seen in Figure 6a, the cutting forces on both sides of x cancel each other out, causing the Fx values to be distributed around 0. The lattice structure on both sides is not consistent after the abrasive grain has cut through the workpiece due to the random distribution of C atoms inside the workpiece, which also contributes to the deviation of Fx up and down at a certain cutting distance. As shown in Figure 6b, the Fy value increases faster at the beginning of the cutting process and gradually smooths out at a later stage. When the cutting angle is 0°, the cutting distance is approximately 50 Å. The abrasive grain has been completely cut into the workpiece at this point, and the cutting process has reached a stable cutting stage, where the Fy value has reached its peak and is stable. The Fy value gradually increases as the cutting angle increases, especially in the middle and later stages of cutting. When the cutting angle is 15° or 20°, Fy continues to rise in the late cutting stage, making it more difficult to achieve the stable cutting stage. If the cutting angle is too large, it is difficult to discharge the chips formed after the abrasive grains enter the workpiece, causing the cutting action to be hampered. As shown in Figure 5c, Fz increases approximately linearly in the early stages of cutting, slowly after the grain has been completely submerged in the work-piece, and then gradually stabilizes in the later stages. Fz allows the atoms beneath the grain to form a machined surface while also overcoming the chip's obstruction to the grain. Fz increases as the cutting angle increases at the same cutting distance. Abrasive grains with a higher cutting angle create deeper cuts in the workpiece, increasing the number of atoms contacted by the grain. To force plastic deformation of the material in the cutting area, the particles must overcome greater bonding energy and break more atomic interactions. As a result, as the cutting angle increases, the abrasive grain cutting forces increase. This is also consistent with previous research, which concluded that increasing cutting angles increases cutting forces within a certain range [32]. Therefore, smaller cutting angles and the presence of fluid improve the quality of the machined workpiece.

3.2. Evolution of Workpiece Surface Morphology

At room temperature, the Fe maintains the BCC lattice structure. Even if a small amount of carbon atoms enter the octahedral gap positions, the workpiece still remains cubic. Under conditions free of external forces, the atoms inside the workpiece are arranged

in an orderly fashion and the lattice structure remains intact. When the abrasive grains machine the workpiece, a build-up of workpiece atoms begins to form on the workpiece surface. At the same time, some areas of the workpiece surface are extruded and deformed, resulting in a substantially altered surface. In order to study the effect of fluid media and different cutting angles on the surface quality of Fe-C alloy workpieces, the surface morphology was observed for cutting processes with and without fluid media selected for cutting distances of 30 Å, 60 Å and 100 Å. The workpiece atoms were colored based on their height along the *z*-axis. At the microscopic size atomic model scale. The surface roughness rule is rarely used because surface roughness is difficult to observe at the microscopic level and data quantification accuracy is low. The roughness level of a workpiece surface is typically calculated by observing the height of the surface bulge as well as the number and arrangement of atoms. Figure 7 depicts the surface profile of the workpiece with fluid lubrication, where the fluid medium and abrasive particles are hidden. Figure 8 depicts the workpiece's surface profile without fluid media.

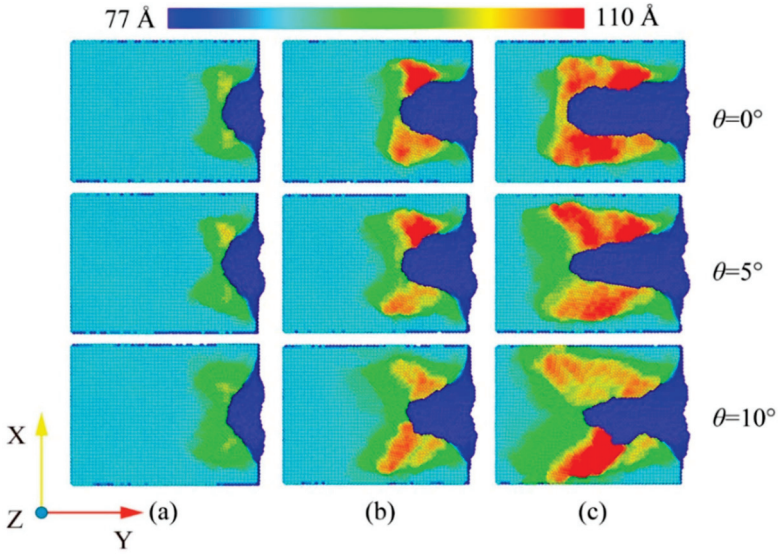

Figure 7. Workpiece surface morphology during wet cutting. (**a**) Cutting distance of 30 Å; (**b**) cutting distance of 60 Å; and (**c**) cutting distance of 100 Å.

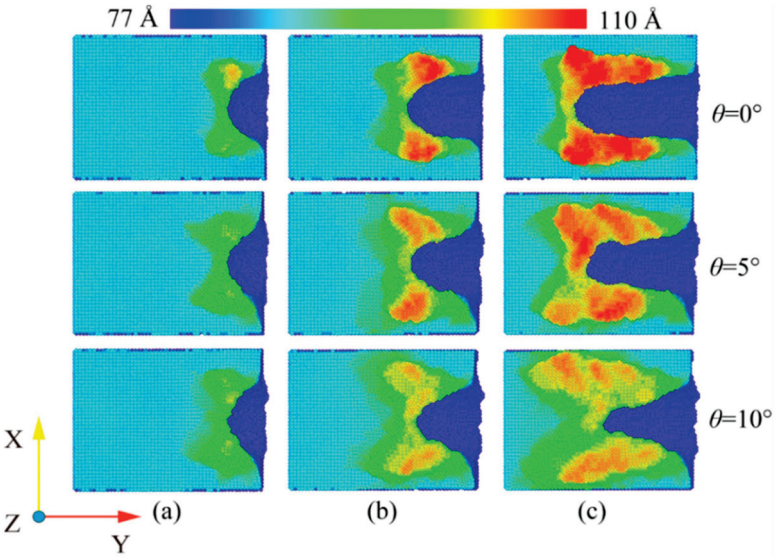

Figure 8. Workpiece surface morphology during dry cutting. (**a**) Cutting distance of 30 Å; (**b**) cutting distance of 60 Å; and (**c**) cutting distance of 100 Å.

The silicon carbide fragments that cut the iron–carbon alloy form an approximately symmetrical pile-up on the (0 0 1) surface. Figures 7 and 8 show that the chips do not gather in front of the abrasive particle, but rather flow to both sides at 45°. The chip atoms are roughly symmetrically distributed on both sides of the groove formed by the abrasive particle's passage. The slip characteristics of the BCC Fe structure determine this build-up behavior, which is unaffected by the presence of fluid media or changes in the cutting angle. Figure 9 shows the slip direction of the BCC Fe crystal. These pile-up features result from the fact that the <1 1 1> slip directions point at 45° to the sides for the cutting process. The number of carbon atoms is small and they are not in the sliding direction, which has little influence on the formation of the pile. However, there is a slight asymmetry in the pile-up due to the atomic and irregular nature of the dislocation generation and reaction process. At the same time, the irregularity in the dispersion of carbon atoms within the workpiece will also cause differences in the stacking height on either side of the slot. This asymmetry appears more pronounced as the angle increases. This is so that the abrasive grains gradually cut into the interior of the workpiece as the cutting angle increases. More interstitial carbon atoms are involved in the chip process affecting the dislocation reaction, resulting in an asymmetry in the pile-up height on the workpiece surface. The groove should be regular when the cutting angle is 0, but as the cutting goes on, more atoms build up on the workpiece's surface, creating a small obscuration above the groove. The radius of the abrasive grain used to cut the atoms on the workpiece's surface diminishes as the cutting angle rises, resulting in a gradual sharpening and irregularity at the front of the flute.

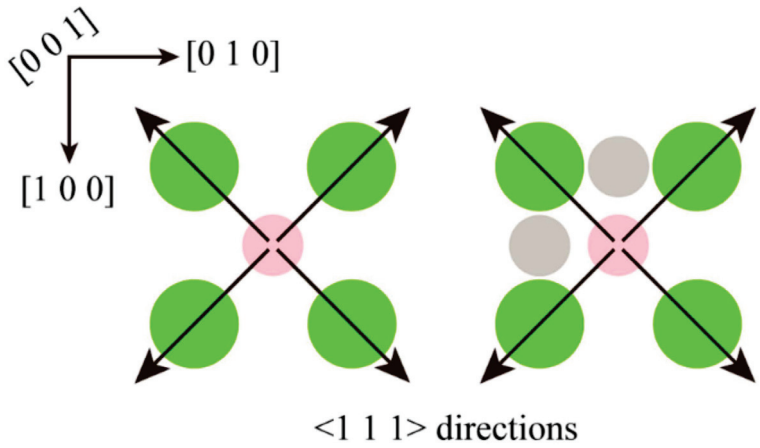

Figure 9. Schematic diagram of the crystal slip direction during cutting. The big green circles (small pink circles) represent the first (second) layer of atoms. The gray circles represent the carbon atoms partly in the octahedral gap. The arrows indicate the <1 1 1> slip direction.

A comparison of Figures 7 and 8 shows that the existence of a fluid medium influences the distribution and symmetry of the surface build-up height. The fluid medium alters the workpiece temperature and friction coefficient influencing the dislocation response within the workpiece during machining. The defect formation and motion causes the complex mechanisms of plastic and elastic deformation, which is reflected in the surface build-up pattern [33]. As can be seen from the color distribution on Figures 7 and 8, the stacking height of the surface atoms gradually decreases with the increasing cutting angle, while the area where displacement changes occur becomes larger. On the one hand, the reduction in stack height is detrimental to chip removal and, on the other hand, the expansion of the workpiece surface deformation area reduces the surface quality of the workpiece. As the cutting angle increases, so does the depth of cut, resulting in more material damage.

In order to reflect more visually the influence of the fluid medium and the cutting angle on the amount of material removed, the number of atoms beyond the surface of the workpiece during the cutting process was counted, as shown in Figure 10. As can be

seen from Figure 9a–c, the fluid medium has a minor effect on the amount of material removed during the cutting process. At cutting angles of 0° and 5°, slightly more atoms are displaced to the workpiece surface during dry cutting. At a cutting angle of 10°, the number of atoms on the surface is nearly the same in both cases. This is explained by the displacement of atoms within the workpiece at a cutting distance of 10 nm, as shown in Figure 11. In the cross-sectional view of the internal atomic displacement of the workpiece when the cutting distance is 10 nm, it can be seen that the atoms are moved into the pile-up on the workpiece surface when the cutting process with a small cutting angle. A large number of atoms with larger displacements do not reach the top at a cutting angle of 10°, but they remain inside the workpiece, and then the upper atoms are squeezed to form pile-up on the workpiece surface. The fluid medium absorbs heat and reduces the thermal movement of the workpiece atoms at small cutting angles, resulting in a slight difference in the number of atoms built up on the surface. However, because the abrasive particle penetrates deep into the workpiece and the atoms in the cutting area are squeezed and moved to the workpiece surface during the large-angle cutting process, they are not very sensitive to the effect of temperature. As shown in Figure 10d,e, the cutting angle has a greater influence on the amount of atomic build-up on the surface. With or without a fluid medium, more atoms within the workpiece are displaced to the workpiece surface as the cutting angle increases. The increase of the cutting angle reduces the surface quality of the workpiece, but it has a significant effect on the material removal to another extent. Figure 11a–c depict the top and side views of the build-up above the workpiece surface at the cutting moment as illustrated in Figures 7 and 8. The surface is free of significant chip deposits during the initial stage of cutting. The surface accumulation of atoms increases in an approximately linear trend as the cutting progresses. The small cutting angle and the presence of the fluid medium reduce workpiece surface damage during the cutting process, which is beneficial for machining.

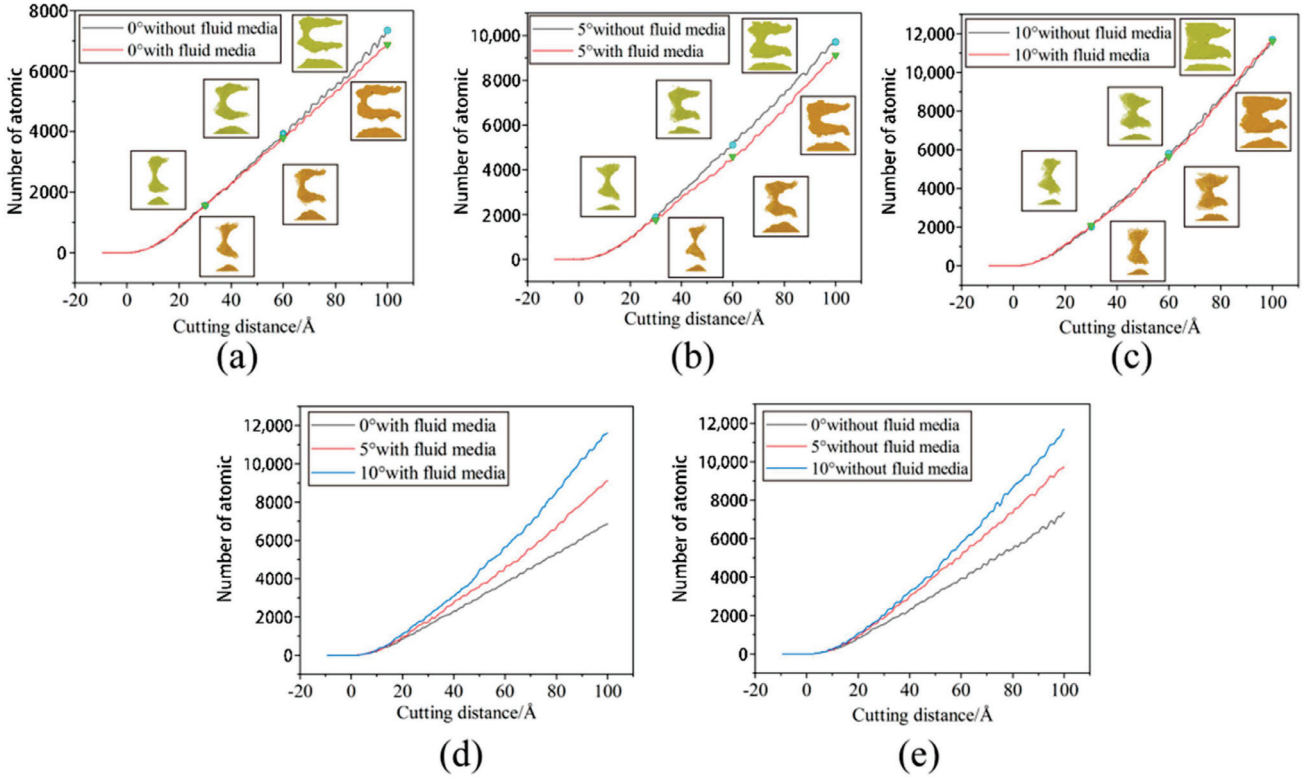

Figure 10. Number of atoms exceeding the workpiece surface. (**a**) θ = 0°; (**b**) θ = 5°; (**c**) θ = 10°; (**d**) wet cutting; and (**e**) dry cutting.

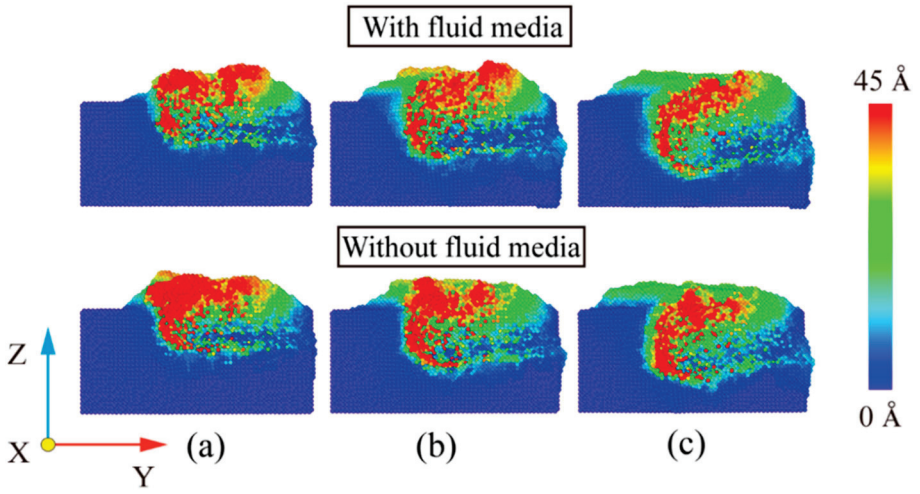

Figure 11. Atomic displacement of cross-section when cutting distance of 10 nm. (**a**) θ = 0°; (**b**) θ = 5°; and (**c**) θ = 10°.

3.3. Analysis of Dislocation Evolution

The dislocations in the iron–carbon alloy workpiece will change with the plastic deformation of the material, and the existence of the dislocations will have a very important impact on the properties of the material. The dislocations in the iron–carbon alloy workpiece will change with the plastic deformation of the material, and the existence of the dislocations will have a very important impact on the properties of the material. In order to investigate the changes of dislocations inside the material during particle microcutting at different cutting angles, the dislocation extraction algorithm (DXA) was used to extract the dislocations inside the workpiece under different conditions of cutting, and the dislocation distribution was obtained for each state. This study found that there is the two dislocations for the Böhler vector b = 1/2 <1 1 1> and b = <1 0 0>, which are in contrast to other dislocations produced by the tool cutting process. The absence of Böhler vectors of 1/3 <1 1 1>, 1/6 <1 1 1> and 1/12 <1 1 1> during the cutting process indicates the absence of a twinning structure. This is consistent with the findings of Katzarov Ivaylo Hristov et al. [34].

When the cutting angle is 0°, the fluid medium does not have a significant effect on the change in the total length of the dislocation, but the dislocation reaction during the cutting process is different. According to Figure 12a, the contact between the abrasive particle and the workpiece in the early cutting stage is an elastic deformation behavior, and there is no dislocation behavior inside the workpiece. First, we analyze the cutting process in the absence of a fluid medium. Before the cutting distance reaches 22 Å, there is a short period of appearance and annihilation of dislocations. In these processes, there is insufficient stress to support dislocation nucleation. When the strain energy reaches a certain threshold, dislocation lines appear one after another. As shown in Figure 12b, a dislocation with Burr's vector b = [1 0 0] appears below the workpiece. As the cutting progresses, this dislocation develops and serves as a link between the dislocation development in front of and below the abrasive grain. When cutting to about 59 Å, the dislocations in the anterior and posterior areas below the abrasive consist of the structure shown in Figure 13a that we call the double-branch structure. This structure is flanked on the left and right by two dislocations with a Burr's vector of b = 1/2 <1 1 1> and connected in the middle by a dislocation with a Burr's vector of b = <1 0 0>. The other structure is called a single-branch structure shown in Figure 13b, which is less than the double-branch structure on one side of the two b = 1/2 <1 1 1> dislocations. Following that, a small part of the deformation damage appears on the lower left of the abrasive, which is considered to be a necessary phenomenon to form the machined surface, which also prevents the development of dislocations at this point. As the cutting progresses to 75 Å, as shown in Figure 11e, the original sub-surface damage is smoothed out, leaving a dislocation of b = 1/2 [1 −1 −1]. The dislocation network

under the abrasive is composed of multiple double-branch structures that are intertwined. As the abrasive continues to move forward, new deformation damage gradually begins to occur in front and temporarily prevents the dislocation from reacting. As shown in Figure 12f, the dislocation reaction under the abrasive does not change significantly, while the deformation in the lower left region accumulates strain energy for further dislocation development. For the wet cutting process, the reaction of the two dislocations inside the workpiece is different. As shown in Figure 12g–i, the b = 1/2 <1 1 1> dislocation reaction within the workpiece dominates in the early cutting process. From a cutting distance of 46 Å to 69 Å, the dislocation of b = 1/2 [1 −1 −1] at the lower left of the abrasive is enlarged. At the same time, the dislocation under the abrasive develops and consists of multiple double-branch structures. As the cutting progresses, we notice that the b = [1 0 0] dislocation, which is made up of the b = 1/2 [1 −1 1] and b = 1/2 [1 1 −1], has grown significantly. From Figure 12j, b = [1 0 0] dislocation has become the link connecting the front and lower areas of the abrasive. As the abrasive continues to advance, multiple dislocation lines regenerate below the abrasive and interrupt the previous b = [1 0 0] long dislocations. The dislocations are reorganized, and a new round of dislocation multiplication begins to generate a new processing surface.

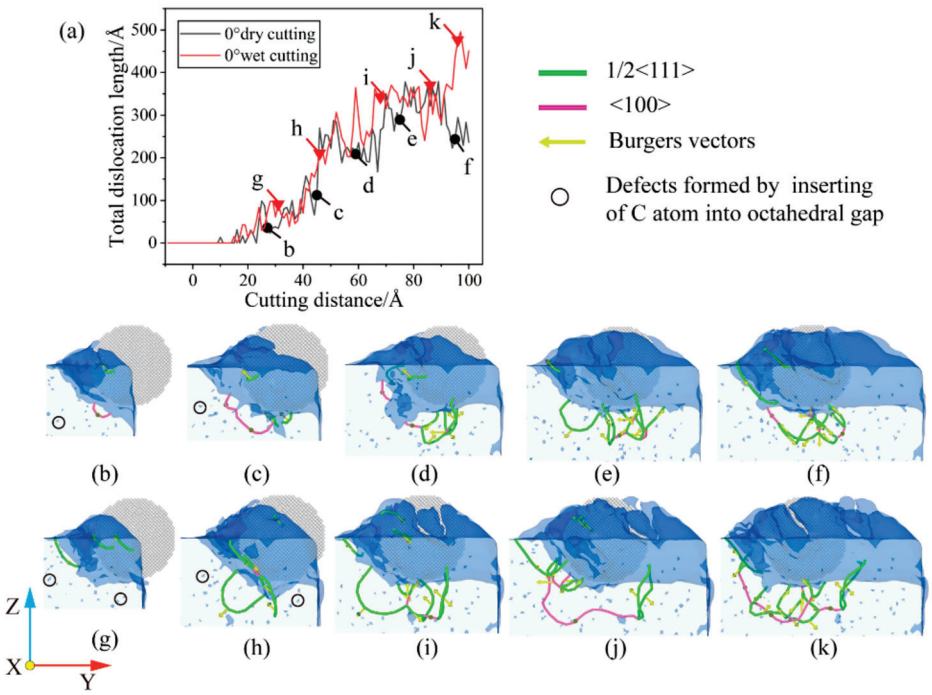

Figure 12. Dislocation evolution under θ = 0°. (**a**) Variation of total length of dislocation with cutting distance; (**b**) cutting distance of 26 Å under dry cutting; (**c**) cutting distance of 45 Å under dry cutting; (**d**) cutting distance of 59 Å under dry cutting; (**e**) cutting distance of 75 Å under dry cutting; (**f**) cutting distance of 95 Å under dry cutting; (**g**) cutting distance of 30 Å under wet cutting; (**h**) cutting distance of 46 Å under wet cutting; (**i**) cutting distance of 69 Å under wet cutting; (**j**) cutting distance of 85 Å under wet cutting; and (**k**) cutting distance of 96 Å under wet cutting.

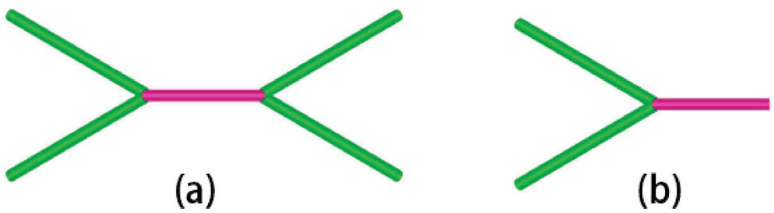

Figure 13. Dislocation structure. (**a**) Double-branch structure; and (**b**) single-branch structure.

For cuts with a cutting angle of 5°, the influence of the presence of the fluid medium on the total dislocation length is also not very obvious. As the cutting angle increases, the abrasive grains gradually move into the workpiece. The contact area between the workpiece and the abrasive grains becomes larger, and more atoms are involved in the process, increasing the intensity of dislocation activity on the subsurface. For the dry cutting process, the dislocation activity in the early stage nucleates stably after the cutting distance is 20 Å, and the total dislocation length increases continuously. When the cutting progress reaches 35 Å, several scattered dislocation lines of b = 1/2 <1 1 1> appear around the abrasive grain, as shown in Figure 14b. Among them, the dislocation line of b = 1/2 [1 1 1] in the lower left of the abrasive gradually expands as the cutting progresses. As shown in Figure 14c, when the cutting distance is 52 Å, the dislocation of b = 1/2 [1 1 1] has developed greatly, and the intersection of multiple dislocations on the front and side of the abrasive grain causes dislocation entanglement. As the abrasive advances, the dislocations accumulated in the front transform into a defective sub-surface. The dislocations under the abrasive develop into a small number of single-branch and double-branch structures. Among them, b = 1/2 <1 1 1> dislocations are not only newly generated with the cutting process, but have also evolved from the previous cutting process. As the cutting progresses, the accumulation of strain energy allows the development and reorganization of each dislocation line beneath the abrasive. It can be seen from Figure 14f that the dislocations under the abrasive have been reorganization, and a number of short dislocations with double-branch structures have been newly derived, which prepares the conditions for a new round of growth in the total dislocation length. As can be seen from Figure 14f, the dislocations below the grain have been reorganized, with a dislocation of b = [1 0 0] connecting the dislocation reactions in front of and below the grain. A number of new short dislocation lines with double-branched structures have been derived, preparing the way for a new round of dislocation growth in the total length. For wet cutting, as shown in Figure 14g,h, the dislocation of b = 1/2 [−1 −1 −1] at the lower left of the abrasive is developed. When the cutting distance is 52 Å, the dislocation under the abrasive is a double-branch structure and absorbs b = 1/2 [−1 −1 −1] dislocation. As the cutting progresses to 69 Å, the dislocations under the abrasive gradually proliferate, and a small amount of deformation damage occurs in front of the grain, which prevents the dislocation from extending. As the abrasive advances, as shown in Figure 14j, the small damage and deformation are gradually engulfed by the new deformed layer, and the dislocations under the abrasive grow to varying degrees. At the same time, a long dislocation of b = [1 0 0] connects the dislocation below and the front sub-surface defect. As the cutting progresses, as shown in Figure 14k, deformation and damage reappear on the lower left of the abrasive grain. A dislocation of b = 1/2 [−1 −1 −1] regrows on the left side of the damage, indicating that a new dislocation growth point will appear.

For cuts with a cutting angle of 10°, the presence of a fluid medium has a greater influence on the total dislocation length in the middle and later stages of the cut. As can be seen in Figure 15a, the total length of dislocations is relatively short in the presence of fluid media. Due to the large cutting angle, the energy exchange between the workpiece and the fluid media is more extensive in the middle and late stages of the cut as the abrasive grains and fluid media penetrate deeper into the workpiece. The fluid medium absorbs some of the energy used to promote the formation of dislocations, resulting in better machining quality and fewer sub-surface defects. For the dry cutting, the total dislocation length steadily increases after the cutting distance is 15 Å. When the cutting distance is 20 Å, a dislocation of b = 1/2 [−1 −1 −1] appears at the lower left of the abrasive, and it develops steadily in the subsequent cutting process. As shown in Figure 15c, the dislocation under the abrasive grain consists of a single and a double-branched structure. The b = 1/2 [−1 −1 −1] dislocation is a component of the double-branch structure and gradually grows. Subsequently, the damage of the abrasive to the workpiece deepens, as shown in Figure 15d, and more short dislocations

are derived from the front of the abrasive grains. The original dislocation line under the abrasive has been greatly increased, especially the b = 1/2 [−1 −1 −1] dislocation plays the role of connecting the front and lower dislocations of the abrasive. At this point, the sub-surface of the abrasive's lower left area has more damage, and the dislocations are derived to a greater extent, so the total dislocation length is rapidly increasing. As the abrasive cuts through the damaged area, the damaged part is smoothed out, and the total dislocation length gradually becomes stable. It is important to note that there are still dislocation lines remaining on the machined surface, which affects the quality of the machined surface. However, when the cutting distance reaches 100 Å, as shown in Figure 15f, new damage appears in the lower left area of the abrasive, which makes the dislocations continue to interweave and multiply. It leads to the formation of a complex dislocation network and heralds the start of a new period of rapid growth. When compared to dry cutting, the dislocation reaction of the cutting process with a fluid medium is less intense. When the cutting distance is 16 Å, a dislocation of b = 1/2 [1 1 1] appears steadily at the lower left of the abrasive grain. As the cut reaches 45 Å, the dislocation below the grain consists of a double-branched structure and absorbs the growing b = 1/2 [1 1 1] dislocation. As the cutting progresses, the damage and deformation layers gradually appear in front and below the abrasive, which also means that the dislocations are reorganized and newly derived. As shown in Figure 15i, damage and deformation in a larger area appear below the abrasive grain, which affects the distribution of the dislocation networks. At this point, there is a single branched structure below the left side of the grain, with a dislocation of b = [−1 0 0] connecting the area in front of and below the grain. As the cut progresses to 77 Å, the defective structure below the grain is smoothed out, while the new damage deformation in front of the grain is deformed by the presence of multiple dislocations. There is a double-branch structure under the abrasive to connect the area under the machined surface and the area under the abrasive. The dislocation of 1/2 [1 −1 −1] is maintained stably at the lower left of the abrasive grain, and the total dislocation length is maintained in a stable state. As the cut reaches 99 Å, the deformed structure beneath the grain is smoothed out and some of the dislocations are obliterated resulting in a decrease in the total dislocation length. This is consistent with the findings of Li Shang-Jie et al. [35]. However, as the cutting continues, the abrasive grains will further damage the workpiece, which will correspondingly initiate the next round of dislocation multiplication.

In order to more intuitively see the changes of dislocation under different cutting conditions, we give the total dislocation length changes of wet and dry cutting under different cutting angles as shown in Figure 15.

Figure 16a illustrates how the total dislocation length gradually increases as the cutting angle rises. This is because the contact area between the workpiece and the abrasive becomes larger when the cutting angle is large, and more workpiece atoms participate in the machining process. The workpiece temperature rises and dislocation activity becomes more frequent under the influence of energy and stress, ultimately resulting in a large number of defective structures in the sub-surface region of the workpiece. Although the cutting angle has the same effect in cutting processes with a fluid medium, as shown in Figure 16b, the presence of the fluid medium causes higher fluctuations in the dislocation variation at some stages. During dry cutting, as shown in Figure 16a, dislocations become easier to nucleate as the cutting angle increases in the early stage of cutting. This is due to the increased strain energy that the additional atoms engaged in the cut release, which ensures the stress necessary for nucleation. As shown in Figure 16b, dislocations nucleate more quickly in the early stages of cutting for cutting with fluid media. From the temperature distribution curve in Figure 4, it can be known that the early temperature of the cutting process with a fluid medium is relatively high, which easily promotes the nucleation of dislocations. On the other hand, from Figures 12f,k, 14f,k and 15f,k, it can be seen that the cutting process with a large cutting angle has a small amount of dislocation residue under the shaped surface of the workpiece at the end of the cut, which has a certain impact on

the quality of the workpiece. According to the analysis above, a smaller cutting angle and the existence of a fluid medium can decrease the quantity of dislocations and the overall length of dislocations, which reduces the generation of sub-surface defect structures.

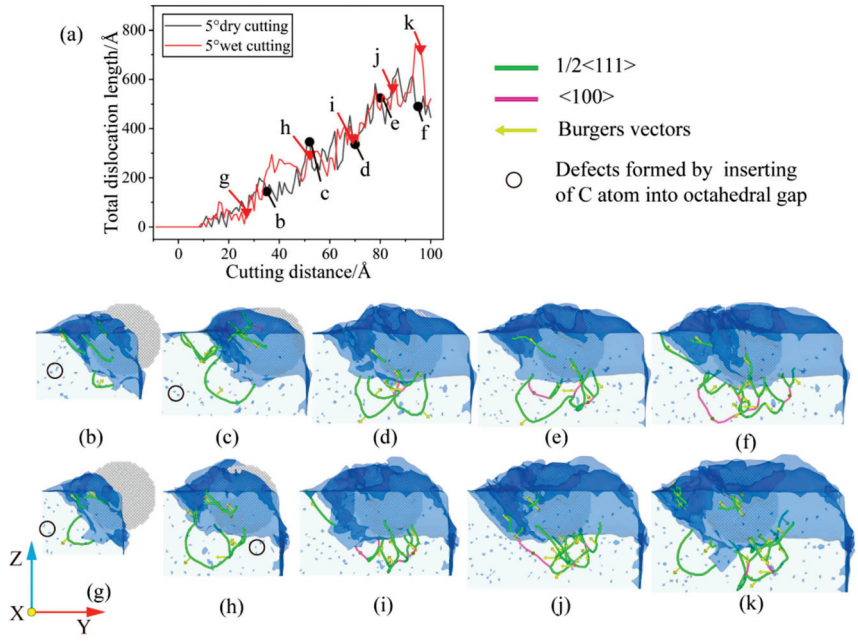

Figure 14. Dislocation evolution under θ = 5°. (**a**) Variation of total length of dislocation with cutting distance; (**b**) cutting distance of 35 Å under dry cutting; (**c**) cutting distance of 52 Å under dry cutting; (**d**) cutting distance of 70 Å under dry cutting; (**e**) cutting distance of 80 Å under dry cutting; (**f**) cutting distance of 94 Å under dry cutting; (**g**) cutting distance of 27 Å under wet cutting; (**h**) cutting distance of 52 Å under wet cutting; (**i**) cutting distance of 69 Å under wet cutting; (**j**) cutting distance of 85 Å under wet cutting; and (**k**) cutting distance of 96 Å under wet cutting.

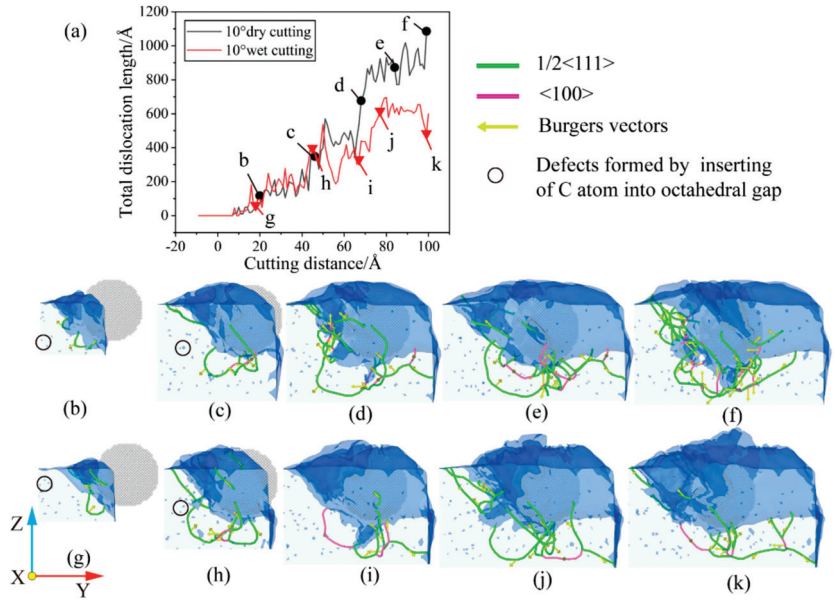

Figure 15. Dislocation evolution under θ = 10°. (**a**) Variation of total length of dislocation with cutting distance; (**b**) cutting distance of 20 Å under dry cutting; (**c**) cutting distance of 46 Å under dry cutting; (**d**) cutting distance of 68 Å under dry cutting; (**e**) cutting distance of 86 Å under dry cutting; (**f**) cutting distance of 100 Å under dry cutting; (**g**) cutting distance of 16 Å under wet cutting; (**h**) cutting distance of 45 Å under wet cutting; (**i**) cutting distance of 66 Å under wet cutting; (**j**) cutting distance of 77 Å under wet cutting; and (**k**) cutting distance of 99 Å under wet cutting.

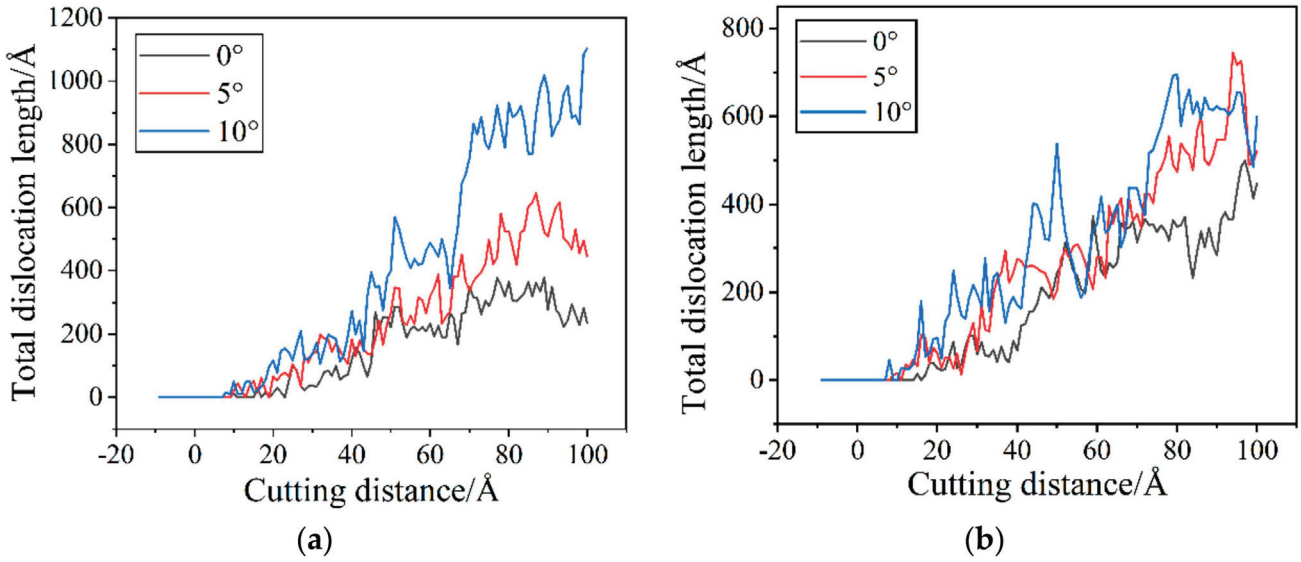

Figure 16. Total dislocation length changes under different cutting angles. (**a**) Dry cutting; and (**b**) wet cutting.

4. Conclusions

In order to reveal the influence of fluid medium and cutting angle on the nano-cutting process, this study establishes a MD model of nano-cutting iron–carbon alloy system with $C_{12}H_{26}$ molecules as the fluid medium. By comparing the dry cutting and wet cutting, the following conclusions are drawn:

1. In comparison to machining without a fluid medium, machining using a fluid medium ($C_{12}H_{26}$) lowers the machining temperature and the coefficient of friction.
2. Temperature and coefficient of friction increase with increasing cutting angle during abrasive flow machining.
3. The cutting angle has a greater influence on the formation of the workpiece's surface profile and the manner in which the workpiece atoms are displaced, whereas the fluid medium has a lesser influence. When the cutting angle is 0°, 5° and 10°, respectively, the workpiece's surface profile flows at 45° to both sides. The height of the atomic accumulation on the workpiece's surface gradually decreases, but at the same time the area where displacement changes occur becomes larger. As the cutting angle increases, so does the depth of cut, resulting in more material damage.
4. The area of displacement gradually expands towards the interior of the workpiece as the cutting angle increases. The number of atoms displaced to the workpiece's surface decreases and remains within the workpiece. The atoms that accumulate inside the workpiece squeeze the uncut area, causing a bulge in the workpiece's surface, which degrades the workpiece's quality, but is beneficial for the removal of large burrs.
5. During the cutting process, a large number of dislocations were discovered at b = 1/2 <1 1 1> and b = <1 0 0>. The b = 1/2 <1 1 1> dislocations dominate, with b = <1 0 0> connecting the dislocations in different areas. The dislocation reaction network is formed by the presence of a large number of single and double-branched structures within the workpiece. During large-angle cutting, the fluid medium can reduce the number of dislocations and the total dislocation length, which in turn reduces the generation of sub-surface defect structures, resulting in better machining quality.

Author Contributions: Conceptualization and methodology, J.L. (Junye Li); writing—original draft preparation, Z.Z.; software, J.L. (Junwei Li); formal analysis, F.X.; validation, R.Q.; writing—review and editing, H.X.; investigation, W.M. All authors have read and agreed to the published version of the manuscript.

Funding: This research was funded by Science and technology development plan project of Jilin province No. 20220201036GX and 20220201056GX, Science and technology research project of Jilin Provincial Department of Education No. JJKH20220734KJ.

Data Availability Statement: Not acceptable.

Acknowledgments: The authors would like to thank Science and technology development plan project of Jilin province No. 20220201036GX and 20220201056GX, Science and technology research project of Jilin Provincial Department of Education No. JJKH20220734KJ.

Conflicts of Interest: The authors declare that they have no affiliations with or involvement in any organization or entity with any financial interest in the subject matter or materials discussed in this manuscript.

References

1. Guo, P. Research on the Evaluation of Nano-Surface Roughness in Ultra-Precision Machining. Master's Thesis, Nanchang University, Nanchang, China, 2022. [CrossRef]
2. Wang, Y.; Yuan, Z.W.; Zhang, Y.J. Overview of material removal theory in ultra-precision machining. *Mech. Des. Manuf.* **2022**, 147–150+155. [CrossRef]
3. Gou, Y. Research on Sub-Surface Damage of Single Crystal Tungsten Cutting Based on Molecular Dynamics. Master's Thesis, Dalian University of Technology, Dalian, China, 2021. [CrossRef]
4. Yang, S.; Cao, H.; Liu, Y.; Yao, P.; Feng, R. Molecular dynamics simulation of the effect of rough surface on material removal and subsurface defects during γ-TiAl processing. *Rare Met. Mater. Eng.* **2022**, *51*, 3236–3243.
5. Du, M. Fundamental Study on the Evolution of Subsurface Defects in Ultra-Precision-Cut Single-Crystal Copper Based on Molecular Dynamics Simulation. Master's Thesis, Huaqiao University, Quanzhou, China, 2022. [CrossRef]
6. Liu, H.; Guo, Y.; Li, D.; Wang, J. Material Removal Mechanism of FCC Single-Crystalline Materials at Nano-Scales: Chip Removal & Ploughing. *J. Mater. Process. Technol.* **2021**, *294*, 117106. [CrossRef]
7. Yue, H. Study on the Removal Mechanism of Monocrystalline Silicon by Three-Body Polishing with Diamond Abrasive Based on Molecular Dynamics. Master's Thesis, Guizhou University, Guiyang, China, 2022. [CrossRef]
8. Ma, Z.; Liang, G.; Lu, M. Molecular dynamics research on anisotropic nano-cutting of monocrystalline silicon. *Mech. Des. Manuf.* **2021**, *8*, 99–102. [CrossRef]
9. Gao, Y.; Urbassek, H.M. Evolution of plasticity in nanometric cutting of Fe single crystals. *Appl. Surf. Sci.* **2014**, *317*, 6–10. [CrossRef]
10. Ma, T.; Xie, H. Mechanism of formation of face-centered cubic phase in single crystal iron along [101] during crystal orientation impact. *J. Phys.* **2020**, *69*, 111–121.
11. Lian, T. Research on Nano-Mechanical Properties and Deformation Mechanism of Single Crystal Iron Carbide. Master's Thesis, Huaqiao University, Quanzhou, China, 2022. [CrossRef]
12. Li, X.; Yin, Y.; Zhang, Y. Point defect types and concentration pairs Molecular dynamics simulation of the effect of plastic deformation behavior of α-Fe. *Rare Met. Mater. Eng.* **2022**, *51*, 2881–2889.
13. Wei, W.; Yu, X. Molecular dynamics study on the effect of lithium on the tensile mechanical behavior of ferrite. *J. Univ. Chin. Acad. Sci.* **2022**, *39*, 13–20.
14. Alhafez, I.A.; Urbassek, H.M. Influence of the Rake Angle on Nanocutting of Fe Single Crystals: A Molecular-Dynamics Study. *Crystals* **2020**, *10*, 516. [CrossRef]
15. Zamzamian, S.M.; Feghhi, S.A.H.; Samadfam, M. A study on the mobility of $\frac{1}{2}$<111> {011} edge dislocation in low-carbon α-Fe and its interactions with damage cascade: On picosecond time scale using molecular dynamics simulations. *J. Nucl. Mater.* **2019**, *527*, 151806. [CrossRef]
16. Jiao, Y.; Dan, W.; Zhang, W. The strain-induced martensitic phase transformation of Fe–C alloys considering C addition: A molecular dynamics study. *J. Mater. Res.* **2020**, *35*, 1803–1816. [CrossRef]
17. Luu, H.-T.; Gunkelmann, N. Pressure-induced phase transformations in Fe-C: Molecular dynamics approach. *Comput. Mater. Sci.* **2019**, *162*, 295–303. [CrossRef]
18. Martin, M.G.; Siepmann, J.I. Transferable Potentials for Phase Equilibria. 1. United-Atom Description of n-Alkanes. *J. Phys. Chem. B* **1998**, *102*, 2569–2577. [CrossRef]
19. Zheng, X.; Zhu, H.; Kosasih, B.; Tieu, A.K. A molecular dynamics simulation of boundary lubrication: The effect of n-alkanes chain length and normal load. *Wear* **2013**, *301*, 62–69. [CrossRef]
20. Liyanage, L.S.I.; Kim, S.-G.; Houze, J.; Kim, S.; Tschopp, M.A.; Baskes, M.I.; Horstemeyer, M.F. Structural, elastic, and thermal properties of cementite (Fe_3C) calculated using a modified embedded atom method. *Phys. Rev. B* **2014**, *89*, 094102. [CrossRef]
21. Girifalco, L.A.; Weizer, V.G. Application of the Morse Potential Function to Cubic Metals. *Phys. Rev.* **1959**, *114*, 687–690. [CrossRef]
22. Hegab, H.; Umer, U.; Soliman, M.; Kishawy, H.A. Effects of nano-cutting fluids on tool performance and chip morphology during machining Inconel 718. *Int. J. Adv. Manuf. Technol.* **2018**, *96*, 3449–3458. [CrossRef]
23. Plimpton, S. Fast Parallel Algorithms for Short-Range Molecular Dynamics. *J. Comput. Phys.* **1995**, *117*, 1–19. [CrossRef]

24. Stukowski, A.; Albe, K. Extracting dislocations and non-dislocation crystal defects from atomistic simulation data. *Model. Simul. Mater. Sci. Eng.* **2010**, *18*, 085001. [CrossRef]
25. Stukowski, A. Visualization and analysis of atomistic simulation data with OVITO–the Open Visualization Tool. *Model. Simul. Mater. Sci. Eng.* **2010**, *18*, 015012. [CrossRef]
26. Ruda, M.; Farkas, D.; Garcia, G. Atomistic simulations in the Fe–C system. *Comput. Mater. Sci.* **2009**, *45*, 550–560. [CrossRef]
27. Cao, H.; Zhang, T.; Chen, Y. Research on Cooling Methods for Cutting Fluids. *Equip. Manag. Maint.* **2021**, *5*, 144–145. [CrossRef]
28. Yang, Y. Study on the Characteristics of Coolant Temperature Field Change during High Speed Cutting. Master's Thesis, Yanshan University, Qinhuangdao, China, 2018.
29. Doan, D.-Q.; Fang, T.-H.; Chen, T.-H. Nanotribological characteristics and strain hardening of amorphous Cu64Zr36/ crystalline Cu nanolaminates. *Tribol. Int.* **2020**, *147*, 106275. [CrossRef]
30. Pan, C.; Wang, C.; Li, W.; Wang, Y.; Yuan, Y.; Wu, H. Development and practical testing of a special micro-lubrication cutting fluid for titanium alloy. *Mould. Manuf.* **2022**, *22*, 70–75.
31. Yang, Y. Research on the Application of Micro-Lubrication Technology of Green Nano Cutting Fluid. Master's Thesis, Hangzhou University of Electronic Science and Technology, Hangzhou, China, 2020. [CrossRef]
32. Wang, H. Cutting Numerical Simulation and Cutter Roller Optimization Design of Drum Chipper. Master's Thesis, Northeast Forestry University, Harbin, China, 2019. [CrossRef]
33. Smith, R.; Christopher, D.; Kenny, S.D.; Richter, A.; Wolf, B. Defect generation and pileup of atoms during nanoindentation of Fe single crystals. *Phys. Rev. B* **2003**, *67*, 245405. [CrossRef]
34. Katzarov, I.H.; Drenchev, L.B. Unveiling the Mechanisms of High-Temperature 1/2[111] Screw Dislocation Glide in Iron–Carbon Alloys. *Crystals* **2022**, *12*, 518. [CrossRef]
35. Li, S.; Chen, Z.; Yun, J.; Zhang, J. Phase-field crystal method investigated the dislocation annihilation and grain boundary migration in grain shrink process. *Acta Phys. Sin.* **2014**, *63*, 128101. [CrossRef]

micromachines

MDPI

Article

In Situ Measurement of Spindle Radial Error for Ultra-Precision Machining Based on Three-Point Method

Hanwei Xu [1,2,3], Zizhou Sun [1,2,3], Yifan Dai [1,2,3,*], Chaoliang Guan [1,2,3], Hao Hu [1,2,3] and Yu Wang [1,2,3]

[1] College of Intelligent Science and Technology, National University of Defense Technology, Changsha 410073, China
[2] Hunan Key Laboratory of Ultra-Precision Machining Technology, Changsha 410073, China
[3] Laboratory of Science and Technology on Integrated Logistics Support, National University of Defense Technology, Changsha 410073, China
* Correspondence: dyf@nudt.edu.cn; Tel.: +86-139-7313-6931

Abstract: The radial error is an important parameter to evaluate the performance of ultra-precision spindles. The three-point method has not yet been well applied in nanometer-scale measurement due to its disadvantages of harmonic suppression and the complicated error separation process. In order to verify that the three-point method can realize the nanometer-scale measurement of the radial error in the machining environment, an in situ measurement and evaluation system is established. Experiments are performed using the system, and a comparative experiment is conducted to verify the accuracy of the system. The average value and standard deviation of the measurement results are 23.096 nm and 0.556 nm, respectively. The in situ measurement result was in good agreement with the Donaldson reversal method using a commercially available spindle analyzer.

Keywords: radial error; ultra-precision spindle; nanometer-scale measurement; three-point method; Donaldson reversal method

Citation: Xu, H.; Sun, Z.; Dai, Y.; Guan, C.; Hu, H.; Wang, Y. In Situ Measurement of Spindle Radial Error for Ultra-Precision Machining Based on Three-Point Method. *Micromachines* **2023**, *14*, 653. https://doi.org/10.3390/mi14030653

Academic Editors: Jiang Guo, Chunjin Wang and Chengwei Kang

Received: 15 February 2023
Revised: 9 March 2023
Accepted: 10 March 2023
Published: 14 March 2023

1. Introduction

Ultra-precision spindles have been widely used in advanced manufacturing and ultra-precision measurement, supporting development in semiconductor electronics, space exploration and other fields [1,2]. Radial error refers to the deviation of the instantaneous axis of the rotating spindle relative to the average axis in the radial direction. Since the spindle drives the tool to rotate, the radial error will directly affect the depth of cut, and then affect the face accuracy of the machined workpiece [3–5]. Therefore, the measurement of the radial error is a key link to design a spindle and evaluate the machining performance of the ultra-precision spindles [6]. Focused on the method of ultra-precision spindle radial error measurement, scholars have carried out a significant amount of research. The proposal of error separation technology is a major breakthrough in the field of spindle radial error measurement [7], promoting the development of spindle metrology. Several error separation techniques were then developed, including the multi-point method [7], multi-step method [8,9] and the Donaldson reversal method [10,11]. The multi-step method is rarely used in the field of ultra-precision measurement because of its complex operation steps.

After the three methods above were put forward, most of the scholars' research was carried out on the basis of these three measurement methods. Compared with the other two methods, the Donaldson reversal method is based on a simpler principle. Cui et al. [12] constructed a nanometer system for measuring the radial error of aerostatic ultra-precision based on the Donaldson reversal method. The effect of the cogging torque of the motor, the angle deviation, artifact eccentricity and spindle axial motion on the measuring accuracy of the spindle were studied. The accuracy of the measurement system and the validity of the Donaldson reversal method were confirmed. Chen et al. [13] measured the uncertainty of the rotary accuracy of an ultra-precision aerostatic spindle based on the Donaldson

reversal method. The results showed that the nonlinear error and the mounting error of the capacitive sensor could affect the measurement accuracy. The Lion Precision Spindle Error Analyzer (SEA) was successfully used by Jerzy Józwik et al. [14] to measure the radial error of the spindle of a DMC 635 eco machining center. The SEA is a representative commercial instrument based on the Donaldson reversal method, but it has extremely high requirements on the accuracy of reverse positioning. It is best to use a precision mechanism for reverse, otherwise a large secondary clamping error will be introduced. In short, although the principle of the Donaldson reversal method is simple, the operation requirements are extremely high, and it is not suitable for the ultra-precision measurement of the radial error of the horizontal spindles.

Another method is the multi-point method [15], mainly including the three-point method and the four-point method [16], which only requires one setup to be measured. According to the research of Eric R. Marsh [17,18], the three-point method can realize nanometer-scale measurement, but experimental technical details were not given. Although the measurement operation of the three-point method is relatively simple, harmonic suppression is a shortcoming of the three-point method that cannot be ignored [19,20]. Research found that the influence of harmonic suppression can be reduced or even ignored by selecting the appropriate sensor angle [21]. Gao et al. [22,23] proposed several new multi-probe methods, which can effectively separate the roundness of the measured workpiece from the spindle radial error, thereby avoiding the problem of harmonic suppression. In addition, some scholars have also systematically studied the three-point method [11,24,25], but most of them have only carried out theoretical research and verified it in the laboratory environment. To sum up, many scholars have conducted in-depth research on the three-point method, but there are still few practical applications of the three-point method in ultra-precision machining measurement.

This paper designs an in situ measurement and evaluation system based on the three-point method, which can realize ultra-precise measurement in the machining environment. The system is used to realize the measurement of 20 nm radial error on an ultra-precision lathe, and the roundness error of the measured standard workpiece can be obtained at the same time. The theoretical analysis and technical details of the experiments are given in detail. The advantages of the three-point method over the Donaldson reversal method in the machining environment is illustrated.

2. Mathematical Model and Error Separation Technology

2.1. Mathematical Model of the Circular Cross-Sectional Profile

The circular cross-sectional profile of shaft parts has a periodic character and can be decomposed into sinusoidal waves of different orders. These sine waves are superimposed in a defined pattern to obtain the cross-sectional profile.

The circular cross-sectional profile of shaft parts is shown in Figure 1, with the solid line indicating the actual profile and the dashed line indicating the ideal profile. It can be found that the shape of the cross-sectional profile of the shaft parts in rotation will exhibit deterministic periodic signal characteristics, which can be expanded by Fourier series as

$$r(\theta_p) = r_0 + \sum_{k=1}^{\infty} (a_k cosk\theta_p + b_k sink\theta_p) \quad (1)$$

where θ_p is the polar angle; r_0 is the average radius of the circular cross-sectional profile of the workpiece; k is the number of harmonics; and a_k and b_k are Fourier coefficients of the roundness error profile.

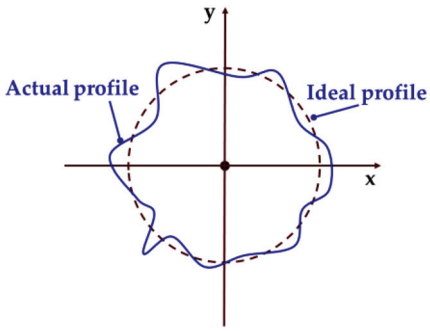

Figure 1. Schematic diagram of one cross-sectional profile.

Since the sampling points are discrete in the actual sampling process, the Fourier coefficients can be calculated by Euler's criterion as

$$a_k = \frac{2}{N}\sum_{n=1}^{N} r(n)\cos\frac{2\pi kn}{N} \tag{2}$$

and

$$b_k = \frac{2}{N}\sum_{n=1}^{N} r(n)\sin\frac{2\pi kn}{N} \tag{3}$$

where N is the number of sampling points in each circle and n is the $n-th$ of the total number of sampling points in each circle.

In the actual sampling, a sensor probe with suitable accuracy is selected for data acquisition. The collected data include synchronous error and asynchronous error, and these errors can be separated. The synchronous error can be obtained by averaging the raw data of multiple turns, and the asynchronous error data is obtained by subtracting the synchronous error from the raw data, as shown in Figure 2.

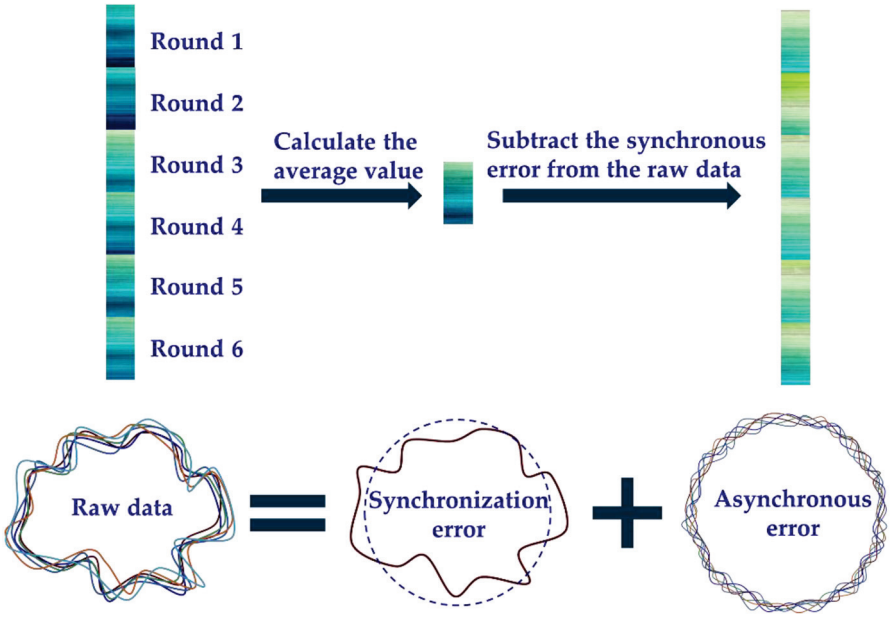

Figure 2. Separation of synchronous and asynchronous errors.

After Fourier transform, the synchronous error data are distributed in integer multiples of the spindle rotation frequency and its neighborhood, and the asynchronous error data are distributed in non-integer multiples of the rotation frequency interval, as shown in Figure 3. The lines marked with asterisks represent the frequency components of synchronous errors, and the lines with circular marks represent the frequency components of asynchronous

errors. The synchronization error data, combined with the data of other probes or other measurement steps, can be further separated into the radial error of the spindle and the roundness error of the standard workpiece. The separation method of the synchronization error will be further introduced below.

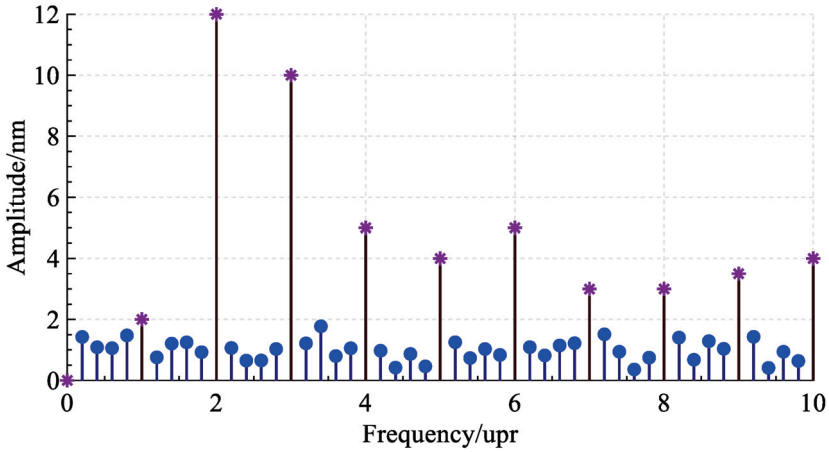

Figure 3. Frequency domain map of original data after Fourier transform.

2.2. Error Separation Techniques

Roundness error separation methods generally include the multi-point method, multi-step method and Donaldson reversal method. Compared with the multi-step method, the three-point method and the reversal method have the advantages of fewer clamping times, thus introducing less error. Therefore, the measurement of radial error of the spindle generally uses the three-point method and the reversal method.

2.2.1. Three-Point Method

As shown in Figure 4, three sensor probes are placed at a certain angle to collect data synchronously. After removing the asynchronous error and the installation eccentricity of the standard workpiece, the data collected by the three sensors can be expressed as

$$\begin{cases} m_A(\theta) = p(\theta) + x(\theta) \\ m_B(\theta) = p(\theta - \alpha) + x(\theta)\cos\alpha + y(\theta)\sin\alpha \\ m_C(\theta) = p(\theta + \beta) + x(\theta)\cos\beta - y(\theta)\sin\beta \end{cases} \tag{4}$$

where θ is the spindle rotation angle; α is the angle between sensor A and sensor B; β is the angle between sensor A and sensor C; $m_A(\theta)$, $m_B(\theta)$, $m_C(\theta)$ respectively represent the readings of the three sensors after removing the asynchronous error and workpiece eccentricity; $p(\theta)$ is the roundness error of the standard workpiece; and $x(\theta)$ and $y(\theta)$ respectively represent the projected components of the radial error of the spindle on the x-axis and y-axis.

The radial error of the spindle and roundness error of the standard workpiece can be obtained by analyzing the weighted sum of each sub-formula of Formula (4) using the Fourier transform method.

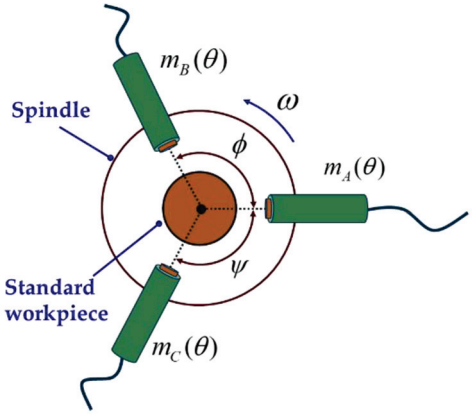

Figure 4. Schematic diagram of sensor distribution of three-point method.

2.2.2. Donaldson Reversal Method

The measurement using the Donaldson reversal method is mainly divided into two steps: first, fix the sensor at the 0° position, and collect the first set of data; then, the measured standard workpiece and the sensor are rotated 180° at the same time to collect the second set of data. The measurement steps of the Donaldson reversal method are shown in Figure 5. Detailed technical details will be introduced in the comparative experiment.

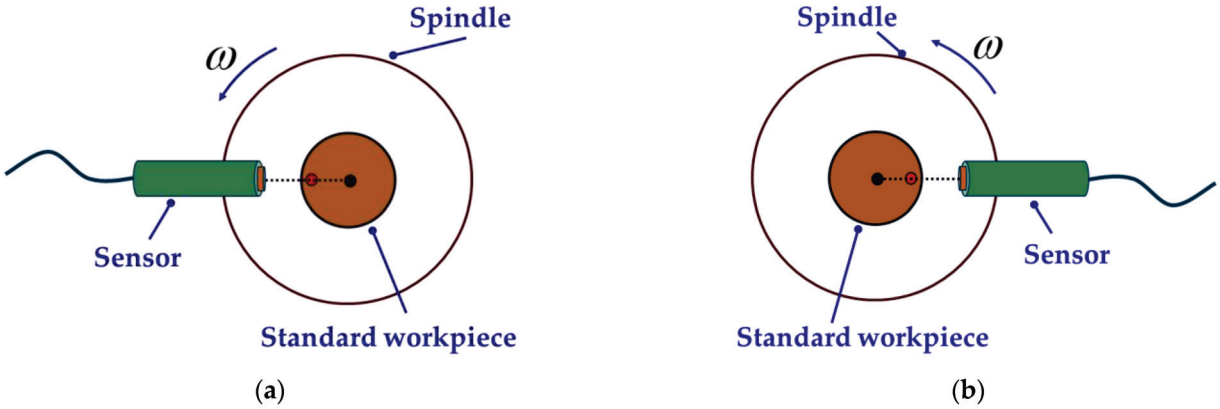

Figure 5. Schematic diagram of Donaldson reversal method measurement: (**a**) before reversal, (**b**) after reversal.

The average value of each point measured before the reversal is T_1, and that after the reversal is T_2:

$$\begin{cases} T_1(\theta_j) = \frac{1}{m}\sum_{1}^{m} C_{ij}, i = 1, 2, \cdots, m; j = 1, 2, \cdots, n \\ T_2(\theta_j) = \frac{1}{m}\sum_{1}^{m} D_{ij}, i = 1, 2, \cdots, m; j = 1, 2, \cdots, n \end{cases} \tag{5}$$

where C_{ij} is the sample value of the $j-th$ point in the $i-th$ cycle before the reversal, and D_{ij} is that after the reversal; i is the number of revolutions sampled; j is the number of sampling points per revolution; and θ_j is the rotated angle of the spindle when the $j-th$ point is sampled.

T_1 and T_2 can also be expressed as

$$\begin{cases} T_1(\theta_j) = s(\theta_j) + p(\theta_j), j = 1, 2, \cdots, n \\ T_2(\theta_j) = s(\theta_j) - p(\theta_j), j = 1, 2, \cdots, n \end{cases} \tag{6}$$

where s is the radial error of the spindle and p is the roundness error of the standard workpiece.

From Equation (13), s and p can be calculated:

$$\begin{cases} s(\theta_j) = \frac{1}{2}(T_1(\theta_j) + T_2(\theta_j)), j = 1, 2, \cdots, n \\ p(\theta_j) = \frac{1}{2}(T_1(\theta_j) - T_2(\theta_j)), j = 1, 2, \cdots, n \end{cases} \tag{7}$$

3. Design of In Situ Measurement and Evaluation System

3.1. Overall Structure of In Situ Measurement and Evaluation System

Based on the previously theoretical derivations, an in situ measurement and evaluation system is designed, and its overall structure diagram is shown in Figure 6. The system consists of a standard workpiece, fixture, digital capacitive micro-displacement sensors, spindle, circular grating, data acquisition card, computer and servo control system of the machine tool. The reason for choosing capacitive sensors is that compared to other sensors, capacitive sensors are more suitable for working in harsh environments, such as ultra-precision machining workshops. The sensor used in this study is the capacitive micro-displacement sensor designed by the Lion Precision Company. The sensor model is CPL190/C8-2. 0, the range is 5.0×10^4 nm, the resolution is 1.0 nm and the linearity is 0.15% F.S.

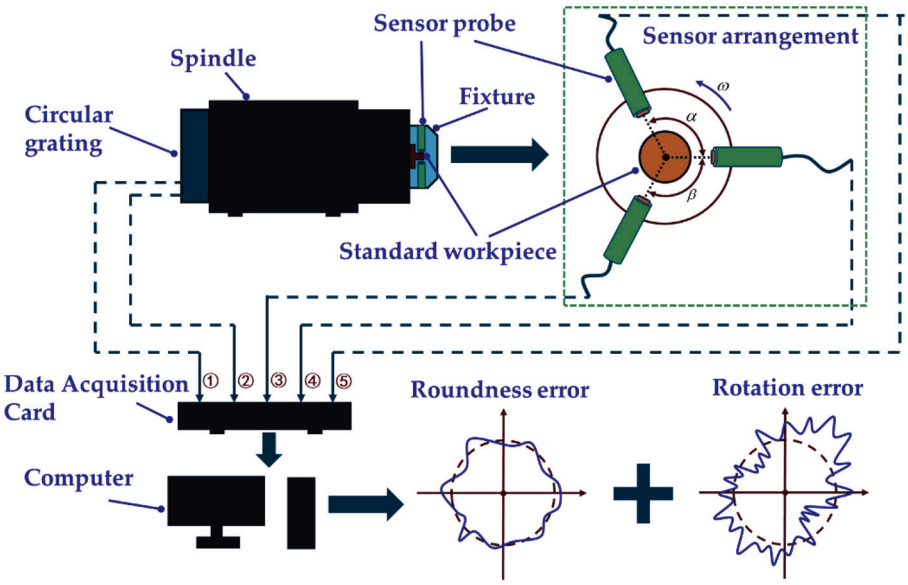

Figure 6. Overall structure of in situ measurement and evaluation system.

The system works as follows: firstly, the standard workpiece, fixture and sensor probes are fixed to the spindle; secondly, a servo control system is used to drive the spindle to rotate at a certain speed, three sensor probes are used to collect data, and two grating data are collected simultaneously; thirdly, the above five signals are imported into the computer and processed. Then, the radial error of the spindle and the roundness error of the standard workpiece can be obtained. Technical details will be given later in the experiments.

3.2. Design of Fixture and Standard Workpiece

3.2.1. Design of Fixture

In order to improve the measurement accuracy of the three-point method, an integrated fixture is designed to ensure the accuracy of the sensor installation position. The fixture can be used for both three-point method measurement and Donaldson reversal method measurement.

The problem of harmonic suppression is the main disadvantage of the three-point method measurement, but it can be reduced or even avoided by choosing an appropriate installation angle for the three sensors. In this paper, angle α and β between the three

sensors are calculated by referring to the methods from previous research [19,26]. Two sets of sensor arrangements applicable to the three-point method are selected:

$$\begin{cases} \alpha_1 = 69.984375^\circ \\ \beta_1 = 70.3125^\circ \end{cases} \tag{8}$$

$$\begin{cases} \alpha_2 = 146.953125^\circ \\ \beta_2 = 152.578125^\circ \end{cases} \tag{9}$$

The fixture designed in this paper is shown in Figure 7.

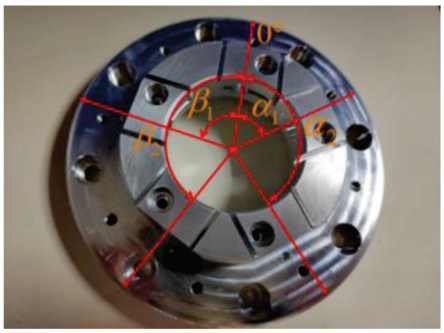

Figure 7. Measuring fixture.

3.2.2. Design of Standard Workpiece

The key to the standard workpiece design is to ensure that the roundness of the standard workpiece is in the same order of magnitude as the radial error of the spindle, so as to ensure the high precision of the error separation.

The radial error of the ultra-precision spindle used in this paper is between 10 nm and 50 nm. Therefore, the roundness of the designed standard workpiece should also be guaranteed in the same order of magnitude through ultra-precision turning. The effective working area of the standard workpiece is a cylinder with a diameter of 20 mm, as shown in Figure 8. According to the performance of the ultra-precision lathe, the roundness of the effective working area of the standard workpiece is between 15 nm and 20 nm.

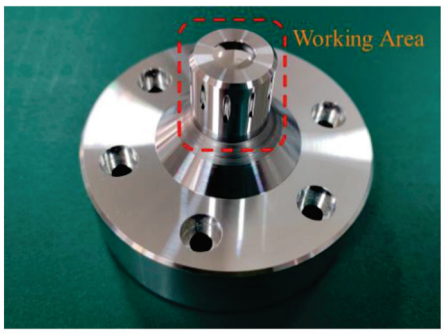

Figure 8. Standard workpiece.

3.2.3. Determination of Sampling Points

The number of sampling points for the three-point method can be determined according to the following algorithm.

The sampling frequency can be expressed by

$$f_s = N\frac{\omega_0}{2\pi} \tag{10}$$

where N is the number of sampling points per revolution and ω_0 is the angular velocity of the spindle.

The frequency component of the signal we want to identify is $f_{\max}$, and the corresponding number of spectral lines is N_{fm}. By Nyquist's sampling theorem, it is required that $f_s \geq 2f_{\max}$.

An anti-alias low-pass filter is usually set to filter out the frequency components above $\frac{f_s}{2}$. When using a capacitive sensor for measurement, since the capacitive sensor probe pole plate has a certain width, it is equivalent to adding a moving average low-pass filter with a cut-off frequency of

$$f_c = \pi \frac{D_r}{D} n \tag{11}$$

where f_c is the cut-off frequency; D_r is the diameter of the standard workpiece; D is the diameter of the capacitive sensor circular pole plate; n is speed of the spindle; and the unit of n is revolutions per minute.

In general, f_c will be lower than the cut-off frequency of the anti-alias low-pass filter available, so N has to satisfy

$$f_s = N \cdot n \geq 2.56 f_c \tag{12}$$

Therefore, N can be chosen as

$$N \geq 2.56\pi \frac{D_r}{D} \tag{13}$$

The diameter of the sensor pole plate used in this paper is 2 mm, and the diameter of the measured cylindrical workpiece is 20 mm. So according to Equation (13), N can be chosen as 512 points. The filtering effect of the capacitive sensor acts as an anti-aliasing low-pass filter.

4. In Situ Measurement and Evaluation Experiment of Radial Error

4.1. In Situ Measurement and Evaluation Experiment of Radial Error Using Three-Point Method

The measurement is carried out in the ultra-precision machining workshop. The temperature of the workshop is kept at 20–24 °C, and the humidity is at 50–60%, which mainly changes with the seasons. During the in situ measurement and evaluation experiment, the temperature and humidity are almost constant. The measurement object is an ultra-precision air-bearing spindle independently developed and manufactured by the laboratory. The spindle is installed on an ultra-precision lathe in the machining workshop and the design value of the radial rotation accuracy of the spindle is 20 nm. The main body of the ultra-precision lathe is granite, and the lathe is installed on a shock-absorbing mechanism to achieve a good shock-absorbing effect and ensure the processing performance.

The in situ measurement and evaluation system is used to perform the experiment. The installation position of the three sensors is decided according to Equation (9). Figure 9 shows the detailed measurement process, which is critical to ensure the accuracy and stability of the in situ measurement and evaluation system. Compared with the traditional operation steps of three-point method of measurement, the in situ measurement and evaluation system is more operable while ensuring the installation accuracy.

First, as shown in Figure 9a, the standard workpiece is adsorbed on the air-bearing spindle by the pressure of the vacuum, and the geometric center of the standard workpiece is roughly aligned with the axis of the standard workpiece; second, as shown in Figure 9b, a dial indicator is used to make rough adjustments so that the eccentricity of the standard workpiece is within 1 μm; third, as shown in Figure 9c, the sensor probe is used for fine adjustments to make the eccentricity of the standard workpiece within 0.1–0.2 μm. The more accurate the centering, the higher the accuracy of the measurement results. Finally, the fixture and sensor probes are mounted in place, as shown in Figure 9d, and the measurement can be performed immediately. The measurement results will be presented and analyzed in Section 5.

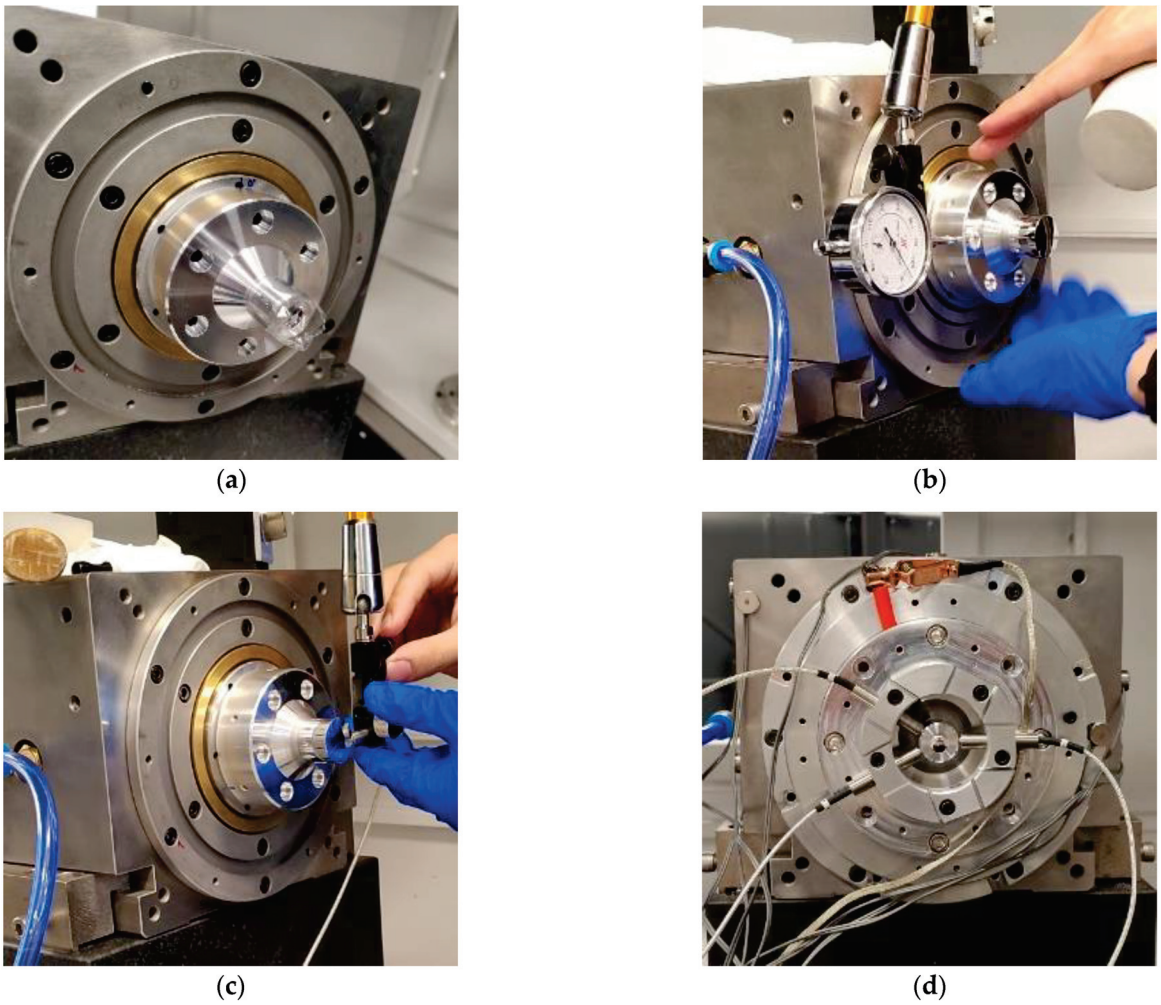

Figure 9. Detailed steps of radial error measurement using three-point method: (**a**) step 1: mounting of standard workpiece, (**b**) step 2: rough adjustment of standard workpiece, (**c**) step 3: fine adjustment of standard workpiece, (**d**) step 4: mounting fixture and sensor probes.

4.2. Comparative Experiment of the Results

The comparative experiment is performed based on the Donaldson reversal method to validate the results measured by the in situ measurement and evaluation system. The spindle analyzer developed by Lion Precision and self-designed experimental equipment are used in the comparative experiment.

The measurement steps of the comparative experiment are as follows: first, the sensor probe is mounted in the 0° direction of the spindle for the first dataset acquisition, as shown in Figure 10a; after this, the fixture, sensor and standard workpiece are reversed 180° at the same time. Then, the sensor probe is in the 180° direction, acquiring the second set of data, as shown in Figure 10b. Before and after reversing, the speed of the spindle should be the same.

The measurement results are shown in Figure 11. The curves in Figure 11a–d show the synchronization error before reversal, the synchronization error after reversal, the roundness error of the standard workpiece and the radial error of the spindle, respectively. The radial error of the spindle is 25.135 nm, and the roundness error of the standard workpiece under testing is 20.515 nm. The measurement results based on the Donaldson reversal method are taken as the reference results. The measurement results obtained using the in situ measurement and evaluation system will be analyzed and discussed together with the reference results in Section 5.

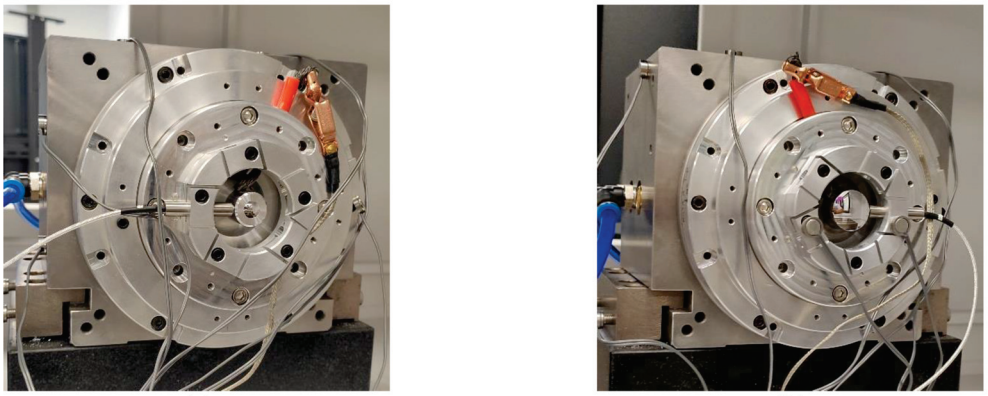

(**a**) (**b**)

Figure 10. Donaldson reversal method measurement device: (**a**) before reversal, (**b**) after reversal.

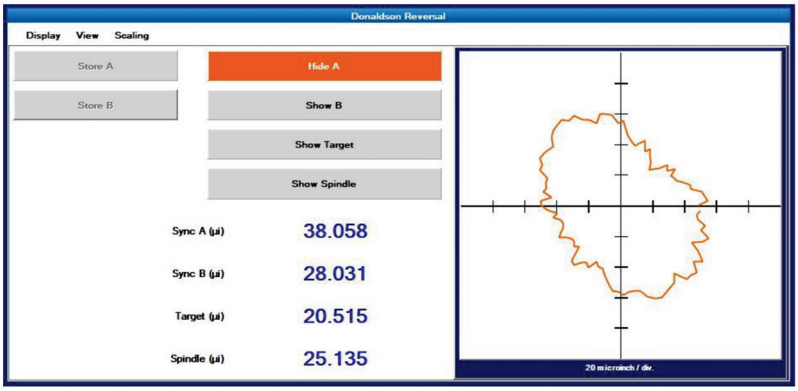

(**a**)

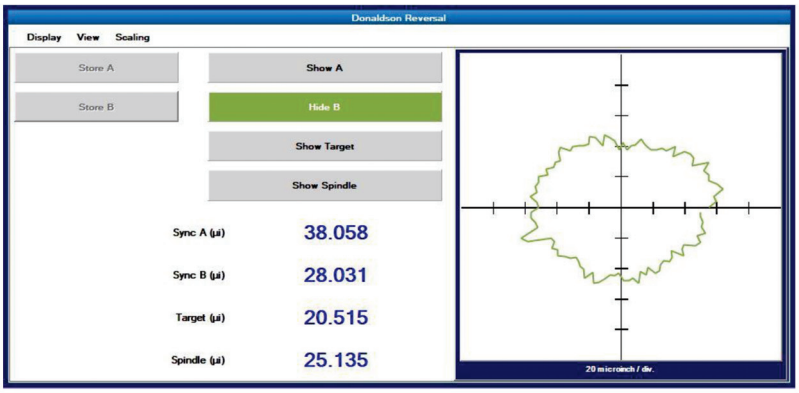

(**b**)

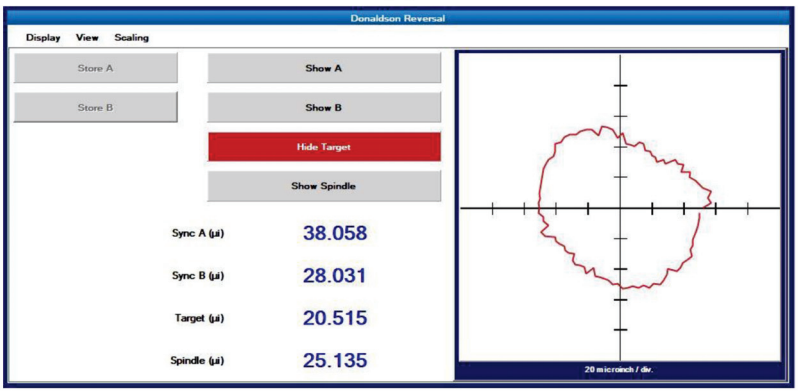

(**c**)

Figure 11. *Cont.*

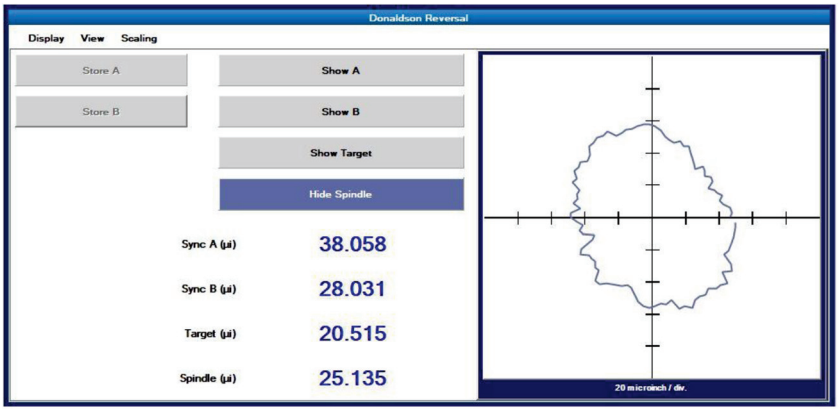

(**d**)

Figure 11. Donaldson reversal method measurement data: (**a**) synchronization error before reversal, (**b**) synchronization error after reversal, (**c**) roundness error of standard workpiece, (**d**) spindle radial error.

5. Result and Discussion

For the convenience of the discussion, the sampling data when the spindle speed is 60 revolutions per minute is selected as the first example. The raw data obtained by the in situ measurement and evaluation system is processed to remove the asynchronous error and eccentricity. Then, the synchronous error data are obtained. Figure 12a–c shows the amplitude phase diagrams of the multi-turn sampling data of the three sensors with the eccentricity and synchronization error removed in the polar coordinate system, respectively. Figure 13a–c show the amplitude phase diagrams of the multi-turn sampling data of the three sensors with the eccentricity and synchronization error removed in the Cartesian coordinate system, respectively.

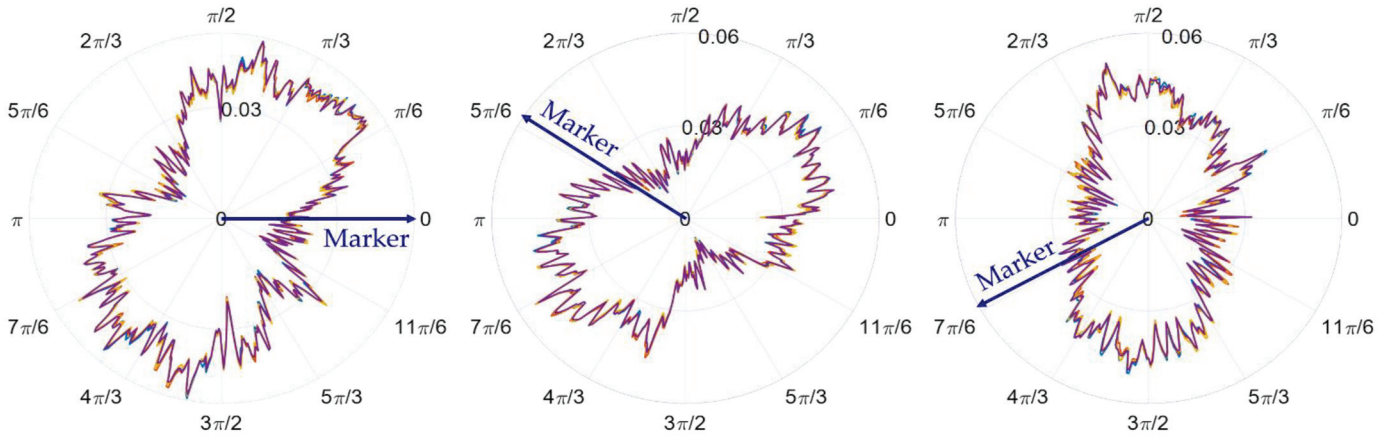

(**a**) (**b**) (**c**)

Figure 12. Amplitude phase diagrams of the multi-turn sampling data of the three sensors with the eccentricity and synchronization error removed in the polar coordinate system: (**a**) data from sensor A, (**b**) data from sensor B, and (**c**) data from sensor C.

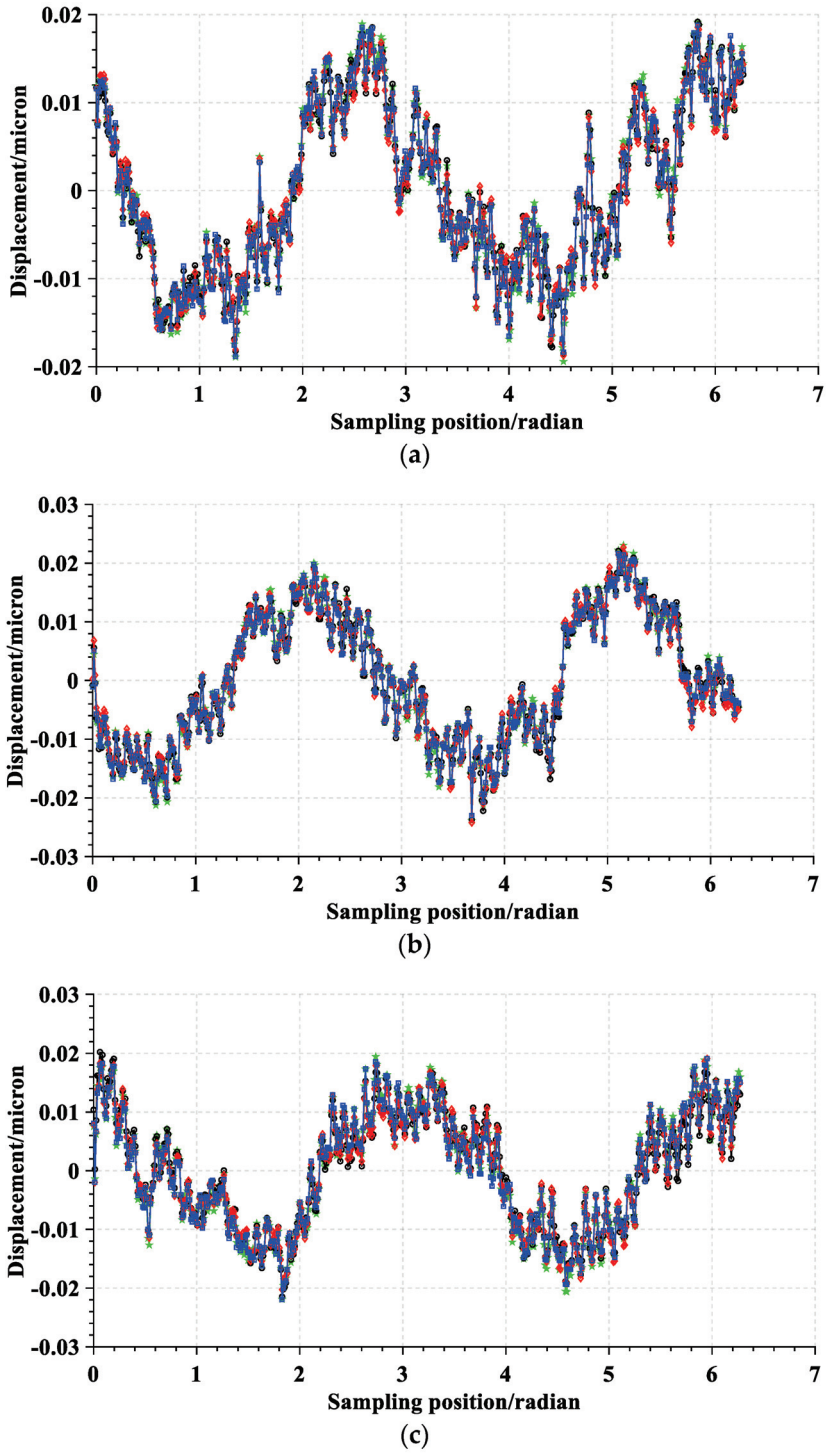

Figure 13. Amplitude phase diagrams of the multi-turn sampling data of the three sensors with the eccentricity and synchronization error removed in the Cartesian coordinate system: (**a**) data from sensor A, (**b**) data from sensor B, and (**c**) data from sensor C.

It is obvious that the repeatability of the data collected by the sensors is good. By comparing the data in the polar coordinate system, it can be observed that the sampled data of the three sensors show a shape characteristic with a fixed-phase deviation just as the marker in Figure 12 shows. The phase deviation is the same as α_2 and β_2 determined in Equation (9), reflecting the correctness and stability of the sampling results.

According to the error separation principle of the three-point method, the radial error and roundness error can be calculated, as shown in Figures 14 and 15. The radial error of

the spindle and the roundness error of the measured standard workpiece are 22.379 nm and 16.362 nm, respectively. Compared with the reference results, the radial error and roundness error differ from the reference results by 2.756 nm and 4.153 nm, respectively. According to the research results of Eric R. March [17,18], the reversal method has more theoretical advantages than the other methods, but it is also easier to couple more error components. The key to ensuring the measurement accuracy of the reversal method is to minimize the installation angle error and eccentricity error before and after the reversal, so the precision mechanism is generally used for reversal and installation positioning. In the comparative experiment, it is difficult to completely eliminate the error components introduced by the installation angle and eccentricity since no precision mechanism is used. As a result, the roundness error and radial error measured by the reversal method are larger and the measurement results of the in situ measurement and evaluation system are believed to be more accurate.

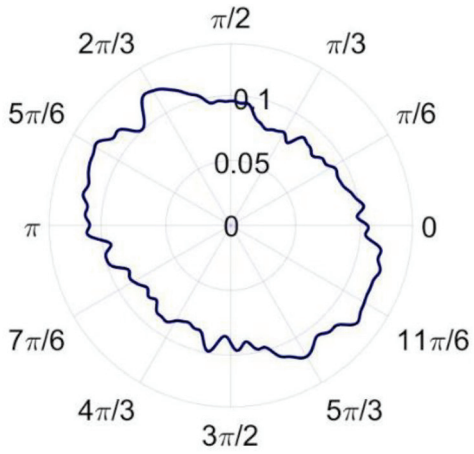

Figure 14. Radial error of the spindle.

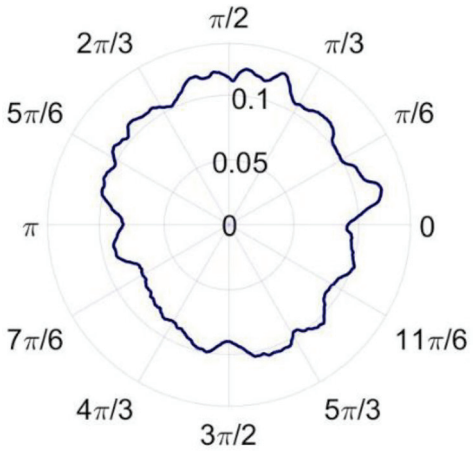

Figure 15. Roundness error of the standard workpiece.

In order to validate the reliability and stability of the in situ measurement and evaluation system, measurements based on the system are performed at different spindle speeds. The measurement results are presented in Table 1, and a line graph is drawn based on the measurement results, as shown in Figure 16.

Table 1. Measurement results of radial error by in situ measurement and evaluation system.

Serial Number	Spindle Speed (rpm)	Radial Error (nm)	Roundness Error (nm)
1	60	22.379	16.362
2	120	22.342	16.311
3	180	23.013	15.953
4	240	22.397	16.649
5	300	22.776	16.901
6	360	22.489	16.203
7	420	22.551	15.622
8	480	23.189	16.163
9	540	23.662	16.121
10	600	23.553	16.951
11	660	23.125	16.882
12	720	23.663	16.935
13	780	23.116	16.236
14	840	22.851	16.754
15	900	23.790	16.525
16	960	23.946	16.168
17	1020	23.785	15.828

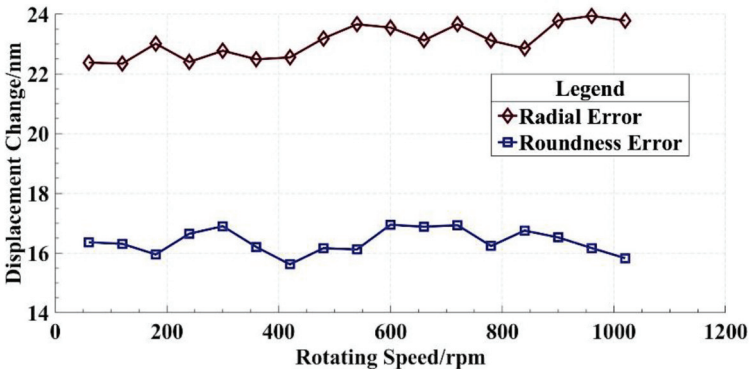

Figure 16. Line graph of measurement results.

The calculation of the statistical results in Table 1 shows that the average value of the radial error and roundness error are 23.096 nm and 16.386 nm, respectively. The standard deviation of the radial error and roundness error are 0.556 nm and 0.408 nm, respectively. The measurement results of the radial error and roundness error are approximately 2 nm and 4 nm smaller than the reference results, respectively. Considering that no precision mechanism was used for inversion in the comparative experiment, the deviations of the measurement results from the reference results are caused by the secondary clamping error in the comparative experiment. From this point of view, the measurement result of the in situ measurement and evaluation system is more accurate than that of the Donaldson reversal method. Environmental factors such as temperature change and vibration can also lead to the deviations, which can also contribute to the fluctuation in the measurement results shown in Figure 16. The control of environmental factors is extremely important to ensure the radial rotation accuracy of the spindles in actual machining.

Based on the analysis above, it is concluded that the in situ measurement and evaluation system can perform accurate in situ measurements of the radial error in the machining environment. The measurement accuracy of the in situ measurement and evaluation system can reach 20 nm. Since the operation of the system is simpler and fewer clamping errors are introduced, it has advantages over the Donaldson reversal method.

6. Conclusions

The three-point method is verified to realize nanometer-scale measurements in the machining environment. An in situ measurement and evaluation system is established and used to perform the experiment. The system simplifies the operation process of the ultra-precision measurement based on the three-point method. In particular, the innovation of the integrated fixture and experimental technical details is the key to improving the in situ measurement accuracy. The accuracy and advantages of in situ measurement and evaluation system are verified through a comparative experiment. The research has a reference function for the practical application of the three-point method.

Author Contributions: Conceptualization, Y.D.; methodology, H.X. and Z.S.; formal analysis, C.G. and H.H.; experiments, H.X. and Z.S.; data curation, H.X.; supervision, Y.D. and H.H.; writing—original draft, H.X.; writing—review and editing, H.X. and Y.W. All authors have read and agreed to the published version of the manuscript.

Funding: This work was financially supported by the National Natural Science Foundation of China (51991371).

Data Availability Statement: The data presented in this study are available upon request from the corresponding author. The data are not publicly available because it is part of an ongoing study.

Conflicts of Interest: The authors declare no conflict of interest. The funders had no role in the design of the study, in the collection, analyses, and interpretation of data, and in the writing of the manuscript, or in the decision to publish the results.

References

1. Yuan, J.; Lyu, B.; Hang, W.; Deng, Q. Review on the progress of ultra-precision machining technologies. *Front. Mech. Eng.* **2017**, *12*, 158–180. [CrossRef]
2. Zhang, S.; To, S.; Wang, S.; Zhu, Z. A review of surface roughness generation in ultra-precision machining. *Int. J. Mach. Tools Manuf.* **2015**, *91*, 76–95. [CrossRef]
3. Chen, G.; Sun, Y.; Zhang, F.; An, C.; Chen, W.; Su, H. Influence of ultra-precision flycutting spindle error on surface frequency domain error formation. *Int. J. Adv. Manuf. Technol.* **2017**, *88*, 3233–3241. [CrossRef]
4. Chen, G.; Sun, Y.; An, C.; Zhang, F.; Sun, Z.; Chen, W. Measurement and analysis for frequency domain error of ultra-precision spindle in a flycutting machine tool. *Proc. Inst. Mech. Eng. Part B J. Eng. Manuf.* **2018**, *232*, 1501–1507. [CrossRef]
5. Gao, W.; Kiyono, S.; Satoh, E.; Sata, T. Precision Measurement of Multi-Degree-of-Freedom Spindle Errors Using Two-dimensional Slope Sensors. *CIRP Ann.* **2002**, *51*, 447–450. [CrossRef]
6. Geng, Z.; Tong, Z.; Jiang, X. Review of geometric error measurement and compensation techniques of ultra-precision machine tools. *Light Adv. Manuf.* **2021**, *2*, 211–227. [CrossRef]
7. Aoki, Y.; Ozono, S. On a New Method of Roundness Measurement Based on the Three-point Method. *J. Jpn. Soc. Precis. Eng.* **1966**, *32*, 831–836. [CrossRef]
8. Whitehouse, D.J. Some theoretical aspects of error separation techniques in surface metrology. *J. Phys. E Sci. Instrum.* **1976**, *9*, 531–536. [CrossRef]
9. Chetwynd, D.G.; Siddall, G.J. Improving the accuracy of roundness measurement. *J. Phys. E Sci. Instrum.* **1976**, *9*, 537–544. [CrossRef]
10. Donaldson, R.R. A simple method for separating spindle error from test ball roundness error. *Ann. CIRP* **1972**, *21*, 125.
11. Liu, X.; Rui, X.; Mi, L.; Tang, Q.; Chen, H.; Xia, Y. Radial Error Motion Measurement and Its Uncertainty Estimation of Ultra Precision Axes of Rotation with Nanometer Level Precision. *Micromachines* **2022**, *13*, 2121. [CrossRef]
12. Cui, H.; Lei, D.; Zhang, X.; Lan, H.; Jiang, Z.; Kong, L. Measurement and analysis of the radial motion error of aerostatic ultra-precision spindle. *Measurement* **2019**, *137*, 624–635. [CrossRef]
13. Cheng, H.; Hu, Q.; Xu, Y. Uncertainty evaluation of aerostatic spindle rotation accuracy by donaldson reversal method. *Modul. Mach. Tool Autom. Manuf. Tech.* **2017**, *58*, 10–13+17. [CrossRef]
14. Jozwik, J. Dynamic Measurement of Spindle Errors of CNC Machine Tools by Capacitive Sensors During Aircraft Parts Machining. In Proceedings of the 2018 5th IEEE International Workshop on Metrology for AeroSpace (MetroAeroSpace), Rome, Italy, 20–22 June 2018; pp. 398–402. [CrossRef]
15. Ding, F.; Luo, X.; Chang, W.; Wang, Z. In Situ Measurement of Spindle Radial and Tilt Error Motions by Complementary Multi-probe Method. *Nanomanufacturing Metrol.* **2019**, *2*, 225–234. [CrossRef]
16. Liu, F.; Liang, L.; Xu, G.; Hou, C.; Liu, D. Four-Point Method in the Measurement and Separation of Spindle Rotation Error. *IEEE/ASME Trans. Mechatron.* **2021**, *26*, 113–123. [CrossRef]

17. Marsh, E.R.; Arneson, D.A.; Martin, D.L. A Comparison of reversal and multiprobe error separation. *Precis. Eng.* **2010**, *34*, 85–91. [CrossRef]
18. Marsh, E.; Couey, J.; Vallance, R. Nanometer-Level Comparison of Three Spindle Error Motion Separation Techniques. *J. Manuf. Sci. Eng.* **2006**, *128*, 180–187. [CrossRef]
19. Baek, S.-W.; Kim, M.-G.; Lee, D.-H.; Cho, N.-G. Multi-probe system design for measuring the roundness and rotation error motion of a spindle using an error separation technique. *Proc. Inst. Mech. Eng. Part B J. Eng. Manuf.* **2019**, *233*, 1547–1560. [CrossRef]
20. Tiainen, T.; Viitala, R. Robust optimization of multi-probe roundness measurement probe angles. *Measurement* **2021**, *168*, 108146. [CrossRef]
21. Cappa, S.; Reynaerts, D.; Al-Bender, F. A sub-nanometre spindle error motion separation technique. *Precis. Eng.* **2014**, *38*, 458–471. [CrossRef]
22. Gao, W.; Kiyono, S.; Nomura, T. A new multiprobe method of roundness measurements. *Precis. Eng.* **1996**, *19*, 37–45. [CrossRef]
23. Gao, W.; Kiyono, S. On-machine roundness measurement of cylindrical workpieces by the combined three-point method. *Measurement* **1997**, *21*, 147–156. [CrossRef]
24. Ma, Y.Z.; Wang, X.H.; Kang, Y.H.; Dong, X. Roundness Measurement and Error Separation Technique. *Appl. Mech. Mater.* **2013**, *303–306*, 390–393. [CrossRef]
25. Huang, R.; Pan, W.; Lu, C.; Zhang, Y.; Chen, S. An improved three-point method based on a difference algorithm. *Precis. Eng.* **2020**, *63*, 68–82. [CrossRef]
26. Jiao, Y.; Huang, M.; Liu, P. Optimal measurement angles of the three-probe spindle error motion separation technique. *Meas. Sci. Technol.* **2019**, *30*, 095001. [CrossRef]

micromachines

Article

Study on the Mechanism of Burr Formation by Simulation and Experiment in Ultrasonic Vibration-Assisted Micromilling

Yuanbin Zhang [1,2], Zhonghang Yuan [3], Bin Fang [1,2,*], Liying Gao [1,2], Zhiyuan Chen [1,2] and Guosheng Su [1,2]

[1] School of Mechanical Engineering, Qilu University of Technology (Shandong Academy of Sciences), Jinan 250353, China
[2] Shandong Institute of Mechanical Design and Research, Jinan 250353, China
[3] School of Mechanical Engineering, Hefei University of Technology, Hefei 230009, China
* Correspondence: fb@qlu.edu.cn

Abstract: Due to the strong plasticity of Inconel 718 and the significant size effect of micromachining, a large number of burrs will be produced in traditional processing. The addition of ultrasonic vibration during machining can reduce the burr problem. The mechanism of burr generation in traditional micromilling (TMM) and ultrasonic vibration-assisted micromilling (UVAMM) was analyzed by simulation, and verified by corresponding experiments. It is found that applying high-frequency ultrasonic vibration in the milling feed direction can reduce cutting temperature and cutting force, improve chip breaking ability, and reduce burr formation. When the cutting thickness will reach the minimum cutting thickness hmin, the chip will start to form. When $A/f_z > 1/2$, the tracks of the two tool heads start to cut, and the chips are not continuous. Some of the best burr suppression effects were achieved under conditions of low cutting speed (V_c), feed per tooth (f_z), and large amplitude (A). When A is 6 μm, the size and quantity of burr is the smallest. When f_z reaches 6 μm, large continuous burrs appear at the top of the groove. The experimental results further confirm the accuracy of the simulation results and provide parameter reference.

Keywords: traditional micromilling; simulation; burr; ultrasonic vibration-assisted micromilling; size effect; cutting performance

Citation: Zhang, Y.; Yuan, Z.; Fang, B.; Gao, L.; Chen, Z.; Su, G. Study on the Mechanism of Burr Formation by Simulation and Experiment in Ultrasonic Vibration-Assisted Micromilling. *Micromachines* **2023**, *14*, 625. https://doi.org/10.3390/mi14030625

Academic Editors: Jiang Guo, Chunjin Wang and Chengwei Kang

Received: 19 February 2023
Revised: 5 March 2023
Accepted: 6 March 2023
Published: 9 March 2023

1. Introduction

Nickel base alloys are widely used in modern aerospace engines because of their excellent high temperature properties [1]. Engine parts have complex structure and high machining accuracy. Micromilling is an important processing method, with high material removal rate and excellent processing flexibility, which can be used to manufacture precision parts [2,3], usually with a diameter of 1–1000 μm tool [4], which is also a common finishing method for nickel base alloys. However, it usually produces a lot of burrs when it is processed. Burr is an important machining defect that affects the quality of machined surface, will affect the performance of parts, and even lead to parts scrapping. In industrial production, deburring is tedious work [5], and the removal effect is often not ideal. Therefore, it is necessary to reduce the formation of burrs during machining. Scholars conducted various studies on the formation of burrs. Hashimura et al. [6] classified burrs into top burrs, inlet burrs, outlet burrs, inlet-side burrs, and outlet-side burrs according to their positions. Under normal conditions, the burr size can be reduced by changing processing parameters, such as feed speed, spindle speed, cutting depth, etc. [7–10]. The conical degree of the tool and the wear of the tool itself can also affect the size of the burr [11,12]. However, the effect is often not ideal. Furthermore, some researchers adopted the means of adding auxiliary technology to reduce the formation of burrs. Additional ultrasonic vibration during cutting can reduce the size of burrs [13,14]. Miranda Giraldo et al. [15] conducted milling research using biopolymers and found that when eddy current cooling is used, the growth of burrs can be effectively suppressed and the width of burrs can be significantly

reduced. In order to further explore the mechanism of burr formation, many researchers simulated and analyzed the burr formation process. Sreenivasulu et al. [16] established a mathematical model for burr formation during drilling, and verified the feasibility of the model by combining it with experiments. Meng et al. [17] studied the cutting performance of carbon fiber reinforced polymer (CFRP) through finite element simulation, and found that the outermost fiber was not cut, but pushed to the side by the cutting edge, and then the fiber rebounded to form burrs. Yadav et al. [18] conducted a finite element simulation study on the formation of burr at the up-milling side of high-speed micromilling Ti6A14V. It was found that when the speed is increased from 10,000 r/min to 200,000 r/min, the burr size decreases sharply. Zou et al. [19] established a finite element model and found that the formation of negative burrs includes eight stages, in which the formation of negative shear bands and stress changes are the main reasons for the formation of negative burrs. The thicker the backup material, the smaller the burr size. Asad [20] used the finite element method to simulate different combinations of V_c, feed speed, and tool edge geometry. It is found that the larger the tool tip radius is, the larger the outlet burr is. Srenivasulu et al. [21] developed a drilling model for aluminum 6061 and 7075 alloys, and found that temperature has no significant effect on the burr height. An et al. [22] proposed a new method for ultra precision cutting and deburring with special single crystal diamond tools, and carried out finite element simulation research, which proved that it is feasible. Chen et al. [23] found that applying vibration in the feed direction can inhibit the formation of burrs. The burrs at the top of the milling side are significantly reduced, and the average height is reduced by 87%. Chen et al. [24] found that microchannel with good surface quality can be obtained by machining with high spindle speed, small cutting depth and medium feed speed close to the tool cutting edge radius. Chen et al. [25] found that when the thickness to be cut is greater than the minimum cutting thickness, the cutting state can be changed to reduce the cutting force, tool wear, and the formation of burrs. In the cutting experiment, it is found that the burr width of ultrasonic vibration-assisted milling decreases from 25 μm to 5 μm compared with traditional milling. Le et al. [26] proposed a method for predicting side burrs and exit fractures of prisms. The results show that ultrasonic vibration can change the machining state and affect the formation of burr, and the number and size of burr can be greatly reduced by applying an appropriate amplitude. Wu et al. [27] established a finite element model and found that the outlet surface angle had an impact on burrs, and burr-free cutting could be achieved when the outlet surface angle was less than 45°. Efstathiou et al. [28] established a drilling finite element model, which can predict the best parameters to suppress burr generation. However, the research work on ultrasonic vibration-assisted micromilling processing parameters and the influence of vibration parameters on the burr size is still less, especially the research on micromilling Inconel 718 material is less, and research and analysis are needed to guide the micromilling work.

In this work, ultrasonic vibration-assisted micromilling was used to process Inconel 718, which restrained the generation of burrs. The tool tip trajectory during machining is simulated and the chip breaking mechanism is analyzed. For clarifying the role of ultrasonic vibration in the micromachining process, burr formation is simulated under different processing parameters. At the same time, traditional micromilling and ultrasonic vibration-assisted micromilling were used to machine high-temperature nickel base alloy for comparative analysis. Finally, the mechanism of burr formation under UVAMM is analyzed based on the simulation and experimental results.

2. Simulation and Experiment

2.1. Simulation Method

The size and cause of the top burr are simulated with Deform-3D software (version number:V6.1; creator: SFTC; sourced from Key Laboratory for High Strength Lightweight Metallic Materials of Shandong Province). In order to improve the calculation efficiency and ensure the calculation accuracy, the tool and workpiece size are reduced in the same proportion, and the original geometric characteristics of the tool are retained. Table 1 shows

the geometric parameters of the tool used, and Table 2 shows the simulation parameters of micromilling. The workpiece size is 0.3 mm × 0.3 mm × 0.1 mm, and the material is Inconel 718. According to the size of the tool and the workpiece, the geometric model of the tool and the workpiece is established in the SolidWorks software (version number: SOLIDWORKS EDU Edition 2016-2017-STAND-ALONE; creator: Dassault Systemes; sourced from Yantai Univ.), and the established model is imported into the software Deform-3D. The simulation process did not consider the influence of tool wear, so the tool model was set as a rigid body and the workpiece was set as an elastic–plastic deformation body. The local mesh refinement method is used to process the tool tip part and the uncut area of the workpiece. This simulation uses tetrahedral mesh to simplify the model and adapt to the boundary features in the mesh. The number of tool meshes is 30,000, and the number of workpiece meshes is 160,000. The model and mesh division are shown in Figure 1.

Table 1. Geometrical parameters of Simulation model.

Geometrical Characteristic	Tool Diameter (mm)	Blade Length (mm)	Cutting Edge Radius (μm)	Helical Angle (°)
Parameter value	0.2	4	5	36
Geometrical characteristic	Rake angle of side edge (°)	Rear angle of side edge (°)	First rear angle of base edge (°)	Second rear angle of base edge (°)
Parameter value	0	9	9	16

Table 2. Simulation parameters.

Experiment Number	Cutting Speed v_c (m/min)	Cutting Depth a_p (μm)	Feed per Tooth f_z (μm/z)	Amplitude A (μm)	Vibration Frequency f (kHz)
Simulation 1	37.7 56.5 75.4	50	6	0 3 6	32
Simulation 2	37.7	50	2 3 4 5 6 7 8	0 3 6	32

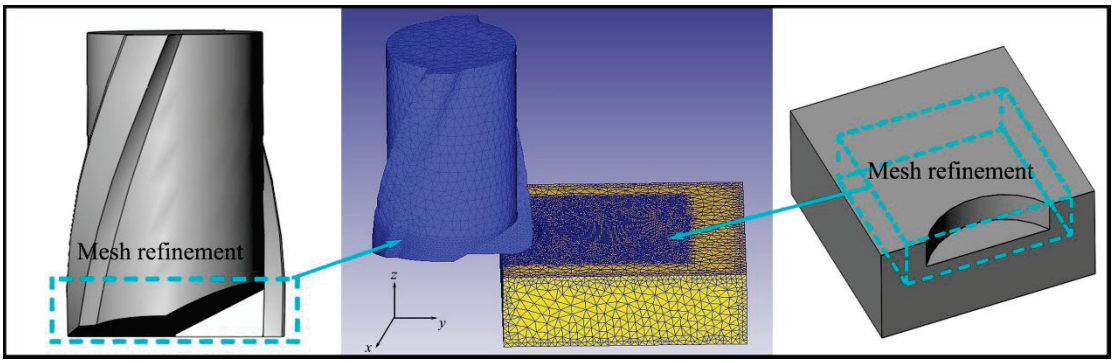

Figure 1. Simulation model and meshing.

In order to better reflect the effects of strain hardening, strain rate strengthening, and thermal softening during the processing of high-temperature nickel-based alloys. In the Deform-3D modeling process, when defining the parameters of the material Inconel 718,

the J-C constitutive model is used to simulate its plastic behavior, as shown in Equation (1), where A = 450 MPa, B = 1700 MPa, n = 0.6, C = 0.017, and m = 1.3 [29].

$$\sigma = [A + B\varepsilon^n]\left[1 + Cln\left(\frac{\dot{\varepsilon}}{\dot{\varepsilon_0}}\right)\right]\left[1 - \left(\frac{T - T_{room}}{T_{melt} - T_{room}}\right)^m\right] \quad (1)$$

where σ is used to indicate the equivalent stress; ε is used to indicate the equivalent plastic strain; $\dot{\varepsilon}$ is used to indicate the equivalent plastic strain rate; $\dot{\varepsilon_0}$ is used to indicate the reference strain rate; T is used to indicate the temperature of the workpiece; T_{room} is used to indicate room temperature; and T_{melt} is used to indicate the melting temperature of the workpiece.

2.2. Experimental Method

The test machine and cemented carbide double edge end milling are shown in Figure 2. The burrs produced by micromilling grooves were studied by scanning electron microscopy (SEM).

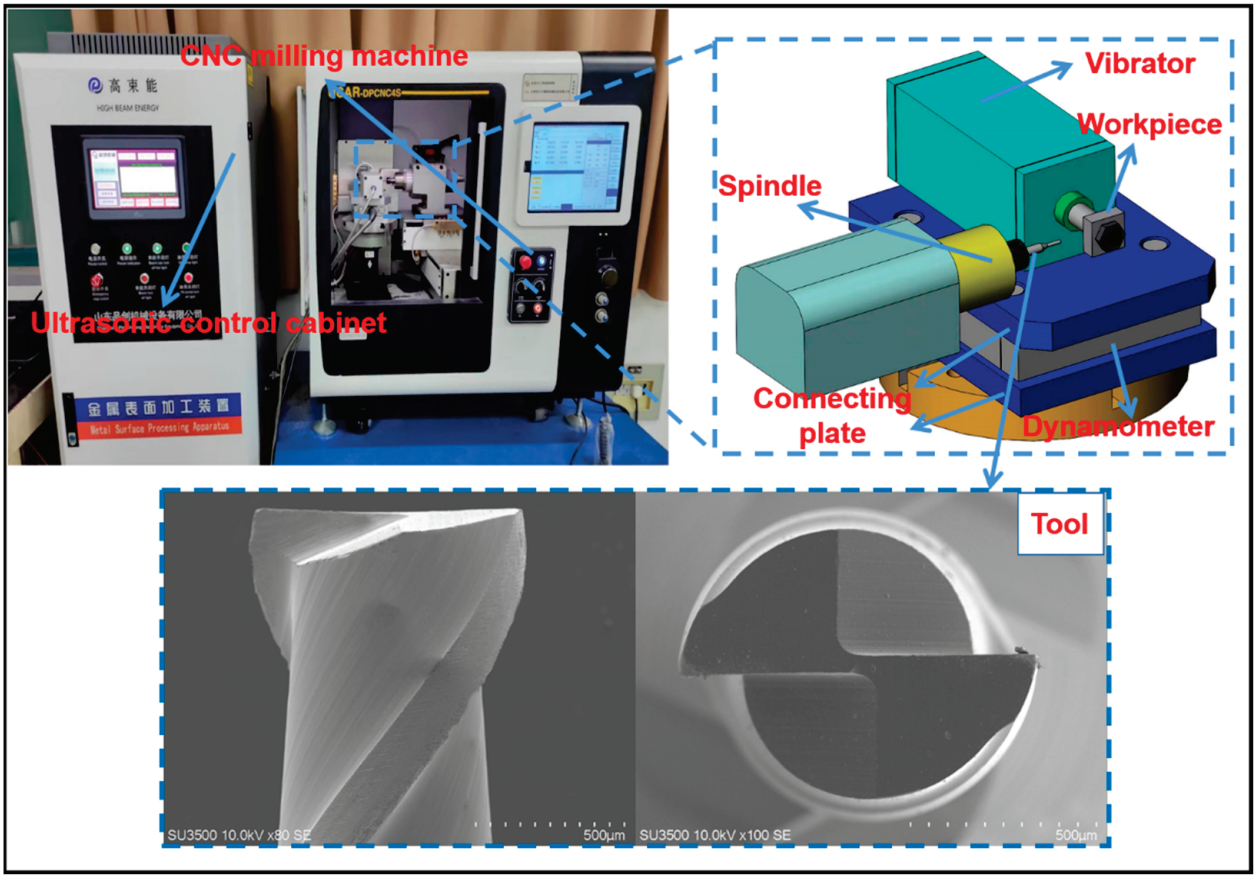

Figure 2. Experimental device.

The profile geometric parameters of micromilling tools are shown in Table 3. The cutting edge radius of the tool is 5 μm. The chemical element composition of workpiece material is shown in Table 4. The machining parameters are shown in Table 5, which is in accordance with Table 2 in order to compare with the simulation results. With V_c and f_z as variables, two groups of single-factor experiments corresponding to the simulation were designed to study the influence of them on the size and shape of burrs generated by ultrasonic vibration-assisted micromilling.

Table 3. Geometrical parameters of micromilling tool.

Geometrical Characteristic	Tool Diameter (mm)	Blade Length (mm)	Cutting Edge Radius (μm)	Helical Angle (°)
Parameter value	1	4	5	36
Geometrical characteristic	Rake angle of side edge (°)	Rear angle of side edge (°)	First rear angle of base edge (°)	Second rear angle of base edge (°)
Parameter value	0	9	9	16

Table 4. Main chemical components of Inconel 718.

Element	Ni	Cr	Fe	Nb	S	Ti
wt%	55.54	18.77	18.17	4.78	1.67	1.07

Table 5. Machining parameters.

Experiment Number	Cutting Speed v_c (m/min)	Cutting Depth a_p (μm)	Feed per Tooth f_z (μm/z)	Amplitude A (μm)	Vibration Frequency f (kHz)
Experiment 1	37.7 56.5 75.4	50	6	0 3 6	32
Experiment 2	37.7	50	2 3 4 5 6 7 8	0 3 6	32

3. Results and Discussion

3.1. Chip Formation

Incomplete chip forming and fracture will eventually lead to burrs in micromilling. In a cutting cycle, the cutting thickness of the up-milling side will gradually increase, and the minimum cutting thickness will not be reached at the beginning. The material will only undergo elastic deformation without chip generation. With the continuous accumulation of cutting materials, the cutting thickness will reach the minimum cutting thickness h_{min}. The stress and strain of the material will increase, and the chip will begin to form and still be an incomplete rebound of the material. Finally, when the stress in the cutting area reaches the yield limit with the increase in the cutting thickness, the material will mainly undergo plastic deformation. From the micro level, the lattice of the extruded cutting area will slip, and when the stress exceeds the fracture limit, the chip is formed normally. On the contrary, in a cutting cycle, the cutting thickness of the down-milling side will gradually decrease, and when the cutting thickness reaches a certain limit, chip breaking will occur, and some will become burrs. Therefore, the extrusion deformation process on the up-milling side will lead to burrs, and the incomplete formation of chips on the down-milling side will also lead to burrs. However, when ultrasonic vibration is introduced, even if the h at any time in TMM is less than h_{min}, it will make h larger, h will periodically exceed him, and will change the cutting form. Figure 3 shows the three stages of chip formation, and the minimum cutting thickness is constant with the effect of ultrasonic vibration on cutting thickness.

3.2. Trajectory Equation of Cutting Edge

During milling, applying high-frequency vibration along the tool feed direction will change the tool tip path, the chip formation process will also change, and will affect the generation of burrs. Therefore, it is necessary to analyze the running track of the tool tip.

Figure 4 shows the trajectory of two tool tips during TMM tool tip movement. The solid line is the path of tool tip 1, and the dotted line is the path of tool tip 2.

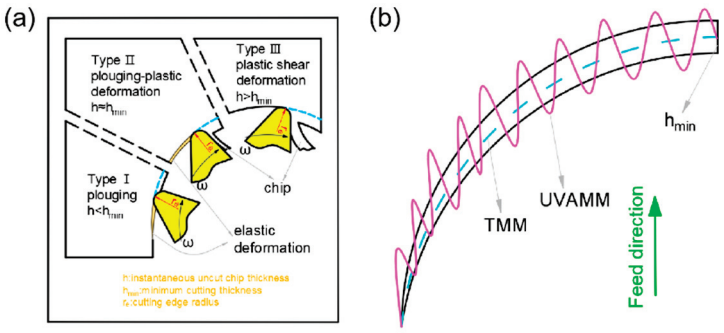

Figure 3. (**a**) Micromilling chip formation process in a single cutting cycle; (**b**) ultrasonic vibration increases h in cutting process.

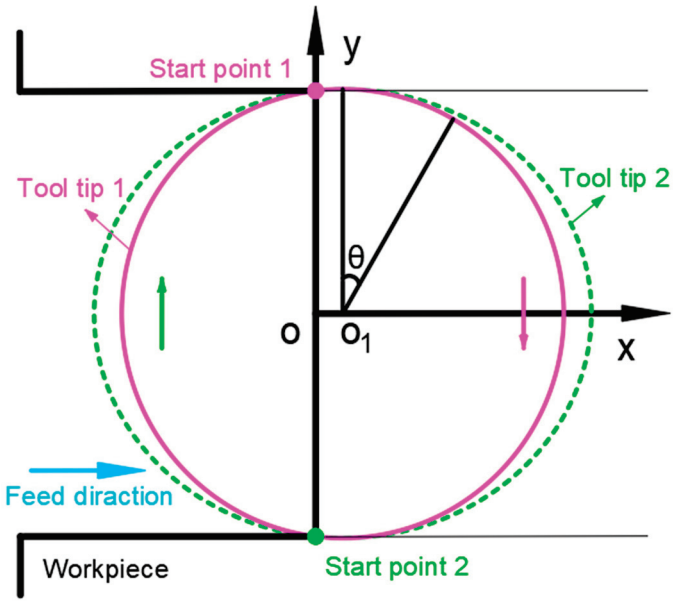

Figure 4. Schematic diagram of tool tip path.

In the coordinate system shown in Figure 4, the motion of the tool tip is decomposed into feed motion and rotation motion, and Equation (2) is used to represent the motion of two tool tips in TMM.

$$\begin{cases} x_i = v_f t + (-1)^{i-1} r sin(\theta) \\ y_i = (-1)^{i-1} r cos(\theta) \end{cases} \quad (2)$$

In the experiment, the vibration signal along the tool feed direction is directly applied to the workpiece. In order to facilitate the synthesis of the motion path, the sinusoidal vibration signal applied to the workpiece is equivalent to the tool. Equations (3) and (4) represent the motion of two tool tips in UVAMM.

$$\begin{cases} x_i = v_f t + (-1)^{i-1} r sin(\theta) + A sin(\lambda \omega t) \\ y_i = (-1)^{i-1} r cos(\theta) \end{cases} \quad (3)$$

$$\theta = 2\pi n t \quad (4)$$

where v_f is used to indicate the milling feed rate; r is used to indicate the tool radius; n is used to indicate the spindle speed; ω is used to indicate the ultrasonic signal angular

frequency; i (i = 1,2) is used to indicate the ith tool tip; and λ is used to indicate the ratio of ultrasonic vibration signal frequency to spindle rotation frequency.

3.3. Simulation and Experiment Results

3.3.1. Trajectory of Cutting Edge

The tool tip trajectory model can be used to predict chip formation. Figure 5 shows the influence of ultrasonic amplitude and f_z on the two tool tip trajectories. When A is 0 μm, it is traditional milling, and the motion tracks of the two tool tips do not intersect, indicating that a cutting edge is continuous cutting in a cutting cycle. When A increases to 3 μm, the running track of tool tip 2 starts to be tangent to the running track of tool tip 1, indicating that a cutting edge starts to cut intermittently in a cutting cycle, and the chip is potentially broken. When A continues to grow, the running track of tool tip 2 intersects with that of tool tip 1. The intersection indicates that tool tip 2 will be separated from the workpiece at this moment, and the chip is not continuous. It shows that the chip breaking form can be changed by changing the size of A when f_z is fixed. According to the motion track characteristics of ultrasonic vibration tool tips, when $A/f_z > 1/2$, the tracks of two tool tips start to cut, and the chips are not continuous.

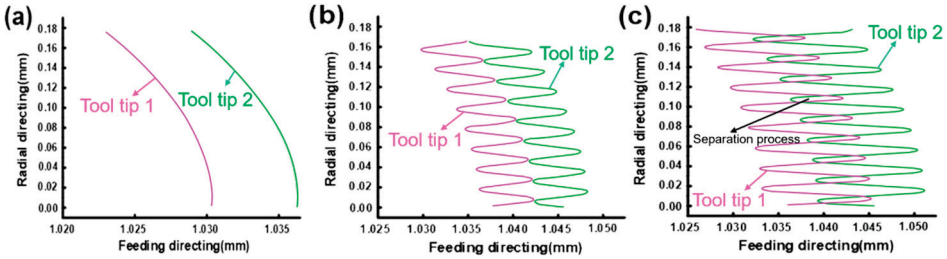

Figure 5. Simulation of tool tip trajectory (**a**) f_z = 6 μm/z, A = 0 μm; (**b**) f_z = 6 μm/z, A = 3 μm; and (**c**) f_z = 6 μm/z, A = 6 μm.

3.3.2. Cutting Force and Cutting Temperature

Cutting force and cutting temperature can intuitively reflect the cutting process. In order to completely understand the processing characteristics of TMM and UVAMM, the cutting force and cutting temperature during the cutting process are simulated and analyzed.

Figure 6 shows the cutting force characteristics of TMM and UVAMM. The axial force (F_z) is the driving force that pushes the chips to bend upward. The feed perpendicular force (F_x) and the feeding force (F_y) are the driving forces that promote chip growth. The resultant cutting force (F_r) is calculated by Equation (5) and the curve is drawn. Figure 6 shows that, compared with TMM, when the tool suddenly contacts the workpiece after the vibration is applied, the cutting force quickly reaches the peak value, which is the contact impact between the tool and the workpiece, and then the cutting force decreases sharply at a high frequency, indicating that the cutting process of UVAMM is intermittent. Therefore, the plough effect on the up-milling side is weakened, and the extrusion deformation of the material is also weakened. On the down-milling side, it can be found that the cutting force dropped sharply, indicating that the chips were broken in advance, so no large burr will be formed on the top of the groove. The high frequency fluctuation of cutting force of UUVAMM results in the average value of the cutting force being lower than that of TMM.

$$F_r = \sqrt{(F_x)^2 + (F_Y)^2 + (F_z)^2} \tag{5}$$

Figure 7 shows the distribution of the cutting temperature field of TMM and UVAMM. It can be found from the temperature field that the highest temperature is mainly distributed in the shear deformation area and gradually diffuses to other parts of the workpiece. The temperature of the contact zone between the tool tip and the material is the highest, and the maximum temperature of TMM and UVAMM is 753 °C and 685 °C, respectively. At

the same time, the temperature diffusion area of TMM is larger than that of UVAMM. The reason is that although the instantaneous cutting thickness of UVAMM is sometimes greater than TMM, because UVAMM is intermittent cutting, it is not conducive to the accumulation of cutting heat, reduces the heat generated by friction between the tool tip and the material, and provides more sufficient time for the heat dissipation process. Wang et al. [30] also pointed out that additional ultrasonic vibration can effectively increase the diffusion time and diffusion space of cutting temperature.

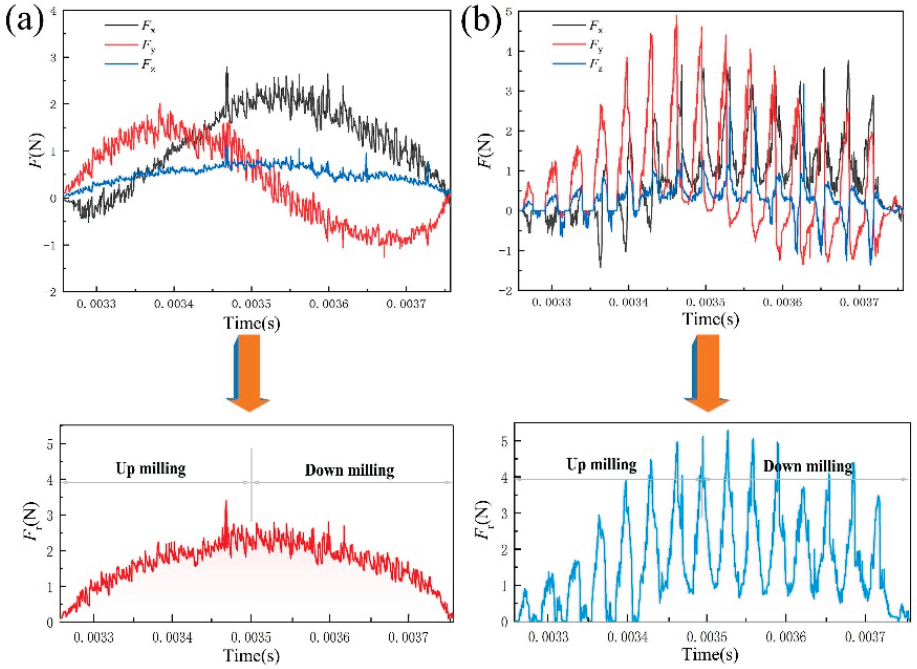

Figure 6. Cutting force changes in a single cutting cycle (**a**) TMM; (**b**) UVAMM.

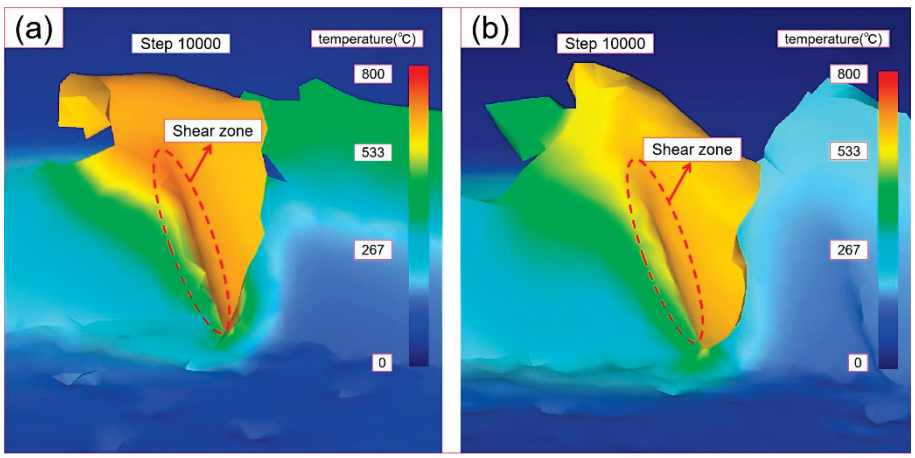

Figure 7. Distribution of cutting temperature field (**a**) TMM (V_c = 37.7 m/min; f_z = 6 μm/z; A = 0 μm); (**b**) UVAMM (V_c = 37.7 m/min; f_z = 6 μm/z; A = 6 μm).

3.3.3. Equivalent Strain Analysis

Figure 8 shows the distribution of equivalent plastic strain and damage in the cutting area when f_z = 8 μm/z. It can be concluded from Figure 8a–c that the equivalent plastic strain is mainly distributed on the side where the chips are generated. The application of ultrasonic vibration expands the equivalent plastic strain range and increases the maximum equivalent plastic strain, which indicates that ultrasonic vibration will increase material deformation during the cutting process. In Figure 8d–f, as the A increases, the damage range

and the maximum damage value decrease. The UVAMM is beneficial to remove materials. The material failure mechanism of UVAMM can be considered as the instantaneous plastic failure of material caused by high-speed impact load. Therefore, UVAMM is helpful to remove chips and reduce the residual burrs on the top of the milling groove.

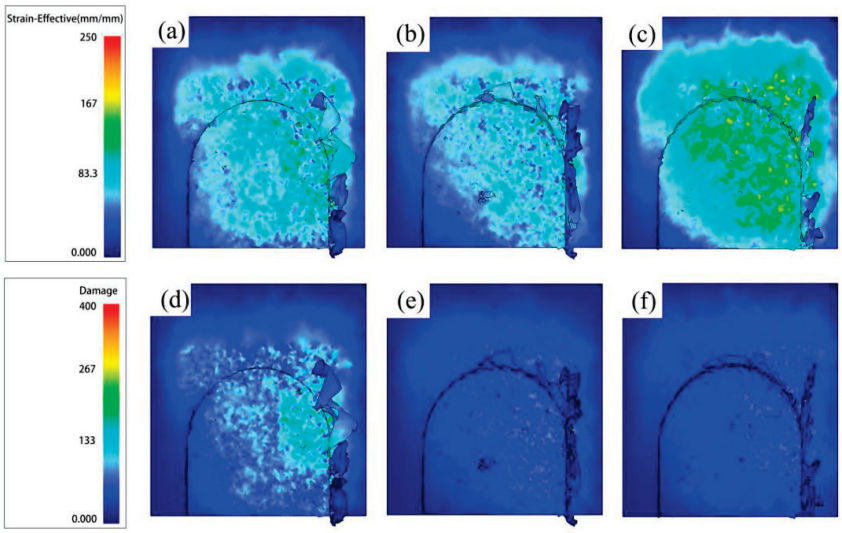

Figure 8. Equivalent plastic strain cloud image and damage cloud image with different A. (**a**,**d**) A = 0 μm; (**b**,**e**) A = 3 μm; and (**c**,**f**) A = 6 μm.

3.3.4. Burr Formation

Burrs can generally be classified into four types, as shown in the Figure 9a. The size of burrs is usually defined in the way shown in the Figure 9b. This paper mainly compares the width of burrs.

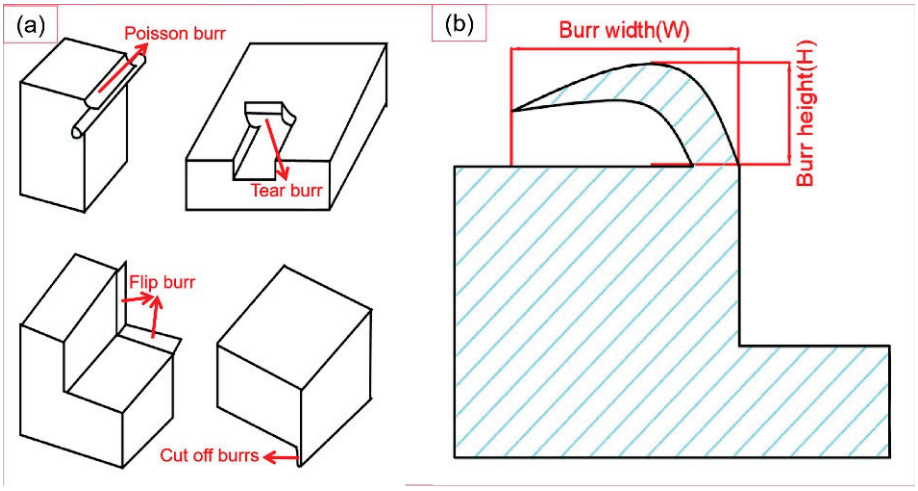

Figure 9. (**a**) Burr types; (**b**) burr size.

(1) Burr formation process.

Figure 10 shows the burr formation process of TMM and UVAMM. When the tool tip just touches the material, the size effect is particularly significant due to the large ratio of the cutting edge radius to the cutting thickness. In the TMM process, the part of the material continuously accumulates along the rotation direction under the extrusion of the tool tip, and the other part of the material is turned out of the groove and forms burrs on the top of the groove, as shown in Figure 10a. When the material accumulates to a certain value, a larger spiral chip forms, as shown in Figure 10b. The spiral chips continue to grow and form larger burrs on the down-milling side, as shown in Figure 10c. After that, due

to the effect of high-frequency ultrasonic vibration, the extrusion of the tool tip on the material is weakened, the burrs on the up-milling side are reduced, as shown in Figure 10d. In addition, UVAMM enhances the destructive effect of the tool on the material. This is in accordance with the results of Figure 8. It can be found from Figure 11e–f that the chips of the up-milling side are smaller than that of the TMM, and the burr is serrated. With the chip growth, the chip size increases gradually. Due to the chip breaking phenomenon in the intermediate process, the chip is a C-type chip, and finally a small burr is formed on the down-milling side. Therefore, compared with TMM, UVAMM can significantly inhibit the growth of burrs and reduce the size of burrs. As shown in Figure 10a,b, the burr surface has a wide texture during TMM, which is formed by material accumulation during processing. After ultrasonic vibration is applied, larger flake burrs gradually change into smaller tear burrs and flocculent burrs, and the burr surface has a more dense texture. Because high-frequency ultrasonic vibration promotes crack growth, and dense vibration cracks remain on the burr surface. Ultrasonic vibration makes materials more vulnerable to damage and cracks more obvious, which is conducive to the transition from ductile fracture to brittle fracture, so the burr is more broken, and the burr size will be smaller, as shown in Figure 11c,d. Chen et al. [25] also found that UVAMM contributed to crack generation and material damage.

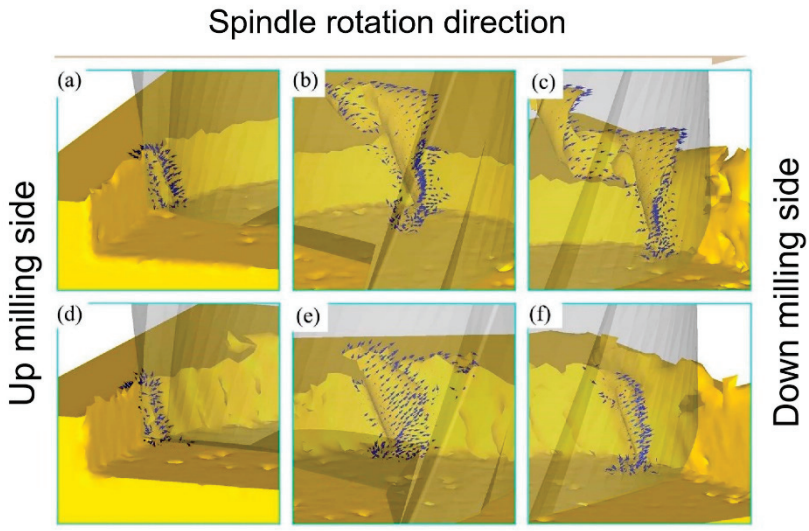

Figure 10. Simulation of burr growth (**a**–**c**) TMM; (**d**–**f**) UVAMM.

(2) Effect of ultrasonic vibration on burr formation at different V_c.

Figure 12 shows the burr morphology generated by simulating TMM and UVAMM with different V_c (f_z = 6 μm/z, a_p = 50 μm). It can be seen from Figure 12 that when the V_c is 37.7 m/min, large flake burrs are produced on the top of the groove. With the increasing of the V_c, the burr size first decreases and then increases without ultrasonic vibration. When vibration is applied, the flake burrs gradually change to tearing burrs, and the size and quantity of burrs reduce. When the A is 6 μm, the size and quantity of burrs are the smallest. In addition, ultrasonic vibration has the most obvious effect on milling at medium and low cutting speed. Zhang et al. [31] also pointed out that the burrs become more with the increase in the cutting speed. Similarly, as shown in Figure 13, it was also observed in the above phenomenon in this experiment (in the Figure, in each groove, the down-milling side is located at the upper side). When traditional micromilling is carried out at V_c = 37.7 m/min cutting speed, a large number of complete sheet burrs are generated at the down-milling side and a large number of strip burrs are generated at the up-milling side. When V_c is increased, it is found that the size of burr is gradually reduced. Because the high cutting speed leads to a shorter single milling cycle time and it is difficult to produce plastic deformation, the burr is smaller. However, higher V_c will also produce higher cutting heat on the down-milling side, and the material will become soft, which

is not conducive to chip fracture and promotes the generation of burrs. During UVAMM processing, it can be found that the burrs on the up-milling side and the down-milling side become more finely broken, because ultrasonic vibration causes the cutting process to be interrupted and the chip formation process is also interrupted, which significantly reduces the burr size.

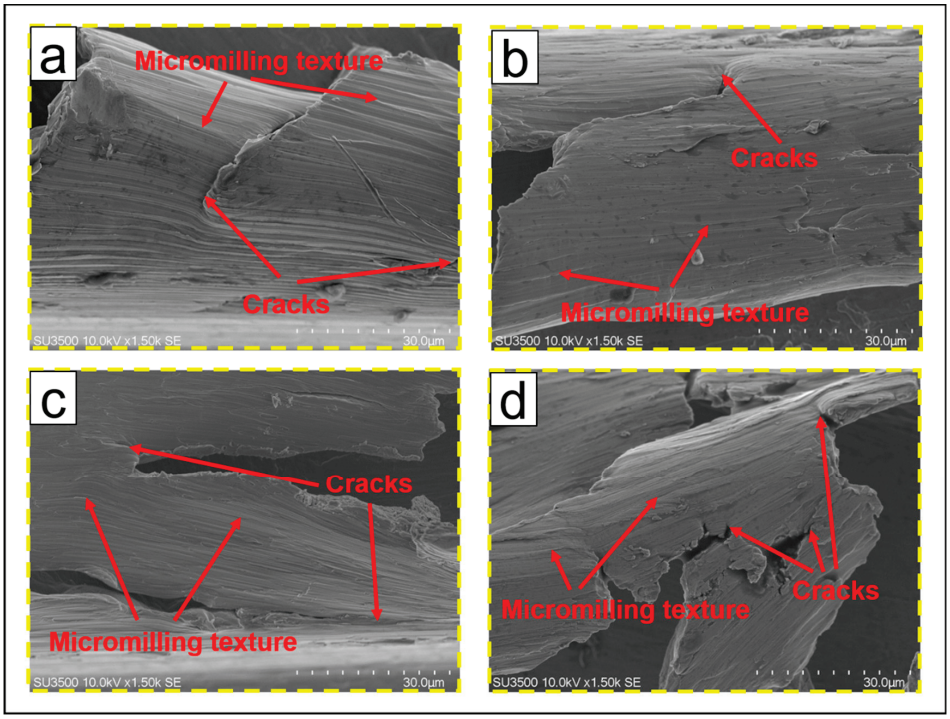

Figure 11. Burr morphology (**a**,**b**) TMM; (**c**,**d**) UVAMM.

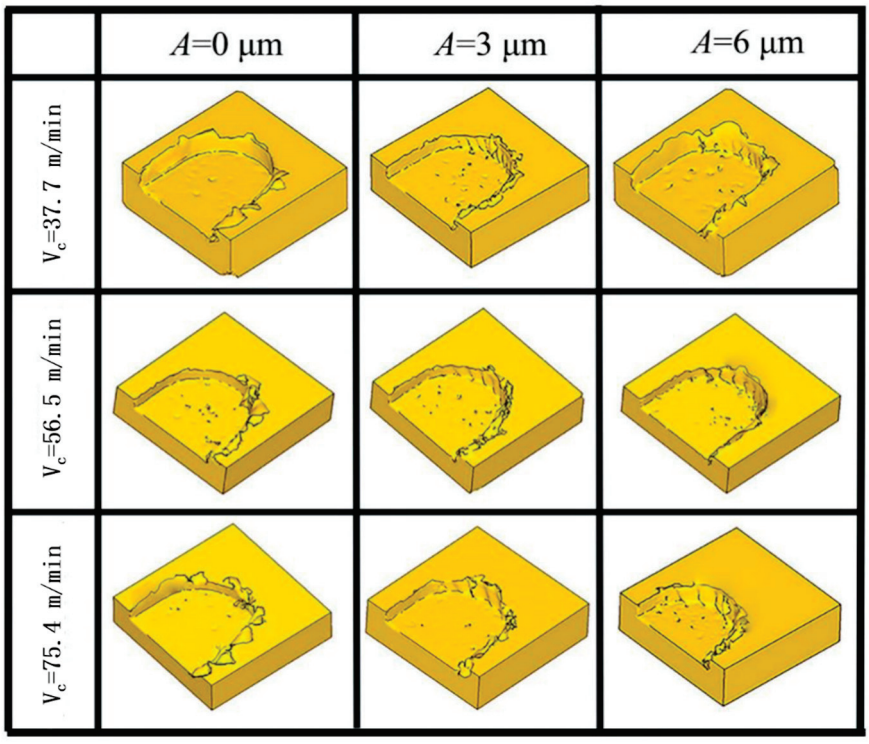

Figure 12. Simulation of burr morphology under different V_c.

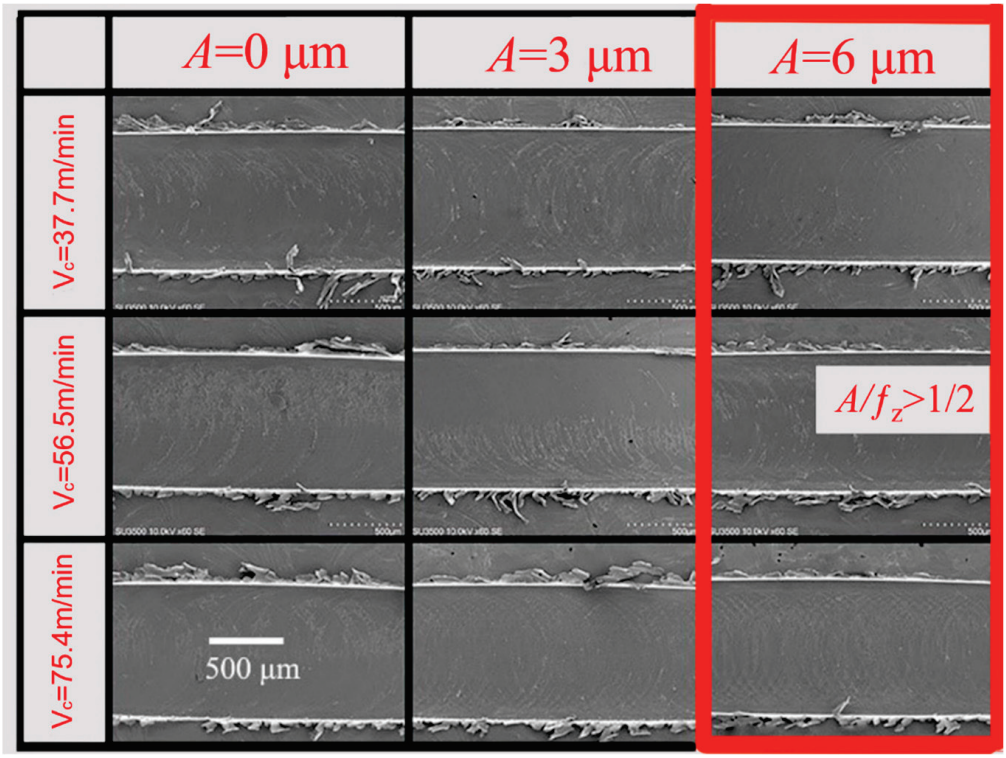

Figure 13. Morphology of burr under different V_c (SEM) (f_z = 6 μm/z, a_p = 50 μm).

(3) Effect of ultrasonic vibration on burr formation at different f_z.

Figure 14 shows the burr morphology of a simulation by the two machining methods with different f_z (V_c = 37.7 m/min, a_p = 50 μm). When the f_z is 2 μm/z, the elastic deformation of the material is serious and chips are difficult to generate. The material is squeezed by the tool and slips upward, forming burrs. The material is easier to remove with the increase of f_z. Large continuous burrs appeared on the top of the groove when f_z reached 6 μm. Under the same f_z condition, the burr generated by UVAMM was smaller than that by TMM, and the burr size decreased with the increase of A. This phenomenon is more obvious under large f_z conditions, especially when f_z is 5–7 μm/z and A is 6 μm. Similarly, as shown in Figure 15, it was also observed in the above phenomenon in the experiment (in the Figure, in each groove, the down-milling side is located at the upper side). When TMM is carried out, f_z gradually becomes larger, resulting in an increase in the cutting amount, and finally leading to larger burr size. During UVAMM, due to the introduction of high-frequency vibration signals in the milling process, the instantaneous cutting thickness changed, which promotes the formation and separation of chips, and at the same time, the burrs are suppressed. This phenomenon is more obvious under the condition of large f_z. When f_z reaches 8 μm/z, the additional ultrasonic vibration cannot significantly suppress the burr, mainly because the f_z is too large to meet the chip breaking condition. Larger chips do not break, they stay at the top of the groove and form burrs. When f_z is small, ultrasonic vibration mainly reduces the size effect and changes the chip formation process, thereby inhibiting the formation of burrs. When f_z is large, the burr size decreases because ultrasonic vibration changes the instantaneous cutting thickness in the milling process and improves the chip-broken ability.

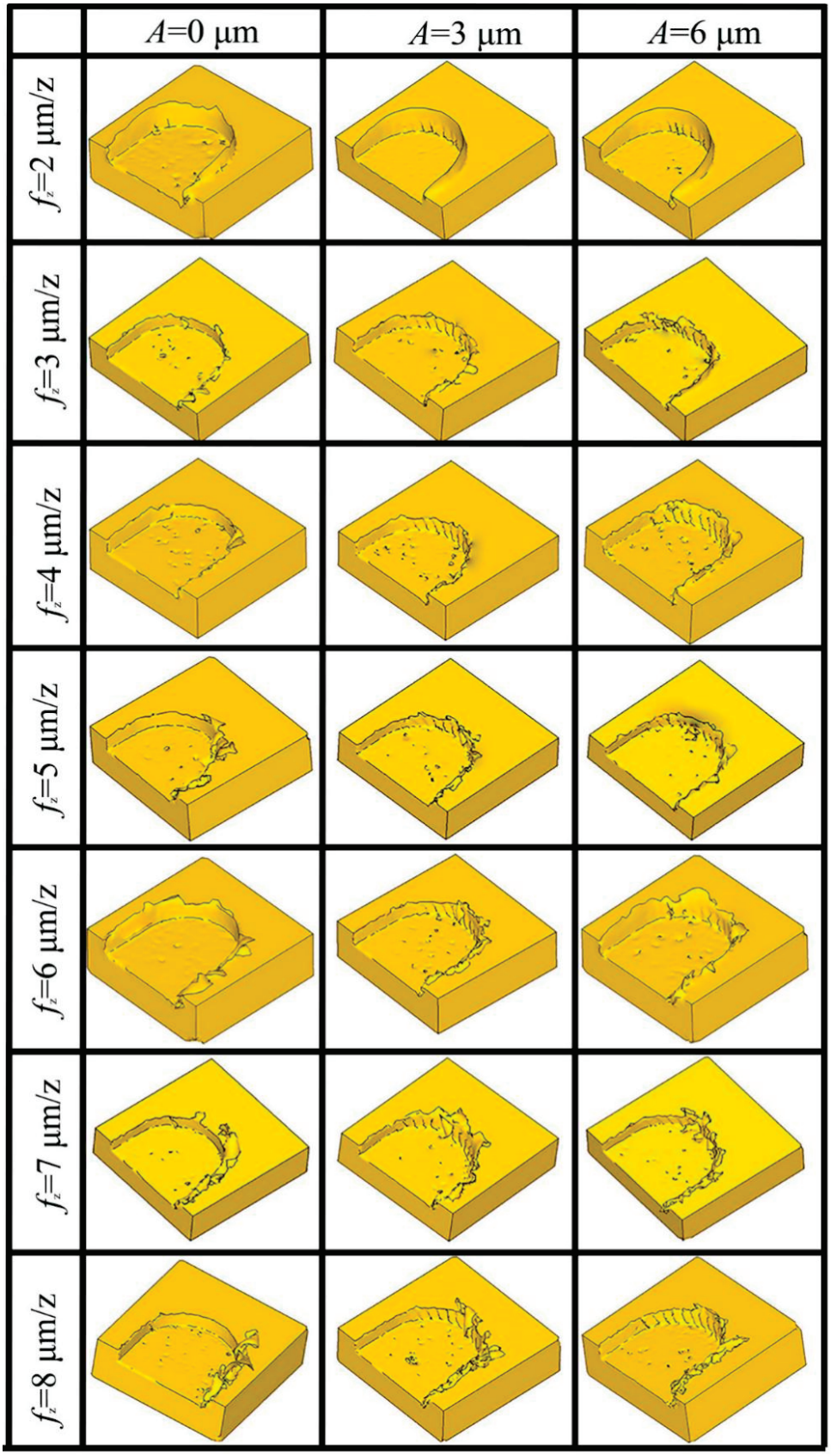

Figure 14. Simulation of burr morphology under different f_z.

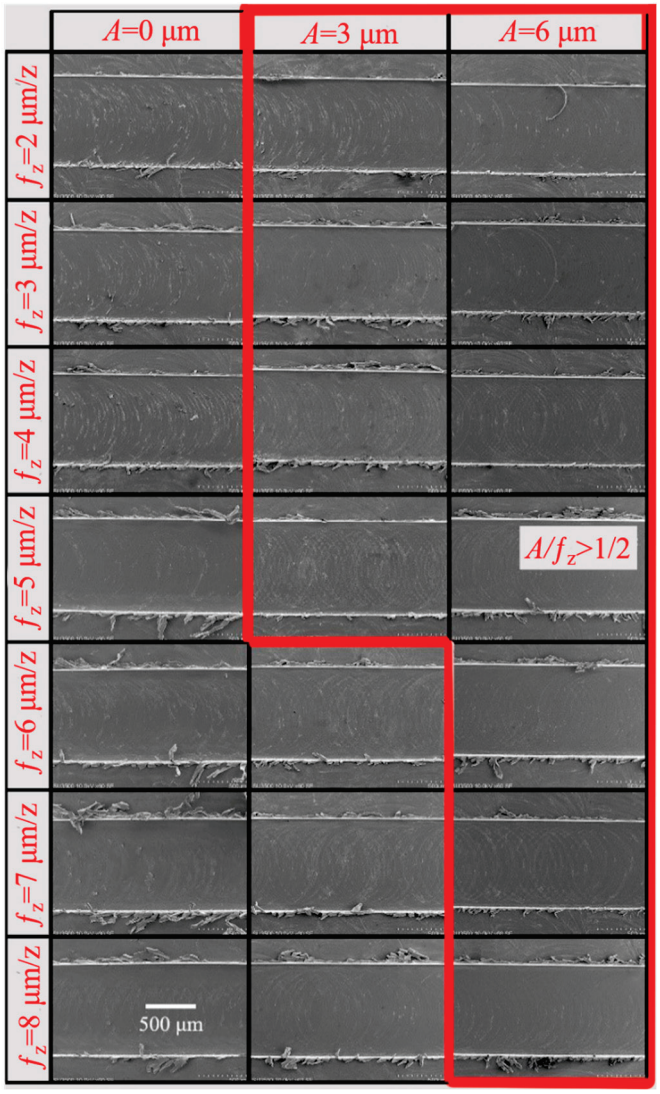

Figure 15. Morphology of burr under different f_z (SEM); (V_c = 37.7 m/min, a_p = 50 μm).

4. Conclusions

The influence of UVAMM on cutting force, cutting temperature, and burr size was analyzed by simulation and experiment. The research findings are as follows:

(1) When ultrasonic vibration is applied and the ratio of A to f_z reaches a certain limit, the UVAMM processing mode will change, and the cutting process will no longer be continuous, but will change to intermittent cutting;

(2) Compared with TMM, the average cutting force and cutting temperature of UVAMM are reduced, the strain range expands by applying ultrasonic vibration, and the energy required for damage reduces;

(3) Through simulation and experiment, it is found that the additional ultrasonic vibration can effectively reduce the burr size in the milling process. The bigger A is, the better the burr suppression effect is;

(4) UVAMM can reduce the size of burr by reducing the size effect and promoting the fracture of burr. When A is 6 μm, the size and quantity of burr is the smallest;

(5) When the f_z is small, UVAMM can reduce the size effect and change the chip formation process to suppress the formation of burr. When f_z is large, the burr size can be reduced by changing the instantaneous cutting thickness to improve the chip breaking ability.

Author Contributions: Conceptualization, Y.Z., Z.Y., B.F., L.G., Z.C. and G.S.; writing—original draft preparation, Y.Z.; writing—review and editing, Y.Z., Z.Y., B.F., L.G., Z.C. and G.S.; supervision, B.F.; project administration, B.F. All authors have read and agreed to the published version of the manuscript.

Funding: This work was supported by Agricultural Key Applied Project of China (No. SD2019NJ015) and National Natural Science Foundation of China (projects No. 52075275).

Institutional Review Board Statement: Not applicable.

Informed Consent Statement: Not applicable.

Data Availability Statement: The data supporting this study's findings are available from the corresponding author upon reasonable request.

Conflicts of Interest: The authors declare no conflict of interest.

References

1. Bücker, M.; Bartolomeis, A.D.; Oezkaya, E.; Shokrani, A.; Biermann, D. Experimental and computational investigations on the effects of deep-temperature emulsion on the turning of Inconel 718 alloy. *CIRP J. Manuf. Sci. Technol.* **2020**, *31*, 48–60. [CrossRef]
2. Sun, Z.; To, S.; Zhang, S.; Zhang, G. Theoretical and experimental investigation into non-uniformity of surface generation in micro-milling. *Int. J. Mech. Sci.* **2018**, *140*, 313–324. [CrossRef]
3. Muhammad, A.; Gupta, M.K.; Mikołajczyk, T.; Pimenov, D.Y.; Giasin, K. Effect of Tool Coating and Cutting Parameters on Surface Roughness and Burr Formation during Micromilling of Inconel 718. *Metals* **2021**, *11*, 167. [CrossRef]
4. Câmara, M.A.; Rubio, J.C.; Abrão, A.M.; Davim, J.P. State of the Art on Micromilling of Materials, a Review. *J. Mater. Sci. Technol.* **2012**, *28*, 673–685. [CrossRef]
5. Biermann, D.; Hartmann, H. Reduction of Burr Formation in Drilling Using Cryogenic Process Cooling. *Procedia CIRP* **2012**, *3*, 85–90. [CrossRef]
6. Hashimura, M.; Hassamontr, J.; Dornfeld, D.A. Effect of In-Plane Exit Angle and Rake Angles on Burr Height and Thickness in Face Milling Operation. *J. Manuf. Sci. Eng.* **1999**, *121*, 13–19. [CrossRef]
7. Pang, X.; Zeng, Y.; Zhang, J.; Deng, W. Analytical model and experimental verification of Poisson burr formation in ductile metal machining. *J. Mater. Process. Technol.* **2021**, *290*, 116966. [CrossRef]
8. Hajiahmadi, S. Burr size investigation in micro milling of stainless steel 316L. *Int. J. Light. Mater. Manuf.* **2019**, *2*, 296–304. [CrossRef]
9. Aslantas, K.; Ekici, E.; Çiçek, A. Optimization of process parameters for micro milling of Ti-6Al-4V alloy using Taguchi-based gray relational analysis. *Measurement* **2018**, *128*, 419–427. [CrossRef]
10. Kobayashi, R.; Xu, S.; Shimada, K.; Mizutani, M.; Kuriyagawa, T. Defining the effects of cutting parameters on burr formation and minimization in ultra-precision grooving of amorphous alloy. *Precis. Eng.* **2017**, *49*, 115–121. [CrossRef]
11. Saptaji, K.; Subbiah, S. Burr Reduction of Micro-milled Microfluidic Channels Mould Using a Tapered Tool. *Procedia Eng.* **2017**, *184*, 137–144. [CrossRef]
12. Li, S.S.; Zou, B.; Xu, K.; Wang, Y.S. Machined channel quality and tool life using cermet micro-mill in micro-milling aluminum alloy. *Int. J. Adv. Manuf. Technol.* **2019**, *101*, 2205–2216. [CrossRef]
13. Xu, J.; Feng, P.; Feng, F.; Zha, H.; Liang, G. Subsurface damage and burr improvements of aramid fiber reinforced plastics by using longitudinal–torsional ultrasonic vibration milling. *J. Mater. Process. Technol.* **2021**, *297*, 117265. [CrossRef]
14. Xiang, D.-H.; Wu, B.-F.; Yao, Y.-L.; Zhao, B.; Tang, J.-Y. Ultrasonic Vibration Assisted Cutting of Nomex Honeycomb Core Materials. *Int. J. Precis. Eng. Manuf.* **2019**, *20*, 27–36. [CrossRef]
15. Giraldo, M.M.; Martínez, D.S.; Bolívar, J.A.P.; Cabrera, J.L.B. Burr formation and control for polymers micro-milling: A case study with vortex tube cooling. *Dyna* **2017**, *84*, 150–159. [CrossRef]
16. Sreenivasulu, R.; SrinivasaRao, C. Modelling, Simulation and Experimental validation of Burr size in Drilling of Aluminium 6061 alloy. *Procedia Manuf.* **2018**, *20*, 458–463. [CrossRef]
17. Meng, Q.; Cai, J.; Cheng, H.; Zhang, K. Investigation of CFRP cutting mechanism variation and the induced effects on cutting response and damage distribution. *Int. J. Adv. Manuf. Technol.* **2020**, *106*, 2893–2907. [CrossRef]
18. Yadav, A.; Kumar, M.; Bajpai, V.; Singh, N.K.; Singh, R.K. FE modeling of burr size in high- speed micro-milling of Ti6Al4V. *Precis. Eng.* **2017**, *49*, 287–292. [CrossRef]
19. Zou, Z.; Liu, L.; Li, B.; Deng, W. Research on burr formation mechanism in metal cutting with a backup material. *Int. J. Adv. Manuf. Technol.* **2016**, *86*, 1895–1907. [CrossRef]
20. Asad, M. Effects of Tool Edge Geometry on Chip Segmentation and Exit Burr: A Finite Element Approach. *Metals* **2019**, *9*, 1234. [CrossRef]
21. Sreenivasulu, R.; Rao, C.S. Some Investigations on Drilling of Aluminium Alloy from FEA-Based Simulation Using DEFORM-3D. In *Advances in Simulation, Product Design and Development*; Springer Nature: Singapore, 2020; pp. 3–15. [CrossRef]
22. An, Q.L.; Dang, J.Q.; Liu, G.Y.; Dong, D.P.; Ming, W.W.; Chen, M. A new method for deburring of servo valve core edge based on ultraprecision cutting with the designed monocrystalline diamond tool. *Sci. China Technol. Sci.* **2019**, *62*, 1805–1815. [CrossRef]

23. Chen, W.; Teng, X.; Zheng, L.; Xie, W.; Huo, D. Burr reduction mechanism in vibration-assisted micro milling. *Manuf. Lett.* **2018**, *16*, 6–9. [CrossRef]
24. Chen, L.; Deng, D.; Pi, G.; Huang, X.; Zhou, W. Burr formation and surface roughness characteristics in micro-milling of microchannels. *Int. J. Adv. Manuf. Technol.* **2020**, *111*, 1277–1290. [CrossRef]
25. Chen, W.; Zheng, L.; Teng, X.; Yang, K.; Huo, D. Finite element simulation and experimental investigation on cutting mechanism in vibration-assisted micro-milling. *Int. J. Adv. Manuf. Technol.* **2019**, *105*, 4539–4549. [CrossRef]
26. Le, D.; Lee, J.-M.; Kim, S.-J.; Lee, D.-Y.; Lee, S.-W. Burr analysis in microgrooving. *Int. J. Adv. Manuf. Technol.* **2010**, *50*, 569–577. [CrossRef]
27. Wu, F.; Liu, Z.; Guo, B.; Sun, Y.; Chen, J. Research on the burr-free interrupted cutting model of metals. *J. Mater. Process. Technol.* **2021**, *295*, 117190. [CrossRef]
28. Efstathiou, C.; Vakondios, D.; Lyronis, A.; Sofiakis, K.; Antoniadis, A. Finite Element Modeling and Experimental Study of Burr Formation in Drilling Processes. In Proceedings of the ASME 2016 International Mechanical Engineering Congress and Exposition, Phoenix, AZ, USA, 11–17 November 2016.
29. Yu, L.; Guo, C.; Ranganath, S.; Talarico, R.A. Multi-phase FE model for machining Inconel 718. In Proceedings of the ASME 2010 International Manufacturing Science and Engineering Conference, Erie, PA, USA, 12–15 October 2010; pp. 263–269.
30. Xie, W.; Wang, X.; Liu, E.; Wang, J.; Tang, X.; Li, G.; Zhang, J.; Yang, L.; Chai, Y.; Zhao, B. Research on cutting force and surface integrity of TC18 titanium alloy by longitudinal ultrasonic vibration assisted milling. *Int. J. Adv. Manuf. Technol.* **2022**, *119*, 4745–4755. [CrossRef]
31. Zhang, Z.; Yuan, Z.; Wang, G. Formation and Control Technology of Top Burr in Micro-Milling. *MATEC Web Conf.* **2017**, *108*, 4003. [CrossRef]

micromachines

MDPI

Article

Femtosecond Laser Cutting of 110–550 μm Thickness Borosilicate Glass in Ambient Air and Water

Edgaras Markauskas *, Laimis Zubauskas, Gediminas Račiukaitis and Paulius Gečys

Center for Physical Sciences and Technology, Savanoriu Ave. 231, LT-02300 Vilnius, Lithuania
* Correspondence: edgaras.markauskas@ftmc.lt; Tel.: +370-5-264-4868; Fax: +370-5-260-231

Abstract: The cutting quality and strength of strips cut with femtosecond-duration pulses were investigated for different thicknesses of borosilicate glass plates. The laser pulse duration was 350 fs, and cutting was performed in two environments: ambient air and water. When cutting in water, a thin flowing layer of water was formed at the front surface of the glass plate by spraying water mist next to a laser ablation zone. The energy of pulses greatly exceeded the critical self-focusing threshold in water, creating conditions favorable for laser beam filament formation. Laser cutting parameters were individually optimized for different glass thicknesses (110–550 μm). The results revealed that laser cutting of borosilicate glass in water is favorable for thicker glass (300–550 μm) thanks to higher cutting quality, higher effective cutting speed, and characteristic strength. On the other hand, cutting ultrathin glass plates (110 μm thickness) demonstrated almost identical performance and cutting quality results in both environments. In this paper, we studied cut-edge defect widths, cut-sidewall roughness, cutting throughput, characteristic strength, and band-like damage formed at the back surface of laser-cut glass strips.

Keywords: femtosecond pulses; cutting; roughness; chipping; characteristic strength; borosilicate glass; filament

Citation: Markauskas, E.; Zubauskas, L.; Račiukaitis, G.; Gečys, P. Femtosecond Laser Cutting of 110–550 μm Thickness Borosilicate Glass in Ambient Air and Water. *Micromachines* **2023**, *14*, 176. https://doi.org/10.3390/mi14010176

Academic Editors: Jiang Guo, Chunjin Wang and Chengwei Kang

Received: 20 December 2022
Revised: 4 January 2023
Accepted: 6 January 2023
Published: 10 January 2023

1. Introduction

The use of femtosecond (fs) pulses has drastically increased over recent years in the processing of brittle transparent materials, such as scribing and cutting [1], femtosecond laser-induced selective etching [2], optical waveguide writing [3,4], and high-density optical storage formation [4,5].

The short duration of the femtosecond laser pulse is advantageous for its reduced thermal accumulation effects and nonlinear absorption compared to longer-duration pulses [1,6,7]. The electron–phonon coupling in dielectrics is usually longer than the fs pulse duration, allowing the delivery of the pulse energy quicker than the thermal diffusion occurs—energy transfer to surrounding material via phonon vibrations [8,9]. As a result, heat-accumulation-related stresses can be reduced and, together with higher energy absorption, can be confined to a smaller volume, improving the quality and strength of machined glass parts [9–11].

The use of femtosecond laser pulses allows the application of a wide variety of glass-cutting approaches, each providing its advantages and drawbacks. The most common laser-based cutting techniques employing femtosecond pulses are top-down cutting via direct laser ablation [12], bottom-up ablation [7,13], and laser stealth dicing [14,15].

Significant cutting speeds can be achieved via the stealth dicing technique. Mishchik et al. [14] reported a straight-line cutting speed of 600 mm/s of 500 μm thickness Eagle XG glass at a 100 kHz pulse repetition rate with fs duration pulses. A laser beam was focused inside the workpiece and scanned in a predetermined trajectory to form a stress layer. Usually, multifocal or Bessel beam processing is employed to improve cutting quality by elongating the modifications [16]. After the laser process, the workpiece is cleaved along

the scanned line by applying mechanical stress. However, this technique is unsuitable for cutting tiny pieces or complex trajectories with a small radius of curvature (1 mm or less). Thus, it is mainly used for cutting straight lines [15].

The bottom-up approach does not have as strict limitations on cutting geometry as the stealth dicing technique while maintaining moderate glass-cutting speed [17,18]. A cutting speed of 9 mm/s of 1 mm thickness soda–lime glass sheet with nanosecond laser pulses was reported in [19]. Kerf formation starts from the back surface of the glass workpiece and gradually approaches the front surface. High cutting rates are reached due to the mechanical material removal nature since laser energy is used to crack the glass into small pieces instead of evaporating the material (a more energy-efficient approach than material ablation). However, the technique suffers from excessive cracking and chipping at the cut edges, with defects reaching up to hundreds of micrometers in size [13,18].

Finally, the direct laser ablation technique is based on the top-down material removal approach, where material ablation starts at the top of the workpiece and ends at the bottom by removing material in a layer-by-layer fashion. This approach allows the cutting of complex shapes consisting of inner and outer contours, coated, opaque, or highly absorptive materials [20]. This approach provides high process flexibility but suffers from low processing speeds and is unsuitable for taper-less cutting [18,21].

In the case of direct laser ablation, slow material cutting speeds can be compensated for by increasing the incident laser power. However, this leads to undesirable heat accumulation in the workpiece, which cannot be avoided even when femtosecond pulses are employed—especially when high pulse repetition rates are increasingly adopted in laser microfabrication [22,23]. Thus, despite the advantages provided by ultrashort femtosecond pulses, multiple undesirable effects could take place in brittle materials during laser–matter interaction: chipping [12,24], surface and subsurface micro-cracking [8,25], refractive index changes [26,27], electronic damage [28], and void formation [25,29]. Ultimately, laser-induced damage (defects) could cause the degradation of the cut-edge strength [7] and resistance to wear and tear, and negatively affect the longevity of laser-cut glass products.

Laser machining of glasses (and other brittle materials) can be conducted in liquids, most commonly in water, to further diminish the detrimental heat accumulation in the materials. In some cases, volatile liquids (ethanol, methanol, ethylene glycol, and others) are used in laser machining to cool down the workpiece [30–32]. However, Kanitz et al. [33] reported the highest specific ablation rate ($\mu m^3/\mu J$ per laser shot) of iron in water, compared to ablation in methanol, ethanol, acetone, or toluene, while Liu et al. [34] observed deeper craters ablated in silicon when the workpiece was submerged in water than in ethanol.

Previously, we demonstrated an improved cut-edge quality for borosilicate glass cutting in water with picosecond pulses [20,35]. Characteristic strength measurements in [35] revealed increased front and back side strengths by 7.2 and 10.9%, respectively, compared to cutting in ambient air.

A comprehensive comparison of multiple laser-based glass-cutting techniques was conducted by Dudutis et al. [19,36]. They compared glass cutting via the bottom-up technique with direct laser ablation in ambient air and water [36] and stealth dicing [19]. In both studies, 1 mm thick soda–lime glass plates were used as the samples. Their findings revealed that in the case of 1064 nm radiation and picosecond (ps) duration pulses, the glass samples cut via direct laser ablation had the smallest sidewall roughness and possessed the highest front side cut-edge quality (smallest defect widths compared to the other two techniques). Furthermore, glass samples cut in water via direct ablation had the highest flexural strength (134 MPa at the front and 131 MPa at the back) compared to other investigated laser-cutting techniques. However, cutting of 1 mm thick soda–lime glass via direct laser ablation was notably slower (0.19 mm/s in ambient air and 0.34 mm/s in water) than the stealth dicing with Bessel beams (100 mm/s) and bottom-up cutting (0.74 mm/s) using 1064 nm wavelength ps pulses [19,36]. The use of 532 nm wavelength nanosecond pulses for the bottom-up cutting increased the glass-cutting speed up to 9 mm/s [19], but

the strength of laser-cut glass remained higher when cutting was conducted in water via direct laser ablation.

Micromachining with femtosecond pulses in a liquid environment can facilitate the formation of filaments within the water layer [24]. Laser beam filamentation can occur in the water layer when the peak pulse power exceeds a critical power P_c [37]. The refractive index of water is $n = 1.329$, and the nonlinear refractive index is $n_2 = 4.1 \times 10^{-20}$ m^2/W for a 1030 nm wavelength radiation [38]. Thus, in water, the P_c value is 2.9 MW for 1030 nm wavelength radiation which for 350 fs duration pulses is reached at a pulse energy of 1.1 μJ. Glass cutting and drilling via femtosecond-pulse filamentation in water were successfully employed in [24,39,40]. The strong electron plasma formation and electron relaxation in the filament facilitated material ablation [41]. Furthermore, filaments can sustain a high beam intensity over a longer distance, allowing cutting and drilling of several-millimeter-deep features without laser beam focal plane readjustment [12,42]. An increase in glass drilling and groove formation speeds was reported in [41].

Glass cutting and milling with ultrashort pulses were thoroughly studied by multiple groups on different glasses and glass thicknesses [1,13,21,25,28,36,43–45]. However, reliable conclusions on how the laser cutting quality, process throughput, and strength of laser-cut glass parts differ at different glass thicknesses cannot be drawn due to the lack of a systematic approach. Furthermore, to the best of our knowledge, no strength measurements were applied for glass cut with femtosecond pulses in water with pulse energies greatly exceeding the critical self-focusing power threshold.

In this work, we experimentally studied the femtosecond laser cutting of borosilicate glass plates via direct laser ablation with 1030 nm wavelength radiation. Three glass thicknesses were studied: 110, 300, and 550 μm. We compared cutting in ambient air and water in terms of cut-edge quality and sidewall roughness, ablation efficiency, effective glass cutting speed, and characteristic strength of the front and back sides of laser-cut glass strips.

2. Materials and Methods

In this study, we used a femtosecond laser FemtoLux 30 (Ekspla), with a central wavelength of 1030 nm and a pulse duration of 350 fs. In the experiments, the pulse repetition rate f was adjusted between 0.4 and 1.1 MHz, resulting in a slight variation in the average laser power P. The highest average laser power P_{max} was 19.3 W at $f = 0.4$ MHz and linearly increased to 21 W at $f = 1.1$ MHz. The power was measured with an Ophir F150(200)A-CM-16 sensor at the sample surface. The thickest investigated glass (thickness $t = 550$ μm) shattered when cutting was conducted in ambient air at P_{max}. As a result, we additionally conducted cutting experiments at a low pulse repetition rate of 100 kHz in ambient air. We used a pulse picker to obtain such a low pulse repetition rate. The pulse picker picked specific pulses to obtain the requested pulse repetition rate at the expense of the average laser power. Thus, the average laser power at 100 kHz decreased to 1.8–3.3 W (P_{min}). Experiments were conducted with a laser beam intensity profile similar to Gaussian (linearly polarized, S polarization).

We used borosilicate glass plates with a thickness of 0.11, 0.3, and 0.55 mm as the samples. Glass plates were thoroughly cleaned prior to the laser treatment and subsequently cut into 26 × 5 mm^2 glass strips.

Laser cutting was realized with a galvanometer scanner IntelliSCAN$_{de}$14 from ScanLab by scanning parallel cut lines separated by hatch distance (see Figure 1). Each cut line was scanned once per scan. After a fixed number of lines, the hatch and the laser beam scanning directions were changed to the opposite. A positive hatch and scanning direction (A to B) were used for odd scans. A negative hatch with the opposite scanning direction (B to A) was used for even scans. The aforementioned number of cut lines and the hatch distance defined the width of the cut. Scans were repeated multiple times until the glass plate was cut through completely.

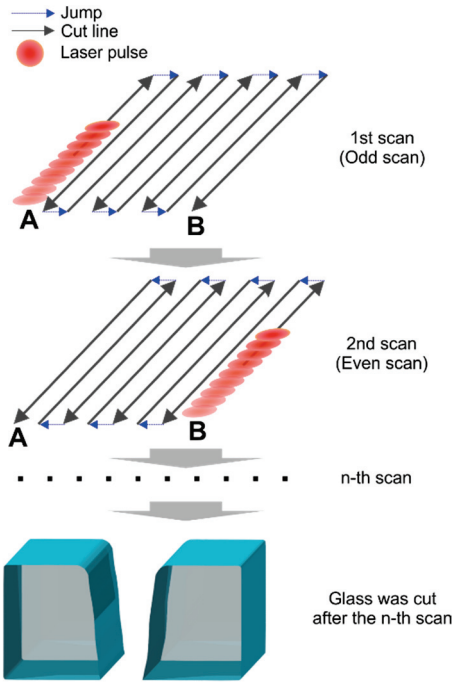

Figure 1. Scan geometry used to cut glass. Arrows represent the laser beam scanning direction for the odd and even scans. For the odd scan, the laser beam scanning direction was from position A to B. For the even scan, the laser beam direction was the opposite (laser beam was scanned from position B to A). Scans were repeated multiple times until the glass was cut through.

The laser beam was focused to a diffraction-limited spot size (diameter) of 27 μm (in both cutting environments) using an f-theta objective with a focal length of 100 mm. We performed spot-size measurements on thin chrome film deposited on glass plates, according to [46]. The focused beam spot size and the laser fluence values reported in this study were evaluated with a laser beam focal point set at the front surface of the glass sample. For the cutting, the focus was set below the front sample surface at a distance equal to 1/2 the thickness of the glass plate, where the highest cutting speed was achieved in ambient air. Thus, the laser beam focal point was shifted from 55 to 275 μm below the front surface, depending on the glass thickness.

In the case of glass cutting in a water environment, cutting was realized through a thin flowing layer of deionized water. The water layer was formed using the water film formation subsystem, which consisted of the compressed air source, an airbrush, a pressure-regulating valve, a deionized water supply tank, and a tray to collect water. The airbrush, connected to pressurized air at 3 bar and a water supply tank, sprayed water mist on top of the glass plate, forming a thin flowing water film (see Figure 2). Constant air pressure and continuously maintained water level in the water tank formed a consistent water film that did not change over time. The nozzle of the airbrush was set 1 cm above the glass surface at an angle of 45 degrees. The liquid flow rate was 11 mL/min. The water mist impingement point was set 5 mm from the laser cutting area (along the water flow direction) to avoid laser beam disturbance with the water mist. The water flow and beam-scanning direction were in parallel. The area covered with the thin flowing water film was 35 mm in length. The width of the film was as wide as the glass plates (the widest plate was 24 mm). The thickness of the water layer decreased linearly with increasing distance from the water mist impingement area. The thickness at the cut line start point was 650 μm, while at the end of the cut, the thickness decreased to 350 μm, giving the average water-layer thickness value of 500 μm throughout the 26 mm long cut line. Initial experiments revealed that the water thickness variation had no significant effect on the ablation efficiency or quality in the laser cutting area. In the experiments, the peak pulse power exceeded the critical power of P_c = 2.9 MW for the laser beam self-focusing in the water layer from 30 to 40 times,

depending on the pulse energy. Butkus et al. [41] simulated the required filament initiation length in water to be 0.5 mm, which coincided with the average water layer thickness used in this study. As a result, we consider that suitable conditions for filament formation in water were ensured. In ambient air, laser ablation was facilitated at the front glass surface, creating favorable conditions for direct material ablation.

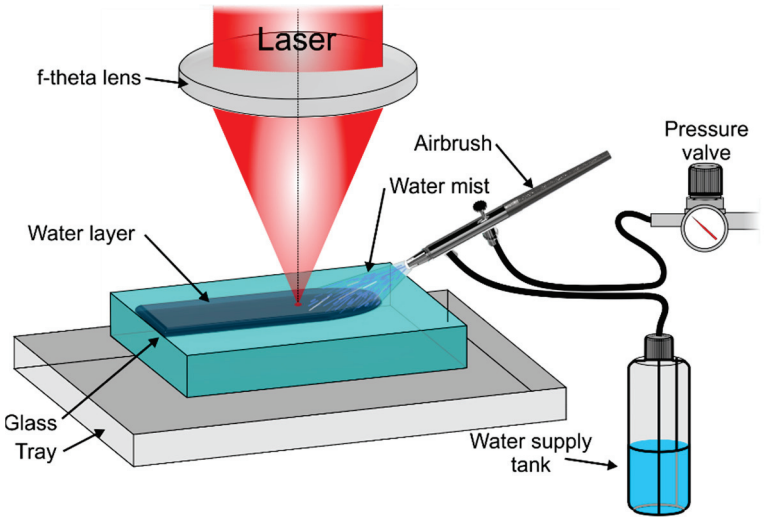

Figure 2. Schematics showing the setup used to form a flowing water layer on top of the glass sample.

After the cutting, glass chipping and cracking were evaluated with an optical microscope Eclipse LV100NDA from Nikon, while cut sidewalls were analyzed with an optical profiler S neox from Sensofar. We used a four-point bending test to determine the maximum bending strength of laser-cut glass strips. The span of supporting and loading rollers was 16 and 6 mm, respectively. Strips were bent from both sides until the failure occurred. We measured the bending strength with a high-precision dynamometer FMI-S30A5 from Alluris. The maximum bending strength was evaluated using the following formula: $\sigma = 3F(L-l)/(2bt^2)$, where F is the loading strength at which the glass strip failed, b is the width of the strip, t is the thickness of the strip, and L and l are the spans of the support and loading rollers, respectively. The σ values obtained were used for the Weibull analysis to extract the characteristic strengths (σ_0) of laser-cut strips. Here, the characteristic strength defines the bending strength at which 63.2% of strips fail. More detailed information on the four-point bending setup and Weibull analysis can be found in [35].

3. Results

3.1. Optimized Cutting Parameters

Strips with dimensions of 26 × 5 mm^2 were cut out of larger glass plates using the laser-cutting parameters presented in Tables 1 and 2. Glass cutting was performed in ambient air and water. Laser-cutting parameters were optimized, prioritizing the process throughput (effective cutting speed). Here, the effective cutting speed is defined as the ratio between the laser beam scanning speed and the total number of scanning passes (the number of cut lines in a single scan multiplied by the number of scans). The laser fluence F, laser beam scanning speed v, hatch, number of scans, and cut widths were individually optimized for glass plate thickness and cutting environment during initial experiments.

Table 1. Glass cutting parameters and performance for fs cutting in ambient air. Values presented outside brackets represent cutting at high laser power (P_{max}), while values inside brackets represent cutting at low laser power (P_{min}). Cutting width, hatch, and the number of cut lines were maintained the same for both high- and low-power cutting.

Glass Thickness (μm)	Average Laser Power (W)	Pulse Repetition Rate (kHz)	Scanning Speed (mm/s)	Number of Cut Lines in a Single Scan	Fluence (J/cm^2)	Hatch (μm)	Cut Width (μm)	Ablation Efficiency (μm^3/μJ)	Effective Cutting Speed (mm/s)
110	21 (1.8)	1100 (100)	1600 (150)	7	6.7 (6.3)	20	150	10.6 (11.3)	20.8 (2)
300	20.8 (3.2)	620 (100)	1000 (170)	13	11.7 (11.2)	22.5	310	8.6 (8.8)	3.2 (0.5)
550	- (3.3)	- (100)	- (250)	17	- (11.5)	20	350	- (7.9)	- (0.17)

Table 2. Glass-cutting parameters and performance for fs cutting in water. Cutting in water was conducted at a high laser power P_{max} only.

Glass Thickness (μm)	Average Laser Power (W)	Pulse Repetition Rate (kHz)	Scanning Speed (mm/s)	Number of Cut Lines in a Single Scan	Fluence (J/cm^2)	Hatch (μm)	Cut Width (μm)	Ablation Efficiency (μm^3/μJ)	Effective Cutting Speed (mm/s)
110	19.5	530	1100	9	12.9	12.5	135	8.7	20.4
300	19.3	433	500	9	15.6	22.5	210	7.2	4
550	19.3	433	500	11	15.6	22.5	260	7.3	1.8

The highest effective cutting speed in ambient air was obtained when the focus position was shifted below the front glass surface at a distance of $t/2$, where t is the glass thickness. We used the same focus positions for cutting in water as in the ambient air since the ablation efficiency in water was insensitive to focus variation in the z direction (in the z range between $z = 0$ and $z = t$).

Also, we used a fixed-beam focus position for glass cutting—the Rayleigh distance in ambient air (560 μm) was longer than the t of all investigated glass plates.

In ambient air, 550 μm thick glass plates shattered during cutting at full laser power (P_{max}) due to excessive stresses caused by heat accumulation. Thus, only t = 110 and 300 μm thickness glass strips were cut without shattering into smaller pieces. For this reason, cutting experiments in ambient air were split into two separate cutting regimes: low laser power (P_{min}, where f was limited to 100 kHz (f_{min})) and high laser power (P_{max}, where the maximum pulse rate f_{max} was used). In the high-laser-power regime, the applied pulse repetition rate was determined by the maximum laser power (at a given f) and laser pulse energy at which optimal fluence was reached. As was mentioned in Section 2, the average laser power at P_{max} was distributed between 19.3 and 21 W, depending on the pulse repetition rate. In the low-laser-power regime, the incident laser power was decreased to 1.8–3.3 W by limiting the pulse repetition rate to 100 kHz (f_{min}) but maintaining optimal laser fluence.

Almost 200 stripes were cut and investigated in this study (eight cutting regimes × 24 glass strips) in terms of cut-edge quality, cut-sidewall roughness, and characteristic strength. More than 70 strips were cut in water, while 120 strips were cut in ambient air.

3.2. Cutting Quality

In this section, we assessed the cutting quality of laser-cut glass strips (26 × 5 mm^2) in terms of (1) cut-sidewall steepness, (2) maximum defect width, (3) mean defect width, and (4) cut-wall roughness. Cutting quality at the front and back sides of laser-cut glass strips was evaluated separately.

The cut-wall steepness a (the taper angle) was evaluated with an optical microscope. A schematic is shown in Figure 3. According to the results, the steepness of the cut sidewalls ablated in water increased with glass thickness from 13.1° to 10.7° with an average taper angle value of 11.9 ± 0.04°. The taper angle in ambient air (insignificant difference between

power levels) was much higher at all investigated glass thicknesses: at t = 110 µm the angle was 27.5 ± 2.6°, at t = 300 µm it was 18.9 ± 0.6°, and at t = 550 µm, the taper angle decreased to 17.3 ± 1°.

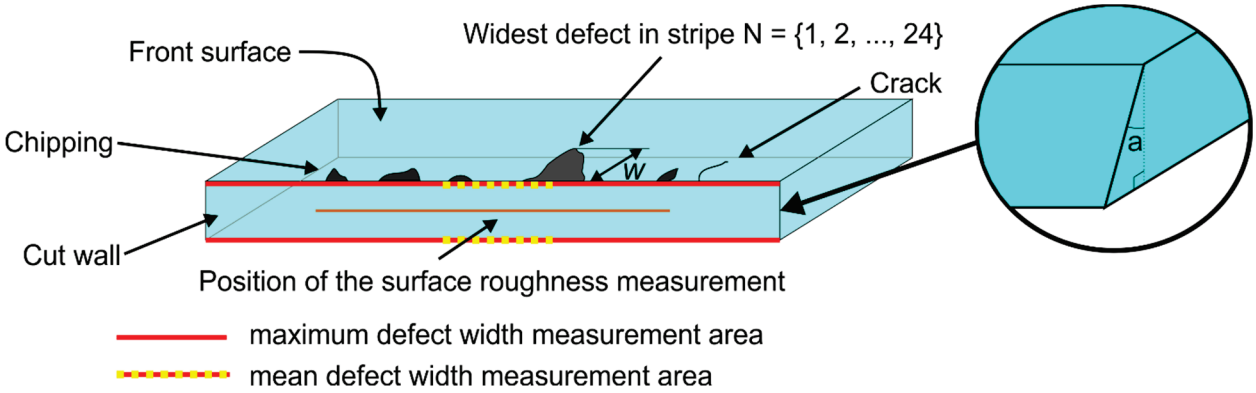

Figure 3. Schematic for evaluating the mean and maximum defect widths. Position for the cut-sidewall roughness measurements and cut-sidewall taper angle (a) are indicated.

The formation of steeper angles in water was conformed in other studies [20,35,47]. Steeper sidewalls (smaller taper angle) allow the maintenance of a higher fluence at greater cut depths due to a flatter bottom of the ablated feature. When cutting in ambient air, a more pronounced V-shape forces one to widen the cut to maintain a high ablation efficiency [20,48]. Otherwise, the flat bottom of the ablated channel transforms into a V-shape quicker than in water-assisted ablation and leads to a larger laser beam impingement area. This, as a result, reduces the laser fluence falling at the glass surface and leads to a quicker loss of material removal rate. The depth of the cut could even saturate. Therefore, in this study, wider cut widths in ambient air achieved an 18.3% higher ablation efficiency than in water (see Tables 1 and 2) at the expense of producing wider cuts by 38%.

Due to steeper cut sidewalls, cuts produced in water could be narrower than in ambient air while maintaining a sufficient ablation efficiency. Therefore, despite the ablation efficiency in water being lower, the actual effective cutting speed was almost identical at t = 110 µm (lower by 2%) and already surpassed cutting in ambient air by 25% at a glass thickness of 300 µm.

The lower effective glass-cutting speed in water at t = 110 µm (compared to cutting in ambient air) could be affected by the laser fluence loss in water (laser beam reflections, distortion, scattering, absorption in the water layer), and also due to the increased glass cooling effect in the ablation zone [49–52]. At greater depths in water, steeper cut walls and flatter groove bottoms mitigated efficiency losses in water.

Next, we evaluated cut-edge defects at the front and back sides of laser-cut glass strips. Chipping or crack formation from the cut edge were considered defects. The mean defect width w_{mean} was evaluated by calculating the average width of every chipping and cracking at the cut edge measured over a distance of 1.5 mm. The measurement area was positioned at the center of the laser cut. The maximum defect width w_{max} was identified as the widest defect per single cut edge along the entire length of the laser cut. The width of defects w was measured normal to the glass surface, as shown in Figure 3. Each strip consisted of four cutting edges (two at the front and two at the back). All laser-cut strips were measured for w_{mean}, w_{max}, and cut-sidewall roughness R_a. Values obtained from strips cut under the same cutting parameters were averaged. Cut-edge quality was evaluated separately for the front and back sides.

The typical cut-edge quality at the front glass side is presented in Figure 4. According to the micrographs, the different cutting conditions (cutting environment, glass thickness, and applied laser parameters) had only a little effect on the visual cut quality. Here, the width of the largest defects remained relatively constant despite different laser processing

parameters or cutting environments. Only the density and length (along the cut line) of large defects increased with increasing glass thickness, by applying higher laser power, or both. As a result, the maximum defect widths at the front side varied in a narrow range from 13.9 ± 3.8 µm (in water) to 15.5 ± 3 µm (in ambient air at P_{max}) with an average value of 14.8 ± 0.8 µm (see Table 3). In the table, we present the values for the maximum defect widths averaged over the different glass thicknesses since the dependency on the glass thickness was insignificant.

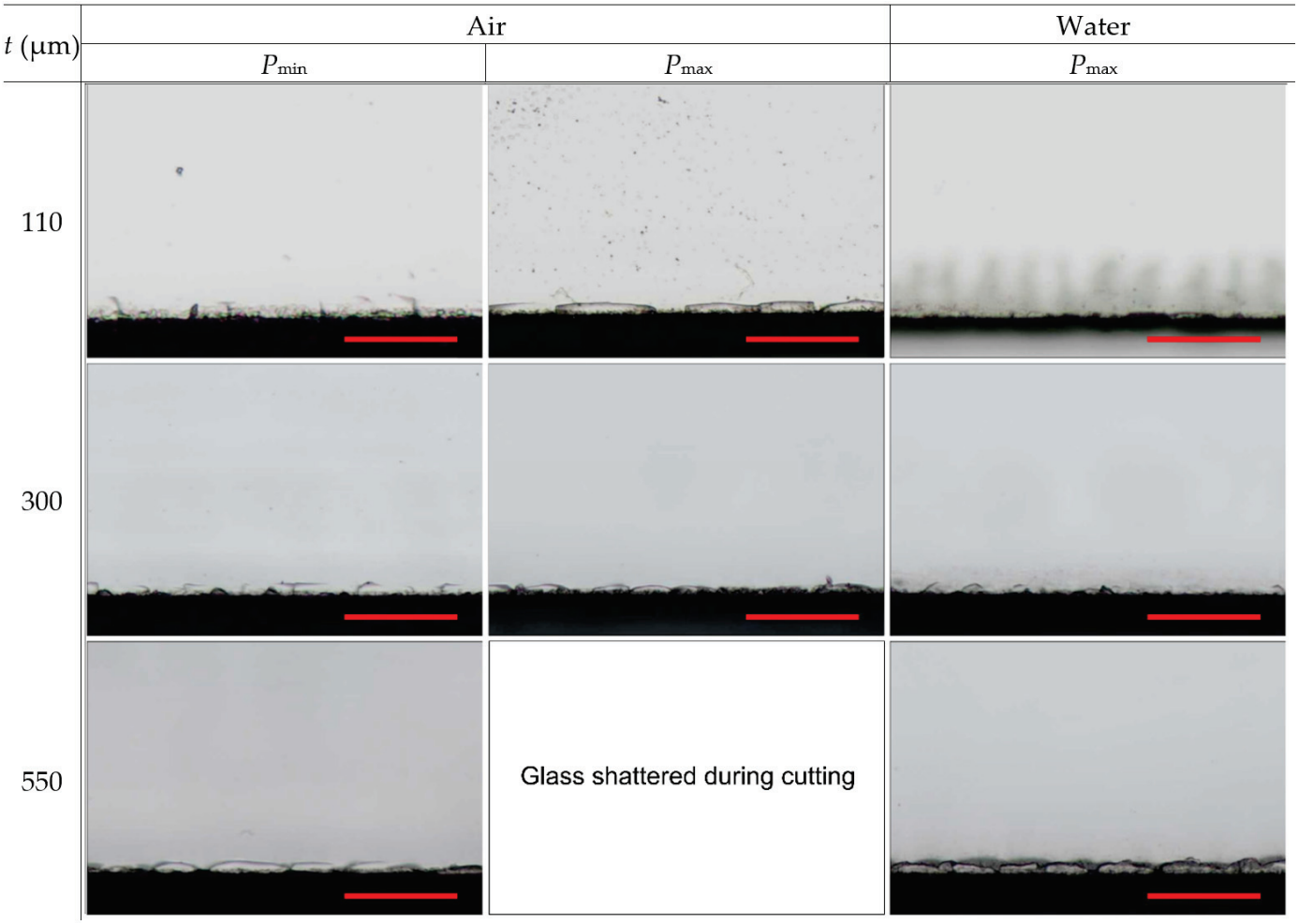

Figure 4. Optical micrographs showing cut edges at the front side of laser-cut glass strips. Rows represent different glass thicknesses, while columns represent different processing conditions. The scale bars represent 100 µm and apply to all panels in the figure.

Table 3. Maximum defect widths averaged over different glass thicknesses (110, 300, and 550 µm). Cases for the front and back sides are presented separately.

Cutting Regime	w_{max} at the Front Side	w_{max} at the Back Side
Air (P_{min}, f_{min})	15 ± 3.4 µm	24.2 ± 12 µm
Air (P_{max}, f_{max})	15.5 ± 3 µm	29.9 ± 5.5 µm
Water (P_{max}, f_{max})	13.9 ± 3.8 µm	25 ± 7.5 µm

Contrary to the consistency of w_{max}, the defects with widths below 10 µm increased with the glass thickness almost linearly. As a result, such development contributed to the increase in w_{mean} in ambient air and water environments (see Figure 5).

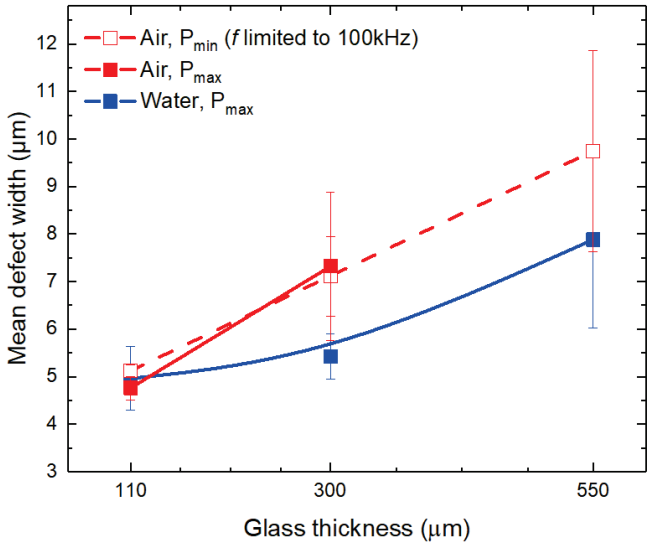

Figure 5. Mean defect widths at the cut edge at the front side of laser-cut glass strips. Dots are connected to guide the eye. Error bars indicate standard deviation.

At t = 110 µm, the mean defect width was almost identical between the different cutting regimes with the average mean defect value of 4.95 ± 0.2 µm (ambient air at P_{max} and P_{min}, and water). However, the mean defect width at higher glass thicknesses was narrower in water: at t = 300 µm it was 25% lower (5.4 ± 0.5 µm versus 7.2 ± 1.2 µm) and 19% lower at t = 550 µm (7.9 ± 1.9 µm versus 9.8 ± 2.1 µm) than in cuts produced in ambient air.

Cut-edge quality at the back side is presented in Figure 6. Micrographs indicated the damage at the back side consisting of defects at the cut edge (chipping and cracking) and periodically recurring band-like damage expanding further away from the cut edge.

The mean defect width's dependency on the glass thickness in ambient air and water was the opposite (see Figure 7). In the ambient air, the mean defect width increased with the glass thickness. At t = 110 µm, cutting in ambient air at two different power levels (P_{min} and P_{max}) produced cuts with almost identical mean defect width values (average w_{mean} value was 6.1 ± 0.2 µm). However, the transition to t = 300 µm showed wider mean defects in strips cut at high laser power (10.1 ± 1.4 µm versus 9.3 ± 1.7 µm), indicating a more pronounced heat accumulation in the glass. Finally, the mean defect width at t = 550 µm and P_{min} reached the highest value of 11.2 ± 1.4 µm. No data at t = 550 µm and P_{max} were available in ambient air due to glass breaking.

Contrary to the results obtained in ambient air, the mean defect width in water decreased with glass thickness. The highest mean defect width (13.1 ± 1.6 µm) was measured in the thinnest glass strips. However, the w_{mean} rapidly decreased: at t = 300 µm, the mean defect width was 9.1 ± 1.8 µm, while at t = 550 µm, it decreased further to 8.8 ± 1.7 µm. At t = 300 µm, the cut-edge quality surpassed cutting in ambient air in terms of mean defect width.

On average, the maximum defect width at the back surface was 1.8 times larger than on the front side (Table 3). The smallest value of 24.2 ± 12 µm was measured in strips cut in ambient air at P_{min}. Transitioning to high laser power (P_{max}) in ambient air increased the maximum defect width to 29.9 ± 5.5 µm. Cutting in water produced a maximum defect width of 25 ± 7.5 µm, which was similar to that measured in ambient air at P_{min}.

Cut-sidewall roughness R_a's dependency on the glass thickness is presented in Figure 8. According to the results, the sidewall roughness was almost identical at t = 110 µm for glass strips cut in ambient air (at P_{min} and P_{max}) and water (at P_{max}), with an average value of 0.5 ± 0.04 µm.

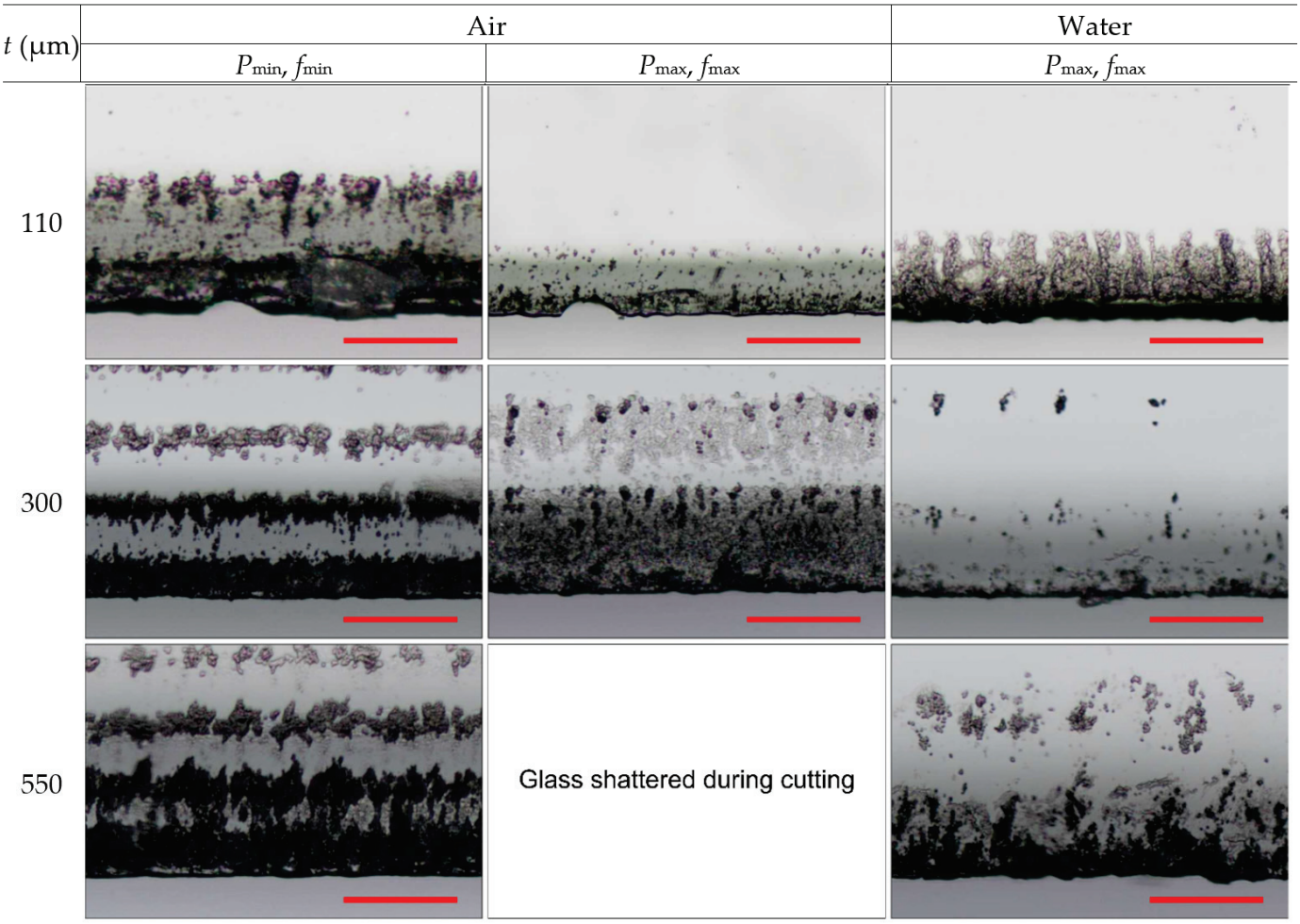

Figure 6. Optical micrographs showing cut edges at the back side of laser-cut glass strips. Rows represent different glass thicknesses, while columns represent different processing conditions. The scale bars represent 100 µm and apply to all panels in the figure.

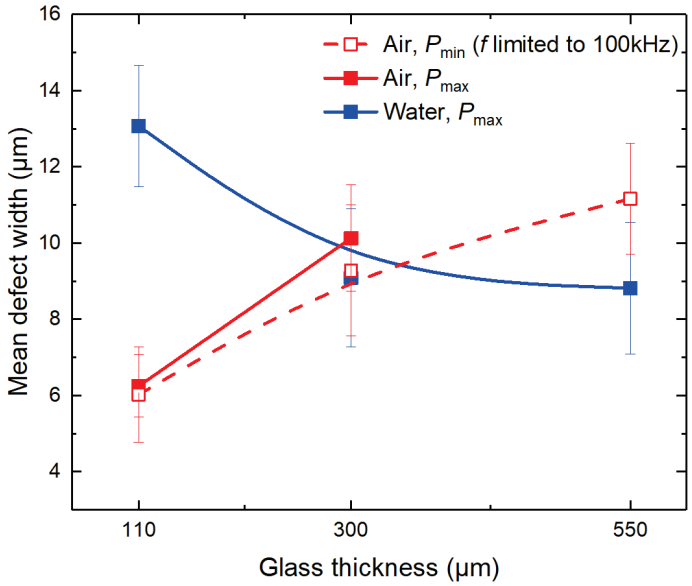

Figure 7. Mean defect widths at the cut edge at the back side of laser-cut glass strips. Dots are connected to guide the eye. Error bars indicate the standard deviation.

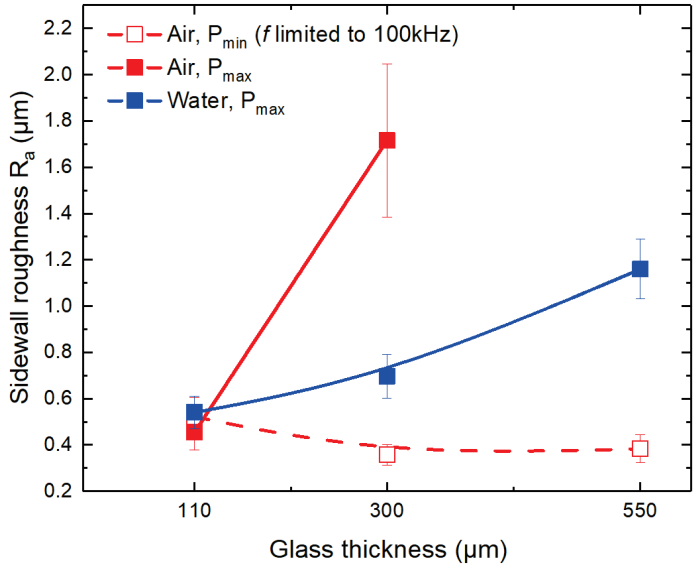

Figure 8. Cut-sidewall roughness versus glass thickness. Glass strips were cut in ambient air and water environments. Dots are connected to guide the eye, while error bars indicate the standard deviation.

In the case of glass cutting in ambient air at limited laser power (P_{min}), glass thickness had an insignificant effect on the cut-sidewall roughness with an average value of R_a = 0.42 ± 0.09 µm. In the case of cutting at P_{max}, the roughness rapidly increased with glass thickness in both ambient air and water environments. In ambient air, the sharp increase in sidewall roughness (from 0.45 ± 0.1 µm at t = 110 µm to 1.7 ± 0.3 µm at t = 300 µm) indicated significant heat accumulation effects in the laser ablation zone. Cutting in water improved cooling; thus, the increase in sidewall roughness was not as significant as in ambient air at P_{max}: 0.7 ± 0.09 µm at t =300 µm and 1.2 ± 0.1 µm at 550 µm.

Nevertheless, cutting in water usually results in higher cut-sidewall roughness compared to cutting in ambient air [35,36]. This is associated with increased mechanical glass erosion in water due to plasma and cavitation bubbles generating shockwaves [20,36,53]. Therefore, even if the increasing heat accumulation could be further suppressed in water, the sidewall roughness would remain higher than in ambient air at P_{min}.

3.3. Band-like Damage

The formation of band-like damage (parallel to the cut edge) at the back surface of transparent media was reported in multiple studies [1,12,54,55]. The cause of the damage was usually associated with laser beam refraction from the sidewall, diffraction from the inverse aperture (the edge of the ablated channel), and multiple reflections between the back and front surfaces of the transparent media.

In this section, we show that the refraction from the cut sidewall was the main effect causing the band-like damage in laser-cut strips. For this, we produced additional cuts in t = 550 µm glass plates in ambient air. The depth and width of cuts were controlled by varying the number of scans (from 24 to 60) and the number of cut lines in a single scan (from 7 to 21), respectively. The hatch distance was fixed at 25 µm. The micrographs showing the back surface of glass plates after the ablation are presented in Figure 9. According to the results, the back side damage occurred after 32 scans. The damage appeared as separate dots clustering into bands. The number of bands increased with the number of scans as the damage accumulated due to repetitive laser beam scanning. Also, the number of individual spots increased and merged into continuous bands after 60 scans.

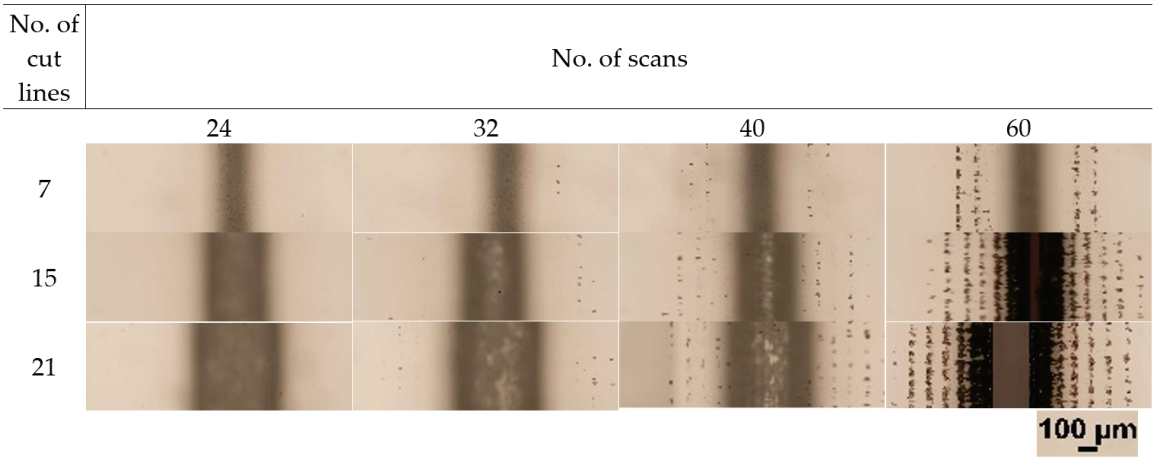

Figure 9. Optical micrographs showing back surface quality after the laser ablation. Rows represent the number of cut lines in a single scan, while columns represent the number of scans. The scale bar shown at the bottom right applies to all the panels in the figure.

The laser beam scanning geometry used (see Figure 1) with strictly fixed cut line positions led to the formation of the cumulative beam intensity on the cut sidewall, as shown in Figure 10. The damage at the back surface was associated with the laser beam refraction from the channel sidewall onto the back surface of the glass plate. Thus, the interband distance could be determined using the laser beam refraction angle, taper angle, and hatch distance:

$$H = \frac{h \cdot \cos(i)}{\sin(a)\sin(i+a)} \quad (1)$$

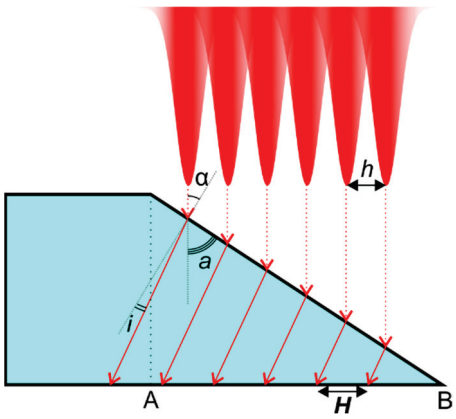

Figure 10. Schematic of the side view of the glass plate indicating a cumulative laser intensity profile falling on the channel (cut) sidewall, laser beam refraction, and impingement onto the back surface. Here, every scan consisted of multiple cut lines separated by the hatch distance *h*. Every cut line was scanned once per single scan.

Here, H is the distance between the bands, h is the hatch, i is the laser beam refraction angle, and a is the taper angle. Snell's law was used to determine the angle of the refraction based on the laser beam incident angle α and refraction indices of glass and ambient air (cutting environment). Furthermore, the formation of such a laser beam profile led to wavy cut sidewalls consisting of ridges and concavities, which were discussed in more detail in [35]. Therefore, the formation of concavities could act as additional focusing elements affecting the laser fluence of the refracted laser beam.

The measured and calculated interband distances for a different number of scan lines coincided well (Table 4). Measurements and calculations were applied for glass strips cut

under laser parameters presented in Table 1 in ambient air, and a high level of coincidence was also observed.

Table 4. The distance (period) between the individual band-like damages formed during glass cutting in ambient air.

Hatch (μm)	No. of Cut Lines	Period between Damage-like Bands	
		Calculated (μm)	Measured (μm)
25	7	89.9	86.4
25	15	79.3	82.8
25	21	88.4	87.7

Figure 6 indicates that the band-like damage in laser-cut glass strips formed in both cutting environments. Most significant damage occurred at the cut's edge and decreased with increasing distance from the cut. The damage intensity was highest in strips cut in ambient air at low laser power. However, cutting at high laser power contributed to a lesser number of bands and damage intensity at the back surface. The band-like damage was further mitigated in strips cut in water. Sun et al. [1] reported that the band-like damage at the back surface could be reduced by immersing the back surface of the glass workpiece in the water due to weakened interference at the glass surface (the surface which is in contact with the water layer). In our case, the water layer was formed only at the front surface of the glass plates, keeping the back surface dry. In addition, we observed decreased damage in strips cut in ambient air at high laser power. Therefore, decreased band-like damage intensity in water and ambient air at high laser power was mainly associated with the increased formation and shielding of plasma and laser beam scattering in water. We believe that higher sidewall roughness observed in thicker glasses (300–500 μm) contributed to the scattering of the laser beam (see Figure 8).

Figure 11a shows that the number of damage bands formed at the back surface increased with the glass thickness. The main contributor to the increase was the cut-sidewall protrusion length (the distance between A and B points in Figure 10). Sidewall protrusion length increased with glass thickness due to the taper angle, determining the number of cut lines projected on the cut sidewall. In ambient air, the number of bands was between two and eight in the 110–550 μm glass thickness range. Fewer bands were formed in water due to the steeper cut sidewalls (one to four bands, depending on the glass thickness).

Figure 11b shows the relationship between the interband distance and the glass thickness. Here, the steepness of the cut wall (taper angle), the hatch distance, and the laser beam refraction angle determined the interband distance. In our case, steeper sidewalls obtained in water contributed to greater interband distances than in ambient air.

Using liquids with other refraction indexes than water would affect the laser beam refraction angle from the cut sidewall. In the case of liquids with a refraction index similar to glass, the refraction angle should decrease, shifting damage bands closer to the cut edge. This would concentrate the back side damage into a smaller area, but the number of damage bands should remain the same. However, it is unclear how the concentrated damage at the edge of the cut could affect the flexural strength of laser-cut glass strips.

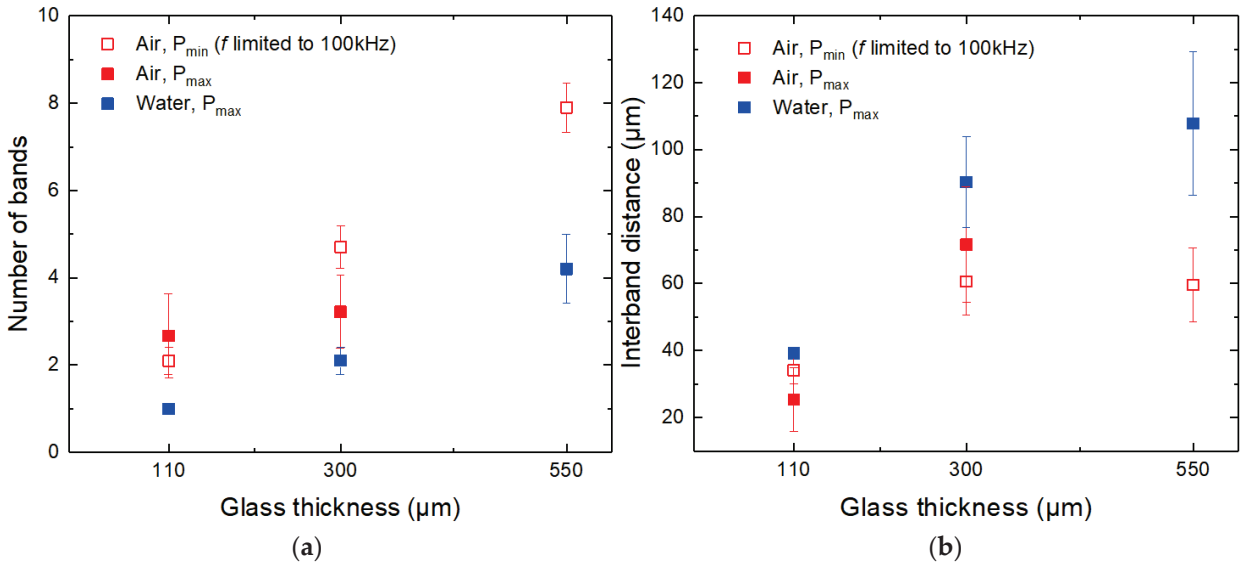

Figure 11. Number of damage bands (**a**) and distance between the bands (**b**) versus glass thickness in water and ambient air cutting environments. Error bars indicate the standard deviation.

3.4. Flexural Strength Measurements and Analysis

In this section, we investigated the characteristic strength of laser-cut glass strips (26×5 mm^2) cut in ambient air and water environments. Laser-cut glass strips were broken using the four-point bending setup described in Section 2 and [35]. The front and back side characteristic strengths were evaluated. Characteristic strength measurements for glass strips with dimensions of 26×5 mm^2 were conducted for t = 300 and 550 μm glass strips. The strength of the thinnest glass plates of t = 110 μm was evaluated by cutting and breaking wider 26×20 mm^2 strips. The width of the strips was increased to ensure sufficient sensitivity and reliability of the breaking force measurement system by increasing the force required to break the glass strips.

According to the measurements presented in Figure 12, the front side characteristic strength in both cutting environments was, on average, 33% higher than at the back side.

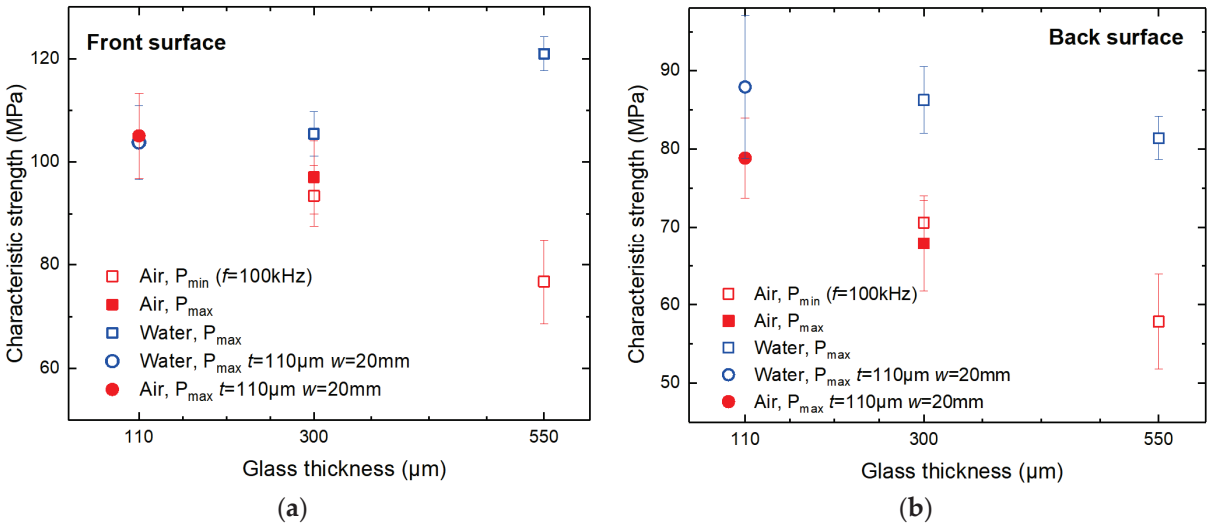

Figure 12. Characteristic strength of laser-cut glass strips. The bending force was applied from the front (**a**) and back (**b**) sides.

We observed that the front side strength dependence on the glass thickness was opposite in strips cut in ambient air and water. In the case of the thinnest glass strips

(t = 110 μm, w = 20 mm wide strips), the characteristic strength at the front side was almost equal between the two cutting environments: cutting in ambient air resulted in a higher front side strength by only 1.3% (103.8 ± 7 versus 105.1 ± 8 MPa). However, as the glass thickness increased, cutting in ambient air became inferior to cutting in water in terms of strip strength. The front side characteristic strength at t = 300 μm was higher in water by 8.6–12.8% than in ambient air (105.5 ± 4.3 MPa in water, 97.1 ± 7 MPa and 93.5 ± 6 MPa in ambient air at P_{max} and P_{min}, respectively). The difference increased further at t = 550 μm, reaching 58% (121 ± 3 versus 76.7 ± 8 MPa).

The strength of strips cut in the ambient air at two different power levels demonstrated similar results. Cutting 300 μm thick glass strips at P_{max} (19.3 W) and P_{min} (3.2 W) resulted in front side glass strip strengths of 97 ± 7.1 and 93.5 ± 6 MPa, respectively. Here, the difference in characteristic strengths was negligible—only 3.6 MPa—and was smaller than the calculated standard deviations of both values (similarly in Figure 12b).

The back side strength of strips cut in both environments decreased with increasing glass thickness (see Figure 12b). However, cutting in water produced strips with a higher characteristic strength. Also, glass strips cut in water lost strength less rapidly than strips cut in ambient air. As a result, the absolute characteristic strength difference at the back side between the two environments increased with glass thickness: at t = 110 μm, the difference was 9.3 MPa (87.9 ± 9.1 MPa versus 78.6 ± 5.1 MPa) and reached 23.5 MPa at t = 550 μm (81.4 ± 2.8 MPa versus 57.9 ± 4.7 MPa).

In Sections 3.2 and 3.3, we investigated cutting quality. The mean and maximum defect width and glass surface damage analysis revealed that in terms of cutting quality, glass cutting in water was superior for glass thicknesses of ≥300 μm. Mean defect widths at the front (Figure 5) and back sides (Figure 7) of laser-cut glass strips were smaller when cutting was performed in water. Also, the number of bands and the intensity of damage at the back surface were reduced (Figures 6 and 11a). Lastly, the maximum defect width at the back side was smaller by 16.4% at the same laser power level as in ambient air (P_{max}, see Table 3).

The improved overall cutting quality in water at t = 300 and 550 μm led to higher characteristic strength than cutting in ambient air. The most significant improvement was observed at 550 μm glass thickness, where the front and back side strengths were higher by 58 and 40%, respectively.

On the other hand, cut-sidewall roughness measurements contradicted the characteristic strength results (Figure 8). Cutting in water produced a sidewall roughness up to three times higher compared to cutting in ambient air at P_{min} at t = 550 μm. Despite that, the strength of strips cut in water was significantly higher than in ambient air. Furthermore, the R_a was distributed in a relatively wide range (from 0.36 ± 0.04 up to 1.72 ± 0.3 μm) at t = 300 μm when cutting was conducted in ambient air at P_{min} and P_{max}. Despite the difference in sidewall roughness, the characteristic strengths of strips cut in ambient air were almost identical at both power levels.

The cut-sidewall roughness is reported to be related to the strength of the glass strips, where an increase in sidewall roughness could lead to strength degradation [45,56]. However, we did not observe such a relationship between glass strength and cut-sidewall roughness in this study. Furthermore, this is supported by our previous studies in [35] (borosilicate glass cutting with 355 nm wavelength ps pulses) and [36] (soda–lime cutting with 1064 nm wavelength ps pulses). In all cases, the cut-wall roughness and characteristic strength were higher in strips cut in water. Thus, we speculate that the sidewall roughness has an insignificant influence on the strength of laser-cut glass strips, at least for low R_a values.

However, a similar cutting quality, characteristic strength, and effective cutting speed were achieved in both cutting environments at a glass thickness of 110 μm. The almost identical front side characteristic strength (the difference was 1.3% only) in water and ambient air was supported with similar w_{mean} and w_{max} defect widths at the front side and sidewall roughness in both cutting environments. However, contradictory results were

achieved on the back side. The characteristic strength at the back side was lower in strips cut in ambient air at P_{max} by 11.5% despite smaller w_{mean}, less intense band-like damage formation, and lower sidewall roughness. Only the higher w_{max} supported the lower back side strength of strips cut in ambient air.

The ability to introduce high average laser power into the material is crucial for achieving high cutting speeds, especially for direct material ablation and cutting via filament techniques. In this study, the water layer formed on top of the glass plate ensured sufficient glass cooling for all three investigated glass thicknesses, preventing the destruction of glass parts during cutting. For this reason, we only investigated glass cutting in water at the high laser power level. However, based on the previous study on the cutting of borosilicate glass in water with 355 nm wavelength picosecond pulses [35], an increase in incident laser power from 2.8 W to 15.5 W (P_{max}/P_{min} ratio was about 5.5) negatively affected the front cut-edge quality (mean defect width increased from 0.75 to 1.5 μm while maximum defect width increased from 10.5 to 20 μm) and increased cut-sidewall roughness by 20%. As a result, the front side strength of strips cut at 15.5 W decreased by 8.5% compared to cutting at 2.8 W. On the other hand, the overall cutting quality at the back side improved at 15.5 W, but only the front side strength was evaluated.

We believe that similar changes in cutting quality and characteristic strength could also occur for fs duration pulses when transitioning from several to several tens of Watts of incident laser power.

4. Conclusions

In this work, three different thicknesses of borosilicate glass plates (110, 300, and 550 μm) were cut with femtosecond duration pulses into 26 mm long glass strips in ambient air and water. The peak pulse power exceeded the critical power P_c = 2.9 MW in water by 30 to 40 times, enabling glass cutting via filament formation when a thin water layer was applied on top of the glass plates. Cutting in water and ambient air was investigated.

The maximum power (P_{max}) of the femtosecond laser was used for cutting glass in water (19.3–19.5 W). Only the two glass plates (110 and 300 μm) could be cut into smaller strips in ambient air, while the thickest glass plate (550 μm thickness) suffered from detrimental damage—glass shattering into smaller pieces. For this reason, we conducted glass cutting at high (P_{max}, 20.8–21 W for 110 and 300 μm thickness glasses) and low (P_{min}, 1.8–3.3 W for all three glass thicknesses) laser powers in ambient air.

The analysis of the band-like damage formation at the back surface of laser-cut strips showed that the refraction of the laser beam from the cut sidewall was responsible for the damage formation at the back surface. The distance between damage bands was evaluated based on the laser beam refraction, cut-sidewall taper angles, and hatch distance.

Experiments revealed that cutting in water was superior for 300 and 550 μm thickness glasses in terms of overall cut-edge quality (mean defect width), effective cutting speed, characteristic strength, and lesser band-like damage at the back surface. Furthermore, the advantage of cutting in water increased with the glass thickness. In the case of ultrathin glass (glass thickness 110 μm), the cutting performance, quality, and characteristic strength were similar in both cutting environments. Thus, cutting ultrathin glass in ambient air might be more attractive due to the simpler laser system setup.

Author Contributions: Conceptualization, E.M., L.Z., G.R. and P.G.; methodology, E.M., L.Z. and P.G.; investigation, E.M. and L.Z.; writing—original draft preparation, E.M. and L.Z.; funding acquisition, G.R. All authors have read and agreed to the published version of the manuscript.

Funding: The research leading to these results has received funding from the European Regional Development Fund (project No 01.2.2-CPVA-K-703-03-0013) under grant agreement with the Central Project Management Agency (CPVA).

Data Availability Statement: The data presented in this study are available on request from the corresponding author.

Conflicts of Interest: The authors declare no conflict of interest.

References

1. Sun, X.; Zheng, J.; Liang, C.; Hu, Y.; Zhong, H.; Duan, J.A. Improvement of rear damage of thin fused silica by liquid-assisted femtosecond laser cutting. *Appl. Phys. A* **2019**, *125*, 461. [CrossRef]
2. Qi, J.; Wang, Z.; Xu, J.; Lin, Z.; Li, X.; Chu, W.; Cheng, Y. Femtosecond laser induced selective etching in fused silica: Optimization of the inscription conditions with a high-repetition-rate laser source. *Opt. Express* **2018**, *26*, 29669–29678. [CrossRef] [PubMed]
3. Eaton, S.M.; Zhang, H.; Ng, M.L.; Li, J.; Chen, W.-J.; Ho, S.; Herman, P.R. Transition from thermal diffusion to heat accumulation in high repetition rate femtosecond laser writing of buried optical waveguides. *Opt. Express* **2008**, *16*, 9443–9458. [CrossRef] [PubMed]
4. Vanagas, E.; Kawai, J.; Tuzhilin, D.; Kudryashov, I.; Mizuyama, A.; Nakamura, K.G.; Kondo, K.I.; Koshihara, S.Y.; Takesada, M.; Matsuda, K.; et al. Glass cutting by femtosecond pulsed irradiation. *J. Micro. Nanolithogr. MEMS MOEMS* **2004**, *3*, 358–363. [CrossRef]
5. Lai, S.; Ehrhardt, M.; Lorenz, P.; Zajadacz, J.; Han, B.; Lotnyk, A.; Zimmer, K. Ultrashort pulse laser-induced submicron bubbles generation due to the near-surface material modification of soda-lime glass. *Opt. Laser Technol.* **2022**, *146*, 107573. [CrossRef]
6. Vázquez de Aldana, J.R.; Méndez, C.; Roso, L. Saturation of ablation channels micro-machined in fused silica with many femtosecond laser pulses. *Opt. Express* **2006**, *14*, 1329–1338. [CrossRef]
7. Shin, H.; Noh, J.; Kim, D. Bottom-up cutting method to maximize edge strength in femtosecond laser ablation cutting of ultra-thin glass. *Opt. Laser Technol.* **2021**, *138*, 106921. [CrossRef]
8. Wang, X.C.; Zheng, H.Y.; Chu, P.L.; Tan, J.L.; Teh, K.M.; Liu, T.; Ang, B.C.Y.; Tay, G.H. High quality femtosecond laser cutting of alumina substrates. *Opt. Lasers Eng.* **2010**, *48*, 657–663. [CrossRef]
9. Ozkan, A.; Migliore, L.; Dunsky, C.; Phaneuf, M. Glass Processing Using Microsecond, Nanosecond and Femtosecond Pulsed lasers. In *Fourth International Symposium on Laser Precision Microfabrication, Proceedings of the SPIE—The International Society for Optical Engineering, Munich, Germany, 21–24 June 2003*; SPIE: Washington, DC, USA, 2003; Volume 5063.
10. Shin, J. Investigation of the surface morphology in glass scribing with a UV picosecond laser. *Opt. Laser Technol.* **2019**, *111*, 307–314. [CrossRef]
11. Nolte, S.; Will, M.; Augustin, M.; Triebel, P.; Zoellner, K.; Tuennermann, A. Cutting of Optical Materials by Using Femtosecond Laser Pulses. In *Lithographic and Micromachining Techniques for Optical Component Fabrication, Proceedings of the International Symposium on Optical Science and Technology, San Diego, CA, USA, 29 July–3 August 2001*; SPIE: Washington, DC, USA, 2001; Volume 4440.
12. Shin, H.; Kim, D. Cutting thin glass by femtosecond laser ablation. *Opt. Laser Technol.* **2018**, *102*, 1–11. [CrossRef]
13. Gečys, P.; Dudutis, J.; Račiukaitis, G. Nanosecond Laser Processing of Soda-Lime Glass. *J. Laser Micro/Nanoeng.* **2015**, *10*, 254–258. [CrossRef]
14. Mishchik, K.; Beuton, R.; Dematteo Caulier, O.; Skupin, S.; Chimier, B.; Duchateau, G.; Chassagne, B.; Kling, R.; Hönninger, C.; Mottay, E.; et al. Improved laser glass cutting by spatio-temporal control of energy deposition using bursts of femtosecond pulses. *Opt. Express* **2017**, *25*, 33271–33282. [CrossRef]
15. Lopez, J.; Mishchik, K.; Chassagne, B.; Javaux-Leger, C.; Hönninger, C.; Mottay, E.; Kling, R. Glass Cutting Using Ultrashort Pulsed Bessel Beams. In *International Congress on Applications of Lasers & Electro-Optics*; Laser Institute of America: Orlando, FL, USA, 2015; Volume 2015, pp. 60–69. [CrossRef]
16. Xie, X.; Zhou, C.; Wei, X.; Hu, W.; Ren, Q. Laser machining of transparent brittle materials: From machining strategies to applications. *Opto-Electron. Adv.* **2019**, *2*, 180017. [CrossRef]
17. Wang, Z.K.; Seow, W.L.; Wang, X.C.; Zheng, H.Y. Effect of laser beam scanning mode on material removal efficiency in laser ablation for micromachining of glass. *J. Laser Appl.* **2015**, *27*, S28004. [CrossRef]
18. Tomkus, V.; Girdauskas, V.; Dudutis, J.; Gečys, P.; Stankevič, V.; Račiukaitis, G. High-density gas capillary nozzles manufactured by hybrid 3D laser machining technique from fused silica. *Opt. Express* **2018**, *26*, 27965–27977. [CrossRef] [PubMed]
19. Dudutis, J.; Pipiras, J.; Stonys, R.; Daknys, E.; Kilikevičius, A.; Kasparaitis, A.; Račiukaitis, G.; Gečys, P. In-depth comparison of conventional glass cutting technologies with laser-based methods by volumetric scribing using Bessel beam and rear-side machining. *Opt. Express* **2020**, *28*, 32133–32151. [CrossRef]
20. Markauskas, E.; Zubauskas, L.; Gečys, P. Efficient milling and cutting of borosilicate glasses through a thin flowing water film with a picosecond laser. *J. Manuf. Process.* **2021**, *68*, 898–909. [CrossRef]
21. Kumkar, M.; Bauer, L.; Russ, S.; Wendel, M.; Kleiner, J.; Grossmann, D.; Bergner, K.; Nolte, S. Comparison of Different Processes for Separation of Glass and Crystals Using Ultrashort Pulsed Lasers. In *Frontiers in Ultrafast Optics: Biomedical, Scientific, and Industrial Applications XIV, Proceedings of the SPIE LASE, San Francisco, CA, USA, 1–6 February 2014*; SPIE: Washington, DC, USA, 2014; Volume 8972.
22. Rihakova, L.; Chmelickova, H. Laser Micromachining of Glass, Silicon, and Ceramics. *Adv. Mater. Sci. Eng.* **2015**, *2015*, 584952. [CrossRef]
23. Wei, C.; Ito, Y.; Shinomoto, R.; Nagato, K.; Sugita, N. Simulation of ultrashort pulse laser drilling of glass considering heat accumulation. *Opt. Express* **2020**, *28*, 15240–15249. [CrossRef]
24. Butkus, S.; Paipulas, D.; Kaskelyte, D.; Gaizauskas, E.; Sirutkaitis, V. Improvement of Cut Quality in Rapid-Cutting of Glass Method via Femtosecond Laser Filamentation. *J. Laser Micro Nanoeng.* **2015**, *10*, 59–63. [CrossRef]

25. Park, S.; Kim, Y.; You, J.; Kim, S.-W. Damage-free cutting of chemically strengthened glass by creation of sub-surface cracks using femtosecond laser pulses. *CIRP Ann.* **2017**, *66*, 535–538. [CrossRef]
26. Homoelle, D.; Wielandy, S.; Gaeta, A.L.; Borrelli, N.F.; Smith, C. Infrared photosensitivity in silica glasses exposed to femtosecond laser pulses. *Opt. Lett.* **1999**, *24*, 1311–1313. [CrossRef]
27. Little, D.J.; Ams, M.; Gross, S.; Dekker, P.; Miese, C.T.; Fuerbach, A.; Withford, M.J. Structural changes in BK7 glass upon exposure to femtosecond laser pulses. *J. Raman Spectrosc.* **2011**, *42*, 715–718. [CrossRef]
28. Sun, M.; Eppelt, U.; Hartmann, C.; Schulz, W.; Zhu, J.; Lin, Z. Damage morphology and mechanism in ablation cutting of thin glass sheets with picosecond pulsed lasers. *Opt. Laser Technol.* **2016**, *80*, 227–236. [CrossRef]
29. Ahsan, M.S.; Rafi, R.S.; Sohn, I.; Choi, H.; Lee, M.S. Characterization of Femtosecond Laser Filamentation in Soda-Lime Glass. In Proceedings of the 2015 International Conference on Electrical Engineering and Information Communication Technology (ICEEICT), Dhaka, Bangladesh, 21–23 May 2015; pp. 1–6.
30. Garcia-Giron, A.; Sola, D.; Peña, J.I. Liquid-assisted laser ablation of advanced ceramics and glass-ceramic materials. *Appl. Surf. Sci.* **2016**, *363*, 548–554. [CrossRef]
31. Jiao, L.S.; Ng, E.Y.K.; Wee, L.M.; Zheng, H.Y. Role of volatile liquids in debris and hole taper angle reduction during femtosecond laser drilling of silicon. *Appl. Phys. A* **2011**, *104*, 1081–1084. [CrossRef]
32. Tangwarodomnukun, V.; Chen, H.-Y. Laser Ablation of PMMA in Air, Water, and Ethanol Environments. *Mater. Manuf. Process.* **2015**, *30*, 685–691. [CrossRef]
33. Kanitz, A.; Hoppius, J.S.; Fiebrandt, M.; Awakowicz, P.; Esen, C.; Ostendorf, A.; Gurevich, E.L. Impact of liquid environment on femtosecond laser ablation. *Appl. Phys. A* **2017**, *123*, 674. [CrossRef]
34. Liu, H.; Chen, F.; Wang, X.; Yang, Q.; Bian, H.; Si, J.; Hou, X. Influence of liquid environments on femtosecond laser ablation of silicon. *Thin Solid Films* **2010**, *518*, 5188–5194. [CrossRef]
35. Markauskas, E.; Zubauskas, L.; Voisiat, B.; Gečys, P. Efficient Water-Assisted Glass Cutting with 355 nm Picosecond Laser Pulses. *Micromachines* **2022**, *13*, 785. [CrossRef]
36. Dudutis, J.; Zubauskas, L.; Daknys, E.; Markauskas, E.; Gvozdaitė, R.; Račiukaitis, G.; Gečys, P. Quality and flexural strength of laser-cut glass: Classical top-down ablation versus water-assisted and bottom-up machining. *Opt. Express* **2022**, *30*, 4564–4582. [CrossRef] [PubMed]
37. Smirnov, N.A.; Kudryashov, S.I.; Danilov, P.A.; Nastulyavichus, A.A.; Rudenko, A.A.; Ionin, A.A.; Kuchmizhak, A.A.; Vitrik, O.B. Femtosecond laser ablation of a thin silver film in air and water. *Opt. Quantum Electron.* **2020**, *52*, 71. [CrossRef]
38. Zheng, C.; Shen, H. Understanding nonlinear optical phenomenon for underwater material ablation by ultrafast laser with high pulse energy. *J. Manuf. Process.* **2021**, *70*, 331–340. [CrossRef]
39. An, R.; Li, Y.; Dou, Y.; Yang, H.; Gong, Q. Simultaneous multi-microhole drilling of soda-lime glass by water-assisted ablation with femtosecond laser pulses. *Opt. Express* **2005**, *13*, 1855–1859. [CrossRef]
40. Butkus, S.; Alesenkov, A.; Paipulas, D.; Gaižauskas, E.; Melninkaitis, A.; Kaškelytė, D.; Barkauskas, M.; Sirutkaitis, V. Analysis of the Micromachining Process of Dielectric and Metallic Substrates Immersed in Water with Femtosecond Pulses. *Micromachines* **2015**, *6*, 2010–2022. [CrossRef]
41. Butkus, S.; Paipulas, D.; Sirutkaitis, R.; Gaižauskas, E.; Sirutkaitis, V. Rapid Cutting and Drilling of Transparent Materials via Femtosecond Laser Filamentation. *J. Laser Micro/Nanoeng.* **2014**, *9*, 213–220. [CrossRef]
42. Butkus, S.; Alesenkov, A.; Paipulas, D.; Baipulas, T.; Kaskelyte, D.; Barkauskas, M.; Sirutkaitis, V. Micromachining of Transparent, Semiconducting and Metallic Substrates Using Femtosecond Laser Beams. *J. Laser Micro/Nanoeng.* **2016**, *11*, 81–86. [CrossRef]
43. Nikumb, S.; Chen, Q.; Li, C.; Reshef, H.; Zheng, H.Y.; Qiu, H.; Low, D. Precision glass machining, drilling and profile cutting by short pulse lasers. *Thin Solid Films* **2005**, *477*, 216–221. [CrossRef]
44. Plat, K.; Witzendorff, P.V.; Suttmann, O.; Overmeyer, L. Process strategy for drilling of chemically strengthened glass with picosecond laser radiation. *J. Laser Appl.* **2016**, *28*, 022201. [CrossRef]
45. Shin, H.; Kim, D. Strength of ultra-thin glass cut by internal scribing using a femtosecond Bessel beam. *Opt. Laser Technol.* **2020**, *129*, 106307. [CrossRef]
46. Liu, J.M. Simple technique for measurements of pulsed Gaussian-beam spot sizes. *Opt. Lett.* **1982**, *7*, 196–198. [CrossRef] [PubMed]
47. Markauskas, E.; Gečys, P. Thin water film assisted glass ablation with a picosecond laser. *Procedia CIRP* **2018**, *74*, 328–332. [CrossRef]
48. Butkus, S.; Gaižauskas, E.; Mačernytė, L.; Jukna, V.; Paipulas, D.; Sirutkaitis, V. Femtosecond Beam Transformation Effects in Water, Enabling Increased Throughput Micromachining in Transparent Materials. *Appl. Sci.* **2019**, *9*, 2405. [CrossRef]
49. Charee, W.; Tangwarodomnukun, V.; Dumkum, C. Laser ablation of silicon in water under different flow rates. *Int. J. Adv. Manuf. Technol.* **2015**, *78*, 19–29. [CrossRef]
50. Zhou, J.; Huang, Y.-X.; Zhao, Y.-W.; Jiao, H.; Liu, Q.-y.; Long, Y.-H. Study on water-assisted laser ablation mechanism based on water layer characteristics. *Opt. Commun.* **2019**, *450*, 112–121. [CrossRef]
51. Tangwarodomnukun, V.; Wang, J.; Mathew, P. A Comparison of Dry and Underwater Laser Micromachining of Silicon Substrates. *Key Eng. Mater.* **2010**, *443*, 693–698. [CrossRef]
52. Kruusing, A. Underwater and water-assisted laser processing: Part 1—General features, steam cleaning and shock processing. *Opt. Lasers Eng.* **2004**, *41*, 307–327. [CrossRef]

53. Lu, J.; Xu, R.Q.; Chen, X.; Shen, Z.H.; Ni, X.W.; Zhang, S.Y.; Gao, C.M. Mechanisms of laser drilling of metal plates underwater. *J. Appl. Phys.* **2004**, *95*, 3890–3894. [CrossRef]
54. Indrišiūnas, S.; Svirplys, E.; Jorudas, J.; Kašalynas, I. Laser Processing of Transparent Wafers with a AlGaN/GaN Heterostructures and High-Electron Mobility Devices on a Backside. *Micromachines* **2021**, *12*, 407. [CrossRef]
55. Collins, A.; Rostohar, D.; Prieto, C.; Chan, Y.K.; O'Connor, G.M. Laser scribing of thin dielectrics with polarised ultrashort pulses. *Opt. Lasers Eng.* **2014**, *60*, 18–24. [CrossRef]
56. Flury, S.; Peutzfeldt, A.; Lussi, A. Influence of Surface Roughness on Mechanical Properties of Two Computer-aided Design/Computer-aided Manufacturing (CAD/CAM) Ceramic Materials. *Oper. Dent.* **2012**, *37*, 617–624. [CrossRef] [PubMed]

micromachines

MDPI

Article

Investigation of Material Removal Distributions and Surface Morphology Evolution in Non-Contact Ultrasonic Abrasive Machining (NUAM) of BK7 Optical Glasses

Zongfu Guo [1,*], Xichun Luo [2], Xiaoping Hu [1] and Tan Jin [3]

[1] School of Mechanical Engineering, Hangzhou Dianzi University, Hangzhou 310018, China
[2] Centre for Precision Manufacturing, DMEM, University of Strathclyde, Glasgow G1 1XJ, UK
[3] College of Mechanical and Vehicle Engineering, Hunan University, Changsha 410082, China
* Correspondence: guozongfu816@163.com; Tel.: +86-138-1914-9270

Abstract: A non-contact ultrasonic abrasive machining approach provides a potential solution to overcome the challenges of machining efficiency in the high-precision polishing of optical components. Accurately modeling the material removal distribution (removal function (RF)) and surface morphology is very important in establishing this new computer-controlled deterministic polishing technique. However, it is a challenging task due to the absence of an in-depth understanding of the evolution mechanism of the material removal distribution and the knowledge of the evolution law of the microscopic surface morphology under the complex action of ultrasonic polishing while submerged in liquid. In this study, the formation of the RF and the surface morphology were modeled by investigating the cavitation density distribution and conducting experiments. The research results showed that the material removal caused by cavitation bubble explosions was uniformly distributed across the entire working surface and had a 0.25 mm edge influence range. The flow scour removal was mainly concentrated in the high-velocity flow zone around the machining area. The roughness of the machined surface increased linearly with an increase in the amplitude and gap. Increasing the particle concentration significantly improved the material removal rate, and the generated surface exhibited better removal uniformity and lower surface roughness.

Keywords: non-contact ultrasonic abrasive machining (NUAM); optical polishing; material removal distributions; surface morphology

Citation: Guo, Z.; Luo, X.; Hu, X.; Jin, T. Investigation of Material Removal Distributions and Surface Morphology Evolution in Non-Contact Ultrasonic Abrasive Machining (NUAM) of BK7 Optical Glasses. *Micromachines* **2022**, *13*, 2188. https://doi.org/10.3390/mi13122188

Academic Editors: Chunjin Wang and Chengwei Kang

Received: 9 November 2022
Accepted: 7 December 2022
Published: 10 December 2022

1. Introduction

Brittle materials, such as Si, SiC, and BK7 optical glass, have been widely used for high-end optical applications for precision detection and navigation. CNC grinding and polishing are usually used to machine them into the desired shape. Although the form accuracy of the ground surfaces can reach the scale of 1 μm/100 mm, the subsurface damage is in the scale of tens of microns to hundreds of microns, which often results in a long polishing time to remove the damaged layer [1,2]. A highly efficient polishing process is therefore required to reduce the machining time for these precision optics. For flat and spherical optics, ring polishers and swing-arm machines are often used to achieve fast polishing [3–5]. For aspheric optics, a small-tool polishing technique [6] is used to correct the sub-aperture surface error and remove the subsurface damage of the grinding surfaces. Bonnet polishing [7,8], magnetorheological finishing (MRF) [9,10], ion beam figuring (IBF) [11,12], and fluid jet polishing (FJP) [13,14] fall into this category, where a sub-nanometer surface finish, a nanometer to tens of nanometers surface form accuracy, and a nanometer-level or zero subsurface damage can be obtained. However, machining efficiency remains a significant challenge in these ultra-precision polishing technologies.

To improve the polishing efficiency, many researchers combine ultrasonic processing technology with the existing polishing technology by applying ultrasonic vibrations to

the polishing tool, workpiece, or polishing fluid. For example, Zhang studied a rotary polishing tool head applied vertically to the surface of BK7 optical glass with the aid of axial ultrasonic vibration (UVAP). The experimental results show that this method can improve both the material removal rate (MRR) and surface quality [15,16]. Suzuki developed a two-axis ultrasonic vibration polishing tool to obtain more complex polishing trajectories. Experiments showed that applying ultrasonic vibration to a polishing tool allows for obtaining a surface roughness Rz of 8 nm [17]. In abrasive waterjet machining, Lv adhered a workpiece to an ultrasonic horn and the workpiece was ultrasonically vibrated by the horn. The experimental results show that the introduction of ultrasound can improve the material removal efficiency by 82% [18,19]. Beaucamp studied the method of applying ultrasonic motion inside a jet nozzle to improve the removal rate of fluid jet polishing and the material removal rate was increased by 380%. The research results of ultrasonic-assisted jet polishing show that the jet fluctuation caused by ultrasonic vibration is the main factor that improves the MRR. As the ultrasonic cavitation zone is far away from the workpiece surface, the cavitation bubbles disappear before reaching the workpiece surface, and thus, the microjets caused by the explosion of the cavitation bubbles did not affect the material removal [20,21].

In addition, Ichida et al. proposed a new non-contact ultrasonic abrasive machining (NUAM) method to machine aluminum alloy (JIS-2014). A schematic of NUAM is shown in Figure 1, where an ultrasonic horn is attached to the ultrasonic transducer and used as a processing tool. There is a gap between the working surface of the ultrasonic horn and the surface of the workpiece that is filled with polishing liquid. The ultrasonic vibration acts on the surface of the workpiece through the polishing liquid to achieve material removal. Three types of material removal modes were found in Ichida's study. They are direct impact removal of microjets produced by cavitation bubble explosion, impact removal by microjet driven abrasive grains, and scratch removal from abrasive grains driven by fluid drag [22]. However, there is no relevant research on the material removal distribution and the evolution of the surface micromorphology of brittle materials, such as optical glass, under this new processing method.

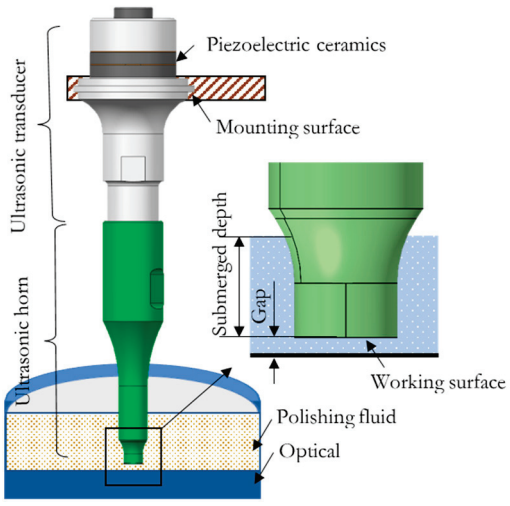

Figure 1. A schematic of non-contact ultrasonic abrasive machining (NUAM).

Among the aforementioned ultrasonic-assisted polishing methods, NUAM technology requires the most simplified device and has the least restrictions on the processing object. It can also avoid problems such as abrasive particle agglomeration and tool wear better than other discrete abrasive polishing methods. This study aimed to investigate the feasibility of further developing NUAM technology into a new high-efficiency polishing method for optical materials. Two key challenges to achieving ultra-precision polishing by NUAM are efficient deterministic material removal and smooth machined surfaces. Therefore,

this study carried out an experimental study on material removal modes, the relationship between the proportion of different removal modes and the MRR and surface quality, and the relationship between the material removal distribution and surface quality and the associated process parameters in the NUAM of BK7, which is a typical brittle material used in the optics industry.

This paper is arranged as follows: Section 2 gives a theoretical analysis of material removal distribution, Section 3 describes the conducted experiments and analysis results, and Section 4 presents the material removal distribution and microscopic surface formation modeling results.

2. Analysis of Material Removal Distribution under NUAM

In a polishing process, the polishing liquid is mainly a suspension that is formed by mixing hard abrasive particles and deionized water. Under the action of ultrasonic vibration, the air dissolved in the liquid water will separate to form bubbles, which become cavitation bubbles. Cavitation bubbles grow, shrink, collapse, or redissolve as the pressure fluctuates [23,24]. Exploding cavitation bubbles will create high-velocity microjets that enable material removal. This section analyzes the material removal distribution caused by cavitation and polishing fluid scouring via theoretical analysis and computer simulation.

2.1. Theory of Cavitation

The material removal rate and material removal distribution caused by cavitation are closely related to the distribution density, collapse strength, and collapse position of ultrasonic cavitation bubbles. Schnerr and Sauer presented a cavitation model to predict the cavitation distribution based on a combination of the VOF (volume of fluid) technique with a model predicting the growth and collapse process of bubbles. The void fraction (α), defined as the volume of vapor divided by the cell volume, can be expressed as Equation (1) [25]:

$$\alpha = \frac{n_0 \cdot \frac{4}{3}\pi R^3}{1 + n_0 \cdot \frac{4}{3}\pi R^3} \tag{1}$$

where n_0 is the number of bubbles in a unit volume of fluid and R is the average cavitation bubble radius. The bubble radius changes with the fluid pressure and can be expressed by the Rayleigh relation, as shown in Equation (2) [25]:

$$R = \sqrt{\frac{2}{3}\frac{p(R) - p\infty}{\rho_l}} \tag{2}$$

where $p(R)$ is the pressure in the liquid at the bubble boundary, $p\infty$ is the pressure in the liquid at a large distance from the bubble, and ρ_l is the fluid density. Cavitation will occur when the liquid additional negative pressure reaches the cavitation threshold. According to the condition of the pressure balance between the inside and outside of the cavitation bubble, Equation (3) [26] was proposed by Neppiras for solving the cavitation threshold:

$$P_B = P_0 - P_V + \frac{2}{3}\left[\frac{\left(\frac{2\sigma}{R_0}\right)^3}{3\left(P_0 - P_V + \frac{2\sigma}{R_0}\right)}\right]^{\frac{1}{2}} \tag{3}$$

where P_0 and P_V are the hydrostatic pressure and saturated vapor pressure in the bubble, respectively; σ is the liquid surface tension coefficient; and R_0 is the initial radius of a cavitation bubble. In the research, a high-speed camera is usually used to observe cavitation bubbles [20,27,28]. The diameter of cavitation bubbles observed in the experiment is generally at the scale of several microns to tens of microns. When ultrasonic vibration acts directly on the water, the cavitation bubble diameter is 10 μm, the saturated vapor

pressure is P_V = 2.34 × 10^3 Pa, and σ = 0.0728 N/m at 20 °C, the cavitation threshold P_B is 9.968 × 10^4 Pa.

According to Luther's work, the average lifetime of cavitation bubbles is equal to 200 acoustic pressure cycles [28]. When the ultrasonic vibration frequency is 26 kHz, the observation results of Beaucamp's work were also very close to this conclusion [20]. The ultrasonic vibration frequency used in this study was 28 kHz, and thus, the lifetime of the cavitation bubbles was considered to be 7 ms. For the polishing fluid suspension, the contained microparticles will increase the cavitation erosion by increasing the number of cavities in the suspension [29,30].

Plesset and Chapman calculated that the microjet velocity is about 130 m/s when a bubble collapses while attached to a wall and about 170 m/s when a bubble collapses near the wall [31]. The pit depth is determined by both the microjet velocity and microjet diameter and increases with their increase. The pit diameter (d_p) is mainly related to the microjet diameter (dj), where $d_p/d_j \approx$ 0.95–1.2, while the pit's diameter-to-depth ratio is mainly negatively correlated with the microjet velocity [32].

2.2. Simulation of Cavitation

Using the computer fluid simulation analysis software Fluent combined with the dynamic mesh technology to simulate the drive of the ultrasonic tool head to the polishing liquid, the pressure and velocity distributions exerted by the ultrasonic vibration on the surface of the workpiece through the polishing liquid were analyzed, along with the distribution of the generated cavitation clouds. Deionized water and hard abrasive particles, such as cerium oxide and alumina, are usually used in polishing, and the suspension formed by mixing is used as a polishing liquid. The mass concentration of abrasive particles is generally 5–40 g/L. At this concentration, the flow characteristics of the suspension and water are very similar, and thus, water is used as the fluid analysis object. Figure 2a shows the finite element model.

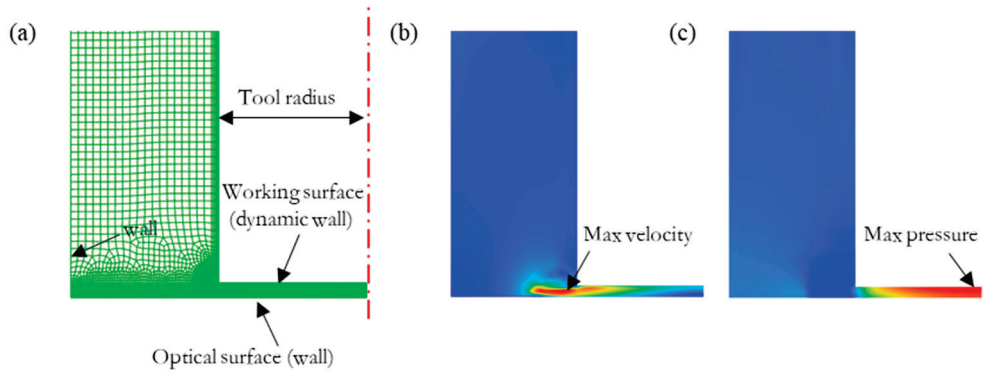

Figure 2. (**a**) FEA mesh model and the (**b**) velocity and (**c**) pressure distributions (gap = 0.25 mm, amplitude = 30 μm).

Without affecting the purpose of the study, the following simplified conditions were used: the effect of particles on the cavitation was ignored, the temperature was kept constant, water was used as the polishing liquid, and a 2D axisymmetric model was used. The detailed simulation parameter settings are shown in Table 1.

The simulation results showed that the liquid velocity caused by ultrasonic vibration reached the maximum at the edge of the gap, as shown in Figure 2b. The pressure in the gap changed periodically with the ultrasonic vibration and was roughly distributed in a Gaussian shape. The maximum velocity at the edge of the gap and the maximum pressure inside the gap decreased exponentially with the increase in the gap and showed a rapidly decreasing trend with the decrease in the amplitude, as shown in Figure 3.

Table 1. Simulation parameters.

Amplitude (μm)	10, 30, 50	**Gap (mm)**	0.1, 0.15, 0.25
Frequency	28 kHz	**Fluid**	Water
Tool radius	4 mm	**Temperature**	20 °C
Homogeneous models	2 Eulerian phases	**Viscous model** [33]	k-omega (SST)
Cavitation model	Schnerr–Sauer	**Vaporization pressure**	3540 Pa
Element size	Minimum 0.01 mm Maximum 0.2 mm		

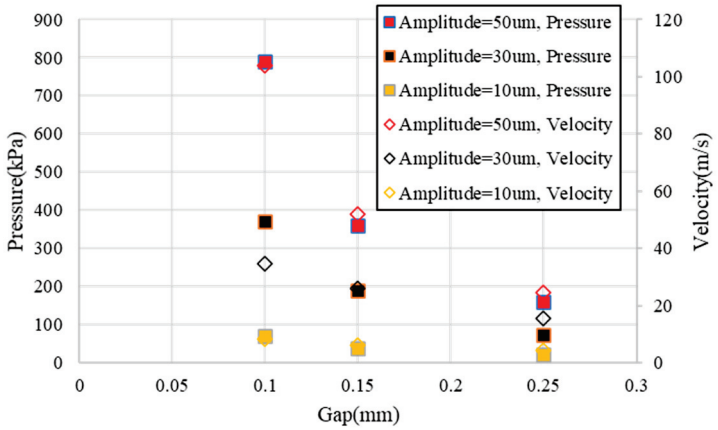

Figure 3. Variation of the maximum speed and pressure with respect to the amplitude and gap.

The variation in cavitation clouds generated by ultrasonic vibration with time was represented by the variation in vapor fraction shown in Figure 4. It can be seen from this figure that under the high-frequency impact of the polishing liquid, the cavitation zone first appeared near the working surface of the horn, the cavitation bubbles overflowed at the edge of the gap in the radial direction, and the overflowing cavitation bubbles moved away from the workpiece surface. When moving away from the surface of the workpiece, the overflowing cavitation bubbles dissolved or disappeared after some time and eventually reached equilibrium.

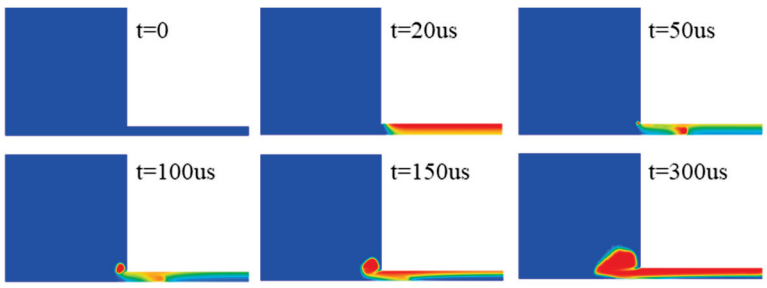

Figure 4. Variation in the vapor fraction over time (gap = 0.25 mm, amplitude = 30 μm).

Figure 5 shows the variation trend of cavitation intensity and cavitation distribution with respect to the gap and amplitude. It can be seen from this figure that increasing the amplitude significantly improved the cavitation rate, while increasing the gap had little effect on the cavitation rate. When the gap was large, if the cavitation rate was not enough, the cavitation cloud gathered near the working face and could not fully exert the erosion processing on the workpiece.

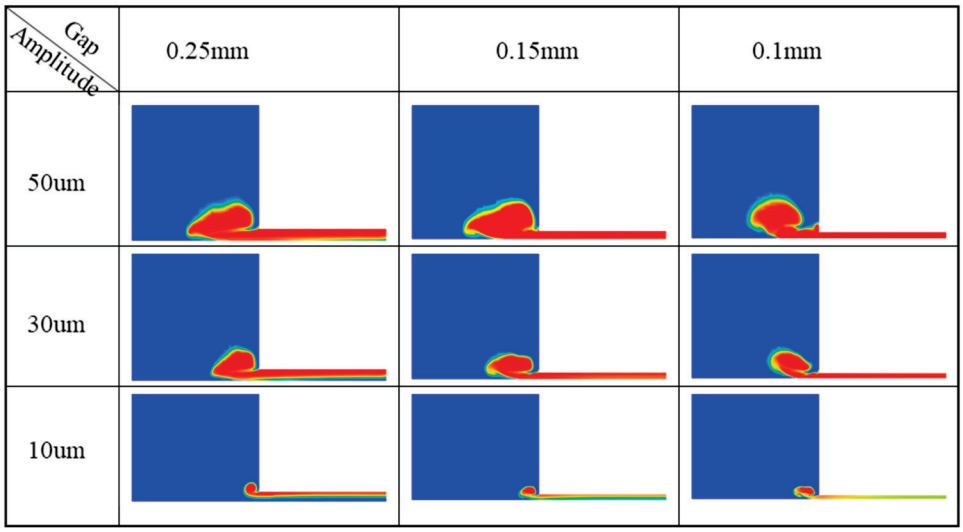

Figure 5. Variation in the vapor fraction with respect to the amplitude and gap (time = 300 μs).

2.3. Removal Theory Using Fluid Scouring

In NUAM, the polishing fluid is driven by an ultrasonic vibration tool to perform high-frequency scouring on the surface of the workpiece. This fluid scouring removal method is very similar to the fluid jet polishing method. Based on the erosion model for FJP and ultrasonic FJP [34], the removal volume (V) of a single abrasive driven by ultrasonic vibration can be described using Equation (4) [21]:

$$V = k\frac{1}{4}m_p v_{vib,r}^2 \left(\frac{1}{4}m_p v_{vib,z}^2\right)^{\frac{2(1-b)}{3}} \tag{4}$$

where $v_{vib,r}$ and $v_{vib,z}$ respectively represent the average values of the vibration velocity along the radius and perpendicular to the surface of the workpiece per unit time, m_p is the abrasive particle mass, k is a material-dependent coefficient that accounts for plastic flow pressure and material springback, and b ($0.5 \leq b \leq 1$) is a material-dependent exponent related to the cross-sectional area of the abrasive indentation.

2.4. Prediction of the Material Removal Distribution

From the distribution of cavitation clouds in the gap, it can be predicted that the material removal caused by cavitation blasting is uniformly distributed in the gap. Due to the cavitation overflow at the edge of the gap, this processing method will have obvious edge effects.

In the fluid jet polishing process, the maximum impact velocity of the polishing liquid on the workpiece surface is usually about 44 m/s (jet pressure = 1 MPa), and the removal depth is at the scale of 1 nm/s [13] and increases exponentially with the increase in the jet pressure [35]. According to the maximum speed and pressure shown in Figure 3, when the amplitude was less than 30 μm and the gap was greater than 0.15 mm, the material removal rate caused by scouring was very low. Through the above Equation (4), it is found that the erosion removal ability of a single abrasive particle mainly depends on its tangential velocity on the workpiece surface. If the abrasive particles are evenly distributed in the polishing solution, it can be inferred that the material erosion removal distribution is consistent with the change curve of the tangential velocity. The maximum velocity according to Figure 2b is located at the edge of the gap, and thus, the distribution of material removal caused by scouring is also concentrated at the edge.

Based on the above analysis, the tool's removal function (RF) of this method can be described as follows:

$$RF = S_{surface} + S_{edge} + S_{scour} \tag{5}$$

where $S_{surface}$ is the shape of the tool's working surface, S_{edge} is the edge removal distribution, and S_{scour} is the removal distribution due to fluid scouring.

3. Experimental Research and Results Analysis

3.1. Experimental Preparation

Figure 6 shows the experimental setup. The ultrasonic frequency was 28 kHz. The ultrasonic horn worked as a tool and three kinds of tool shapes were used (a plane with a diameter of 8 mm, a plane with microgrooves, and a plane with a protruding five-pointed star). The amplitude of the working face of the horn could be adjusted by adjusting the output power. The workpiece was a flat mirror with a diameter of 50 mm and the material was BK7. The surface roughness (*Sa*) of the workpiece before processing was 0.5 nm. The workpiece was submerged in the polishing fluid to a depth of 20 mm. The fluid was filled with CeO_2 abrasive particles, where the average diameter of the particles was 1 micron. The detailed experimental conditions setting are shown in Table 2.

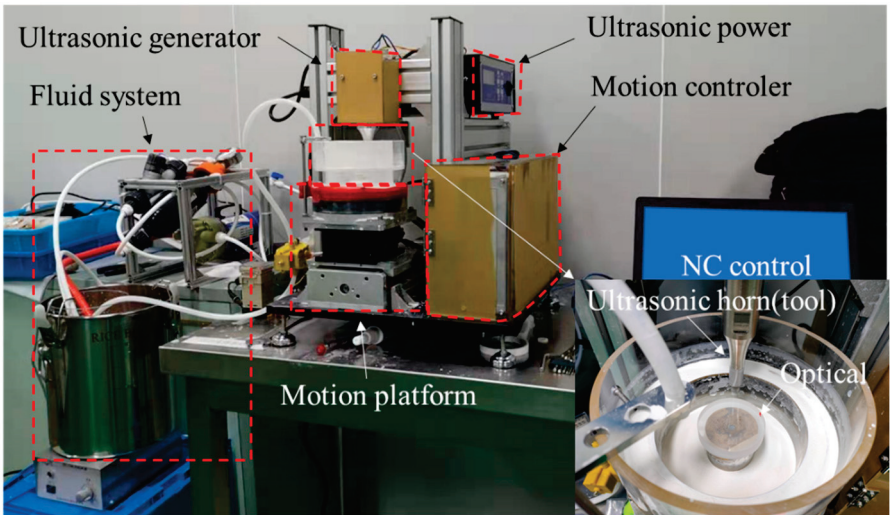

Figure 6. Experimental setup.

Table 2. Experimental conditions.

Resonance frequency (kHz)	28
Amplitude (μm)	20, 30, 40, 50 (peak to peak)
Abrasive	CeO_2 (1 μm in mean diameter)
Machining fluid	Water
	Water mixed with abrasive grains (10 g/L)
	Water mixed with abrasive grains (20 g/L)
	Water mixed with abrasive grains (40 g/L)
Machining time (s)	150, 300, 450, 600
Gap (mm)	0.1, 0.15, 0.2, 0.25
Fluid temperature (°C)	25
Workpiece	BK7 flat optical glass
	Surface roughness (Sa): 0.5 nm
	Hardness (HK100): 610 kg/mm^2
	Dimensions: φ 50 × 10 mm

Table 2. *Cont.*

Submerged depth (mm)	20
Working surface on the horn	Plane (diameter: 8 mm)
	Rectangle groove (diameter: 10 mm)
	Five-pointed star (diameter: 10 mm)
Testing equipment	Zygo GPI for material removal distribution
	Zygo Newview9000 for surface morphology

3.2. Material Removal Distribution

3.2.1. Under the Action of the Plane Tool

The horn with the flat working surface was used to carry out a fixed-point processing experiment with different process parameters. Figure 7 shows the removal pit shapes, which were measured using a laser interferometer (Zygo GPI).

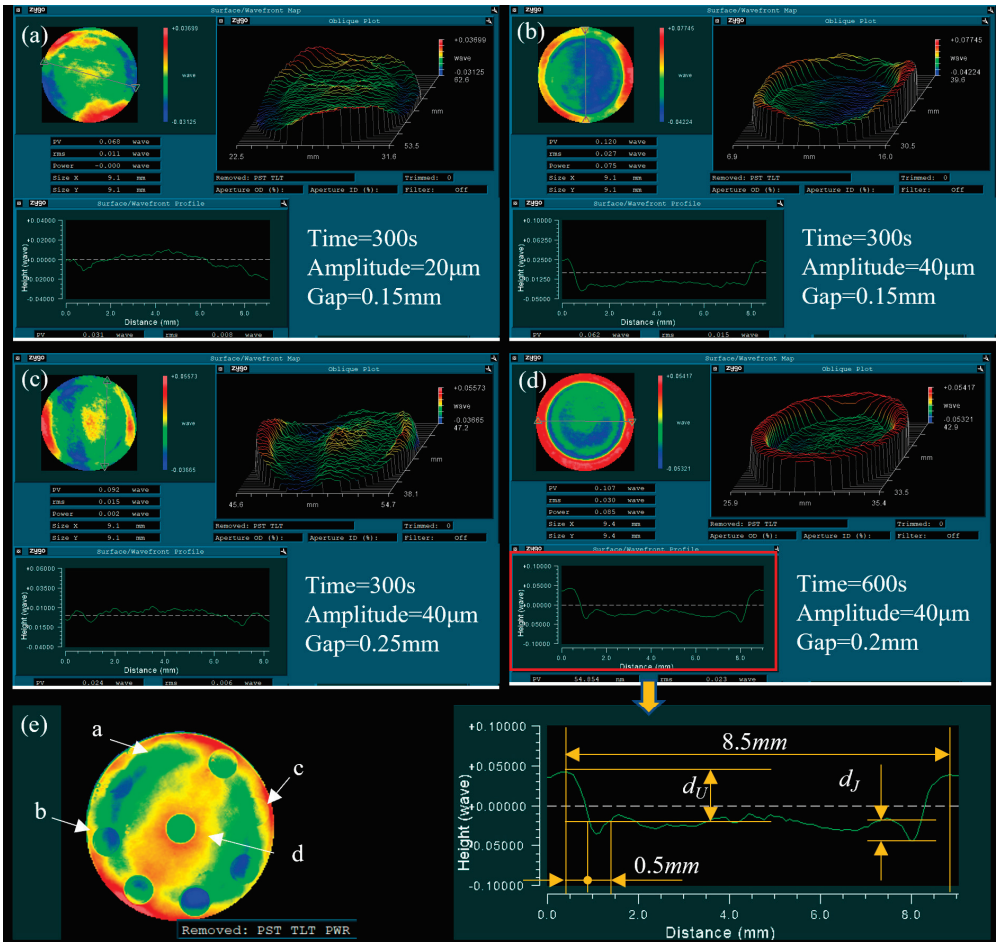

Figure 7. Removal pit profiles after using the ultrasonic tool: (**a**) removal pit under the processing parameters of time = 300 s, amplitude = 20 μm, and gap = 0.15 mm; (**b**) removal pit under the processing parameters of time = 300 s, amplitude = 40 μm, and gap = 0.15 mm; (**c**) removal pit under the processing parameters of time = 300 s, amplitude = 40 μm, and gap = 0.25 mm; (**d**) removal pit under the processing parameters of time = 60 s, amplitude = 4 μm, and gap = 0.2 mm; and (**e**) the lens's overall surface shape error distribution after the experimental processing.

The measurement results clearly showed that the distribution of the removed material was like a tool head shape (round). Figure 7e shows the lens's overall surface shape error distribution after processing. By analyzing the shape changes in the bottom surface of the

removal pits and the pit's position on the lens, it was found that the initial surface shape of the lens was retained. This showed that the changing trend in the overall surface shape at the pits was consistent with the changing trend at the bottom of the pits, which meant that the material removal in the tool processing surface was uniformly distributed. There was a groove on the edge of the removal pit, which can be seen clearly in Figure 7b,d, and the groove depth (d_J) increased with the increase in removal depth (d_U), as seen by comparing the cross-sectional profile. The ratio of d_J and d_U changed under different process parameters. For example, the ratio of d_J and d_U in Figure 7b was clearly larger than in Figure 7d. The width of the groove was about 0.5 mm. The center of the removal area was slightly raised, which can be seen clearly in Figure 7c. The diameters of removal pits under different process parameters were basically the same at about 8.5 mm, which was 0.5 mm larger than the tool diameter.

Based on the simulation results of the speed and pressure distribution in the gap (Figure 2), the fluid speed increased sharply in the machine edge and the max value decreased as the gap increased; therefore, we can conclude that the groove was generated by the fluid scouring. The material removal in the processing area was basically evenly distributed, and it can be concluded that the polishing liquid scouring removal in the processing area played a secondary role and the cavitation jet scouring removal played a major role. Therefore, the ratio of the pit removal depth d_J to the average removal depth d_U reflects the ratio of jet erosion removal to ultrasonic cavitation microjet removal in the vicinity. The edge effect was around 0.25 mm, which indicated that the overflowing cavitation cloud did not produce significant material removal. This may have been because the pressure fluctuation outside the action zone was small, most of the cavitation bubbles redissolved and disappeared, or the distance away from the workpiece surface under the action of the drag force exceeded the action range of the blasting jet.

3.2.2. Under the Action of the Tool with a Complex Structure

Figure 8 shows the material removal distribution formed by different geometric structures on the working surface of ultrasonic vibration tools. It can be seen from Figure 8a that interference formed when the spacing of the geometric structures was less than 0.5 mm. It did not matter whether the structure was inside or at the edge of the ultrasonic vibrating surface. This further indicated that the material removal caused by fluid scouring was small. It can be seen from Figure 8b that the corresponding removal distribution at the apex of the five-pointed star became an excessive arc, where the radius of the arc was about 0.25 mm. It can be known from the above experimental results that this processing method produced an edge effect of 0.25 mm. Therefore, if the geometric structure of the tool's working surface is larger than 0.5 mm, the structure can be copied to the workpiece surface using this method.

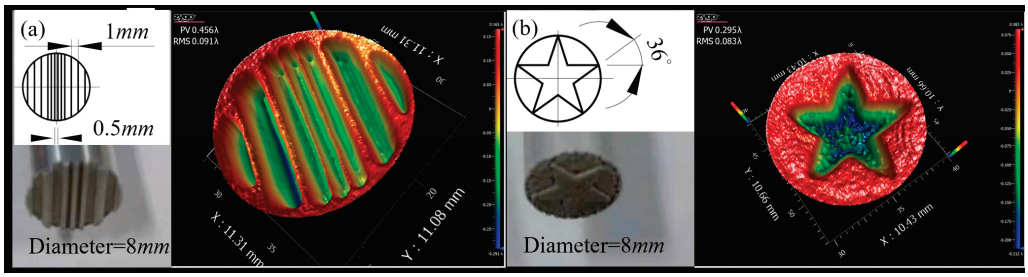

Figure 8. Material removal distribution formed using different geometric structures on the surface of ultrasonic vibration tools: (**a**) rectangle groove and (**b**) five-pointed star (time = 300 s, amplitude = 40 μm, gap = 0.1 mm).

3.2.3. Interaction Analysis of the Removal Pits

Figure 9 shows the material removal distribution under different coverage ratios formed by adjusting the center distance during two machining operations using an ultra-

sonic vibration tool with a diameter of 8 mm. It can be seen from the figure that there was almost no mutual interference between the two processing operations; therefore, peaks or valleys of different scales can be obtained by adjusting the center distance during the two processing operations, and this feature also satisfies the deterministic polishing process. This means that in the future, the processing of special-shaped complex parts can be realized, such as commonly used etalons and array structures, by combining path planning, tool head geometry design, and deterministic polishing control technology.

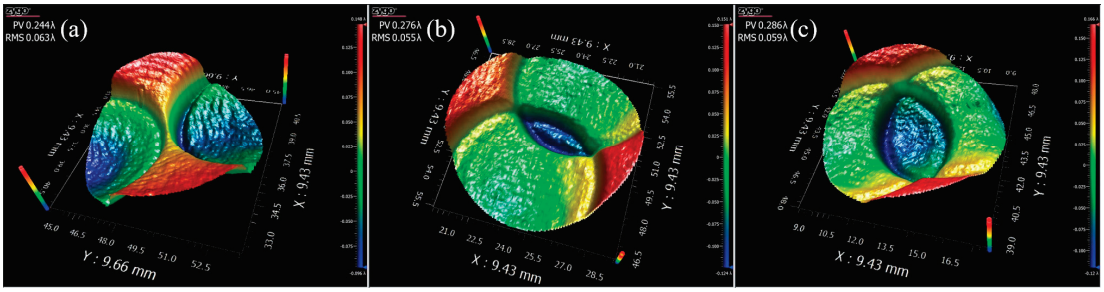

Figure 9. The material removal distribution under different overlap ratios: (**a**) center distance = 8.5 mm, (**b**) center distance = 6.5 mm, and (**c**) center distance = 4.5 mm (time = 300 s, amplitude = 40 μm, gap = 0.1 mm).

3.3. Removal Depth and Surface Morphology

The morphology of the removal pit's bottom was observed using a white light interferometer (Zygo Newview, Connecticut, United States). The plane ultrasonic horn was used to carry out the experiment to investigate the influence of the process parameters.

Figure 10a shows that the removal depth increased exponentially and the surface roughness increased linearly with the increase in amplitude. It can be known from the above analysis that as the amplitude increased, the cavitation density and cavitation intensity also increased, which meant that more and stronger cavitation bubbles participated in the material removal, increasing the removal rate. Figure 10b shows that the surface morphology exhibited more obvious discreteness and randomness compared with the surface formed by small tool head polishing or jet polishing [36]. As the amplitude increased from 20 μm to 40 μm, the removal uniformity became significantly worse and it appears that the red area representing the convex peaks on the figure became smaller and more dispersed. This was because the blasting energy of the cavitation bubbles increased, thereby increasing the removal depth. Furthermore, after the amplitude increased to 50 μm, the red area blocks on the figure became significantly larger. This was because the peaks formed on the surface became slenderer as the amplitude increased and the polishing fluid flow velocity in the gap increased, resulting in the removal of the microstructure peaks.

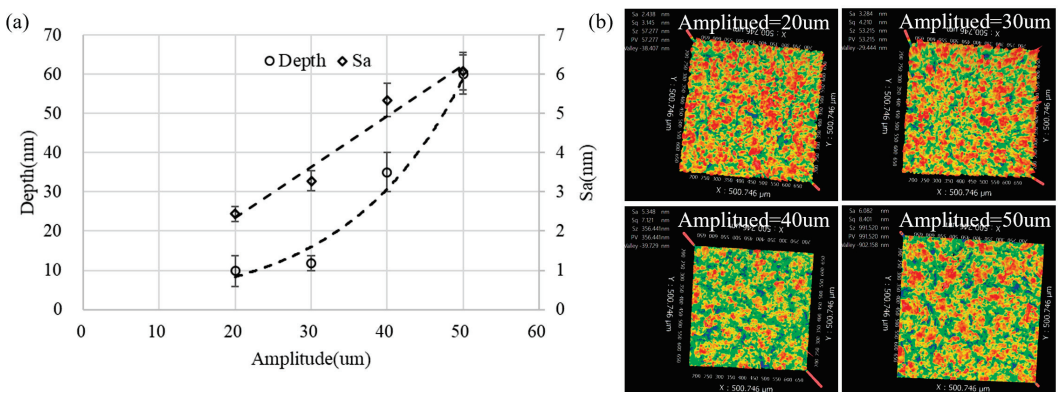

Figure 10. The influence of amplitude on the removal pit: (**a**) the depth and the bottom surface roughness and (**b**) the bottom surface morphology (gap = 0.15 mm, time = 300 s).

The above analysis shows that the surface microstructure was generated by the combined action of polishing fluid scouring and cavitation jet erosion, and the cavitation jet erosion was stronger than the material removal effect of high-frequency scouring.

Figure 11 shows that the surface roughness at the machining edge was larger than the center area and had more obvious dispersion. The surface microstructure at the edge groove significantly reduced the dispersion and surface roughness. According to the research results of Section 2, it can be known that the pressure fluctuation at the machining edge was smaller than that of the machining center, the blast density of cavitation bubbles was reduced, and a more favorable growth into larger bubbles with greater bursting power occurred. Therefore, the removal uniformity was poor and the surface roughness was higher at the edge. The flow velocity at the groove was large and the scour of the polishing fluid played a certain role in reducing the surface roughness. The roughnesses in the central area and the grooves were not much different, but the area in red was larger in the figure, which indicated better removal uniformity. This was due to the higher density of cavitation bubbles bursting in the central region under high pressure fluctuations, but the bursting energy of individual bubbles was reduced.

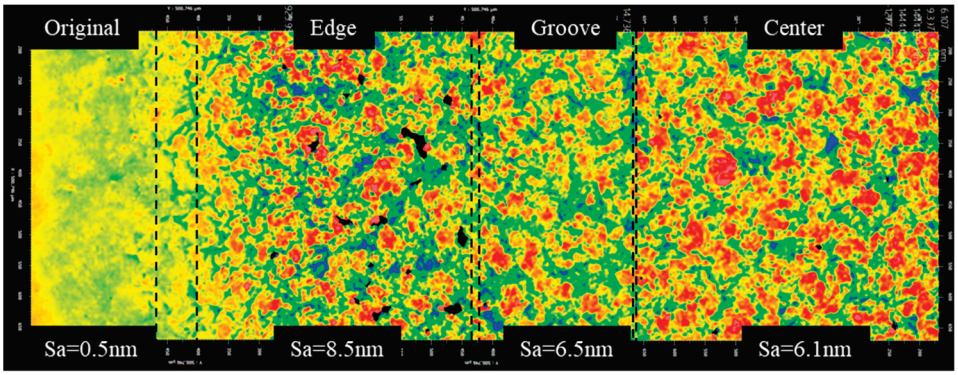

Figure 11. Change in the surface morphology along the radius of the removal pit (gap = 0.15 mm, amplitude = 40 μm, time = 300 s).

Figure 12a shows that the removal depth decreased exponentially and the surface roughness increased linearly with the increase in the gap. When the removal depth was larger, the measurement error caused by the unevenness of the starting surface was larger, and thus, the error bar range was larger. Figure 12b shows that as the gap increased, the red areas representing the microscopic peaks on the surface were lower and the distribution was more dispersed. Based on the simulation results of Section 2, it can be known that the pressure fluctuation amplitude increased as the gap decreased, which caused the cavitation bubbles to be more likely to collapse, which also meant that the burst concentration of the cavitation bubbles was higher and the cavitation bubbles did not grow into strong, large bubbles. A higher bubble burst concentration means more uniform removal. Moreover, when the gap is small, the flow velocity in the gap is larger, which is more conducive to the scouring removal of microstructure peaks.

Figure 13 shows that the removal depth increased linearly with the increase in processing time. The growth rate of the surface roughness became slower with the increase in time, and the larger the gap, the larger the roughness value. It can also be seen from Figure 13b that as the processing time increased, the number and area of the red regions representing the micro-convex peaks decreased (compare time = 300 s and time = 450 s); the blue area representing the lowest point was also decreasing (compare time = 450 s and time = 600 s). This was because the initial surface roughness of the sample used was very low (Sa = 0.5 nm) and the initial surface was not completely removed in the early stage of processing, and thus, the roughness gradually increased. When the newly machined surface formed and the density of effective cavitation bubbles had stabilized, the roughness stabilized.

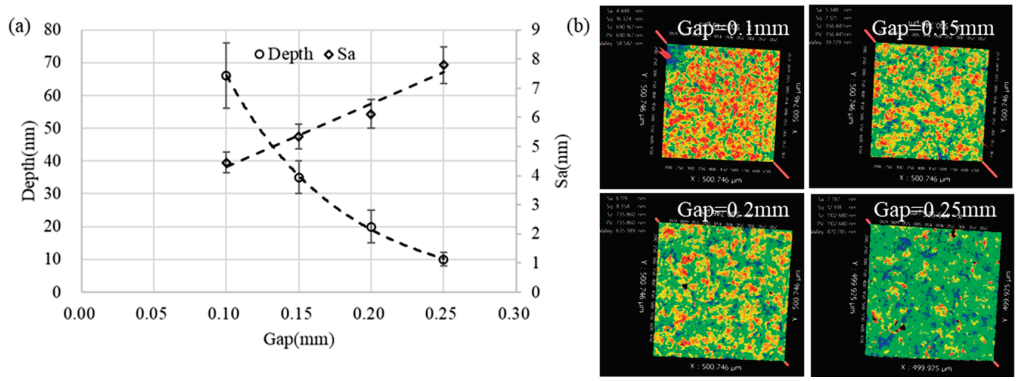

Figure 12. The influence of the gap on the removal pit: (**a**) the depth and the bottom surface roughness and (**b**) the bottom surface morphology (time = 300 s, amplitude = 40 μm).

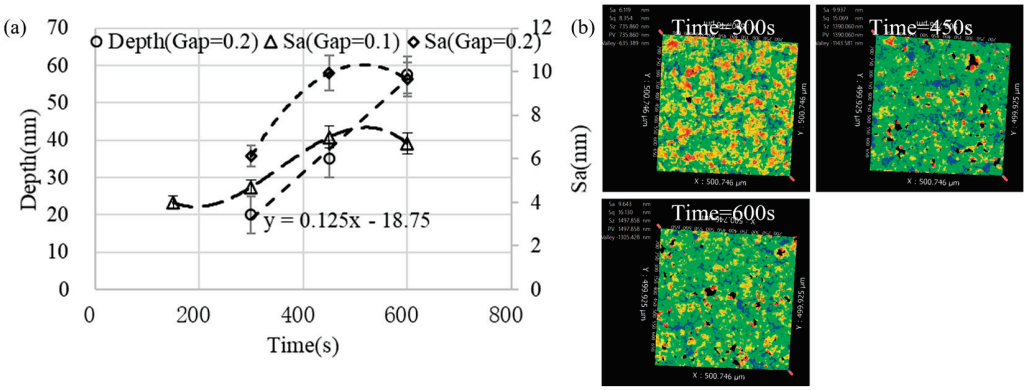

Figure 13. The removal pit changes with processing time: (**a**) the depth and the bottom surface roughness and (**b**) the bottom surface morphology (amplitude = 40 μm, gap = 0.2 mm).

As can be seen from Figure 14a, as the particle concentration increased, the depth of the removal increased exponentially with a slight decrease in the surface roughness. From the microstructure shown in Figure 14b, the area of the blue region representing the pit was larger at lower concentrations, which indicated that the removal uniformity in the microscopic range was poor. When the concentration increased, the red area representing the convex peak on the microscopic surface increased, which indicated that the scouring removal effect was significantly enhanced. Previous research showed that the presence of particles in liquids can cause bubbles to burst more easily [33]. Therefore, as the particle concentration increased, the burst concentration of cavitation bubbles increased, which contributed to the improvement of removal uniformity.

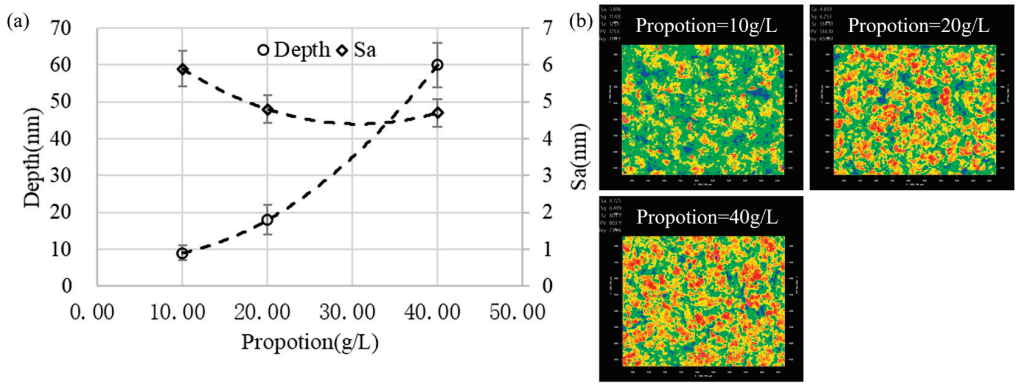

Figure 14. The influence of the fluid proportion on the removal pit: (**a**) the depth and the bottom surface roughness and (**b**) the bottom surface morphology (gap = 0.1 mm, time = 300 s, amplitude = 40 μm).

4. Modeling of Material Removal Distributions and Surface Morphology

4.1. Material Removal Distributions Model

Based on the experimental results of Section 3.2, each part of the *RF* could be described as follows:

$$S_{surface} = H \times S_{Tool} \times t \tag{6}$$

$$H = -k_1 e^{k_2(h_{amplitude} - k_3 h_{gap})} \tag{7}$$

where H is the cavitation removal rate; $h_{amplitude}$ is the amplitude; h_{gap} is the gap value; S_{tool} is the shape of the tool's working surface; and k_1, k_2, and k_3 are constants related to the fluid concentration and the optical material.

$$S_{edge} = H \times \frac{R_{edge} * L_{Tool}}{\left| R_{edge} * L_{Tool} \right|} \left(U_{ones} - U_{ones} \bigcap S_{Tool} \right) \times t \tag{8}$$

$$R_{edge} = -e^{-\frac{x^2}{2c^2}} \tag{9}$$

where L_{Tool} is the edge of the tool's working surface, R_{edge} is the edge function, * is the convolution operation, and c is the width of the edge effect. In this study, the width of the edge effect was c = 0.25 mm. U_{ones} is an all-ones matrix of size equal to R*L_{Tool}.

In the NUAM processing method, the polishing liquid in the narrow gap mainly moves tangentially on the surface of the workpiece under the drive of ultrasonic vibration, and thus, the material removal distribution realized by fluid scouring can be simplified to

$$S_{scour} = kv^a \times t \tag{10}$$

where k and a are constants and v is the normalized near-wall velocity distribution.

By adjusting the relevant parameters in equations 4 to 10 according to the experimental detection results, the geometric model of the tool removal function can be established, as shown in Figure 15.

4.2. Evolution of the Surface Micromorphology

The surface of BK7 optical glass processed using NUAM was observed by an atomic force microscope, as shown in Figure 16. According to the three material removal modes, the surface microtopography shown in Figure 16 could be divided into deep pits (mode-A) formed by the impact of cavitation bubble blasting and a large amount of crossing slender scratches (mode-B). It can be seen from the figure that the number of slender scratches in mode-B was significantly higher than the number of pits in mode-A, and the shape of the removed pits in both modes was very irregular. To facilitate the modeling and analysis, this study regarded the erosion pits of mode-A and mode-B formed under the same process parameters as circular pits with Gaussian shape changes and elliptical pits with Gaussian shape changes, respectively. Therefore, the shape of the mode-A pit formed by a single impact can be described as follows:

$$RF_A = -h_A \times e^{-\frac{2r^2}{d_A^2}} \tag{11}$$

where h_A is the depth of the erosion pit and d_A is the diameter of the erosion pit.

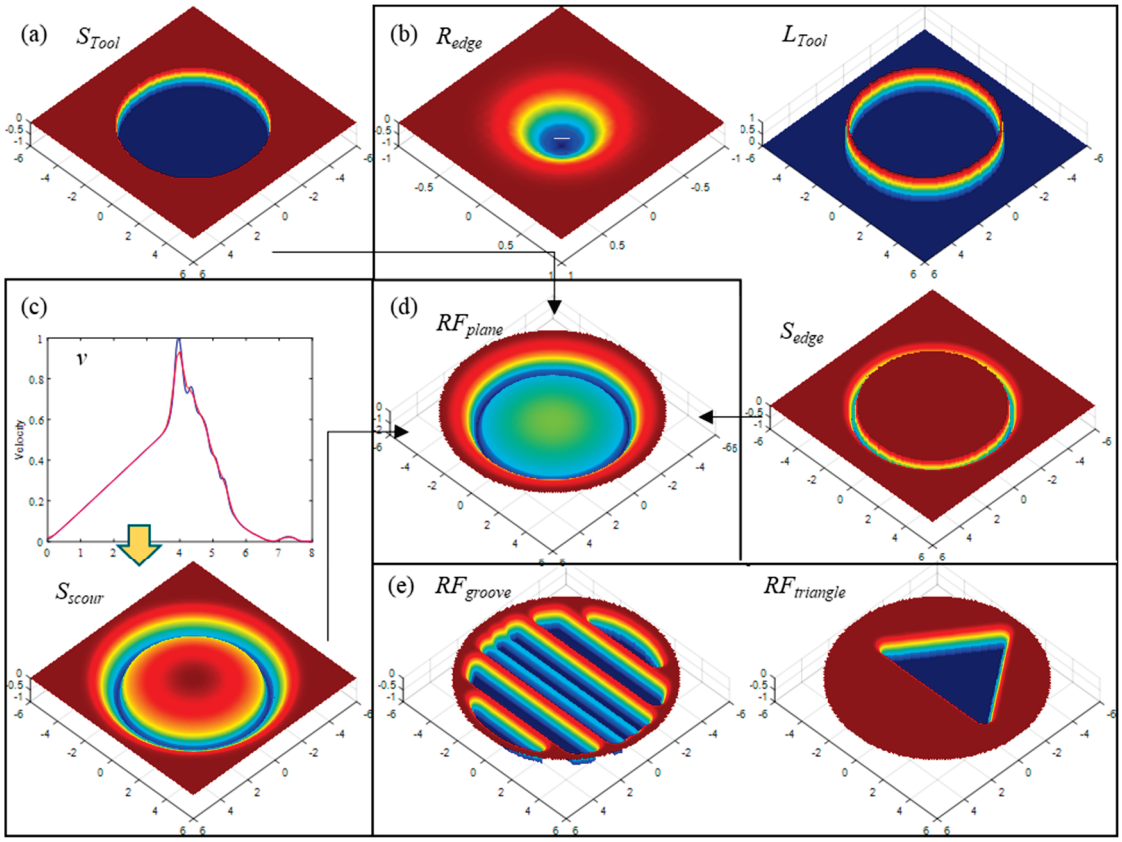

Figure 15. Removal distributions model: (**a**) the shape of the tool's working surface, (**b**) the edge removal distribution model, (**c**) the fluid scouring removal model, (**d**) the plane tool's removal function, and (**e**) the tool's removal function with complex working surfaces.

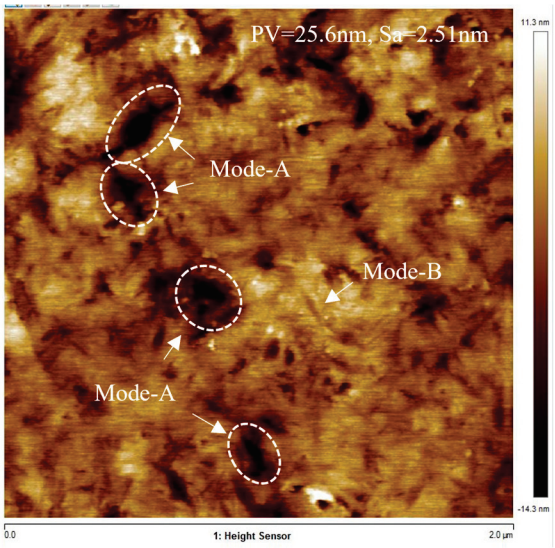

Figure 16. AFM images of the finished surfaces (time = 300 s, gap = 0.15 mm, amplitude = 30 µm).

The material removal distribution formed by mode-A pits on the workpiece surface per unit time is given by the following formula:

$$\sum RF_A = RF_A * D_A \tag{12}$$

where RF_A is the pit formed by a single impact, D_A is the pits distribution, and * is the convolution operation symbol.

The shape of the mode-B pit formed by a single impact can be described as follows:

$$RF_B = -h_B \times e^{-\frac{2x^2}{l_{B1}^2} - \frac{2y^2}{l_{B2}^2}} \tag{13}$$

where h_B is the depth of the erosion pit, l_{B1} is the length of the long side of the erosion pit, and l_{B2} is the length of the short side of the erosion pit.

The material removal distribution formed by mode-B pits on the workpiece surface per unit time is given by the following formula:

$$\sum RF_B = \sum_{i=0,45,\ 90,135} f(\theta_i) \times RF_B * D_B^i \tag{14}$$

where RF_B is the pit formed by a single impact, ${D_B}^i$ is the removal distribution of the angle biased toward θ_i, and $f(\theta)$ is the rotation matrix. To simplify the analysis, the directions of RF_B are summarized as four directions: 0°, 45°, 90°, and 135°.

The volume of material removed using NUAM processing per unit time can be expressed by the following formula:

$$V = \sum_{i=0}^{M} RF_{A_i} + \sum_{j=0}^{N} RF_{B_j} + RF_C \tag{15}$$

where M is the number of mode-A pits generated per unit time, N is the number of mode-B pits generated per unit time, and RF_C is the material removal caused by polishing liquid scouring. Within the range of process parameters investigated in this study, the material removal rate achieved by abrasive particles under liquid drag is very low compared with mode-A and mode-B, and thus, it is not considered in this section.

According to Figure 16, within the detection range of 2 μm × 2 μm, the diameter d_A of the mode-A pit was about 100–200 nm, the depth h_A was between 14 and 24 nm, and the number M was about 4. The length of the long side l_{B1} of the mode-B pit was about 100 nm, the length of the short side l_{B2} was about 10 nm, the depth h_B was between 14 and 24 nm, and the number N was about 400. The evolution process of the surface generated by the combined action of mode-A pits and mode-B pits is shown in Figure 17.

If the generated surface is represented by a matrix A of size M × N, the roughness of the generated surface can be calculated according to the following equation:

$$S_a = \frac{1}{MN} \sum_{i=0}^{M} \sum_{j=0}^{N} |A(i,j) - mean(A)| \tag{16}$$

Figure 17c shows the surface morphology after processing per unit of time. Since the parameter settings in Table 3 were obtained according to the observation of the microscopic topography shown in Figure 16, the unit time was the processing time of the microscopic topography shown in Figure 16, which was 300 s. By comparing the simulation results shown in Figure 17c with the experimental detection results shown in Figure 16, it can be found that the simulation results were significantly smaller than the measurement results. According to the analysis, this was the difference caused by the fact that the starting surface of the test sample was not an ideal plane. Figure 17f shows that after 100 units of processing time, the surface roughness reached 15.7 nm, which was also in line with the change trend of the processed surface roughness with processing time shown in Figure 13.

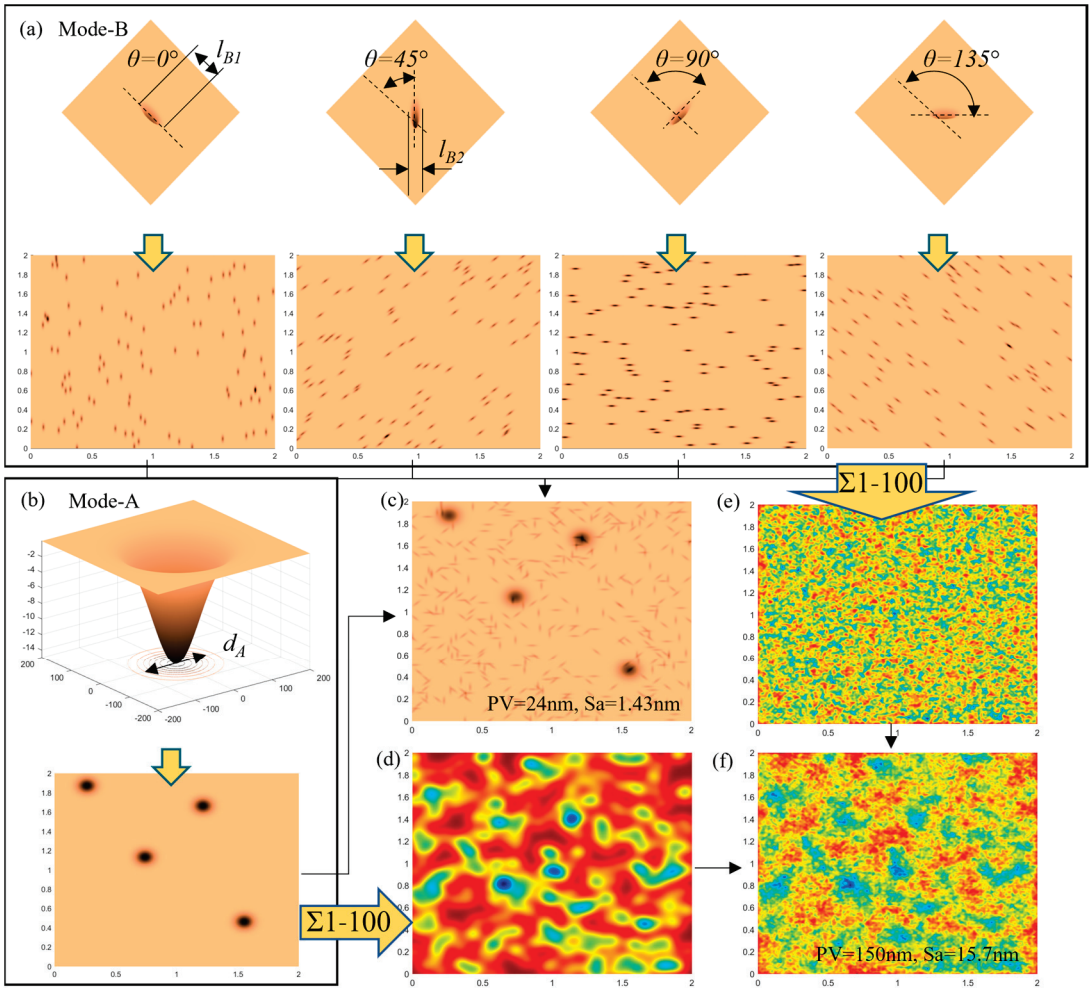

Figure 17. Removal pit shape and formed surface morphology in different modes: (**a**) four directions of mode-B removal pit and a random distribution, (**b**) mode-A removal pit and a random, distribution, (**c**) surface morphology using mode-A and mode-B per unit of time, (**d**) surface morphology using mode-A after 100 units of time, (**e**) surface morphology using mode-B after 100 units of time, and (**f**) surface morphology using mode-A and mode-B after 100 units of time.

Table 3. Surface morphology generation simulation parameters.

Mode-A	Diameter	d_A = 150 nm
	Depth	h_A = 19 nm
	Number	M = 4
Mode-B	Major axis	l_{B1} = 100 nm
	Minor aixs	l_{B2} = 10 nm
	Depth	h_B = 5 nm
	Number	N = 400

Based on the above studies, the evolution trends of machining removal depth and machined surface roughness with machining time are shown in Figure 18.

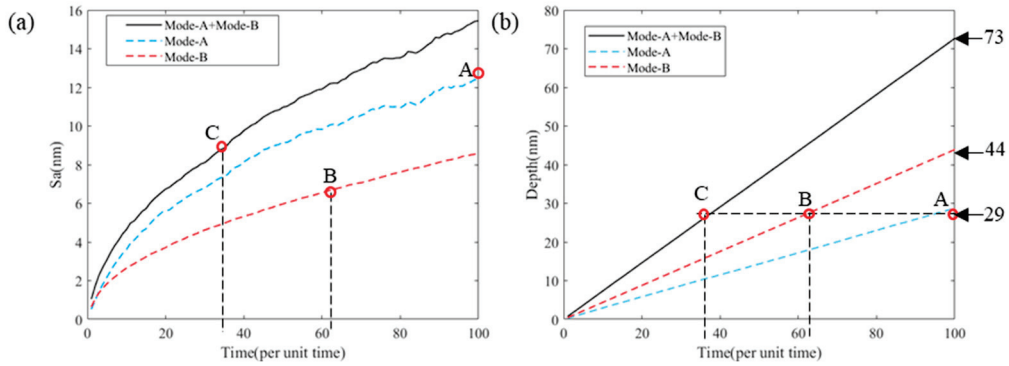

Figure 18. Surface roughness (Sa) and removal depth change with the number of iterations: (**a**) the influence of different modes on the surface roughness and (**b**) the influence of different modes on removal depth.

Figure 18a shows that the surface roughness increased with time and gradually decreased with increasing speed. The surface processed with mode-A and mode-B had a higher roughness than the surfaces processed separately. The surface roughness increase formed by mode-B was very smooth, while the surface roughness increase curve formed using mode-A and mode-A+B had a certain fluctuation, which indicated that the influence of mode-A on the surface roughness was significantly greater than that of mode-B. Therefore, when wanting to obtain a higher machined surface quality, the occurrence of mode-A in machining should be suppressed or avoided, and when wanting to obtain higher machining efficiency, the frequency of occurrence of mode-A should be promoted. How to improve the processing efficiency while satisfying a surface quality requirement, it is necessary to adjust the frequency of occurrence of different modes by optimizing the process parameters.

Figure 18b shows that the removal depth increased linearly with time. The removal depth of mode-A and mode-B processing together equalled the depth when using each processing mode alone. Under the parameter settings listed in Table 3, the material removal rate ratio of mode-A and mode-B was 28:44. The point A, B, and C represent the processing time of different methods for the same removal depth, corresponding to the points with the same name in Figure 18a. The points A, B, and C in Figure 18 show that when the same depth of material was removed, the roughness of the surface formed by mode-A was the largest and the roughness of the surface formed by mode-B was the smallest.

The variation curve of Sa with time t in Figure 18a can be represented by fitting the following exponential function:

$$S_a = a \cdot t^b \tag{17}$$

where the larger the b is, the greater the rate of increase of the surface roughness with time. The size of the goodness of fit can reflect the fluctuation of the surface roughness curve compared with the function curve.

Since the random distribution function was used in the solution operation, each solution result had a certain fluctuation, but the fluctuation size was not enough to change the influence law, and thus, there is no error range added to the data in the table.

From the data changes in Table 4, the following conclusions can be drawn: Under the same material removal rate, as the proportion of mode-A pits increased, the surface roughness increased. The change in surface roughness under the action of mode-A and mode-B exhibited an obvious exponential change ($R^2 \approx 1$) with the exponential size b ≈ 0.5. The surface roughness change rate caused by mode-A was significantly larger than that of mode-B. The fluctuation of surface roughness was mainly affected by mode-A. As the number of impacts increased, there was no obvious trend in the rate of surface roughness increase. The surface roughness can be reduced by increasing the frequency of mode-A or mode-B per unit removal depth.

Table 4. Changes in the surface roughness caused by the proportion of pits in different removal modes.

No.	M	N	Sa (nm)	Depth (nm)	Sa/Depth	a	b	Goodness of Fit (R^2)
1	3	466	15.16	72.75	0.208	1.287	0.532	0.9991
2	3	0	11.51	21.37	0.54	0.8873	0.563	0.9947
3	0	466	9.35	51.38	0.18	0.8842	0.5089	0.9998
4	4	400	15.69	72.37	0.217	0.133	0.5482	0.9992
5	4	0	13.08	28.45	0.46	1.073	0.5561	0.9966
6	0	400	8.539	43.92	0.19	0.7974	0.5166	0.9998
7	5	334	16.16	72.46	0.223	1.488	0.5183	0.9983
8	5	0	14.23	35.58	0.4	1.236	0.5327	0.9972
9	0	334	7.73	36.89	0.21	0.7609	0.5053	0.9996

5. Conclusions

In conclusion, NUAM technology was introduced into the polishing process of optical components, and theoretical and simulation analyses were carried out for the material removal distribution, material removal rate, and surface quality when using precision polishing. The removal function model and the evolution model of the microscopic surface morphology under this processing method were established. Some conclusions can be described as follows:

1. The material removal caused by cavitation bubble explosion was uniformly distributed on the entire working surface and had a 0.25 mm edge influence range. The flow scouring removal was mainly concentrated in the high-velocity flow zone around the machining area.
2. The material removal rate increased exponentially with the decrease in machining gap and the increase in amplitude, and remained constant with machining time. This feature is suitable for deterministic polishing.
3. Under the combined action of cavitation erosion and fluid erosion, the machined surface roughness increased linearly with the increase in amplitude and gap due to the reduced removal uniformity.
4. Increasing the particle concentration significantly improved the material removal rate, and the generated surface exhibited a better removal uniformity and a lower surface roughness.
5. Increasing the blasting density of cavitation bubbles while avoiding near-wall blasting, such as increasing the concentration of abrasive particles, could improve the material removal rate and achieve a higher surface quality.

Author Contributions: Conceptualization, Z.G.; methodology, Z.G. and X.H.; software, Z.G.; validation, Z.G., X.L. and T.J.; formal analysis, Z.G.; investigation, Z.G.; resources, X.H.; data curation, Z.G.; writing—original draft preparation, Z.G.; writing—review and editing, Z.G. and X.L; visualization, Z.G.; supervision, X.L. and T.J.; project administration, X.H.; funding acquisition, Z.G. All authors read and agreed to the published version of the manuscript.

Funding: This research was funded by Zhejiang Province Public Welfare Technology Application Research Project (grant number LGG22E050030), National Natural Science Foundation of China (grant number 51975173), and the UK Engineering and Physical Sciences Research Council (EPSRC, EP/T024844/1).

Data Availability Statement: Not applicable.

Acknowledgments: The authors would like to thank the LT Co., Ltd., for providing the testing services.

Conflicts of Interest: The authors declare no conflict of interest.

References

1. Li, P.; Chen, S.; Xiao, H.; Chen, Z.; Qu, M.; Dai, H.; Jin, T. Effects of local strain rate and temperature on the workpiece subsurface damage in grinding of optical glass. *Int. J. Mech. Sci.* **2020**, *182*, 105737. [CrossRef]
2. Beaucamp, A.; Namba, Y. Super-smooth finishing of diamond turned hard X-ray molding dies by combined fluid jet and bonnet polishing. *Cirp Ann.-Manuf. Technol.* **2013**, *62*, 315–318. [CrossRef]
3. Chen, G.; Yi, K.; Yang, M.; Liu, W.; Xu, X. Factor effect on material removal rate during phosphate laser glass polishing. *Mater. Manuf. Process.* **2014**, *29*, 721–725. [CrossRef]
4. Cai, G.; Lu, Y.; Cai, R.; Zheng, H. Analysis on lapping and polishing pressure distribution. *CIRP Ann.* **1998**, *47*, 235–238. [CrossRef]
5. Zhao, D.; Lu, X. Chemical mechanical polishing: Theory and experiment. *Friction* **2013**, *1*, 306–326. [CrossRef]
6. Cheng, H.; Dong, Z.; Ye, X.; Tam, H.-Y. Subsurface damages of fused silica developed during deterministic small tool polishing. *Opt. Express* **2014**, *22*, 18588–18603. [CrossRef]
7. Wang, C.; Wang, Z.; Yang, X.; Sun, Z.; Peng, Y.; Guo, Y.; Xu, Q. Modeling of the static tool influence function of bonnet polishing based on FEA. *Int. J. Adv. Manuf. Technol.* **2014**, *74*, 341–349. [CrossRef]
8. Walker, D.D.; Freeman, R.; Morton, R.; McCavana, G.; Beaucamp, A. Use of the 'precessions'™ process for prepolishing and correcting 2D & $2\frac{1}{2}$D form. *Opt. Express* **2006**, *14*, 11787–11795.
9. Golini, D.; Kordonski, W.I.; Dumas, P.; Hogan, S.J. Magnetorheological finishing (MRF) in commercial precision optics manufacturing. *Int. Soc. Opt. Photonics* **1999**, *3782*, 80–91.
10. Shi, F.; Tian, Y.; Peng, X.; Dai, Y. Combined technique of elastic magnetorheological finishing and HF etching for high-efficiency improving of the laser-induced damage threshold of fused silica optics. *Appl. Opt.* **2014**, *53*, 598–604. [CrossRef]
11. Wang, T.; Huang, L.; Vescovi, M.; Kuhne, D.; Tayabaly, K.; Bouet, N.; Idir, M. Study on an effective one-dimensional ion-beam figuring method. *Opt. Express* **2019**, *27*, 15368–15381. [CrossRef] [PubMed]
12. Weiser, M. Ion beam figuring for lithography optics. *Nucl. Instrum. Methods Phys. Res. Sect. B Beam Interact. Mater. At.* **2009**, *267*, 1390–1393. [CrossRef]
13. Guo, Z.; Jin, T.; Xie, G.; Lu, A.; Qu, M. Approaches enhancing the process accuracy of fluid jet polishing for making ultra-precision optical components. *Precis. Eng.* **2019**, *56*, 20–37. [CrossRef]
14. Wang, C.; Cheung, C.; Ho, L.; Loh, Y. Development of a fluid line-jet polishing process for rotational axisymmetric surfaces. *J. Manuf. Process.* **2021**, *61*, 15–24. [CrossRef]
15. Zhang, T.; Guan, C.; Zhang, C.; Xi, W.; Yu, T.; Zhao, J. Predictive modeling and experimental study of generated surface-profile for ultrasonic vibration-assisted polishing of optical glass BK7 in straight feeding process. *Ceram. Int.* **2021**, *47*, 19809–19823. [CrossRef]
16. Zhang, T.; Wang, Z.; Yu, T.; Chen, H.; Dong, J.; Zhao, J.; Wang, W. Modeling and prediction of generated local surface profile for ultrasonic vibration-assisted polishing of optical glass BK7. *J. Mater. Process. Technol.* **2021**, *289*, 116933. [CrossRef]
17. Suzuki, H.; Hamada, S.; Okino, T.; Kondo, M.; Yamagata, Y.; Higuchi, T. Ultraprecision finishing of micro-aspheric surface by ultrasonic two-axis vibration assisted polishing. *CIRP Ann.* **2010**, *59*, 347–350. [CrossRef]
18. Lv, Z.; Huang, C.; Zhu, H.; Wang, J.; Wang, Y.; Yao, P. A research on ultrasonic-assisted abrasive waterjet polishing of hard-brittle materials. *Int. J. Adv. Manuf. Technol.* **2015**, *78*, 1361–1369. [CrossRef]
19. Lv, Z.; Hou, R.; Wang, T.; Huang, C.; Zhu, H. Research on cavitation involved in ultrasonic-assisted abrasive waterjet machining. *Int. J. Adv. Manuf. Technol.* **2018**, *101*, 1879–1886. [CrossRef]
20. Beaucamp, A.; Katsuura, T.; Kawara, Z. A novel ultrasonic cavitation assisted fluid jet polishing system. *CIRP Ann.* **2017**, *66*, 301–304. [CrossRef]
21. Beaucamp, A.; Katsuura, T.; Takata, K. Process mechanism in ultrasonic cavitation assisted fluid jet polishing. *CIRP Ann.* **2018**, *67*, 361–364. [CrossRef]
22. Ichida, Y.; Sato, R.; Morimoto, Y.; Kobayashi, K. Material removal mechanisms in non-contact ultrasonic abrasive machining. *Wear* **2005**, *258*, 107–114. [CrossRef]
23. Du, J.; Chen, F. Cavitation dynamics and flow aggressiveness in ultrasonic cavitation erosion. *Int. J. Mech. Sci.* **2021**, *204*, 106545. [CrossRef]
24. Pandit, A.V.; Sarvothaman, V.P.; Ranade, V.V. Estimation of chemical and physical effects of cavitation by analysis of cavitating single bubble dynamics. *Ultrason. Sonochem.* **2021**, *77*, 105677. [CrossRef] [PubMed]
25. Sauer, J.; Schnerr, G.H. Unsteady cavitating flow—A new cavitation model based on a modified front capturing method and bubble dynamics. In Proceedings of the 2000 ASME Fluid Engineering Summer Conference, Boston, MA, USA, 11–15 June 2000; Volume 251, pp. 1073–1079.
26. Neppiras, E. Acoustic cavitation thresholds and cyclic processes. *Ultrasonics* **1980**, *18*, 201–209. [CrossRef]
27. Kadivar, E.; el Moctar, O.; Skoda, R.; Löschner, U. Experimental study of the control of cavitation-induced erosion created by collapse of single bubbles using a micro structured riblet. *Wear* **2021**, *486–487*, 204087. [CrossRef]
28. Luther, S.; Mettin, R.; Koch, P.; Lauterborn, W. Observation of acoustic cavitation bubbles at 2250 frames per second. *Ultrason. Sonochem.* **2001**, *8*, 159–162. [CrossRef]
29. Li, S. Cavitation enhancement of silt erosion—An envisaged micro model. *Wear* **2006**, *260*, 1145–1150. [CrossRef]

30. Haosheng, C.; Jiadao, W.; Darong, C. Cavitation damages on solid surfaces in suspensions containing spherical and irregular microparticles. *Wear* **2009**, *266*, 345–348. [CrossRef]
31. Plesset, M.S.; Chapman, R.B. Collapse of an initially spherical vapour cavity in the neighbourhood of a solid boundary. *J. Fluid Mech.* **2006**, *47*, 283–290. [CrossRef]
32. Ye, L.; Zhu, X. Analysis of the effect of impact of near-wall acoustic bubble collapse micro-jet on Al 1060. *Ultrason. Sonochem.* **2017**, *36*, 507–516. [CrossRef] [PubMed]
33. Teran, L.A.; Laín, S.; Rodríguez, S.A. Synergy effect modelling of cavitation and hard particle erosion: Implementation and validation. *Wear* **2021**, *478–479*, 203901. [CrossRef]
34. Cao, Z.-C.; Cheung, C.F. Theoretical modelling and analysis of the material removal characteristics in fluid jet polishing. *Int. J. Mech. Sci.* **2014**, *89*, 158–166. [CrossRef]
35. Guo, Z.; Jin, T.; Ping, L.; Lu, A.; Qu, M. Analysis on a deformed removal profile in FJP under high removal rates to achieve deterministic form figuring. *Precis. Eng.* **2018**, *51*, 160–168. [CrossRef]
36. Namba, Y.; Beaucamp, A.; Freeman, R. Ultra-precision fluid jet and bonnet polishing for next generation hard x-ray telescope application. In Proceedings of the ASPE 2010 Annual Meeting, Atlanta, GA, USA, 5–31 October 2010.

micromachines

Article

Investigating the Effect of Grinding Time on High-Speed Grinding of Rails by a Passive Grinding Test Machine

Pengzhan Liu [1,*], Wenjun Zou [1], Jin Peng [1] and Furen Xiao [2]

[1] Henan Engineering Lab for Super-Hard Grinding Gomposites, College of Materials Science & Engineering, Henan University of Technology, Zhengzhou 450007, China
[2] Key Lab of Metastable Materials Science & Technology, Hebei Key Lab for Optimizing Metal Product Technology and Performance, College of Materials Science & Engineering, Yanshan University, Qinhuangdao 066004, China
* Correspondence: pengzhan_liu@outlook.com

Abstract: High-speed rail grinding is a unique passive grinding maintenance strategy that differs from conventional grinding techniques. Its grinding behavior is dependent on the relative motion between the grinding wheel and rail; hence, it possesses great speed and efficiency. In this study, the effects of the duration of grinding time and the increase in the number of grinding passes on the grinding of high-speed rails were investigated using passive grinding tests with a single grinding time of 10 s and 30 s and grinding passes of once, twice, and three times, respectively. The results show that when the total grinding time was the same, the rail removal, grinding ratio of grinding wheels, rail grinding effect, grinding force, and grinding temperature were better in three passes of 10 s grinding than in one pass of 30 s grinding, indicating that the short-time and multi-pass grinding scheme is not only conducive to improving the grinding efficiency and grinding quality in the high-speed rail grinding but can also extend the service life of the grinding wheels. Moreover, when the single grinding times were 10 s and 30 s, respectively, the grinding removal, grinding efficiency, grinding marks depth, and surface roughness of rail increased with the number of grinding passes, implying that the desired rail grinding objective can be achieved by extending the grinding time via the multi-pass grinding strategy. The results and theoretical analysis of this study will contribute to re-conceptualizing the practical operation of high-speed rail grinding and provide references for the development of the grinding process and grinding technology.

Keywords: high-speed rail grinding; passive grinding; grinding time; grinding pass; grinding wheel

Citation: Liu, P.; Zou, W.; Peng, J.; Xiao, F. Investigating the Effect of Grinding Time on High-Speed Grinding of Rails by a Passive Grinding Test Machine. *Micromachines* **2022**, *13*, 2118. https://doi.org/10.3390/mi13122118

Academic Editors: Jiang Guo, Chunjin Wang and Chengwei Kang

Received: 31 October 2022
Accepted: 28 November 2022
Published: 30 November 2022

1. Introduction

As one of the principal modes of contemporary transportation, railways hold an unrivaled strategic position and significance [1,2]. The construction of high-speed railway networks in China, Japan, and Western Europe has been essentially completed, giving the nearly 200-year-old industry new vigor and vitality [3,4]. This is especially true with the introduction of a large number of high-speed trains traveling at speeds of more than 250 km per hour [5]. With the growth in train operation hours, frequency, and load capacity, however, the damage caused by trains to railways is increasing daily. This has resulted in a substantial increase in the number and generation rate of rail defects [6]. Currently, rail grinding is widely recognized as an advanced and effective technique for rail maintenance in the leading railway nations, as it can eliminate a variety of rail defects, including wave wear, rolling contact fatigue (RFC), and rail wear damage, without disassembling the rail [7]. This accomplishes the purposes of restoring the rail surface, limiting rail surface fatigue, and reshaping the rail profile [8]. There are multiple methods for grinding rails. Active grinding is the prevalent approach for rails, in which the motor rotates the grinding wheels to grind the rail [9]. Active rail grinding is characterized by its sluggish operation speed and substantial rail wear. This is a maintenance-type grinding strategy developed in the early

stages of rail maintenance technology to repair rail surface damage. It largely eliminates existing rail surface defects that affect the operational quality of trains by removing a substantial amount of rail [10]. Nevertheless, since the time spent on rail maintenance operations in the rail transportation plan is being reduced year by year with the increase of train operation time, in addition to a large amount of rail grinding that will reduce the service life of rails, the concept of rail maintenance grinding is gradually shifting from maintenance-type grinding with extensive metal removal to preventive grinding operations with short intervals and less metal removal [11,12]. Therefore, the active rail grinding method has become less adapted to the current high-speed rail transportation situation, and a new high-speed rail grinding technology has come into being [13,14].

Because there is no active drive for the grinding wheel, rail high-speed grinding is also known as passive grinding [15]. High speed refers to the forward speed of the grinding train, not the linear speed of the grinding wheel. The grinding wheel needs to follow the high-speed grinding train to advance rapidly on the surface of the rail, relying solely on the grinding pressure provided by the passive grinding mechanism and the friction force generated by the relative movement of the grinding wheel and the rail to passively rotate and complete the grinding behavior of rail [16]. The structure design and operation principle of passive high-speed grinding allow the grinding train to execute rail grinding at speeds between 60 and 80 km per hour. In contrast to the common active grinding train at 3 and 15 km per hour, the passive high-speed grinding train does not require a unique "window" to close the railway and does not require the dismantling of any railway signal equipment or rail accessories prior to grinding [17]. Consequently, the adoption of passive high-speed grinding technology in the preventive grinding of rail has unmatched efficiency and cost advantages. For the application of rail high-speed grinding technology, the United Kingdom, Germany, and other nations have spent over a decade demonstrating through practice the unparalleled application value of high-speed grinding technology for rail preventive grinding in the long straight length of rail track [18,19]. According to the data and technical experience acquired by the German railway maintenance, the preventive grinding maintenance of rails every four months using high-speed grinding technology can achieve the same rail maintenance effect as the repairing grinding maintenance by active grinding performed every 4.5 MGT of the total train passing weight [20]. This considerably extends the rails' service life, as demonstrated in Figure 1 [17,21].

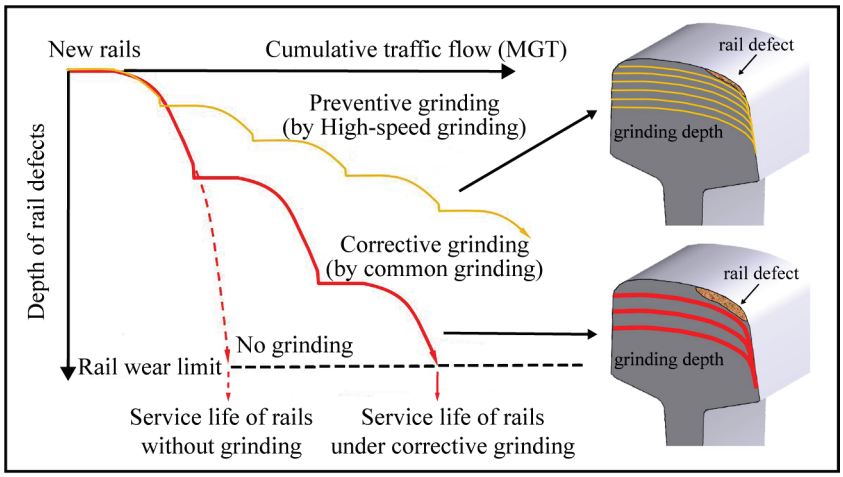

Figure 1. Effect of different grinding technologies on the service life of rails [17,21].

Notably, the rail high-speed grinding maintenance process must sometimes adjust the rail grinding time based on the state of rail surface wear to accomplish the desired effect of regulating rail grinding [22]. There are two conventional methods for controlling the grinding time. One is to increase or decrease the length of the grinding train to change the number of high-speed grinding wheels, thereby altering the time of grinding in a single

pass of high-speed grinding; the other is to perform multiple grindings of rails during a maintenance operation, which is also a disguise to alter the time of grinding wheels grinding rails [23]. Since increasing the length of the grinding train will raise the operating costs of rail maintenance and there are upper limits on the length of the grinding train, the passive grinding process of repeated multiple passes in one rail maintenance is generally used to regulate the high-speed grinding time [8].

However, in addition to the significant differences in rail service life, grinding wheel life and rail maintenance effects caused by the difference in total grinding time, the single long-time passive grinding process, and the multiple short-time passive grinding process will produce different results for high-speed rail grinding with the same total grinding time. Yet, there is little relevant research studying the impact of grinding time on railways, and the majority of discussions regarding rail grinding time focus on the prevalent active rail grinding technique. Lin et al. [24] investigated the influence of grinding time and grinding pass of active rail grinding on rail surface temperature and burn behavior. This study found that the surface of the rail samples was burned to varying degrees when the rotating speed of the grinding stone exceeded 2600 r/min and the grinding pressure above 1000 N during the 8 s active rail grinding tests. Moreover, when the linear velocity of the grinding stone and the pressure were held constant, the maximum grinding temperature rose differently as the number of grinding passes increased. This shows that the variation of grinding time affects the surface grinding quality of the rails. Zhang et al. [25] discussed the impact of grinding passes and direction on the behavior of material removal in the rail grinding process. The authors illustrated that the increase in the number of grinding passes increased the wear of the grinding wheel, resulting in a decrease in rail removal, grinding efficiency, and rail surface roughness, by developing a three-dimensional finite element model of active rail grinding. Wu et al. [26] examined the effect of grinding time on the wear characteristics of brazed diamond grinding tools for rail grinding using a custom-built active rail grinding tester. This study revealed that the intermittent grinding strategy of single grinding for 6 s and cumulative grinding for 5 passes resulted in less grinding tool wear and rail surface roughness than the single pass grinding for 30 s. This showed that the short time and multi-pass grinding process extended the service life of the grinding tools and optimized the rail surface morphology after grinding. The aforementioned studies on active rail grinding provide a reference for the setting of grinding time parameters in high-speed rail grinding, but they cannot be used to guide the grinding time in high-speed rail grinding line operations or to illustrate the effect of single long-time passive grinding and multiple short-time passive grinding on high-speed rail grinding results and grinding wheels.

The purpose of this article was to optimize the effect of rail high-speed grinding and extend the service life of high-speed grinding wheels, and a self-designed passive grinding test machine was used to investigate the effect of grinding time and grinding passes on the high-speed grinding of rails. During grinding, the grinding efficiency, service life of the grinding wheel, grinding effect on rails, grinding force, and grinding temperature are discussed. Due to the fact that water, coolant, and other grinding media are undesirable in practical rail grinding operations, dry grinding is the appropriate grinding state. This is because rail maintenance must take into account operating safety and environmental protection. Consequently, the focus of this work is on the outcomes of grinding tests conducted under dry grinding conditions with no further grinding aids employed. This study will contribute to an in-depth understanding of the passive grinding operation in high-speed rail grinding and to the formulation of grinding process specifications.

2. Experiment

2.1. Grinding Testing Machine

Research involving high-speed rail grinding is challenging to conduct on rail lines. This is because, first, it is expensive to perform frequent rail grinding tests on in-service railway lines; second, it will result in test errors due to the varying initial state of the

railways; and thirdly, the high speed of the rail high-speed grinding train makes it difficult to measure the grinding process and the grinding results. Figure 2 depicts the structure of the self-designed passive grinding test machine utilized for grinding testing in this work. In the preceding study, the structural design, grinding principle, and technical feasibility of the test machine were discussed and explained in detail [16]. Therefore, the content related to the grinding test machine will not be discussed in this study.

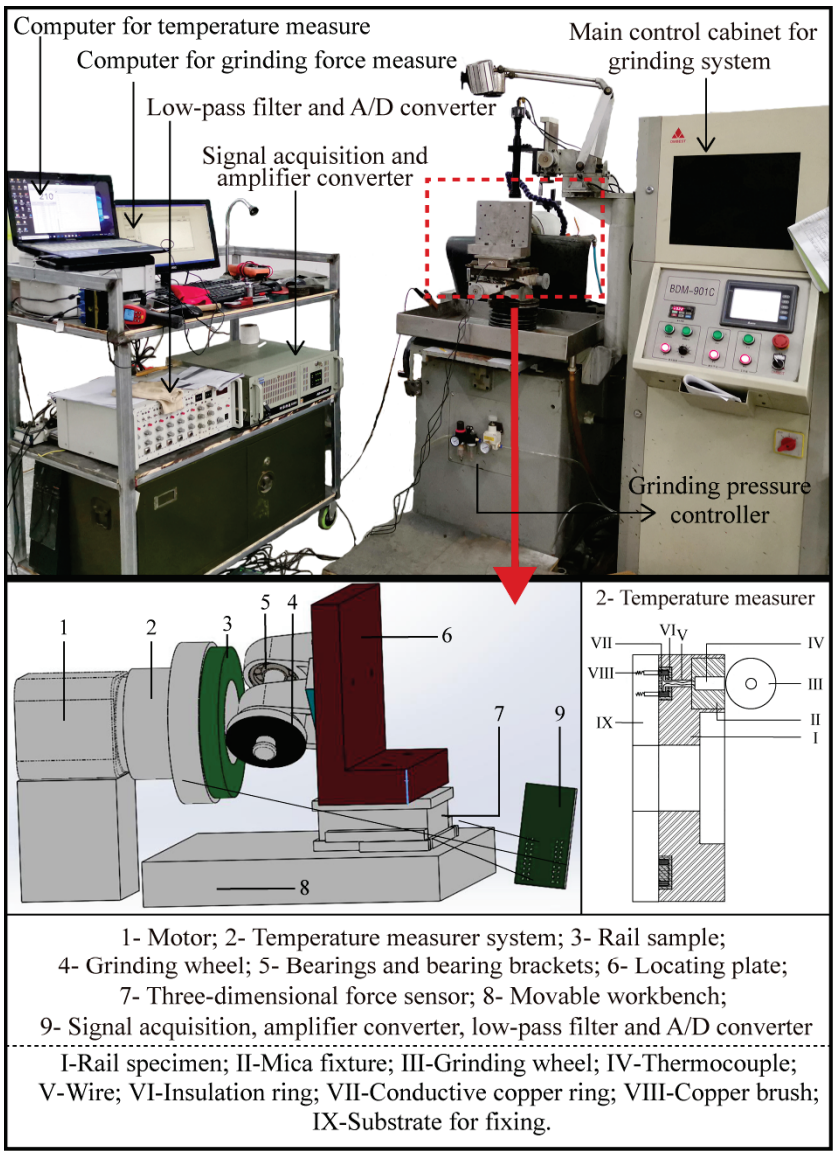

Figure 2. Structure of the grinding test machine.

Utilizing the grinding force measurement system and the grinding temperature monitoring system of the grinding test machine, the grinding force and grinding temperature were measured during the grinding test. The three-dimensional mechanical sensor was used to measure the grinding pressure and grinding force in the grinding force measurement system. The gathered mechanical signals were analyzed by the Labview force measurement program in the computer via the signal acquisition system and amplifier converter, and the resulting waveform array and oscillogram were constructed in the computer. In the grinding temperature monitoring system, the insertion thermocouple was modified to monitor the grinding temperature, and the thermoelectric effect served as the basis for measuring the temperature. The thermoelectric potential generated by the thermocouple was transmitted to the temperature acquisition module through wires

and brushes. Through the A/D converter, low-pass filter, and amplifier, the signals are converted to digital signals, and then they are stored in the computer. The entire test procedures and data processing for the mechanical and thermoelectric signals can also be found in the published study [16], which describes these processes in depth. Equation (1) was used to calculate the rotation speed of rail sample based on the operation speed of the grinding train [16].

$$Rotation\ speed\ of\ rail\ sample\ (r/min) = \frac{v_w(km/h) \times 10^6}{\pi \times d_s \times 60} \quad (1)$$

In the formula, v_w is the speed of the grinding train, and d_s is the diameter of the rail sample. Significantly, grinding wheels with varied angles are typically used to trim rails during the high-speed rail grinding process. To control the variables and accurately reflect the influence of grinding time on the high-speed grinding of rails, only the top of the rail material was ground at a vertical angle for testing.

2.2. Experimental Materials

The test rail samples were acquired from the Mn-steel rail installed in the field (Chinese brand: U71Mn). It is widely used on the Chinese railways, and its elemental composition in weight (%) is listed in Table 1. Table 2 provides a summary of the mechanical parameters of this rail steel, and the typical heat treatment for this steel is hot rolling [27]. The rail specimen was assembled directly from the rail head cut into eight identical sectors, as depicted in Figure 3. Before the test, the surface of each rail specimen was machined to the same roughness to ensure similar test conditions.

Table 1. Chemical compositions (wt%) of U71Mn rail steel [27].

Elemental	C	Si	Mn	P	S	V	Nb
content	0.65–0.76	0.15–0.58	0.70–1.20	≤ 0.035	≤ 0.030	0.030	≤0.010

Table 2. Mechanical properties of U71Mn rail steel [27].

Steel Material	Tensile Strength σb (MPa)	Elongation Rate δ (%)	Fracture Toughness K_{IC} (Mpa·$m^{1/2}$)	Hardness (HB)
U71Mn	≥880	≥ 10	≥26	260–300

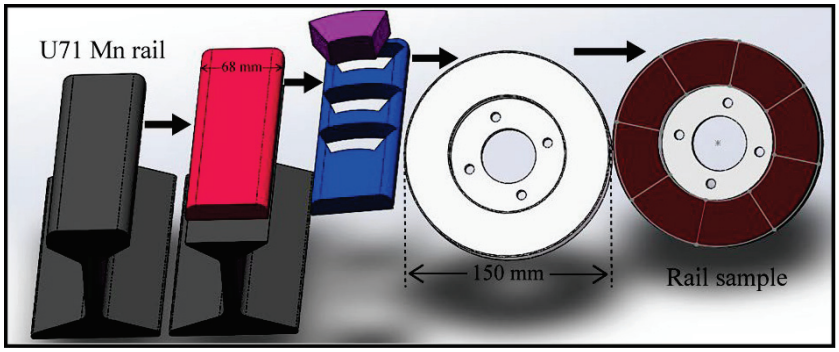

Figure 3. Preparation and morphology of rail sample.

In this work, a grinding wheel corresponding to the size of the rail sample was used for grinding tests. The material composition of grinding wheels and production formula were developed from the actual high-speed rail grinding wheel [28]. The grinding wheel's

outer diameter, inner diameter, and thickness are 80, 10, and 10 mm, respectively, and its material and composition are detailed in Table 3.

Table 3. Composition of passive grinding wheels.

Grinding Wheel Type	Hot Pressed Resin Grinding Wheel
Abrasive	fused alumina zirconia, brown fused alumina, ceramics corundum abrasives
Abrasive size	14–60 mesh
Binder	high toughness heat-resistant resin
Auxiliary materials (fillers/heat dissipation material)	pyrites (FeS_2)

2.3. Grinding Test

The grinding tests investigated the effects of passive grinding time and grinding passes on the railway surface. The grinding test settings were based on the actual operational parameters and maintenance requirements of the rail high-speed grinding (HSG-2) train [17]. Each group was subjected to three passive grinding procedures, as detailed in Table 4. The single passive grinding time of Group A was 30 s, whereas that of Group B was 10 s. In Group A and Group B tests, rail samples were ground one, two, and three passes, respectively. The grinding passes represent the total number of repetitions of a single grinding time test. To simulate the forward speed of an 80 km/h high-speed grinding train, the linear velocity of the rail sample was set to 22.2 m per second. The grinding pressure was set at 240 N, which was calculated using the standard pressure load of 12 MPa for passive grinding machines. Additionally, the grinding state of the grinding wheel on the rail is dry grinding, meaning that the auxiliary liquid media material in the grinding process is not involved.

Table 4. Grinding parameters of grinding time on grinding tests.

No.	Grinding Wheel Angle	Rotation Speed of Rail Sample	Grinding Pressure	Grinding Time	Grinding Passes
A_1	45°	2831 r/min	240 N	30 s	1
A_2	45°	2831 r/min	240 N	30 s	2
A_3	45°	2831 r/min	240 N	30 s	3
B_1	45°	2831 r/min	240 N	10 s	1
B_2	45°	2831 r/min	240 N	10 s	2
B_3	45°	2831 r/min	240 N	10 s	3

All studies were conducted in the same conditions (20~24 °C, 40~60% relative humidity). Each group of tests was repeated six times with new grinding wheels to acquire the final experimental results. Before the test, the surface of the rail sample and grinding wheels were cleaned with anhydrous ethanol to eliminate the influence of contaminants. Before and after the grinding test, the rail samples and the grinding wheels were weighed using an electronic analytical balance (GL623i; measurement accuracy: 0.001 g). The mass loss of grinding per unit time for the rail sample was defined as the material removal ratio of rail or grinding efficiency, and the grinding ratio was defined as the ratio of grinding mass loss between the rail and grinding wheel. The grinding ratio indicates the grinding life or durability of grinding wheels. The removal of the rail samples was determined by the change in weight. The topography of the surface was observed using an ultra-fine digital microscope (VHX-7000, KEYENCE, Osaka, Japan). The surface roughness of rail samples was measured and recorded by a 3D optical surface profilometer (Ze Gage TM, Zygo, Connecticut, America) before and after the grinding test.

3. Results and Discussion

3.1. Rail Removal and Grinding Wheel Wear

In order to visualize the effects of grinding time and grinding passes on the grinding results, the weight changes of the rail samples and grinding wheels were measured before and after the grinding test, as seen in Figure 4. With the same number of grinding passes, the longer the single grinding time, the greater the rail removal and grinding wheel loss. Multiple grinding passes of the grinding wheel on the rail samples further increased rail removal and grinding wheel loss. However, under the same total grinding time, the mean value of the sum of rail removal after three passes of 10 s passive grinding (i.e., the sum of rail removal in the B_1, B_2, and B_3 three groups of grinding tests) was 0.3 g higher than that in the Group A_1 with only one pass of 30 s passive grinding, while the mean value of the sum of grinding wheel wear loss in the B_1, B_2, and B_3 three groups of grinding tests was 0.1 g lower than that in the Group A_1. This suggests that the intermittent grinding strategy of extending the grinding time by increasing the grinding passes has effects on the grinding results of passive grinding. The test findings indicate that the short-time and multiple-pass grinding approach is advantageous for increasing rail removal and decreasing grinding wheel wear.

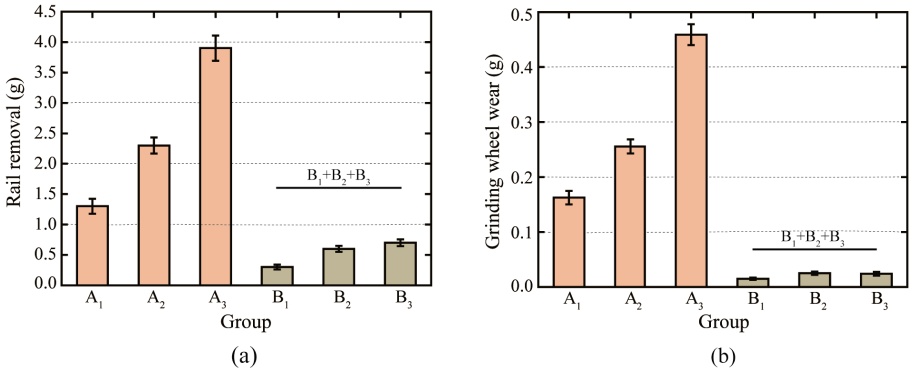

Figure 4. (**a**) Removal of rail samples by grinding wheels and (**b**) wear of grinding wheels at different grinding times.

3.2. Grinding Efficiency and Grinding Ratio

Figure 5 illustrates the grinding efficiency and grinding ratio for passive grinding tests with various grinding times and passes. For the grinding efficiency, as the number of grinding passes increased, the grinding efficiency of the second pass of repetition was higher than the grinding efficiency of the first pass, and the grinding efficiency of the third pass of repetition was higher than that of the second pass, both for Group A with a single grinding time of 10 s and for Group B with a single grinding time of 30 s. Comparing the Groups A and B with different single grinding times, although the grinding efficiency of the first 10 s passive grinding (B1) was lower than that of the first 30 s passive grinding (A1), the grinding efficiency of the second and third 10 s passive grinding (B2 and B3) was higher than that of the 30 s passive grinding completed in one pass (A1). For a total grinding time of 30 s, the average grinding efficiency was 10 mg/s greater when the passive grinding process was conducted in three times of 10 s than when it was completed in one time of 30 s. In conjunction with the amount of rail removed as seen in Figure 4a, it can be concluded that the passive grinding method with multiple passes helps in enhancing the grinding efficiency.

For the grinding ratio, multi-pass passive grinding with 10 s can improve the grinding ratio of the grinding wheel, whereas multi-pass passive grinding with 30 s cannot considerably improve the grinding ratio of the grinding wheel. This indicates that the short time and multiple passes of passive grinding can effectively extend the service life of high-speed grinding wheels. The passive grinding state of the grinding wheel on the rail

was essentially stable when the single grinding time was 30 s. Multiple passes of passive grinding hence have little effect on the durability performance of the grinding wheel.

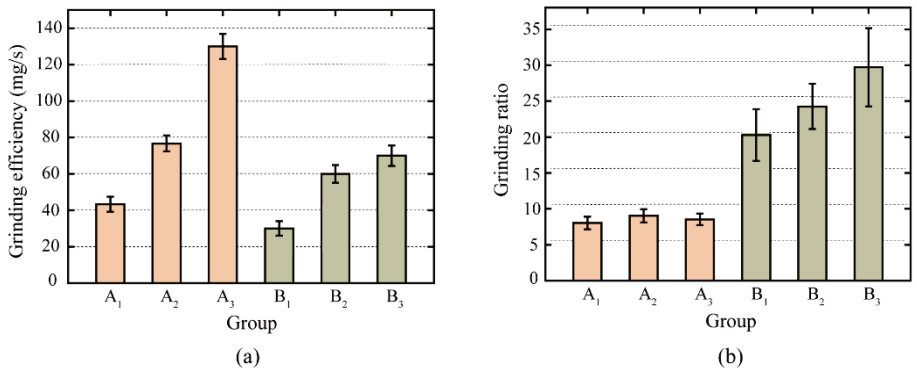

Figure 5. (**a**) Grinding efficiency and (**b**) grinding ratio of grinding wheels at different grinding times.

3.3. Morphology and Roughness of Rail Surface

The surface integrity of rails after grinding is one of the most essential criteria for evaluating grinding quality, as it has a considerable effect on the adhesion characteristics and damage of wheel/rail contact [29]. The surface roughness and grinding marks depth of the rail surface before and after the passive grinding tests were counted, as shown in Figure 6. In addition, the surface morphology and the average state of the three-dimensional profile of the rail samples were visualized, as shown in Figures 7 and 8 respectively. In these figures, Sa and Sz represent the surface roughness and average topographical depth of the rail sample, respectively. After several train rides, rails with good surface roughness from grinding operations would become flat and smooth again [30]. Following a grinding operation, the lower the rail surface roughness and the depth of the grinding marks, the better it is to restore the rail from the grinding profile to the conventional smooth profile. The subsequent use of rail will be harmed if the surface roughness of the rail is excessive or the depth of grinding marks are too deep [31].

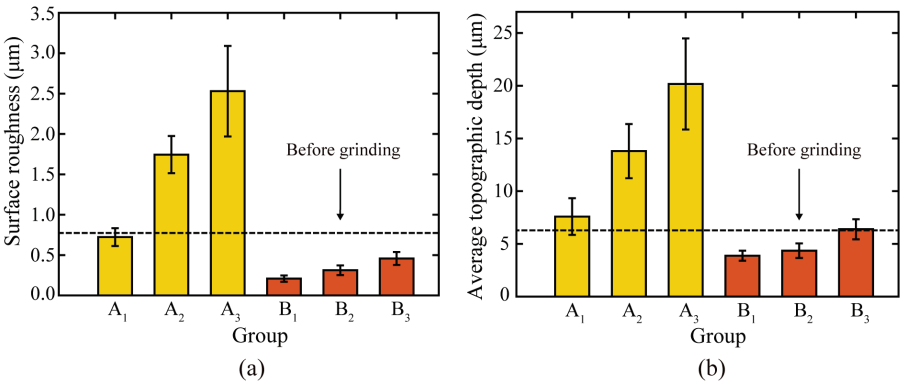

Figure 6. (**a**) Average roughness of rail samples surface and (**b**) average wear depth of grinding marks.

Through independent analysis of Groups A and B, it was found that the surface roughness and grinding mark depth of the rail samples rise as the number of grinding passes of the grinding wheel on the rail increases. This indicates that multiple repetitions of passive grinding will continue to change the surface morphology of the rails following passive grinding. A comprehensive comparison of the rail surface grinding results in Group A and Group B reveals that an increase in grinding time will result in an increase in rail surface roughness and grinding mark depth. However, it is noteworthy that differences exist between the surface morphology and surface quality of Group B_3 rail samples that have been passively ground three times for 10 s and Group A_1 rail samples that have been

passively ground only once for 30 s. Even though the total grinding duration was the same at 30 s, the average surface roughness and average grinding mark depth of the rail samples in Group B_3 with three grinding passes of 10 s were 0.46 μm and 6.39 μm, respectively, while they were 0.72 μm and 7.96 μm in Group A_1 with one grinding pass of 30 s. The surface roughness and average grinding mark depth of the rail samples in Group B_3 were lower than those in Group A_1, indicating that the short time and multiple passes grinding strategy improved the grinding quality.

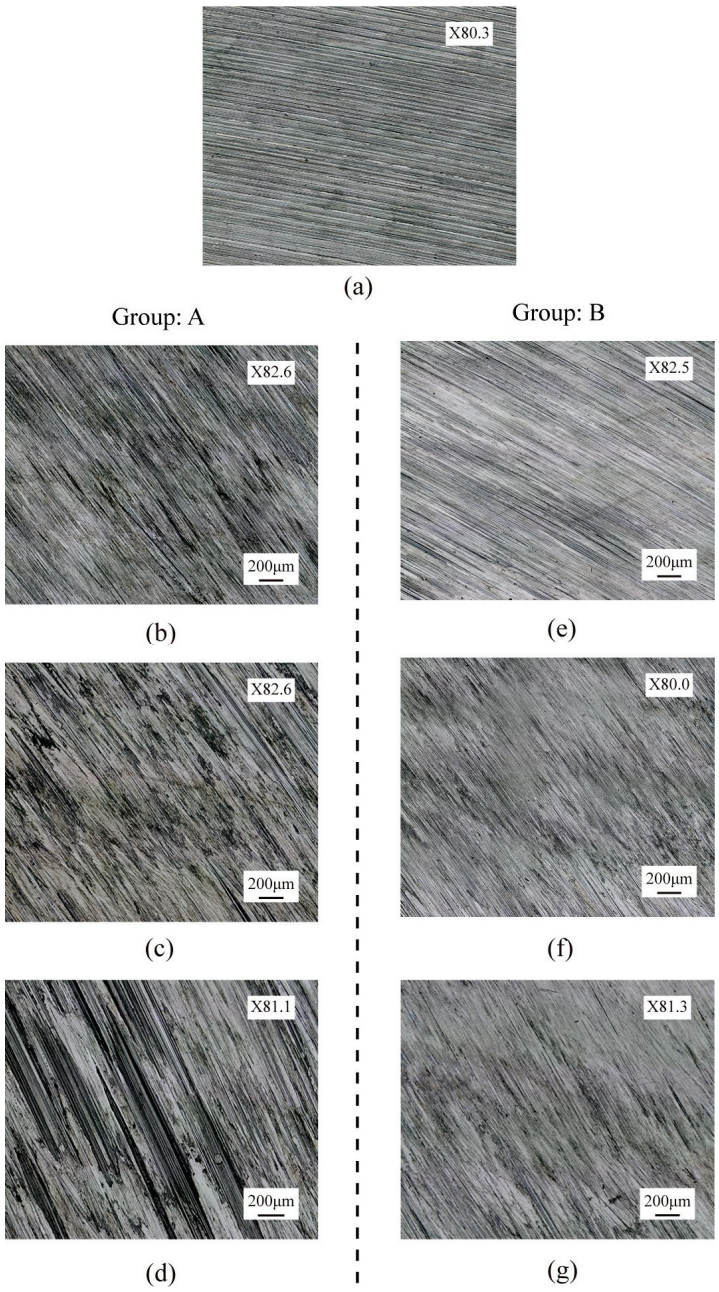

Figure 7. Optical morphologies of rail samples: (**a**) before grinding; (**b**) 30 s first grinding (A_1); (**c**) 30 s second grinding (A_2); (**d**) 30 s third grinding (A_3); (**e**) 10 s first grinding (B_1); (**f**) 10 s second grinding (B_2); (**g**) 10 s third grinding (B_3).

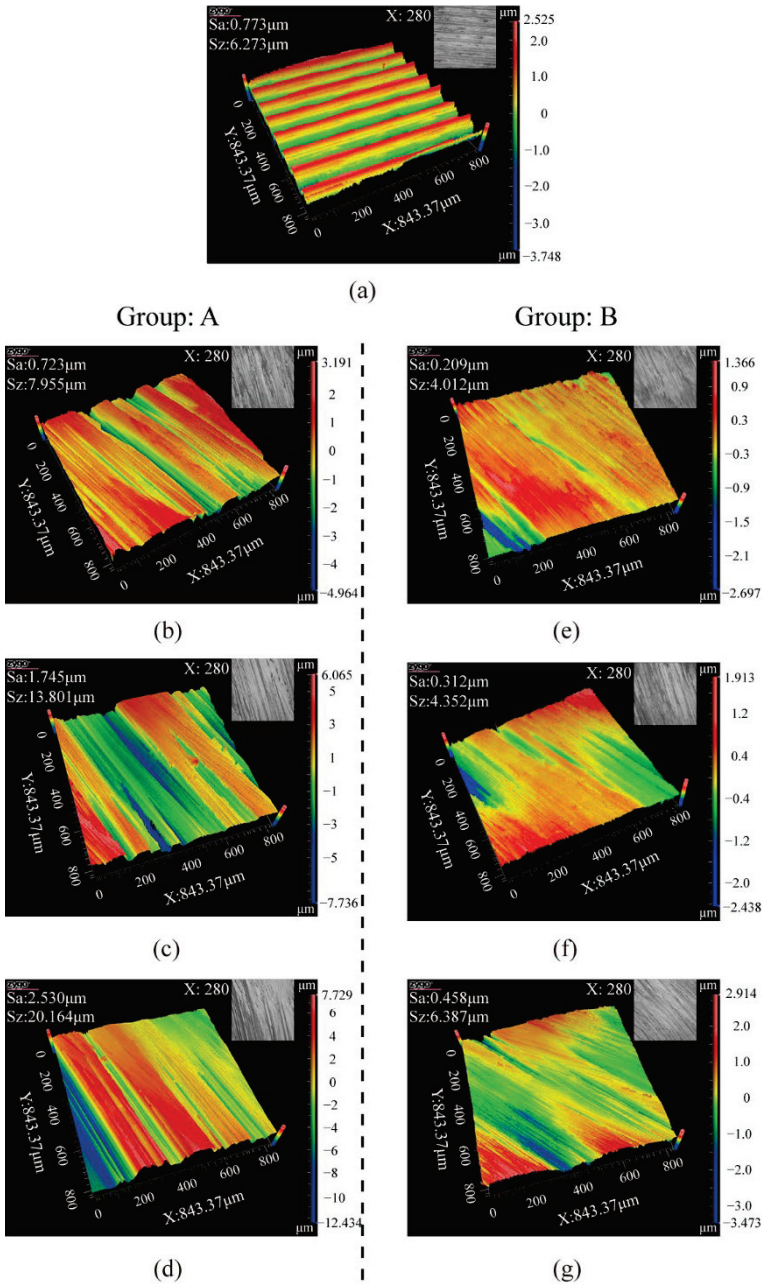

Figure 8. 3D profile of rail sample surfaces: (**a**) before grinding; (**b**) 30 s first grinding (A_1); (**c**) 30 s second grinding (A_2); (**d**) 30 s third grinding (A_3); (**e**) 10 s first grinding (B_1); (**f**) 10 s second grinding (B_2); (**g**) 10 s third grinding (B_3).

3.4. Surface Topography of Grinding Wheel

Figure 9 depicts the surface morphology of the grinding wheel before and after the grinding tests. The surface of the grinding wheel exhibited varying degrees of wear as grinding time and grinding passes increased, and the self-sharpening state of grinding wheels differed as well. Under the conditions of a single grinding time of 10 s, the grinding wheel surface gradually displayed slight wear as the number of grinding passes increased; under the conditions of a single grinding time of 30 s, the wear on the grinding wheel surface tended to become pronounced as the number of grinding passes increased. After 30 s of passive grinding with three passes, visible hole structures emerged on the surface of the grinding wheel, as well as slight wear and self-sharpening of the zirconia abrasive. With the same total grinding time, the wear and self-sharpening degree of the abrasives

on grinding wheel surfaces after three 10 s passive grinding passes were comparable to those after one 30 s passive grinding pass; however, the state of the resin binder and the heat dissipation filler (Pyrite: main component FeS_2) of grinding wheels was significantly different. The filler pyrite was held by the resin binder and dispersed among the abrasives. In the 10 s passive grinding of Group B, the pyrite filler (FeS_2) in the grinding wheel was depleted gradually as the number of grinding passes increased, and the loss of pyrite in the grinding wheel after three passes of 10 s passive grinding was significantly greater than that after a single pass of 30 s passive grinding. In contrast, only a small amount of pyrite filler was lost in the grinding wheel during the first 30 s of passive grinding for Group A. The pyrite was gradually depleted as the number of 30 s passive grinding passes increased, and due to the disintegration of the oxidation process, holes appeared in the structure of the grinding wheel after the second and third passive grinding passes. These holes will increase the wear and cracking of the phenolic resin binder during the grinding process, resulting in a bigger hole structure on the grinding wheel surface, which in turn accelerates the wear and self-sharpening of the grinding wheel.

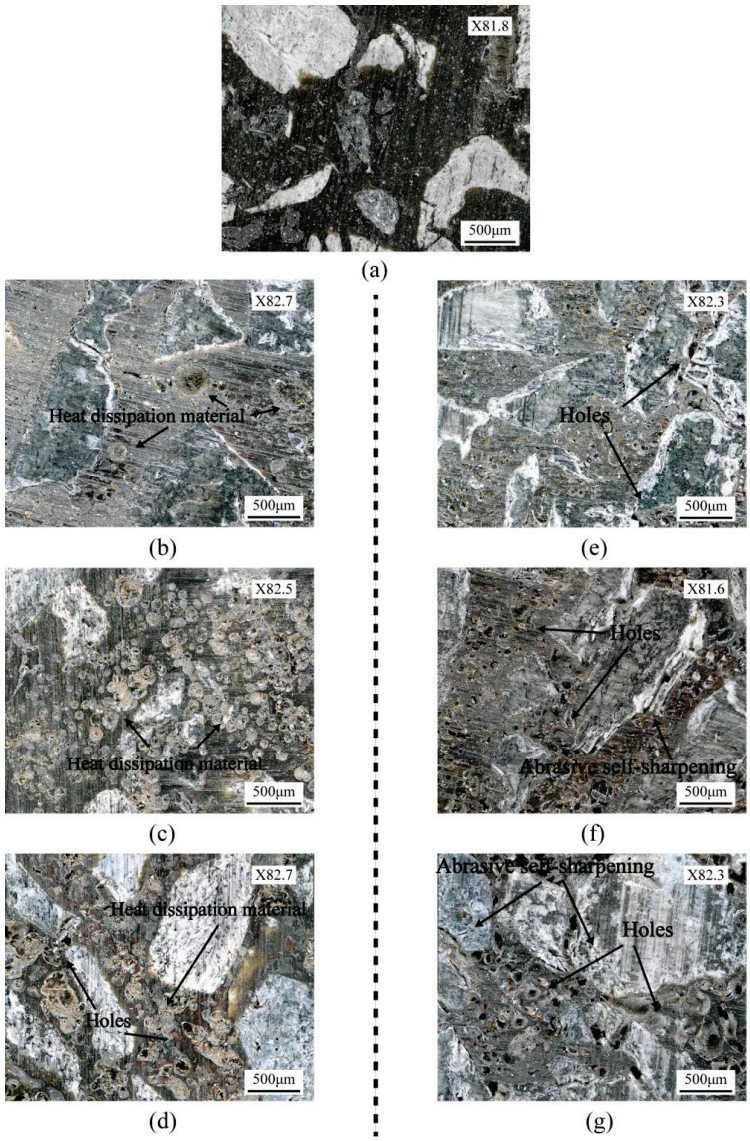

Figure 9. The surface of grinding wheel samples: (**a**) before grinding; (**b**) after the first pass of 10 s passive grinding (B_1); (**c**) after the second pass of 10 s passive grinding (B_2); (**d**) after the third pass of 10 s passive grinding (B_3); (**e**) after the first pass of 30 s passive grinding (A_1); (**f**) after the second pass of 30 s passive grinding (A_2); (**g**) after the third pass of 30 s passive grinding (A_3).

Pyrite (FeS_2) is frequently used as a filler in the manufacturing of high-speed rail grinding wheels. In order to minimize rail oxidation and burning caused by grinding, one of its primary roles is to reduce the transiently high temperatures generated during the grinding operation. Pyrite absorbs grinding heat and combines with oxygen to break down into ferric oxide (Fe_2O_3) and sulfur dioxide (SO_2), as shown in Equation (2).

$$4FeS_2 + 11O_2 \xrightarrow{grinding\ heat} 2Fe_2O_3 + 8SO_2 \quad (2)$$

The surface morphology of the grinding wheel after grinding indicates that the phase in which pyrite exerts its heat absorption effect is primarily concentrated during the initial phase of passive grinding. Since the dry grinding process without grinding fluid has just begun at this stage, a substantial amount of grinding heat will be produced, resulting in a high immediate temperature. The pyrite will then absorb the grinding heat and react with oxygen to lower the grinding temperature. As the grinding process continues, the vast amount of grinding debris formed in the grinding process will absorb a portion of the grinding heat, while the grinding heat will progressively conduct and diffuse to the outside world via media such as the rail, grinding wheel, and air. This causes the grinding heat to begin to gradually accumulate, resulting in a steady increase in grinding temperature, as opposed to continuing to produce a large amount of sudden high temperature. This change will moderately delay the oxidation reaction rate of pyrites, resulting in the pyrite's progressive depletion when the grinding temperature is kept increasing.

3.5. Grinding Force

The grinding forces of the grinding wheels on the rail samples in each test group are shown in Figure 10. According to the figure, the grinding force rose as the number of grinding passes increased for both a single grinding time of 10 s and a single grinding time of 30 s. Contrasting the grinding forces of Group A_1 and Group B for the same total grinding time of 30 s reveals that the average grinding forces of Groups B_1, B_2, and B_3 were marginally higher than those of Group A_1 in the first 10 s, middle 10 s, and final 10 s of the grinding process, respectively. Moreover, the change trend of grinding force was more stable in Group B than in Group A_1. These reasons make the grinding effect of rail samples by high-speed grinding wheels in Group B better than in Group A_1, and explain why the intermittent and short-time passive grinding process can make the grinding process of the grinding wheel on the rail more stable. In addition, the grinding forces of A_2 and A_3 in Group A fluctuated, particularly in the second half of the grinding time exceeding 15 s. Comparing the three 30 s passive grinding tests in Group A (A_1, A_2, and A_3), the grinding force in Group A_2 increased slightly relative to Group A_1, whereas the grinding force in Group A_3 increased significantly relative to Group A_2. For these reasons, the comprehensive performance of the passive grinding force in three passes of 10 s grinding time was better than that after one pass of 30 s. Not only was the maximum value of the grinding force (43.39 N) in three passes of 10 s higher than the maximum value of the grinding force (42.41 N) in one pass of 30 s, but also the stability of the grinding force was better. The maximum value of the grinding force in the third pass of 30 s grinding time was 50.35 N, which was greater than the value of 43.99 N in the second pass of 30 s grinding time and the value of 42.41 N in the first pass of 30 s grinding time. Nevertheless, its stability was weaker, which could negatively impact the rail grinding results.

In general, the grinding force of high-speed grinding wheels on rails in Groups A_1, A_2, and A_3 exhibited an upward trend as the number of grinding passes and cumulative grinding time increased. When the grinding wheel produces more and deeper grinding marks on the rail surface, the average grinding area of the abrasive decreases during passive grinding. Therefore, more energy is required to cut off a unit volume of rail material, which is macroscopically presented as an increase in grinding force. This relates to the dimensional effect of the grinding force of the grinding wheel. In addition, the surface state of the rail in 3.3 shows that the surface roughness and the depth of grinding marks of the rail exhibit

a trend of first decreasing and then increasing with the increase of grinding passes and the accumulation of grinding time. This indicates that the grinding force generated by the grinding wheel on the rail during passive grinding is proportional to the rail surface roughness after surface defects are removed, namely, the higher the rail surface roughness, the greater the grinding force generated by the grinding wheel on the rail during passive grinding.

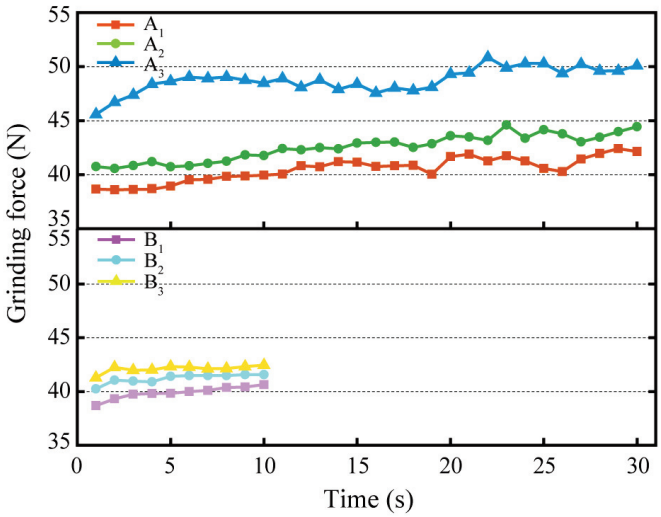

Figure 10. Grinding forces of grinding wheels on rail samples under different grinding times.

3.6. Grinding Temperature

Figure 11 illustrates the grinding temperatures of the grinding wheel on the rail samples under varied grinding time conditions. As can be seen, there are also variations in the grinding temperatures for different grinding times and grinding passes.

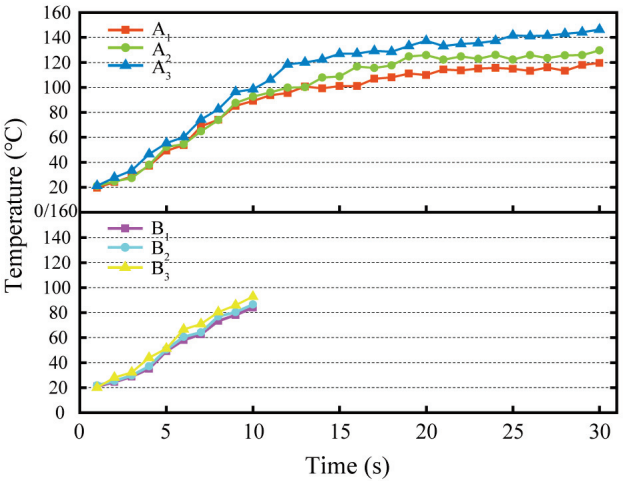

Figure 11. Grinding temperature of rail samples by grinding wheels under different grinding times.

Grinding time is one of the influential factors on rail grinding temperature. The longer the grinding time, the more the grinding heat accumulates, resulting in a higher grinding temperature. In addition, as the number of grinding passes increases, the grinding temperature rises faster and is higher at the same point in time. At the end of the third pass of 30 s grinding, the highest grinding temperature of 148.4 °C in the six groups of grinding tests was exhibited. The variation of rail grinding temperature with time for rail grinding

wheels is related to the energy consumed to remove a unit volume of metal, i.e., the specific grinding energy (E_s), as shown in Equation (3) [32].

$$E_s = \frac{v_s F_t}{v_w a_p b} \tag{3}$$

In the formula, vs. is the linear velocity of grinding wheel (m/s), F_t is the grinding force (N), v_w is the linear velocity of rail sample (m/s), a_p is the grinding depth, and b is the grinding width. The higher the grinding force, the greater the specific grinding energy of passive grinding, which generates more grinding heat and accelerates the rate at which the grinding temperature rises. Even though the grinding temperature increased with grinding time and the number of grinding passes, the maximum grinding temperature did not exceed 400 °C in any of the grinding test groups, which was below the oxidation burn temperature of the rail material [24]. As seen in Figure 7, there is no "blue" or "yellow" rail oxidation burn exhibited on the ground of rail samples. Burning of the rail surface during the active rail grinding process is common [16]. Monitoring results of grinding temperature demonstrate that the passive high-speed rail grinding procedure is less likely to cause rail burn due to grinding maintenance than the active rail grinding process.

3.7. Comprehensive Evaluation and Analysis

According to the high-speed grinding conditions of rails, three passes of passive grinding tests with 30 s grinding time in Group A and 10 s grinding time in Group B were designed to investigate the effects of a single grinding time and the number of grinding passes on grinding wheel performance and passive grinding results. As stated in the introduction, the essence of increasing the number of passive grinding passes is to extend the grinding time of the grinding wheel on the rails in an alternative manner. Nevertheless, based on the results of the grinding tests, even if the total grinding time is the same, the grinding performance of the grinding wheels and the passive grinding results of the rail in multiple grinding passes are relatively distinct from those in a single grinding pass.

Independent analysis of the Group A grinding test results revealed that the grinding efficiency, rail removal in a single pass, grinding temperature, surface roughness of the rail samples after the grinding tests, and depth of the grinding marks increased as the number of rail grinding passes increased, even though the other grinding parameters such as grinding time, grinding pressure, and grinding speed remained unchanged. This is related to the grinding state of the grinding wheel on the rails. Insufficient grinding time prevents the passive grinding behavior of grinding wheels on the rail from reaching a stable peak condition. In the three passes of 30 s of passive grinding, the grinding ratio of the grinding wheel stabilized, but the surface roughness of the rail samples and the grinding force increased with each additional pass. This change can be regarded as a continuation of the grinding state taking over the rail grinding again after the last time rail passive grinding. The continuity of the values for grinding force and rail surface roughness across various grinding passes demonstrates this point. And the grinding test results indicated that the passive grinding for 3 passes of 30 s improved the grinding efficiency without affecting the service life of the grinding wheels, which is advantageous for increasing the amount of rail grinding and can be used for grinding maintenance of the rail surface with severe damage.

Comparing the grinding test results of Group A_1 with those of Groups B_1, B_2, and B_3, it was discovered that, under the same conditions of total grinding time and remaining grinding parameters, the grinding performance of the grinding wheels and the grinding results of the rail samples were slightly different when the 30 s of passive grinding was completed in one pass versus when it was completed in three passes of 10 s. Not only were the surface roughness and grinding mark depth of the rail sample after the third 10 s of passive grinding lower than those after the first 30 s of passive grinding, but the total grinding removal of the rail after the three 10 s passive grinding passes was slightly greater than that after the first 30 s of passive grinding, and the total grinding wheel wear was

also lower after the third 10 s of passive grinding pass. Equation (4) displays the empirical formula for grinding efficiency per unit time [33].

$$Q_w = \frac{v_s \cdot \sqrt[x]{F_t}}{f} \tag{4}$$

In the formula, Q_w is the grinding efficiency per unit time (mg/s), vs. is the linear velocity of grinding wheel (m/s), F_t is the grinding force (N), and x and f are the grinding constants. According to Figure 10, the grinding forces of Groups B_1, B_2, and B_3 are somewhat higher than those of Group A_1 at the corresponding grinding time node. Consequently, Equation (4) demonstrates that the grinding efficiency and total rail removal of multi-pass passive grinding are higher than those of single-pass passive grinding. In addition, the grinding forces of Group A_1 in the final 10 s of grinding fluctuated significantly, while the grinding forces of Groups B_1, B2, and B3 in the three passes of 10 s grinding tests were relatively stable. This indicates that the short-time state of passive grinding is more steady. Furthermore, the monitoring results of the grinding temperature revealed that although the maximum grinding temperature increased after each 10 s of passive grinding, the grinding temperature after 30 s of passive grinding was higher than that of all 10 s of passive grinding tests. This is due to the accumulation of grinding heat caused by the continuous grinding on the one hand, and the filler (Pyrite/FeS_2) of the rail grinding wheel on the other hand. The accumulation of grinding heat caused by prolonged dry grinding accelerates the wear of the grinding wheels. This would not only shorten the service life of the grinding wheel but also limit its grinding performance, thus diminishing the grinding quality of the wheel on the rail [28,34]. For the implementation of preventive grinding of rails, a short-time grinding program of 1 or 3 passes is reasonable because the low degree of rail disease does not require a large amount of rail grinding.

In conclusion, the passive grinding operation with the short time and multiple passes is conducive to the performance of the passive grinding, improving the grinding efficiency of the rail within the same grinding time, optimizing the grinding quality of the grinding wheel to the rail, and extending the service life of the grinding wheel.

4. Conclusions

This study investigated the effects of grinding time and number of grinding passes on the grinding efficiency, rail grinding effect, and service life of grinding wheels of the passive grinding process, as well as their underlying principles, under the conditions of a constant relative rail motion speed and grinding wheel deflection angle. The main conclusions are as follows:

1. The passive rail grinding strategy of repetitions with three passes is conducive to overcoming the challenge that the grinding removal and rail surface roughness cannot reach the desired level during the high-speed rail grinding process to achieve the expected rail grinding objective.
2. When the total grinding time was thirty seconds, the grinding removal and rail surface roughness of the passive grinding performed in three passes of ten seconds were better than those of the passive grinding completed in one pass of thirty seconds. It indicates that the passive grinding mode with short time and multiple passes improves the grinding efficiency of the high-speed rail grinding process and the rail grinding quality compared to completing the rail grinding operation in a single pass.
3. The maximum grinding temperature at the conclusion of the testing was 148.4 °C, which is lower than the initial temperature of 400 °C at which the rail produces oxidation burns. Due to the fast relative motion speed of grinding wheels and rails, high-speed grinding of rails does not easily cause apparent oxidation burns on the rail surface.
4. Three passes of intermittent grinding for ten seconds provide a greater grinding ratio, lower grinding temperature, and more steady grinding force than one pass of single

grinding for thirty seconds. It reveals that the short-time and multiple-pass passive grinding mode can reduce the accumulation of grinding heat, slow the wear of the grinding wheel to extend its service life, and stabilize the grinding process of the grinding wheel on the rail.

Author Contributions: P.L.: validation, software, formal analysis, methodology, visualization, investigation, data curation, writing—original draft, supervision, and editing. W.Z. and J.P.: resources, funding acquisition, project administration. F.X.: conceptualization. All the authors confirm that the manuscript has been read and approved, and the order of authors listed in the manuscript has been approved by all of the authors. All authors have read and agreed to the published version of the manuscript.

Funding: This research was funded by Science and Technology Department of Henan Province, grant number No. 181200212000. The study did not involve humans or animals.

Data Availability Statement: The datasets used or analyzed during the current study are available from the corresponding author on reasonable request.

Conflicts of Interest: The authors declare that they have no known competing financial interest or personal relationships that could have appeared to influence the work reported in this paper.

References

1. Gao, Y.; Zheng, J. The impact of high-speed rail on innovation: An empirical test of the companion innovation hypothesis of transportation improvement with China's manufacturing firms. *World Dev.* **2020**, *127*, 104838. [CrossRef]
2. Cavallaro, F.; Bruzzone, F.; Nocera, S. Spatial and social equity implications for High-Speed Railway lines in Northern Italy. *Transp. Res. Part A Policy Pract.* **2020**, *135*, 327–340. [CrossRef]
3. Miwa, N.; Bhatt, A.; Morikawa, S.; Kato, H. High-Speed rail and the knowledge economy: Evidence from Japan. *Transp. Res. Part A Policy Pract.* **2022**, *159*, 398–416. [CrossRef]
4. Calzada-Infante, L.; Adenso-Díaz, B.; Carbajal, S.G. Analysis of the European international railway network and passenger transfers. *Chaos Solitons Fractals* **2020**, *141*, 110357. [CrossRef]
5. Li, S.; Li, Z.; Yuan, J. Examining the impact of high-speed railways on land value and government revenue: Evidence from China. *China Econ. Rev.* **2020**, *63*, 101502. [CrossRef]
6. Ma, L.; Guo, J.; Liu, Q.; Wang, W. Fatigue crack growth and damage characteristics of high-speed rail at low ambient temperature. *Eng. Fail. Anal.* **2017**, *82*, 802–815. [CrossRef]
7. Satoh, Y.; Iwafuchi, K. Effect of rail grinding on rolling contact fatigue in railway rail used in conventional line in Japan. *Wear* **2008**, *265*, 1342–1348. [CrossRef]
8. Krishna, V.V.; Hossein-Nia, S.; Casanueva, C.; Stichel, S. Long term rail surface damage considering maintenance interventions. *Wear* **2020**, *460*, 203462. [CrossRef]
9. Gu, K.; Lin, Q.; Wang, W.; Wang, H.; Guo, J.; Liu, Q.; Zhu, M. Analysis on the effects of rotational speed of grinding stone on removal behavior of rail material. *Wear* **2015**, *342*, 52–59. [CrossRef]
10. Mesaritis, M.; Shamsa, M.; Cuervo, P.; Santa, J.; Toro, A.; Marshall, M.; Lewis, R. A laboratory demonstration of rail grinding and analysis of running roughness and wear. *Wear* **2020**, *456*, 203379. [CrossRef]
11. Tian, Q.; Wang, H. Optimization of preventive maintenance schedule of subway train components based on a game model from the perspective of failure risk. *Sustain. Cities Soc.* **2014**, *81*, 103819. [CrossRef]
12. Reddy, V.; Chattopadhyay, G.; Larsson-Kråik, P.-O.; Hargreaves, D.J. Modelling and analysis of rail maintenance cost. *Int. J. Prod. Econ.* **2007**, *105*, 475–482. [CrossRef]
13. Von Diest, K. High Speed Grinding: Evolution of the established technology. *Chron. Railw. Technol.* **2015**, *64*, 54–57.
14. Von Diest, K.; Meyer, R. German turnouts get the high-speed grinding treatment. *Int. Railw. J.* **2016**, *56*, 36–38.
15. Liu, P.-Z.; Zou, W.-J.; Peng, J.; Song, X.-D.; Xiao, F.-R. Study on the Effect of Grinding Pressure on Material Removal Behavior Performed on a Self-Designed Passive Grinding Simulator. *Appl. Sci.* **2021**, *11*, 4128. [CrossRef]
16. Liu, P.-Z.; Zou, W.-J.; Peng, J.; Song, X.-D.; Xiao, F.-R. Designed a Passive Grinding Test Machine to Simulate Passive Grinding Process. *Processes* **2021**, *9*, 1317. [CrossRef]
17. Vossloh, A.G. HSG-2 Grinding Train—80 km/h and in Sync with the Timetable. Available online: https://www.vossloh.com/en/products-and-solutions/product-finder/product_20609.php (accessed on 7 September 2021).
18. Grassie, S.L. Rolling contact fatigue on the British railway system: Treatment. *Wear* **2005**, *258*, 1310–1318. [CrossRef]
19. Singleton, R.; Marshall, M.B.; Lewis, R.; Evans, G. Rail grinding for the 21st century—Taking a lead from the aerospace industry. *Proc. Inst. Mech. Eng. Part F J. Rail Rapid Transit* **2014**, *229*, 457–465. [CrossRef]
20. Von Diest, K.; Ferrarotti, G.; Kik, W.; Neto, A.C. Wear Analysis of the High-Speed-Grinding Vehicle HSG-2: Validation, Simulation and Comparison with Measurements. In *The Dynamics of Vehicles on Roads and Tracks*; CRC Press: Boca Raton, FL, USA, 2017; pp. 925–930.

21. Von Diest, K.; Puschel, A. High speed grinding—Railway noise reduction through regular rail grinding without traffic interruptions. In Proceedings of the Inter-Noise and Noise-Con Congress and Conference Proceedings 2013, Innsbruck, Austria, 15–18 September 2013.
22. Bedoya-Zapata, A.; León-Henao, H.; Mesaritis, M.; Molina, L.; Palacio, M.; Santa, J.; Rudas, J.; Toro, A.; Lewis, R. White Etching Layer (WEL) formation in different rail grades after grinding operations in the field. *Wear* **2022**, *502*, 204371. [CrossRef]
23. Mohammadi, R.; He, Q. A deep reinforcement learning approach for rail renewal and maintenance planning. *Reliab. Eng. Syst. Saf.* **2022**, *225*, 108615. [CrossRef]
24. Lin, B.; Zhou, K.; Guo, J.; Liu, Q.; Wang, W. Influence of grinding parameters on surface temperature and burn behaviors of grinding rail. *Tribol. Int.* **2018**, *122*, 151–162. [CrossRef]
25. Zhang, S.; Zhou, K.; Ding, H.; Guo, J.; Liu, Q.; Wang, W. Effects of Grinding Passes and Direction on Material Removal Behaviours in the Rail Grinding Process. *Materials* **2018**, *11*, 2293. [CrossRef]
26. Wu, H.; Xiao, B.; Xiao, H.; Xiao, B.; Yan, X.; Liu, S. Wear characteristics of brazed diamond sheets with different grinding time. *Wear* **2019**, *432*, 202942. [CrossRef]
27. Lu., Z.W. Selection of rail materials for high-speed railway. *China Railw.* **2004**, *10*, 35–38. (In Chinese) [CrossRef]
28. Liu, P.-Z.; Yao, Y.; Zou, W.-J.; Peng, J.; Song, X.-D.; Xiao, F.-R. Design of a CBN composite abrasive to improve the performance of HSG rail maintenance grinding wheel. *Constr. Build. Mater.* **2022**, *319*, 126073. [CrossRef]
29. Zhou, K.; Ding, H.; Wang, W.; Wang, R.; Guo, J.; Liu, Q. Influence of grinding pressure on removal behaviours of rail material. *Tribol. Int.* **2019**, *134*, 417–426. [CrossRef]
30. Cuervo, P.; Santa, J.; Toro, A. Correlations between wear mechanisms and rail grinding operations in a commercial railroad. *Tribol. Int.* **2015**, *82*, 265–273. [CrossRef]
31. Magel, E.; Roney, M.; Kalousek, J.; Sroba, P. The blending of theory and practice in modern rail grinding. *Fatigue Fract. Eng. Mater. Struct.* **2003**, *26*, 921–929. [CrossRef]
32. Hwang, T.; Malkin, S. Upper bound analysis for specific energy in grinding of ceramics. *Wear* **1999**, *231*, 161–171. [CrossRef]
33. Malkin, S. *Grinding Technology-Theory and Applications of Machining with Abrasives*; Wiley: New York, NY, USA, 1989. [CrossRef]
34. Wu, H.; Xiao, B.; Xiao, H.; Zhang, Y.; Dou, L. Study on wear characteristics of brazed diamond sheet for rail's composite grinding wheel under different pressures. *Wear* **2019**, *424*, 183–192. [CrossRef]

micromachines

MDPI

Article

Study on the CBN Wheel Wear Mechanism of Longitudinal-Torsional Ultrasonic-Assisted Grinding Applied to TC4 Titanium Alloy

Junli Liu, Zhongpeng Liu, Yanyan Yan * and Xiaoxu Wang

School of Mechanical and Power Engineering, Henan Polytechnic University, Jiaozuo 454003, China
* Correspondence: yyy@hpu.edu.cn

Abstract: In this study, the CBN (cubic boron nitride) wheel wear model of TC4 titanium alloy in longitudinal-torsional ultrasonic-assisted grinding (LTUAG) was established to explore the grinding wheel wear pattern of TC4 titanium alloy in LTUAG and to improve the grinding efficiency of TC4 titanium alloy and the grinding wheel life. The establishment of the model is based on the grinding force model, the abrasive surface temperature model, the abrasive wear model, and the adhesion wear model of TC4 titanium alloy in LTUAG. The accuracy of the built model is verified by the wheel wear test of TC4 titanium alloy in LTUAG. Research has shown that the grinding force and grinding temperature in LTUAG increase with the increase of the grinding depth and workpiece feed rate and decrease with the increase of the longitudinal ultrasonic amplitude. It also shows that the grinding force gradually decreases with the increase of the grinding wheel speed, while the grinding temperature gradually increases with the increase of the grinding wheel speed. In addition, the use of LTUAG can significantly reduce the wear rate of the grinding wheel by 25.2%. It can also effectively reduce the grinding force and grinding temperature.

Keywords: TC4 titanium alloy; longitudinal-torsional ultrasonic grinding; grinding force; grinding temperature; grinding wheel wear

Citation: Liu, J.; Liu, Z.; Yan, Y.; Wang, X. Study on the CBN Wheel Wear Mechanism of Longitudinal-Torsional Ultrasonic-Assisted Grinding Applied to TC4 Titanium Alloy. *Micromachines* **2022**, *13*, 1480. https://doi.org/10.3390/mi13091480

Academic Editors: Jiang Guo, Chunjin Wang and Chengwei Kang

Received: 6 August 2022
Accepted: 30 August 2022
Published: 6 September 2022

1. Introduction

Since its inception in the middle of the last century, titanium alloy has been used as an ideal material for key spacecraft components such as space shuttle skins and compressor blades because of its excellent physical properties, such as corrosion resistance, heat resistance, fatigue resistance, and high specific strength [1–4]. However, the hardness and strength of titanium alloy are high, and the coefficient of thermal conductivity is poor, so the cutting performance is poor. The large cutting force and cutting temperature also lead to the poor surface quality of the workpiece, and the tool wear is more serious, which affects the promotion and application of titanium alloy material. In recent years, the ultrasonic-assisted grinding technology developed by combining conventional grinding technology and ultrasonic vibration processing technology has exhibited characteristics such as instantaneous effect, intermittent contact, high-frequency cutting, and so on, which have a positive effect on reducing the grinding force, grinding heat, and wheel wear. Therefore, ultra-precision machining of titanium alloy material can be achieved [5–7]. At the same time, scholars have also conducted related research on the wear of grinding wheels under longitudinal-torsional ultrasonic-assisted grinding (LTUAG) of titanium alloys.

Through a large number of experimental studies, Bhushan [8] classified grinding wheel wear types into mechanical wear, chemical wear, and diffusion wear. Among them, the typical forms of mechanical wear include abrasive wear, plastic wear, and thermal stress fracture. Churi et al. [9] studied the grinding wheel wear mechanism of Ti6Al4V titanium alloy during LTUAG, and the study showed that the diamond grinding wheel wear form of longitudinal ultrasonic vibration grinding of Ti6Al4V titanium alloy is abrasive wear,

abrasive particle shedding, abrasive particle crushing, and binder fracture. Abrasive grains on the edge of the end face of the grinding wheel are more obviously broken and fall off after grinding, and abrasive particles near the center of the wheel end face are less worn.

Qin [10] established a tool wear model for titanium alloy in rotary ultrasonic grinding based on dimensional analysis, which reflects the influence of tool structure parameters, grinding process parameters, and ultrasonic parameters on tool wear. The validity and significance test of the model found that the F distribution value of the model was 45.04, which was much higher than the critical value of the F distribution, indicating that the established tool wear model had a high degree of significance and could predict tool wear to a certain extent. Liu [11] established a finite element model for multi-abrasive rotary ultrasonic grinding of Ti6Al4V titanium alloy, and on this basis, the secondary development of the wear subprogram of Deform software was carried out. Thus, the finite element simulation of the model was realized. The research results show that the wear amount of the grinding wheel under the rotating ultrasonic grinding of Ti6Al4V titanium alloy decreases with the increase of the abrasive particle size and grinding wheel speed and increases with the increase of the abrasive concentration, workpiece feed rate, and ultrasonic frequency. The finite element simulation results are consistent with the variation pattern of the experimental results, thus proving the correctness of the finite element model. Li et al. [12] conducted ordinary grinding and ultrasonic-assisted grinding tests for TC4 titanium alloy. The study found that compared to ordinary grinding, the abrasive debris adhering to the surface of the workpiece after ultrasonic-assisted grinding was significantly reduced, which proved that ultrasonic-assisted grinding can effectively reduce the abrasive debris adhesion phenomenon in the process of titanium alloy grinding and can improve the adhesion and blockage of the grinding wheel surface, thereby improving the surface quality of the TC4 titanium alloy.

To sum up, there is little research on the wheel wear mechanism of titanium alloy ultrasonic-assisted grinding by scholars, and the related research mainly focuses on the grinding wheel wear mechanism under the condition of one-dimensional ultrasonic-assisted grinding, where vibration is applied to the grinding wheel or workpiece. The grinding wheel wear mechanism under the LTUAG of titanium alloy is rarely involved. From this background, TC4 titanium alloy was chosen as the research object, and the LTUAG method was adopted. The grinding wheel wear during LTUAG of TC4 titanium alloy is studied from the perspective of theoretical modeling and experimental research, which is expected to provide a theoretical reference for the high-efficiency precision grinding of TC4 titanium alloy by longitudinal-torsion ultrasonic-assisted grinding.

2. Establishment of a Wheel Wear Model of TC4 Titanium Alloy in LTUAG

2.1. Analysis of Kinematics Characteristics of TC4 Titanium Alloy in LTUAG

The LTUAG system is shown in Figure 1a, which is mainly composed of a longitudinal-torsional ultrasonic vibration system and a ceramic-based CBN (cubic boron nitride) grinding wheel. The longitudinal-torsional ultrasonic vibration system is composed of an ultrasonic generator (working frequency range: 20–50 kHz), a wireless transmission system, a BT40 ultrasonic shank (Huizhuan Technology Group Co., Ltd., Guangzhou, China), a piezoelectric ceramic transducer, and a longitudinal-torsion ultrasonic vibration amplitude transformer. According to Figure 1b, and assuming that the workpiece is stationary relative to the grinding wheel, the movement of the abrasive particles on the surface of the grinding wheel during LTUAG includes the feed movement along the x-axis with a speed of v_w, the motion work in the xoy plane includes rotational motion around the z-axis with a rotational speed of n, a torsional ultrasonic vibration with an amplitude of b, and a longitudinal ultrasonic vibration with an amplitude of a along the z-axis.

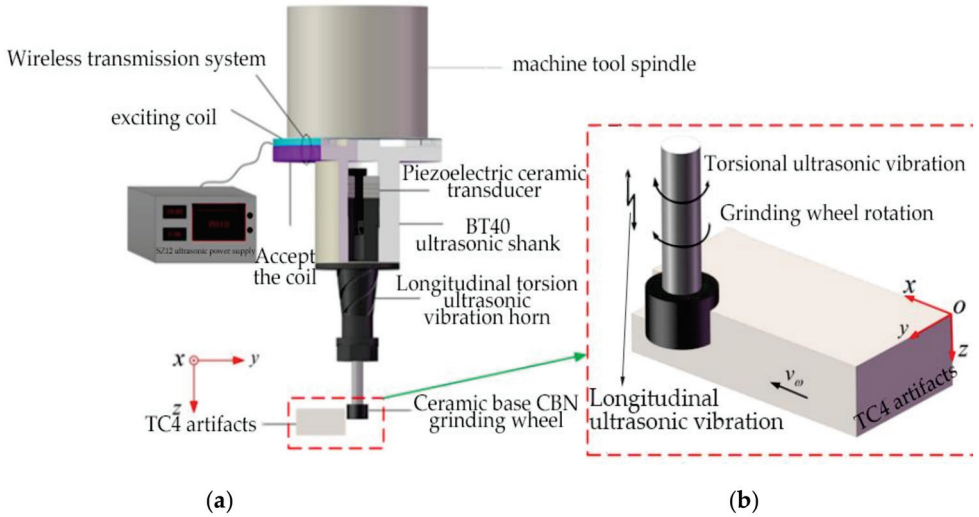

Figure 1. Schematic diagram of the longitudinal-torsional ultrasonic-assisted grinding (LTUAG) system and its motion model. (**a**) Schematic diagram of the grinding system in LTUAG. (**b**) Schematic diagram of the motion model in LTUAG.

To facilitate the analysis of the kinematic characteristics of abrasive particles, it is assumed that the workpiece material is uniform and isotropic, the abrasive particles on the surface of the grinding wheel are uniformly distributed in the longitudinal and axial directions, and the frequency and output amplitude of the longitudinal-torsional ultrasonic vibration system remain stable during the machining process. According to the coordinate system shown in Figure 1b, the motion of a single abrasive particle during LTUAG can be expressed as:

$$\begin{cases} x(t) = v_w \cdot t + R \cdot sin[\omega tb \cdot sin(2\pi f_b t + \varphi)/R] \\ y(t) = R \cdot cos[\omega t + b \cdot sin(2\pi f_b t + \varphi)/R] \\ z(t) = asin(2\pi f_a t) \end{cases} \tag{1}$$

where v_w is the workpiece feed speed, R is the grinding wheel radius, ω is the grinding wheel angular speed, b is the torsional ultrasonic vibration amplitude, a is the longitudinal ultrasonic vibration amplitude, f_b is the torsional-ultrasonic vibration frequency, f_a is the longitudinal ultrasonic vibration frequency, and φ is the phase difference between longitudinal and torsional vibration.

According to Equation (1), taking the derivative of time, the velocity of a single abrasive particle in LTUAG can be obtained as:

$$\begin{cases} v_x = x\prime(t) = v_w + [\omega R + 2\pi fbcos(2\pi ft + \varphi)]cos\left[\omega t + \frac{b}{R}sin(2\pi ft + \varphi)\right] \\ v_y = y\prime(t) = -[\omega R2\pi fbcos(2\pi ft + \varphi)]sin\left[\omega t + \frac{b}{R}sin(2\pi ft + \varphi)\right] \\ v_z = z\prime(t) = 2\pi fcos(2\pi ft) \end{cases} \tag{2}$$

According to Equation (2), the grinding arc length, l_c, of a single abrasive particle in LTUAG in one vibration cycle can be obtained as:

$$\begin{aligned} l_c &= \int_0^t \sqrt{v_x^2 + v_y^2 + v_z^2}dt \\ &= \int_0^t \sqrt{\begin{array}{c} v_w^2 + 2v_w cos\left[\omega t + \frac{b}{R}sin(2\pi ft + \varphi)\right][\omega R + 2\pi fbcos(2\pi ft + \varphi)] + \\ [\omega R + 2\pi fbcos(2\pi ft + \varphi)]^2 + (2\pi fa)^2 cos^2(2\pi ft) \end{array}} dt \end{aligned} \tag{3}$$

When $a = b = 0$, according to Equation (3), the ordinary grinding arc length, l_p, of a single abrasive particle can be expressed as:

$$l_p = \int_0^t \sqrt{{v_w}^2 + v_a^2 + 2v_w v_a cos(\omega t)}dt \tag{4}$$

where v_a is the rotational speed of the grinding wheel. According to Figure 2 and Equation (4), the removal volume, V_p, of a single abrasive grain material during ordinary grinding can be obtained as:

$$V_p = S_p l_p = \frac{1}{2}(2u + 2a_p tan\theta)a_p \int_0^t \sqrt{{v_w}^2 + v_a^2 + 2v_w v_a cos(\omega t)}\mathrm{dt} \tag{5}$$

where S_p is the cross-sectional area of ordinary grinding chips.

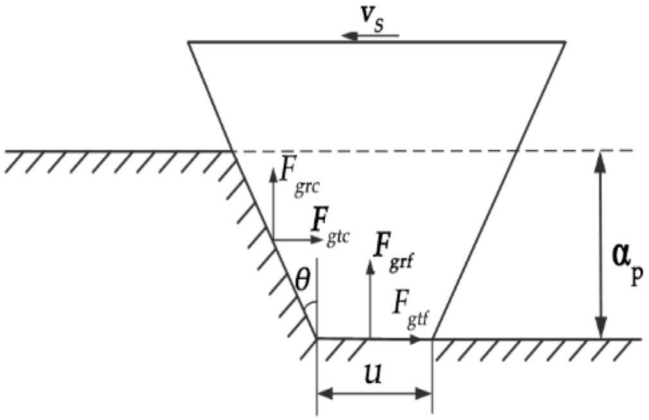

Figure 2. Grinding force model of a single CBN abrasive particle in LTUAG. (In the figure: v_s is the grinding linear speed, a_p is the grinding depth of a single abrasive particle in LTUAG, F_{gtc} is the tangential deformation force for wear debris of a single abrasive particle, F_{gtf} is the tangential friction of a single abrasive particle, F_{grc} is the radial deformation force for wear debris of a single abrasive particle, F_{grf} is the radial friction of a single abrasive particle.).

It can be seen from Equation (3) that the arc length of the single abrasive particle in LTUAG is related to the workpiece feed rate, the linear speed of the grinding wheel, the longitudinal torsional ultrasonic vibration frequency, the longitudinal ultrasonic vibration amplitude, and the torsional ultrasonic vibration amplitude. It can be seen from Equations (3)–(5) that, under the same grinding conditions, the arc length of the single abrasive particle in LTUAG is longer than that in ordinary grinding. This means that LTUAG introduced changes to the grinding mechanism of the single abrasive particle and improved the time for the single abrasive particle to participate in grinding. Therefore, it is beneficial to improve the material removal rate of LTUAG.

2.2. Establishment of a Grinding Force Model for Titanium Alloy in LTUAG

The grinding force and grinding heat generated in LTUAG increase the mechanical stress and thermal stress acting on the surface of the abrasive particle, which exceeds the strength of the abrasive particle and the binding agent itself, which causes the breaking and shedding of abrasive grains, eventually leading to grinding wheel wear. Therefore, the study of the grinding force of titanium alloy in LTUAG is of great significance for the subsequent establishment of the grinding wheel wear model of the titanium alloy in LTUAG. In the study, a single CBN abrasive particle was simplified as a flat-ended quadrangular pyramid. The cross-sectional shape of the abrasive grain can be approximated as an isosceles trapezoid. According to the cross-sectional shape of CBN abrasive grains and the force in LTUAG, the grinding force model of a single CBN abrasive particle in LTUAG was established, as shown in Figure 2.

As shown in Figure 2, the grinding force is mainly composed of two parts: one is the tangential and radial deformation resistance of the abrasive particles acting on the rake face of the abrasive grain, and the other is the tangential and radial friction force between the bottom surface of the abrasive grain and the workpiece surface. The tangential grinding force, F_{gt}, and the radial grinding force, F_{gr}, of a single abrasive particle in LTUAG can be expressed as:

$$\begin{cases} F_{\mathrm{gt}} = F_{gtc} + F_{gtf} \\ F_{gr} = F_{grc} + F_{grf} \end{cases} \tag{6}$$

where F_{gtc} is the tangential deformation force for wear debris of a single abrasive particle, F_{gtf} is the tangential friction of a single abrasive particle, F_{grc} is the radial deformation force for wear debris of a single abrasive particle, and F_{grf} is the radial friction of a single abrasive particle. According to the research of Yan et al. [13], the tangential grinding force, F_{gt}, and radial grinding force, F_{gr}, of a single abrasive particle in LTUAG can be expressed as:

$$\begin{cases} F_{gt} = F_{gtc} + F_{gtf} = \dfrac{\pi F_0 a_p^{2r} \tan^{r-1}\theta \cdot \left(u + a_p \tan\theta\right) a_p \int_0^t \sqrt{{v_w}^2 + v_a^2 + 2v_w v_a \cos(\omega t)}\, dt}{4 \int_0^t \sqrt{v_w^2 + {v_s}^2 + 2v_w v_s \cos\left[\omega t + \frac{b}{R}\sin(2\pi f t + \varphi)\right] + (2\pi f a)^2 \cos^2(2\pi f t)}\, dt} \\ \qquad + \mu k_1 {a_p}^{a_1} k_2 {a_p}^{a_2} \\ F_{gr} = F_{grc} + F_{grf} = \dfrac{F_0 a_p^{2r} \tan^{r}\theta \cdot \left(u + a_p \tan\theta\right) a_p \int_0^t \sqrt{{v_w}^2 + v_a^2 + 2v_w v_a \cos(\omega t)}\, dt}{\int_0^t \sqrt{v_w^2 + {v_s}^2 + 2v_w v_s \cos\left[\omega t + \frac{b}{R}\sin(2\pi f t + \varphi)\right] + (2\pi f a)^2 \cos^2(2\pi f t)}\, dt} \\ \qquad + k_1 {a_p}^{a_1} k_2 {a_p}^{a_2} \end{cases} \tag{7}$$

From Equation (7), it can be seen that the grinding force of a single abrasive particle in LTUAG is related to the grinding depth, a_p, grinding linear speed, v_s, feed speed, v_w, longitudinal ultrasonic amplitude, a, torsional ultrasonic amplitude, b, and longitudinal-torsional ultrasonic vibration frequency, f. During LTUAG, the grinding force increases with the increase of the grinding depth and the feed rate and decreases with the increase of ultrasonic amplitude, grinding linear velocity, and longitudinal-torsional ultrasonic vibration frequency. According to Equations (3) and (4), the grinding arc length of a single abrasive particle in LTUAG is longer than that of a single abrasive particle in ordinary grinding. The grinding force in LTUAG is smaller than that in ordinary grinding under the same grinding conditions.

2.3. Establishment of an Abrasive Particle Surface Temperature Model for TC4 Titanium Alloy in LTUAG

During the LTUAG of TC4 titanium alloy, intense friction is generated between the surface of the abrasive grain and the workpiece, and a large amount of frictional heat is generated, causing the temperature of the workpiece surface and the surface of the abrasive grain to rise, which in turn generates a temperature field on the surface of the abrasive grain and the workpiece, which eventually causes the thermal stress of the abrasive grain to fragment.

Figure 3 shows the surface temperature rise model of a single abrasive particle during LTUAG of TC4 titanium alloy. According to Komanduri et al. [14,15], and assuming that the coordinate of a point in a single abrasive particle is N(x, y, z), then the temperature at the abrasive grain N(x, y, z) can be expressed as:

$$T(x,y,z) = \frac{q_m}{2\pi\lambda_t} \int_0^{L^t} B(s) \int_{-\frac{w}{2}}^{\frac{w}{2}} \left(\frac{1}{R_{ts}} + \frac{1}{R_{ts}\prime} \right) dx_i dy_i \tag{8}$$

where λ_t is the tool's thermal conductivity, q_m is the heat source density, L^t is the fixed heat source's length, $B(s)$ is the proportionality coefficient of grinding heat transfer into the grinding grain generated during grinding, w is the unit cutting width, R_{ts} is the distance from the fixed heat source to a point inside the tool, and $R_{ts}\prime$ is the distance from the mirror image heat source to a point inside the tool.

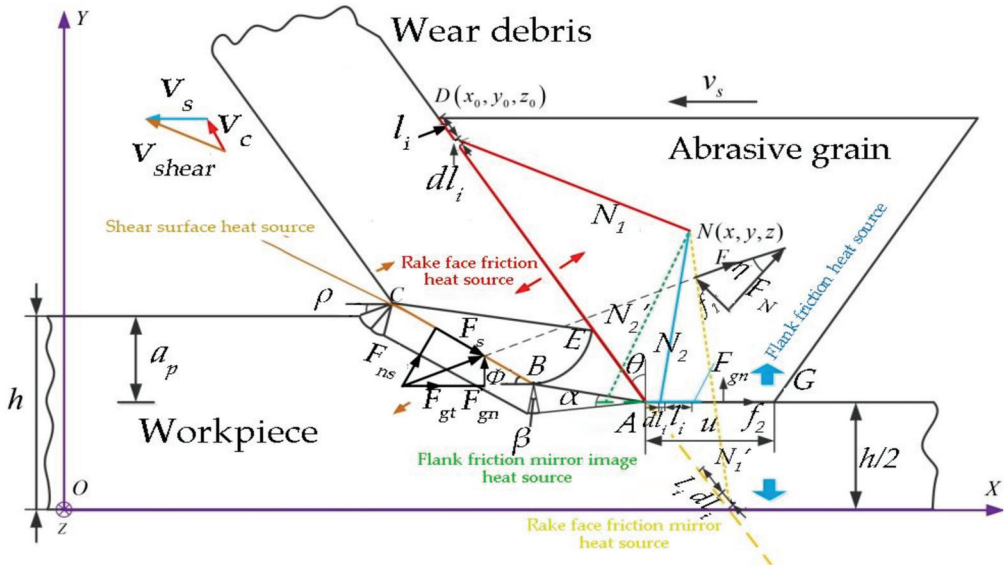

Figure 3. Model of surface temperature rise of a single abrasive particle in LTUAG.

As can be seen from Figure 3, the heat that causes the temperature of the grinding grain to increase during the grinding process is mainly composed of two parts: one is the frictional heat generated by the relative sliding between the rake face of the abrasive particle and the chip, and the other is the frictional heat generated by the relative sliding between the bottom surface of the abrasive particle and the workpiece surface. The shear heat generated by the shear deformation of the workpiece material can only be transferred to the abrasive particle through the path of the shear surface heat source–chip–rake face of the abrasive particle, and the poor thermal conductivity of TC4 titanium alloy material leads to less heat transfer into the grinding grain. Therefore, this study does not consider the influence of the internal shear surface heat source of the workpiece on the surface temperature of the abrasive particles.

According to Figure 3, chip flow velocity, v_c, and the length of the contact surface between abrasive particles and chips, l_{AD}, can be expressed as:

$$\begin{cases} v_c = \frac{v_s sin\phi}{cos(\theta+\phi)} \\ l_{AD} = \frac{a_p sin(\phi+\eta-\theta)}{sin\phi cos\eta} \end{cases} \tag{9}$$

where v_s is the grinding line speed, ϕ is the shear angle, a_p is the grinding depth, and η is the friction angle.

According to Figure 3, combined with Equation (9), the friction heat source density on the rake face and the friction heat source density on the flank face of a single abrasive particle during LTUAG can be obtained (q_{f1}, q_{f2}) as:

$$\begin{cases} q_{f1} = \frac{f_1 \cdot v_c}{w \cdot l_{AD}} = \frac{\left(F_{gt}cos\phi - F_{gr}sin\phi\right)sin(2\eta)sin^2\phi \cdot v_s}{w \cdot a_p sin[2(\phi+\eta-\theta)]cos(\theta+\phi)} \\ q_{f2} = \frac{f_2 \cdot v_s}{w \cdot l_{AG}} = \frac{\mu \cdot F_{gr} \cdot v_s}{w \cdot u} \end{cases} \tag{10}$$

where f_1 is the friction force between the rake face of the abrasive particle and the chip interface, f_2 is the friction force between the flank face of the abrasive particle and the workpiece surface, w is the unit cutting width, l_{AG} is the length of the flank face of the abrasive grain, $l_{AG} = u$, and F_{gt} and F_{gr} are the tangential grinding force and radial grinding force of a single abrasive particle in LTUAG.

It can be seen from Equation (10) that the friction heat source density for the rake face and flank face of a single abrasive particle in LTUAG is related to the tangential grinding

force, F_{gt}, the radial grinding force, F_{gr}, the grinding linear speed, v_s, and the grinding depth, a_p. The friction heat source density on the rake face of the abrasive grain in LTUAG increases with the increase of the tangential grinding force, F_{gt}, radial grinding force, F_{gr}, and grinding linear velocity, v_s, and decreases with the increase of grinding depth, a_p. The friction heat source density of the abrasive flank face increases with the increase of radial grinding force, F_{gr}, and grinding linear velocity, v_s, in LTUAG of a single abrasive particle.

During LTUAG, the heat generated by the friction heat source on the rake face of the abrasive particles is mainly transferred into the abrasive particles and chips, and the heat generated by the friction heat source on the flank face is mainly transferred into the abrasive particles and the workpiece. Therefore, the proportional coefficient, $B(s)$ [16], of the grinding heat into the abrasive grains can be expressed by Equation (11):

$$B(s) = \left(1+0.974k_g / \sqrt{r_0 v_s K_{to} \rho c}\right)^{-1} \tag{11}$$

Substituting Equations (10) and (11) into Equation (8), the temperature of the abrasive particle at N(x, y, z) in LTUAG can be obtained as:

$$\begin{aligned} T_{total} &= T_{f1}+T_{f2}+T_{room} \\ &= \frac{q_{f1}}{2\pi\lambda_t}\int_0^{l_{AD}} B(s)\int_{-\frac{w}{2}}^{\frac{w}{2}}\left(\frac{1}{N_1}+\frac{1}{N_1'}\right)dl_i dz_i + \frac{q_{f2}}{2\pi\lambda_t}\int_0^{l_{AG}} B(s)\int_{-\frac{w}{2}}^{\frac{w}{2}}\left(\frac{1}{N_2}+\frac{1}{N_2'}\right)dl_i dz_i + T_{room} \\ &= \frac{\left(\frac{1+0.974k_g}{\sqrt{r_0 v_s K_{to}\rho c}}\right)^{-1}}{2\pi\lambda_t}\left[\begin{array}{l} \int_0^{l_{AD}} q_{f1}\int_{-\frac{w}{2}}^{\frac{w}{2}}\left(\frac{1}{\sqrt{(x-x_0-l_i sin\theta)^2+(y_0-y-l_i cos\theta)^2+(z-z_i)^2}} + \frac{1}{\sqrt{\left[l_i cos\left(\frac{\pi}{2}-\theta\right)\right]^2+y^2+(z-z_i)^2}}\right)dl_i dz_i \\ + \int_0^{l_{AG}} q_{f2}\int_{-\frac{w}{2}}^{\frac{w}{2}}\left(\frac{1}{\sqrt{(x-x_0-l_{AD}sin\theta-l_i)^2+\left(y-\frac{t}{2}\right)^2+(Z-Z_i)^2}} + \frac{1}{\sqrt{(x-x_0-l_{AD}sin\theta+l_i)^2+\left(y-\frac{t}{2}\right)^2+(z-z_i)^2}}\right)dl_i dz_i \end{array}\right] + T_{room} \end{aligned} \tag{12}$$

where T_{total} is the average temperature inside the abrasive grain, T_{f1} is the temperature rise caused by the friction heat source of the abrasive grain's rake face, T_{f2} is the temperature rise caused by the friction heat source of the abrasive grain's flank face, and T_{room} is the room temperature.

It can be seen from Equation (12) that the temperature at the abrasive particle N(x, y, z) during LTUAG is related to the grinding linear velocity, v_s, and the friction heat source density of the abrasive grain rake face and flank face (q_{f1}, q_{f2}). During the grinding process, the surface temperature of the abrasive grains increases with the increase of the grinding linear velocity, v_s, and the friction heat source density on the rake face and the flank face of the abrasive grains. In addition, according to Equations (7) and (10), the introduction of longitudinal-torsional ultrasonic vibration makes the tangential grinding force and the radial grinding force of a single abrasive particle (F_{gt}, F_{gr}), and the friction heat source of the density of the rake face and flank face of the abrasive grain (q_{f1}, q_{f2}), decrease. To a certain extent, the surface temperature of the abrasive grains is reduced, thereby reducing the influence of the temperature field of the abrasive grain surface on the fatigue wear of the abrasive grains and improving the durability of the grinding wheel.

2.4. Establishment of a Grinding Wheel Wear Model in LTUAG for TC4 Titanium Alloy

Grinding wheel wear of titanium alloy is an extremely complex physicochemical process, and its grinding wheel wear mechanism is relatively diverse. According to the research of scholars [17], the grinding wheel wear mechanism of titanium alloy in the grinding process is mainly abrasive wear and adhesive wear. To more accurately reflect the change of grinding wheel wear of TC4 titanium alloy in the process of LTUAG, the abrasive wear and adhesion wear mechanisms should be comprehensively considered, and a corresponding grinding wheel wear model should be established.

According to the research of Rabinowicz et al. [18,19], the tool wear rate caused by abrasive wear during tool cutting can be expressed as:

$$\frac{dW_{\mathrm{ab}br}}{dt} = Gv_r \tag{13}$$

where $\frac{dW_{abr}}{dt}$ is the tool wear rate caused by abrasion wear, G is the characteristic correlation coefficient of abrasive wear of CBN, and v_r is the workpiece feed rate during cutting.

According to the research of Usui et al. [20], the tool wear rate caused by the adhesive wear of workpiece material in the cutting process can be expressed as:

$$\frac{dW_{adh}}{dt} = A_w v_n p_n exp\left(\frac{-B_w}{T_m}\right) \tag{14}$$

where A_w and B_w are the characteristic correlation coefficients of adhesive wear of CBN, V_n is the relative sliding velocity of the chip contact surface, P_n is the positive pressure of the contact surface between the tool and the workpiece, and T_m is the tool surface temperature during cutting.

According to Figure 3, the positive pressure, F_N, of the abrasive particle face during LTUAG can be expressed as:

$$F_N = \frac{\left(F_{gt}cos\phi - F_{gr}sin\phi\right)cos\eta}{cos(\eta - \theta + \phi)} \tag{15}$$

As the abrasive particle will be chunk-broken, fall off, and binder-broken in both the initial wear stage and the rapid wear stage [21], it has a large impact on wheel wear, while the abrasive particle in the stable wear stage is in the form of abrasive wear and debris adhesion wear, and the abrasive wear rate changes are more stable. Assuming the grinding wheel enters the stable wear stage, the abrasive debris that is not discharged in time gradually fills the entire abrasive grain gap and adheres to the bottom surface of the abrasive grains participating in the grinding, thereby increasing the grinding force and grinding heat of the abrasive grain surface. The abrasive particles begin to break up and wear away. At this time, the abrasive particle breakage caused by the adhesion of abrasive debris is similar to the adhesive wear of the tool.

Substituting Equations (9) and (15) into Equation (14), and adding them to Equation (13) to obtain the grinding wheel wear rate, $r_{wheel}(t)$, of the stable wear stage in LTUAG can be expressed as:

$$\begin{aligned} r_{wheel}(t) &= \frac{dW_{wheel}}{dt} = \frac{dW_{abr}}{dt} + \frac{dW_{adh(ch-t)}}{dt} + \frac{dW_{adh(t-w)}}{dt} \\ &= Gv_w + \left[A_w p_1 v_c exp\left(\frac{-B_w}{T_{f1}}\right) + A_w p_2 v_w exp\left(\frac{-B_w}{T_{f2}}\right)\right] \\ &= Gv_w + A_w\left[\frac{\left(F_{gt}cos\phi - F_{gr}sin\phi\right)sin\phi cos\eta}{cos(\phi + \eta - \theta)\cdot cos(\theta + \phi)v_s} exp\left(\frac{-B_w}{T_{f1}}\right) + F_{gr}v_w exp\left(\frac{-B_w}{T_{f2}}\right)\right] \end{aligned} \tag{16}$$

where $\frac{dW_{adh(ch-t)}}{dt}$ is the bonded wear rate at the interface between abrasive particles and chips, $\frac{dW_{adh(t-w)}}{dt}$ is the bond wear rate between the abrasive bottom surface and the workpiece contact surface, and t is the cutting time.

It can be seen from Equation (16) that the wear rate of the grinding wheel during LTUAG is related to the workpiece feed speed, v_w, the grinding linear speed, v_s, and the tangential grinding force and the radial grinding force of a single abrasive particle in LTUAG (F_{gt}, F_{gr}). The abrasive rake face temperature, T_{f1}, and the abrasive flank temperature, T_{f2}, are also related. It can be seen from Equations (7) and (12) that the grinding force of LTUAG and the surface temperature of abrasive grains increase with the increase of grinding depth and decrease with the increase of ultrasonic amplitude. Therefore, the grinding wheel wear rate of TC4 titanium alloy in LTUAG increases with the increase of the grinding depth and the workpiece feed rate and decreases with the increase of the grinding linear speed and the ultrasonic amplitude.

3. Verification and Analysis of the Grinding Wheel Wear Test of TC4 Titanium Alloy in LTUAG

3.1. Test Conditions and Program

The test platform of TC4 titanium alloy during LTUAG is shown in Figure 4. The test of TC4 titanium alloy during LTUAG was carried out on the VMC850E vertical machining center (Shenyang Shenyi Lathe Manufacturing Co., Ltd., Shenyang, China). The relevant parameters of the VMC850E vertical machining center are shown in Table 1. The longitudinal-torsional ultrasonic vibration system consisting of a wireless transmission device, an ultrasonic tool-holder, a longitudinal-torsional ultrasonic horn, and a ceramic CBN grinding wheel was installed on the spindle of the vertical machining center, and an external SZ12 intelligent ultrasonic generator (Hangzhou Jingzhen Ultrasonic Technology Co., Ltd., Hangzhou, China) to realize longitudinal ultrasonic vibration and torsional ultrasonic vibration of the grinding wheel. The relevant parameters of the SZ12 intelligent ultrasonic generator are shown in Table 2. After that, the grinding force and grinding temperature during the grinding process were collected by the Kistler 9257B dynamometer (Kistler Instrumente AG, Shanghai, China) and the DH5933D fast-response thermocouple acquisition instrument (Jiangsu Donghua Testing Technology Co., Ltd., Jingjiang, China), respectively.

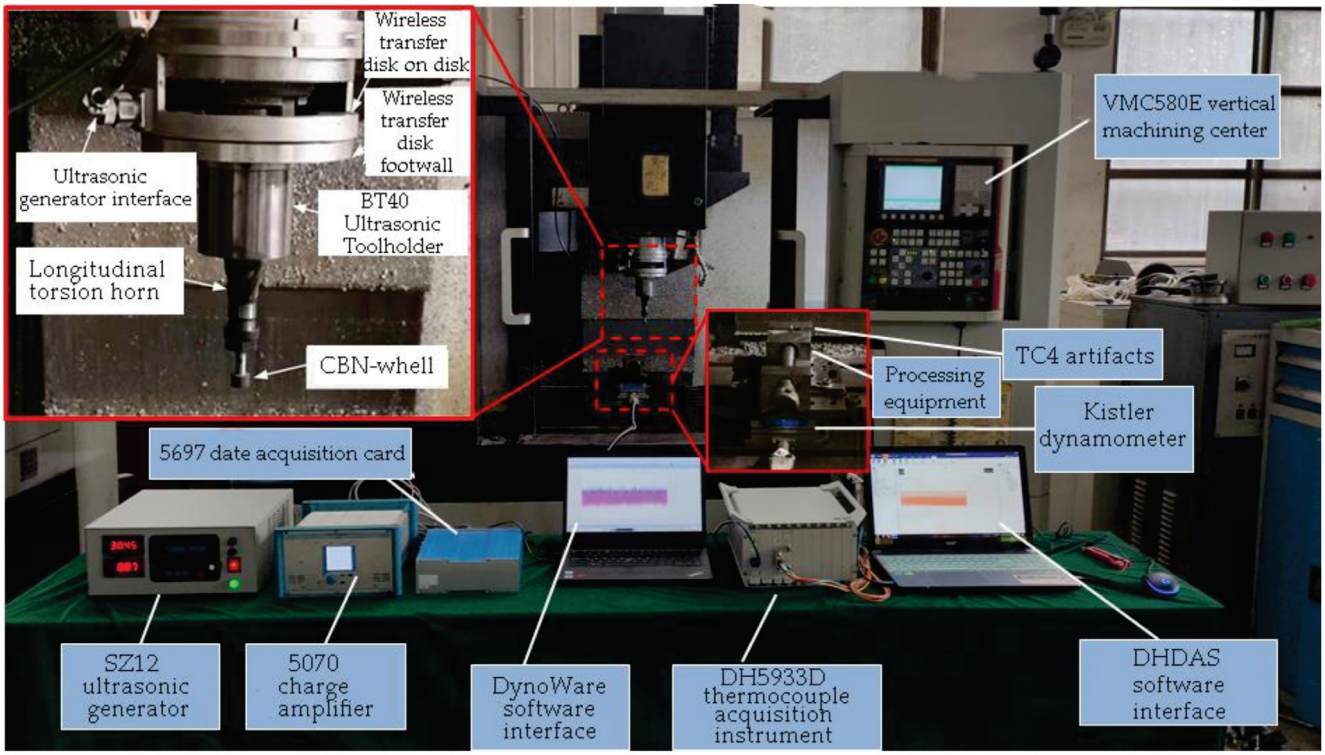

Figure 4. Test platform of TC4 titanium alloy in LTUAG.

Table 1. The parameters of VMC850E machining center performance.

Project	Parameter
The maximum travel of the table (*x*-axis)	850 mm
The maximum travel of the table (*y*-axis)	500 mm
Maximum stroke of spindle (*z*-axis)	540 mm
Range of rotation	50~8000 r/min
Maximum spindle power	11 kW
Maximum output torque	35.8 N·m
Positioning accuracy	0.005 mm

Table 2. Performance parameters of the SZ12 ultrasonic frequency generator.

Project	Parameter
Input voltage	AC voltage 220 V
Frequency	50 Hz
Output power	Greater than 250 W
Frequency adjustable range	18–23 KHz

In this experiment, a ceramic base CBN grinding wheel with a diameter of 15 mm and a particle size of 200# was used for grinding. The test piece used was TC4 titanium alloy (30 × 15 × 10 mm). The grinding wheel and workpiece are shown in Figure 5a,b, and the related information is shown in Tables 3 and 4. The FA1004 precision electronic analytical balance (accuracy of 0.0001 g) produced by Zhejiang Lichen Technology Co., Ltd. (Shaoxing, China.) was used to detect the wear amount of the grinding wheel before and after the LTUAG test of TC4 titanium alloy.

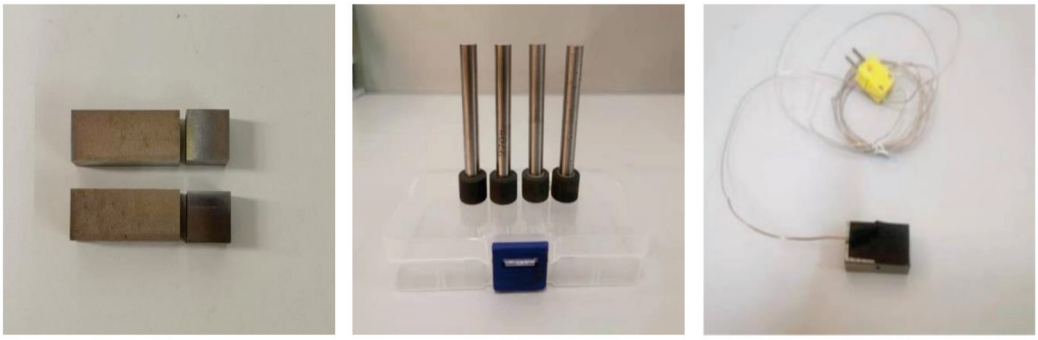

(**a**) (**b**) (**c**)

Figure 5. Workpieces, grinding wheels, and temperature test pieces used in the test. (**a**) TC4 workpiece. (**b**) Ceramic base CBN grinding wheel. (**c**) Temperature test piece.

Table 3. Grinding wheel specifications.

Project	Parameter
Grinding wheel model	1A1W-type ceramic base CBN flat grinding wheel
Manufacturer	Zhengzhou Abrasives Grinding Research Institute Co., Ltd.
Grinding wheel length/mm	10
Wheel diameter/mm	15
Grinding wheel particle size	100#, 200#, 300#
Grinding wheel concentration	100%

Table 4. Physical and mechanical properties of TC4 titanium alloy.

Elongation δ5 (%)	Coefficient of Thermal Conductivity	Density	Tensile Strength	Hardness
≥10	7.955 W/m·K	4.5 g/cm^3	≥850 MPa	HRC30

The temperature measurement specimen equipped with the thermocouple sensor is shown in Figure 5c. The whole measurement process was as follows: Firstly, a through hole with a diameter of 1 mm was machined by the CNC milling machine in the TC4 titanium alloy workpiece. Secondly, the K-type thermocouple sensor was put into the through hole, and the thermocouple tip was placed 0.3 mm away from the workpiece surface to ensure that the grinding wheel surface is in contact with the thermocouple tip during the grinding process, which can improve the accuracy of the measurement results. Thirdly, the thermocouple sensor and workpiece were tightly wrapped with insulating tape, the working end of the thermocouple sensor was fixed near the machining area of the workpiece, and the

sensor output was connected to the thermocouple collector; then, the grinding temperature measurement system was built. The working principle of the thermocouple acquisition instrument is shown in Figure 6.

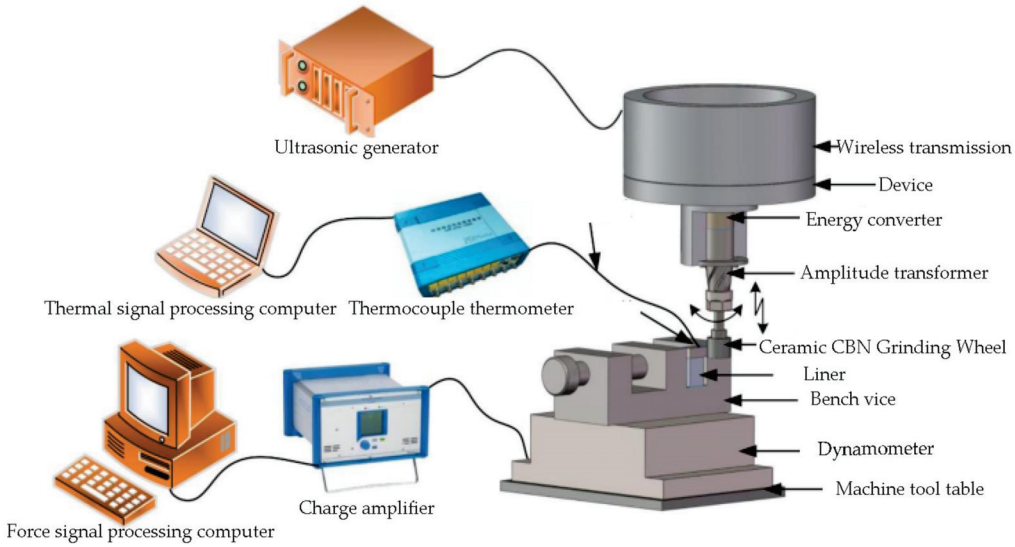

Figure 6. The working principle of force and thermocouples.

To analyze the influence of grinding process parameters and longitudinal-torsional ultrasonic parameters on the grinding force, grinding temperature, and grinding wheel wear rate in the process of LTUAG of TC4 titanium alloy, in this study, the longitudinal-torsional ultrasonic single-factor grinding test of TC4 titanium alloy was carried out. The parameters of the single-factor grinding test are shown in Table 5.

Table 5. Longitudinal-torsional ultrasonic single-factor grinding parameters of TC4 titanium alloy.

Exp. Number	Grinding Depth (μm)	Speed of Grinding (Wheel r/min)	Feed Speed (mm/min)	Ultrasonic Amplitude (μm)
1	1/3/5/7	4000	150	4
2	3	2000/3000/4000/5000	150	4
3	3	4000	100/150/200/250	4
4	3	4000	150	0/2/4/6

3.2. Test Results and Analysis

3.2.1. Influence of Process Parameters on Grinding Force in LTUAG

Figure 7 shows the variation of grinding force under different parameters during LTUAG. Figure 7a shows that the grinding force during LTUAG increased with the grinding depth. The radial grinding force and tangential grinding force showed an increasing trend during LTUAG when the grinding depth exceeded 5 μm, and the trend gradually slowed down. The volume of material removed increased with the grinding depth, which resulted in an increase of the grinding force. When the grinding depth exceeded 5 μm, the temperature induced by the grinding was higher than the recrystallization temperature of the workpiece, and the microhardness of the workpiece was lower than the original microhardness of the workpiece. As a result, when the grinding depth was further increased, the increasing trend of the grinding force became slower.

Figure 7b shows that the grinding force during LTUAG decreased as the grinding wheel speed increased. The number of abrasive grains and the grinding arc length of the abrasive grains also increased as the speed of the grinding wheel increased, which in turn reduced the cross-sectional area of abrasive debris and the degree of adhesion wear of the single abrasive particle. Ultimately, the grinding force during LTUAG was reduced.

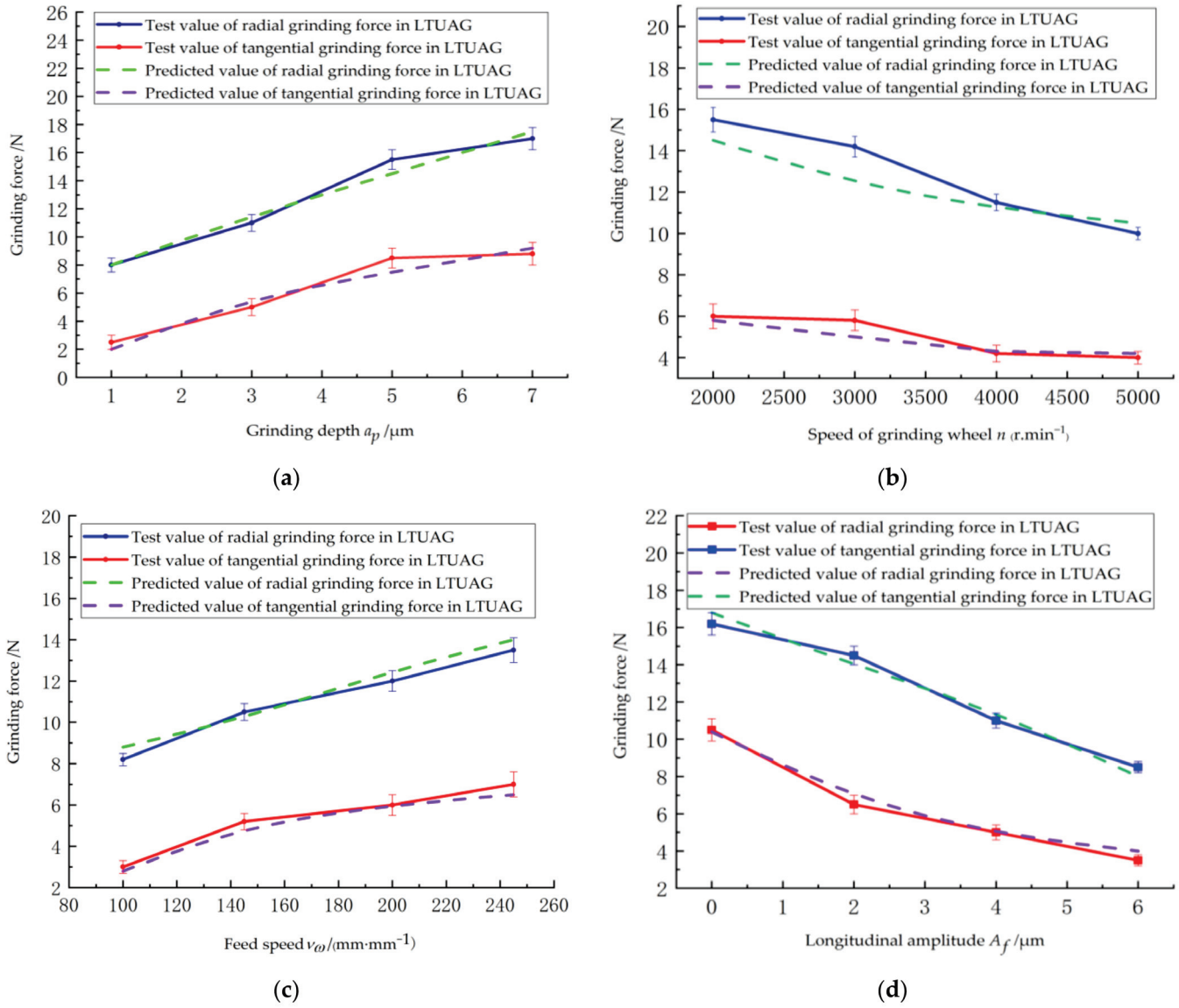

Figure 7. Influence of process parameters on the grinding force of LTUAG. (**a**) Depth of grinding. (**b**) Speed of the grinding wheel. (**c**) Feed rate. (**d**) Lengthening amplitude.

Figure 7c shows that the grinding force during LTUAG generally increased as the workpiece feed rate increased. With the increase of the feed rate, the volume of the workpiece material removed by the abrasive particles during the grinding process increased, and the deformation resistance of the workpiece material to the grinding wheel also increased, which led to an increase in the grinding force.

Figure 7d shows that the grinding force during LTUAG decreased as the longitudinal ultrasonic amplitude increased. As the longitudinal ultrasonic amplitude increased, the grinding arc length of the single abrasive particle lengthened, the cross-sectional area of the material removed decreased, and the chip deformation force decreased. The friction between the bottom surface of the abrasive grains and the workpiece was reduced, resulting in a reduction in the grinding force.

The experimental results of the grinding force under different process parameters during LTUAG are consistent with the changing trend of the theoretical prediction results of the grinding force during LTUAG, which verifies the accuracy of the grinding force model of LTUAG established in this study, as shown in Figure 7a–d.

3.2.2. Effect of Process Parameters on Grinding Temperature of LTUAG

Figure 8 shows the temperature variation of LTUAG under different process parameters. Figure 8a shows that the grinding temperature of LTUAG gradually increased as the grinding depth increased. The grinding force required to remove the workpiece material during LTUAG also increased as the grinding depth increased. This in turn led to the increase of the frictional heat source density on the contact surface of the abrasive grain and the workpiece as well as the increase of the grinding temperature. At the same time, the increase in grinding depth made the contact between the abrasive grain and the workpiece closer. The grinding area was more fully affected by the grinding heat and was not easily dissipated, which further accelerated the rising trend of the grinding temperature.

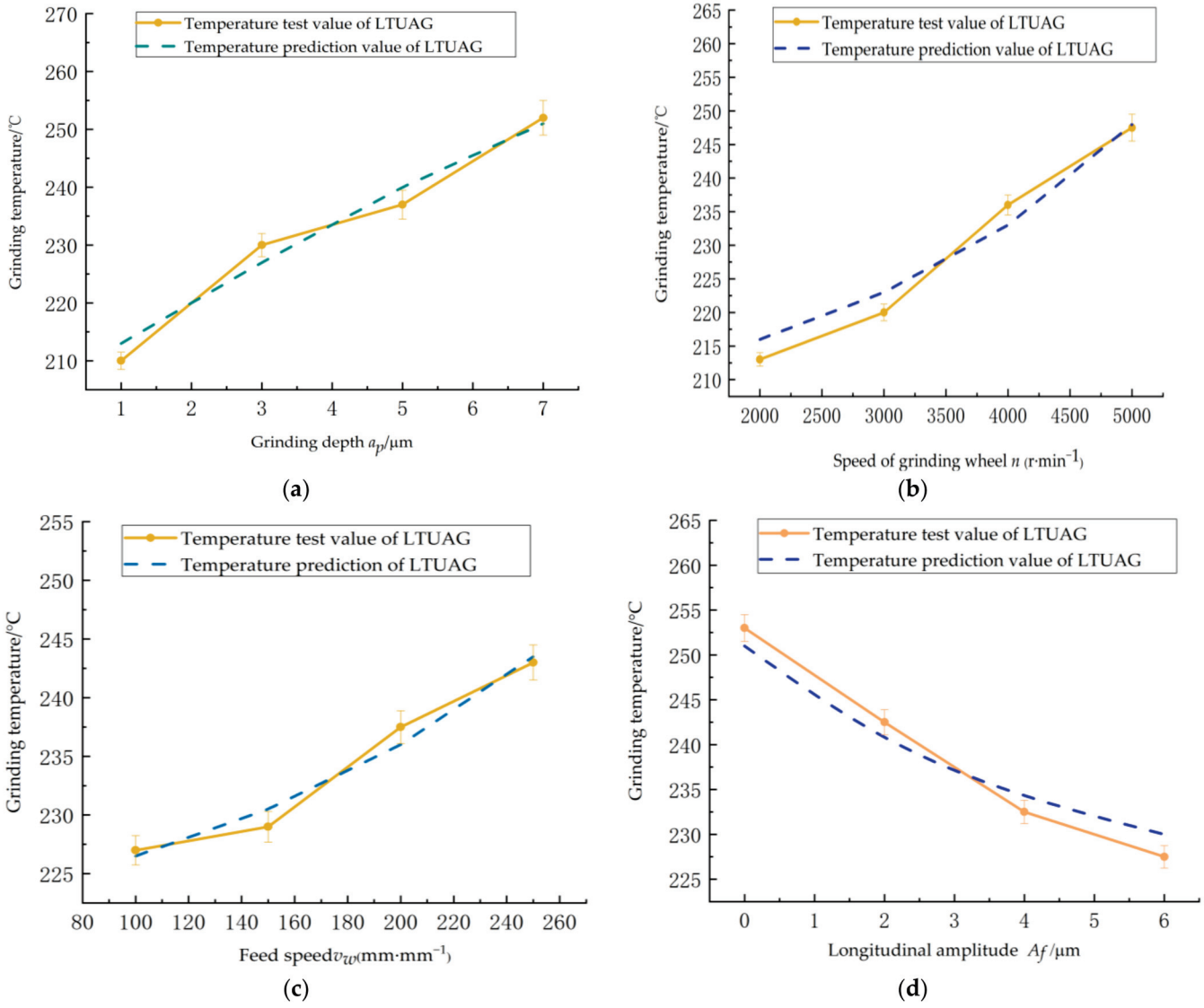

Figure 8. The influence of process parameters on the grinding temperature of LTUAG. (**a**) Depth of grinding. (**b**) Speed of the grinding wheel. (**c**) Feed rate. (**d**) Longitudinal amplitude.

Figure 8b shows that the grinding temperature of LTUAG gradually increased as the grinding wheel speed increased, and the temperature of LTUAG started to rise faster when the grinding wheel speed exceeded 4000 r/min. This is because the friction heat source density between the abrasive particles and the workpiece increased as the grinding wheel speed increased, which in turn led to an increase in the grinding temperature. The vibration characteristics of LTUAG were weakened when the rotational speed of the grinding wheel

exceeded 4000 r/min, which in turn reduced the heat dissipation rate of grinding, resulting in a faster rise in the grinding temperature.

Figure 8c shows that the grinding temperature of LTUAG gradually rose as the workpiece feed rate increased. This is because with the increase of the workpiece feed rate, the volume of TC4 material removed by the abrasive particles in LTUAG increased in unit time, which in turn led to an increase in the grinding force of LTUAG. The friction heat source density increased on the contact surface between the abrasive particles and the workpiece, and the grinding temperature increased.

Figure 8d shows that as the longitudinal-torsional ultrasonic amplitude increased, the grinding temperature of LTUAG decreased overall. This is due to the increase in the longitudinal-ultrasonic amplitude and the decrease in the grinding force generated by the shear deformation of the workpiece material and the ploughing slip. In turn, the friction heat source density of the contact surface between the abrasive particles and the workpiece increased. At the same time, the contact-separation characteristics of the abrasive particles on the surface of the grinding wheel and the workpiece were strengthened, and the speed of grinding heat dissipation was accelerated. This led to a significant reduction in the temperature of the grinding area.

As shown in Figure 8a–d, the experimental results of the grinding temperature under different process parameters during LTUAG are consistent with the changing trend of the theoretical prediction results of the grinding temperature of LTUAG, confirming the accuracy of the grinding temperature model in LTUAG established in this study.

3.2.3. The Effect of Process Parameters on the Wear Rate of Grinding Wheels in LTUAG

A single-factor test on the grinding wheel wear rate of TC4 titanium alloy was carried out according to the single-factor grinding test scheme shown in Table 5, and the results of the single-factor test are shown in Table 6. The variation of the grinding wheel wear rate for LTUAG with different process parameters is shown in Figure 9.

Figure 9a shows that as the grinding depth increased, the wear rate of the grinding wheel under LTUAG increased overall. This is because with the increase in the grinding depth, the grinding force and grinding temperature also increased, which led to an increase in stress on the surface of abrasive particles caused by the coupling of mechanical stress and thermal stress. The crushing degree of abrasive particles was intensified, and the wear rate of the grinding wheel showed an increasing trend.

Table 6. Single-factor experimental results of grinding wheel wear rate in LTUAG of TC4 titanium alloy.

Grinding Depth (μm)	Wheel Speed ($r \cdot min^{-1}$)	Feed Speed ($mm \cdot min^{-1}$)	Longitudinal Amplitude (μm)	Grinding Length (mm)	Wear Rate (g/s)
1	4000	150	4	150	0.0813
3	4000	150	4	150	0.0951
5	4000	150	4	150	0.1313
7	4000	150	4	150	0.1525
3	2000	150	4	150	0.1090
3	3000	150	4	150	0.1130
3	4000	150	44	150	0.0950
3	5000	150	4	150	0.0910
3	4000	100	4	150	0.1183
3	4000	150	4	150	0.1255
3	4000	200	4	150	0.1294
3	4000	250	4	150	0.1378
3	4000	150	0	150	0.1317
3	4000	150	2	150	0.1196
3	4000	150	4	150	0.0953
3	4000	150	6	150	0.1079

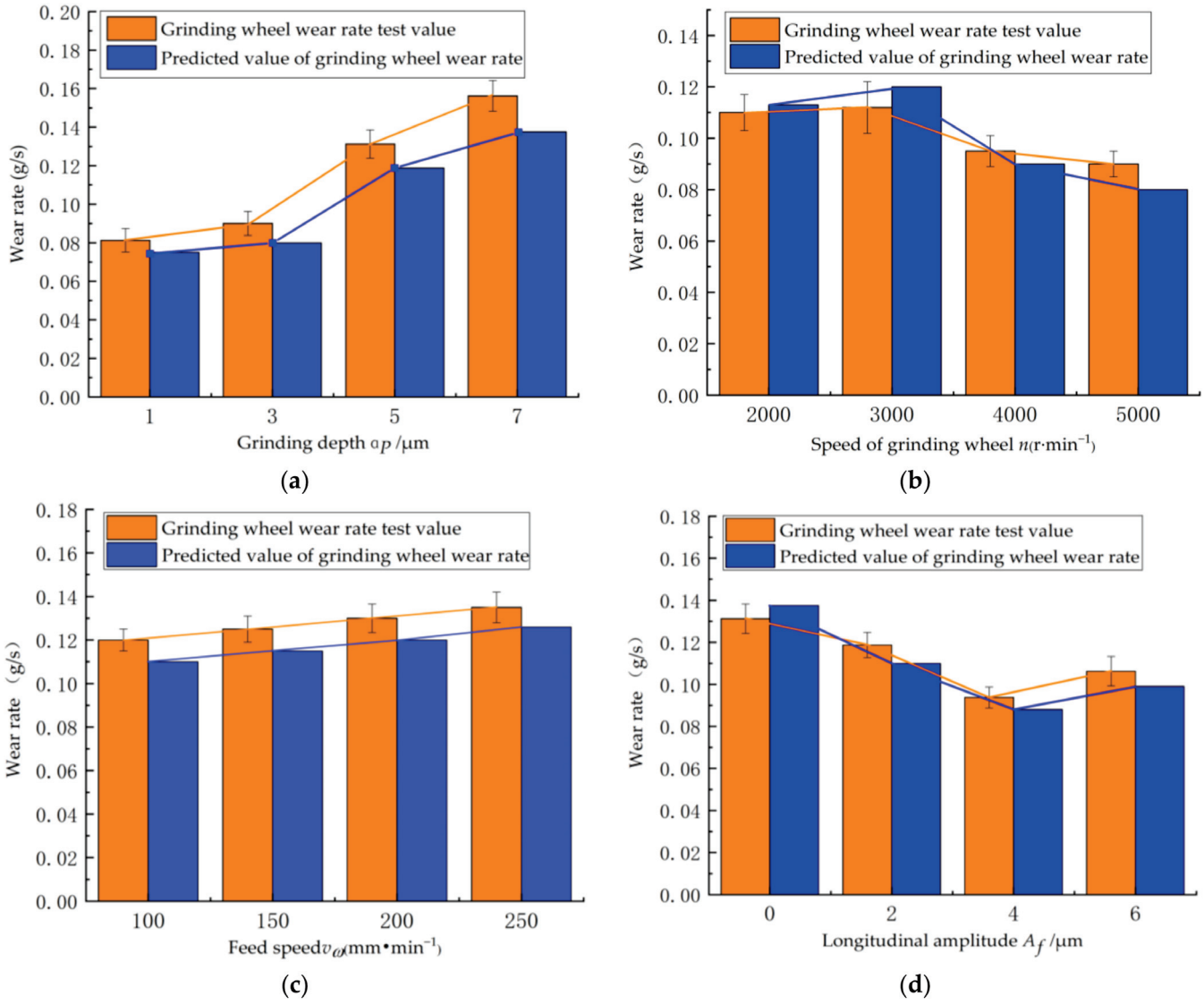

Figure 9. Influence of process parameters on grinding wheel wear rate in LTUAG. (**a**) Depth of grinding. (**b**) Speed of the grinding wheel. (**c**) Feed rate. (**d**) Lengthening amplitude.

Figure 9b shows that with the increase of the grinding wheel speed, the grinding wheel wear during LTUAG increased and then decreased. This is because with the increase of the grinding wheel speed, the relative sliding speed of the contact surface between the abrasive grain and the workpiece increased, which led to an increase in the temperature of the front and flank surfaces of the abrasive grain, resulting in a gradual increase in the wear rate of the grinding wheel. When the grinding wheel speed exceeded 3000 r/min, the increase of grinding grains on the grinding wheel surface made the grinding force decrease, and the rising trend of grinding temperature slowed down, thus alleviating the grinding wheel wear to a certain extent, and the grinding wheel wear rate decreased.

Figure 9c shows that the wear rate of the grinding wheel under LTUAG increased as the workpiece feed speed increased. This is because as the feed speed increased, the contact pressure and temperature increased, which further intensified the degree of bond wear of abrasive particles. The wear amount caused by the bonding wear of the front and rear tool surfaces of the abrasive particles gradually increased.

Figure 9d shows that the grinding wheel wear rate decreased as the longitudinal ultrasonic amplitude increased and increased when the longitudinal ultrasonic amplitude exceeded 4 μm. This is because the grinding force and grinding heat during LTUAG were

reduced as the longitudinal amplitude increased, which in turn led to the reduction of the wear rate. The excessively large, high ultrasonic amplitude increased the instantaneous high-frequency impact between the grinding wheel and the workpiece when the longitudinal amplitude exceeded 4 μm, which in turn led to an increase in the internal stress of the abrasive particles on the surface of the grinding wheel and the bonding agent. The degree of fragmentation of the abrasive particles and the bonding agent was increased, and the wear rate of the grinding wheel significantly increased. In addition, under the same processing conditions, the wear rate of the grinding wheel during LTUAG was reduced by 25.2% compared with ordinary grinding, indicating that LTUAG helped to improve the durability of the grinding wheel.

Figure 9a–d show that the experimental results of the grinding wheel wear rate during LTUAG under different process parameters agree with the theoretical prediction results of the grinding wheel wear rate of LTUAG. The changing trend was consistent, which verified the accuracy of the grinding wheel wear model during LTUAG established in this study.

4. Conclusions

1. The grinding force model and the grinding abrasive surface temperature model of LTUAG were established based on the single-grain grinding arc length model in LTUAG, and on this basis, the grinding wheel wear model of LTUAG was established by combining the wear model and the bond wear model. The theoretical analysis results showed that the grinding wheel wear rate of LTUAG increased as the grinding depth and workpiece feed rate increased and decreased as the grinding linear speed and ultrasonic amplitude decreased.
2. The single-factor test of LTUAG of TC4 titanium alloy showed that the grinding force and grinding temperature increased as the grinding depth and workpiece feed rate increased and decreased as the longitudinal amplitude increased. The grinding force gradually decreased as the grinding wheel speed increased, and the grinding temperature gradually increased as the grinding wheel speed increased. In addition, the variation trend of the experimental results of the grinding force and grinding temperature under different process parameters was consistent with the theoretical prediction results, which verified the accuracy of the established grinding force model and grinding temperature model in LTUAG.
3. The single-factor test results of the grinding wheel wear rate of TC4 titanium alloy in LTUAG showed that the use of longitudinal-torsional ultrasonic vibration reduced the wear rate of the grinding wheel by 25.2%, thereby increasing the service life of the grinding wheel and improving the machining efficiency of TC4 titanium alloy. The experimental results of the grinding wheel wear rate were consistent with the theoretical prediction results during LTUAG, which verified the accuracy of the grinding wheel wear model in LTUAG established in this study.

Author Contributions: Conceptualization, Y.Y.; methodology, J.L. and Y.Y.; software, J.L. and Z.L.; validation, J.L.; formal analysis, Y.Y.; investigation, J.L., Z.L. and X.W.; resources, Y.Y. and J.L.; data curation, J.L.; writing—original draft preparation, J.L. and X.W.; writing—review and editing, Y.Y. and Z.L.; visualization, Z.L. and X.W.; supervision, Y.Y.; project administration, J.L.; funding acquisition, Y.Y. All authors have read and agreed to the published version of the manuscript.

Funding: This research was sponsored by Henan Science and Technology Research Project (No.212102210047) and the National Natural Science Foundation of China (No.51575163).

Institutional Review Board Statement: Not applicable.

Informed Consent Statement: Not applicable.

Data Availability Statement: Not applicable.

Conflicts of Interest: The authors declare no conflict of interest.

References

1. Baltatu, M.S.; Vizureanu, P.; Sandu, A.V.; Florido-Suarez, N.; Saceleanu, M.V.; Mirza-Rosca, J.C. New Titanium Alloys, Promising Materials for Medical Devices. *Materials* **2021**, *14*, 5934. [CrossRef] [PubMed]
2. Guo, L.; He, W.X.; Zhou, P.; Liu, B. Research Status and Development Prospect of Titanium and Titanium Alloy Products in China. *Hot Work. Technol.* **2020**, *49*, 22–28.
3. Guo, J.; Goh, M.H.; Wang, P.; Huang, R.; Lee, X.; Wang, B.; Nai, S.M.L.; Wei, J. Investigation on surface integrity of electron beam melted Ti-6Al-4 V by precision grinding and electropolishing. *CJA* **2020**, *34*, 28–38. [CrossRef] [PubMed]
4. Wang, K.H.; Wang, L.L.; Zheng, K.L.; He, Z.B.; Politis, D.J.; Liu, G.; Yuan, S.Y. High-efficiency forming processes for complex thin-walled titanium alloys components: State-of-the-art and perspectives. *Int. J. Extrem. Manuf.* **2020**, *2*, 20–43. [CrossRef]
5. Bhaduri, D.; Soo, S.L.; Aspinwall, D.K.; Novovic, D.; Bohr, S.; Harden, P.; Webster, J.A. Ultrasonic Asisted Creep Feed Grinding of Gamma Titanium Aluminide Using Conventional and Superabrasive Wheels. *CIRP Ann. Manuf. Techn.* **2017**, *66*, 341–344. [CrossRef]
6. Yan, Y.Y.; Yan, H.Z.; Liu, J.L.; Niu, Y.; Wang, X.B. The Thermo-mechanical Coupling Model and Experimental Research of Longitudinal and Torsional Ultrasonic Grinding of TC4 Titanium Alloy. *CMES* **2021**, *209*, 1–13.
7. Han, S. Simulation and Experimental Research on Ultrasonic Assisted Grinding of GH4169 Superalloy. Ph.D. Thesis, Dalian University of Technology, Dalian, China, 2021.
8. Bhushan, B. *Mordern Tribology Handbook*, 1st ed.; CRC Press: Boca Raton, FL, USA, 2000; pp. 273–312.
9. Churi, N.J.; Pei, Z.J. Wheel Wear Mechanisms in Rotary Ultrasonic Machining of Titanium. *IMECE* **2007**, *3*, 399–407.
10. Liu, F.; Qin, N.; Niu, J.D.; Zheng, L. Tool Wear Model of Rotary Ultrasonic Grinding for Titanium Alloy Based on Dimensional Analysis Method. *Mach. Build. Autom.* **2018**, *47*, 93–95+113.
11. Liu, F.; Qin, N.; Niu, J.D.; Zheng, L. Finite Element Simulation and Experimental Research on Rotary Ultrasonic Grinding of Titanium Alloy. *Chin. J. Eng. Des.* **2017**, *24*, 162–167.
12. Li, Y.Q.; Xiao, G.; Li, T. Effect of Ultrasonic Assisted Grinding Force for TC4 Titanium Alloy. *Master Mech. Eng.* **2019**, *43*, 10–13+63.
13. Yan, Y.Y.; Wang, X.X.; Zhao, B.; Liu, J.L. Study on the Surface Residual Stress and Experimental of TC4 Titanium Alloy by Longitudinal Torsional Ultrasonic Grinding of TC4 Titanium Alloy. *Surf. Technol.* **2021**, *50*, 119–129.
14. Komanduri, R.; Hou, Z.B. Thermal Modeling of the Metal Cutting Process—Part II: Temperature Rise Distribution due to Frictional Heat Source at the Tool-chip Interface. *Int. J. Mech. Sci.* **2001**, *43*, 57–88. [CrossRef]
15. Komanduri, R.; Hou, Z.B. Thermal Modeling of the Metal Cutting Process—Part III: Temperature Rise Distribution due to the Combined Effects of Shear Plane Heat Source and the Tool-chip Interface Frictional Heat Source. *Int. J. Mech. Sci.* **2001**, *43*, 89–107. [CrossRef]
16. Mao, C. The Research on the Temperature Field and Thermal Damage in the Surface Grinding. Ph.D. Thesis, Hunan University, Hunan, China, 2008.
17. Liu, F. Research on Grinding Force and Tool Wear in Rotary Ultrasonic Grinding of Titanium Alloy. Ph.D. Thesis, Xi'an Jiaotong University, Xi'an, China, 2017.
18. Rabinowitwicz, E.; Dunn, L.A.; Russell, P.G. A Study of Abrasive Wear under Three-body Conditions. *Wear* **1961**, *4*, 345–355. [CrossRef]
19. Liu, X.S. Research on the Mechanism and Key Technology of Double Wheel Follow-Up Grinding of High-speed Railway. Ph.D. Thesis, Zhejiang University of Technology, Hangzhou, China, 2012.
20. Usui, E.; Shirakashi, T.; Kitagawa, T. Analytical Prediction of Cutting Tool Wear. *Wear* **1984**, *100*, 129–151. [CrossRef]
21. Su, C. Research on Key Theory and Technology of Virtual Grinding. Ph.D. Thesis, Northeastern University, Boston, MA, USA, 2009.

micromachines

Article

Finite Element Investigation on Cutting Force and Residual Stress in 3D Elliptical Vibration Cutting Ti6Al4V

Shiyu Li [1], Jinguo Han [1,2,*], Haiqiang Yu [1], Jinhui Wang [1], Mingming Lu [3], Yebing Tian [1] and Jieqiong Lin [3]

[1] School of Mechanical Engineering, Shandong University of Technology, Zibo 255049, China
[2] Shandong Provincial Key Laboratory of Precision Manufacturing and Non-Traditional Machining, Shandong University of Technology, Zibo 255049, China
[3] School of Mechatronic Engineering, Changchun University of Technology, Changchun 130012, China
* Correspondence: hankeyee@163.com

Abstract: Titanium alloy is a typical difficult-to-machine material with features of superhigh strength and hardness, and low elastic modulus. It is difficult to guarantee the processing quality and efficiency due to the high cutting force and tool wear in conventional cutting. Elliptical vibration cutting (EVC) as an effective method can improve the machinability of titanium alloys. In this paper, the finite element method (FEM) was adopted to study the cutting force and residual stress of 3D EVC in machining of Ti6Al4V. The Johnson-Cook constitutive model was utilized to illustrate the plastic behavior of Ti6Al4V alloy. The kinematics of the 3D EVC was described, and then the influence of various cutting speeds, vibration amplitudes, vibration frequencies and depths of cut on cutting force and residual stress were carried out and analyzed. The simulation results show that the cutting speed, vibration amplitude *a*, vibration frequency and depth of cut have larger effect on principal force. In addition, the compressive stress layer can be easily obtained near the machined surface by using 3D EVC, which is helpful to improve the working performance of workpiece.

Keywords: Ti-6Al-4V alloy; 3D EVC; cutting force; residual stress; finite element method

Citation: Li, S.; Han, J.; Yu, H.; Wang, J.; Lu, M.; Tian, Y.; Lin, J. Finite Element Investigation on Cutting Force and Residual Stress in 3D Elliptical Vibration Cutting Ti6Al4V. *Micromachines* **2022**, *13*, 1278. https://doi.org/10.3390/mi13081278

Academic Editors: Chengwei Kang, Chunjin Wang and Jiang Guo

Received: 27 July 2022
Accepted: 6 August 2022
Published: 8 August 2022

1. Introduction

Titanium alloy is widely used in aerospace, shipbuilding, communication equipment, medical equipment and other fields due to its low density, high strength and stable performance under extreme conditions. However, for titanium alloy it is hard to obtain the ideal machining results by traditional machining methods. The characteristics of low thermal conductivity and high elasticity of titanium alloy produce a lot of heat during the cutting period, and the friction between the tool and the workpiece is serious, which makes the cutting force too large [1]. The high chemical reactivity of titanium alloy leads to a compound wear mechanism, which aggravates tool wear [2]. These disadvantages limit the application of titanium alloy in many fields.

Aiming to improve the machinability and increase machining efficiency of titanium alloy, many researchers have studied cutting methods of titanium alloy in recent years, including laser machining [3], electrical discharge machining (EDM) [4], electron beam machining (EBM) [5], vibration cutting [6] and so on. Among these methods, elliptical vibration cutting (EVC) technology has been considered as an effective way to improve the machinability of titanium alloys. As a new material processing method, EVC was first introduced by Shamoto and Moriwaki in 1994 [7]. The characteristics of EVC is intermittent contact and separation between the tool and the workpiece within an elliptical vibration cycle. Moreover, the reversal of friction force direction on tool rake face, which is helpful in chip removal, is another interesting phenomenon [8]. EVC has the advantages of reducing cutting force [9], improving machining surface quality [10], reducing tool wear [11,12], inhibiting burr generation [13] and reducing residual stress after machining [14] compared with conventional cutting (CC) methods. In recent years, EVC has been widely used in

the processing of difficult-to-machine materials [15–17], especially in the fabrication of micro-nano structure surfaces, which highlight great advantages [18–20].

However, as the commonly used EVC only moves elliptically in the machining plane, i.e., two-dimensional EVC (2D-EVC), the tool has a low degree of freedom, which has limitations in machining complex free-form surfaces. Aiming to meet the processing requirements of complicated surfaces, Shamoto introduced three-dimensional EVC (3D-EVC) technology [21]. This method is a spatial elliptical vibration cutting technique. The higher modulation ability of 3D-EVC makes it more suitable for machining free-form surfaces [22]. Compared with 2D-EVC, the more parameters of 3D-EVC can be dynamically adjusted with the characteristics of the workpiece [23]. In addition, 3D-EVC can reduce cutting force more effectively, enhance chip removal efficiency and improve the machining surface quality of the workpiece [24,25]. At present, for 3D-EVC, researchers mainly focus on the studies of optimization of machining parameters [26], reduction of tool wear [27], preparation of micro-nano structures [28] and the procession of composite materials [29]. Research on cutting force and residual stress is rare.

Generally, cutting force and residual stress are important parameters that influence the workpiece machining process and workpiece accuracy after machining. The popular methods for cutting force and residual stress studying are the experimental method and the finite element method (FEM). Compared with the experimental method, FEM not only has the characteristics of low cost and high efficiency, but also is more flexible. Therefore, FEM is favored by many researchers. Currently, there are many studies about studying the cutting mechanism of titanium alloy during machining by FEM [30–33], while few studies have been carried out on the cutting force and residual stress in 2D-EVC of titanium alloy. Xie et al. [34] used FEM to study the changes of cutting force in EVC titanium alloy with vibration frequency, amplitude and cutting speed. The results show that the tangential force decreases with the increase of vibration frequency, tangential amplitude and thrust amplitude, but decreases with the decrease of cutting speed. The positive and negative thrust force decreases with the increase of frequency and tangential amplitude but decreases with the decrease of cutting speed and thrust amplitude. Wang et al. [35] discussed the material removal mechanism of ultrasonic EVC under different cutting paths. Through simulation and experiment, the material removal mechanism of medical β titanium alloy in ultrasonic elliptical vibration cutting was studied from the aspects of cutting deformation, cutting force and residual stress. The cutting force and residual stress of EVC on some other difficult-to-machine materials are also investigated by FEM. Zhou et al. [36] established a finite element model of elliptical vibration cutting SiCp/Al composite material to study the material removal mechanism, cutting force changes and surface roughness in EVC process. The results show that EVC not only reduces the average cutting force, but also avoids the scratches caused by SiC particles on the machined surface, thus improving the machined surface quality. Kurniawan et al. [37] used FEM to study the difference between ultrasonic EVC and CC of AISI 1045. The cutting force and residual stress have been studied. The results show that the average cutting force of ultrasonic EVC increases with the increase of speed ratio and feed speed, and the average cutting force decreases with the increase of vibration amplitude. In addition, the surface residual stress of the two cutting techniques is tensile stress, and the maximum compressive stress of ultrasonic EVC process is larger than that of CC process due to the compression effect of the vibrated cutting tool.

Above all, the research on the cutting force and residual stress in 3D-EVC needs to be further studied. Therefore, FEM was adopted to investigate the effect on cutting force and residual stress of different processing parameters, such as cutting speed, vibration amplitude, vibration frequency and depth of cut.

2. Kinematic of 3D-EVC

The motion trajectory of the tool tip in 3D-EVC is shown in Figure 1. In each cutting cycle, the tool contacts the workpiece from point t_0, from which the tool cuts the surface remaining from the previous cycle until point t_1, which is the lowest point of the trajectory

in the y direction, where the tool velocity is zero. The tool leaves the workpiece material at point t_2, ending the effective cutting stage. The next cycle of cutting starts at point t_3.

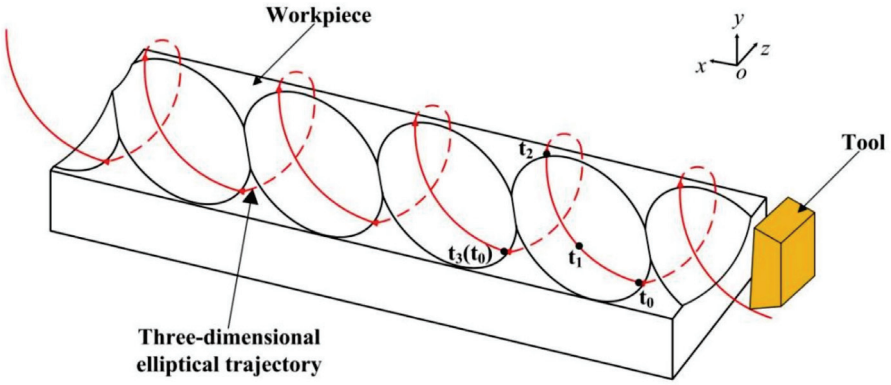

Figure 1. Principle of 3D-EVC.

The trajectory projections of 3D-EVC on the cutting plane and vertical plane are both ellipses. The elliptical path of the tool is synthesized by the sinusoidal motion of three axes at a certain frequency. The motion equation of the tool can be summarized as follows:

$$\begin{cases} x(t) = a\cos(\omega t + \varphi_x) - v_c t \\ y(t) = b\cos(\omega t + \varphi_y) \\ z(t) = c\cos(\omega t + \varphi_z) \end{cases} \quad (1)$$

where a, b and c are, respectively, the vibration amplitudes in x, y and z directions, ω is the vibration angular frequency. φ_x, φ_y and φ_z are the initial phase angles in the x, y and z directions. v_c is the cutting speed. As shown in Figure 2, by synthesizing the trajectory equations of the three axes, the spatial trajectory of 3D-EVC can be obtained. In addition, from the projection of each direction in Figure 2, it can be seen that 3D-EVC is reciprocating on the three projection planes.

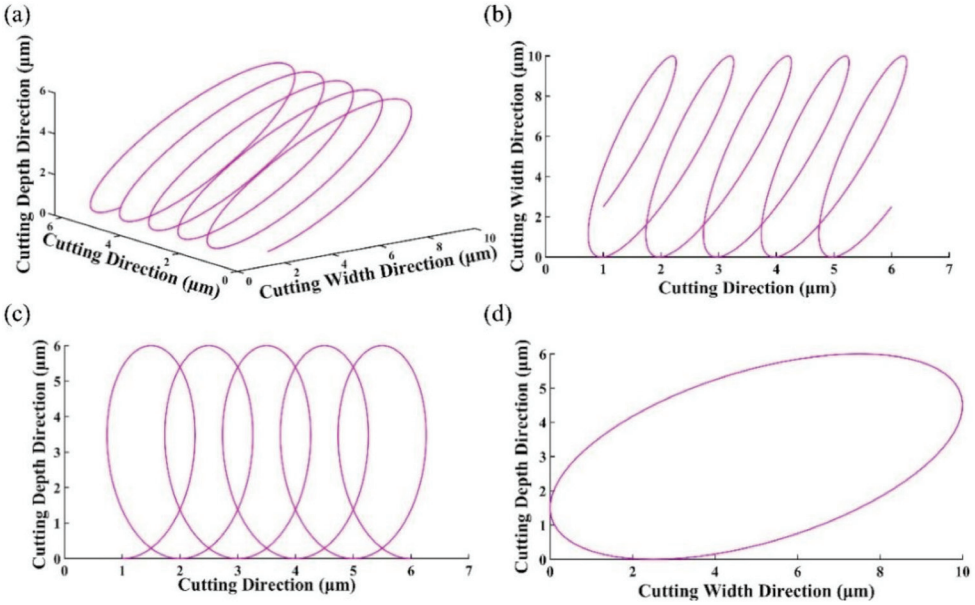

Figure 2. The trajectory and its projection of tool in 3D-EVC (**a**) 3D view (**b**) the projection of trajectory in XoZ plane (**c**) the projection of trajectory in XoY plane (**d**) the projection of trajectory in YoZ plane.

Generally, the cutting speed of the tool is required to be lower than the maximum vibration speed during the 3D-EVC process to ensure the tool has separated from the workpiece and chip during each vibration cycle.

3. Finite Element Method

3.1. Material Constitutive Model

In the process of metal cutting, in order to ensure that the elastic-plastic deformation of the material in the simulation is the same as that in the real processing, the stress-strain relationship of the material must be determined reasonably in the simulation of metal cutting. In this paper, the Johnson-Cook constitutive model is adopted to describe the stress-strain relationship of metal materials. The Johnson-Cook constitutive model can be expressed as:

$$\sigma = [A + B\varepsilon^n]\left[1 + c\ln(\frac{\dot{\varepsilon}}{\dot{\varepsilon_0}})\right]\left[1 - (\frac{T - T_r}{T_m - T_r})^m\right] \quad (2)$$

where $\dot{\varepsilon_0}$ is the reference strain rate, A is the elastic limit of the material, B is the hardening modulus, C is the strain rate dependency coefficient, n is the strain hardening index of the material, m is the thermal softening index of the material. T_m is the melting temperature of the workpiece and T_r is the ambient temperature. In this paper, the parameters of Johnson-Cook constitutive model are shown in Table 1.

Table 1. Johnson-Cook parameters for Ti6Al4V alloy [38].

A (MPa)	B (MPa)	C	n	m	T_m (°C)	T_r (°C)
782.7	498.4	0.028	0.28	1	1660	20

3.2. The Criterion of Material Failure

In the finite element model of cutting process, the critical value of plastic strain accumulation is usually taken as the criterion of element failure. The material damage model selected in this study is the Johnson-Cook damage model, which is based on the equivalent plastic strain of each element. The damage principle of each element can be determined by:

$$D = \sum \frac{\Delta\bar{\varepsilon}}{\varepsilon_D} \quad (3)$$

where D is the fracture failure parameter, $\Delta\bar{\varepsilon}$ is the equivalent plastic strain increment, ε_D is the failure strain. When the fracture failure parameter D exceeds 1, the element begins to sustain damage, but at this point the element does not fail completely. The fracture failure strain of the material is expressed as follows:

$$\varepsilon_D = \left[d_1 + d_2\exp(d_3\frac{p}{q})\right]\left[1 + d_4\ln(\frac{\dot{\varepsilon}}{\dot{\varepsilon_0}})\right]\left[1 + d_5\left(\frac{T - T_r}{T_m - T_r}\right)\right] \quad (4)$$

where p and q are the compressive stress and von Mises stress, d_1~d_5 are the material failure constants, as shown in Table 2.

Table 2. Johnson-Cook damage parameters [39].

d_1	d_2	d_3	d_4	d_5	$\dot{\varepsilon_0}$ (s^{-1})
−0.09	0.25	−0.5	0.014	3.87	0.001

After the material is damaged, the simple stress-strain relationship cannot accurately express the damage failure behavior of the material. Hillerborg et al. [40] described the softening phenomenon of materials after damage by establishing the stress-displacement relationship, and defined fracture energy G to represent the energy required for cracking of materials per unit area, thus reducing dependence on the model mesh. In the damage evolution stage, the strain energy of the material is taken as the failure criterion, and

fracture energy is the integral of the stress-strain of a material from the initial stage of damage to complete failure. It can be determined by:

$$G_f = \int_{\overline{\varepsilon}_0}^{\overline{\varepsilon}_f} L_0 \sigma_{y0} d\varepsilon = \int_0^{\overline{u}_f} \sigma_{y0} d\overline{u} \quad (5)$$

where $\overline{\varepsilon}_0$ and $\overline{\varepsilon}_f$ are the equivalent plastic strain at initial damage and material failure, L_0 is the element feature length in the simulation model, σ_{y0} is the yield stress at initial damage, $\overline{u}$ is the equivalent plastic displacement of material failure process, $\overline{u}_f$ is the equivalent plastic displacement when the material fails completely.

In this paper, displacement-based failure is adopted as the material failure criterion. It can be seen from Equation (5) that the failure displacement value defined in ABAQUS is related to the element feature length L_0 of the simulation model. Therefore, the initial failure displacement value is determined according to L_0. Then, according to the comparison between the cutting force in the simulation and the cutting force in the experiment, the appropriate failure displacement value is finally obtained.

3.3. The Establishment of Finite Element Model

The three-dimensional finite element model of EVC is shown in Figure 3. The model simulates the turning method in the actual process. Figure 3a is the front view of the model, and Figure 3b is the left view of the model. The model was established by ABAQUS software, and the workpiece size was 3 mm × 1.5 mm × 1 mm. Diamond tools are used in the model. The rake angle of the tool is 10 degrees, and the clearance angle of the tool is 10 degrees.

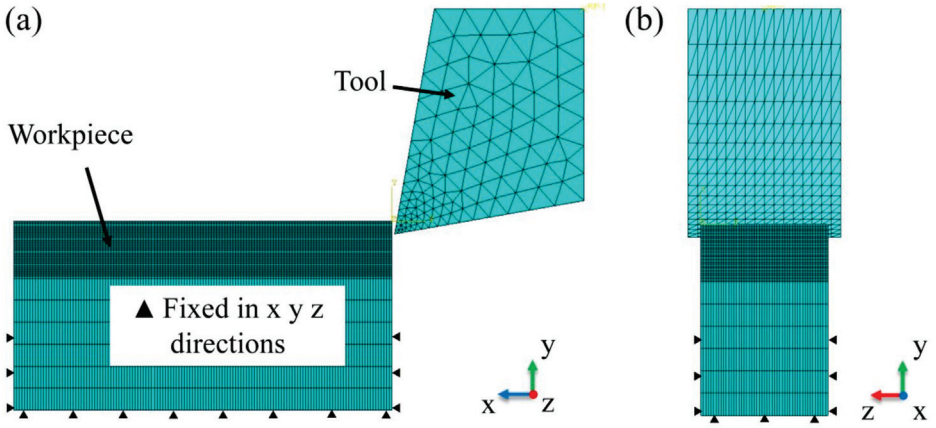

Figure 3. 3D finite element cutting model (**a**) front view (**b**) left view.

The material used for the workpiece is Ti6Al4V, and the material used for the tool is PCD. The material parameters of the tool and the workpiece are shown in Table 3. The tool material has high hardness, which is much higher than that of the workpiece material, so it is assumed that the tool is rigid.

Table 3. The material parameters of tool and workpiece [39].

Properties	Ti6Al4V	PCD
Density (kg/m^3)	4440	14,450
Young's modulus (GPa)	119	640
Poisson's ratio	0.29	0.22
Specific heat (J/kg/K)	661	220
Thermal conductivity (W/m/K)	6.8	75.4

The mesh type of the workpiece is set to be C3D8RT, and the number of meshes is 322,000. The mesh type of the tool is set to be C3D4T, and the number of meshes is 8037. In order to improve the calculation efficiency, the workpiece model is divided into two parts, namely chip layer and base layer. The chip layer is in contact with the tool to form chips. The base layer has imposed constraints to simulate the workpiece being clamped onto the machine tool. The mesh density of the chip layer is much higher than that of the base layer.

4. Results and Discussions

4.1. Effect of Cutting Parameters on Cutting Forces

The geometric relationship of each cutting force is shown in Figure 4, where N is the resultant force, N' is the projection of the resultant force on the normal plane, F_p, F_t and F_n are the principal force, thrust force and normal force respectively [41].

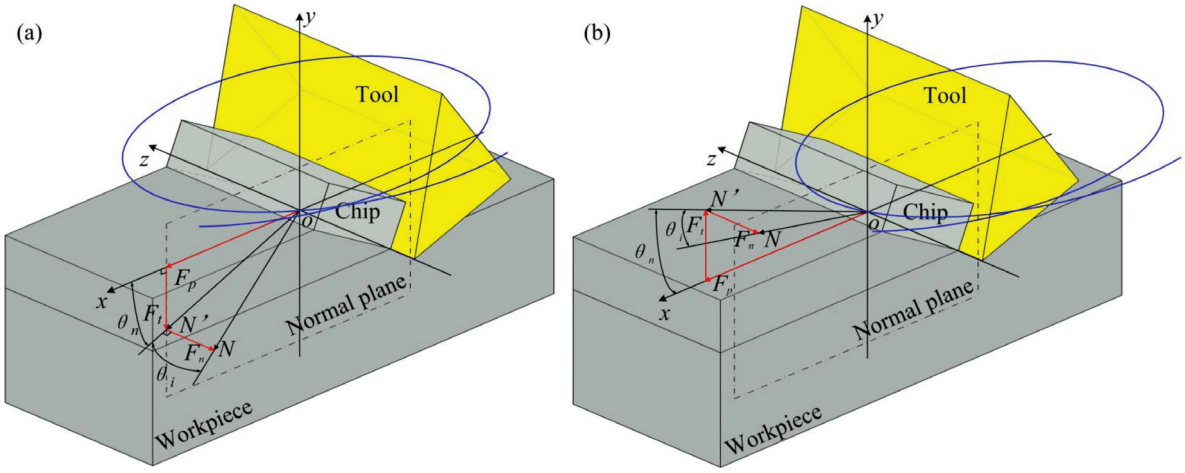

Figure 4. Analysis of the cutting force of the cutting tool acting on the workpiece (**a**) the stage similar to ordinary cutting (**b**) the stage of friction reversal.

This section uses a single variable method to explore the effect of each cutting parameter on the cutting force. When exploring the effect of one cutting parameter on cutting force, the other cutting parameters take the default values. The default values are that the amplitude of the three directions of x, y and z is 15 μm, the vibration frequency is 20 kHz, the cutting depth is 0.1 mm, the cutting speed is 0.3 m/s and the rake and clearance angles of the tool are both 10 degrees.

4.1.1. Effect of Cutting Speed on Cutting Force

Figure 5 shows the change of real-time cutting force and average cutting force at different cutting speeds. In addition, the curve of transient thickness of cut (TOC) changing with time is attached. It can observe the change of material removal under different cutting parameters. The cutting speed is altered between 0.1 m/s and 0.4 m/s with an interval of 0.1. All the above cutting speeds meet the condition of separate EVC.

The maximum principal force increases with the increase of cutting speed, and the average principal cutting force increases with the increase of cutting speed, as shown in Figure 5a,d. The average principal force is 26.62 N at 0.1 m/s, and 48.41 N at 0.4 m/s, increasing by 81.9%. The reason is that, as the cutting speed increases, the elliptical path of the cutting tool becomes longer over a cutting cycle. It means that there is a longer contact time between the tool and the workpiece. As shown in Figure 5e, after the tool has finished cutting the residual workpiece of the previous cycle, the TOC has an instantaneous increase. This trend intensifies with the increase of cutting speed. Moreover, more material is removed in a cutting cycle as the cutting speed increases. These result in an increasing of principal force peak value.

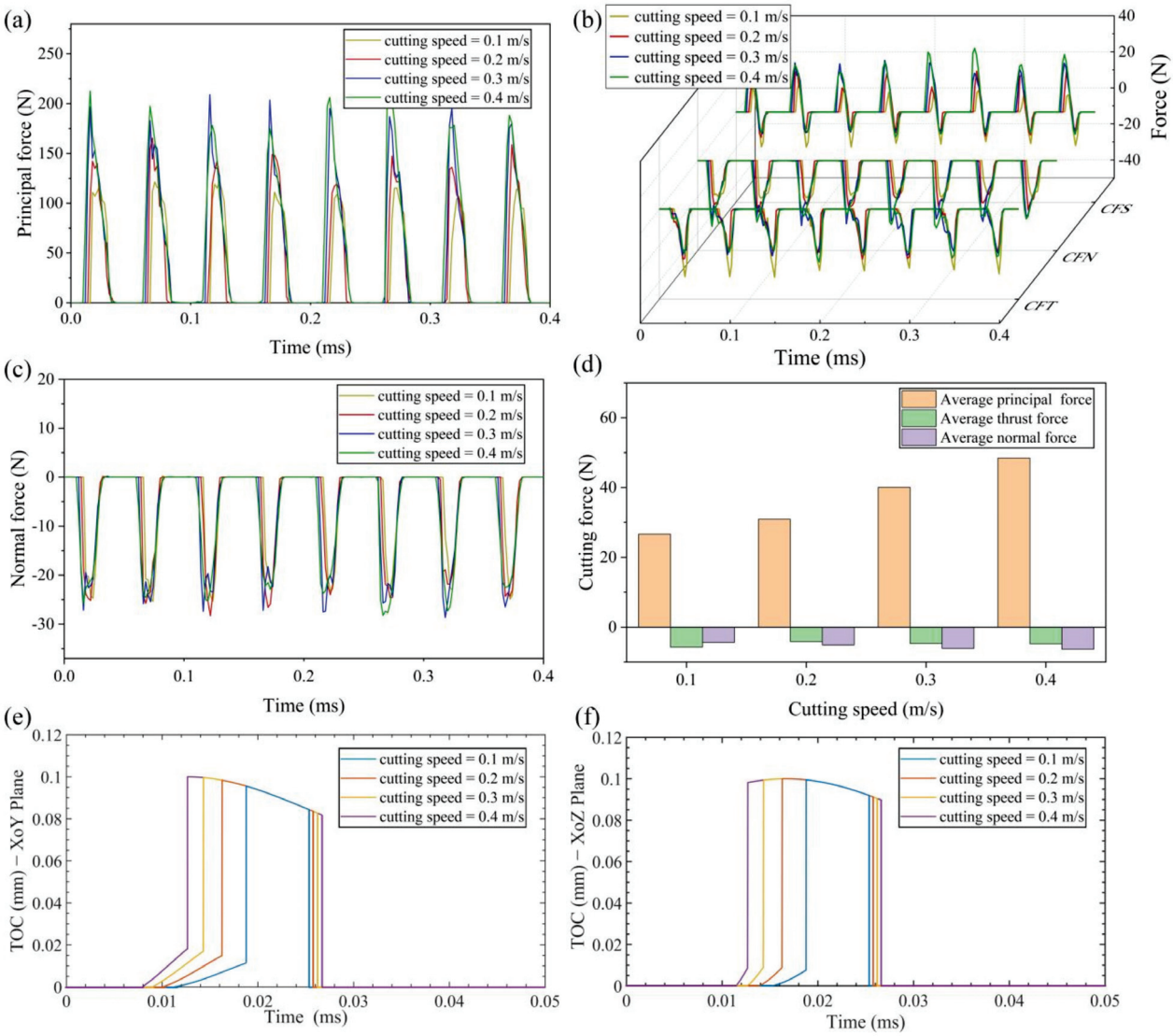

Figure 5. Results of cutting force and TOC with various cutting speeds (**a**) principal force (**b**) thrust force (**c**) normal force (**d**) average cutting force (**e**) TOC with various cutting speeds in XoY plane (**f**) TOC with various cutting speeds in XoZ plane.

The thrust force consists of the force due to contact pressure and the force due to frictional stress. In this paper, CFT is the thrust force, CFN is the force due to contact pressure and CFS is the force due to frictional stress. It can be seen from Figure 5b that, with an increase of cutting speed, CFS increases gradually in the stage similar to ordinary cutting and decreases gradually in the stage of friction reversal. CFN increases gradually with increasing cutting speed. CFT is the combination of CFS and CFN. The effect of cutting speed on thrust force is lower when compared with principal force. This is also validated by the change trend of average thrust force.

As shown in Figure 5c, the maximum real-time normal force has little change with the change of cutting speed. This is because the maximum TOC at the various cutting speeds differ little as shown in Figure 5f. Thus, there is no significant difference in the maximum normal force at different speeds. In addition, increasing the cutting speed can increase the effective cutting time. The average normal force increases as the cutting speed increases. The average normal force is −4.38 N at 0.1 m/s, and −6.33 N at 0.4 m/s, increasing by 44.5%.

4.1.2. Effect of Vibration Amplitude on Cutting Force

Figures 6–8 show the change of real-time cutting force and average cutting force at different vibration amplitudes in three directions. The value of amplitudes *a*, *b* and *c* are set to 8 μm, 13 μm, 18 μm and 23 μm, respectively.

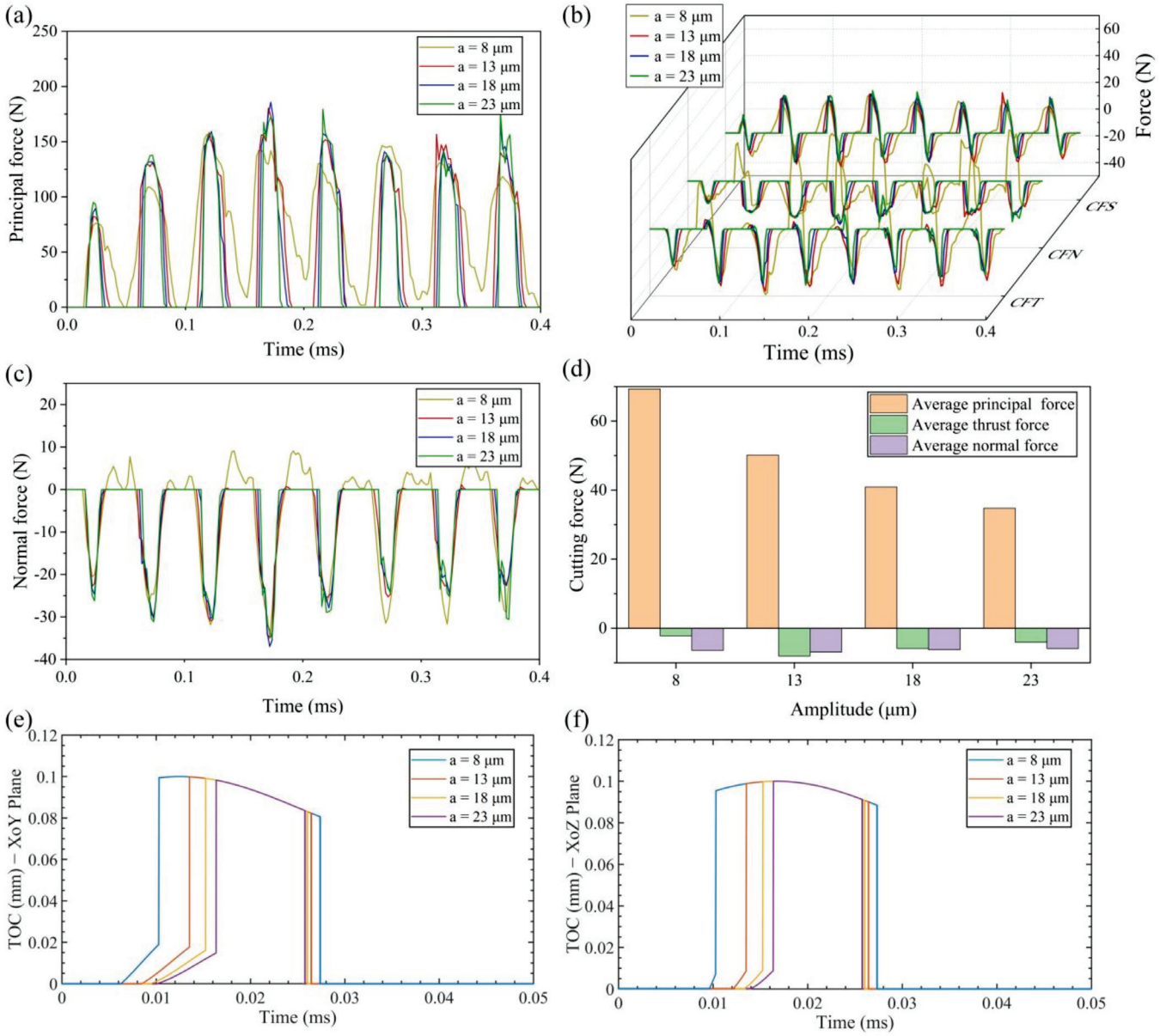

Figure 6. Results of cutting force and TOC with various amplitudes *a* (**a**) principal force (**b**) thrust force (**c**) normal force (**d**) average cutting force (**e**) TOC with various amplitudes *a* in XoY plane (**f**) TOC with various amplitudes *a* in XoZ plane.

(1) Effect of amplitude *a*

As shown in Figure 6a, the maximum principal force increases gradually with the increase of amplitude *a*. The reason is that, after the tool finishes cutting the residual workpiece of the previous cycle, the TOC has an instantaneous increase. This trend intensifies with the increase of amplitude *a*, which makes the peak value of the principal force increase. On the other hand, the decrease of average principal force is the result of the decrease in speed ratio ($V_c/2\pi fa$). With the increase of amplitude *a*, the effective cutting time decreases in a cutting cycle. It can be seen from Figure 6d that the average principal force is 69.32 N at 8 μm, and 34.75 N at 23 μm, decreasing by 49.9%.

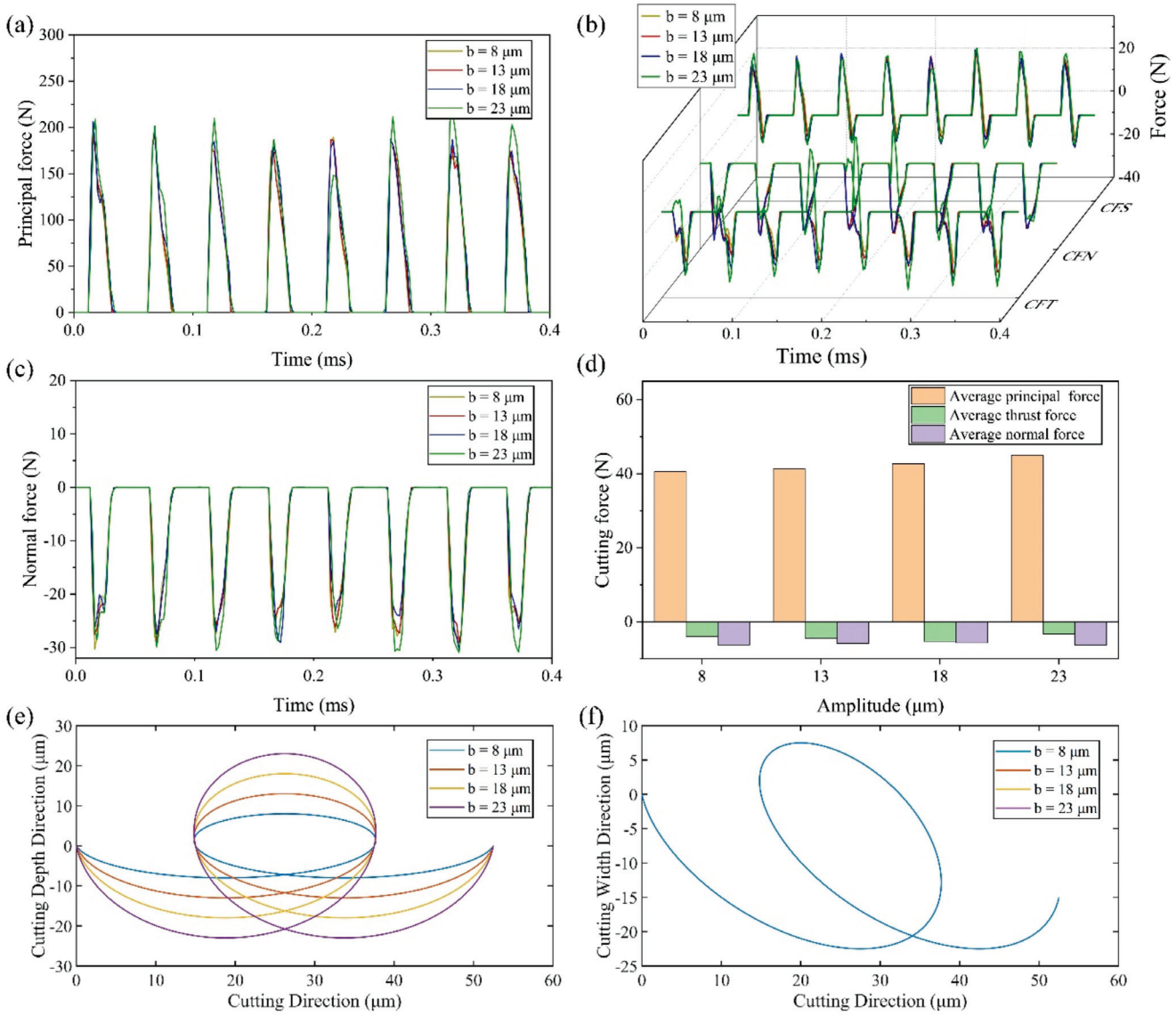

Figure 7. Results of cutting force and tool trajectories with various amplitudes *b* (**a**) principal force (**b**) thrust force (**c**) normal force (**d**) average cutting force (**e**) cutting trajectory with various amplitudes *b* in XoY plane (**f**) cutting trajectory with various amplitudes *b* in XoZ plane.

As can be seen from Figure 6b, the CFS is almost unchanged in the stage similar to ordinary cutting, and gradually decreases in the stage of friction reversal with the increase of amplitude *a*. The CFN is almost constant with the increase of amplitude *a*. However, when the amplitude *a* is 8 μm, the tool and workpiece cannot be separated completely, which causes a slight change both in CFN and normal force. CFT is influenced by both CFN and CFS, and it decreases with the increase of amplitude *a*. It can also be seen from Figure 6e that the maximum TOC in XoY plane decreases with the increase of amplitude *a*. It means that, at the same cutting depth, the higher magnitude of amplitude *a*, the smaller the cutting resistance in the cutting depth direction. In addition, the average thrust force will decrease with the increase of amplitude *a* at the condition of separated EVC. It should be noted that the CFN in the stage similar to ordinary cutting is too large due to the continuous contact of tool and workpiece when the amplitude *a* is 8 μm, so the average thrust force is small. The average thrust force is −8.03 N at 13 μm, and −4.04 N at 23 μm, decreasing by 49.7%.

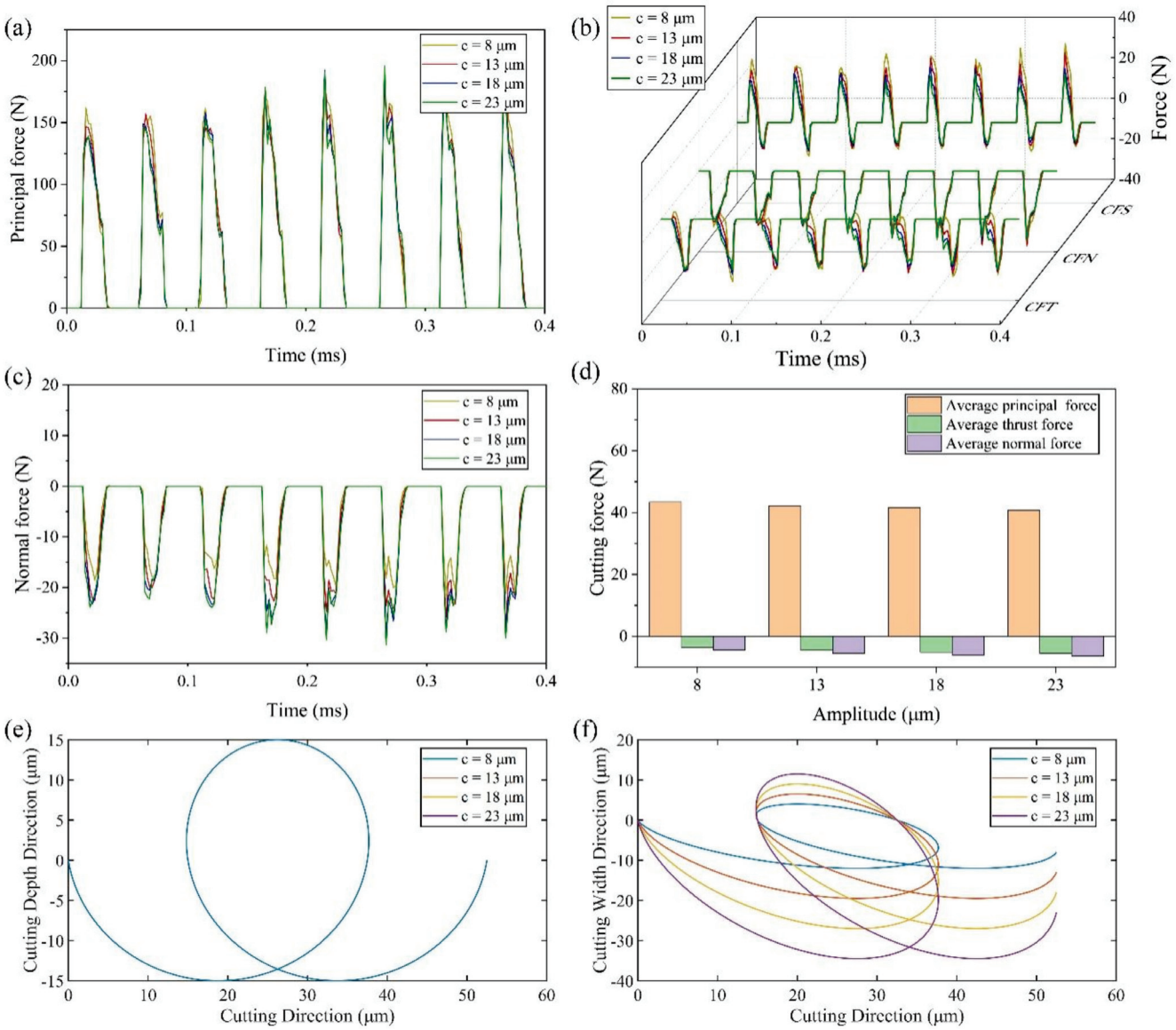

Figure 8. Results of cutting force and tool trajectories with various amplitudes *c* (**a**) principal force (**b**) thrust force (**c**) normal force (**d**) average cutting force (**e**) cutting trajectory with various amplitudes *c* in XoY plane (**f**) cutting trajectory with various amplitudes *c* in XoZ plane.

It can be seen from Figure 6f that the maximum TOC in XoZ plane in the cutting process remains unchanged with the increase of amplitude *a*. It makes the maximum normal force almost constant with the increase of amplitude *a*, as shown in Figure 6c. However, increasing amplitude *a* will reduce the effective cutting time within a single cutting cycle. Therefore, the average normal force decreases as the amplitude *a* increases at the condition of separated EVC. The average normal force is −6.87 N at 13 μm, and −5.87 N at 23 μm, decreasing by 14.6%.

(2) Effect of amplitude *b*

As demonstrated in Figure 7a,c, the real-time principal cutting force and the real-time normal force increase slightly with the increase of the amplitude *b*. The average principal force and the average normal force have the same trend with slightly changing shown in Figure 7d. The average principal cutting force and the average normal force are respectively 40.6 N and −6.21 N at 8 μm, 44.98 N and −6.27 N at 23 μm, increasing by 10.8% and 1%. Therefore, the changing of amplitude *b* has little effect on the principal force and normal

force. The reason can be attributed to the same cutting trajectory in the XoZ plane shown in Figure 7f.

It can be seen from Figure 7b that, with the increase of amplitude b, CFS has little change in the stage similar to ordinary cutting, while increases gradually in the stage of friction reversal. CFN changes little except the singular period. The maximum thrust force increases gradually with the increase of amplitude b due to the increasing volume of material that needs to be removed, which can be deduced through the trajectories shown in Figure 7e. Additionally, the friction reversal effect was shown clearly since the positive thrust force appeared in the stage similar to ordinary cutting when the amplitude b is 23 μm. Therefore, a smaller average thrust force was obtained when the amplitude b is 23 μm.

(3) Effect of amplitude c

Figure 8a,b shows that the real-time principal cutting force and thrust force are slightly affected by the amplitude c. The reason is that the amplitude c mainly affects the inclination-degree of the tool elliptical trajectory. It has no significant effect on the cutting force in the cutting direction and the cutting depth direction since the cutting trajectory in XoY plane are the same as shown in Figure 8e. The average principal force shown in Figure 8d has the value of 43.43 N at 8 μm, and 40.74 N at 23 μm, decreasing by 6.2%.

With the increase of amplitude c, CFS decreases gradually in the stage similar to ordinary cutting, and nearly remains constant in the friction reversal stage. CFN is almost unchanged. Therefore, the average thrust force increases gradually with the increasing of amplitude c. The average thrust force is −3.65 N at 8 μm, and −5.52 N at 23 μm, increasing by 51.2%.

Figure 8c,d show the increase in the real-time normal force and average normal force when increasing the amplitude c. The average normal force is −4.43 N at 8 μm, and −6.35 N at 23 μm, increasing by 43.3%. It can be seen from Figure 8f that the higher the amplitude c is, the smaller the inclination of the elliptical trajectory of the tool is. The decrease of inclination of elliptical trajectory will lead to the increase of the displacement of the tool in the feed direction, which means that more material needs to be removed in the feed direction, i.e., the maximum normal force increases.

4.1.3. Effect of Vibration Frequency on Cutting Force

Figure 9a–c shows the changes of real-time cutting force with different vibration frequencies (5–20 kHz) at cutting speed of 0.2 m/s. It can be seen from Figure 9a–c that the real-time cutting forces in three directions decrease gradually with the increase of vibration frequency. As demonstrated in Figure 9d, the average principal cutting force and normal force decrease with the increase of vibration frequency. The decrease ratio from frequency of 5 kHz to frequency of 20 kHz are respectively 57.4% and 36.3%. However, the changing trend of average thrust force is increase first and then decrease due to the friction reversal effect. The critical cutting speed ($2\pi fa$) increases directly as the vibration frequency increases, which results in more cutting cycles at the same distance, as shown in Figure 9e,f. With the increasing of vibration frequency, the less volume of material needs to be removed in a single cutting cycle, resulting in a lower cutting component force in three directions.

4.1.4. Effect of Cutting Depth on Cutting Force

Figure 10a–c shows the changes of real-time cutting force at different cutting depths (0.02–0.08 mm). It can be seen from Figure 10a–c that, with the increase of cutting depth, the real-time principal force, the real-time thrust force and the real-time normal force increase significantly. Figure 10d shows the changing trend of average cutting force. The average cutting force in three directions increases with the increase of the cutting depth, except the average thrust force at cutting depth of 0.06 mm. The abnormal value of average thrust force is due to the abnormal periods of CFN. The average forces in three directions are: 18.92 N, −3.11 N and −8.72 N at 0.02 mm, 34.13 N, −3.91 N and −13.12 N at 0.08 mm, increasing by 80.4%, 25.7% and 50.5%, respectively. The reason can be attributed to the cutting area in EVC being proportional to the cutting depth [19]. As the cutting depth

increases, the volume of material that needs to be removed increases significantly, resulting in an increase in cutting force.

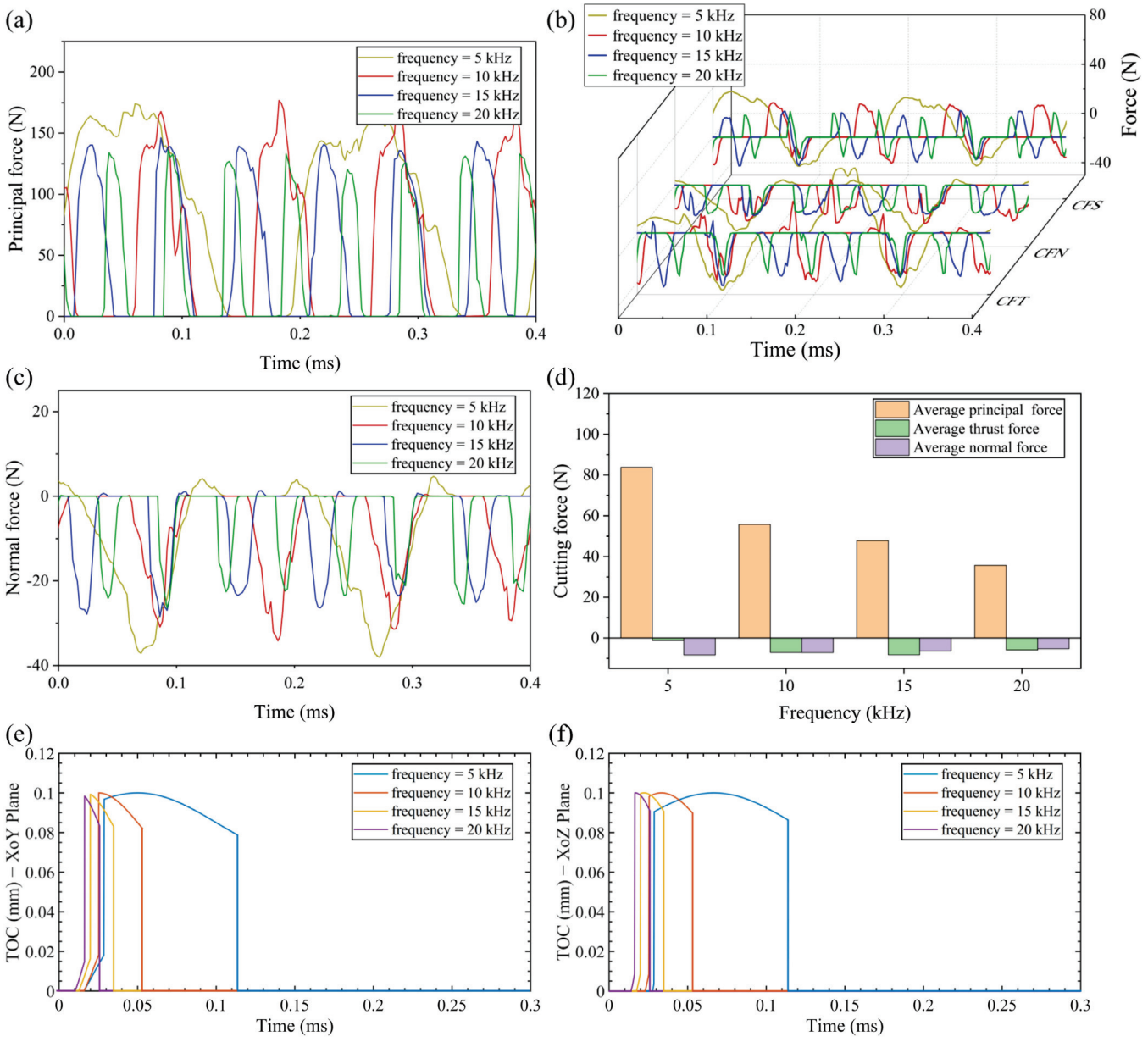

Figure 9. Results of cutting force and TOC with various vibration frequencies (**a**) principal force (**b**) thrust force (**c**) normal force (**d**) average cutting force (**e**) TOC with various vibration frequencies in XoY plane (**f**) TOC with various vibration frequencies in XoZ plane.

4.2. Effect of Cutting Parameters on Residual Stress

Considering that residual stress analysis involves multiple analysis steps, in order to reduce the calculation time and improve the calculation accuracy, the model used in this section is modified: the workpiece size is 2 mm × 1 mm × 1 mm, and the total number of workpiece and tool meshes is 260,000 and 4506, respectively. The calculation process of residual stress in actual production is divided into four stages [42]: cutting, tool removal, boundary constraint removal and cooling. While the steps in the finite element simulation are set as cutting, tool removal and cooling. When cooling is set, the clamping mode of the workpiece is changed from fixing the bottom and both sides of the workpiece to fixing three endpoints of the workpiece, so that the boundary constraint removal step in actual production can be approximately simulated. As shown in Figure 11, the sampling path

is set as the intersection line of two middle planes to study the effect of different cutting parameters on the residual stress.

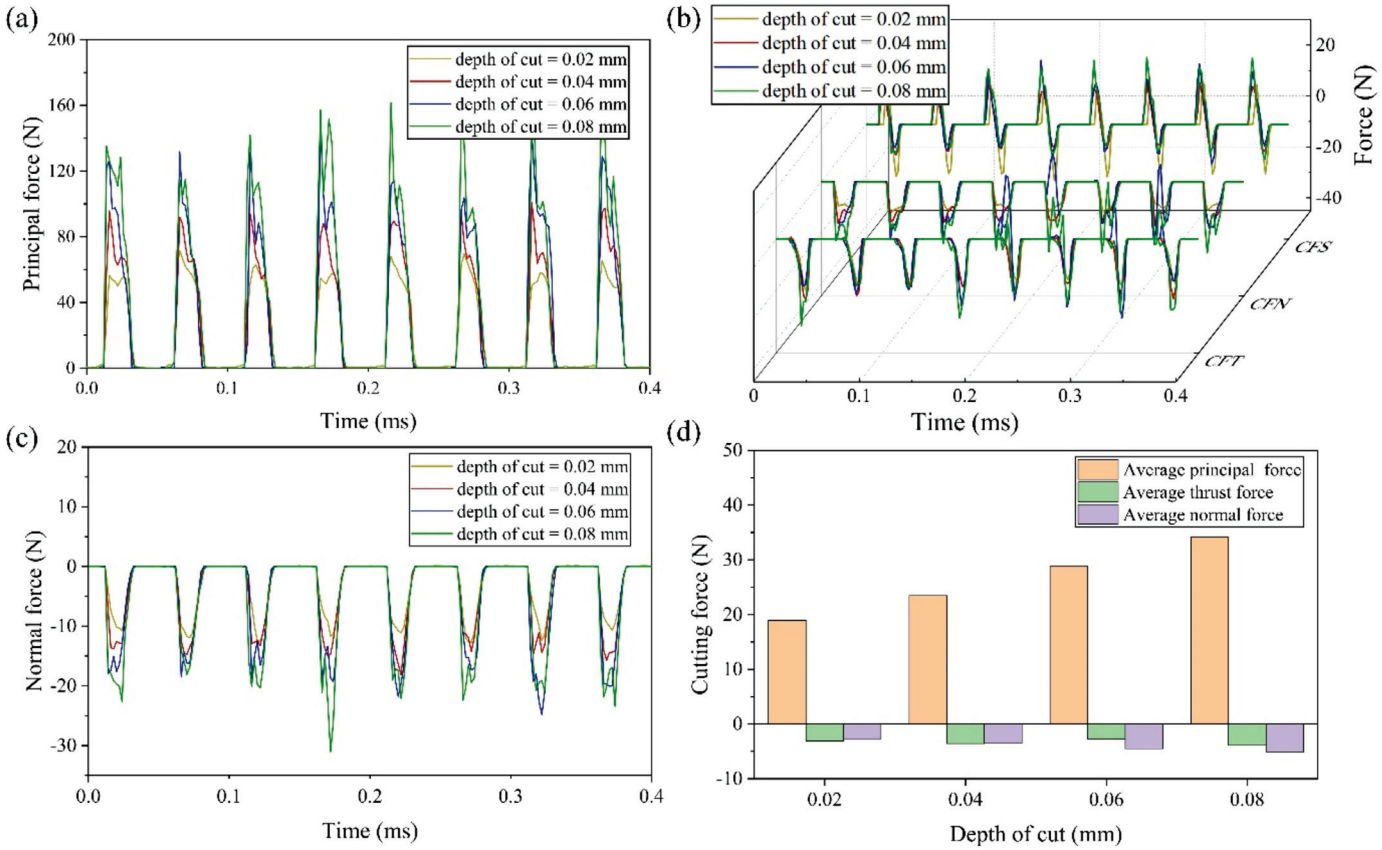

Figure 10. Results of cutting force with various cutting depths (**a**) principal force (**b**) thrust force (**c**) normal force (**d**) average cutting force.

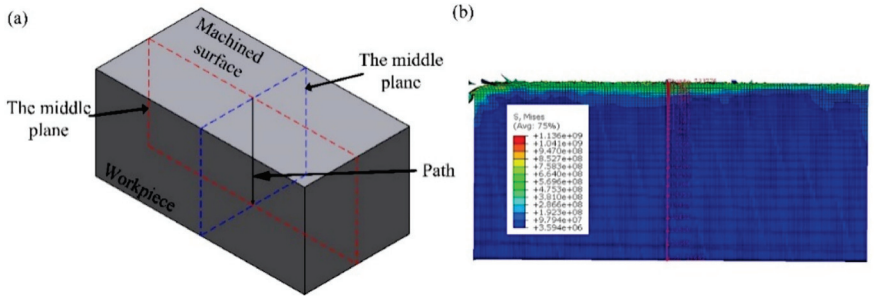

Figure 11. The path of obtained residual stress. (**a**) 3D view (**b**) front view.

This section also uses a single variable method to explore the effect of each cutting parameter on the residual stress. When exploring the effect of one cutting parameter on residual stress, the other cutting parameters take the default values. The default value is that the amplitudes of a, b and c are 10 μm, 15 μm and 18 μm, respectively, the vibration frequency is 20 kHz, the cutting depth is 0.08 mm, the cutting speed is 0.4 m/s and the rake and clearance angles of the tool are both 10 degrees.

4.2.1. Effect of Cutting Speed on Residual Stress

Figure 12 shows the residual stress in three directions with different cutting speeds (0.3–0.5 m/s). Figure 12a shows that, when the cutting speed is 0.3 m/s, the stress-xx of the machined surface layer of the workpiece is compressive stress. As the distance

from the machined surface increases, the compressive stress increases and reaches the maximum value when the distance from the machined surface is about 0.03 mm. Then the compressive stress gradually decreases and reversely changes to tensile stress. The tensile stress firstly increases to the maximum value and then decreases gradually and finally approaches zero. The variation trend of residual stress at 0.4 m/s and 0.5 m/s is similar to that at 0.3 m/s. However, with the increase of the speed, the compressive stress of the machined surface layer of the workpiece increases gradually, and the maximum compressive stress also increases gradually.

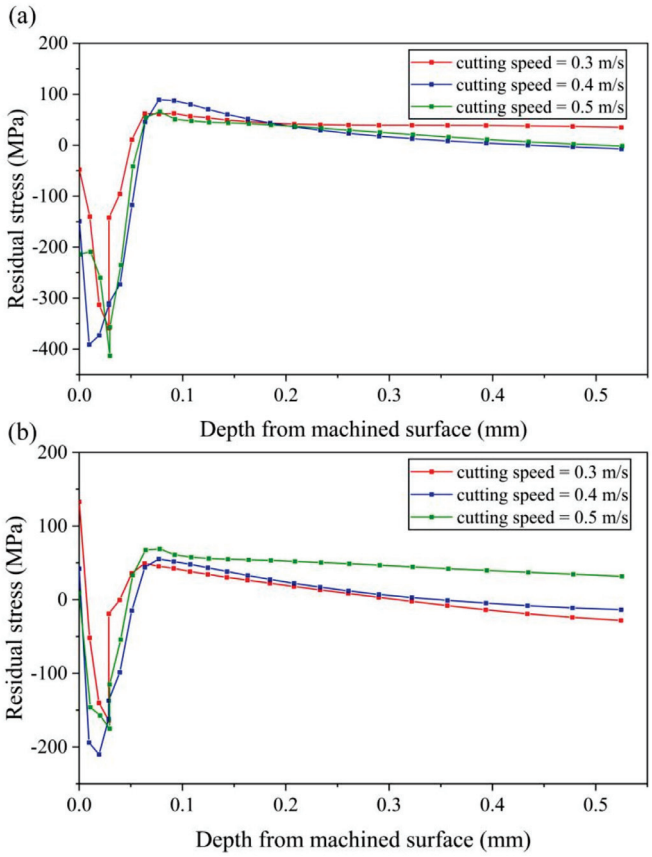

Figure 12. Results of residual stress with various cutting speeds (**a**) stress-xx (**b**) stress-zz.

Figure 12b shows that the stress-zz of the machined surface layer of the workpiece is tensile stress. With the increase of cutting speed, the tensile stress of the machined surface layer of the workpiece decreases gradually. As the distance from the machined surface increases, stress-zz tends to decrease in tensile stress and changes to compressive stress. After the compressive stress reaches the maximum value, it decreases and then changes to tensile stress with the increases of the distance from the machined surface. Finally, tensile stress tends to a stable value close to zero.

4.2.2. Effect of Vibration Amplitude on Residual Stress

Figures 13–15 shows the change of residual stress at different vibration amplitudes in three directions, setting amplitudes a, b and c, to 10 μm, 15 μm and 18 μm, respectively.

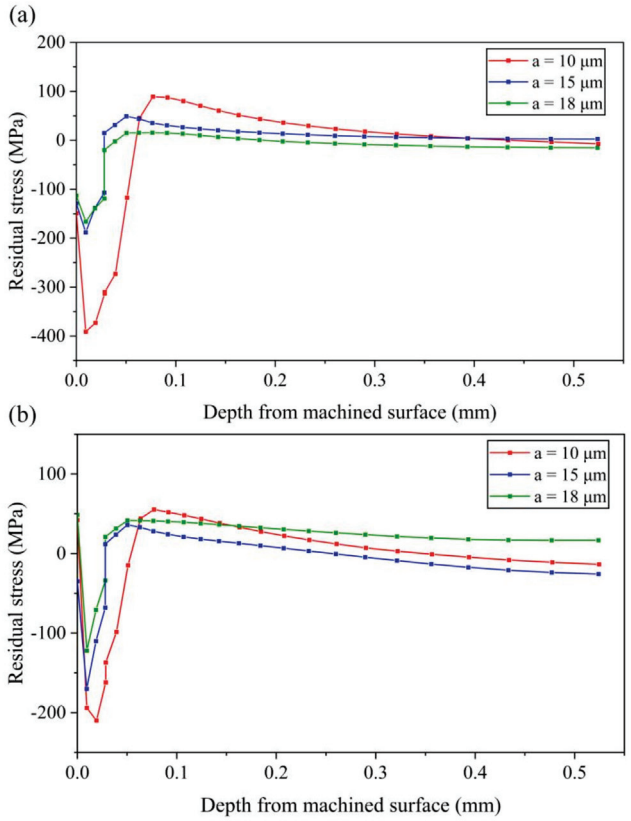

Figure 13. Results of residual stress with various amplitudes *a* (**a**) stress-xx (**b**) stress-zz.

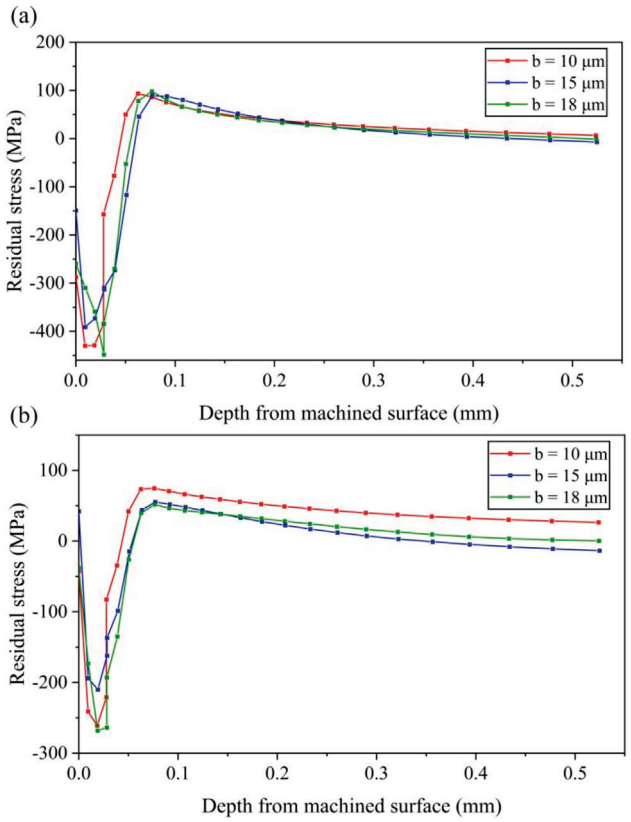

Figure 14. Results of residual stress with various amplitudes *b* (**a**) stress-xx (**b**) stress-zz.

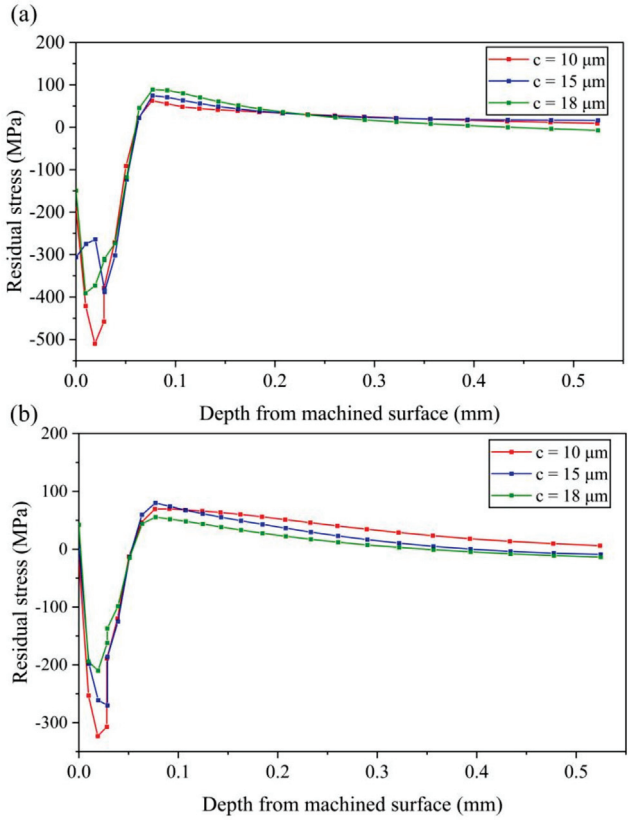

Figure 15. Results of residual stress with various amplitudes *c* (**a**) stress-xx (**b**) stress-zz.

(1) Effect of amplitude *a*

It can be seen from Figure 13a that the compressive stress of the machined surface layer of the workpiece decreases gradually with the increase of amplitude *a*. The maximum values of tensile stress and compressive stress decrease with the increase of amplitude. Especially when the amplitude *a* increases from 10 μm to 15 μm, both tensile stress and compressive stress decrease greatly. It can be concluded that, when the amplitude *a* is small, the stress-xx of the machined surface layer easily becomes a large compressive stress.

As shown in Figure 13b, with the increase of amplitude *a*, the maximum value of the compressive stress decreases, while the maximum value of tensile stress decreases first and then increases with the increase of amplitude *a*.

(2) Effect of amplitude *b*

It can be seen from Figure 14a that stress-xx changes little with the increase of amplitude *b*. The compressive stress on the machined surface layer of the workpiece decreases first and then increases with the increase of amplitude *b*. Both the maximum tensile stress and compressive stress decrease first and then increase with the increase of amplitude *b*. For stress-zz, the change trend of maximum compressive stress is the same as stress-xx, as shown in Figure 14b, while the maximum tensile stress decreases with the increase of amplitude *b*. According to the results of residual stress with vary amplitude *b*, it can be concluded that the effect of amplitude *b* on the residual stress is small.

(3) Effect of amplitude *c*

It can be seen from Figure 15a that, with the increase of amplitude *c*, the compressive stress on the machined surface layer increases first and then decreases. Increasing amplitude *c* can effectively reduce the maximum compressive stress. The maximum tensile stress increases with the increase of amplitude *c*, but the variation is small.

As can be seen from Figure 15b, the maximum compressive stress decreases with the increase of amplitude *c*. The maximum tensile stress increases first and then decreases. Therefore, it can be concluded that the large compressive stress can be obtained under the

machined surface layer by setting a small amplitude c, which is helpful to improve the working performance of the workpiece.

4.2.3. Effect of Vibration Frequency on Residual Stress

Setting different vibration frequencies to 10 kHz, 15 kHz and 20 kHz, respectively, the cutting speed is 0.3 m/s to ensure the cutting process be a separated EVC. The results of residual stress corresponding to different vibration frequency are shown in Figure 16.

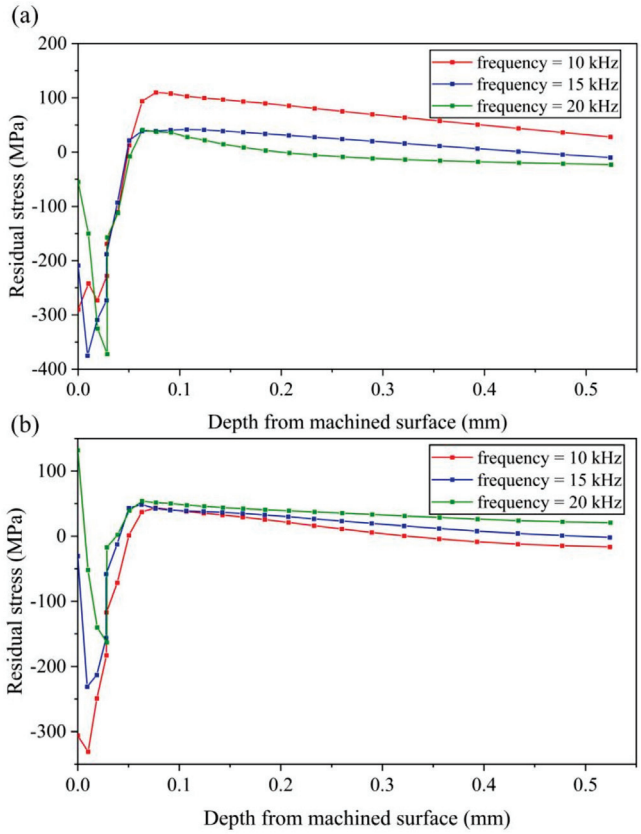

Figure 16. Results of residual stress with various vibration frequencies (**a**) stress-xx (**b**) stress-zz.

As can be seen from Figure 16a, with the increase of vibration frequency, the stress-xx of the machined surface decreases gradually, and the maximum tensile stress also decreases gradually. As the distance from the machined surface increases, the tensile stress tends to zero with the increase of frequency. As shown in Figure 16b, with the increase of frequency, the maximum compressive stress of stress-zz decreases gradually, and the maximum tensile stress changes little.

4.2.4. Effect of Cutting Depth on Residual Stress

The effect of cutting depth on residual stress is shown in Figure 17. It can be seen that, with the increase of cutting depth, both the maximum tensile stress and the maximum compressive stress increase first and then decrease. The residual stress on machined workpiece surface also increases first and then decreases. Compared with the stress-xx at cutting depth of 0.08 mm shown in Figure 16a, it can be concluded that, with the increasing of cutting depth, it is much easier to obtain a larger magnitude of compressive stress layer near the machined surface. The same conclusion can be obtained for stress-zz when compared with the stress-zz at cutting depth of 0.08 mm shown in Figure 16b.

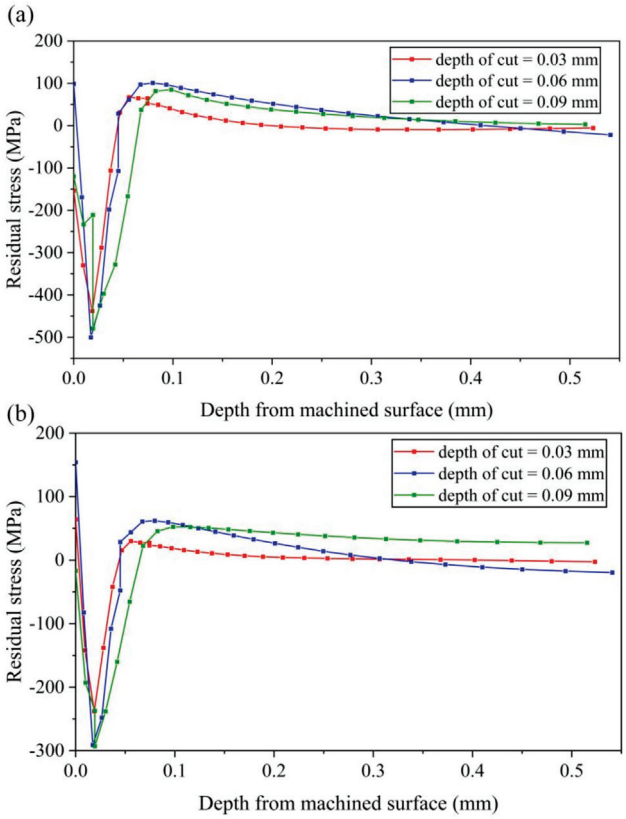

Figure 17. Results of residual stress with various cutting depths (**a**) stress-xx (**b**) stress-zz.

5. Conclusions

In this paper, the Finite Element Method was utilized to investigate the influence of processing parameters on cutting force and residual stress. A Johnson-Cook constitutive model was adopted to illustrate the plastic behavior of Ti6Al4V alloy. The kinematics of the 3D EVC were described first, and then the effect of vary cutting speed, vibration amplitude, vibration frequency and depth of cut on cutting force and residual stress were carried out and analyzed.

Compared with the effect of changing cutting parameters on thrust force and normal force, simulation results show that the change of cutting speed, vibration amplitude a, vibration frequency and depth of cut have larger effect on principal force. The principal force increases gradually with the increase of cutting speed from 0.1 m/s to 0.4 m/s. The increase ratio in average principal force can reach up to 81.9%. The maximum principal force increases with the increase of amplitude a. However, the average principal force decreases with the increase of amplitude a due to the decrease of effective cutting time in a cutting cycle. The decrease ratio is about 49.9% from amplitude of 8 μm to 23 μm. The principal force decreases with the increase of vibration frequency. The decrease ratio of average principal force is about 57.4% from a frequency of 5 kHz to 20 kHz. Meanwhile, the principal force increases with the increase of cutting depth. The decrease ratio of average principal force is about 80.4% from cutting depth of 0.02 mm to 0.08 mm. In addition, an interesting phenomenon should be noted: the friction reversal effect can not be found from the thrust force curve due to the combination of CFN and CFS, but this reversal effect does exist which can be seen clearly from the CFS curve.

Moreover, changing various cutting parameters have different effects on residual stress of machined workpiece surface in x direction and z direction. The simulation results show that the stress-xx on machined workpiece surface increases with the increase of cutting speed, decreases with the increase of amplitude a and vibration frequency. It first increases and then decreases with the increase of amplitude c and first decreases and then increases

with the increase of amplitude *b* and cutting depth. The stress-zz on machined workpiece surface decreases with the increase of amplitude *b* and cutting speed. It first increases and then decreases with the increase of cutting depth. Meanwhile, it first decreases and then increases with the increase of amplitude *a*, amplitude *c* and vibration frequency. Above all, it can be seen from the study of residual stress that the compressive stress layer can be easily obtained near the machined surface by using 3D EVC, which is helpful to improve the working performance of workpiece.

Author Contributions: Conceptualization, S.L. and J.H.; methodology, S.L. and J.H.; software, S.L.; validation, S.L., J.H. and H.Y.; formal analysis, S.L. and J.W.; investigation, S.L.; resources, J.H., M.L. and J.L.; data curation, S.L.; writing—original draft preparation, S.L.; writing—review and editing, J.H. and Y.T.; visualization, S.L.; supervision, J.H. and Y.T.; project administration, J.H.; funding acquisition, J.H. All authors have read and agreed to the published version of the manuscript.

Funding: This research was funded by National Natural Science Foundation of China, grant number 51905322, and the China postdoctoral Science Foundation, grant number 2021T140420.

Institutional Review Board Statement: Not applicable.

Informed Consent Statement: Not applicable.

Data Availability Statement: Not applicable.

Conflicts of Interest: The authors declare no conflict of interest.

References

1. Arrazola, P.J.; Garay, A.; Iriarte, L.M.; Armendia, M.; Marya, S.; Maître, F.L. Machinability of titanium alloys (Ti6Al4V and Ti555.3). *J. Mater. Process. Technol.* **2009**, *209*, 2223–2230. [CrossRef]
2. Corduan, N.; Himbart, T.; Poulachon, G.; Dessoly, M.; Lambertin, M.; Vigneau, J. Wear mechanisms of new tool materials for Ti-6AI-4V high performance machining. *CIRP Ann.* **2003**, *52*, 73–76. [CrossRef]
3. Muthuramalingam, T.; Moiduddin, K.; Akash, R.; Krishnan, S.; Mian, S.H.; Ameen, W. Influence of process parameters on dimensional accuracy of machined Titanium (Ti-6Al-4V) alloy in Laser Beam Machining Process. *Opt. Laser Technol.* **2020**, *132*, 106494. [CrossRef]
4. Singh, N.K.; Singh, Y.; Sharma, A.; Prasad, R. Experimental investigation of flushing approaches on EDM machinability during machining of titanium alloy. *Mater. Today. Proc.* **2021**, *38*, 139–145. [CrossRef]
5. Patrycja, S.Z.; Grzegorz, Z.; Viktoria, H.; Małgorzata, R.; Karol, K.; Marcin, M. Improved quality and functional properties of Ti-6Al-4V ELI alloy for personalized orthopedic implants fabrication with EBM process. *J. Manuf. Processes* **2022**, *76*, 175–194. [CrossRef]
6. Su, Y.S.; Li, L. An Investigation of Cutting Performance and Action Mechanism in Ultrasonic Vibration-Assisted Milling of Ti6Al4V Using a PCD Tool. *Micromachines* **2021**, *12*, 1319. [CrossRef]
7. Shamoto, E.; Moriwaki, T. Study on elliptical vibration cutting. *CIRP Ann.* **1994**, *43*, 35–38. [CrossRef]
8. Maroju, N.K.; Jin, X.L. Effect of speed ratio on shear angle and forces in elliptical vibration assisted machining. *J. Mater. Process. Technol.* **2022**, *302*, 117498. [CrossRef]
9. Ahn, J.H.; Lim, H.S.; Son, S.M. Improvement of micromachining accuracy by 2-Dimensional vibration cutting. *Proc. Aspe.* **1999**, *20*, 150–153.
10. Suzuki, N.; Haritani, M.; Yang, J.; Hino, R.; Shamoto, E. Elliptical Vibration Cutting of Tungsten Alloy Molds for Optical Glass Parts. *CIRP Ann.* **2007**, *56*, 127–130. [CrossRef]
11. Matthew, A.C. *Elliptical Diamond Milling: Kinematics, Force and Tool Wear*; North Carolina State University: Raleigh, NC, USA, 2001.
12. Shamoto, E.; Moriwaki, T. Ultaprecision diamond cutting of hardened steel by applying elliptical vibration cutting. *CIRP Ann.* **1999**, *48*, 441–444. [CrossRef]
13. Ma, C.X.; Shamoto, E.; Moriwaki, T. Study on the thrust cutting force in ultrasonic elliptical vibration cutting. *Mater. Sci. Forum.* **2004**, *471*, 396–400. [CrossRef]
14. Liu, X.B.; Xiong, R.L.; Xiong, Z.W.; Zhang, S.J.; Zhao, L. Simulation and experimental study on surface residual stress of ultra-precision turned 2024 aluminum alloy. *J. Braz. Soc. Mech. Sci.* **2020**, *42*, 386. [CrossRef]
15. Saito, H.; Jung, H.; Shamoto, E. Elliptical vibration cutting of hardened die steel with coated carbide tools. *Precis. Eng.* **2016**, *45*, 44–54. [CrossRef]
16. Nath, C. *A study on ultrasonic vibration cutting of difficult-to-cut materials*; National University of Singapore: Singapore, 2008.
17. Song, Y.C.; Park, C.H.; Moriwaki, T. Mirror finishing of Co-Cr-Mo alloy using elliptical vibration cutting. *Precis. Eng.* **2010**, *34*, 784–789. [CrossRef]
18. Guo, P.; Lu, Y.; Pei, P.C.; Ehmann, K.F. Fast generation of micro-channels on cylindrical surfaces by elliptical vibration texturing. *J. Manuf. Sci. Eng. ASME* **2014**, *136*, 041008. [CrossRef]

19. Kurniawan, R.; Kiswanto, G.; Ko, T.J. Micro-dimple pattern process and orthogonal cutting force analysis of elliptical vibration texturing. *Int. J. Mach. Tools Manuf.* **2016**, *106*, 127–140. [CrossRef]
20. Xu, S.L.; Shimada, K.; Mizutani, M.; Kuriyagawa, T. Development of a novel 2D rotary ultrasonic texturing technique for fabricating tailored structures. *Int. J. Adv. Manuf. Technol.* **2017**, *89*, 1161–1172. [CrossRef]
21. Shamoto, E.; Suzuki, N.; Hino, R. Analysis of 3D elliptical vibration cutting with thin shear plane model. *CIRP Ann.* **2008**, *57*, 57–60. [CrossRef]
22. Lin, J.Q.; Li, Y.C.; Zhou, X.Q. Tool path generation for fabricating optical freeform surfaces by non-resonant three-dimensional elliptical vibration cutting. *Proc. Inst. Mech. Eng. Part C J. Manuf. Eng. Sci.* **2014**, *228*, 1208–1222. [CrossRef]
23. Lin, J.Q.; Lu, M.M.; Zhou, X.Q. Development of a Non-Resonant 3D Elliptical Vibration Cutting Apparatus for Diamond Turning. *Exp. Tech.* **2016**, *40*, 173–183. [CrossRef]
24. Lin, J.Q.; Liu, J.H.; Gao, X.P.; Wang, S.Q. Modeling and Analysis of Machining Force in Elliptical Vibration Cutting. *Adv. Mater. Res.* **2013**, *2384*, 2464–2469. [CrossRef]
25. Lu, M.M.; Zhou, J.K.; Lin, J.Q.; Gu, Y.; Han, J.G.; Zhao, D.P. Study on Ti-6Al-4V alloy machining applying the non-resonant three-dimensional elliptical vibration cutting. *Micromachines* **2017**, *8*, 306. [CrossRef] [PubMed]
26. Li, Y.C.; Zhou, X.Q.; Lu, M.M.; Lin, J.Q.; Sun, J.B. Parameters Optimization for Machining Optical Parts of Difficult-To-cut Materials by Genetic Algorithm. *Mater. Manuf. Processes* **2013**, *29*, 9–14. [CrossRef]
27. Lin, J.Q.; Jing, X.; Lu, M.M.; Gu, Y.; Han, J.G. Study on the tool wear of 3-D elliptical vibration cutting. *Mech. Sci.* **2017**, *8*, 215–220. [CrossRef]
28. Kurniawan, R.; Ali, S.; Ko, T.J. Measurement of wettability on rhombohedral pattern fabricated by using 3D-UEVT. *Measurement* **2020**, *160*, 107784. [CrossRef]
29. Wang, H.; Hu, Y.B.; Cong, W.L.; Hu, Z.Y.; Wang, Y.Q. A novel investigation on horizontal and 3D elliptical ultrasonic vibrations in rotary ultrasonic surface machining of carbon fber reinforced plastic composites. *J. Manuf. Processes* **2020**, *52*, 12–25. [CrossRef]
30. Outeiro, J.; Cheng, W.Y.; Chinesta, F.; Ammar, A. Modelling and Optimization of Machining of Ti-6Al-4V Titanium Alloy Using Machine Learning and Design of Experiments Methods. *J. Manuf. Mater. Process.* **2022**, *6*, 58. [CrossRef]
31. Friderikos, O.; Sagris, D.; David, C.N.; Korlos, A. Simulation of Adiabatic Shear Bands in Orthogonal Machining of Ti6Al4V Using a Rigid-Viscoplastic Finite Element Analysis. *Metals.* **2020**, *10*, 338. [CrossRef]
32. Sun, Z.T.; Shuang, F.; Ma, W. Investigations of vibration cutting mechanisms of Ti6Al4V alloy. *Int. J. Mech. Sci.* **2018**, *148*, 510–530. [CrossRef]
33. Airao, J.; Nirala, C.K.; Outeiro, J.; Khanna, N. Surface integrity in ultrasonic-assisted turning of Ti6Al4V using sustainable cutting fluid. *Procedia CIRP* **2022**, *108*, 55–60. [CrossRef]
34. Xie, H.B.; Wang, Z.J. Study of cutting forces using FE, ANOVA, and BPNN in elliptical vibration cutting of titanium alloy Ti-6Al-4V. *Int. J. Adv. Manuf. Technol.* **2019**, *105*, 5105–5120. [CrossRef]
35. Wang, Z.D.; Pan, Y.Z.; Zhang, Y.J.; Men, X.H.; Fu, X.L.; Ren, S.F. Study on the Material Removal Mechanism of Ultrasonic Elliptical Vibration Cutting of Medical β Titanium Alloy. *Micromachines* **2022**, *13*, 819. [CrossRef]
36. Zhou, J.K.; Lu, M.M.; Lin, J.Q.; Du, Y.S. Elliptic vibration assisted cutting of metal matrix composite reinforced by silicon carbide: An investigation of machining mechanisms and surface integrity. *J. Mater. Res. Technol.* **2021**, *15*, 1115–1129. [CrossRef]
37. Kurniawan, R.; Ali, S.; Ko, T.J. Finite Element Analysis in Ultrasonic Elliptical Vibration Cutting (UEVC) During Micro Grooving in AISI 1045. *Int. J. Precis. Eng. Man.* **2021**, *22*, 1497–1515. [CrossRef]
38. Lee, W.S.; Lin, C.F. High-temperature deformation behavior of Ti6Al4V alloy evaluated by high strain-rate compression tests. *J. Mater. Process. Technol.* **1998**, *75*, 127–136. [CrossRef]
39. Chen, G.; Ren, C.Z.; Yang, X.Y.; Jin, X.M.; Guo, T. Finite element simulation of high-speed machining of titanium alloy (Ti–6Al–4V) based on ductile failure model. *Int. J. Adv. Manuf. Technol.* **2011**, *56*, 1027–1038. [CrossRef]
40. Hillerborg, A.; Modéer, M.; Petersson, P.E. Analysis of crack formation and crack growth in concrete by means of fracture mechanics and finite elements. *Cem. Concr. Res.* **1976**, *6*, 773–781. [CrossRef]
41. Lin, J.Q.; Han, J.G.; Zhou, X.Q.; Hao, Z.P.; Lu, M.M. Study on predictive model of cutting force and geometry parameters for oblique elliptical vibration cutting. *Int. J. Mech. Sci.* **2016**, *117*, 43–52. [CrossRef]
42. Shet, C.; Deng, X. Residual stresses and strains in orthogonal metal cutting. *Int. J. Mach. Tools Manuf.* **2003**, *43*, 573–587. [CrossRef]

micromachines

Article

An Investigation into the Densification-Affected Deformation and Fracture in Fused Silica under Contact Sliding

Changsheng Li [1,2], Yushan Ma [3], Lin Sun [1,*], Liangchi Zhang [4,5,6], Chuhan Wu [7], Jianjun Ding [1,*], Duanzhi Duan [1], Xuepeng Wang [3] and Zhandong Chang [3]

1 State Key Laboratory for Manufacturing Systems Engineering, Xi'an Jiaotong University, Xi'an 710049, China; li.changsheng@xjtu.edu.cn (C.L.); dzduan@163.com (D.D.)
2 State Key Laboratory of Mechanical System and Vibration, Shanghai Jiaotong University, Shanghai 200240, China
3 Wuzhong Instrument Co., Ltd., Wuzhong 751199, China; mys@wzyb.com.cn (Y.M.); 18729961058@163.com (X.W.); czd@wzyb.com.cn (Z.C.)
4 Shenzhen Key Laboratory of Cross-scale Manufacturing Mechanics, Southern University of Science and Technology, Shenzhen 518055, China; zhanglc@sustech.edu.cn
5 SUSTech Institute for Manufacturing Innovation, Southern University of Science and Technology, Shenzhen 518055, China
6 Department of Mechanics and Aerospace Engineering, Southern University of Science and Technology, Shenzhen 518055, China
7 School of Mechanical and Manufacturing Engineering, The University of New South Wales, Sydney, NSW 2052, Australia; chuhan.wu@unsw.edu.au
* Correspondence: sunlin@xjtu.edu.cn (L.S.); dianjianjun@126.com (J.D.)

Abstract: Subsurface damage of fused silica optics is one of the major factors restricting the performance of optical systems. The densification-affected deformation and fracture in fused silica under a sliding contact are investigated in this study, via three-dimensional finite element analysis (FEA). The finite element models of scratching with 70.3° conical and Berkovich indenters are established. A refined elliptical constitutive model is used to consider the influence of densification. The finite element models are experimentally verified by elastic recovery, and theoretically verified by hardness ratio. Results of densification and plastic deformation distributions indicate that the accuracy of existent sliding stress field models may be improved if the spherical/cylindrical yield region is replaced by an ellipsoid/cylindroid, and the embedding of the yield region is considered. The initiation sequence, and the locations and stages of radial, median, and lateral cracks are discussed by analyzing the predicted sliding stress fields. Median and radial cracks along the sliding direction tend to be the first cracks that emerge in the sliding and unloading stages, respectively. They coalesce to form a big median–radial crack that penetrates through the entire yield region. The fracture behavior of fused silica revealed in this study is essential in the low-damage machining of fused silica optics.

Keywords: sliding contact; fused silica; densification; finite element analysis; cracks

Citation: Li, C.; Ma, Y.; Sun, L.; Zhang, L.; Wu, C.; Ding, J.; Duan, D.; Wang, X.; Chang, Z. An Investigation into the Densification-Affected Deformation and Fracture in Fused Silica under Contact Sliding. *Micromachines* **2022**, *13*, 1106. https://doi.org/10.3390/mi13071106

Academic Editors: Chengwei Kang, Chunjin Wang and Jiang Guo

Received: 30 June 2022
Accepted: 9 July 2022
Published: 14 July 2022

1. Introduction

Fused silica, or silica-rich glass optics, are widely used in laser nuclear fusion devices [1], large astronomical telescopes [2], semiconductor technology [3,4], and consumer electronics. Subsurface damage has plenty of negative effects on the performance of optics, e.g., increasing optical scatter, reducing mechanical strength, and increasing laser-induced damage (LID). For instance, the subsurface damage is one of the precursors resulting in LID. The LID of fused silica optics is one of the key factors restricting the output power and a key challenge for the long-term and stable operation of high-power laser facilities [5]. Therefore, an in-depth understanding of the material removal and damage formation mechanisms of fused silica subjected to machining is essential to fabricate damage-free optics.

Fused silica optics are generally fabricated by abrasive grain-based methods, e.g., grinding and polishing. Therefore, indentation/scratching mechanics are widely used to study the fracture of fused silica subjected to machining [6,7]. In addition to the contact pressure between the indenter and the sample, the indentation stress field also results from a misfit between the plastic zone beneath the indentation and the surrounding elastic matrix. Therefore, the elastic indentation models, e.g., the classical Boussinesq solution and Hertzian field [8] for elastic contact, are insufficient. Later on, Hill et al. [9] developed a model for the wedge indentation of the rigid–perfectly-plastic materials. However, this model is not suitable for indentation with blunt indenters, or with materials with a low ratio of Young's modulus to yield stress. To this end, Johnson et al. [10] proposed the expanding-cavity model that treats the indentation-induced plastic zone as an expanding zone. This model was successfully used by Lawn et al. [11] to analyze the indentation damage in ceramics.

Different from most materials, fused silica suffered from significant permanent volume contraction under high hydrostatic pressure. This phenomenon is known as densification [12]. The aforementioned indentation stress field models ignore the influence of densification, which limits the accuracy for fused silica. In order to solve this problem, Yoffe [13] proposed the Blister stress field model, which, for the first time, integrates the material densification. Li et al. [14] modified the ECD model to make it suitable for materials with densification. Compared with the Yoffe model, the modified ECD model considers the distribution characteristics of the contact pressure between the indenter and the sample. In addition, the center of the plastic zone is not restricted in the sample surface.

The grinding and polishing processes are more analogous to successive scratching compared with indentations. The studies on analytical sliding stress fields are rather limited. Hamilton and Goodman [15] proposed an elastic model for sliding contact. Ahn et al. [16] developed the sliding blister stress field model by extending the Yoffe model to scratching, in which the plastic deformation and material densification were considered. Similar models were used to analyze the cracking behavior of BK7 glass [17], fused silica [17], and silicon [18] subjected to scratching. However, these models assume that the indenter is conical and the center of plastic zone locates in the sample surface, which limits the prediction accuracy.

The finite element method is a powerful tool to investigate the deformation, friction [19], wear [20], and fracture [21] of brittle materials subjected to scratching. It should be noted, however, that in these studies the constitutive models used were either purely elastic or von Mises [22], and that the effects of material densification were neglected. Imaoka et al. [23] and Gadelrab et al. [24] developed the positive linear models to consider densification. The mean hydrostatic stress is linear with the equivalent shear stress in these models. Xin et al. [25] proposed a negative linear model to explain the unique features of fused silica during grinding and polishing. Kermouche et al. [26] proposed an elliptical constitutive model to consider the shear-assisted densification. This model considers the hardening of yield pressure with densification, which is neglected in the linear models. The elliptical model is widely used to investigate the indentation deformation and fracture in fused silica [12,27]. Later on, the elliptical constitutive model was refined by Li et al. [28], to consider the influence of densification on elastic properties and the saturation of densification with hydrostatic pressure. This refined elliptical model was successfully used to study the indentation mechanisms [28,29] and sliding friction behavior [30].

This paper aims to establish three-dimensional finite element models for conical and Berkovich scratching using the refined elliptical model. Finite element simulations are performed to investigate the densification and deformation in fused silica subjected to scratching to reveal the stress field more precisely. The influence of friction on indentation and scratching hardness is investigated, and the cracking behavior of fused silica under scratching explored.

2. Scratching Tests

As shown in Figure 1, fused silica samples (Corning UV 7980, Corning Corp., Corning, NY, USA) were scratched by an edge-forward Berkovich tip on a nanoindentation machine (TI-950 TriboIndenter, Hysitron Inc., Eden Prairie, MN, USA). The samples were carefully polished to achieve a surface roughness small than 2 nm. Scratching tests were performed under constant normal loads of 1 mN, 2 mN, 4 mN, 200 mN, 400 mN, 600 mN, 1 N, and 1.2 N. The sliding length was 250 μm, which is significantly greater than the scratching depth. The scratching process consists of the approaching stage Ⓐ, the preliminary profiling stage Ⓑ (to obtain the original surface profile), the indentation stage Ⓒ, the scratching stage Ⓓ, the unloading stage Ⓔ, and the postmortem profiling stage Ⓕ (to obtain the residual surface profile). The variations of normal load, normal displacement, lateral load, and lateral displacement with time were recorded during scratching.

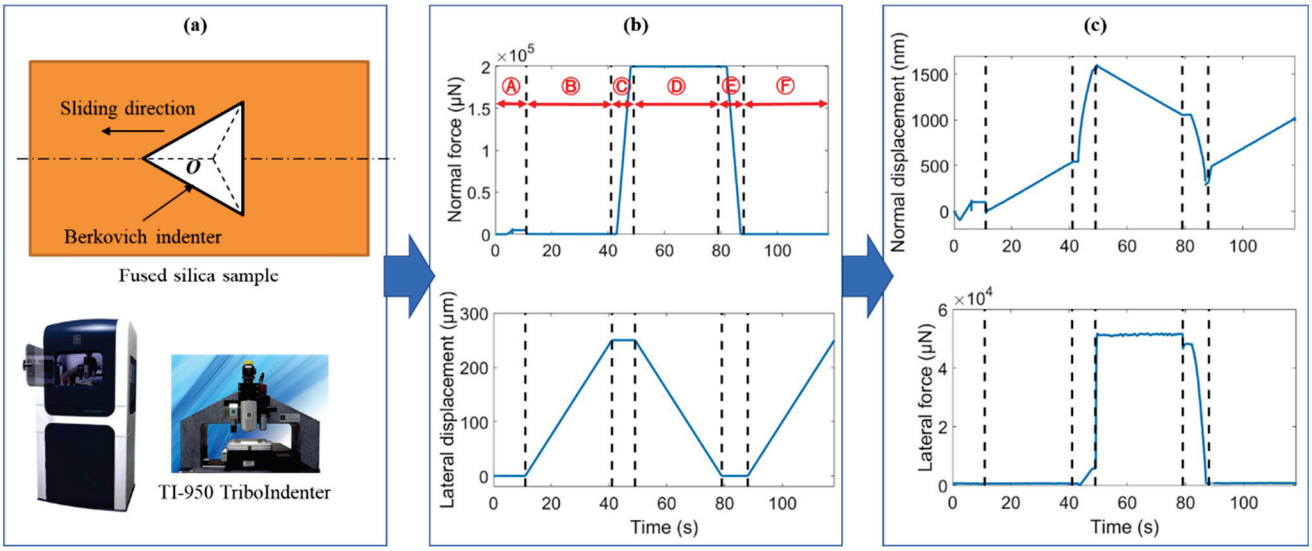

Figure 1. (**a**) Schematic diagram of edge-forward Berkovich scratching, (**b**) the applied normal force and lateral displacement for the normal load of 200 mN, and (**c**) the resulting normal displacement and lateral force.

After scratching, the samples were measured by an atomic force microscope (AFM) (Innova, Veeco, Plainview, NY, USA) to obtain the three-dimensional topography of the impression. After etching by the buffered HF solution to open the surface cracks [31], the morphology of the cracks was characterized by a scanning electron microscope (SEM) (SU3500, Hitachi, Japan).

3. Finite Element Modeling

The finite element analysis of scratching with an edge-forward Berkovich indenter and a conical indenter was performed on a commercial finite element code ABAQUS. A modified elliptical constitutive model [28,30] was used to consider the influence of densification on the deformation in fused silica:

$$f(\sigma_{ij}) = \left(\frac{q}{d}\right)^2 + \left(\frac{p}{p_b}\right)^2 - 1 = 0 \quad (1)$$

where q is equivalent shear stress; p is hydrostatic pressure; d is the von Mises yield stress under pure shear; and p_b is the hydrostatic yield stress for pure compression. The relationship between hydrostatic pressure p and the densification ζ is modeled by:

$$\zeta = \frac{\zeta_{\max}}{1 + e^{-k(p-p_0)}} \quad (2)$$

where ζ_{max} (%) is the saturated densification under compression, and p_0 (GPa) is the hydrostatic pressure under which a densification of $\zeta_{max}/2$ is produced. The parameters of the modified elliptical model used in this study are taken from the ref. [28].

In the finite element model, an infinitely sharp Berkovich edge-forward indenter slides along the x-axis on the top surface of a deformable parallelepiped with a dimension of $W \times W \times (l + 2W)$, as shown in Figure 2. The diamond indenter is assumed to be rigid because its Young's modulus [32] and hardness [33] are much higher than those of the fused silica samples [14]. An eight-node linear brick element with reduced integration and hourglass control is used. Refined FE mesh with an element size of l_e is used in a parallelepiped with a dimension of $a \times a \times (l + 2W)$, and graded FE mesh is used in the residual region. For conical scratching, the semi-included angle α of the conical indenter is set as 70.3°, to ensure that the projected area-to-indentation depth function is the same as the commonly used Vickers and Berkovich indenters. $A = 2.79\ h_{max}$ is the nominal contact radius for 70.3° conical scratching.

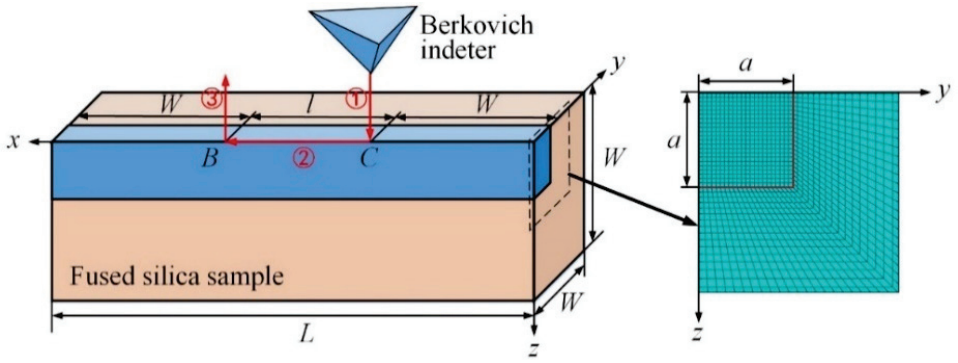

Figure 2. The finite element model of scratching with a Berkovich indenter.

As shown in Figures 2 and 3, the sliding process is divided into three stages, i.e., the indentation stage ①, the sliding stage ②, and the unloading stage ③. The scratching depth, length, and speed are denoted as h_{max}, l, and v, respectively. The Coulomb friction model is used to model the adhesion friction behavior between the indenter and the sample. The coefficient of adhesion friction f was determined to be 0.04, by comparing FEA and scratching tests.

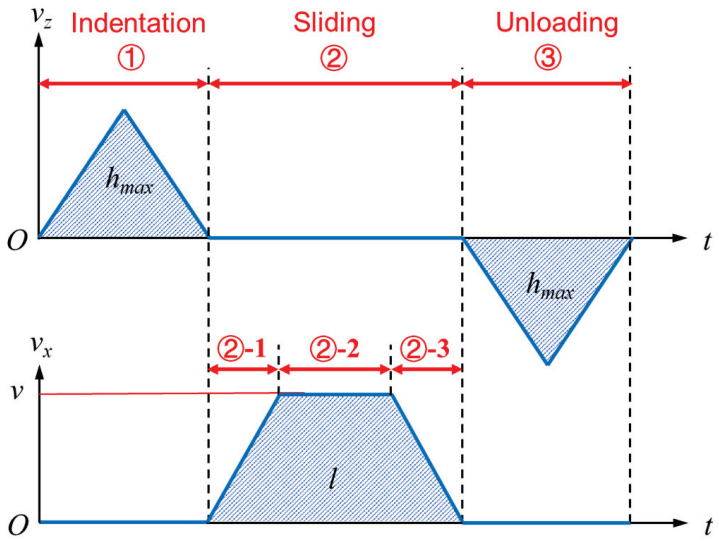

Figure 3. The velocity of the indenter during the FEA of scratching.

The single-variable method is used to optimize the cross-section dimension W, sliding length l, and element size l_e. The appropriate parameters result in stable and convergent normal and tangential loads, and apparent coefficient of friction in the sliding stage. h_{max} is assumed to be 1 μm. Results show that a cross-section dimension of $5a \times 5a$, a sliding length of 10 h_{max}, and a mesh size of 1/8 h_{max} are appropriate for the simulations.

4. Verification of Finite Element Models

4.1. Experimental Verification of Elastic Recovery

The elastic recovery ratio f_e for scratching reflects the extent of elastic deformation relative to the whole deformation. In addition, f_e can be conveniently measured by AFM. Therefore, f_e is used to verify the finite element model in this study.

As shown in Figure 4, the leading end of the impression induced by scratching with an edge-forward Berkovich indenter is measured by AFM to obtain its three-dimensional topography. Pile-up is obvious on the lateral sides of the impression. Figure 4 also indicates that the residual depth h_f (see Figure 5) slightly decreases with the distance d to the unloading position of indenter tip. The profile shown in Figure 5 is obtained by averaging five equally spaced cross-section profiles of the middle part of the impression. The residual scratch depth h_f after elastic recovery, determined from Figure 5, is 668 nm.

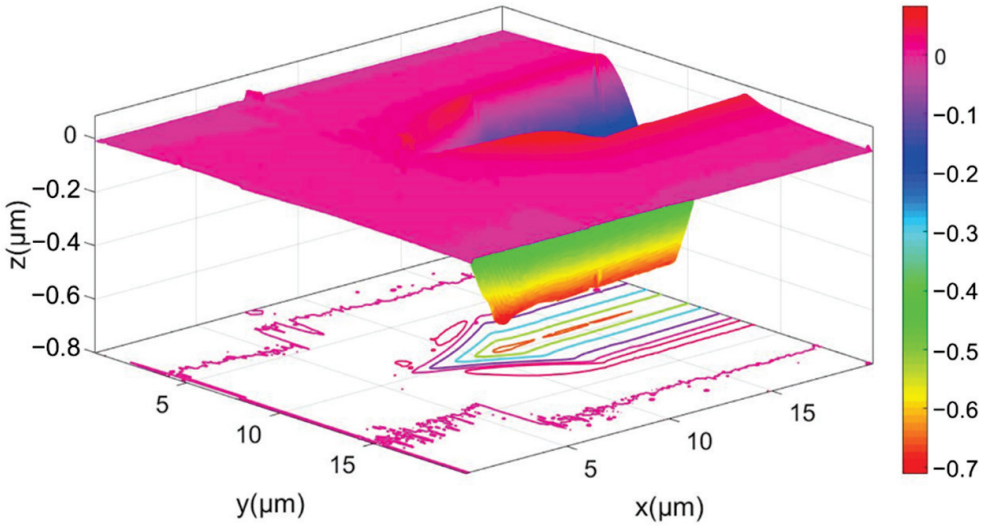

Figure 4. The AFM-measured three-dimensional topography of the scratching impression induced by an edge-forward Berkovich indenter under the normal load of 200 mN.

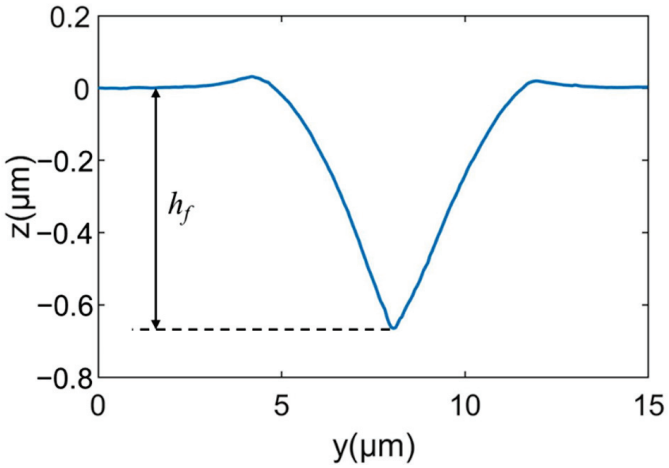

Figure 5. The average cross-section profile of the scratching impression.

In order to determine the scratching depth directly from the displacement curve, the normal displacement of the indenter (see Figure 1c) during the scratching process was corrected by the original profile of the sample surface. The corrected normal displacement in the scratching stage Ⓓ was calculated by subtracting the uncorrected displacement from t_2 to t_1 in the stage Ⓑ from the uncorrected displacement from t_3 to t_4. Similarly, the corrected normal displacement in the postmortem profiling stage Ⓕ was calculated by subtracting the uncorrected displacement from t_1 to t_2 from the uncorrected displacement from t_5 to t_6. The evolution of the corrected normal displacement with time is shown in Figure 6. The maximum scratching depth and residual depth are 1063 nm and 479 nm, respectively. It is worth noting that this value of residual depth is smaller than that measure by AFM (i.e., h_f = 668 nm). This is possibly because the indenter did not strictly follow the scratching path in stage Ⓕ, due to the movement of the sample or the motion error of the indentation test in the lateral direction. By contrast, the AFM probe accurately detects the lowest positions of the residual scratching profiles for two reasons. First, the tip radius of the AFM probe is much smaller than that of the Berkovich indenter. Second, the AFM probe is scanning across the impression. Using the AFM-measured h_f, the elastic recovery ratio is calculated to be $f_e = 1 - h_f/h_{amx}$ = 37.2%. Ba analyzing the FEA-predicted profiles of the scratching impression at the fully-loaded and fully-unloaded states shown in Figure 7, the value of f_e predicted by FEA is 37%, which is very close to the experimental value.

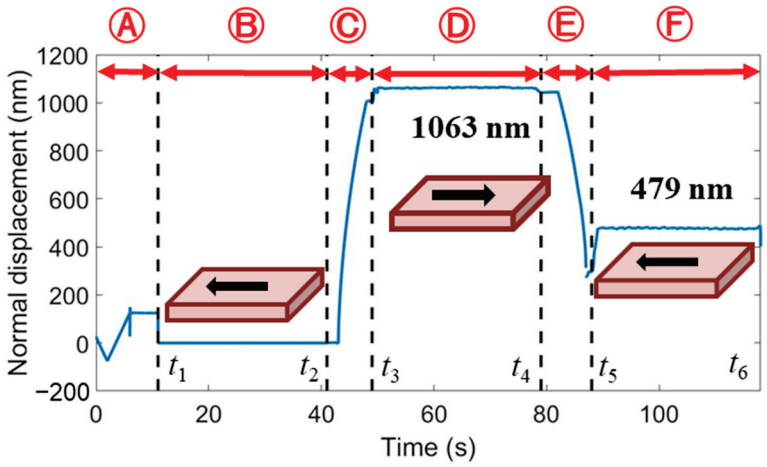

Figure 6. The evolution of the corrected normal displacement with time for scratching with an edge-forward Berkovich indenter, under the normal load of 200 mN.

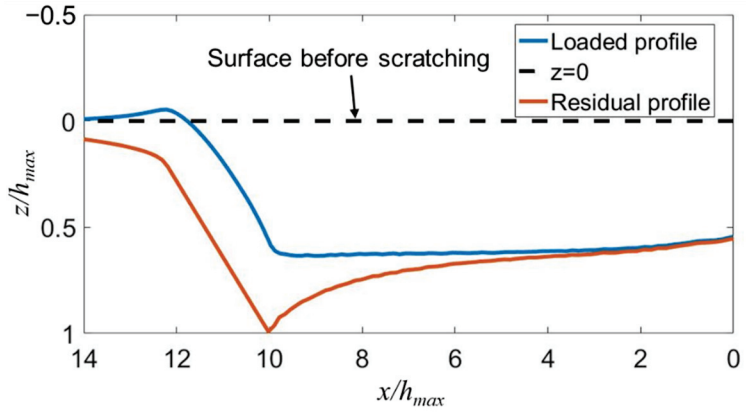

Figure 7. The FEA-simulated profiles of the scratching impression at the fully loaded and fully unloaded states for an edge-forward Berkovich indenter.

4.2. Theoretical Verification of Hardness Ratio

As shown in Figure 8, FEA predicts that the hardness ratio $k_H^p = H_T^p / H_s^p$ is slightly larger than utility, and nearly independent of the sharpness of the indenter, where H_T^p and H_s^p are the ploughing hardness along the sliding and vertical directions, respectively. This is consistent with theoretical analysis, as detailed below.

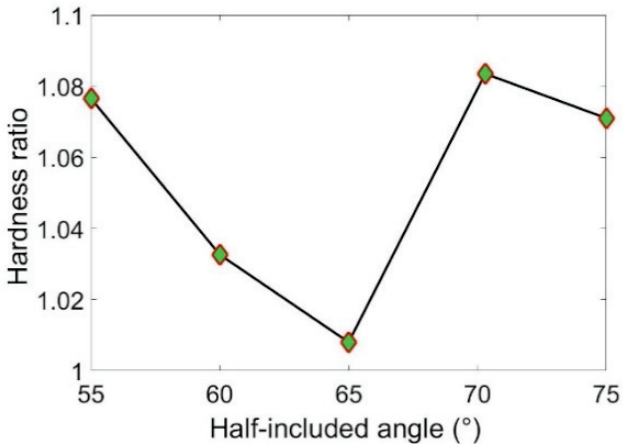

Figure 8. The variation of hardness ratio k_H^p with the half-included angle of the conical indenters.

For an infinitesimal contact area dA, the contact force is normal to dA. Therefore, the forces along the sliding and vertical directions, i.e., dF_T and dF_N, have the following relationship:

$$\frac{dF_T}{dA_{pl}} = \frac{dF_N}{dA_{pv}} = p(h, \beta) \tag{3}$$

where A_{pl} and A_{pv} are the laterally and vertically projected contact areas, respectively; $p(h,\beta)$ is the contact pressure at the point (h,β) on the indenter surface; and β and h are the phase and the height measured from the indenter tip, respectively. According to the definition of hardness, the ploughing hardness can be expressed by:

$$H_s^p = \frac{\int p(h,\beta) dA_{pv}}{A_{pv}} \tag{4}$$

and

$$H_T^p = \frac{\int p(h,\beta) dA_{pl}}{A_{pl}} \tag{5}$$

The contours of the contact stress induced by conical scratching and Berkovich scratching resemble concentric circles and triangles, respectively [30]. Therefore, $p(h,\beta)$ is nearly independent of β. As the geometries of the conical and Berkovich indenters are self-similar, the vertically and laterally projected areas of the contact zone with a height from h to $h + dh$, i.e., $dA_{pl,h\sim h+\Delta h}$ and $dA_{pv,h\sim h+\Delta h}$ have the following relationship:

$$\frac{dA_{pl,h\sim h+\Delta h}}{dA_{pv,h\sim h+\Delta h}} \approx \frac{A_{pl}}{A_{pv}} \tag{6}$$

Therefore, the hardness ratio:

$$k_H^p = \frac{H_T^p}{H_s^p} = \frac{\int_{h=0}^{h_c} p(h) dA_{pl,h\sim h+\Delta h}}{\int_{h=0}^{h_c} p(h) dA_{pv,h\sim h+\Delta h}} \cdot \frac{A_{pv}}{A_{pl}} \approx 1 \tag{7}$$

By combining Equations (3), (12) and (18) in ref. [30], the following expression can be obtained for a conical indenter:

$$\frac{k_H}{k_H^p} \approx 1 + \frac{f}{\mu_0 \sin \alpha} \tag{8}$$

where $k_H = H_T/H_s$ is the ratio of tangential hardness and scratching hardness; and μ_0 is the friction coefficient induced by ploughing. As $k_H^p \approx 1$, we can conclude from Equation (8) that $k_H > 1$ when friction exists, i.e., $H_T > H_s$. This is consistent with the scratching tests [34]. It is worth noting that the above analysis considers the non-uniform distribution of the contact pressure. This is more accurate than the widely adopted assumption that the contact pressure is uniformly distributed [35].

5. Deformation and Fracture in Fused Silica under Scratching

5.1. Scratching Hardness

Scratching hardness is widely used to model the scratching load that is a key factor determining the fracture behavior. Although it is reported that friction only plays a small role in indentation hardness for blunt indenters [36], Figure 9 shows that the indentation hardness H_i (the hardness at the end of stage ①) for edge-leading Berkovich scratching is slightly increased with the rise in friction. By contrast, the scratching hardness (the hardness in the right red box) is nearly independent of friction.

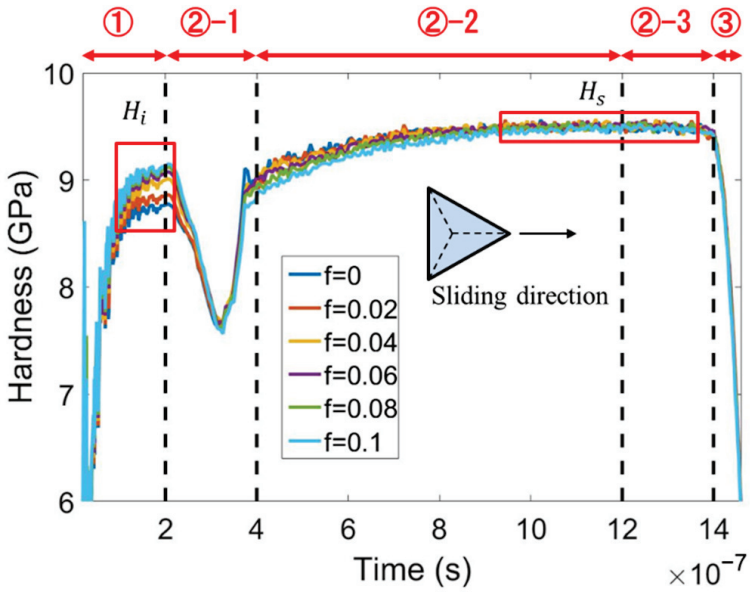

Figure 9. The variation of hardness with time at various values of adhesion friction coefficient f for edge-leading Berkovich scratching.

In order to understand the above phenomena, the evolutions of the contact area and normal force with time are plotted in Figure 10a,b, respectively. During the transition from indentation to sliding, i.e., in the stage ②-1, the contact area is considerably reduced because the support for the indenter rear is removed. If no elastic recovery occurs, the rear face of the indenter is entirely separated from the sample surface, and the contact area decreases to two-thirds. However, Figure 10a shows that the contact area during the steady sliding stage (in the right red box) is significantly bigger than two-thirds of that during indentation (in the left red box). This is due to elastic recovery.

The moving direction of the indenter relative to the sample determines the influence of friction on the contact area. The contact area during static indentation is slightly decreased by friction, because the friction-induced downward shear stress applied to the sample surface results in a decrease in the contact area, as shown in Figure 10a. By contrast, friction

leads to an increase in the contact area during the steady sliding stage because the friction-induced shear stress on the sample surface is upward. The indentation hardness increases with friction, while the contact area decreases with friction. Therefore, the normal force during indentation is nearly independent of friction, as shown in Figure 10b. During the steady sliding stage, the scratching hardness is nearly independent of friction because the friction increases both the contact area and the normal force.

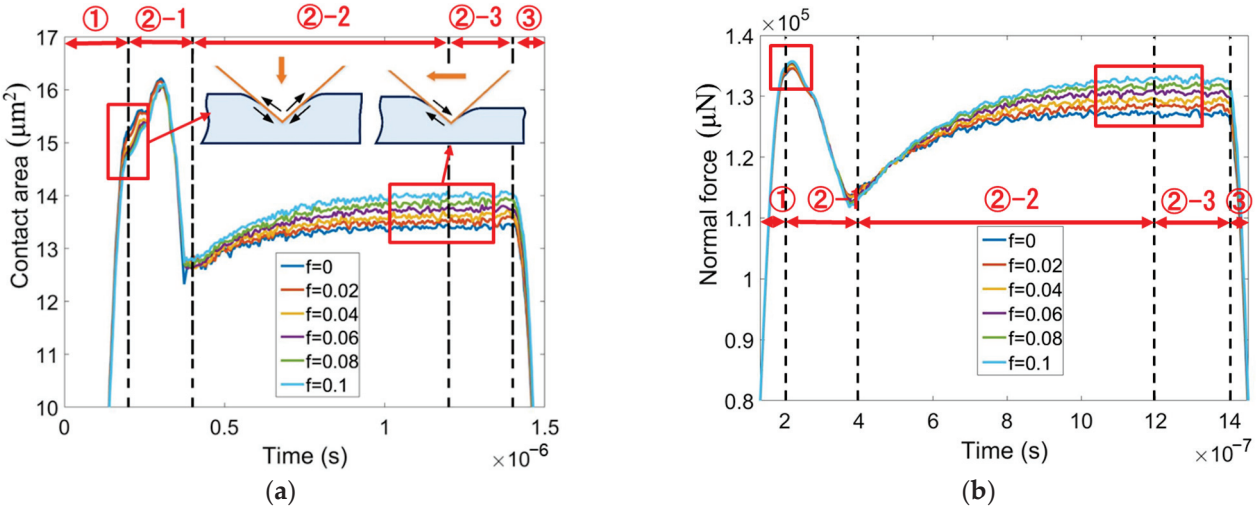

Figure 10. The evolutions of (**a**) contact area and (**b**) normal force with time at various friction coefficients for edge-leading Berkovich scratching.

Although the scratching hardness H_s for Berkovich indenter is independent of f, H_s for conical indenter is linearly decreased with f, as demonstrated in Figure 11. The scratching hardness induced by ploughing, i.e., H_s^p, remains nearly unchanged when f increases from 0 to 0.2.

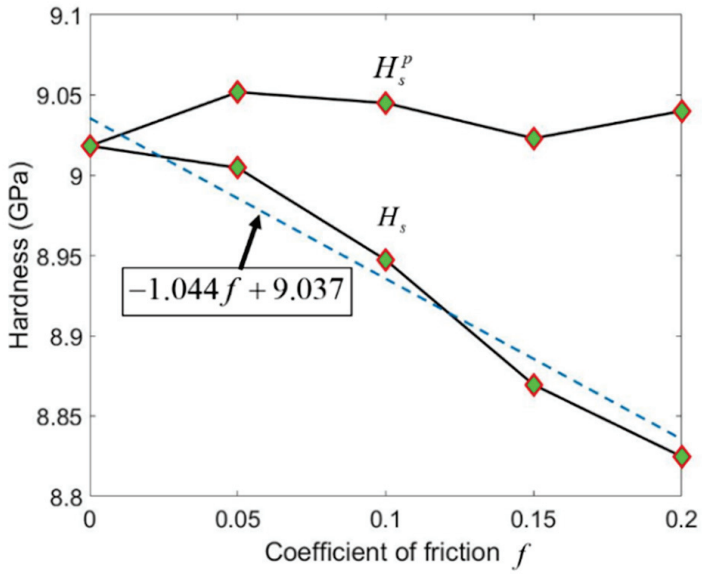

Figure 11. The hardness during scratching as a function of adhesion friction coefficient f for scratching with a 70.3° conical indenter. The value pairs of (H_s, f) is fitted to obtain the dash line.

5.2. Plastic Deformation

It is reported that the stress and deformation are relieved by densification [13,25]. The stress distribution is significantly influenced by the geometry and location of the elastic–plastic boundary [14,37]. In the analytical models of sliding stress fields, e.g., the Ahn

model [16] and the Wang model [17], the plastic region is assumed to be a sphere with the center on the sample surface.

As shown in Figure 12, the maximum densification locates in the region that the indenter tip passes. The maximum value of densification predicted by FEA, i.e., 22.6%, is close to the measured saturated densification, i.e., 21% [38]. By comparing the densification contours in the top surface and the *xz*-cross-section shown in Figure 12, it is found that the contours in the *yz*-cross-sections are flat ellipses. Figure 12 also indicates that the densification in fused silica caused by scratching is bigger than that caused by indentation.

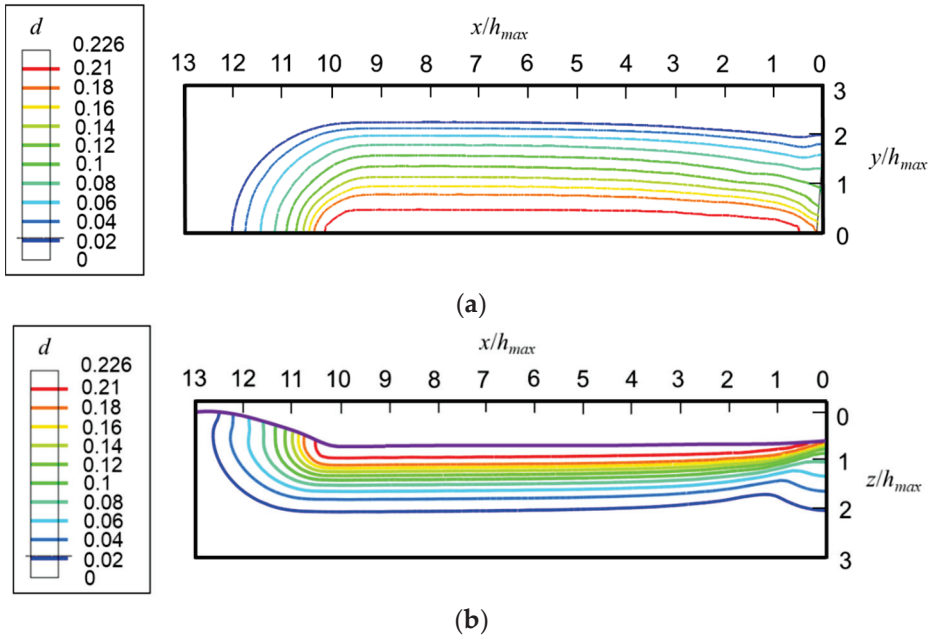

Figure 12. Contours of densification at the fully unloaded state induced by scratching with a 70.3° conical indenter in (**a**) the top surface and (**b**) *xz*-cross-section.

Figure 13a shows that the elastic–plastic boundary in fused silica induced by scratching deviates from a circle. By contrast, Figure 13b demonstrates that the boundary can be tightly fitted by an ellipse. Figures 13 and 14 indicate that the yield region is an ellipsoid in the front of the indenter ($x/h_{max} > 10$), and a cylindroid at the rear of the indenter ($x/h_{max} \leq 10$).

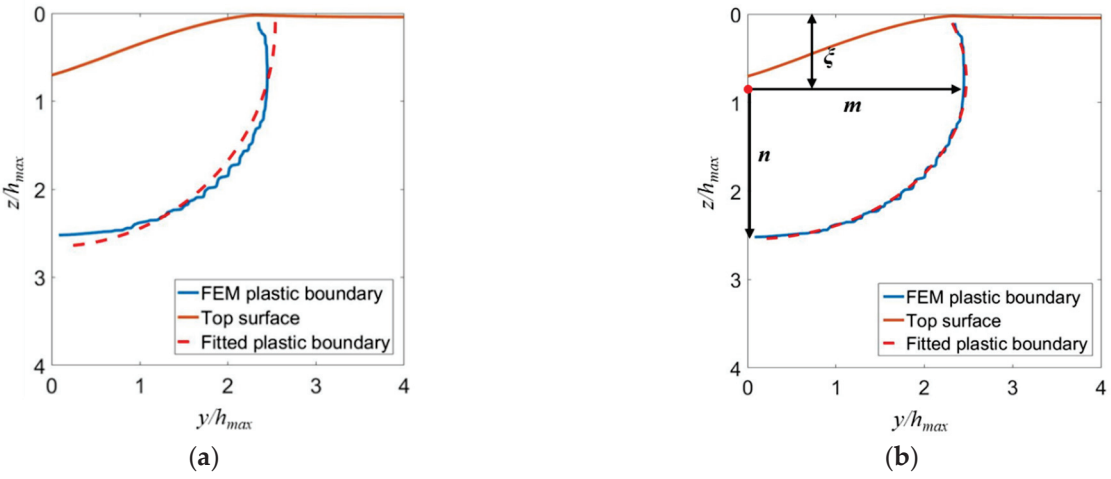

Figure 13. The elastic–plastic boundaries defined by a von Mises equivalent plastic strain of 10^{-2} in the *yz*-cross-section at the fully unloaded state for 70.3° conical scratching. The simulated boundaries are fitted by (**a**) a circular arc and (**b**) an elliptical arc.

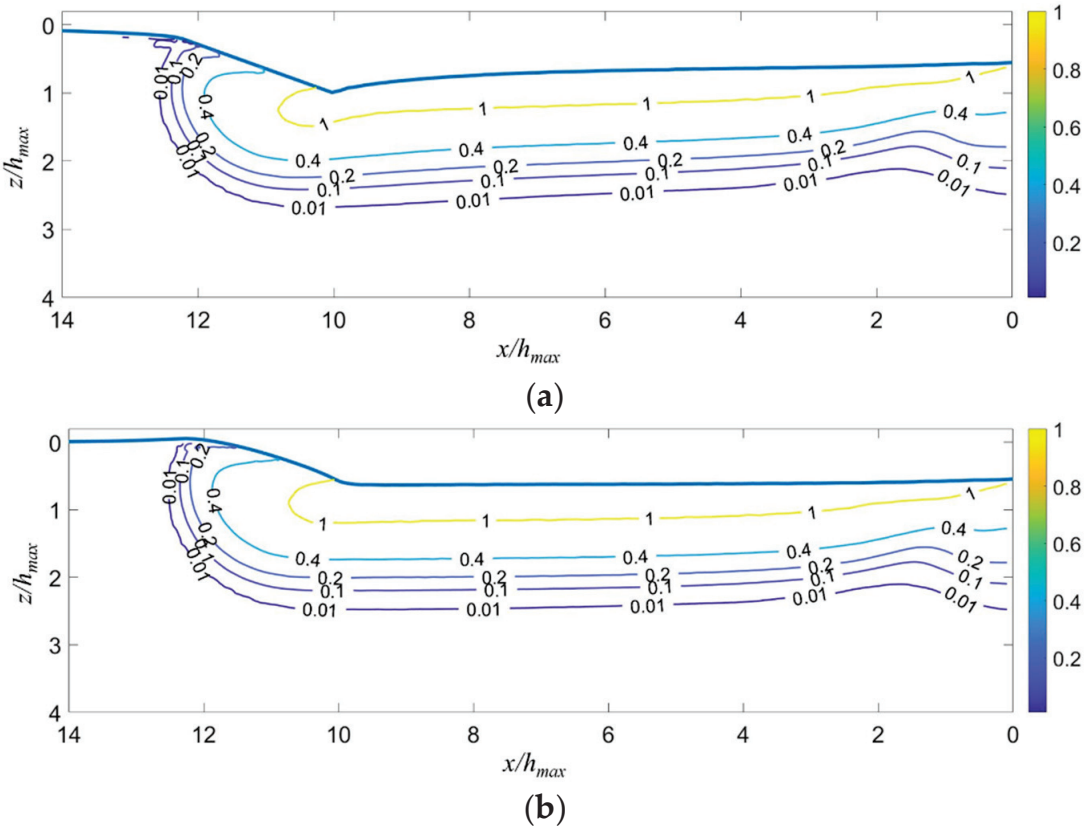

Figure 14. The contours of von Mises equivalent plastic strain in the *xz*-cross-section (**a**) at the fully loaded and (**b**) fully unloaded states.

As shown in Figure 13b, the shape of the elastic–plastic boundary is characterized by the length m of the semi-major axis, the length n of the semi-minor axis, and the depth ξ of the elastic–plastic boundary center. The semi-major and semi-minor axes are along the lateral and vertical directions, respectively. These parameters can be determined by fitting the elastic–plastic boundary by the following formula:

$$\left(\frac{y}{m}\right)^2 + \left(\frac{z-\xi}{n}\right)^2 = 1 \tag{9}$$

The fitted results are shown in Figure 15. The real contact radius a_r predicted by FEA equals 2.24 h_{max}. Figure 15a shows that m is bigger than a, while n is smaller than a. After unloading, m remains nearly unchanged, but n in the cross-section close to point B increases, due to the significant elastic recovery. m is significantly larger than n in the steady sliding stage. Therefore, the prediction accuracy of the existent sliding stress field models may be greatly improved if the spherical/cylindrical yield region is replaced by an ellipsoid/cylindroid. Figure 15b shows that the depth of the elastic–plastic boundary center in the *yz*-cross-section behind the indenter decreases rapidly when the indenter moves far away from it. ξ for scratching is much bigger than that for indentation (close to ξ at l_B = 9.5 h_{max}) at both the fully loaded and the fully unloaded states. This indicates that the Ahn and Wang models should be refined to allow for the embedding of the center of the plastic zone.

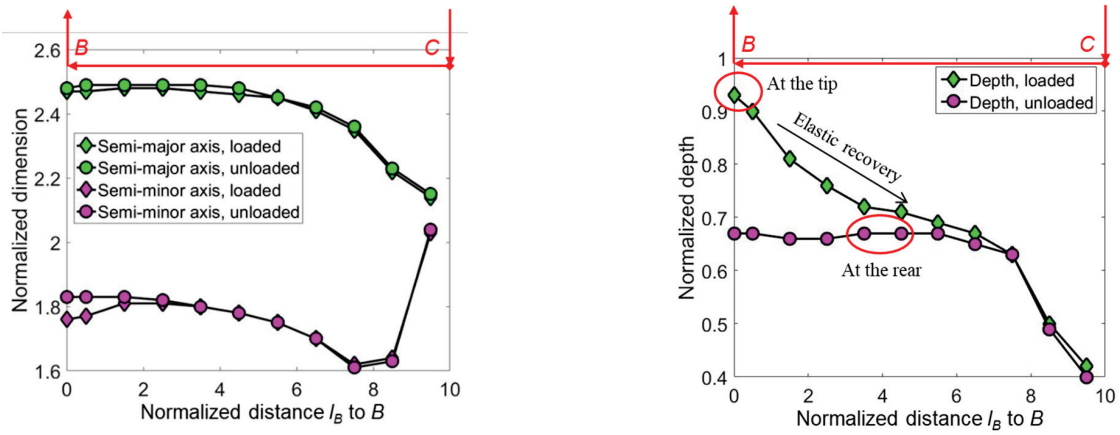

(**a**) (**b**)

Figure 15. The fitted (**a**) dimension and (**b**) depth of the elastic–plastic boundary normalized by h_{max}. The indenter moves from the point *C* to the point *B* in the scratching stage (see Figure 2).

5.3. Stress Fields and Cracking Behavior

5.3.1. In the Sliding Stage

The scratching-induced stress contours under a conical indenter at the end of the sliding stage ② are shown in Figure 16. In the front of the indenter tip, i.e., in the region $x \geq 0$, the shape of the contour lines induced by scratching is similar to those induced by indentation [29]. By contrast, at the back of the indenter tip, the contours are flattened, due to the plastic deformation left by the sliding indenter.

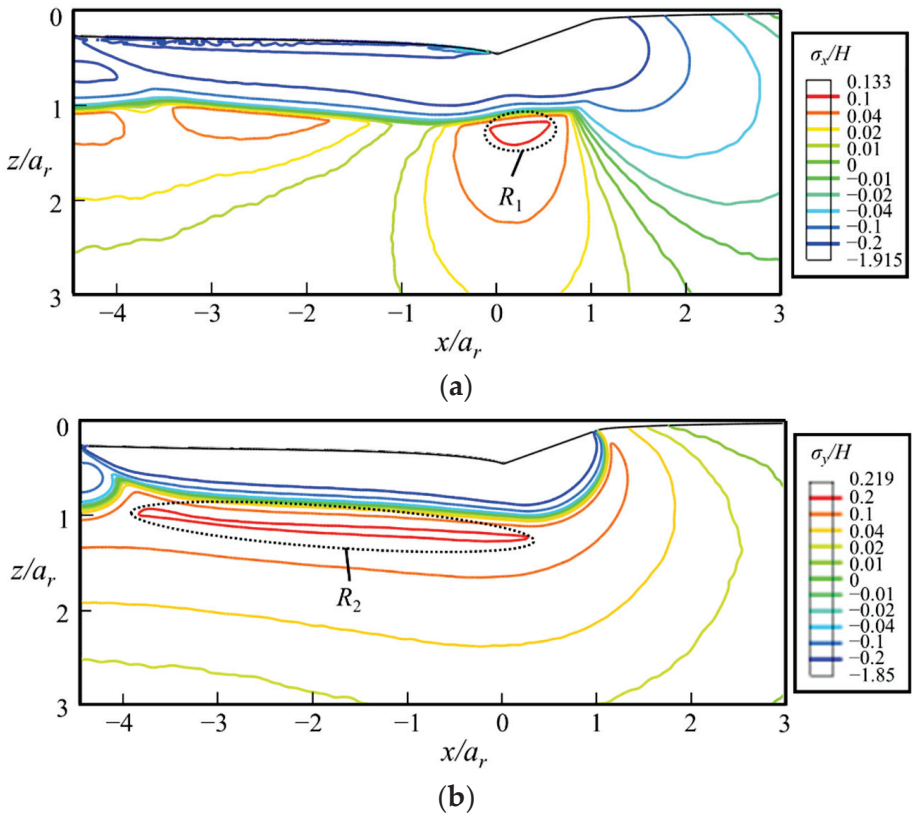

Figure 16. *Cont.*

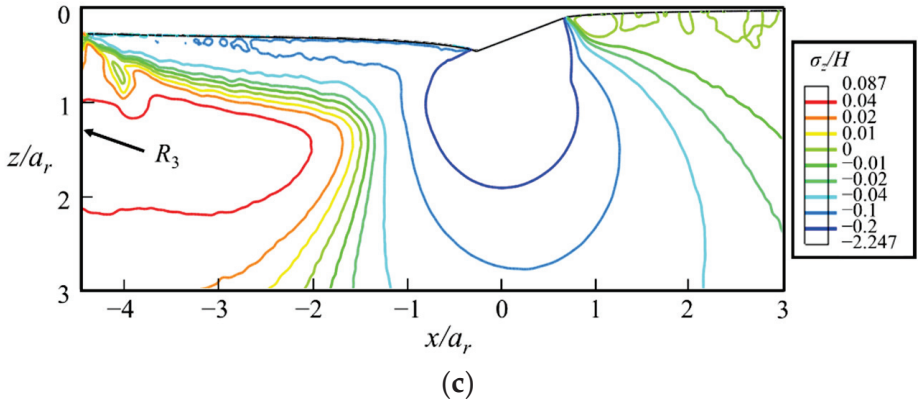

(c)

Figure 16. The contours of (**a**) σ_x/H, (**b**) σ_y/H, and (**c**) σ_z/H at the end of the sliding stage ② in the xz-cross-section, where a_r = 2.24 h_{max} is the real contact radius evaluated by FEA, and H is the hardness measured by indentation tests. The indenter moves along the positive direction of the x-axis.

The maximal values of σ_x and σ_y are identified in the regions below the indenter tip just outside the elastic–plastic boundary, i.e., the regions R_1 and R_2 shown in Figure 16, respectively. They are the driving forces of median cracks. As the maximal σ_y is higher than the maximal σ_x, the median crack along the sliding direction tends to initiate prior to that along the lateral direction. The maximal value of σ_z locates at the far rear of the indenter (region R_3), which is the driving force of lateral cracks. In the sliding stage, the driving force of median cracks is higher than that of lateral cracks.

5.3.2. At the Fully-Unloaded State

After unloading, as shown in Figure 17a, the stress contours predict a high σ_y on the sample surface at the front of the indenter (region R_4), which is the driving force of radial cracks along the sliding direction, i.e., the radial crack 1 in Figure 18a. σ_y at the bottom of the yield region remains nearly unchanged after unloading. Therefore, median cracks along the sliding direction remain open in the unloading stage if they initiate in the sliding stage. The maximal σ_z increases from 0.087H to 0.137H during the unloading process. This indicates that the lateral crack emerges more easily in the unloading stage compared with the sliding stage.

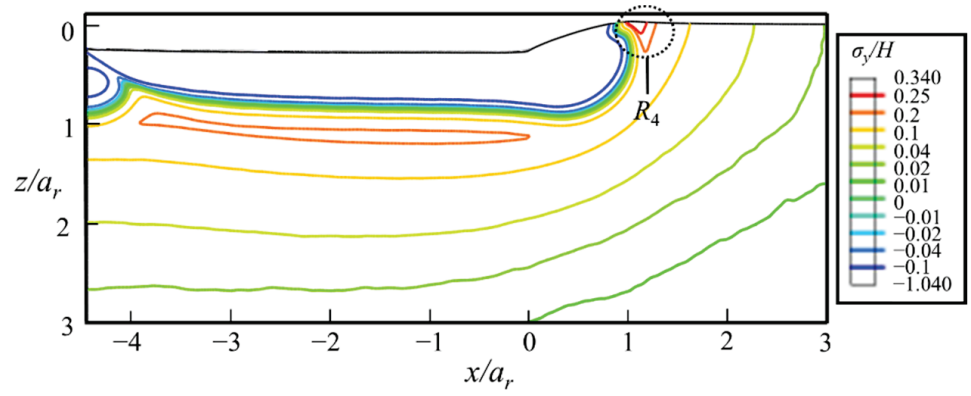

(a)

Figure 17. *Cont.*

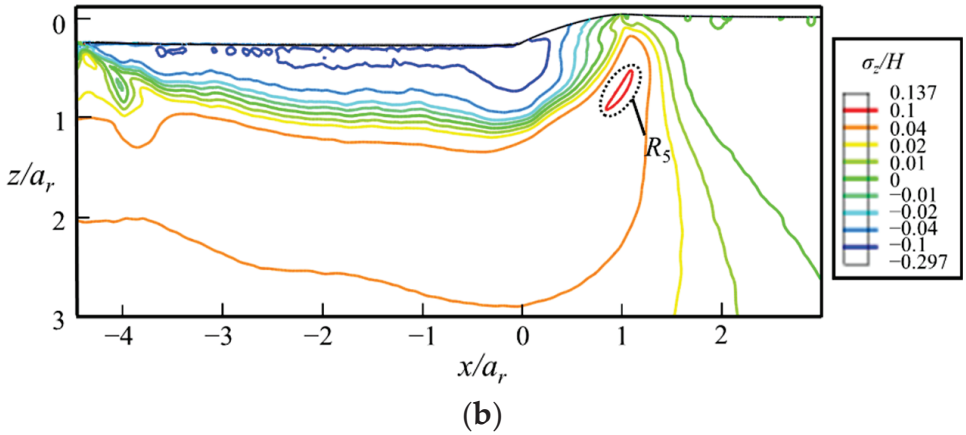

Figure 17. The contours of (**a**) σ_y/H and (**b**) σ_z/H at the fully unloaded state in the xz-cross-section predicted by FEA. The indenter moves along the positive direction of x-axis.

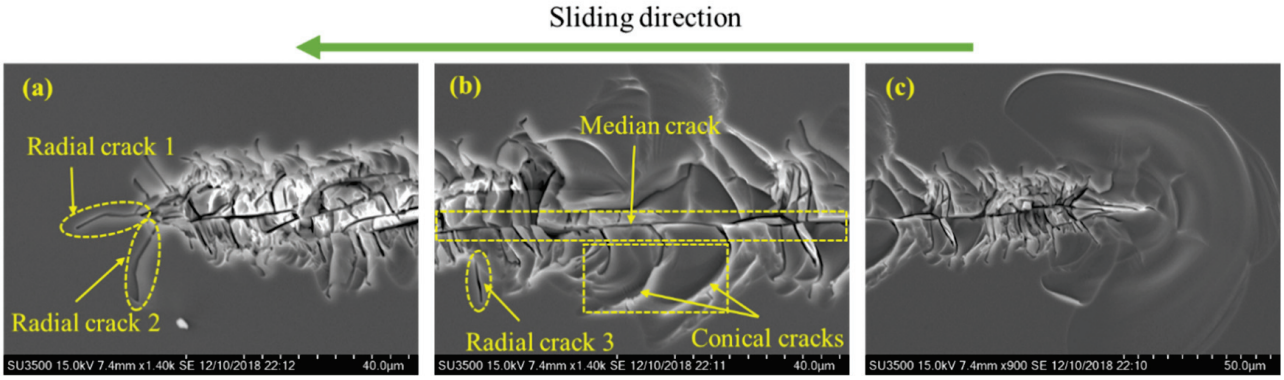

Figure 18. The SEM images of the impression at the (**a**) end, (**b**) middle, and (**c**) start of the edge-forward Berkovich scratching, under the normal load of 600 mN.

5.3.3. Maximum Principal Stress

The contours of σ_1/H shown in Figure 19 indicate that the median crack along the sliding direction tends to be the first crack to appear during the sliding stage. It initiates below the yield region at the rear of the indenter, i.e., in the region R_2. Once initiated in the xz-cross-section, the median crack propagates along the sliding direction during scratching. As the value of σ_1 in region R_3 is smaller than that in region R_2, the initiation load of median crack under indentation is higher than that under scratching. This is consistent with experimental observations. Though median crack is absent during indentation tests under the normal load of 40 N [39], it is observed during scratching tests under the normal load of 600 mN, as shown in Figure 18b. During the unloading stage, radial cracks may initiate from the sample surface at the front of the indenter, i.e., region R_4, as shown in Figure 18a. As σ_y in region R_4 is small before unloading, and significantly increases during the unloading process, radial cracks tend to emerge in the unloading stage. If both radial and median cracks form, they coalesce to form a big median–radial crack that penetrates through the entire yield region, as verified by the experiments (see Figure 18).

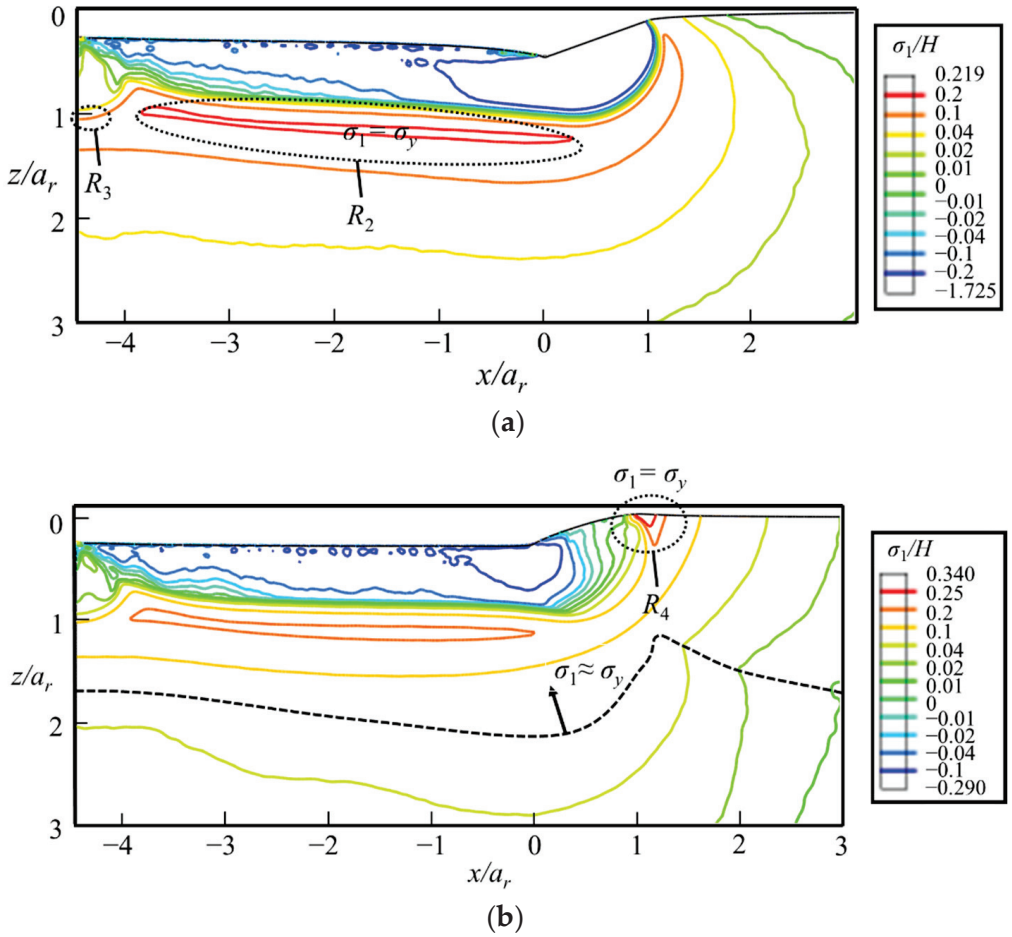

Figure 19. The contours of σ_1/H at the (**a**) fully loaded and (**b**) fully unloaded states in the *xz*-cross-section. The thick dash line is the boundary between $\sigma_1 \approx \sigma_y$ and $\sigma_1 \approx \sigma^*$, where σ^* is the in-plane principal stress.

6. Conclusions

This study developed three-dimensional finite element models of scratching on fused silica with 70.3° conical and Berkovich indenters. A refined elliptical model was used to consider the influence of densification on elastic properties and the saturation of densification with hydrostatic pressure. By analyzing the predicted scratching hardness, plastic deformation, and stress fields, the following conclusions are obtained:

(1) The tangential hardness is slightly larger than the scratching hardness, and their ratio linearly increases with the adhesion friction coefficient *f*. The scratching hardness for an edge-leading Berkovich indenter is nearly independent of *f*, because the friction increases both the contact area and the normal force. By contrast, the scratching hardness for a conical indenter linearly decreases with *f*. These findings are helpful to model the friction-affected forces induced by scratching;

(2) The densification effect should not be ignored if one aims for a damage-free process in fabrication. It is found that the material's densification under scratching is bigger than that under indentation. This indicates that the prediction accuracy of the sliding stress analyses can be improved if the material's densification is properly integrated into the modelling, e.g., replacing the spherical/cylindrical plastic zone with an ellipsoid/cylindroid, and considering the embedding of the plastic zone center;

(3) Median cracks along the sliding direction tend to be the first cracks that emerge in the sliding stage. Radial cracks may initiate under a smaller load in the sample surface at the front of the indenter during the unloading stage. Radial and median cracks coalesce to form a big median–radial crack that penetrates through the entire yield region.

Author Contributions: Conceptualization, C.L. and L.Z.; methodology, C.L., L.S., and X.W.; validation, C.L. and D.D.; formal analysis, C.L. and Y.M.; writing—original draft preparation, C.L.; writing—review and editing, L.Z. and C.W.; supervision, J.D.; project administration, J.D. and Z.C. All authors have read and agreed to the published version of the manuscript.

Funding: This research was funded by the Fellowship of China National Postdoctoral Program for Innovative Talents, grant number BX20200268; the National Natural Science Foundation of China, grant number 51720105016; the Research Project of State Key Laboratory of Mechanical System and Vibration in China, grant number MSV202103; Key Research and Development Projects of Shaanxi Province in China, grant number 2021GXLH-Z-051; the Guangdong Specific Discipline Project, grant number 2020ZDZX2006; and the Shenzhen Key Laboratory of Cross-scale Manufacturing Mechanics Project, grant number ZDSYS20200810171201007.

Data Availability Statement: Some or all data, models, or codes generated or used during the study are available from the corresponding author by request.

Conflicts of Interest: The authors declare no conflict of interest.

References

1. Campbell, J.H.; Hawley-Fedder, R.A.; Stolz, C.J.; Menapace, J.A.; Borden, M.R.; Whitman, P.K.; Yu, J.; Runkel, M.; Riley, M.O.; Feit, M.D.; et al. NIF optical materials and fabrication technologies: An overview. In Proceedings of the Optical Engineering at the Lawrence Livermore National Laboratory II: The National Ignition Facility, San Jose, CA, USA, 25–29 January 2004; pp. 84–101.
2. Gray, P.; Ciattaglia, E.; Dupuy, C.; Gago, F.; Guisard, S.; Marrero, J.; Ridings, R.; Wright, A. E-ELT Assembly, Integration, and Technical Commissioning Plans. In Proceedings of the Ground-Based and Airborne Telescopes VI, Edinburgh, UK, 26 June–1 July 2016.
3. Hrdina, K.E.; Duran, C.A. ULE®Glass with Improved Thermal Properties for EUVL Masks and Projection Optics Substrates. *Int. J. Appl. Glas. Sci.* **2014**, *5*, 82–88. [CrossRef]
4. Hergenhan, G.; Taubert, J.; Grimm, D.; Tilke, M.; Panitz, M.; Ziener, C. *Realization of Thermally Stable Transmissive Optical Elements for the EUV Wavelength Range*; SPIE: Bellingham, WA, USA, 2020; Volume 11323.
5. Zhao, L.-J.; Cheng, J.; Chen, M.-J.; Yuan, X.-D.; Liao, W.; Yang, H.; Liu, Q.; Wang, H.-J. Development of Integrated Multi-Station System to Precisely Detect and Mitigate Surface Damage on Fused Silica Optics. *Int. J. Precis. Eng. Manuf.* **2021**, *22*, 95–105. [CrossRef]
6. Malkin, S.; Hwang, T. Grinding mechanisms for ceramics. *CIRP Ann.* **1996**, *45*, 569–580. [CrossRef]
7. Suratwala, T.I.; Steele, W.A.; Wong, L.L.; Tham, G.C.; Destino, J.F.; Miller, P.E.; Ray, N.J.; Menapace, J.A.; Feigenbaum, E.; Shen, N. Subsurface mechanical damage correlations after grinding of various optical materials. *Opt. Eng.* **2019**, *58*, 092604. [CrossRef]
8. Hertz, H. Über die Berührung fester elastischer Körper. *J. Reine Angew. Math.* **1882**, *92*, 22.
9. Hill, R.; Lee, E.H.; Tupper, S.J. The theory of wedge indentation of ductile materials. *Proc. R. Soc. Lond. Ser. A Math. Phys. Sci.* **1947**, *188*, 273–289.
10. Johnson, K.L. The correlation of indentation experiments. *J. Mech. Phys. Solids* **1970**, *18*, 115–126. [CrossRef]
11. Lawn, B.R.; Evans, A.G.; Marshall, D.B. Elastic/plastic indentation damage in ceramics: The median/radial crack system. *J. Am. Ceram. Soc.* **1980**, *63*, 574–581. [CrossRef]
12. Bruns, S.; Uesbeck, T.; Fuhrmann, S.; Tarragó Aymerich, M.; Wondraczek, L.; de Ligny, D.; Durst, K. Indentation densification of fused silica assessed by raman spectroscopy and constitutive finite element analysis. *J. Am. Ceram. Soc.* **2020**, *103*, 3076–3088. [CrossRef]
13. Yoffe, E.H. Elastic Stress-Fields Caused by Indenting Brittle Materials. *Philos. Mag. A* **1982**, *46*, 617–628. [CrossRef]
14. Li, C.; Zhang, L.; Sun, L.; Yang, S.; Wu, C.; Long, X.; Ding, J.; Jiang, Z. A quantitative analysis of the indentation fracture of fused silica. *J. Am. Ceram. Soc.* **2019**, *102*, 7264–7277. [CrossRef]
15. Hamilton, G.M.; Goodman, L.E. The stress field created by a circular sliding contact. *J. Appl. Mech.* **1966**, *33*, 371–376. [CrossRef]
16. Ahn, Y.; Farris, T.N.; Chandrasekar, S. Sliding microindentation fracture of brittle materials: Role of elastic stress fields. *Mech. Mater.* **1998**, *29*, 143–152. [CrossRef]
17. Wang, W.; Yao, P.; Wang, J.; Huang, C.; Kuriyagawa, T.; Zhu, H.; Zou, B.; Liu, H. Elastic stress field model and micro-crack evolution for isotropic brittle materials during single grit scratching. *Ceram. Int.* **2017**, *43*, 10726–10736. [CrossRef]
18. Yao, L.; Zhang, L.; Ge, P.; Gao, Y.; Wang, H. Study on nucleation and propagation of median cracks generated by scratching single crystal silicon. *Mater. Sci. Semicond. Process.* **2020**, *105*, 104691. [CrossRef]
19. Lee, K.; Marimuthu, K.P.; Kim, C.-L.; Lee, H.J.T.I. Scratch-tip-size effect and change of friction coefficient in nano/micro scratch tests using XFEM. *Tribol. Int.* **2018**, *120*, 398–410. [CrossRef]
20. Arjmandi, M.; Ramezani, M. Finite element modelling of sliding wear in three-dimensional textile hydrogel composites. *Tribol. Int.* **2019**, *133*, 88–100. [CrossRef]
21. Asqari, M.A.; Akbari, J. Investigation of cohesive FE modeling to predict crack depth during deep-scratching on optical glasses. *Ceram. Int.* **2018**, *44*, 16781–16790. [CrossRef]

22. Shim, S.; Oliver, W.C.; Pharr, G.M. A comparison of 3D finite element simulations for Berkovich and conical indentation of fused silica. *Int. J. Surf. Sci. Eng.* **2007**, *1*, 259–273. [CrossRef]
23. Imaoka, M.; Yasui, I. Finite element analysis of indentation on glass. *J. Non-Cryst. Solids* **1976**, *22*, 315–329. [CrossRef]
24. Gadelrab, K.R.; Bonilla, F.A.; Chiesa, M. Densification modeling of fused silica under nanoindentation. *J. Non-Cryst. Solids* **2012**, *358*, 392–398. [CrossRef]
25. Xin, K.; Lambropoulos, J.C. Densification of fused silica: Effects on nanoindentation. In Proceedings of the International Symposium on Optical Science and Technology, San Diego, CA, USA, 30 July–4 August 2000; Volume 4102, pp. 112–121. [CrossRef]
26. Kermouche, G.; Barthel, E.; Vandembroucq, D.; Dubujet, P. Mechanical modelling of indentation-induced densification in amorphous silica. *Acta Mater.* **2008**, *56*, 3222–3228. [CrossRef]
27. Bruns, S.; Johanns, K.E.; Rehman, H.U.; Pharr, G.M.; Durst, K. Constitutive modeling of indentation cracking in fused silica. *J. Am. Ceram. Soc.* **2017**, *100*, 1928–1940. [CrossRef]
28. Li, C.; Zhang, L.; Sun, L.; Wu, C.; Duan, D.; Lin, Q.; Ding, J.; Jiang, Z. A finite element study on the effects of densification on fused silica under indentation. *Ceram. Int.* **2020**, *46*, 26861–26870. [CrossRef]
29. Li, C.; Ding, J.; Zhang, L.; Wu, C.; Sun, L.; Lin, Q.; Liu, Y.; Jiang, Z. Densification effects on the fracture in fused silica under Vickers indentation. *Ceram. Int.* **2021**, *48*, 9330–9341. [CrossRef]
30. Fang, X.; Li, C.; Sun, L.; Sun, H.; Jiang, Z. Hardness and friction coefficient of fused silica under scratching considering elastic recovery. *Ceram. Int.* **2020**, *46*, 8200–8208. [CrossRef]
31. Menapace, J.A.; Davis, P.J.; Steele, W.A.; Wong, L.L.; Suratwala, T.I.; Miller, P.E. MRF applications: Measurement of process-dependent subsurface damage in optical materials using the MRF wedge technique. In Proceedings of the Boulder Damage Symposium XXXVII: Annual Symposium on Optical Materials for High Power Lasers, Boulder, CO, USA, 19–21 September 2005.
32. Broitman, E. Indentation Hardness Measurements at Macro-, Micro-, and Nanoscale: A Critical Overview. *Tribol. Lett.* **2017**, *65*, 23. [CrossRef]
33. Brookes, C.A. Plastic Deformation and Anisotropy in the Hardness of Diamond. *Nature* **1970**, *228*, 660–661. [CrossRef]
34. Li, K.; Shapiro, Y.; Li, J.C.M. Scratch test of soda-lime glass. *Acta Mater.* **1998**, *46*, 5569–5578. [CrossRef]
35. Chamani, H.R.; Ayatollahi, M.R. The effect of Berkovich tip orientations on friction coefficient in nanoscratch testing of metals. *Tribol. Int.* **2016**, *103*, 25–36. [CrossRef]
36. Cai, X. Effect of friction in indentation hardness testing: A finite element study. *J. Mater. Sci. Lett.* **1993**, *12*, 301–302. [CrossRef]
37. Feng, G.; Qu, S.; Huang, Y.; Nix, W.D. An analytical expression for the stress field around an elastoplastic indentation/contact. *Acta Mater.* **2007**, *55*, 2929–2938. [CrossRef]
38. Rouxel, T.; Ji, H.; Hammouda, T.; Moreac, A. Poisson's ratio and the densification of glass under high pressure. *Phys. Rev. Lett.* **2008**, *100*, 225501. [CrossRef] [PubMed]
39. Cook, R.F.; Pharr, G.M. Direct Observation and Analysis of Indentation Cracking in Glasses and Ceramics. *J. Am. Ceram. Soc.* **1990**, *73*, 787–817. [CrossRef]

micromachines

MDPI

Article

Experimental Investigation on the Effect of Surface Shape and Orientation in Magnetic Field Assisted Mass Polishing

Yee-Man Loh, Chi-Fai Cheung *, Chunjin Wang * and Lai-Ting Ho

State Key Laboratory in Ultra-Precision Machining Technology, Department of Industrial and Systems Engineering, The Hong Kong Polytechnic University, Hong Kong, China;
yee-man-kristy.loh@connect.polyu.hk (Y.-M.L.); lai.ting.ho@polyu.edu.hk (L.-T.H.)
* Correspondence: benny.cheung@polyu.edu.hk (C.-F.C.); chunjin.wang@polyu.edu.hk (C.W.);
Tel.: +852-2766-7905 (C.-F.C.); +852-3400-3190 (C.W.)

Abstract: Magnetic field assisted finishing (MFAF) technology has been widely used in industries such as aerospace, biomedical, and the optical field for both external and internal surface finishing due to its high conformability to complex surfaces and nanometric surface finishing. However, most of the MFAF methods only allow polishing piece-by-piece, leading to high post-processing costs and long processing times with the increasing demand for high precision products. Hence, a magnetic field-assisted mass polishing (MAMP) method was recently proposed, and an experimental investigation on the effect of surface posture is presented in this paper. Two groups of experiments were conducted with different workpiece shapes, including the square bar and roller bar, to examine the effect of surface orientation and polishing performance on different regions. A simulation of magnetic field distribution and computational fluid dynamics was also performed to support the results. Experimental results show that areas near the chamber wall experience better polishing performance, and the surface parallel or inclined to polishing direction generally allows better shearing and thus higher polishing efficiency. Both types of workpieces show notable polishing performance where an 80% surface roughness improvement was achieved after 20-min of rough polishing and 20-min of fine polishing reaching approximately 20 nm.

Keywords: magnetic field assisted finishing; polishing; material removal; surface shape; ultra-precision machining

Citation: Loh, Y.-M.; Cheung, C.-F.; Wang, C.; Ho, L.-T. Experimental Investigation on the Effect of Surface Shape and Orientation in Magnetic Field Assisted Mass Polishing. *Micromachines* **2022**, *13*, 1060. https://doi.org/10.3390/mi13071060

Academic Editor: Cyril Mauclair

Received: 29 May 2022
Accepted: 27 June 2022
Published: 30 June 2022

1. Introduction

In most of the machining processes for ultra-smooth surfaces applied in various fields such as optics, imaging, biomedical engineering, and the aerospace and automotive fields [1,2], polishing is usually required as a final and crucial step to remove defects and to smoothen the surfaces. Different kinds of polishing technologies have been developed, including ion beam finishing [3], bonnet polishing [4], fluid jet polishing [5], plasma finishing [6], magnetic field assisted finishing (MFAF) [7], etc. MFAF technology, being one of the most promising technologies in achieving ultra-smooth surface finishing, was first developed in the 1930s and has been widely researched and applied in various industries such as aerospace, biomedical, optics, etc. [7–9]. This technology shows advantages over polishing difficult-to-access surface [10], freeform surface [11] and microstructures [12] due to its high flexibility and conformity to the workpiece shape. MFAF can now be divided into two main streams depending on the polishing media: Magnetic Abrasive Finishing (MAF) and Magnetorheological Finishing (MRF).

MAF adopts magnetic abrasive particles which are made up of the combination of magnetic particles and abrasive particles to perform surface finishing [13]; with a different combination of magnetic abrasive particles and magnetic poles movement, both external and internal surface finishing can be achieved. Guo et al. [14] developed a localized vibration-assisted magnetic abrasive polishing method for various types of microstructures

and achieved surface roughness reduction by 80% while maintaining the form accuracy. A rotating-vibrating MAF process was also proposed [15] for additive manufactured components with complex internal structures, which successfully improved surface roughness from 7 μm to 0.5 μm on both surfaces within 3 h. Vahdati and Rasouli [11] studied and optimized the parameters for freeform surface MAF polishing and reported the characteristic of magnetic abrasives. Sumit and Chhikara [16] and Deepak et al. [17] proved that MAF is able to efficiently polish flat surfaces, internal and external surfaces of tube-like workpieces to a mirror surface with surface roughness on the order of a few nanometers. Amnieh et al. [18] presented a MAF setup which is able to finish internal grooves of a cylindrical tube, and various experiments on the effectiveness of parameters were performed. With the trapezium shaped grooves, a permanent magnet tool was ground to form the appropriate shape to ensure uniform gap distance between the magnetic tool and workpiece wall. Experimental results indicate that the proposed MAF setup is able to improve the surface quality of internal grooves by 70%, from 1.12 μm to 0.32 μm, with only 30 mg material loss, which further verifies the capability of MAF in internal surface finishing. Mulik and Pandey [19] developed the ultrasonic-assisted magnetic abrasive finishing (UMAF) process which combines ultrasonic vibration and MAF to achieve quick surface finishing, and was successfully achieved to polish a hardened steel workpiece to 22 nm in 80 s. Sihag et al. [20] further enhanced the UMAF process into a chemo ultrasonic assisted magnetic abrasive finishing, resulting 86% surface roughness reduction. Research on magnetic abrasive particles (MAPs) was also conducted in the literature [21,22], which summarized the polishing performance of various types of MAPs fabricated by different processes, and concluded that sintered MAPs show the strongest bonding and highest material removal.

On the other hand, MRF utilizes a magnetorheological fluid which stiffens under the magnetic field to create a highly conforming abrasive lap to polish the workpiece surface [23], in which the stiffness and shape of the formed MR brush can be controlled by the magnetic field strength [24]. This technology has been widely used and commercialized in the field of high-precision surface finishing, which is capable of achieving the nanometric finishing of freeform optics. MRF was first invented by Kordonski et al. in the 1980s, and the first computer-controlled MRF machine prototype was proposed later in 1995 [25,26]. Kordonski et al. [27] then widened the application of MRF to freeform and concave surfaces by introducing Magnetorheological Jet Finishing (MRJF), which is able to provide a more stable and precise material removal function compared to the common abrasive-water jet polishing. Experimental results proved that MRJF could produce ultra-precise surfaces on the order of tens of nanometers peak-to-valley together with surface roughness smaller than 1 nm rms on various materials such as metals, ceramics and glasses. Pattanaik and Agarwal [28] and Kumar et al. [29] innovatively developed a different MRF process of Rotational-Magnetorheological abrasive flow finishing (R-MRAFF), and it was pointed out that the magnetic flux density and the polishing angle (inclination) of the polished surface were two significant parameters affecting the roughness improvement and uniformity. A steel knee joint implant of 200 nm initial roughness was polished to a mirror surface, which has verified its practicality in the biomedical field. Saraswathamma et al. [30] conducted experiments on the ball end MRF to investigate the effects of parameters on silicon wafers and revealed that the working gap plays a crucial role in surface roughness improvement. Kansal et al. [31] introduced an innovative tool for MRF of diamagnetic materials which is capable of reducing surface roughness from 274 nm to 29 nm within 7.5 min, further widening its application in the electronics field. Anwesa and Manas [32] developed a polishing tool for freeform surface finishing and adopted finite element analysis to determine the optimal design configuration of the tool; experiments were conducted on a titanium workpiece and 95% surface roughness improvement was obtained from 180 nm to 10 nm. An MRF method for internal surface finishing of titanium tubes was also proposed and the effect of various parameters were investigated and optimized [33]. The application of MRF in polishing alloys and ceramics was also investigated and was

proven to have high efficiency in achieving nanometer scale surface roughness without surface or subsurface damage [34–36].

However, most of the above MFAF processes focus on precision polishing of the workpiece one-by-one, which leads to high polishing costs and is time consuming when polishing a large amount of workpieces. With the increasing demand of ultra-precision complex and freeform surfaces, more and more attention has been paid to increase the production efficiency of the polishing process. Hence, our research group [37] recently developed a novel magnetic field assisted mass polishing (MAMP) system which can polish tens of freeform surfaces simultaneously and obtain nanometric surface roughness. A feasibility study and the effects of some key parameters have been conducted and measured in our previous research. However, the target surface for polishing in our previous research [38,39] was only one side surface facing the external wall of the annular chamber.

Hence, an experimental investigation on the effects of the workpiece posture and orientation during MAMP was conducted in this paper. The experimental setup and design of experiments are presented in Section 2. Sections 3 and 4 present the experimental results of the polishing experiments as well as the discussion on the simulated computational fluid dynamics (CFD) model and magnetic field simulation. Finally, a conclusion is presented to summarize the research work in this paper in Section 5.

2. Experimental Procedures

2.1. Experimental Setup

The schematic diagram of the MAMP device is shown in Figure 1. In this device, workpieces are mounted on the cover and inserted into a Teflon (PTFE) annular chamber for polishing. The chamber is held by a frame to reduce vibration during polishing. Magnetic abrasives are poured into the chamber and two permanent magnetic pairs are placed around the chamber. Magnetic abrasives were then attracted towards the magnetic poles, forming two magnetic abrasive brushes within the chamber. The magnets were controlled to rotate along the fixed annular chamber, driving the abrasive brushes to continuously impinge on the workpiece surface leading to material removal.

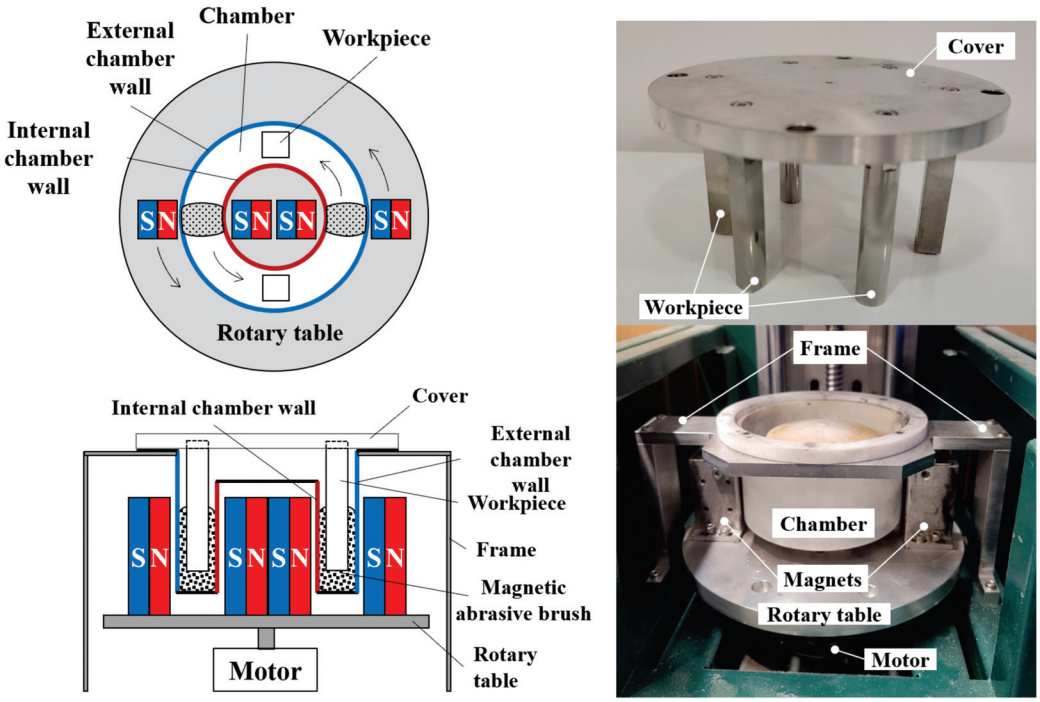

Figure 1. Schematic diagram of the MAMP device.

In this experiment, bonded magnetic abrasives which are made of iron particles (i.e., average 100~200 μm, 80 wt.%) and alumina abrasive (i.e., average ~2 μm, 20 wt.%), lubricated by silicon oil were used for rough polishing of the workpieces [39], while loose magnetic abrasive composed of carbonyl iron particles (CIP) (i.e., average ~3 μm, 80 wt.%) and polishing fluid (i.e., 150 nm alumina mixed with carrier fluid, 20 wt.%) were used for fine polishing of workpiece [38].

Two different shapes of workpiece were prepared as shown in Figure 2, including the square bar and roller. The side length of the square bar is 10 mm, and the diameter of the roller is also 10 mm. The material is 304 stainless steels (SS304). All workpieces were lapped with #400 silicon carbide (SiC) sandpaper before polishing.

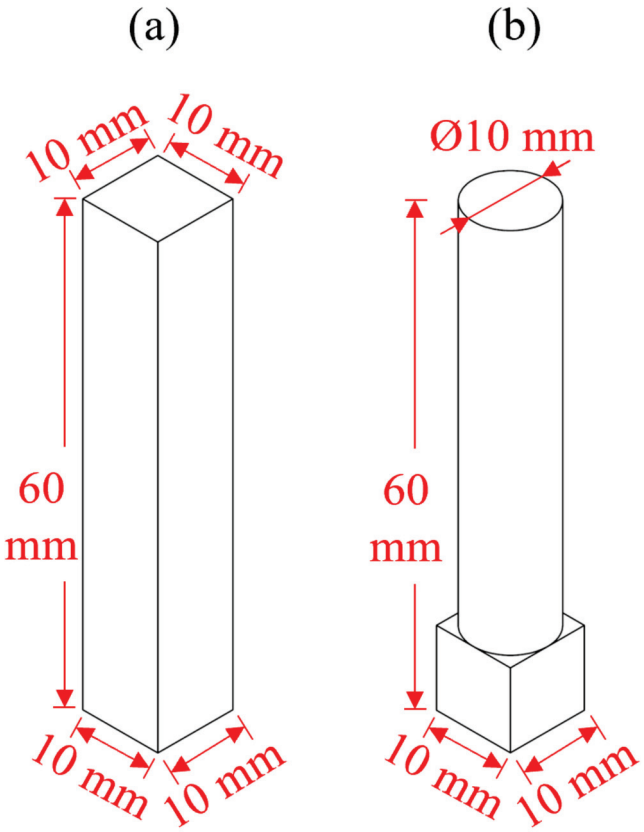

Figure 2. Workpiece design (**a**) square bar (**b**) roller.

2.2. Experimental Design

To further investigate the polishing performance of the MAMP device, two groups of experiments were designed. In each experiment, the workpieces were first rough polished for 20 min and then fine polished for another 20 min with the polishing parameters as presented in Table 1. The first group of experiments was conducted on rectangular bars to evaluate the polishing performance on flat surfaces and examine the effect of surface orientation. Two square bar workpieces were fixed on the chamber cover and mounted into the chamber, with a 2.5 mm gap distance between both the external and internal wall of the chamber. The polishing performance was evaluated based on the surface roughness of all four surfaces of the workpiece, namely plane 1~4 as shown in Figure 3. Plane 1 and plane 3 were perpendicular to the polishing direction, while plane 2 and plane 4 were parallel to the polishing direction. Each plane was divided into three regions (A, B, C) for surface roughness analysis. The workpiece was measured every 5 min. A Taylor Hobson Talysurf profilometer PGI1240 was used to measure the arithmetic surface roughness (S_a) of all four surfaces of the workpiece, and five measurements with a total length of 9 mm were taken on each surface, and a Gaussian filter and 0.08 mm cutoff length (L_c) was

applied for surface roughness analysis. The surface form profile was also measured by PGI1240 profilometer.

Table 1. Polishing parameters in experiments.

Parameters	Values
Rotational speed	1500 rpm
Polishing abrasive	Rough polishing 500~1000 μm Al_2O_3 sintered magnetic abrasives Fine polishing ~2 μm CIP (80 wt.%) + 150 nm Al_2O_3 (20 wt.%)
Polishing time	20 min
Workpiece	Square bar (10 × 10 × 60 mm); SS304 Roller (Ø10 × 60 mm); SS304
Magnets	N52 Neodymium permanent magnets, 25.4 × 25.4 × 50.8 mm;

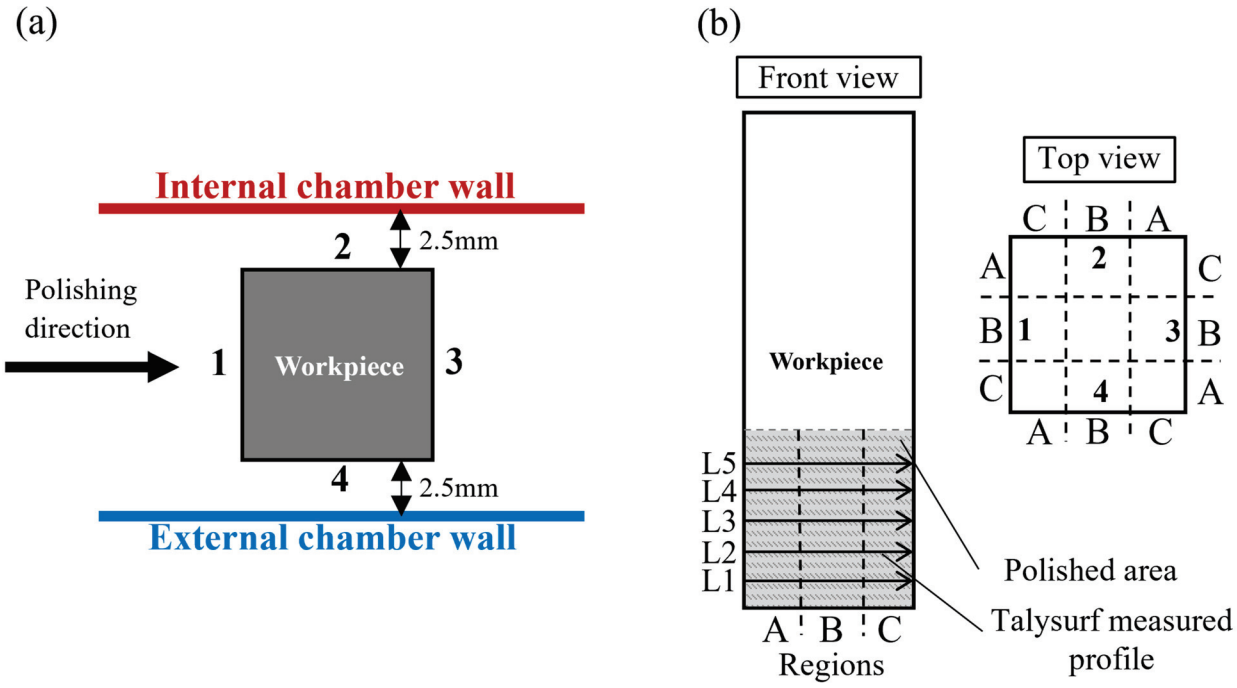

Figure 3. Square bar workpiece surface roughness measurement illustration (**a**) planes (**b**) regions.

The second group of experiments was aimed at studying the polishing performance of an MAMP device on the roller surface and to observe the effect of different impact angles. Two roller workpieces were rough polished for 20 min and then fine polished for another 20 min; seven measurement profiles were taken vertically along the workpiece as shown in Figure 4, including 0°, 30°, 60°, 90°, 120°, 150° and 180°. Theoretically, the polishing direction would form different angles with the tangents of a circle at different positions, which implies a different impingement angle of the abrasive brush on the workpiece surface. Measurements were taken along each angle of the workpiece every 5 min of polishing to record the surface roughness change at each angle.

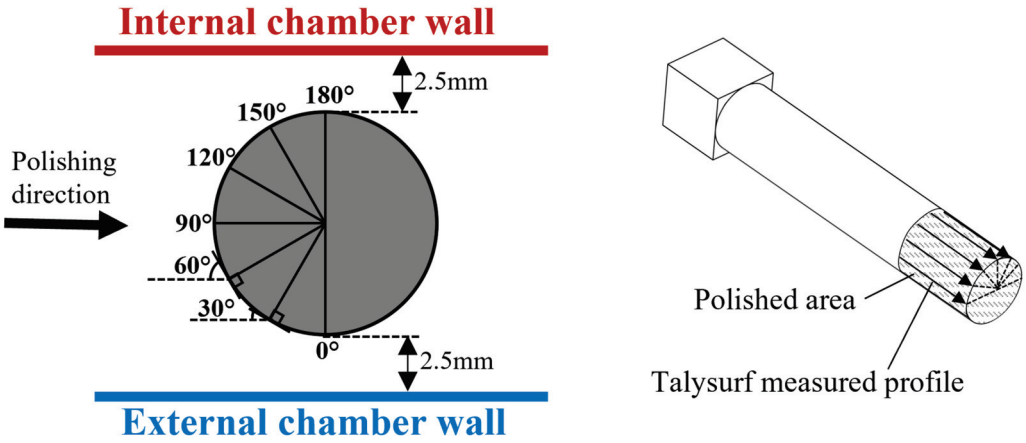

Figure 4. Roller workpiece surface roughness measurement illustration.

3. Results

3.1. Polishing Performance in Four Different Orientations

Figure 5 shows the surface roughness results measured in each plane of the square bar workpiece after 20 min of rough polishing. The result shows that plane 1, which was perpendicular to the polishing direction, has very little improvement, whereas plane 2 and plane 4, which were parallel to the polishing direction, shows a significant roughness reduction. The lowest surface roughness was obtained in plane 4, and a drastic decrease can be observed in the first 5 min. Moreover, plane 4 has achieved the limits of rough polishing of the MAMP system at around 40–50 nm, which is around 70% surface roughness convergence. A significant decrease in surface roughness deviation can be observed in plane 1, 2 and 4 after 20 min polishing, however, plane 3 shows no improvement in surface roughness after rough polishing. The reason is that plane 3 was not able to be polished in this case. Under an anticlockwise polishing direction, the surface behind the workpiece (plane 3) can hardly be polished, as the magnetic abrasive brush cannot make contact with the surface under a high-speed rotational movement.

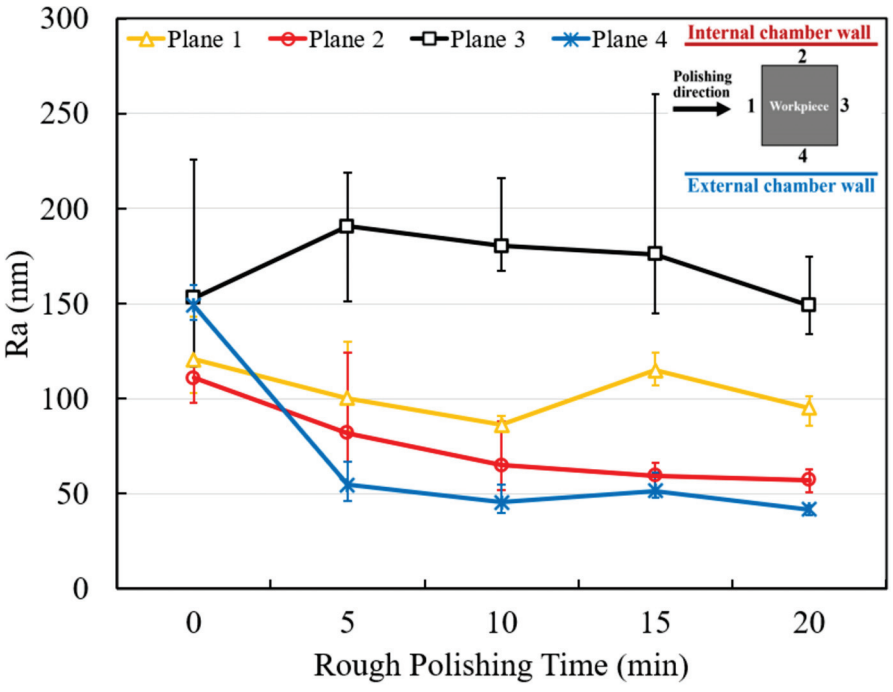

Figure 5. Overall surface roughness of rough polished square bar.

The rough polished workpieces were then fine polished for 20 min and the results are shown in Figure 6. The surface roughness of plane 2 before fine polishing shows 3 different starting points varying from 40 to 120 nm, indicating an uneven polishing performance on the three regions of plane 2 during rough polishing. It reveals that region A experienced the least material removal; region B was slightly polished while region C was fully polished, reaching around 40 nm roughness.

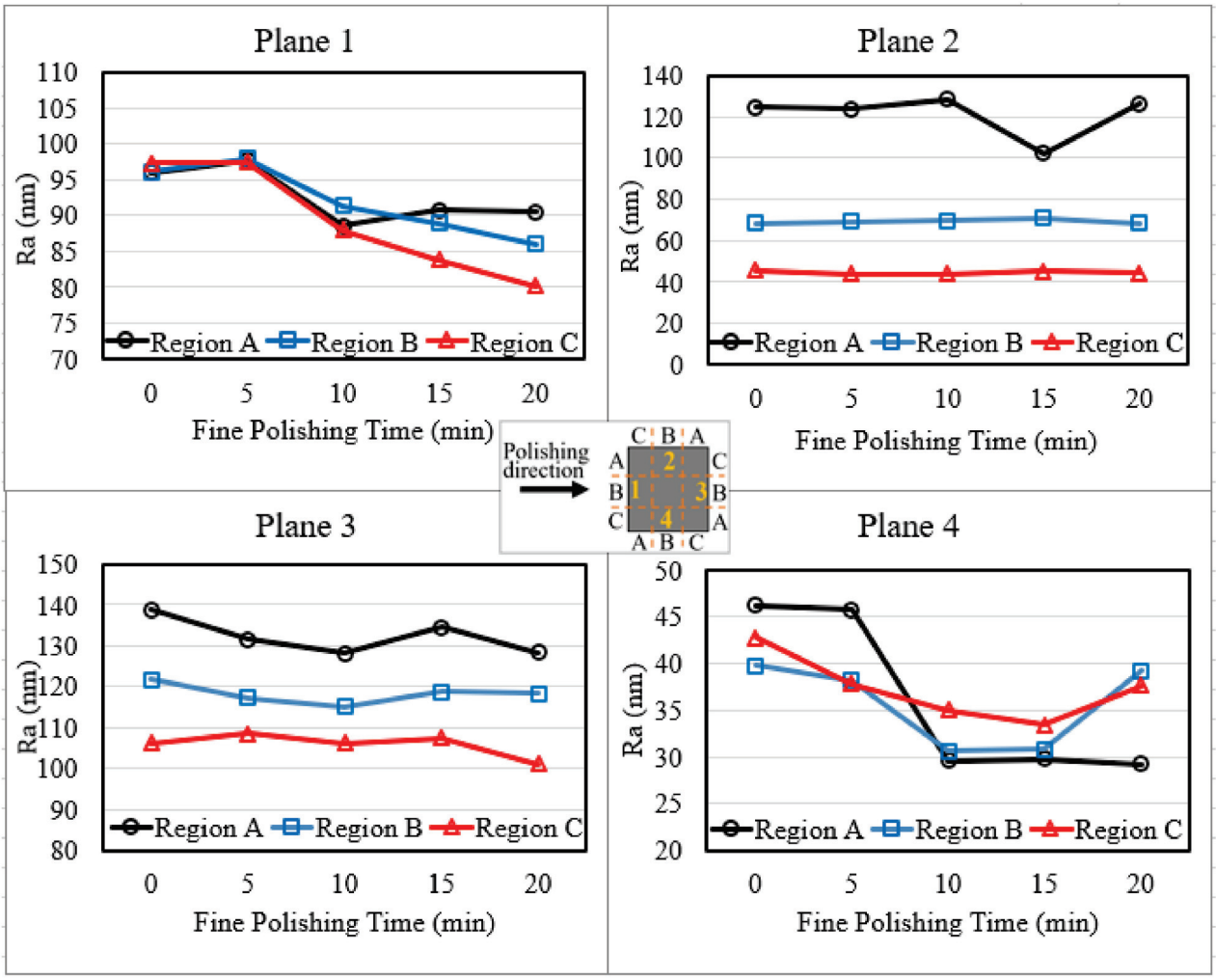

Figure 6. Planer surface roughness of fine polished square bar workpiece.

Looking into the fine polishing results, it can be seen that all regions in plane 2 and 3 show nearly no improvement along the 20 min fine polishing, and only plane 4 shows a significant decrease in surface roughness to around 30 nm, with region A having the lowest value. Figure 7 has summarized the average surface roughness of each plane before polishing, after rough polishing and after fine polishing. It can be observed that plane 4 shows the most significant improvement, and plane 2 has recorded the largest surface roughness deviation within the plane after fine polishing.

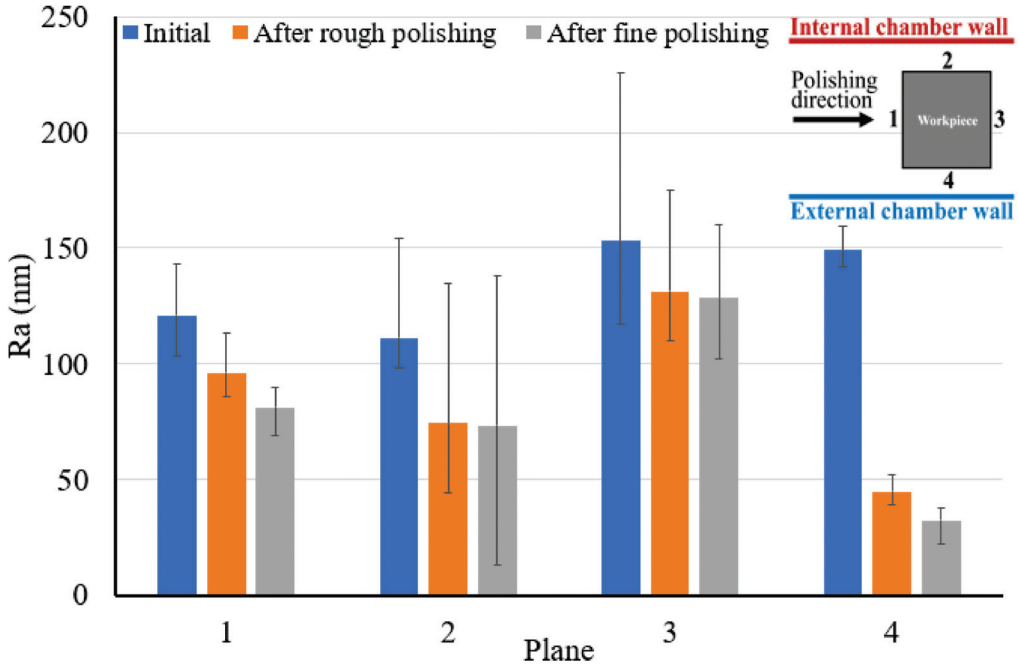

Figure 7. Summary of average surface roughness in each plane of square bar.

Figure 8 presents the snapshots of the fine polished surface of a square bar. It can be seen that plane 4 shows a much clearer reflected image than the other three planes, whereas plane 3 shows the poorest. The surface roughness profile of plane 4 of the square bar before and after polishing was shown in Figure 9. It is observed that the rough peaks were largely sheared off after the polishing process as shown in Figure 9a, and the overall surface height deviations were improved. Figure 9b,c shows the 3D contour of surface roughness measured by a Zygo Nexview white light interferometer, and the arithmetical mean height (S_a) has improved from 146 nm to 26 nm, and the root-mean-square roughness has also reduced from 193 nm to 36 nm, which signifies the polishing performance of the process. Figure 10 shows the surface integrity of the workpiece captured by a Scanning Electron Microscope (Hitachi tabletop microscope-TM3000). Most of the scratches and defects have been removed after rough polishing and the surface was further smoothened after fine polishing. Figure 11 demonstrates the comparison of the surface profile before and after polishing, indicating that the surface form accuracy can be well maintained along the height direction of the square bar after the MAMP process.

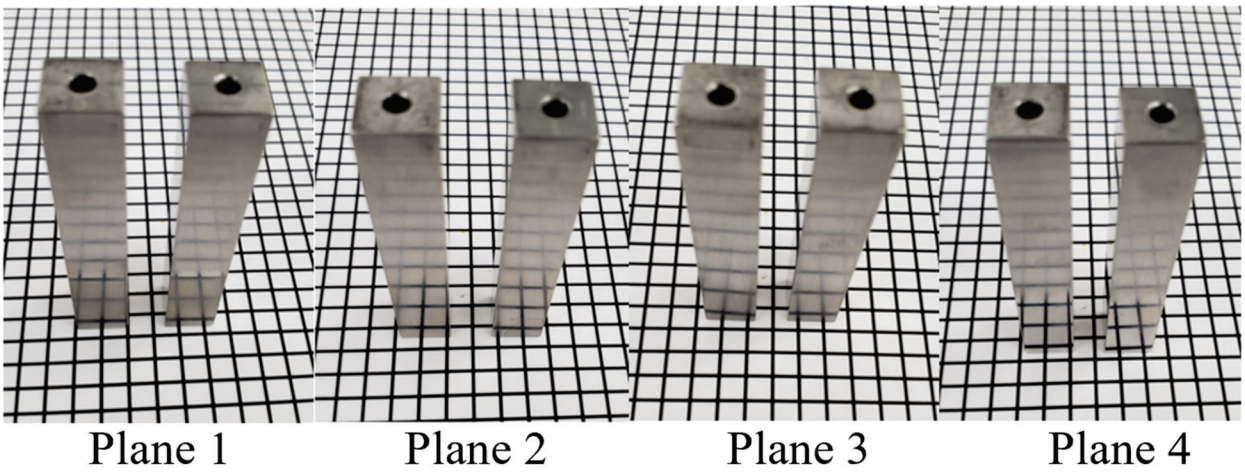

Figure 8. Snapshots of square bar after fine polishing.

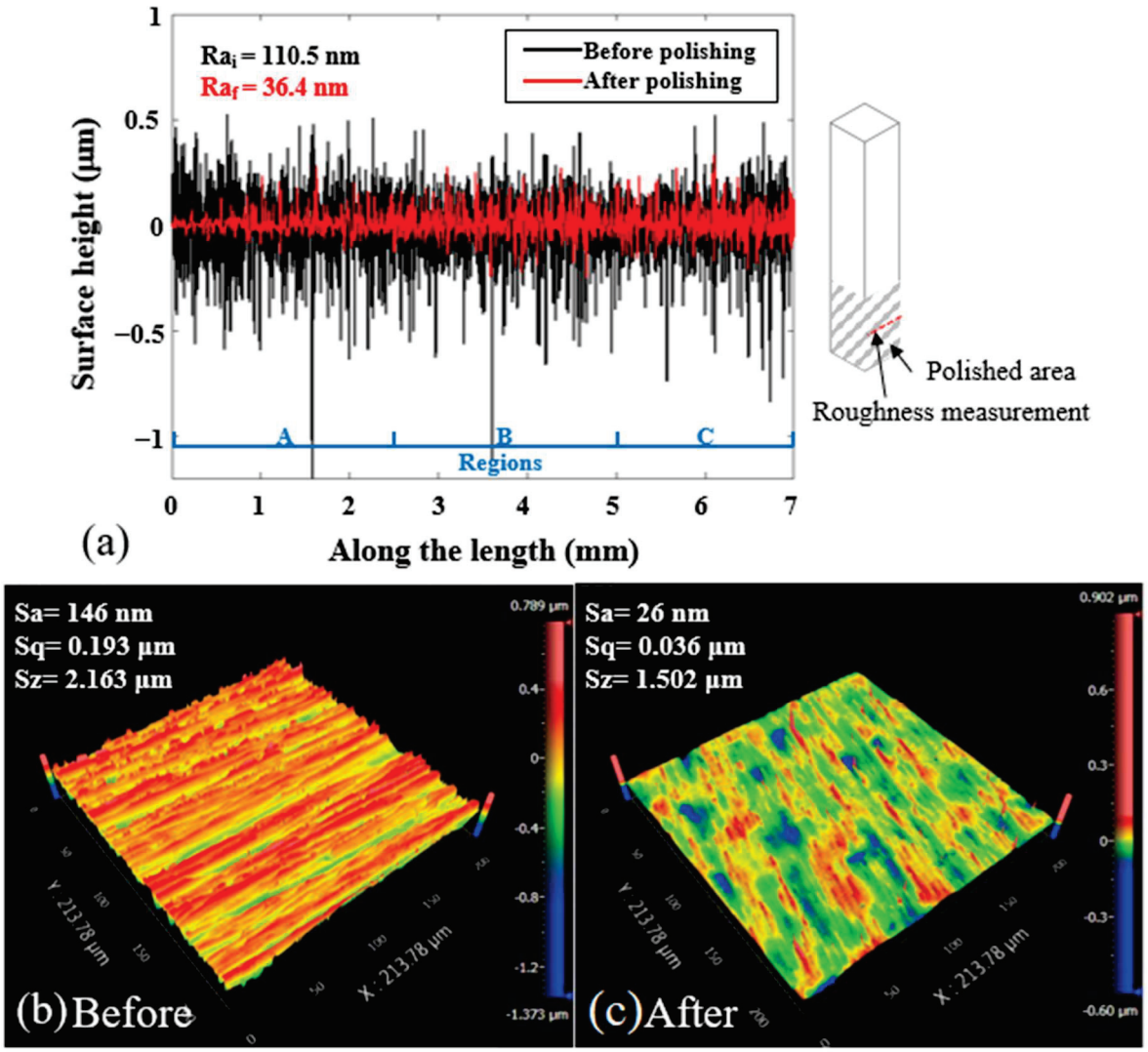

Figure 9. Surface roughness (**a**) profile of square bar plane 4 (L3); Ra_i signifies the arithmetic roughness of the profile before polishing. Ra_f signifies the arithmetic roughness of the profile after fine polishing. 3D surface topography of the square bar plane 4 (**b**) before and (**c**) after polishing, measured from a ZYGO Nexview 3D optical interferometer.

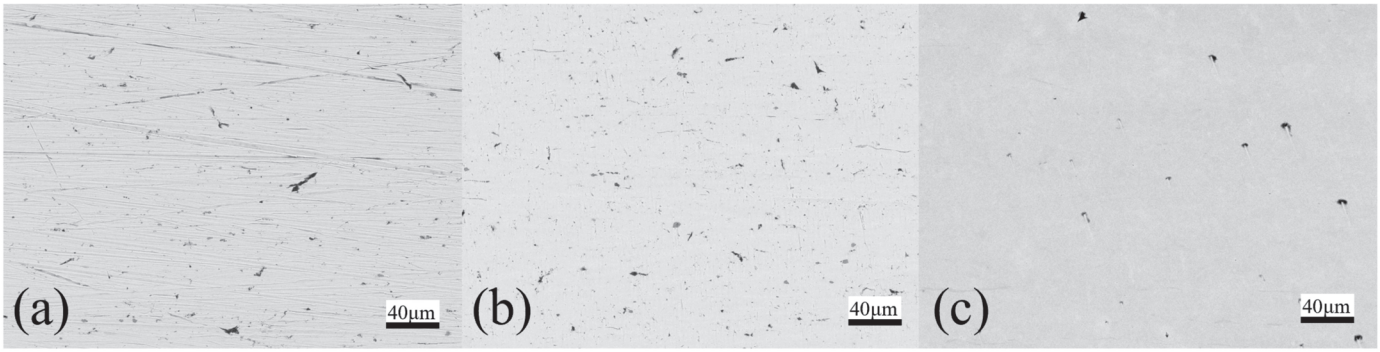

Figure 10. SEM photographs of workpiece (**a**) before polishing (**b**) rough polished (**c**) fine polished.

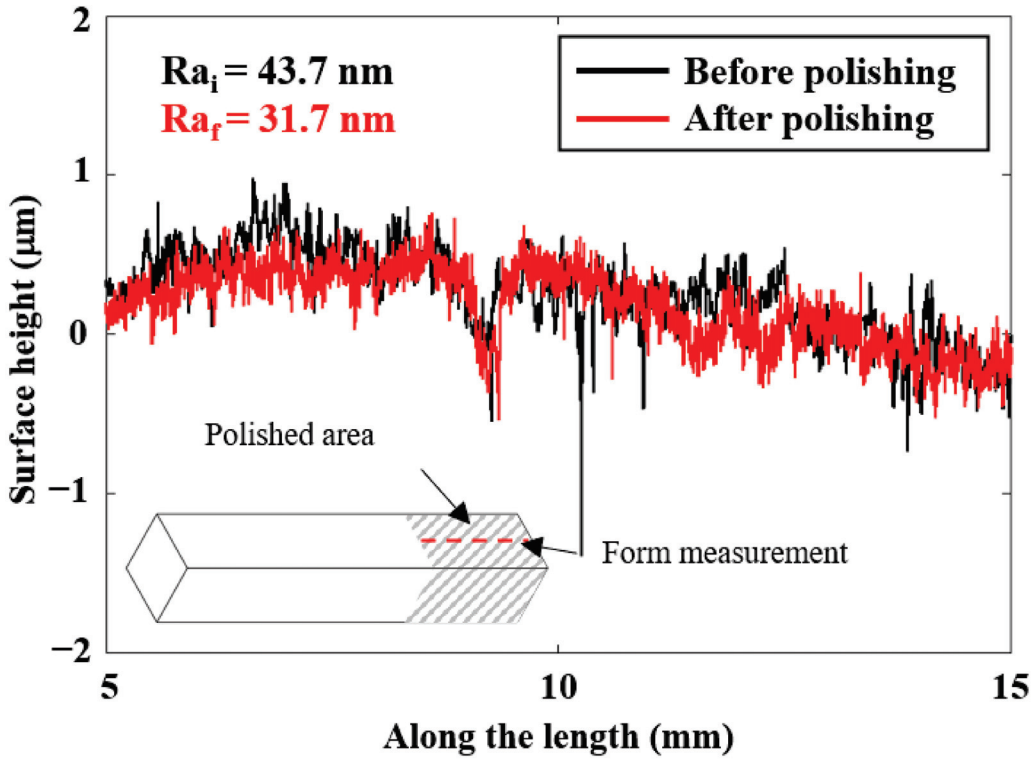

Figure 11. Surface profiles of square bar plane 4.

3.2. Polishing Performance on the Roller Surfaces

Roller type workpieces were polished to examine the effect of the polishing angles. A snapshot of the roller surface before and after polishing was shown in Figure 12, where a smoother surface was obtained after rough polishing, and a shiny and reflective surface can be observed after the fine polishing process. The rough polished and fine polished surface roughness change was shown in Figure 13, and the varied polishing performance can be observed after fine polishing, where 0°, 30° and 60° have experienced a more dramatic fall in surface roughness reaching around 25 nm; 150° and 180° shows a very gradual decrease during both rough and fine polishing; and 90° and 120° received nearly no improvement in the rough polishing process and a slight decrease after the fine polishing process. From the results, under the same impact angle, where 0° corresponds to 180°, a different value was obtained after the whole polishing process; better polishing performance was observed near the external chamber wall and the reason is discussed in the section below.

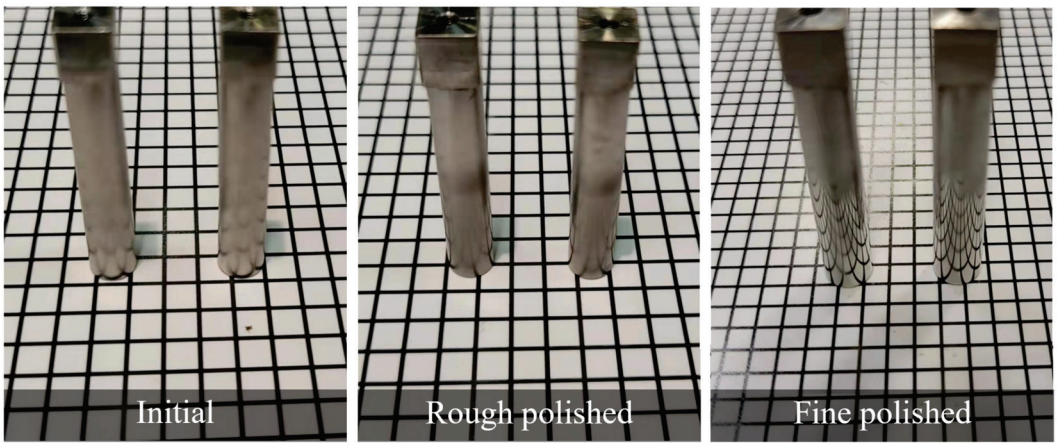

Figure 12. Snapshot of roller workpieces before and after polishing.

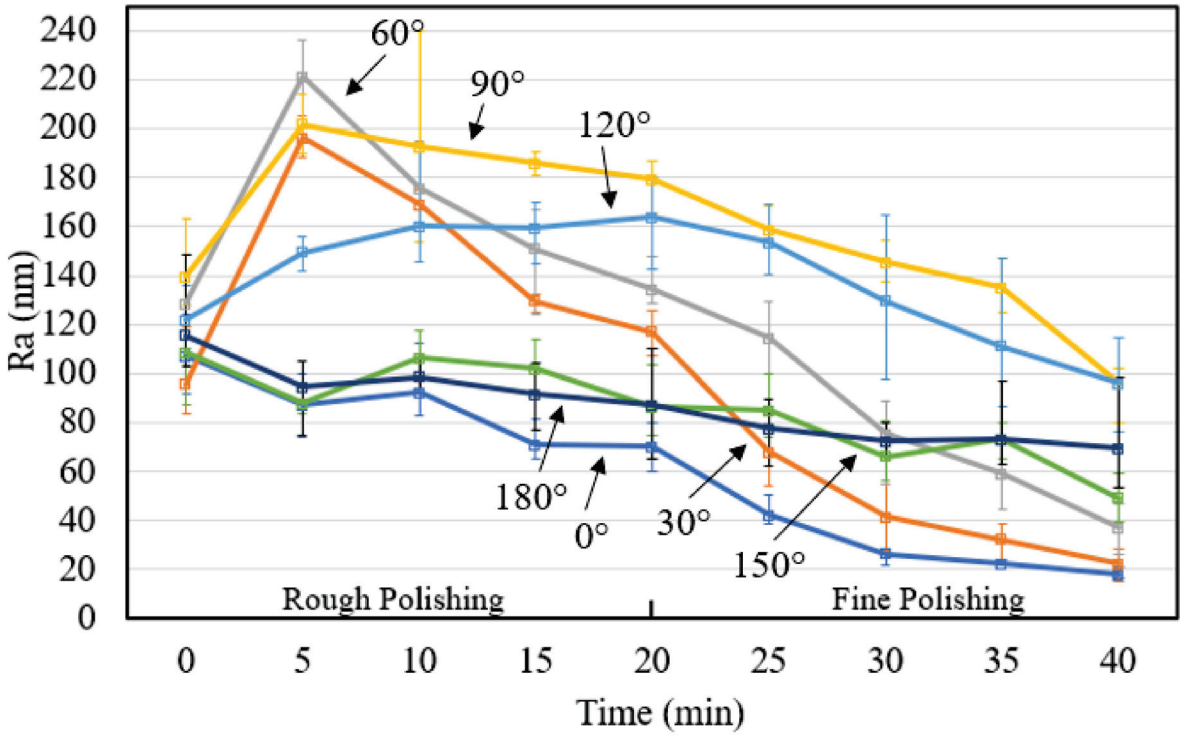

Figure 13. Surface roughness change of roller workpiece at different angles.

3.3. Simulations

3.3.1. Simulation of the Magnetic Field Distribution

In MFAF, the magnetic force is critical to the polishing performance. Hence, the magnetic flux density distribution in MAMP was modelled based on the finite element method (FEM) to explain the phenomenon of uneven roughness results. A simulation of the magnetic flux density distribution was performed using ANSYS Maxwell. A magnetostatic solver was adopted to solve Maxwell's equations in a setup as shown in Figure 14. The default boundary condition with 100% padding was applied to ensure sufficient room for fringing, and an automatic adaptive meshing for 10 passes was set. Four non-model lines were drawn on the surface of the four planes of the workpiece to extract the numerical value of the magnetic flux density of the different planes. Figure 15 shows the magnetic flux density distribution of the system, and Figure 16 presents the graphical value of magnetic flux density along the horizontal line of each plane. From Figures 15 and 16, plane 1 and 3 were experiencing a weaker magnetic field of 430 mT compared to 470 mT in plane 2 and 450 mT in plane 4. This is due to the increase of distance between the magnets and the plane, as plane 2 and 4 were closer to the chamber wall and parallel to the magnets surface, thus experiencing a higher magnetic force. Whereas plane 1 and 3 lies in between the two magnets, it experiences magnetic force from both sides of the permanent magnets at the edges but less magnetic forces in the middle of the plane. Theoretically, a stronger magnetic force indicates a tougher magnetic abrasive brush as the bonding in the magnetic abrasive chain is stronger, thus areas near the chamber wall should have a higher material removal rate.

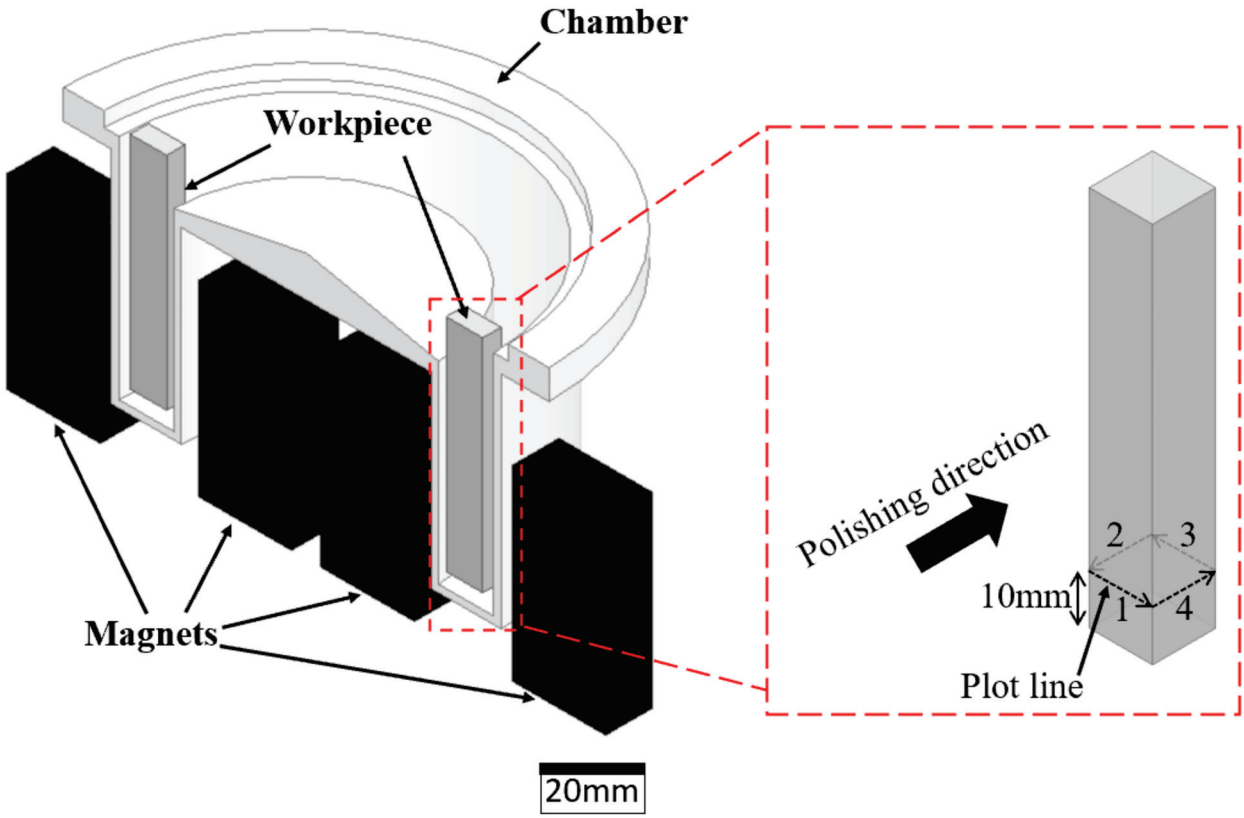

Figure 14. Finite element analysis model.

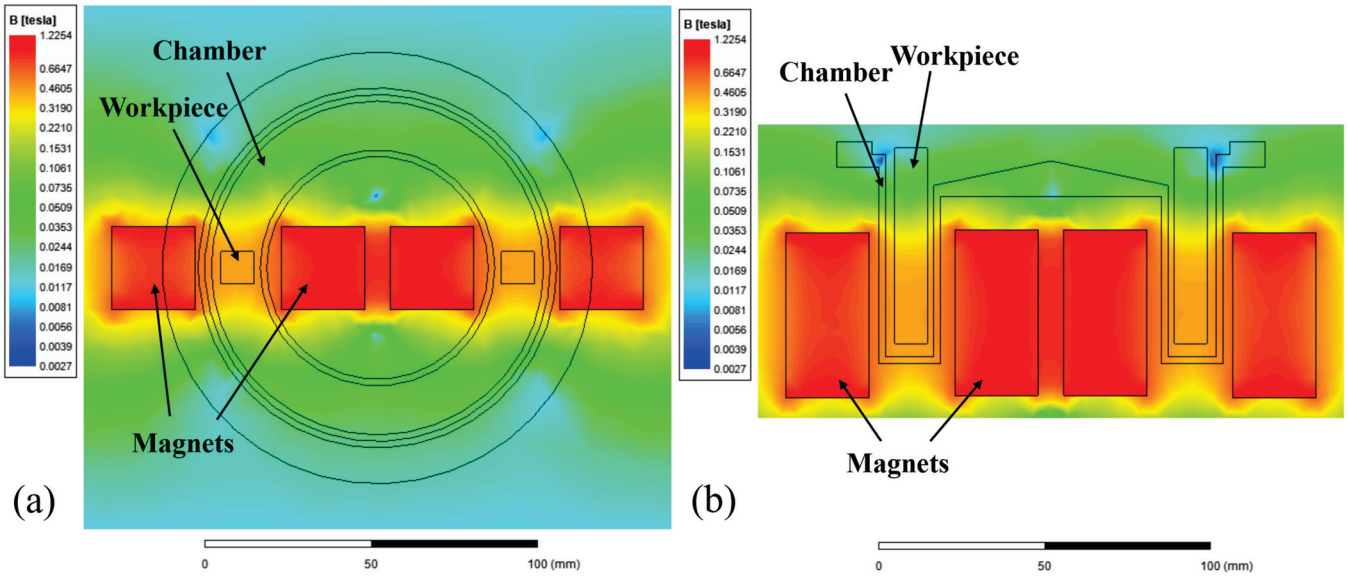

Figure 15. Simulation result of magnetic flux density distribution in (**a**) top view (**b**) front view (sectioned).

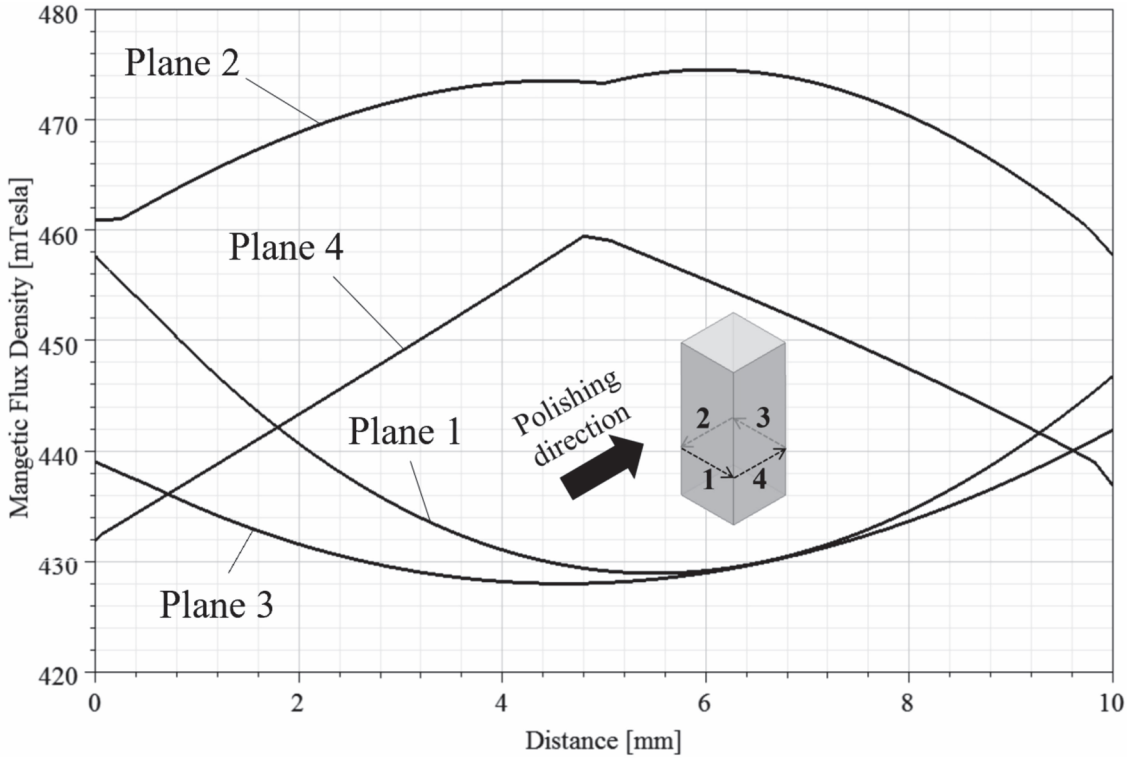

Figure 16. Simulation result of magnetic flux density horizontally along each workpiece plane.

3.3.2. Simulation of Impingement

In addition to the magnetic field distribution, the movement of the magnetic flow can also be attributed to the difference in polishing performance at different orientations. Hence, the movement of the fluid flow was also modelled by ANSYS Fluent in this study to provide a deeper understanding on the effect of the fluid flow movement when polishing different shapes of the workpiece. The rotational symmetry structure during polishing makes it possible to simplify the simulation down to a 2D axisymmetric problem. The Navier-Stokes's equation with incompressible form is applied to solve the fluid velocity field. To describe multiphase systems, a simple algorithm and Volume of Fluid (VOF) model were employed to solve the pressure-velocity coupling and model the continuous multiphase, respectively. Considering the effect of turbulence on flow field, the Shear-Stress Transport (SST) was used to express the turbulent fluid flow in the inner region of the boundary layer as well as in the outer part of the boundary layer for a wide range of the Reynolds number. The inlet was defined as the velocity inlet with a velocity of 6.6 m/s, which is calculated based on 1500 revolutions per minute, with a 42 mm distance from the rotational axis; and the outlet was a pressure outlet. Furthermore, the fluid viscosity was set to 0.001 kg/s to simulate the property of polishing slurry. Figure 17 shows the mesh generation methods, and all the boundary layers were refined to guarantee the simulation accuracy. Looking into Figure 18, according to the polishing direction, the abrasive brush flows from the left to the right, first impinges plane 1 in Figure 18a, then separates into two streams and rubs the surface of plane 2 and plane 4, while plane 3 remained uncontacted. As for the roller workpiece as shown in Figure 18b, the abrasive flows along the curvature, so half of the workpiece was polished while the other half at the back was not.

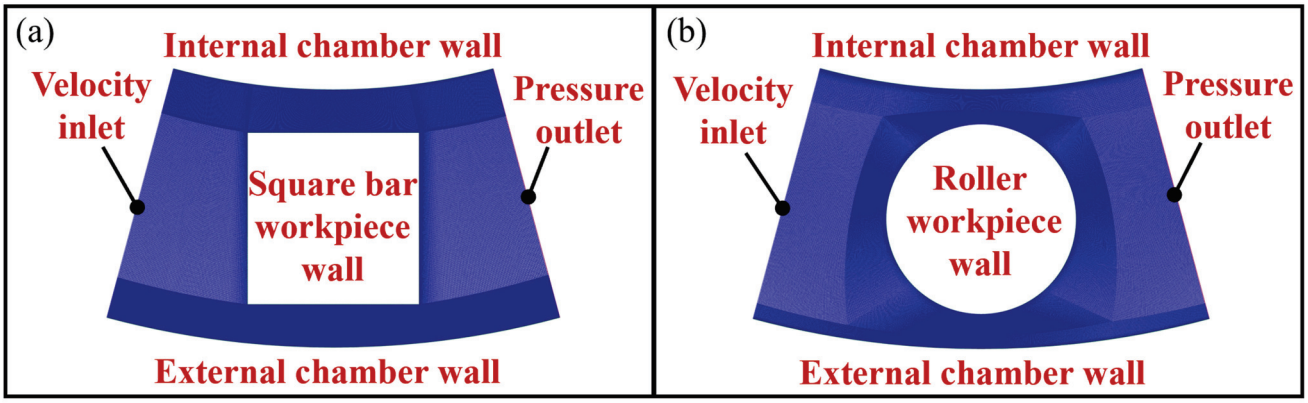

Figure 17. Mesh generation in CFD model simulation of (**a**) square bar (**b**) roller workpiece.

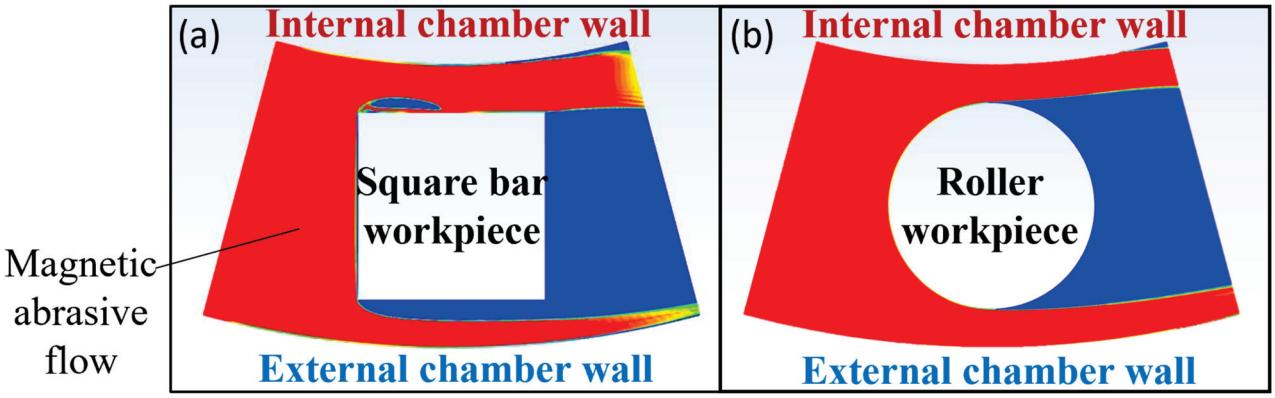

Figure 18. Simulation result of fluid flow in the polishing process of (**a**) square bar (**b**) roller.

4. Discussion

4.1. Discussion on the Effect of Surface Orientation

The experimental results show that the MAMP method has different polishing performance at different posture and orientation; better polishing performance can be observed in the surfaces parallel to or slightly inclined to the polishing direction. In the square bar workpiece, plane 2 and 4 shows significant roughness reduction, plane 1 has little improvement and plane 3 has no obvious change. Whereas in the roller workpiece, 0° and 30° impact angles show the lowest roughness after the polishing process. This result can be explained by the varying abrasive brush stiffness and abrasive flow. The stiffness of the abrasive brush is considered to be related to the magnetic pressure which is mainly produced by magnetization. This magnetic pressure expression can be written as follows [40]

$$P_m = \frac{B^2}{2\mu_0}\left(1 - \frac{1}{\mu_r}\right) \quad (1)$$

where μ_0 is the free space permeability, μ_r is the relative magnetic permeability of the magnetic brush, and B is the magnetic flux density on the target surface, which can be obtained from the simulation model of magnetic field distribution. It is known from Equation (1) that the greater the value of B, the larger the P_m. According to the magnetic field simulation results, the magnetic flux density near the chamber wall was stronger than that of the middle region by around 40 mT, and magnetic force is found to be proportional to the magnetic field strength [41]. Thus, it can be deduced that a stronger magnetic pressure can be found near the chamber wall (plane 2 and 4) while a lower magnetic pressure was formed at the middle of the tunnel (plane 1) which would lead to a weaker impingement and material removal. Whereas plane 3 was not able to be polished as demonstrated in the CFD simulation shown in Figure 18. From the roller type experiments, a perpendicular

impact angle shows poorer improvements, while 0° and 30° polishing angles had achieved the lowest surface roughness of 20 nm, which also conforms to the results of the bar type workpiece. In addition, the perpendicular polishing angle has not allowed effective shearing, as the magnetic abrasives were stopped by the surface when hitting the perpendicular surface, resulting in near zero velocity along the polishing direction that material removal can hardly occur, whereas an angled surface allows the abrasives to slide through and shears off the material from the surface during the impingement, and thus the middle area of the roller workpiece appears to have a higher surface roughness after polishing.

However, although plane 2 and plane 4 of the square bars were both parallel to the polishing direction, and that 0° and 180° of the rollers shall share the same impact angle, the polishing performance of these identical angle pairs did not show a similar efficiency. It was found that lower surface roughness values were recorded in surfaces near the outer circle (external chamber wall), especially during the fine polishing process, as compared to surfaces near the inner circle (internal chamber wall) despite the stronger magnetic force in the inner circle. This might be due to the centrifugal force brought by the rotational movement of the abrasive brush. In the polishing process, magnetic abrasives were attracted to two pairs of magnetic poles, and rotated at a high-speed of 1500 rpm; centrifugal force can be loaded on the magnetic abrasives which tend to be swung outwards, leading to a less concentrated brush in the inner circle of the chamber. The magnetic force F_m on the magnetic particles under the magnetic field can be expressed by [42]:

$$F_m = V \cdot X_m \cdot H \cdot \nabla H \tag{2}$$

where V is the volume of magnetic particle and X_m is the mass susceptibility, H is the magnetic field strength and ∇H is the gradient of H. From Equation (2), it is known that with a greater volume of magnetic particle (V), a larger magnetic force (F_m) can be obtained. Similarly, in fine polishing, the magnetic particles are smaller in size and loosely bonded, and a weaker magnetic force and linkage was experienced as compared to the large magnetic abrasives used in rough polishing. Thus, the weak magnetic force may not withstand the strong centrifugal force experienced by the fine polishing abrasive as reported by Shukla and Pandey [43], abrasives in the inner circle would have been thrown outwards and accumulate on the external wall that area near internal chamber wall cannot be reached by the abrasives, leading to the different polishing pattern between rough and fine polishing. Thus, with the current design of the MAMP system, the target surface should be mounted facing outwards to ensure the best polishing performance.

4.2. Discussion on the Effect of Different Region on the Same Surface

Looking into the performance in the parallel direction of the square bar workpiece, the results show that regions at the beginning of impingement were better polished in both plane 2 and 4, while plane 4 had a larger variation of roughness among the three regions after fine polishing. The fluid simulation also conforms with the polishing results that only plane 1, 2 and 4 were able to be reached, with fluid being slightly blocked apart from the surfaces of both plane 2 and plane 4. Figure 19 has summarized the polishing performance at different regions of impingement in plane 2 and 4, while plane 2 region C and plane 4 region A belongs to the beginning of impingement while plane 2 region A and plane 4 region C belongs to the end of the impingement. Generally, only regions at the beginning and middle can be significantly polished. Magnetic abrasives may be retained at the highest point of the workpiece (at the middle of region B), so that the sliding of the abrasive cannot continue on regions at the end of the impingement. With the magnetic abrasive being blocked due to the surface shape, the high flow-speed magnetic abrasive brush might not have allowed enough time for the abrasives to re-link themselves under the magnetic force and thus cannot completely conform to the surface, leading to a varying polishing performance. To overcome this problem, a larger gap distance between workpiece surface and the chamber wall is believed to be able to allow smoother pass through of the

stiffened brush, and thus a more complete contact. Moreover, keeping the target surface at an inclined angle against the polishing direction is important to allow efficient shearing.

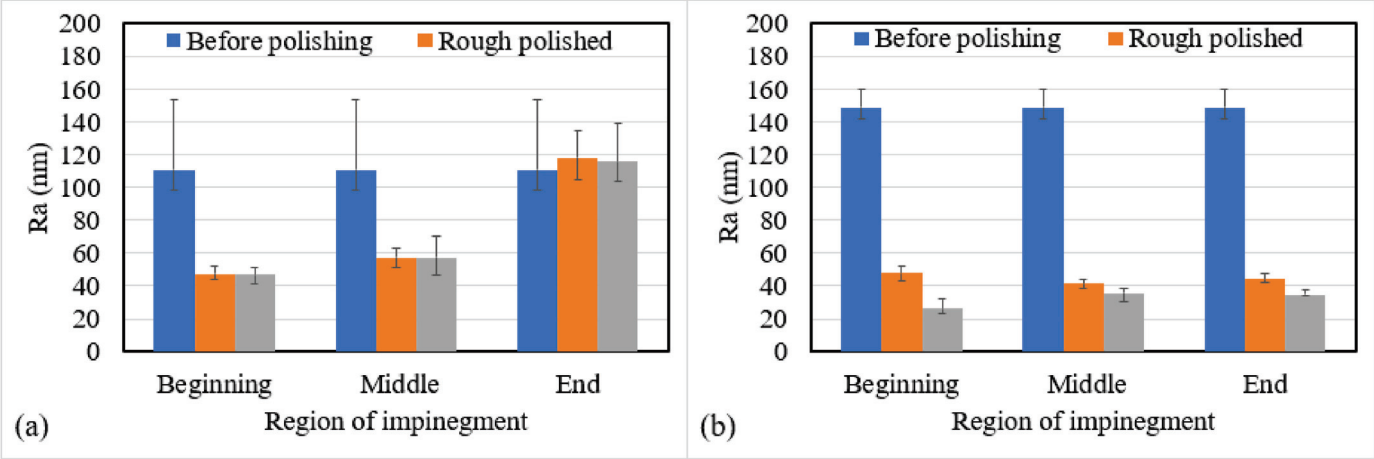

Figure 19. Polishing performance at different regions of impingement in square bar (**a**) plane 2 and (**b**) plane 4.

4.3. Discussion on the Edge-Rounding Effect of Square Bar Surface

After a 20-min rough polishing and 20-min fine polishing, the square bar component has a great surface roughness improvement on plane 4, especially at the beginning area of impingement. Figure 20 shows the edge width of the square bar before and after polishing. It can be observed that the edge width has a slight increase from approximately 100 µm to 110 µm after polishing, and the sharp and clear edge (white area) has diminished slightly, symbolizing a small round edge despite the similar width of the white area. The edge rounding effect is mainly induced by the rough polishing process as the abrasive particle size was larger, however, since the rough polishing process was not performed for a long period, the edge rounding effect was insignificant in this study. In addition, the edge rounding effect during rough polishing can be minimized by controlling the polishing time and polishing angle, whereas in fine polishing, edge-rounding effect was not found [38].

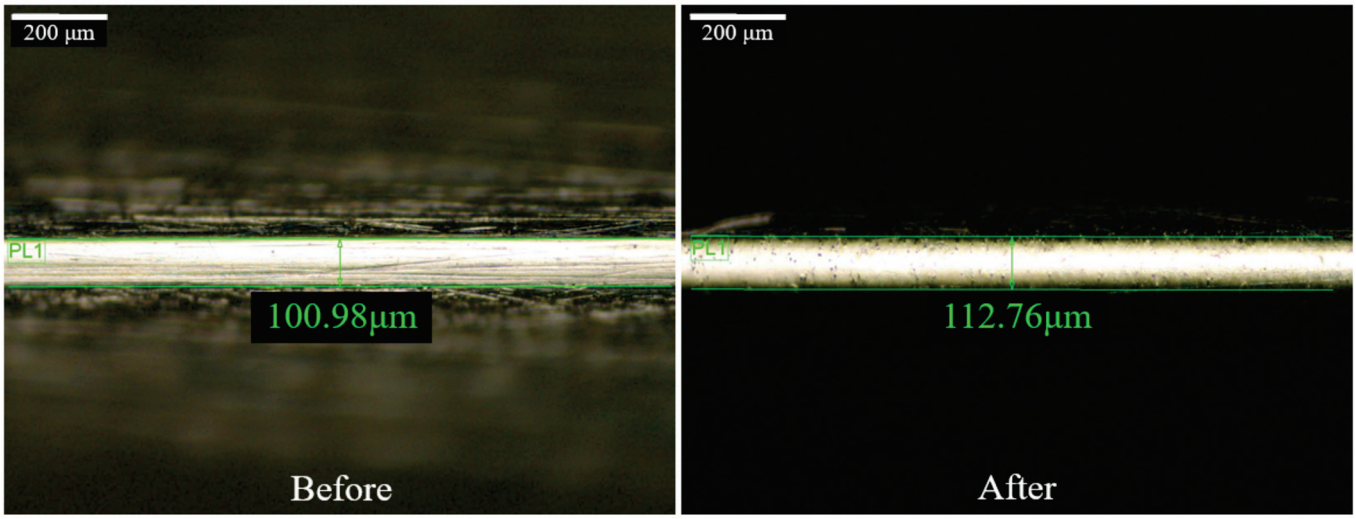

Figure 20. Edge width of square bar workpiece before and after polishing.

4.4. Discussion on the Methods to Improve the Polishing Uniformity

From the experimental results, it can be deduced that the target surface should be facing outwards when polishing a non-revolving surface. Moreover, an effective polishing

angle should be determined to allow uniform material removal. For a revolving surface (i.e., roller) that requires polishing of the entire surface, the extra rotation of the workpiece can be added to ensure uniform polishing of the whole surface. Driving the magnetic brush to run both in a clockwise and anti-clockwise direction should also be helpful to obtain uniform polishing of the whole surface. Another possible approach might be controlling the workpiece to self-rotate or performing overlapping polishing by adding a motor to match the polishing direction and impact angle. As it was found that an area with 0–30° impact angle achieves better performance, therefore by rotating the component and changing the orientation of the surface to the effective polishing angle repetitively and constantly, the material removal uniformity can be improved.

5. Conclusions

In this study, experimental investigation and simulation on the effect of surface shapes and orientations in the MAMP process was conducted on the square bar and roller. The obtained conclusions are as follows:

(1) Surfaces near the chamber wall experience higher magnetic strength, a stiffer magnetic brush is formed and thus generally performs better, and the target surface should be mounted facing outwards.
(2) Regions at the beginning of impingement were polished better, as the abrasive brush was either obstructed or not conforming to the regions behind it due to the workpiece shape and high rotational speed; polishing angle adjustment will be needed to eliminate the limitations.
(3) Both types of workpieces have partially achieved a final surface roughness of Ra = 20 nm after fine polishing.
(4) Further investigation is still needed to study the polishing mechanism and improve the polishing uniformity.

Author Contributions: Conceptualization, Y.-M.L. and C.W.; methodology, Y.-M.L. and C.W.; formal analysis, Y.-M.L.; investigation, Y.-M.L.; resources, C.-F.C.; writing—original draft preparation, Y.-M.L.; writing—review and editing, C.-F.C., C.W. and L.-T.H.; supervision, C.-F.C. and C.W.; funding acquisition, C.-F.C. and C.W. All authors have read and agreed to the published version of the manuscript.

Funding: This research was funded by a grant from the Research Grants Council of the Government of the Hong Kong Special Administrative Region, China (Project No. 15203620) and the financial support from the Guangdong Natural Science Foundation Program 2019–2020 (Project No. 2019A1515012015). In addition, the authors would also like to express their sincere thanks to the funding support from the Research Office of The Hong Kong Polytechnic University (Project code: BBXN) and the research studentships (Project code: RH3Y).

Institutional Review Board Statement: Not applicable.

Informed Consent Statement: Not applicable.

Conflicts of Interest: The authors declare that they have no conflict of interest.

References

1. Kim, D.W.; Burge, J.H.; Davis, J.M.; Martin, H.M.; Tuell, M.T.; Graves, L.R.; West, S.C. New and improved technology for manufacture of GMT primary mirror segments. In Proceedings of the SPIE Astronomical Telescopes and Instrumentation, Edinburgh, UK, 26 June–1 July 2016; SPIE: Bellingham, WA, USA, 2016; pp. 1–8.
2. Fang, F.; Zhang, X.; Weckenmann, A.; Zhang, G.; Evans, C. Manufacturing and measurement of freeform optics. *CIRP Ann. Manuf. Technol.* **2013**, *62*, 823–846. [CrossRef]
3. Chkhalo, N.; Kaskov, I.; Malyshev, I.; Mikhaylenko, M.; Pestov, A.; Polkovnikov, V.; Salashchenko, N.; Toropov, M.; Zabrodin, I. High-performance facility and techniques for high-precision machining of optical components by ion beams. *Precis. Eng.* **2017**, *48*, 338–346. [CrossRef]
4. Wang, C.; Wang, Z.; Wang, Q.; Ke, X.; Zhong, B.; Guo, Y.; Xu, Q. Improved semirigid bonnet tool for high-efficiency polishing on large aspheric optics. *Int. J. Adv. Manuf. Technol.* **2016**, *88*, 1607–1617. [CrossRef]

5. Wang, C.; Cheung, C.; Liu, M. Numerical modeling and experimentation of three dimensional material removal characteristics in fluid jet polishing. *Int. J. Mech. Sci.* **2017**, *133*, 568–577. [CrossRef]
6. Yunata, E.E.; Aizawa, T.; Tamaoki, K.; Kasugi, M. Plasma Polishing and Finishing of CVD-Diamond Coated WC (Co) Dies for Dry Stamping. *Procedia Eng.* **2017**, *207*, 2197–2202. [CrossRef]
7. Yamaguchi, H.; Shinmura, T.; Sato, T.; Taniguchi, A.; Tomura, T. Study of Surface Finishing Process using Magneto-rheological Fluid (MRF). *J. Jpn. Soc. Precis. Eng. Contrib. Pap.* **2006**, *72*, 100–105. [CrossRef]
8. Hashimoto, F.; Yamaguchi, H.; Krajnik, P.; Wegener, K.; Chaudhari, R.; Hoffmeister, H.-W.; Kuster, F. Abrasive fine-finishing technology. *CIRP Ann.-Manuf. Technol.* **2016**, *65*, 597–620. [CrossRef]
9. Yamaguchi, H.; Shinmura, T.; Kaneko, T. Development of a new internal finishing process applying magnetic abrasive finishing by use of pole rotation system. *Int. J. Jpn.* **1996**, *30*, 317–322.
10. Yamaguchi, H.; Shinmura, T. Study of an internal magnetic abrasive finishing using a pole rotation system: Discussion of the characteristic abrasive behavior. *Precis. Eng.* **2000**, *24*, 237–244. [CrossRef]
11. Vahdati, M.; Rasouli, S.A. Study of magnetic abrasive finishing on freeform surface. *Int. J. Surf. Eng. Coat.* **2016**, *94*, 294–302. [CrossRef]
12. Guo, J.; Liu, K.; Wang, Z.F.; Tnay, G.L. Magnetic field-assisted finishing of a mold insert with curved microstructures for injection molding of microfluidic chips. *Tribol. Int.* **2017**, *114*, 306–314. [CrossRef]
13. Yang, S.; Li, W. *Surface Quality and Finishing Technology, in Surface Finishing Theory and New Technology*; Springer: Berlin/Heidelberg, Germany, 2017; pp. 1–64.
14. Guo, J.; Feng, W.; Jong, H.J.H.; Suzuki, H.; Kang, R. Finishing of rectangular microfeatures by localized vibration-assisted magnetic abrasive polishing method. *J. Manuf. Process.* **2019**, *49*, 204–213. [CrossRef]
15. Guo, J.; Au, K.H.; Sun, C.-N.; Goh, M.H.; Kum, C.W.; Liu, K.; Wei, J.; Suzuki, H.; Kang, R. Novel rotating-vibrating magnetic abrasive polishing method for double-layered internal surface finishing. *J. Mater. Process. Technol.* **2018**, *264*, 422–437. [CrossRef]
16. Sumit, Y.; Chhikara, G. Modern magnetic abrasive Finishing process. *Int. J. Enhanc. Res. Sci. Technol. Eng.* **2014**, *3*, 460–462.
17. Deepak, B.; Walia, R.S.; Suri, N.M. Effect of rotational motion on the flat work piece magnetic abrasive Finishing. *Int. J. Surf. Eng. Mater. Technol.* **2012**, *2*, 550–554.
18. Amnieh, S.K.; Mosaddegh, P.; Tehrani, A.F. Study on magnetic abrasive finishing of spiral grooves inside of aluminum cylinders. *Int. J. Adv. Manuf. Technol.* **2017**, *91*, 2885–2894. [CrossRef]
19. Mulik, R.S.; Pandey, P.M. Ultrasonic assisted magnetic abrasive finishing of hardened AISI 52100 steel using unbonded SiC abrasives. *Int. J. Refract. Met. Hard Mater.* **2011**, *29*, 68–77. [CrossRef]
20. Sihag, N.; Kala, P.; Pandey, P.M. Analysis of Surface Finish Improvement during Ultrasonic Assisted Magnetic Abrasive Finishing on Chemically treated Tungsten Substrate. *Procedia Manuf.* **2017**, *10*, 136–146. [CrossRef]
21. Singh, L.; Khangura, S.S.; Mishra, P. Performance of abrasives used in magnetically assisted finishing: A state of the art review. *Int. J. Abras. Technol.* **2010**, *3*, 215–227. [CrossRef]
22. Jiang, L.Z.; Zhang, G.X.; Du, J.J.; Zhu, P.X.; Cui, T.L.; Cui, Y.T. Processing performance of Al_2O_3/Fe-based composite spherical magnetic abrasive particles. *J. Magn. Magn. Mater.* **2021**, *528*, 167811. [CrossRef]
23. Hong, S.-W.; Yoon, J.-Y.; Kim, S.-H.; Lee, S.-K.; Kim, Y.-R.; Park, Y.-J.; Kim, G.-W.; Choi, S.-B. 3D-Printed Soft Structure of Polyurethane and Magnetorheological Fluid: A Proof-of-Concept Investigation of its Stiffness Tunability. *Micromachines* **2019**, *10*, 655. [CrossRef]
24. Yin, X.; Guo, S.; Song, Y. Magnetorheological Fluids Actuated Haptic-Based Teleoperated Catheter Operating System. *Micromachines* **2018**, *9*, 465. [CrossRef]
25. Jacobs, S.D.; Golini, D.; Hsu, Y.L.; Puchebner, B.E.; Strafford, D.; Prokhorov, I.V.; Fess, E.M.; Pietrowski, D.; Kordonski, W.I. Magnetorheological finishing: A deterministic process for optics manufacturing. In Proceedings of the International Conference on Optical Fabrication and Testing, Tokyo, Japan, 5–7 June 1995; SPIE: Bellingham, WA, USA, 1995.
26. Harris, D.C. History of magnetorheological finishing. In Proceedings of the Window and Dome Technologies and Materials XII, Orlando, FL, USA, 25–29 April 2011; Volume 8016.
27. Kordonski, W.; Shorey, A.B.; Sekeres, A. New magnetically assisted finishing method: Material removal with magnetorheological fluid jet. In Proceedings of the International Conference on Optical Manufacturing and Testing V, San Diego, CA, USA, 22 December 2003.
28. Pattanaik, L.N.; Agarwal, H. Magnetorheological Finishing (MRF) of a Freeform Non-magnetic Work Material. *J. Manuf. Sci. Prod.* **2015**, *15*, 249–256. [CrossRef]
29. Kumar, S.; Jain, V.K.; Sidpara, A. Nanofinishing of freeform surfaces (knee joint implant) by rotational-magnetorheological abrasive flow finishing (R-MRAFF) process. *Precis. Eng.* **2015**, *42*, 165–178. [CrossRef]
30. Saraswathamma, K.; Jha, S.; Rao, P. Experimental investigation into Ball end Magnetorheological Finishing of silicon. *Precis. Eng.* **2015**, *42*, 218–223. [CrossRef]
31. Kansal, H.; Singh, A.K.; Grover, V. Magnetorheological nano-finishing of diamagnetic material using permanent magnets tool. *Precis. Eng.* **2018**, *51*, 30–39. [CrossRef]
32. Anwesa, B.; Manas, D. Design and fabrication of a novel polishing tool for finishing freeform surfaces in magnetic field assisted finishing (MFAF) process. *Precis. Eng.* **2017**, *49*, 61–68.

33. Song, W.; Peng, Z.; Li, P.; Shi, P.; Choi, S.-B. Annular Surface Micromachining of Titanium Tubes Using a Magnetorheological Polishing Technique. *Micromachines* **2020**, *11*, 314. [CrossRef]
34. Wang, R.; Xiu, S.; Sun, C.; Li, S.; Kong, X. Study on Material Removal Model by Reciprocating Magnetorheological Polishing. *Micromachines* **2021**, *12*, 413. [CrossRef]
35. Xiao, X.-L.; Li, G.-X.; Mei, H.-J.; Yan, Q.-S.; Lin, H.-T.; Zhang, F.-L. Polishing of Silicon Nitride Ceramic Balls by Clustered Magnetorheological Finish. *Micromachines* **2020**, *11*, 304. [CrossRef]
36. Guo, J.; Wang, H.; Goh, M.H.; Liu, K. Investigation on Surface Integrity of Rapidly Solidified Aluminum RSA 905 by Magnetic Field-Assisted Finishing. *Micromachines* **2018**, *9*, 146. [CrossRef] [PubMed]
37. Wang, C.; Cheung, C.F.; Ho, L.T.; Yung, K.L.; Kong, L. A novel magnetic field-assisted mass polishing of freeform surfaces. *J. Mater. Process. Technol.* **2020**, *279*, 116552. [CrossRef]
38. Wang, C.; Loh, Y.M.; Cheung, C.F.; Wang, S.; Ho, L.T.; Li, Z. Shape-adaptive magnetic field-assisted batch polishing of three-dimensional surfaces. *Precis. Eng.* **2022**, *76*, 261–283. [CrossRef]
39. Wang, C.; Loh, Y.M.; Cheung, C.F.; Wang, S.; Chen, K.; Ho, L.T.; Cheng, E. Magnetic field-assisted batch superfinishing on thin-walled components. *Int. J. Mech. Sci.* **2022**, *223*, 107279. [CrossRef]
40. Shinmura, T. Study on Free Form Surface Finishing by Magnetic Abrasive Finishing Process: 1st Report, Fundamental Experiments. *Trans. Jpn. Soc. Mech. Eng. Ser. C* **1987**, *53*, 202–208. [CrossRef]
41. Shinmura, T.; Takazawa, K.; Hatano, E.; Matsunaga, M.; Matsuo, T. Study on magnetic abrasive finishing. *CIRP Ann. Manuf. Technol.* **1990**, *39*, 325–328. [CrossRef]
42. Fox, M.; Agrawal, K.; Shinmura, T.; Komanduri, R. Magnetic Abrasive Finishing of Rollers. *CIRP Ann.* **1994**, *43*, 181–184. [CrossRef]
43. Shukla, V.C.; Pandey, P.M. Experimental investigations into sintering of magnetic abrasive powder for ultrasonic assisted magnetic abrasive finishing process. *Mater. Manuf. Process.* **2016**, *32*, 108–114. [CrossRef]

micromachines

MDPI

Article

Study on Wavelet Packet Energy Characteristics on Friction Signal of Lapping with the Fixed Abrasive Pad

Zhankui Wang [1,2,*], Zhao Zhang [1], Shiwei Wang [1], Minghua Pang [1], Lijie Ma [1] and Jianxiu Su [1]

[1] Postdoctoral Research Base, Henan Institute of Science and Technology, Xinxiang 453003, China; zhangzhao_zz0309@126.com (Z.Z.); wangshiwei_1208@163.com (S.W.); pangminghua909@163.com (M.P.); mlj001@163.com (L.M.); dlutsu2004@126.com (J.S.)
[2] Postdoctoral Station, Henan University of Science and Technology, Luoyang 471000, China
* Correspondence: luckywzk@126.com

Abstract: The surface condition of the fixed abrasive pad (FAP) has a significant impact on its machining performance, workpiece material removal rate (MRR), and surface roughness. To clarify the wavelet packet energy characteristics of friction signal under different surface conditions of FAP and its mapping relationship with MRR and workpiece surface quality, FAP samples in different processing stages were obtained through a consolidated abrasive grinding quartz glass experiment. Then, the friction signals in different stages were received by the friction and wear experiment between the FAP and quartz glass workpiece, and the wavelet packet analysis was carried out. The experimental results show that with the increase of lapping time, the surface wear degree of the FAP increased gradually, and the MRR of the workpiece, the surface roughness of the FAP, and the surface roughness of the workpiece decreased slowly. In the wavelet packet energy of friction signal during machining, the energy proportion of frequency band 7 showed an upward trend with the increase of lapping time. The energy proportion of frequency band 8 showed a downward trend with the increase of lapping time. The change characteristics of the two are significantly correlated with the surface condition of the FAP.

Keywords: fixed abrasive pad; friction and wear; quartz glass; material removal rate; surface quality; wavelet packet energy coefficient

Citation: Wang, Z.; Zhang, Z.; Wang, S.; Pang, M.; Ma, L.; Su, J. Study on Wavelet Packet Energy Characteristics on Friction Signal of Lapping with the Fixed Abrasive Pad. *Micromachines* **2022**, *13*, 981. https://doi.org/10.3390/mi13070981

Academic Editors: Chengwei Kang, Chunjin Wang and Jiang Guo

Received: 20 May 2022
Accepted: 20 June 2022
Published: 21 June 2022

1. Introduction

With the development of science and technology, people put forward higher requirements for the quality control and machining efficiency of ultra-precision machining technology [1]. The traditional free abrasive machining technology has the following disadvantages: uncontrolled abrasive trajectory, low abrasive utilization, high production cost, environmental pollution, and so on [2–5]. To overcome the shortcomings of free abrasive, the 3M company first proposed the consolidated abrasive polishing technology, which consolidates the abrasive on the cushion substrate and transforms the three-body removal of workpiece material into two-body removal, which is easier to control [6,7].

In consolidated abrasive polishing, the surface material of the workpiece is mainly removed by mechanical and chemical actions such as friction and extrusion between abrasive particles and the workpiece. The friction signal between its interface reflects the real-time tribological characteristics of the polishing pad surface [8], and it is a non-stationary signal, which is difficult to be analyzed by traditional Fourier transform. Therefore, when analyzing the friction signal, it is necessary to use the analysis methods of non-stationary signal, such as wavelet transform, short-time Fourier transform, Hilbert Huang transform, etc. [9–11]. At present, many scholars have studied the analysis of non-stationary signals. Xiong et al. [12] proposed a novel bearing fault diagnosis method based on the Wavelet Packet Transform (WPT) and a lightweight variant of Deep Residual Networks (DRN). The accuracy of fault identification is high, which has great potential in the practical application

of industrial fault diagnosis. Habbouche et al. [13] proposed a new data-driven approach for bearing prognostics based on the decomposition of wavelet packets and bidirectional long short-term memory for preprocessing and tracking degradation. Han et al. [14] proposed the modal parameter identification method and damage diagnosis method based on Hilbert Huang Transform (HHT) to monitor the bridge structure. Lan et al. [15] used short-time Fourier transform to analyze the vibration signal and explored structural vibration's time-varying characteristics and modal frequency characteristics. Xu et al. [16] proposed a rolling bearing fault detection method based on Translation-Invariant Denoising (TID) and HHT, which can effectively extract the fault features of bearings. Li et al. [17] realized the feature extraction of weak friction vibration signal through harmonic wavelet packet transform. J. Rabi et al. [18] proposed a method based on wavelet transform and empirical mode decomposition to analyze the defect vibration signal of friction stir welding tunnel. Yao et al. [19] proposed a rolling bearing fault diagnosis method based on wavelet packet analysis and a limit learning machine, which can accurately diagnose the bearing fault category.

To sum up, there have been many research reports on the analysis and processing of non-stationary signals, but how to analyze the friction in the process of lapping and find the characteristics of friction signal reflecting the surface condition of the FAP has not been studied. Therefore, this paper proposes to use the wavelet packet analysis method to analyze the mechanical friction signal in the processing of the FAP by comparing the proportion of wavelet packet energy in each frequency band of friction force signal under different FAP surface conditions to obtain the friction signal characteristics reflecting the surface condition of the FAP.

2. Basic Principles

Wavelet packet analysis is a new method based on wavelet analysis [20] which can decompose the high-frequency and low-frequency parts of the signal more finely and conduct a more comprehensive signal analysis [21]. Each wavelet packet decomposition will obtain two sub-bands of low frequency and high frequency. The three-layer wavelet packet decomposition is shown in Figure 1. For the n-layer decomposed wavelet packet signal, 2n sub-bands are obtained. The decomposition calculation formula is as follows:

$$d_{i,j,2m} = \sum_k h(k-2i) d_{k,j+1,m} \tag{1}$$

$$d_{i,j,2m+1} = \sum_k \mathrm{g}(k-2i) d_{k,j+1,m}$$

The calculation formula of wavelet packet reconstruction is as follows:

$$d_{i,j+1,m} = \sum_k h(i-2k) d_{i,j,2m} + \sum_k \mathrm{g}(i-2k) d_{i,j,2m+1} \tag{2}$$

where, $d_{i,j,m}$ is the i-th wavelet packet coefficient of the m-th node of layer j; and $h(k)$ and $g(k)$ are low-pass and high pass filter coefficients, respectively.

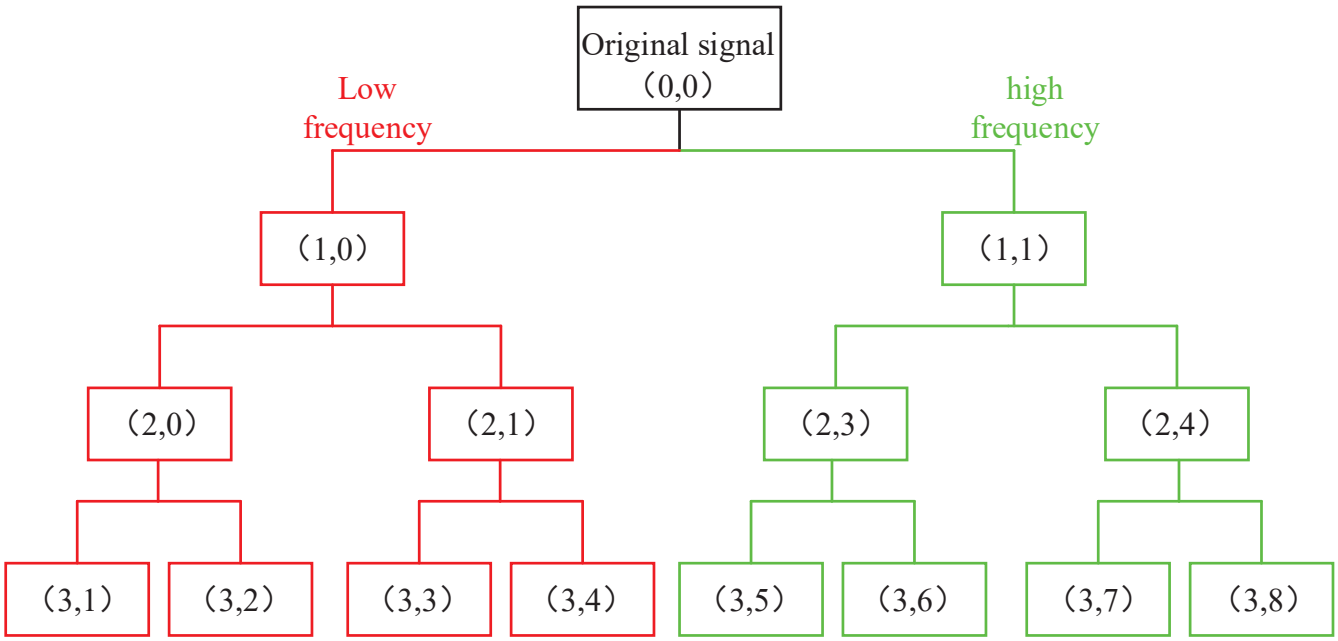

Figure 1. Decomposition diagram of three-layer wavelet packet.

The principle of wavelet packet energy is to solve the signal energy on different decomposition scales and arrange these energy values into eigenvectors according to the scale order for recognition [22,23]. Wavelet packet energy contains rich signal characteristics, and its wavelet packet decomposition result is $d_{i,j}(k)$ energy E in different frequency bands $E_{i,j}$. The calculation formula is:

$$E_{i,j} = \sum_{k=1}^{N} \left| d_{i,j}(k) \right|^2, j = 0, 1, \cdots 2^i - 1 \tag{3}$$

where N is the original signal length. All $E_{i,j}$ constitute the wavelet packet energy spectrum. The proportion of wavelet packet energy $P_{i,j}$, the calculation formula is as follows:

$$P_{i,j} = \frac{E_{i,j}}{\sum_{j=0}^{2^i-1} E_{i,j}} \tag{4}$$

3. Experimental Part

3.1. Experimental Design

The test part mainly includes the lapping test and the wear test. The lapping test is carried out on the ZDHP-30B ultra precision plane polishing machine. The lapping pad is W7 fixed abrasive pad, and the lapping workpiece is a quartz glass wafer with a diameter of 50 mm and a thickness of 3 mm. Its initial surface roughness is 60–70 nm. The total lapping time is 180 min. Every 30 min in the lapping process is a stage. After each stage, the quality difference of the workpiece is measured to calculate the MRR of the processing stage. The processing performance of the FAP is characterized by the material removal rate. FAP samples are obtained from the surface of the polishing pad for standby to observe the surface wear condition of FAP samples. The FAP does not need to be dressed. The next stage of lapping quartz glass is carried out, and so on until the grinding time reaches 180 min. The lapping test processing equipment and processing principle are shown in Figure 2. Other process parameters are shown in Table 1. The wear test is performed after each stage of the lapping test. The wear test was carried out on a microcomputer controlled reciprocating friction and wear tester (MWF-500). Its working principle is that the spindle rotates to drive the slider crank mechanism to move, so as to realize reciprocating linear

motion. Paste the FAP samples of each processing stage obtained from the lapping test on the cylindrical workbench. The FAP samples lap the quartz glass in a straight-line reciprocating motion on the reciprocating friction and wear tester with a reciprocating distance of 6 mm. Thus, the friction signal generated in the process of FAP lapping quartz glass can be obtained. The test equipment and FAP sample diagram are shown in Figure 3: 150 r/min refers to the rotation speed of the spindle of MWF-500 in the wear test; the unit of the instrument is r/min; 100 rmp represents the rotation speed of the polishing disc of ZDHP-30B in the lapping test. The unit of the instrument is rpm. The effect of the two instruments is consistent at specific speeds. When the spindle speed of the wear test is 150 r/min, the effect is consistent with that of the polishing disc speed of 100 rmp in the lapping test. Other parameters are shown in Table 2. The experimental flow chart is shown in Figure 4.

Table 1. Process parameters of lapping experiment.

Parameter	Condition
Lapping fluid	Deionized water
Lapping pressure	26.7 kPa
Slurry flow rate	50 mL/min
Speed	100 rpm

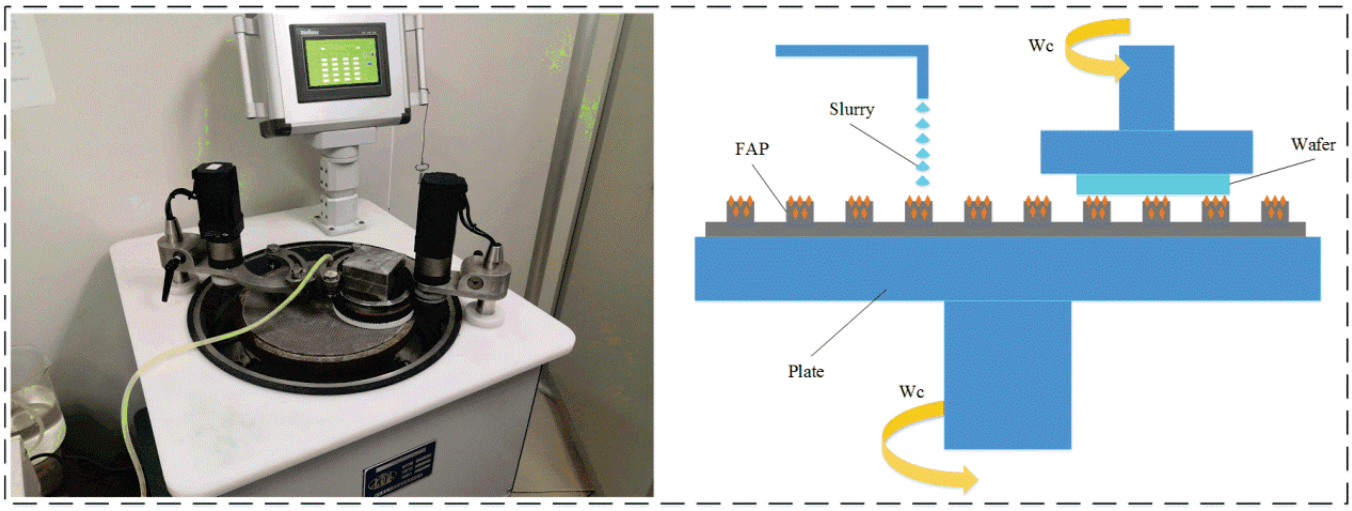

Figure 2. Ultra-precision plane lapping and polishing machine and its processing principle.

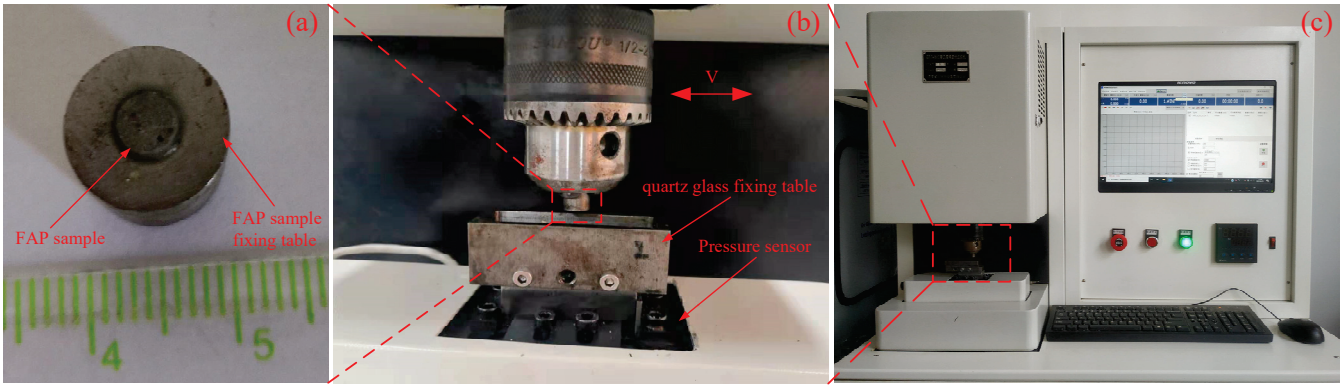

Figure 3. The experimental equipment and partial enlarged view. Note: (**a**) FAP sample; (**b**) local amplification; (**c**) experimental equipment.

Table 2. Wear test parameters.

Parameter	Condition
Spindle speed	150 r/min (100 rpm)
Pressure	26.7 kPa
Wear time	1 min

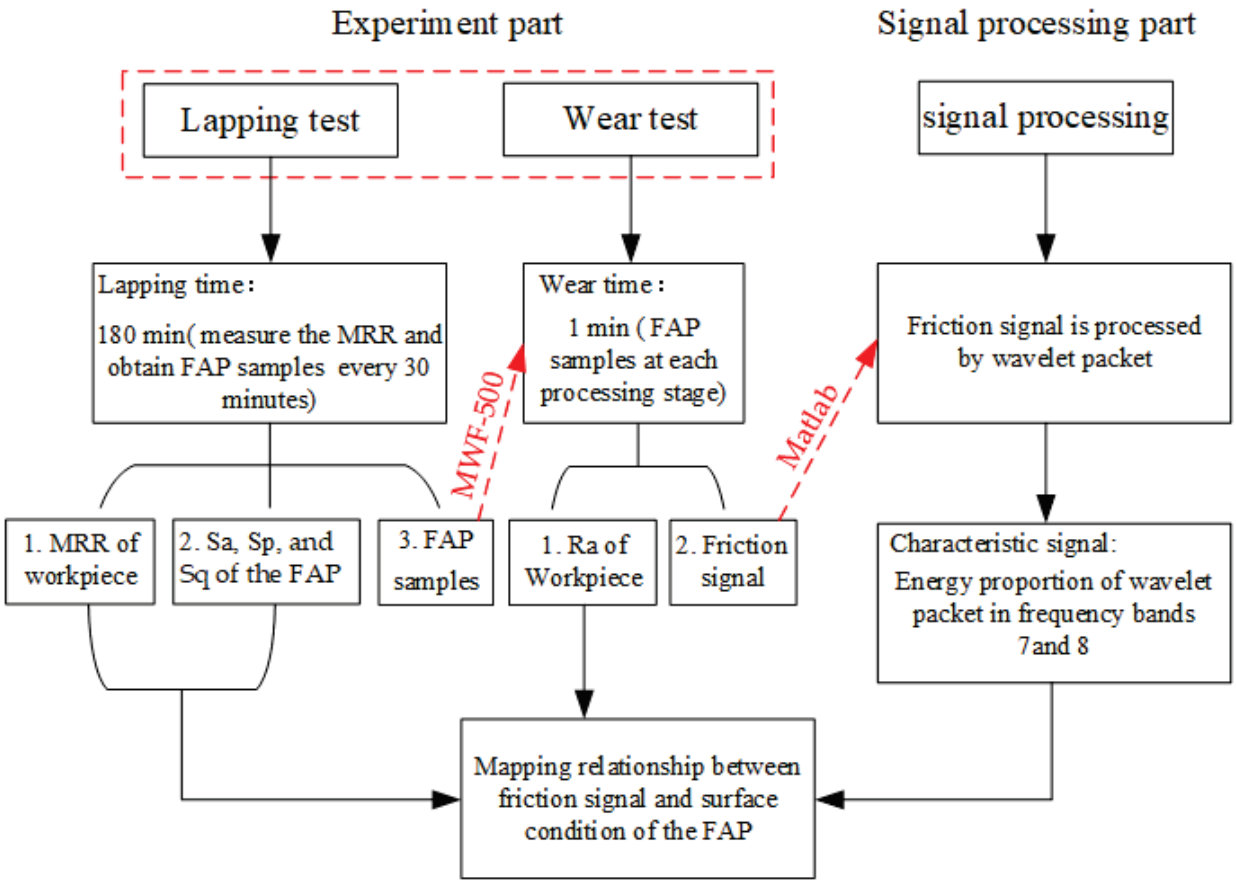

Figure 4. Flow chart for experiment.

3.2. Measurement and Characterization

3.2.1. Material Removal Rate

In each lapping experiment, SatoriousCP225D precision balance is used to weigh the mass of quartz glass samples before and after processing. The diameter of quartz glass is measured with a micrometer. Finally, the weight loss method calculates the MRR of the quartz glass in the lapping process.

$$\mathrm{MRR} = \frac{\Delta m}{\rho \times s \times t} \times 10^7 \quad (5)$$

where "MRR" is the material removal rate, nm/min; Δm is the poor quality of quartz glass before and after processing, g; ρ is the density of quartz glass, ρ = 2.2 g/cm^3; s is the workpiece area, cm^2; and t is the processing time, min.

3.2.2. Observation of Surface Roughness and Three-Dimensional Morphology

Before and after the lapping test, Contour GT-X3/X8 white light interferometer was used to measure the surface roughness Sa and three-dimensional surface morphology of the FAP. Before and after the wear test, Contour GT-X3/X8 white light interferometer was used to measure the surface roughness Sa of the workpiece. When the measuring point

was selected in the experiment, we chose 3 points on a straight line on the surface of the polished workpiece as measurement points, which can better reflect the surface roughness Sa and three-dimensional topography of the polished workpiece, and the average value was taken as the final measurement result.

4. Results and Discussion

4.1. Relationship between the MRR and Energy Proportion of Wavelet Packet

MATLAB software was used to process the friction signal, and the db2 wavelet function was selected; the length of the signal was N = 600, and the theoretical maximum number of decomposition layers was 4. After three-layer wavelet packet decomposition, 8 frequency bands from low to high were obtained to meet the subdivision of the signal and reduce the amount of calculation. Finally, three-layer wavelet packet decomposition was selected. When the decomposition scale was 3, the corresponding frequency bands of the 8 signal nodes are shown in Table 3. The distribution of energy in different frequency bands was calculated, and the proportion of wavelet packet energy in each processing stage was obtained, as shown in Figure 5. It can be seen from Figure 5 that the energy was mainly concentrated in frequency bands 7 and 8, and the energy of the low-frequency part accounted for a relatively low proportion. Therefore, the fault signal mainly existed in the high-frequency part. The relationship between the energy proportion in frequency bands 7 and 8 and the MRR was obtained by associating frequency band 7 and 8 with the MRR, as shown in Figure 6.

Table 3. The corresponding frequency bands of the 8 signal nodes.

Serial Number	1	2	3	4	5	6	7	8
Node	(3,1)	(3,2)	(3,3)	(3,4)	(3,5)	(3,6)	(3,7)	(3,8)
Frequency band (Hz)	0–0.625	0.625–1.25	1.25–1.875	1.875–2.5	2.5–3.125	3.125–3.75	3.75–4.375	4.375–5

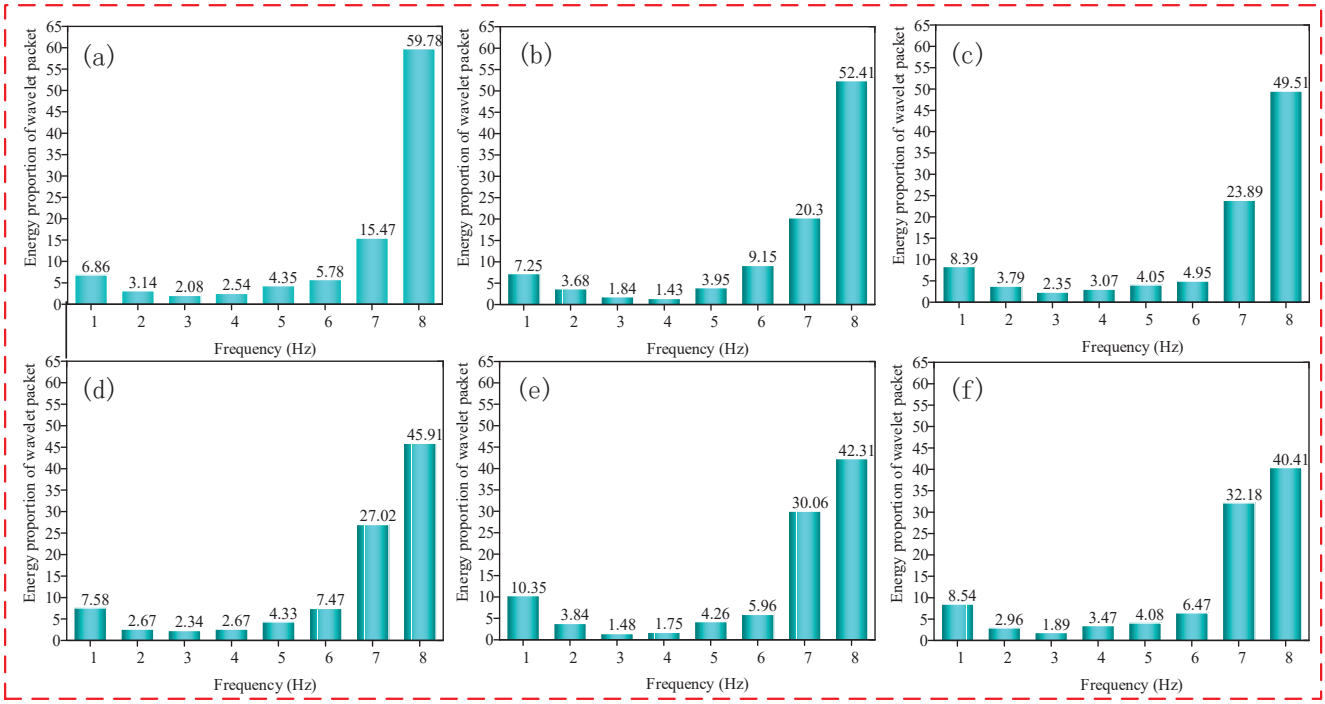

Figure 5. Proportion of wavelet packet energy in each processing stage of the FAP. Note: (**a**) Lapping time 0–30 min; (**b**) lapping time 30–60 min; (**c**) lapping time 60–90 min; (**d**) lapping time 90–120 min; (**e**) lapping time 120–150 min; (**f**) lapping time 150–180 min.

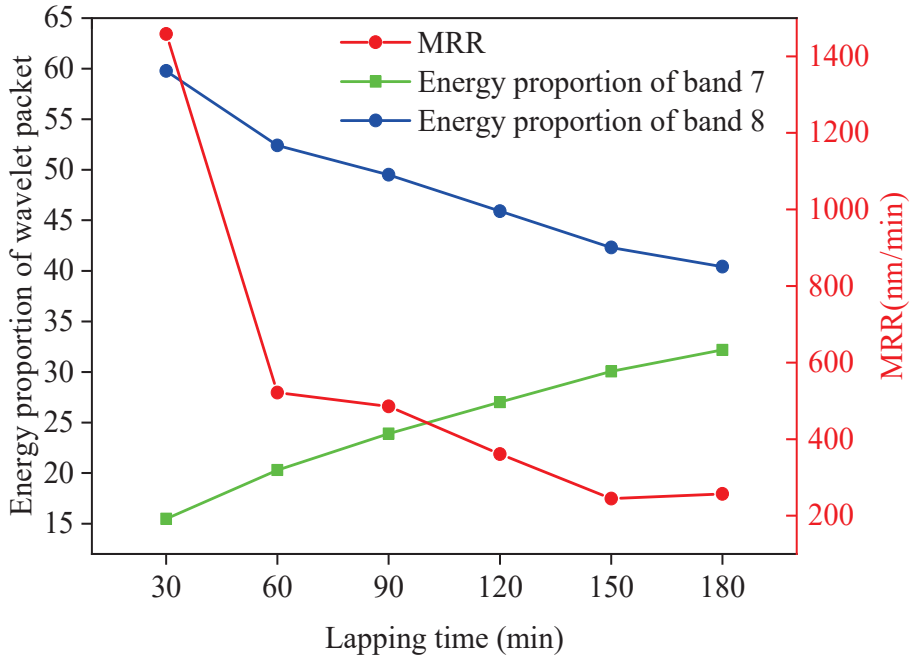

Figure 6. Relationship between the MRR and energy proportion of frequency bands 7 and 8.

4.2. Relationship between Surface Roughness of the FAP and Energy Proportion of Wavelet Packet

The surface roughness and three-dimensional surface parameters of the FAP after each processing were measured. It can be seen from the literature that the size of peak SP can characterize the protruding height of surface abrasive particles, and the size of arithmetic square root Sq can characterize the condition of surface texture [24]. The surface roughness and three-dimensional surface parameters of the FAP in each processing stage are shown in Table 4. The three-dimensional surface parameters Sp and Sq of FAP at each processing stage are shown in Figure 7. The relationship between the surface roughness of the FAP in each processing stage and the energy proportion of frequency bands 7 and 8 are as shown in Figure 8. The three-dimensional morphology of its surface is shown in Figure 9. It can be seen from Figure 7 that Sp and Sq gradually decreased with the increase of lapping time because the FAP surface abrasive particles were constantly worn during the lapping process, resulting in the continuous reduction of the abrasive particle height on the FAP surface. It can be seen from Figure 8 that the changing trend of energy proportion in frequency band 8 of wavelet packet was consistent with the changing trend of surface roughness of the FAP, which decreased with the increase of lapping time. The energy proportion in frequency band 7 of the wavelet packet was opposite to the changing trend of surface roughness of the FAP and increased with the increase of lapping time. This is because, at the initial stage of lapping, there were many exposed abrasive particles on the FAP surface, and the exposed height of abrasive particles is high. The edge tip of the abrasive particles was complete, the micro-cutting ability of the abrasive particles was strong, and the surface roughness was large. During the lapping process, a large number of abrasive particles scratched the surface of the workpiece. The energy of the wavelet packet in frequency band 8 was large, and that in the frequency band 7 was small. With the increase in lapping time, the abrasive particles on the surface of the FAP aggravated the wear and fall off. More and more matrix materials were exposed on the surface, and their SP and Sq decreased. FAP surface roughness was small, which affected the micro-cutting ability of the abrasive particles to a certain extent. A large number of substrates contacted and scratched the workpiece, which increased the energy of frequency band 7 and decreased the energy of frequency band 8 of the wavelet packet.

Table 4. Surface roughness and three-dimensional surface parameters of the FAP in each processing stage.

Lapping Time	Sa/nm	Sp/nm	Sq/nm
30 min	1294.08	7855.92	1713.72
60 min	966.01	6186.56	1372.41
90 min	940.32	5778.66	1343.55
120 min	873.51	5018.38	1251.19
150 min	830.26	4629.98	1190.13
180 min	782.09	3626.41	1100.47

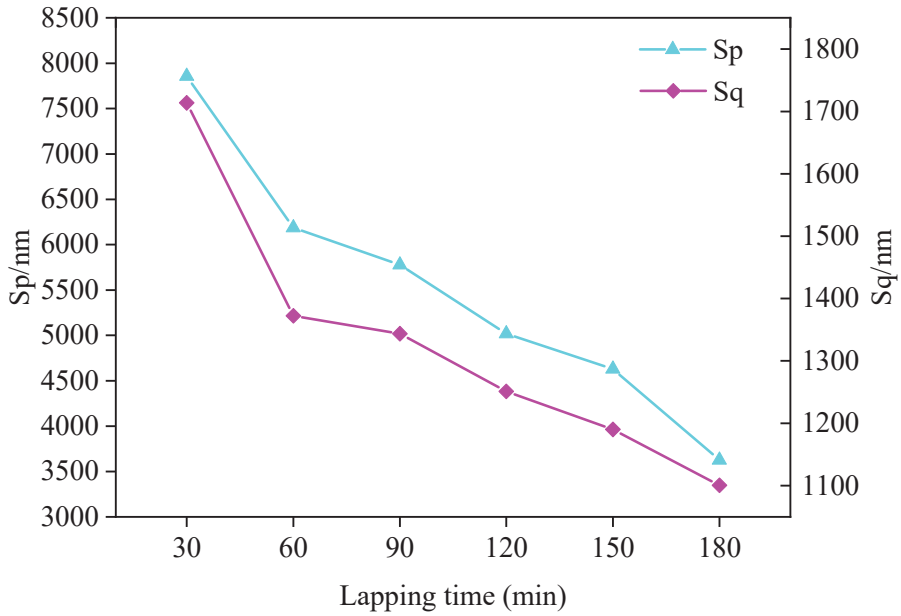

Figure 7. The three-dimensional surface parameters Sp and Sq of FAP at each processing stage.

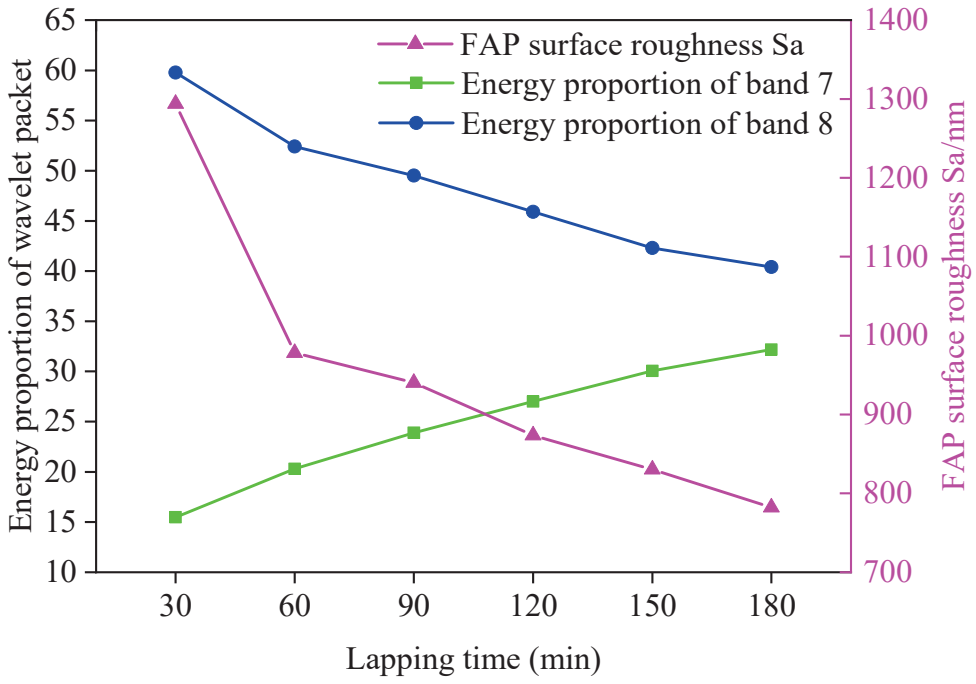

Figure 8. Relationship between surface roughness of the FAP and energy proportion of frequency bands 7 and 8.

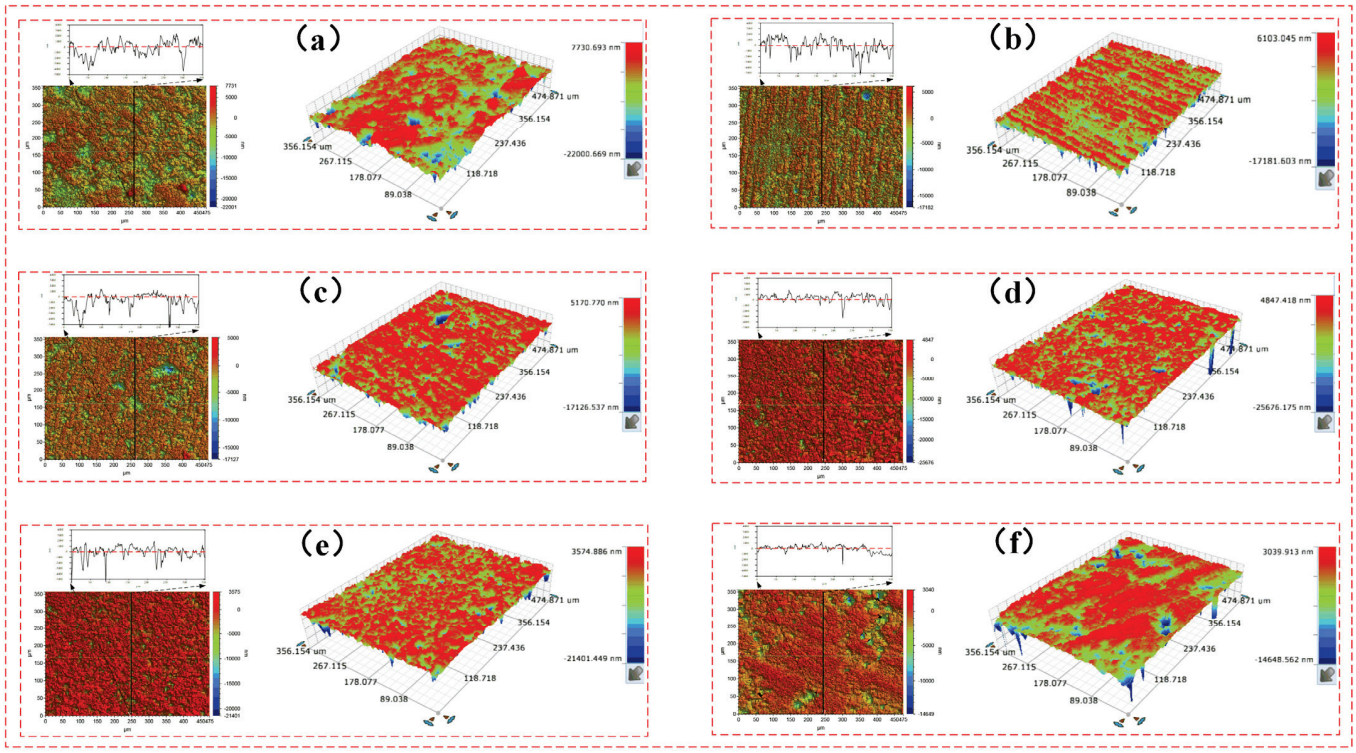

Figure 9. Three-dimensional surface morphology of the FAP in different processing stages. Note: (**a**) Lapping time 0–30 min; (**b**) lapping time 30–60 min; (**c**) lapping time 60–90 min; (**d**) lapping time 90–120 min; (**e**) lapping time 120–150 min; (**f**) lapping time 150–180 min.

4.3. Relationship between Surface Roughness of Workpiece after Wear and the Energy Proportion of Wavelet Packet

In order to observe the micro cutting performance of FAP surface abrasive particles and the surface roughness of workpiece at different machining stages more intuitively, the FAP samples were ground back and forth on a microcomputer controlled reciprocating friction and wear tester (MWF-500). The surface roughness and three-dimensional morphology of lapping quartz glass of FAP samples were measured at different processing stages after each wear test. The surface roughness of lapping quartz glass of FAP samples at each processing stage is shown in Table 5. The relationship between the surface roughness of quartz glass and the energy proportion of frequency bands 7 and 8 is shown in Figure 10. The three-dimensional morphology of quartz glass workpiece lapping by FAP samples at different processing stages is shown in Figure 11. It can be seen from Figure 10 that the changing trend of energy proportion in frequency band 8 of wavelet packet was consistent with the changing trend of surface roughness of quartz glass workpiece, which decreased with the increase of lapping time. The energy proportion of frequency band 7 was the opposite of the changing trend of the surface roughness of quartz glass workpiece and increased with the increase of lapping time. This is because many abrasive particles were exposed to the FAP surface at the initial stage of lapping, and the height was high. The abrasive particles scratched the workpiece surface during the lapping process and left large scratches. The workpiece surface roughness was large, and the abrasive particles had a strong micro-cutting performance. The energy proportion of frequency band 8 was large, and the energy proportion of frequency band 7 was small. The abrasive particles wore and fell off with the increased lapping time, and many matrices were exposed and scratched on the workpiece surface. The damage to the workpiece surface was small, the surface roughness was reduced, and the micro-cutting ability of abrasive particles was weakened. The energy proportion of frequency band 7 was large, and the energy proportion of frequency band 8 was small.

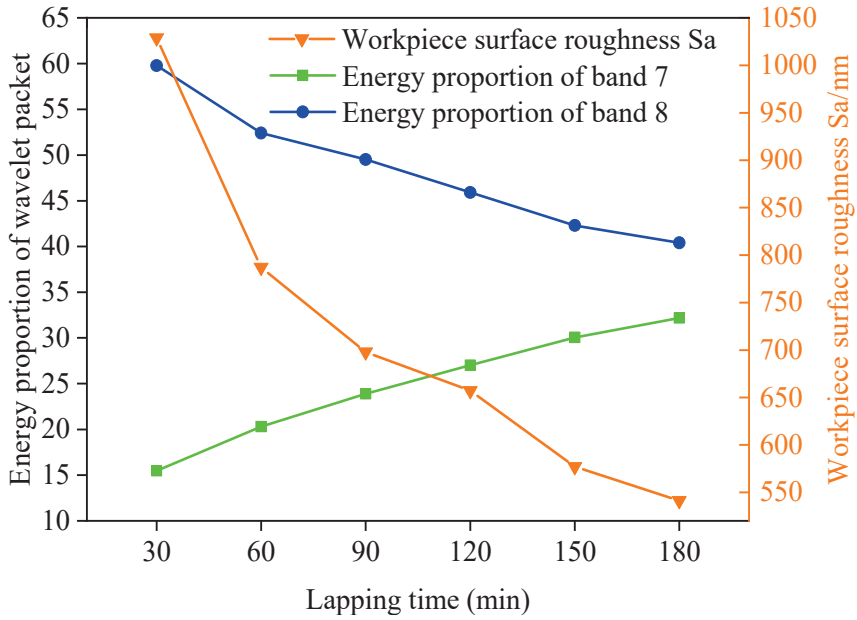

Figure 10. Relationship between workpiece surface roughness and energy proportion of frequency bands 7 and 8.

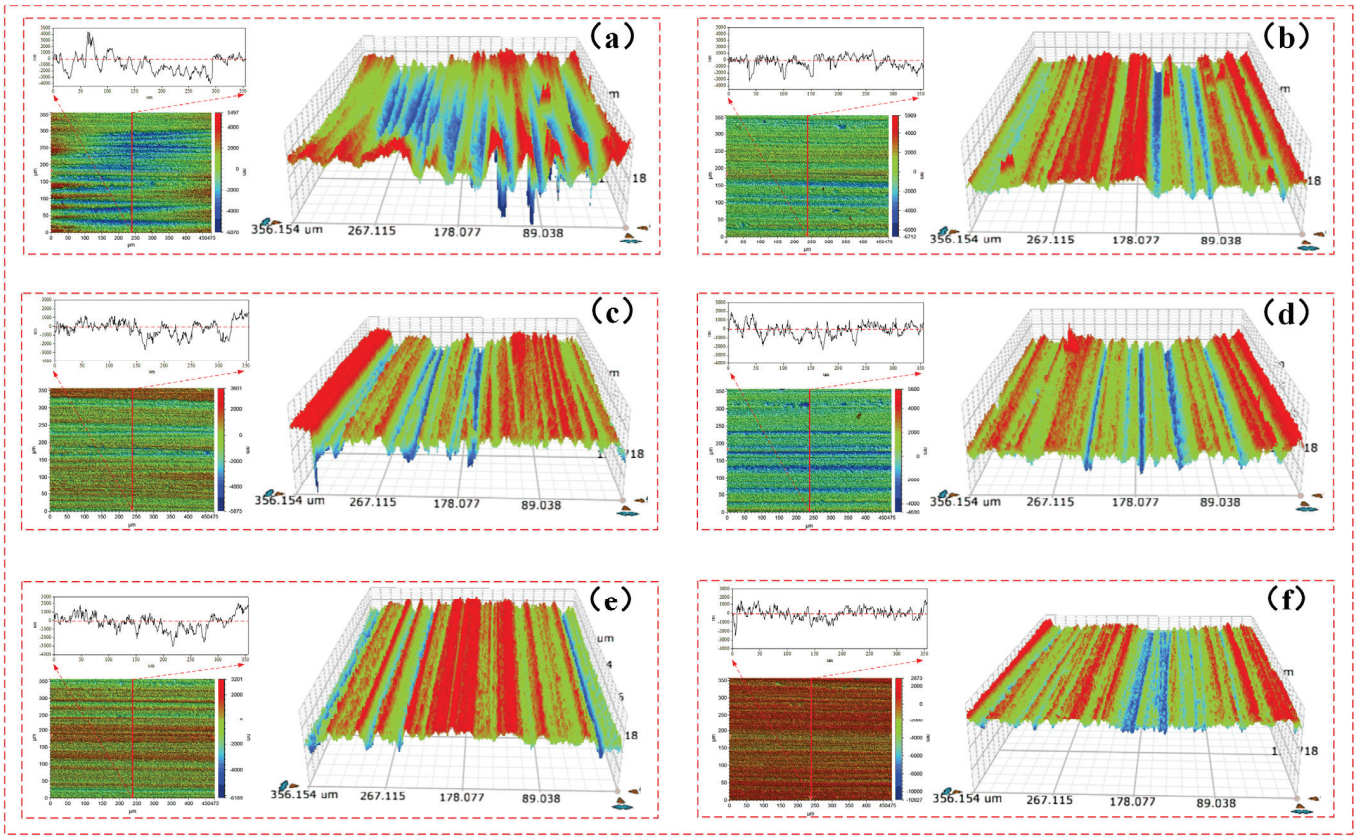

Figure 11. The three-dimensional morphology of quartz glass workpiece lapping by FAP samples at different processing stages. Note: (**a**) The FAP samples (0–30 min) lapping quartz glass workpiece; (**b**)the FAP samples (30–60 min) lapping quartz glass workpiece; (**c**) the FAP samples (60–90 min) lapping quartz glass workpiece; (**d**) the FAP samples (90–120 min) lapping quartz glass workpiece; (**e**) the FAP samples (120–150 min) lapping quartz glass workpiece; (**f**) the FAP samples (150–180 min) lapping quartz glass workpiece.

Table 5. The surface roughness of lapping quartz glass of FAP samples at each processing stage.

Lapping Time	Sa/nm
30 min	1028.838
60 min	787.058
90 min	697.936
120 min	657.071
150 min	577.03
180 min	541.184

4.4. Discussion

It can be seen from the above that the MRR of the workpiece was consistent with the change law of the surface roughness of the FAP and the surface roughness of the workpiece, which generally showed a downward trend with the increase of lapping time. The energy proportion in frequency bands 7 and 8 of the wavelet packet was relatively high. The energy proportion in the frequency band 7 increased with the increase of lapping time, and the energy proportion in the frequency band 8 decreased with the increase of lapping time.

The FAP was mainly composed of diamond abrasive particles and resin matrix. It can be seen that there are two reasons for the change of energy proportion in frequency bands 7 and 8. On the one hand, there were a large number of diamond abrasive particles on the surface of the FAP. The diamond abrasive particles achieved a certain MRR by scratching and ploughing the workpiece surface in the processing process. At the initial stage of lapping, the wear degree of the abrasive particles on the surface of the FAP was small, most of the abrasive particles retained the complete blade tip, the surface morphology was relatively convex, and the surface roughness was large, as shown in Figure 9a. Its processing performance was not greatly affected. The abrasive tip cut deep into the workpiece surface, scratched the plough workpiece's surface, and left deep scratches. There were many waste chips generated by scratching, and its MRR was large, as shown in Figure 12a. In machining, the scrap and abrasive particles contact together and scratch the workpiece surface, resulting in the change of wavelet packet energy. Therefore, the energy of frequency band 8 was the largest in the initial lapping stage. With the increase in lapping time, the abrasive particles on the surface of the FAP were constantly worn, part of the abrasive particles were forced to fall off from the surface of the FAP, and the edge tips of the other abrasive particles had a large area of edge collapse. The abrasive protrusion on the surface of the FAP decreased, the surface became relatively smooth, and the surface roughness decreased. The cutting performance of worn abrasive particles was greatly reduced. In machining, the depth of abrasive particles cutting into the surface of the workpiece became shallow, and the amount generated debris became smaller. The times of scraping the surface of the workpiece with debris and abrasive particles were reduced, and the energy proportion in frequency band 8 were reduced.

On the other hand, the FAP was mainly composed of a resin matrix, and the abrasive particles were fixed on the matrix. At the initial stage of lapping, the abrasive particles on the surface of the FAP were only slightly worn, and the abrasive particles were more prominent. The abrasive particles scratched the cutting workpiece to remove the material in the lapping process. Only a small part of the matrix with high protrusion contacted the workpiece surface. The energy change caused by this part of the matrix scratching the workpiece surface was small, so the energy proportion of frequency band 7 was small in the initial lapping stage. As the lapping continued, the abrasive particles on the surface of the FAP accelerated the wear, a large number of abrasive particles fell off or collapsed on the surface, the height of abrasive particles decreased, and more matrices were exposed and participated in scratching the workpiece surface, as shown in Figure 12e. The energy change caused by the matrix scratching the workpiece surface increased, and the energy proportion in the frequency band 7 increased. Due to the large difference in hardness between the matrix and diamond abrasive particles, the scratches left by the matrix scratching the workpiece surface were shallow and dense. The workpiece surface morphology was relatively smooth

and had small surface roughness, as shown in Figure 11f. This is consistent with the experimental results in Section 4.3.

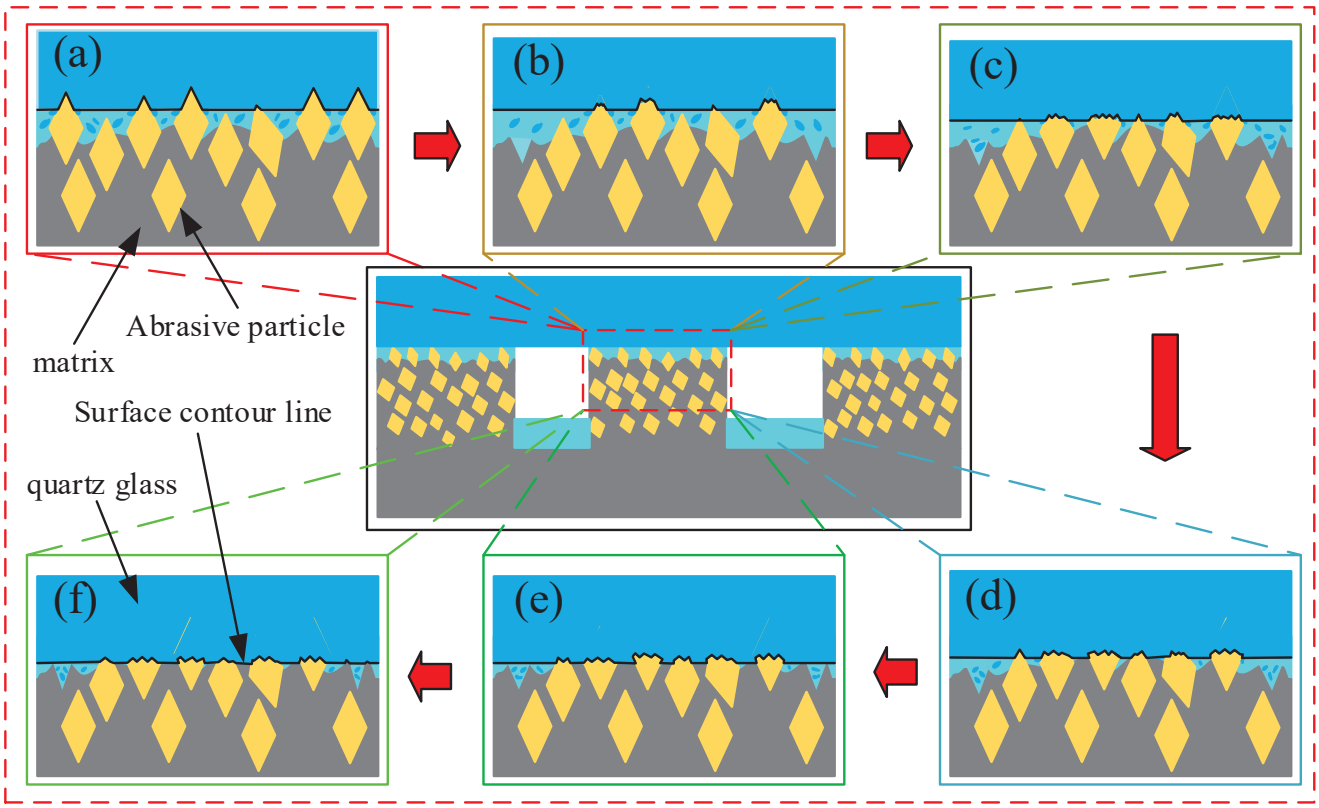

Figure 12. Machining wear principle of the FAP. Note: (**a**) Lapping time 0–30 min; (**b**) lapping time 30–60 min; (**c**) lapping time 60–90 min; (**d**) lapping time 90–120 min; (**e**) lapping time 120–150 min; (**f**) lapping time 150–180 min.

5. Conclusions

With the increase of lapping time, the MRR of the workpiece, the surface roughness of the FAP, and the surface roughness of the workpiece after wear were consistent, and all showed a downward trend with the increase of lapping time.

The wavelet packet energy was mainly concentrated in the high-frequency part of the lapping process. The energy proportion in the frequency band 7 increased with the increase of lapping time, and the energy proportion in the frequency band 8 decreased with the increase of lapping time.

The energy proportion of frequency band 7 was related to the surface of the workpiece scratched by the matrix. In contrast, the energy of frequency band 8 was connected to the scratched workpiece scratched by abrasive particles and debris. Therefore, the processing performance of FAP can be detected by the energy of frequency band 8, and the energy of frequency band 7 can detect the matrix exposure on the surface of FAP.

Author Contributions: Conceptualization, Z.W. and Z.Z.; methodology, Z.W.; software, Z.Z.; validation, Z.Z., S.W. and M.P.; formal analysis, Z.Z.; investigation, L.M.; resources, J.S.; data curation, Z.Z.; writing—original draft preparation, Z.Z.; writing—review and editing, Z.Z.; visualization, Z.W.; supervision, Z.W.; project administration, J.S.; funding acquisition, Z.W. All authors have read and agreed to the published version of the manuscript.

Funding: This research was funded by [The National Natural Science Foundation of China, Project funded by China Postdoctoral Science Foundation, Science and Technology Plan Projects of Henan province, Postdoctoral Research Project of Henan Province] grant number [U1804142, 2020M672220, 212102210062, 201903045], And The APC was funded by [The National Natural Science Foundation

of China, Project funded by China Postdoctoral Science Foundation, Science and Technology Plan Projects of Henan province, Postdoctoral Research Project of Henan Province].

Acknowledgments: This study was supported by the National Natural Science Foundation of China (U1804142), project funded by China Postdoctoral Science Foundation (2020M672220), Science and Technology Plan Projects of Henan province (212102210062), and Postdoctoral Research Project of Henan Province (201903045).

Conflicts of Interest: The authors declare that they have no known competing financial interests or personal relationships that could have appeared to influence the work reported in this paper.

References

1. Fang, T.; Chen, P.C.; Lee, M.H. A New Permanganate-Free Slurry for GaN-SiC CMP Applications. *Mater. Sci. Forum* **2020**, *1004*, 199–205.
2. Jiang, W.; Zhou, H.; Ji, J.; Ren, X.; Zhu, Z. Semi-Consolidated Grinding Process of Easily Cleaved Gallium Oxide Wafer. *Surf. Technol.* **2022**, *51*, 178–185.
3. Niu, F.; Wang, K.; Sun, T.; Zhou, P.; Hu, W.; Zhu, Y. Lapping performance of mixed-size agglomerated diamond abrasives in fixed abrasives pads. *Diam. Relat. Mater.* **2021**, *118*, 108499. [CrossRef]
4. Wang, J.B.; Zhu, Y.W.; Xie, C.X.; Xu, J.; Ju, Z.L. Role of slurry in single crystal sapphire lapping with fixed abrasive pad. *Opt. Precis. Eng.* **2014**, *22*, 3004–3011. [CrossRef]
5. Gagliardi, J.J.; Kim, D.; Sokol, J.J.; Zazzera, L.A.; Romero, V.D.; Atkinson, M.R.; Nabulsi, F.; Zhang, H. A case for 2-body material removal in prime LED sapphire substrate lapping and polishing. *J. Manuf. Process.* **2013**, *15*, 348–354. [CrossRef]
6. Wang, Z.; Yang, Y.; Pang, M.; Li, Y.; Ma, L.; Yao, J.; Zhu, Y.; Su, J. Response surface model of processing parameters for lapping quartz glass with a fixed abrasive pad. *Surf. Technol.* **2021**, *50*, 376–385.
7. Luo, X.; Yang, W.; Qian, Y. Fixed abrasive polishing: The effect of particle size on the workpiece roughness and sub-surface damage. *Int. J. Adv. Manuf. Technol.* **2021**, *115*, 3021–3035. [CrossRef]
8. Lin, Z.; Yan, Z.; Xiao, M.; Zhu, X.; Cheng, D. Analysis of reciprocating friction signal based on Hilbert-Huang Transform. *Lubr. Eng.* **2015**, *40*, 92–96.
9. Chen, Z.; Hu, Y.; Tian, S.; Lu, M.; Xu, L. Non-stationary signal combined analysis based fault diagnosis method. *J. Commun.* **2020**, *41*, 187–195.
10. Zhang, H.; Yin, Y.; Yin, K. Non-Stationary Signals Analysis and Processing Based on Wavelet Transform. *J. Nanjing Norm. Univ.* **2014**, *14*, 63–69.
11. Tang, F.; Liu, S. Research on fault feature extraction method of nonlinear non-stationary signal based on generalized local frequency. *J. Mech. Eng.* **2015**, *51*, 176.
12. Xiong, S.; Zhou, H.; He, S.; Zhang, L.; Shi, T. Fault diagnosis of a rolling bearing based on the wavelet packet transform and a deep residual network with lightweight multi-branch structure. *Meas. Sci. Technol.* **2021**, *32*, 085106. [CrossRef]
13. Habbouche, H.; Benkedjouh, T.; Zerhouni, N. Intelligent prognostics of bearings based on bidirectional long short-term memory and wavelet packet decomposition. *Int. J. Adv. Manuf. Technol.* **2021**, *114*, 145–157. [CrossRef]
14. Han, J.; Zheng, P.; Wang, H. Structural modal parameter identification and damage diagnosis based on Hilbert-Huang transform. *Earthq. Eng. Eng. Vib.* **2014**, *13*, 101–111. [CrossRef]
15. Lan, Z.; Zhao, Y.; Guo, J.; Zhou, Z.; Xing, J.; Bai, G.; Lu, H.; Li, H. The measurement and analysis of ice induced vibration of JZ9-3WHPB oil platform in Bohai Sea. *Strateg. Study CAE* **2011**, *13*, 79–87.
16. Liu, Q.; Cao, X.; Xu, S. Research on fault diagnosis of rolling bearings based on wavelet packet transform and ELM. *J. Saf. Environ.* **2021**, *21*, 2466–2472.
17. Xu, L. Study on Fault Detection of Rolling Element Bearing Based on Translation-Invariant Denoising and Hilbert-Huang Transform. *J. Comput.* **2012**, *7*, 1155–1162. [CrossRef]
18. Li, G.B.; Ren, Z.Y.; Wang, H.Z.; Wei, H.J. Characteristics Extraction of Friction Vibration Signal Using Harmonic Wavelet Packet Transforms. *J. Saf. Environ.* **2011**, *31*, 452–456.
19. Rabi, J.; Balusamy, T.; Jawahar, R.R. Analysis of vibration signal responses on pre induced tunnel defects in friction stir welding using wavelet transform and empirical mode decomposition. *Def. Technol.* **2019**, *15*, 885–896. [CrossRef]
20. Guo, J.; Hang, D.; Zhu, X. Prediction of Crack Propagation in U-Rib Components Based on the Markov Chain. *J. Bridge Eng.* **2020**, *25*, 04020089. [CrossRef]
21. Yang, Y.; Fu, P. Rolling-Element Bearing Fault Data Automatic Clustering Based on Wavelet and Deep Neural Network. *Shock Vib.* **2018**, *2018*, 3047830. [CrossRef]
22. Guo, J.; Zhong, H. Vibration Analysis and Wavelet Packet Energy Ratio of Stay Cable Based on Measured Date. *Bridge Constr.* **2021**, *51*, 25–31.
23. He, C.; Wu, T.; Gu, R.; Qu, H. Bearing fault diagnosis based on wavelet packet energy spectrum and SVM. *J. Phys. Conf. Ser.* **2020**, *1684*, 012135. [CrossRef]
24. Zhang, Z.; Yao, P.; Zhang, Z.; Xue, D.; Wang, C.; Huang, C.; Zhu, H. A novel technique for dressing metal-bonded diamond grinding wheel with abrasive wateret and touch truing. *Int. J. Adv. Manuf.* **2017**, *93*, 3063–3073. [CrossRef]

micromachines

MDPI

Article

Efficient Water-Assisted Glass Cutting with 355 nm Picosecond Laser Pulses

Edgaras Markauskas *, Laimis Zubauskas, Bogdan Voisiat and Paulius Gečys

Center for Physical Sciences and Technology, Savanoriu Ave. 231, LT-02300 Vilnius, Lithuania; laimis.zubauskas@ftmc.lt (L.Z.); bogdan.voisiat@ftmc.lt (B.V.); paulius.gecys@ftmc.lt (P.G.)
* Correspondence: edgaras.markauskas@ftmc.lt; Tel.: +370-5-264-4868; Fax: +370-5-260-231

Abstract: In this study, the cutting of borosilicate glass plates in ambient air and water with a 355 nm wavelength picosecond laser was carried out. Low (2.1–2.75 W) and high (15.5 W) average laser power cutting regimes were studied. Thorough attention was paid to the effect of the hatch distance on the cutting quality and characteristic strength of glass strips cut in both environments. At optimal cutting parameters, ablation efficiency and cutting rates were the highest but cut sidewalls were covered with periodically recurring ridges. Transition to smaller hatch values improved the cut sidewall quality by suppressing the ridge formation, but negatively affected the ablation efficiency and overall strength of glass strips. Glass strips cut in water in the low-laser-power regime had the highest characteristic strength of 117.6 and 107.3 MPa for the front and back sides, respectively. Cutting in a high-laser-power regime was only carried out in water. At 15.5 W, the ablation efficiency and effective cutting speed per incident laser power increased by 16% and 22%, respectively, compared with cutting in water in a low-laser-power regime.

Keywords: picosecond laser; glass cutting; characteristic strength; surface roughness; hatch

Citation: Markauskas, E.; Zubauskas, L.; Voisiat, B.; Gečys, P. Efficient Water-Assisted Glass Cutting with 355 nm Picosecond Laser Pulses. *Micromachines* **2022**, *13*, 785. https://doi.org/10.3390/mi13050785

Academic Editor: Xichun Luo

Received: 11 April 2022
Accepted: 12 May 2022
Published: 18 May 2022

1. Introduction

Glass is one of the most widely adopted engineering materials, preferred for its mechanical strength, chemical inertness, high thermal stability, and electrical resistance [1,2]. It is widely used in multiple areas, ranging from mass consumer electronics to specific applications, such as microfluidics, photonics, or microelectromechanical systems (MEMSs) [2–4].

Among different glass fabrication methods, glass cutting remains one of the most common and fundamental operations [5,6]. Mechanical glass cutting is typically performed by scoring and breaking, which produces large micro-cracks and splinters [5]. As a result, defects inflicted during cutting reduce the strength of the glass element [7], which ultimately could lead to glass shattering.

Nevertheless, the requirements for faster processing, higher precision, excellent surface finish, and tighter-than-ever tolerances are constantly increasing. For this reason, one of the most promising and versatile techniques for the drilling, milling, and cutting of fine features in the glass is direct laser ablation. Direct laser ablation enables the possibility of seamlessly switching between the machining of different types of features in glasses, unlike well-established mechanical methods. Furthermore, the laser beam can be sharply focused, allowing the production of micrometre-sized features with very high accuracy. Additionally, the laser process is flexible, highly repeatable, and easily automated [8,9]. The technology allows the cutting of features with a complex shape, consisting of inner and outer contours [10]. Opaque and highly absorptive glasses can be processed, unlike other common laser-based techniques, such as rear side ablation [11] and the internal scribing approach [9,12].

The transition from continuous-wave and short (nanosecond) pulses to ultrashort lasers reduces thermal damage in glasses [13]. Furthermore, the dominant mechanism

causing ablation shifts from avalanche ionisation to multiphoton ionisation for pulses shorter than 50 ps [14]. This improves the localisation of absorbed laser energy and reduces thermal damage. The avoidance of such defects is crucial for cutting and scribing applications because they determine the strength of the machined element [7,15]. Therefore, laser ablation with ultrashort pulses has become an attractive method for the precise machining of thin glasses (<1 mm) [15].

The average laser power of modern ultrashort lasers is constantly growing, allowing one to achieve higher-than-ever processing speeds. Thus, with decent (industrially accessible) laser focusing, such systems can easily surpass optimal laser fluence levels for most engineering materials. In order to utilise full laser potential at optimal material processing conditions, one must either increase the laser beam spot size at the expense of machining accuracy or increase the laser pulse repetition rate to maintain optimal fluence levels. Unfortunately, excessive heat would accumulate in either case and ultimately lead to fractures and destruction of the brittle material even for ultrashort pulses [16,17].

Fortunately, excessive heat which is generated during the laser processing can effectively be taken away by introducing liquid into the laser ablation zone [16,18–21]. As a result, brittle material can withstand higher thermal loads, and higher laser power can be irradiated into the workpiece, increasing the process throughput. Additionally, multiple studies have reported the improved extraction of ablation products, reduced plasma shielding, and the generation of high-pressure mechanical shockwaves, which further contributed to material removing rates [22,23]. Additionally, improved machining quality was also observed: reduced heat-affected zones (HAZs), micro-cracks, and the re-deposition and recast of ablative debris [21,24–27].

Water is most commonly used as a laser ablation assisting liquid since it is cheap, harmless, and recyclable [20,28]. Water can be introduced into the ablation zone in multiple ways: by submerging the workpiece into standing [22,26,29,30] or flowing water [20,21,31,32]; by guiding a laser beam in the water jet [33,34]; or by spraying water mist [18] or a water jet [19,28] next to the laser beam. Most studies have investigated laser ablation with workpieces submerged into a standing or low-velocity liquid flow with a liquid layer thickness of a few to tens of millimetres. The key limitations of such a design were noted in [20,28,35]: laser heating formed bubbles around the ablation zone, generating waves at the surface of the liquid. Consequently, waves caused instability in laser processing conditions—variations in laser focus position, beam diffraction, and refraction angles; as a result, hampering the continuity and uniformity of ablated grooves [35]. Furthermore, Tangwarodomnukun et al. [35] reported a substantial 6.5% loss of laser power in a 2 mm thick water layer for 1080 nm wavelength radiation, whereas Kruusing et al. [36] observed the laser (heating) power loss due to the water cooling.

Fortunately, air–water interface instability and laser absorption in the water layer can be addressed by employing a thin and flowing water film [16,18]. This can be achieved by spraying a water mist into the ablation zone instead of submerging the workpiece into the liquid. Transitioning to shorter laser wavelengths can further reduce laser radiation absorption in the water layer. For example, absorption of the 355 nm wavelength radiation is about 300 times lower than the absorption of the widely used 1064 nm wavelength [36]. The highest absorption length in water is reportedly in the range of 400–600 nm, with the peak value at 500 nm [36]. However, transitioning to UV wavelengths can improve laser energy coupling in glasses [14] and localise laser-induced damage into a smaller area [13]. For 355 nm, higher ablation efficiency and lower ablation thresholds compared with 532 and 1064 nm wavelengths were reported in [14]. As a result, glass chipping and microcrack formation can be further reduced, improving cut edge strength and making glass more resistant to tensile stresses.

In our previous study, we demonstrated the efficient milling and cutting of borosilicate glasses using a picosecond laser working at a 1064 nm wavelength in a water-assisted environment [16]. Water introduction into the ablation zone significantly improved effective

glass cutting speeds and the morphology of the cut wall compared with glass ablation in ambient air.

As stated above, the transition to a shorter wavelength could further improve the cut quality due to better laser energy coupling, improving the strength of the laser-cut glass elements. To the best of our knowledge, no research involving efficient borosilicate glass cutting with UV picosecond pulses in a water-assisted environment has been conducted thus far. Additionally, we investigated the impact of the hatch distance on the cut wall quality and the characteristic strength of laser-cut glasses when the cut line consisted of multiple lines scanned in parallel.

Here, we experimentally studied the cutting of 0.4 mm thick borosilicate glass plates with a picosecond laser working at 355 nm radiation wavelength. Glass ablation was carried out in ambient air and water using optimised laser processing parameters for efficient glass ablation. The glass shattered at elevated laser powers (above 4 W) in ambient air; therefore, low (2.1–2.75 W) and high (15.5 W) average laser power cutting regimes were investigated separately. The cutting quality was evaluated using an optical microscope and a profiler. Four-point bending tests were conducted to determine the bending strength of laser-cut glass strips.

2. Materials and Methods

Glass cutting experiments were performed using a picosecond laser: Atlantic from Ekspla. The emission wavelength was 355 nm, the pulse width was 10 $\pm$ 3 ps, and the maximum average laser power at the sample's surface was 15.5 W. The laser pulse repetition rate was adjustable between 0.4 and 1 MHz. The emitted light intensity profile was similar to Gaussian and had linear polarisation. Cutting experiments were carried out using P polarisation only (the polarisation vector was perpendicular to the laser beam scanning direction).

The optical setup consisted of a laser, a beam expander, mirrors to direct the laser beam to the scanning system, and a focusing lens. The laser beam movement was controlled with a galvanometer scanner: IntelliSCAN$_{de}$14 from ScanLab. For focusing, we used an f-theta lens with a focal distance of 100 mm. Laser beam spot sizes were measured using Liu's method [37]. At the focal position, the minimal diffraction-limited spot size (diameter) was 15 μm with a beam expander installed in the laser beam path and 30 μm without the expander. The laser fluence F (values reported further in the text) was evaluated using the expression $F = 2E/(\pi r^2)$, where E is the laser pulse energy and r is the radius of the focused laser beam. The focal plane was set on top of the glass sample for the laser fluence and spot size measurements. For glass cutting experiments, the laser beam focal point was shifted 200 μm below the surface of the glass sample.

In this study, we used borosilicate glass plates (D263m) with a thickness of 400 μm. The length and the width of the glass plates were 26 mm and 20 mm, respectively. Glass plates were cleaned before the laser cutting with high-purity acetone. Cutting quality was analysed with an optical microscope: Eclipse LV100NDA from Nikon. The cut sidewall topographies were recorded with the S neox optical profiler from Sensofar.

Morphology and topography analyses were followed by glass cleaving experiments to determine the characteristic strength of laser-cut samples. For this, glass plates were cut into rectangular 26 $\times$ 6 mm^2 glass strips. The bending force was measured with an Alluris FMI-S30A5 dynamometer.

The laser scanning geometry used for cutting the borosilicate glass is presented in Figure 1. Multiple lines were scanned in parallel, separated by the hatch (the distance between two scanned lines). The number of lines in a single scan defined the cut's width. After each scan, the hatch direction was changed to the opposite. In the case of an odd scan, the scanning started at position A and ended at position B. An even scan started where the odd scan had ended (position B) and returned to position A by following the same scan path backwards.

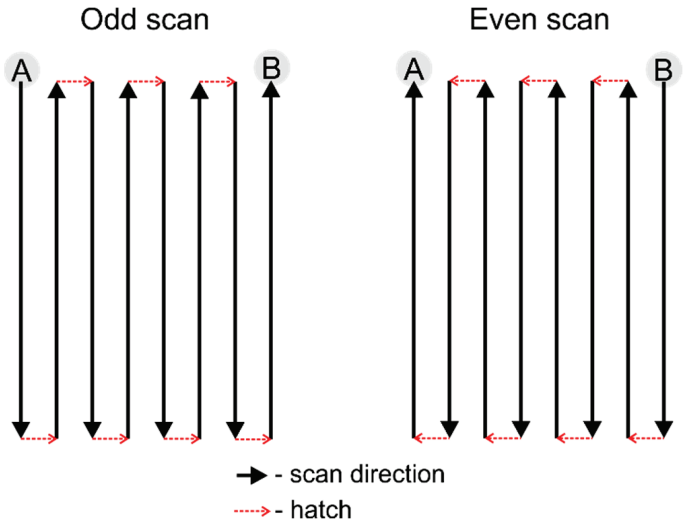

Figure 1. Graphical representation of the scan geometry used for cutting glass.

A thin flowing water film was formed at the surface of the glass workpiece by spraying water mist (see Figure 2). The mist was formed with a commercially available airbrush connected to a pressurised air (3 bar). Here, high-velocity air atomised water into droplets which then were sprayed onto the glass surface and formed a liquid film flowing through the laser ablation zone. The liquid layer was the thickest at the beginning and gradually thinned out as the distance from the nozzle tip increased. In this study, the liquid film flow direction was parallel to the laser scanning direction. At the start of the cut line, the thickness of the liquid layer was 750 µm, whereas at the end of the cut line (26 mm away), the thickness decreased to 450 µm. Variation in layer thickness had no significant effect on ablation efficiency over the length of the cut.

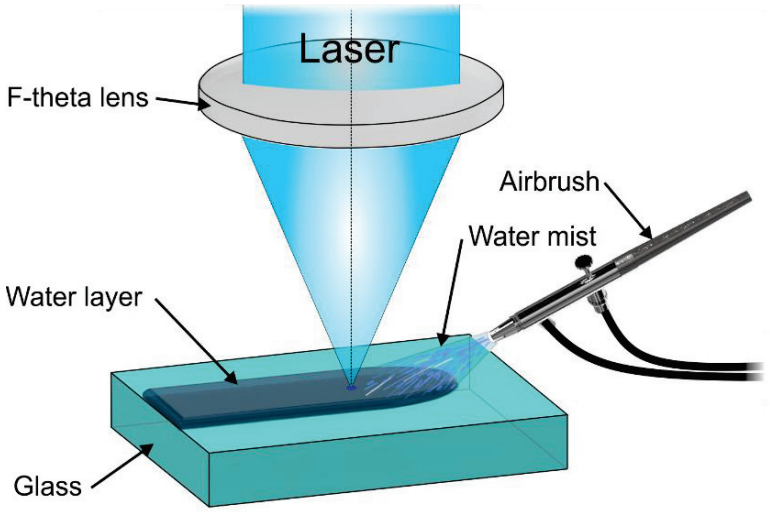

Figure 2. Experimental setup. Airbrush sprayed water mist onto the glass surface, forming thin and flowing water film.

A four-point bending test was performed to assess the characteristic strength of glass strips cut with a laser. The bending test setup is presented in Figure 3. The testing setup consisted of two inner loading rollers with an inner span of 6 mm and two support rollers with a span of 16 mm. The diameter of loading and support rollers was 2 and 6 mm, respectively. During the load, the side of the glass sample in contact with support rollers was under the tensile load, whereas the opposite side was under the compressive load.

Both sides underwent a different type of load during a test; therefore, bending tests were conducted on both sides of glass samples. The loading rate was 1.7 MPa/s.

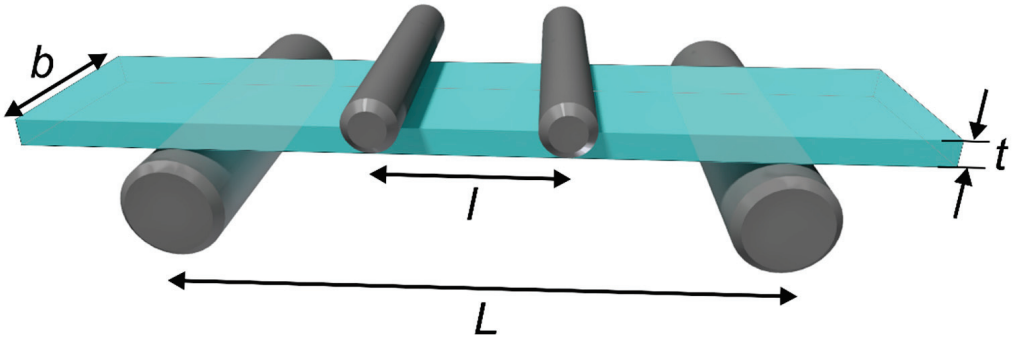

Figure 3. The four-point bending test setup.

The maximum bending strength σ is given by the following formula [38]:

$$\sigma = \frac{3F(L-l)}{2bt^2}, \tag{1}$$

where F is the load at glass sample failure, b is the width, t is the thickness of the sample, and l, L are the distance between the loading and supporting rollers, respectively.

Glass is a brittle material that usually presents a widely scattered strength. Some samples cut under the same processing parameters may break under light load, whereas others will withstand significant bending forces [39]. For this reason, Weibull cumulative distribution is often employed to describe the distribution of the characteristic strength of such materials [40]:

$$P_f(\sigma) = 1 - exp\left(-\frac{\sigma}{\sigma_0}\right)^m \tag{2}$$

Here, σ_0 and m are the characteristic strength and shape parameters of the Weibull modulus. Characteristic strength defines the bending strength at which 63.2% of all samples fail, whereas the shape parameter indicates the dispersion [39], and P_f is the fracture probability.

During tests, a force was applied on laser-cut strips. The maximum bending strength of each strip was calculated based on the measured F at which glass failure occurred. Obtained σ values were ranked in ascending order, i = 1,2, . . . ,n. Probability of fracture should be assigned to every calculated σ_n, where $0 < P_f < 1$, but because the exact probability values for each σ_n is not known, an estimator was used to find these values [41]:

$$P_{f,\,i}(\sigma) = \frac{(i-0.5)}{n}. \tag{3}$$

This is one of the most commonly used estimators and preferred one for smaller sample sizes of fewer than 50 measurements [42]. Finally, Equation (3) was fitted with Weibull cumulative distribution (Equation (2)) to extract σ_0 and m parameters.

3. Results and Discussion

3.1. Low-Laser-Power Cutting Regime

3.1.1. Cutting Process Optimisation

Thin glass plates are sensitive to thermal stresses caused by laser ablation and can easily shatter when higher laser power is irradiated into the material [16]. Glass plates used in this research fractured in ambient air if incident laser power exceeded 4 W. For this reason, glass cutting experiments were split into two parts: low and high (average) laser power regimes. This section presents laser parameter optimization for efficient borosilicate glass cutting at low laser power (<4 W). In Section 3.2, results on high-laser-power cutting are presented.

Firstly, laser ablation parameters for cutting borosilicate glass in ambient air and water were optimised. Initial (not optimised) ablation parameters were the same for both cutting environments: ν = 400 kHz (laser pulse repetition rate), V = 200 mm/s (laser beam scanning speed), h = 4 µm (hatch), and P_{avg} = 4 W (average laser power). The length and width of the optimisation cuts were 5 and 0.3 mm, respectively. During the optimisation step, a number of parameters were optimised: laser fluence, laser beam scanning speed, pulse repetition rate, and the hatch. For every laser parameter set, a minimum number of laser scans was found for a complete and consistent cut-through.

First, the laser fluence was optimised in both environments. The laser fluence was varied from 2 to 12 J/cm^2 by changing the laser pulse energy. The results are presented in Figure 4. The shapes of both ablation efficiency curves were similar, despite different ablation environments. However, the peak of the ablation efficiency curve in water was higher by 63.6% (3.57 versus 5.84 µm^3/µJ) and shifted towards higher fluencies (from 3.5 J/cm^2 to 6.1 J/cm^2).

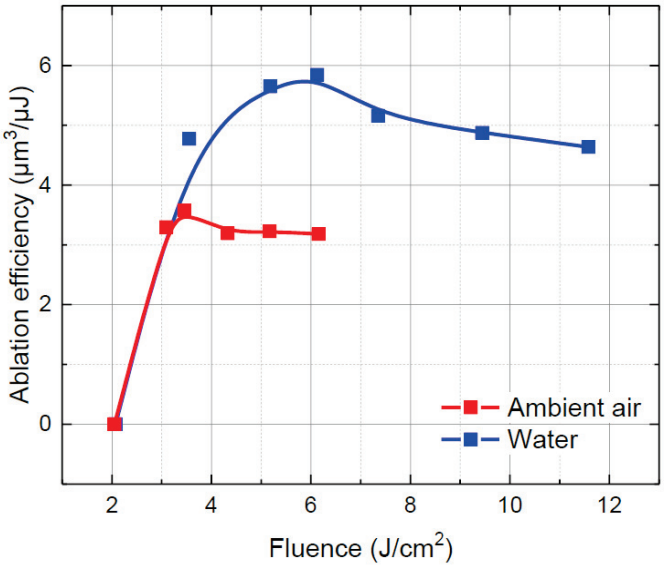

Figure 4. Ablation efficiency versus laser fluence in ambient air and water. Dots are connected to guide the eye.

After the optimal laser fluence was found, the laser pulse repetition rate was re-adjusted, keeping in mind that the average laser power should be maintained below 4 W to avoid glass fracture in ambient air. Laser wavelength conversion efficiency from 1064 nm (fundamental wavelength) to 355 nm (third harmonic of the fundamental wavelength) depends on the pulse intensity. Thus, increasing the pulse repetition rate above 400 kHz and keeping the pump level fixed resulted in a slight decrease in laser output power.

With that being said, further optimisation in water was carried out at 529 kHz and the average laser power of 2.75 W, whereas optimisation in ambient air was conducted at ν = 653 kHz and P_{avg} = 2.1 W. Laser fluence was maintained optimal in both environments, despite slightly different average laser power levels.

Then, the laser beam scanning speed was varied from 200 to 1000 mm/s (see Figure 5). Glass ablation in water remained more efficient in the investigated scanning speed range. Additionally, varying the scanning speed outside the optimal values in water was not as detrimental as in ambient air. The optimal laser beam scanning speed for glass ablation in water was lower (600 mm/s) compared with ablation in ambient air (800 mm/s). Here, the difference in the optimal scanning speed was determined by the different pulse repetition rates in both environments.

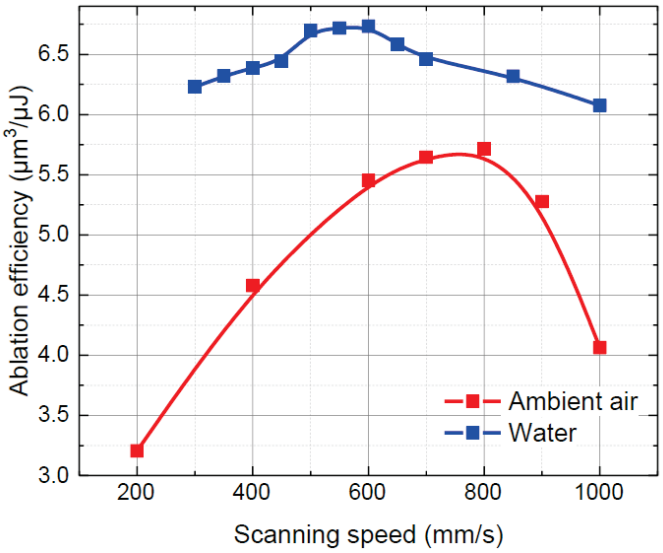

Figure 5. Ablation efficiency versus the laser beam scanning speed in ambient air and water. Dots are connected to guide the eye.

A decrease in ablation efficiency at scanning speeds below optimal in ambient air was associated with increasing laser beam shielding with plasma and debris due to heat accumulation, whereas ablation efficiency loss at scanning speeds above optimal was associated with decreasing temperature in the ablation zone from the optimal due to the increasing distance between laser pulses [43,44].

Finally, a hatch distance was optimised. The distance between the scan lines was varied between 2 and 14 μm to find an optimal hatch value. Additionally, the number of parallel cut lines was adjusted to maintain a constant cut width. Ablation efficiency dependence on the hatch distance is presented in Figure 6. Here, the peak efficiency was obtained at the same hatch distance (10 μm) in both environments, which indicated that the hatch distance mostly depended on the laser beam spot size, but not on the processing environment. At a 10 μm hatch distance, the laser ablation efficiency in ambient air was 6.6 $\mu m^3/\mu J$. The ablation efficiency in water was 14% higher, reaching 7.5 $\mu m^3/\mu J$.

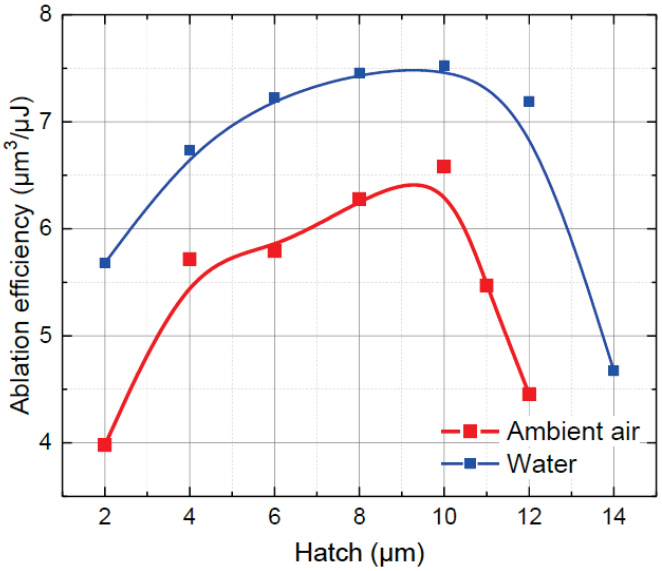

Figure 6. Ablation efficiency versus hatch distance in ambient air and water. Dots are connected to guide the eye.

After the optimised laser parameters were determined, we varied the laser fluence, pulse repetition rate, laser beam scanning speed, and hatch again (only in a narrower parameter range). Despite this, the parameter values yielding the highest ablation efficiency remained unchanged, indicating the optimal glass cutting parameter set.

Therefore, the final (optimised) processing parameters for cutting 0.3 mm wide cuts in a low-laser-power regime are presented in Table 1. Under optimised glass ablation parameters, the effective cutting speed of 0.4 mm thick glass plates in water was 0.26 mm/s. Cutting in ambient air was slower—0.19 mm/s. The difference in effective cutting speed mostly resulted from the difference in incident laser power between two environments (2.75 W in water and 2.1 W in ambient air). Considering this, the effective cutting speed per incident laser power (W) was 0.095 mm/s/W in water and 0.09 mm/s/W in ambient air.

Table 1. Optimised glass cutting parameters (low-laser-power cutting regime).

Cutting Environment	Average Laser Power, W	Ablation Efficiency, $\mu m^3/\mu J$	Fluence, J/cm^2	Scan Speed, mm/s	Pulse Energy, μJ	Pulse Repetition Rate, kHz	Hatch, μm	Cut Width, μm
Air	2.1	6.6	3.5	800	3.2	653	10	300
Water (low power)	2.75	7.5	6.1	600	5.2	529	10	300

Despite the 14% higher ablation efficiency in water-assisted conditions, the improvement in effective cutting speed per Watt was modest (5.5%). The reason for the discrepancy between the ablation efficiency and effective cutting speed was caused by the steeper cut walls produced in water [16]. Strong shockwaves are created during laser ablation in a liquid environment that impinge on the cut sidewalls, producing shallower taper angles [16]. As a result, a larger volume of material was removed, yielding a higher ablation efficiency, despite removing the same material layer thickness per laser scan.

3.1.2. Cut Sidewall Quality

The hatch (h) is the distance between two scanned lines that defines the degree of laser beam overlap between two neighbouring cut lines. The effect of hatch distance on the bottom of milled cavities has been investigated in multiple papers [44–47]. However, we could not find extensive research on the influence of the hatch on the quality of laser cutting.

For this reason, rectangular glass strips (26×6 mm^2) were cut out of the larger glass plates using the optimised laser parameter sets presented in Table 1 (2.1 W in ambient air and 2.75 W in water). The optimal hatch in both environments was 10 μm. Nevertheless, we produced additional cuts with the following hatch values: 2, 4, 6, 8, and 12 μm. Here, only the hatch value was varied, whereas other parameters remained unchanged. Micrographs of laser-cut walls are depicted in Figure 7.

Cut sidewalls were covered with periodically recurring ridges. These formations were parallel to the laser beam scanning direction and spanned uninterrupted throughout the length of the cut. Ridges are visible as the dark lines in Figure 7 separated by lighter areas—the concavities.

In the experiments, we used a Gaussian laser beam intensity profile. Thus, these formations resulted from the cumulative beam intensity distribution projected onto the glass plate after multiple laser scans (Figure 8). The accumulated laser intensity distribution (the distance between intensity minimums and maximums) depended on the hatch distance between individual cut lines. Concavities represent the laser beam intensity peaks, where more material was removed. In Figure 8, dashed lines (normal to the glass plate surface) were extrapolated from the laser intensity peaks to the inclined cut sidewall, indicating positions where concavities would be formed. Ridges were formed in intensity minimums between the cut lines, thus removing less material. However, as the hatch distance decreased to 2 μm in ambient air and 4 μm in water, the ridges became indistinguishable to the eye. Hatch became comparable to the pitch, yielding a relatively uniform overlap in both directions.

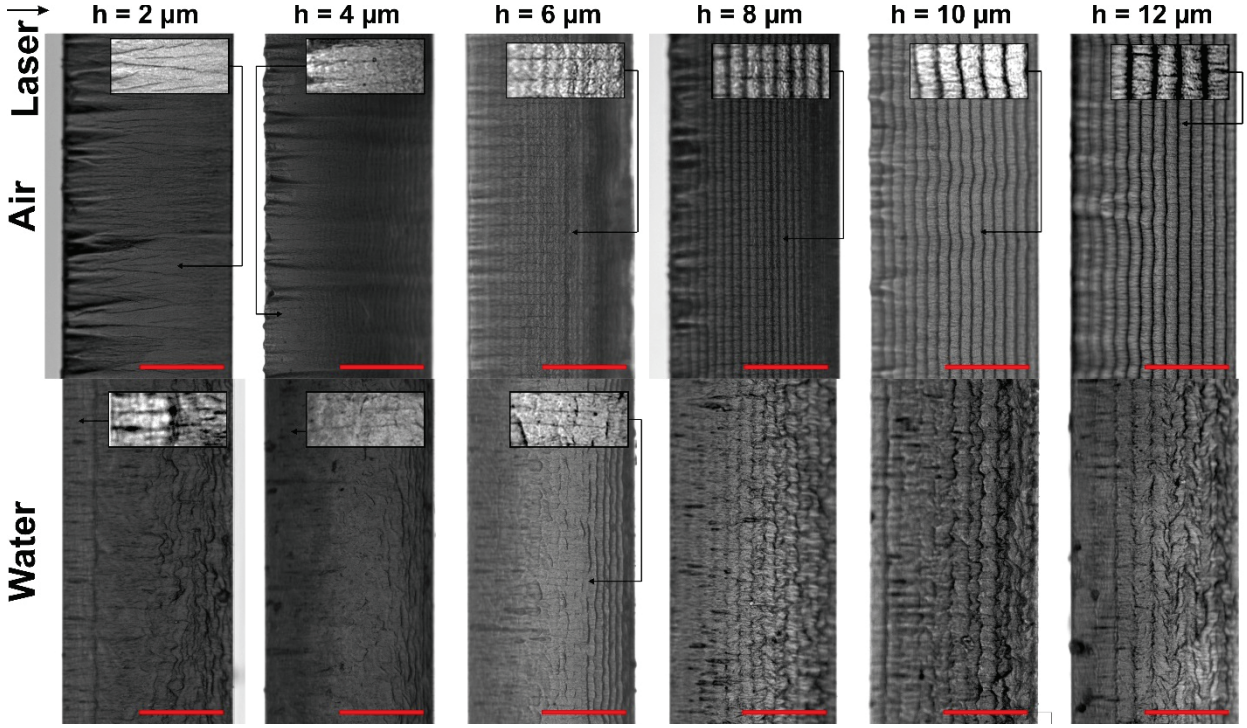

Figure 7. Optical micrographs of cut sidewalls. Cases for cutting in ambient air and water at different hatch values are presented. Scale bars represent 0.2 mm and apply to all panels in this figure. The laser beam entry side is indicated with an arrow.

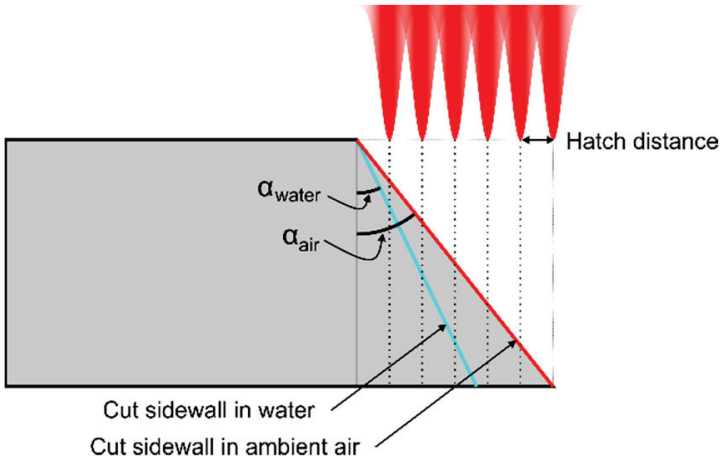

Figure 8. Schematic of the side view of the glass plate. Above the glass plate, a cumulative laser intensity profile is shown. Dashed lines (normal to the glass surface) extrapolated from the cumulative laser intensity peaks indicate positions where concavities were formed on the inclined cut wall. Ridges were formed between the concavities.

The period of ridges H depended on the hatch distance and the cut wall taper angle: $\sin(\alpha) = h/H$ (see Figure 8), where α is the taper angle obtained in water (α_{water}) or in ambient air (α_{air}). According to the measurements, the average taper angle in water was 16°, whereas the angle in ambient air was larger—23.4°. As a result, fewer ridges were projected on glass strips that were cut in water, resulting in larger ridge periods. The period of ridges versus the hatch distance is presented in Figure 9. At h = 6 µm, the ridge period in ambient air was 15.1 µm, whereas in water, it was almost two times larger (30.9 µm). The ridge period increased more quickly in water with the hatch. As a result, the difference in periods gradually increased to almost 20 µm at h = 12 µm.

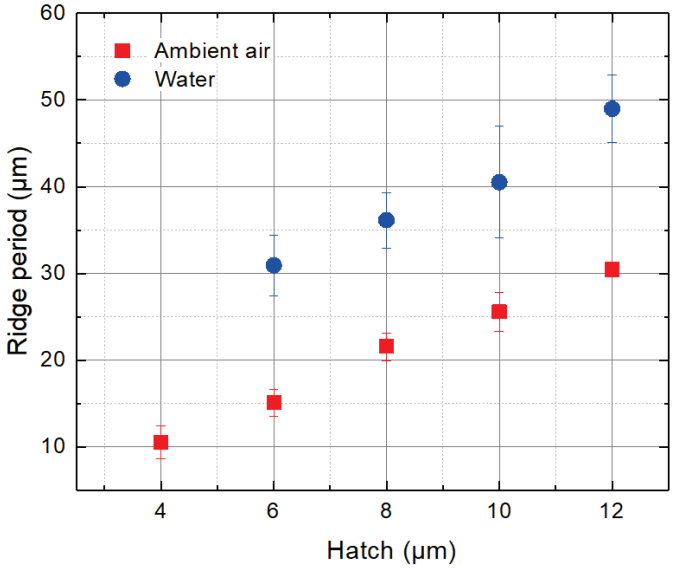

Figure 9. The period of ridges versus the hatch distance.

In both cutting environments, cut wall steepness decreased slightly near the bottom of the cut. This resulted in a denser ridge formation in that area. Nevertheless, the relationship between the ridge period, taper angle, and hatch distance remained valid.

The waviness of ridges seen in Figure 7 in ambient air was caused by glass chipping at the front surface of the glass plate. Chips originated at the front glass surface and propagated more deeply into the glass plate during the cutting, forming oblong concavities perpendicular to the laser beam scanning direction. The dense chipping at the cut edge is a characteristic of glass ablation in ambient air due to heat accumulation [16]. Vertical oblong concavities tended to grow with the decreasing hatch distance. This indicated increasing heat accumulation [48].

In the case of water-assisted cutting, chipping at the cut edge and the consequent formation of oblong vertical concavities was suppressed by efficient cooling. However, ridges were wavy near the bottom surface of the cut sidewall due to laser beam distortion by the water layer. This effect was attributed to the laser beam disturbance in a liquid–vapour layer, which increased with the depth of the cut (water flow instability, formation and collapse of bubbles, liquid vaporisation [49–51]). According to the micrographs, glass melting was pronounced in distorted areas.

Additionally, we observed vertical cracks formed at the cut sidewall normal to the glass surface (a network of cracks spanned between the front and the back surfaces, as shown in the insets in Figure 7). Cracks were more visible on cut sidewalls produced in ambient air due to a much smoother cut wall surface (see insets at h = 2, 6, 8, 10, and 12 µm). In the case of cutting in water, a network of vertical cracks was visible in smoother areas of the sidewall where surface distortion was minimal. Here, cracks were clearly visible at h = 2, 4, and 6 µm. The melting was more pronounced in distorted areas of the cut sidewall. Thus, the network of cracks could have been covered with re-solidified melt, hindering their detectability [52]. However, we could not identify cracks in distorted areas in the micrographs presented in Figure 7.

At h between 6 and 8 µm, the direction of the cracks was strictly vertical in ambient air, propagating from the front surface towards the bottom of the glass strip. However, as the h decreased and ridges could not be distinguished any more (h = 2), the direction of propagating cracks became not as strict, allowing individual cracks to deviate up to an angle of 14° from the normal to the glass surface. In some cases, cracks intersected each other. Furthermore, the density of the crack network was highest at h = 2 µm, indicating the highest thermal damage. At the largest investigated hatches (10 and 12 µm), cracks became discontinuous and short and were prone to abruptly change direction between ridges.

3.1.3. Cut Edge Quality

A high edge quality is critical for the mechanical robustness of glass parts. Minimising glass chipping and microcrack formation at the cut edge reduces the loss of strength of machined glass elements [7]. Furthermore, such defects tend to grow under the tensile strength and, over time, could cause the fracture of glass elements [53].

We assessed the front and back surface edge quality in more detail for the following hatch distances:

Optimal hatch yielding the highest ablation efficiency (10 μm in ambient air and water);

Ridge-free hatch (2 μm in ambient air and 4 μm in water);

An intermediate hatch between the optimal and ridge-free hatch values (6 μm in ambient air and 7 μm in water).

Multiple studies have shown that band-like damage can occur at the back surface of transparent media during laser scribing and cutting [53–56], potentially hindering the mechanical robustness of brittle glass elements [55]. This damage is mainly associated with laser beam refraction and reflection from the ablated crater/channel walls and can be avoided, or at least minimised, by properly selecting the laser beam polarisation direction. In this study, we did not observe any formation of band-like damage next to a laser cut at P polarisation. For this reason, experiments were conducted using P polarisation only, and no other polarisation states were investigated.

A total of 48 strips were cut for every preselected hatch (24 in ambient air and 24 in water). Each strip was cut with two laser cuts along the longer edge of the glass plate. This way, four cut edges were inspected per single glass strip—two edges at the front and two at the back surface of each strip.

We evaluated the cut edge quality of glass by assessing the mean maximum and the average chipping widths on both sides of laser-cut glass strips (see Figure 10). The mean maximum chipping width is defined as the width of the single widest chip per cut edge averaged over all strips cut under the same laser parameter set. The average chipping width (w) is an average cut edge deviation from the cut line due to glass chipping measured normal to the glass surface, as shown in Figure 10. The cut edge quality at the front and back surfaces was assessed separately. The mean maximum chipping and the average chipping widths were evaluated in a central part of the cut edge over distances of 10 and 1 mm, respectively.

The most noticeable difference in cut edge quality between the two environments was observed at the front surface of the laser-cut glass strips (see Figure 11). Cutting in water was superior to cutting in ambient air in terms of cut edge quality. The average chipping width in water was 7.2 ± 1.2 times smaller than in air (see Table 2). Furthermore, variation in hatch distance in the water had an insignificant effect on the average chipping width, which was distributed between 0.75 and 0.85 μm. Here, the smallest value of 0.75 ± 0.35 μm was observed at the optimal hatch distance (h = 10 μm).

Cutting in ambient air produced rougher cut edges. The smallest value of 4.3 ± 1.8 μm was measured at the optimal hatch. Transition to smaller hatch values increased the average chipping width by up to 49% to 6.2–6.4 μm, depending on the hatch distance.

However, contrasting results were observed at the back surface (see Figure 12). Here, cutting in ambient air outperformed cutting in water by producing smoother cut edges. Furthermore, cut edges at the back surface were smoothest at the smallest hatch distance. In ambient air at h = 2 μm, the average chipping width was only 3.9 ± 2.9 μm. In water, at h = 4 μm, the average chipping width was 13% higher than in air (4.4 ± 2.2 μm). Unexpectedly, the highest average chipping width was observed at the optimal hatch distance (h = 10 μm) in both environments: in ambient air, the value was 6.7 ± 3.3 μm, whereas in water, it was even larger—6.9 ± 4.3 μm.

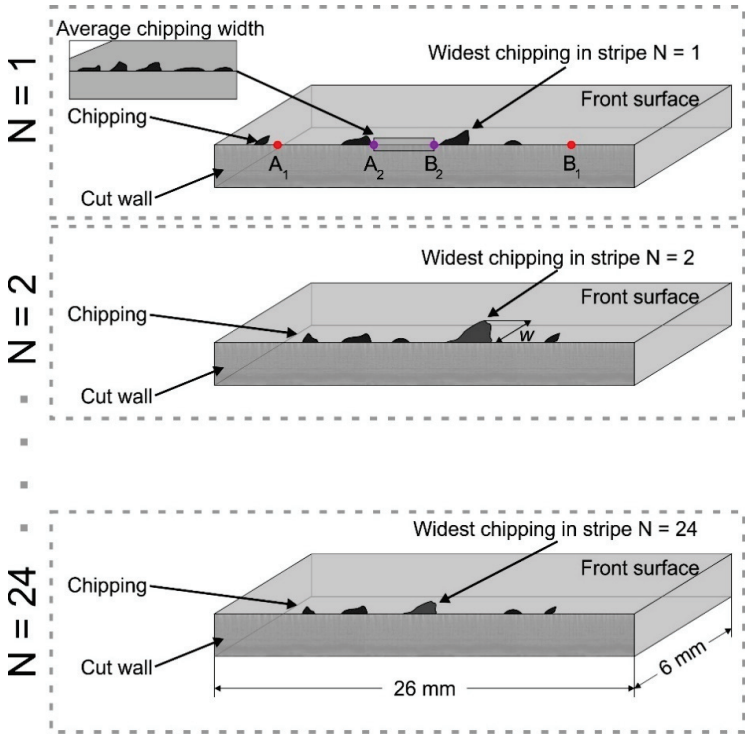

Figure 10. Schematics for evaluating the mean maximum and the average chipping widths at the cut edge. The mean maximum chipping width was evaluated over a distance of 10 mm (between points A_1 and B_1). An average chipping width was evaluated over a distance of 1 mm (between points A_2 and B_2).

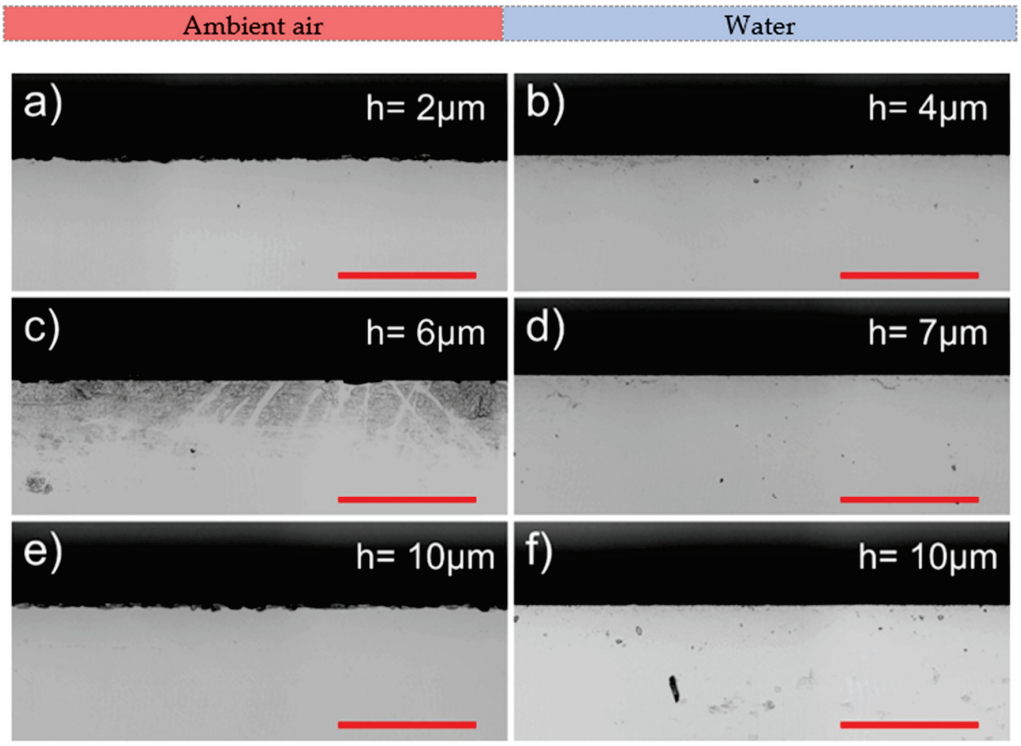

Figure 11. Optical micrographs showing cut edges at the front surface produced in ambient air (to the left) and water (to the right). Rows represent different hatch distances: ridge-free (**a**,**b**), intermediate (**c**,**d**), and optimal (**e**,**f**). The scale bars represent 200 μm and apply to all panels in the figure.

Table 2. Average chipping widths.

	Cutting in Ambient Air			Cutting in Water		
Hatch, µm	**2 µm**	**6 µm**	**10 µm**	**4 µm**	**7 µm**	**10 µm**
Front surface, µm	6.4 ± 3.7	6.2 ± 2.9	4.3 ± 1.8	0.85 ± 0.4	0.8 ± 0.4	0.75 ± 0.35
Back surface, µm	3.9 ± 2.9	5.4 ± 3.2	6.7 ± 3.3	4.4 ± 2.2	6.7 ± 2.6	6.9 ± 4.3

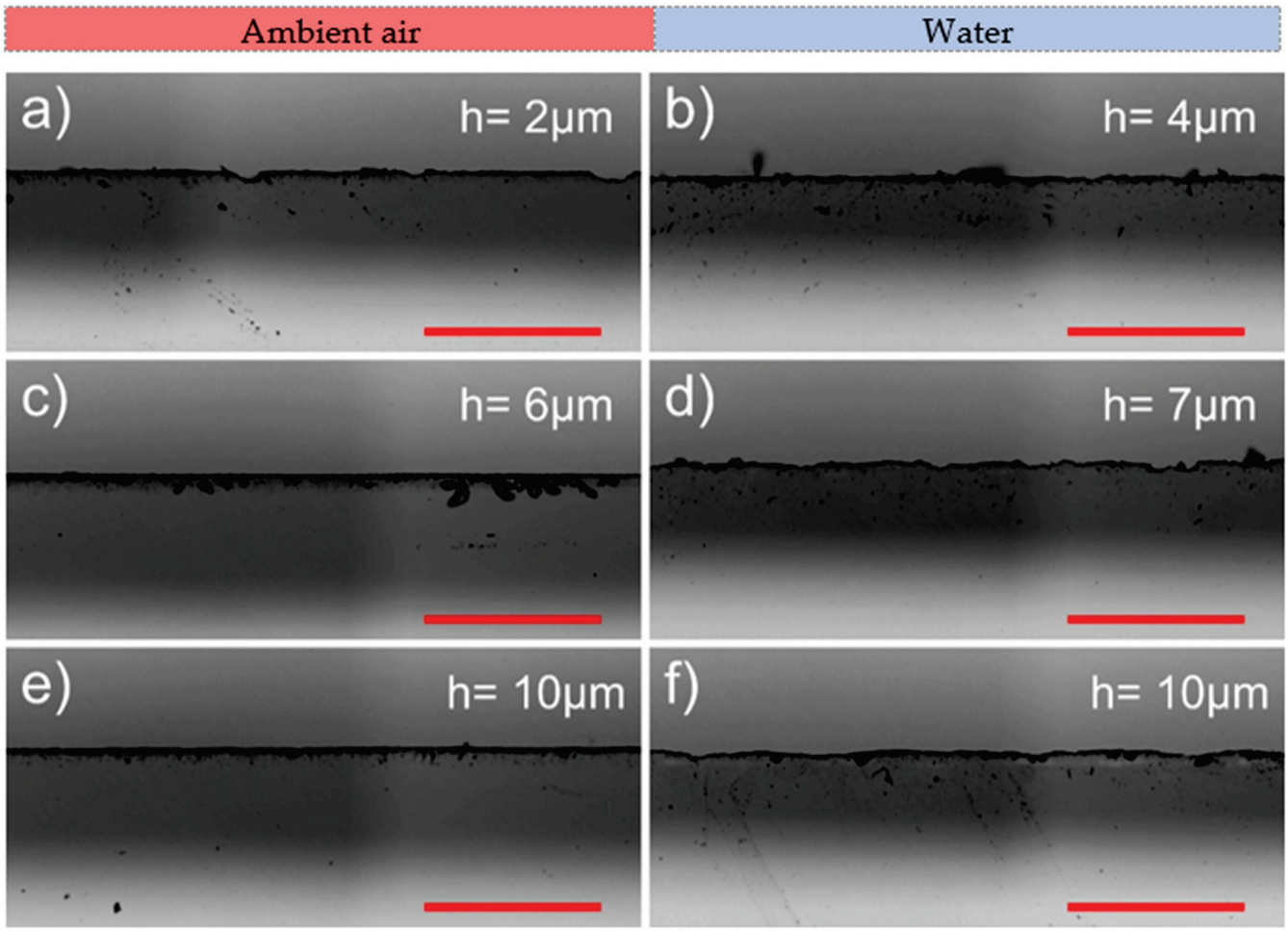

Figure 12. Optical micrographs showing cut edges at the back surface produced in ambient air (to the left) and water (to the right). Rows represent different pitch distances: ridge-free (**a**,**b**), intermediate (**c**,**d**), and optimal (**e**,**f**). The scale bars represent 200 µm and apply to all panels in the figure.

Next, we evaluated the mean maximum chipping widths at the back and the front surfaces. The formation of wide chippings that were significantly wider than the average chipping width was scarce. However, this could not be avoided entirely, even when cutting under optimal laser processing parameters. The mean maximum chipping width at the back surface was distributed between 34 and 44 µm in both cutting environments, with the smallest widths at h = 2–4 µm (see Figure 13). At the front surface, maximum chipping was smaller in water by 43% (9.3 ± 0.9 µm in water and 16.2 ± 2 µm in ambient air). Furthermore, error bars in Figure 13 reveal that the mean maximum chipping width was more consistent at the front surface than at the back.

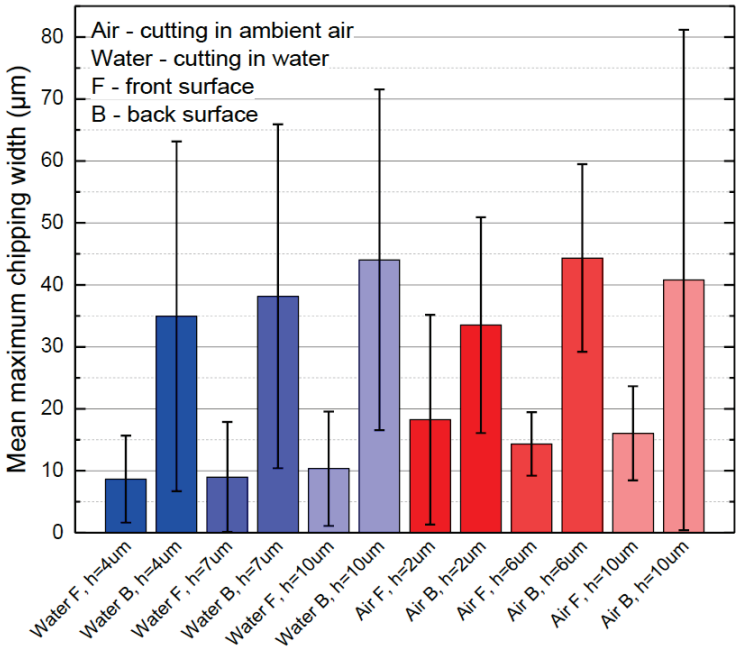

Figure 13. Mean maximum chipping width at the cut edge.

3.1.4. Cut Wall Roughness

A rougher sidewall could indicate the presence of larger defects which negatively affect the strength of glass strips [17]. For this reason, we studied the roughness of laser-cut sidewalls produced in ambient air and water at preselected hatch values (optimal, ridge-free and intermediate). Recorded 3D topologies at different h values are depicted in Figure 14.

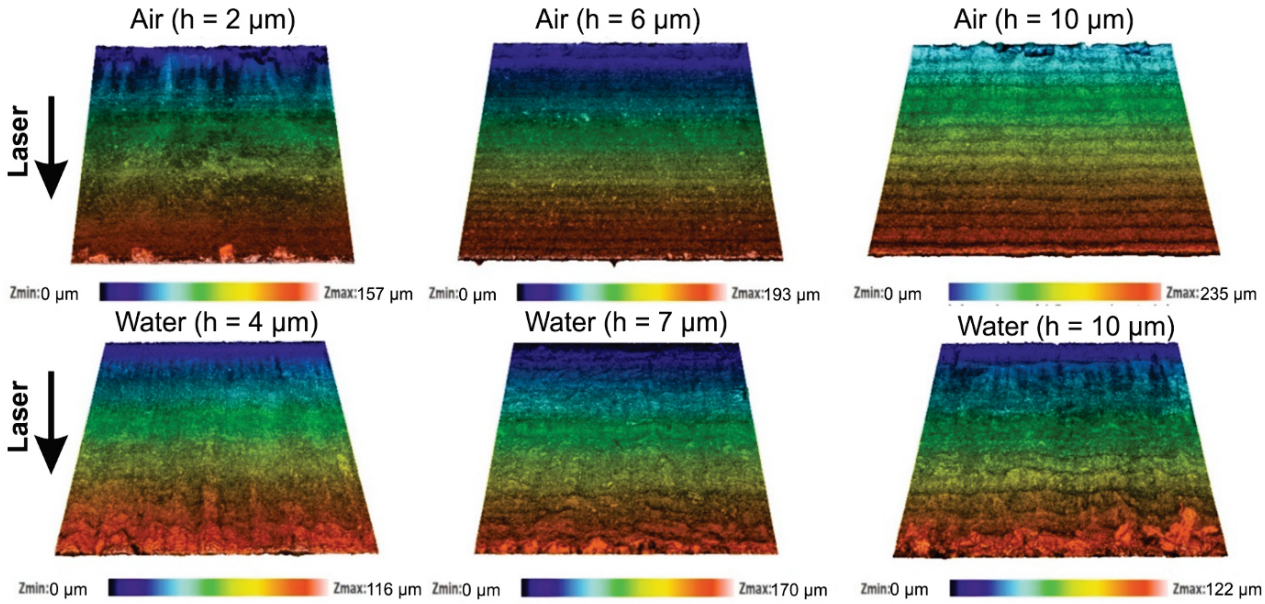

Figure 14. Topographies of cut sidewalls produced in ambient air and in water. Cases for three different hatch distances are presented (optimal, intermediate and ridge-free). Laser beam entry side is indicated with an arrow and applies to all panels in the figure.

The surface roughness (R_a) was measured along the laser beam scanning direction 200 µm below the glass surface. Cutting in water produced a consistent cut sidewall surface roughness of $R_a = 0.69 \pm 0.1$ µm in the investigated h range (see Figure 15).

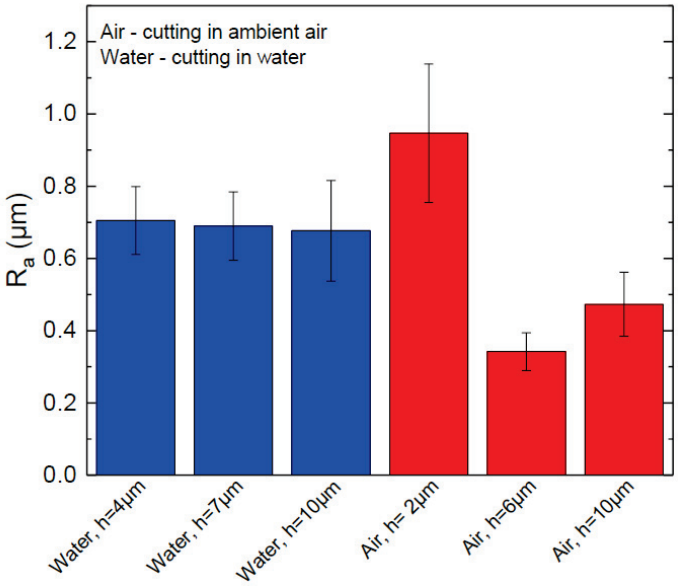

Figure 15. Cut wall roughness (R_a) versus hatch in ambient air and water. Error bars indicate standard deviation.

On the other hand, cut wall roughness varied greatly in ambient air. At the intermediate and optimal hatch values, cut sidewalls were smoother than in water. The overall smoothest sidewall of 0.34 μm was measured at h = 6 μm in ambient air. However, the maximum roughness of 0.95 ± 0.2 μm was also measured in the air at h = 2 μm. An abrupt increase in roughness at h = 2 μm was associated with the formation of vertical oblong concavities.

Improved glass cooling in water avoided cut sidewall quality degradation related to heat accumulation, showing a consistent surface roughness irrespective of the hatch value. The roughness was higher than in ambient air due to increased mechanical forces acting on the glass wall during the laser ablation (collapse of cavitation bubbles, confined plasma generated shockwaves), which led to a more mechanical glass erosion and porous-looking cut wall surface [16,17,57].

3.1.5. Flexural Strength

Laser-cut glass strips were broken using the four-point bending setup shown in Figure 3. The failure occurred at the tensioned side of the glass strip, facing support rollers. For this reason, we conducted bending tests on both sides of glass strips. We broke 12 samples per side for every preselected hatch value in both cutting environments. Extracted characteristic strength (the bending strength at which 63.2% of all samples fail) and shape parameters are presented in Figure 16. Glass strips were cut using average laser powers of 2.1 and 2.75 W in ambient air and water, respectively.

Glass strips cut in the water had higher strength than those cut in ambient air. The highest front side strength of 117.6 ± 12 MPa was recorded at the optimal hatch (h = 10 μm), whereas the highest back side strength was recorded at the ridge-free hatch value of h = 4 μm (101 MPa). Nevertheless, the strength at the back side at the optimal h value was only lower by 7 MPa compared with the maximum strength recorded at the back side.

For the front side bending in ambient air, characteristic strength increased with the hatch. The smallest characteristic strength of 96.8 ± 10 MPa was obtained at h = 2 μm, and reached the highest value of 107.3 ± 5 MPa at h = 10 μm. The lowest strength at the back side was also measured at the smallest hatch value of 2 μm (76 ± 7 MPa), but the strength increased to 89 ± 8 MPa at h = 6–10 μm.

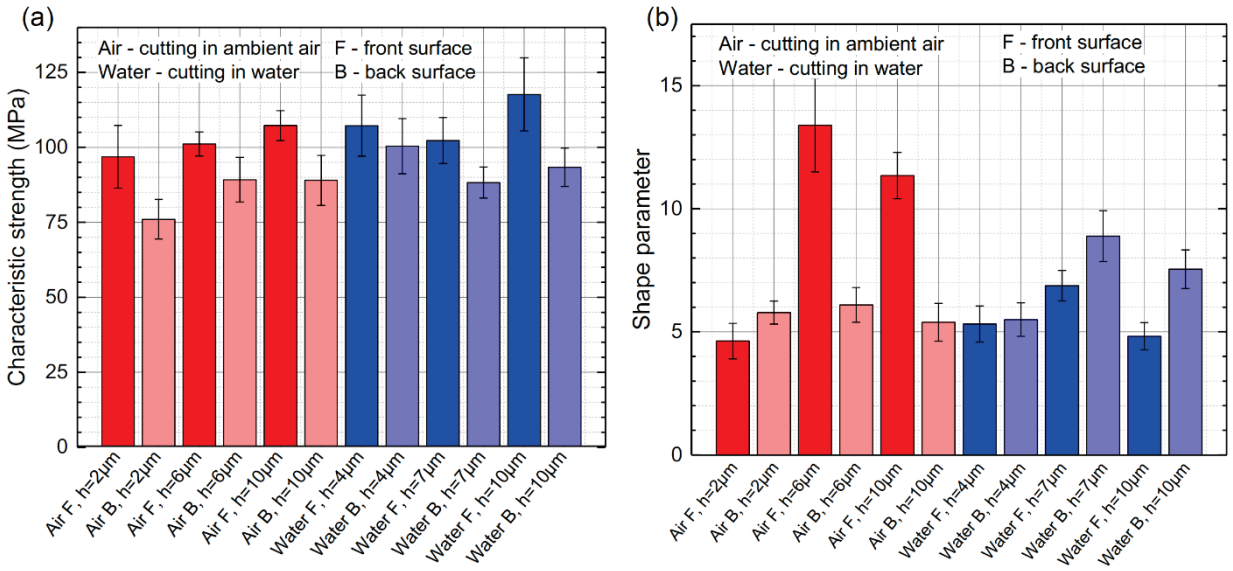

Figure 16. Characteristic strength (**a**) and shape parameter (**b**) when loading force is applied from the front and the back glass strip sides. Cases for cutting in ambient air and water are presented.

Overall, the strength at the front side (surface) was higher than at the back, between 7% and 27%, depending on the h value and the cutting environment.

As noted in Section 2, the shape parameter is dimensionless and indicates the dispersion of the characteristic strength. Therefore, measurements with a higher m parameter are less scattered, giving more predictable and consistent results. For front side bending, the highest shape parameters were extracted in ambient air at intermediate and optimal hatch values. Although the characteristic strength was smaller in ambient air, the strength was more consistent at these hatch values. The highest m parameter for back side bending was obtained in glass strips cut in water at intermediate and optimal hatch distances (8.9 ± 1 and 7.5 ± 0.8). In other cases, the m parameter was relatively consistent, with an average value of 5.6 ± 0.7.

Characteristic strength was distributed over a narrow range of values regardless of the applied hatch distance. Therefore, we present averaged characteristic strength for the front and the back side bending in Table 3. On average, cutting in water improved the front side strength by 7.2% to 109 ± 8 MPa and back side strength by 10.9% to 93.9 ± 7 MPa, compared with cutting in ambient air.

Table 3. Average characteristic strength of glass strips cut in ambient air and water for the front and back side bending cases. Strength was averaged in terms of hatch distance.

Cutting Environment	Front Side	Back Side
Ambient air	101.7 ± 6 MPa	84.7 ± 7 MPa
Water	109 ± 8 MPa	93.9 ± 7 MPa

The front side strength of glass strips cut in ambient air decreased with the hatch. The decrease in strength coincided well with increasing average and mean maximum chipping widths and cut sidewall roughness (at h = 2 μm). However, the back side strength of glass strips decreased with the hatch, contradicting the improving cut edge quality at smaller hatch values (average and mean maximum chipping widths) and was only supported with the increasing cut sidewall roughness. Furthermore, the vertical oblong concavities visible in Figure 7 were the largest and most dense at h = 2 μm at the front surface, which should cause more drastic losses of front side strength. However, relative strength losses were very similar on both sides of the glass strip. Moreover, the relative strength losses were similar

to those cut in water, even though oblong vertical concavities did not form during cutting in water.

In the case of cutting in water, the cut sidewall surface roughness remained constant regardless of the hatch and should not affect the strength of glass strips differently in the investigated h range. The mean maximum chipping width decreased with the hatch; therefore, the change in the characteristic strength at the front side of the strips could only be supported by the increase in average chipping width. In the case of back side strength, the maximum value was obtained at the smallest hatch value of 2 μm and was supported with the decrease in average and mean maximum chipping widths.

As a result, we did not observe a relationship between the sidewall roughness measurements or the average and mean maximum chipping widths with the characteristic strength of glass strips at different hatch values.

However, the formation of vertical cracks on the glass strip sidewalls was correlated with characteristic strength measurements. According to Figure 7, the cracks were short, formed between ridges and were mostly discontinuous in both cutting environments at the optimal hatch value (h = 10 μm), resulting in the highest characteristic strength. However, the length and density of cracks increased with the decreasing hatch, indicating the loss of strength in both environments. Thus, we believe that the evolution of the crack network at the cut sidewall is mostly responsible for the characteristic strength degradation of strips cut at smaller hatch distances than the optimal.

Furthermore, we speculate that the characteristic strength of glass strips cut in water was higher due to more efficient cooling. Laser cutting generates high temperature gradients, causing significant stress fields in the ablation zone [58]. Therefore, better cooling lessens the heat diffusion into the material, as well as the generated stresses [8], consequently decreasing the crack depth and increasing the mechanical strength of samples [52].

3.2. High-Laser-Power Cutting Regime

Scaling up the manufacturing throughput is one of the major objectives for successfully implementing direct laser ablation technology for glass cutting applications. Considering that the direct ablation is much more energy-demanding than other laser-based glass cutting techniques (such as internal scribing and rear side ablation), significantly higher average laser power should be used to keep the cutting speed and material removal rates competitive. Unfortunately, glass is a brittle material with low heat conductivity, limiting the practical use of the full potential of high-power lasers. As mentioned in Section 3.1.1, glass plates used in the experiment could not withstand incident laser power above 4 W and shattered during the cutting. Fortunately, water ensured sufficient cooling, enabling glass to be cut into smaller strips at higher laser power.

For this reason, additional high-power glass cutting experiments were performed in water at an incident laser power of 15.5 W. The laser beam spot size was increased to 30 μm by removing the beam expander from the laser beam optical path. This was performed to maintain optimal laser fluence at maximum laser power while staying in the lasers' operating pulse repetition rate range. Cutting width was not changed (300 μm) to keep experimental conditions similar to that in the low-power cutting regime. Other laser processing parameters, such as pulse repetition rate, hatch and laser beam scanning speed, were re-optimised for larger beam width and higher average laser power.

The optimised processing parameters for cutting glass in a high-power regime are presented in Table 4. At 15.5 W, the borosilicate glass ablation efficiency was 8.7 $\mu m^3/\mu J$, giving an effective cutting speed of 1.8 mm/s, whereas the effective cutting speed per incident laser power was 0.116 mm/s/W. Compared with the low-power cutting regime in water, ablation efficiency and effective cutting speed per incident laser power increased by 16% and 29%, respectively. The increase in both parameters was associated with the more pronounced glass cracking and disintegration at higher laser power. However, the optimal laser fluence remained unchanged (6.1 J/cm^2).

Table 4. Optimised glass cutting parameters. High-laser-power cutting in water.

Cutting Environment	Average Laser Power, W	Ablation Efficiency, $\mu m^3/\mu J$	Fluence, J/cm^2	Scan Speed, mm/s	Pulse Energy, µJ	Pulse Repetition Rate, kHz	Hatch, µm	Cut Width, µm
Water (high power)	15.5	8.7	6.1	1250	21.4	725	15	300

For the sake of brevity, in further text, only the cuts produced at the optimal hatch will be discussed.

The micrographs of the front and back surface cut edges produced in water at 15.5 W are presented in Figure 17. The average chipping and mean maximum chipping widths at the front surface were 1.5 ± 0.7 µm and 20 ± 19 µm, respectively. Both parameters doubled in the high-laser-power cutting regime, compared with cutting in water at 2.75 W. Despite this, the average chipping width remained almost three times smaller compared with cutting in ambient air at 2.1 W.

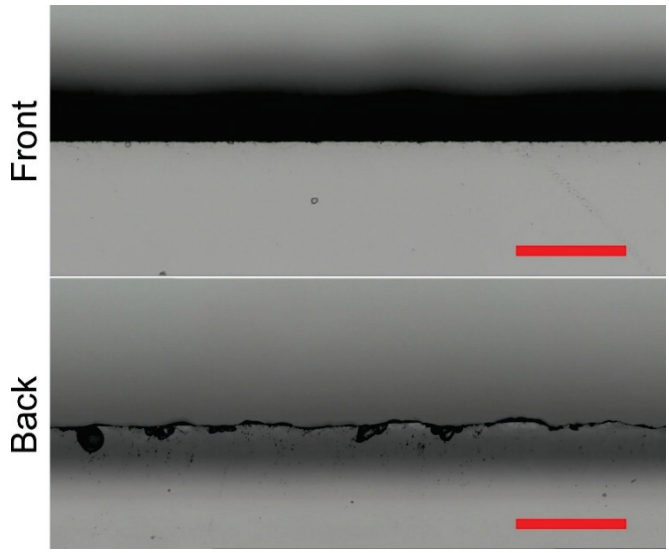

Figure 17. Optical micrographs showing front and back surface cut edges. Cutting was performed in water at 15.5 W. The scale bars represent 200 µm and apply to all panels in the figure.

At the bottom surface, higher incident laser power had almost no effect on the average chipping width, which increased only by 3% to 7.1 ± 4 µm, compared with glass cutting in water at 2.75 W. The mean maximum chipping width in the high-power regime was 30 ± 10 µm. Compared with cutting at low laser power in water and ambient air, the mean maximum chipping widths decreased by 32% and 26%, respectively.

The 3D topology and the optical micrograph of the cut wall produced at 15.5 W are shown in Figure 18. The micrographs revealed that the sidewall was covered with vertical notches. The direction of notches was normal to the glass surface, the same as the direction of cracks formed in glass strips in Figure 7. According to the micrographs, some notches were long and could span between several ridges, whereas the length of others was limited to the period of ridges. The variation in length was similar to vertical cracks formed in glass strips cut in ambient air at low average laser power (see Figure 7). Thus, we believe that the notches were formed during the coalescence of adjacent cracks during the laser ablation at higher incident power.

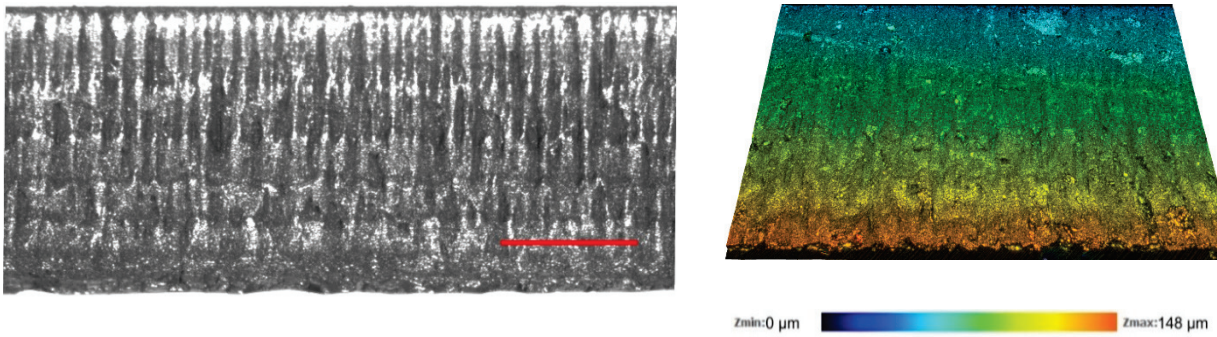

Figure 18. Optical micrograph (**left**) and the topography (**right**) of the cut sidewall produced in water at 15.5 W. The scale bar in the left panel represents 200 µm.

The sidewall remained covered with periodically recurring ridges, as in the strips cut under the low-power cutting regime (Figure 18). The period of ridges corresponded well with the relationship between the cut sidewall taper angle and the hatch distance given in Section 3.1.2. The ridges could be easily identified in the optical micrograph. However, they were difficult to distinguish in topographical images, indicating that the ridge height was similar to the surface roughness of the cut wall, which was 0.82 µm. Compared with the low-power cutting regime in water, the R_a increased by 20%. The formation of notches at the cut sidewall seen in Figure 18 was primarily responsible for the increase in surface roughness.

Finally, bending tests were applied on laser-cut glass strips, and the tension was applied only on the stronger (front surface) side of the glass strips. The obtained average characteristic strength was 107.5 ± 6.6 MPa. According to the results, the strength of glass strips cut at 15.5 W decreased by 8.5% compared with strips cut at 2.75 W in water, and almost equally with the strength of glasses cut in ambient air at 2.1 W. However, the glass strips were broken more predictably in the high-power cutting regime than at 2.75 W: the shape parameter of strips cut at 15.5 W was 9.2 ± 0.9, whereas at 2.75 W, the shape parameter was 4.8 ± 0.6.

4. Conclusions

In this study, we investigated borosilicate glass cutting in ambient air and water with 355 nm wavelength picosecond laser pulses. Laser pulse repetition rate, fluence, beam scanning speed and hatch parameters were optimised to cut 400 µm thick glass plates into 26 × 6 mm^2 strips under efficient ablation conditions in both environments. Cutting under optimised laser parameters in a low-laser-power regime (2.1 W in ambient air and 2.75 W in water) was more efficient in water (7.5 $\mu m^3/\mu J$) than in ambient air (6.6 $\mu m^3/\mu J$), by 14%. Nevertheless, the effective glass cutting speed per incident laser power remained similar in both cutting environments (0.095 mm/s/W in water and 0.09 mm/s/W in ambient air). The reason for the discrepancy between ablation efficiency and effective cutting speed per incident power was mainly caused by the laser cut taper angle, which was shallower in water. As a result, steeper cut walls in water contributed to a higher ablation efficiency, but had little effect on the thickness of the removed material layer per single laser scan.

Additionally, more efficient cooling in water allowed us to cut glass at the maximum average laser power of 15.5 W, whereas glass in ambient air fractured when the incident laser power exceeded 4 W. As a result, effective glass cutting speed increased from 0.26 mm/s (at 2.75 W) to 1.8 mm/s (at 15.5 W) in water. Additionally, at higher incident laser power, the ablation efficiency increased by 16% to 8.7 $\mu m^3/\mu J$ and effective glass cutting speed per incident laser power increased to 0.116 mm/s/W. Improved ablation efficiency and effective cutting speed were associated with the increased cracking and disintegration of brittle glass material at higher power levels.

Under the optimal cutting parameters (in terms of ablation efficiency), glass strips cut in the water had the highest characteristic strength: 117.6 MPa when bending was

applied from the front side and 107.3 MPa from the back side of laser cut glass strips. In comparison, glass strips cut in ambient air had a lower characteristic strength on both sides (107.3 MPa and 88.9 MPa at the front and back surface sides, respectively). The average front side surface characteristic strength of samples cut at 15.5 W in water was 107.5 MPa. The strength of strips in the high-power cutting regime degraded but remained slightly higher than strips cut in ambient air at 2.1 W.

The variation in the hatch had the largest impact on the visual quality of the cut sidewall due to the formation of ridges, ablation efficiency and the characteristic strength of glass strips. The formation of ridges at the cut sidewall was prominent at the optimal hatch value (10 μm). The height and the period of ridges decreased with the hatch until ridges could not be distinguished any more (h = 2 μm in ambient air and h = 4 μm in water), improving the sidewall quality. However, this negatively affected the ablation efficiency and overall strength of glass strips. Ablation efficiency and strength losses were associated with overheating the glass plate, because the heat accumulation increased with decreasing spacing between the neighbouring cut lines (hatch). The decrease in characteristic strength was associated with the formation of vertical cracks on the cut sidewalls. Micrographs revealed that at the optimal hatch distance, the cracks were short and discontinuous. However, as the hatch decreased, the length of cracks notably increased, spanning between multiple ridges.

The experimental results show that the borosilicate cutting in water was superior to the ablation in ambient air, and represents a promising candidate for wider applications in the industrial cutting of high-quality glass parts.

Author Contributions: Conceptualization, E.M., B.V. and P.G.; methodology, E.M. and P.G.; validation, E.M., L.Z. and B.V.; formal analysis, E.M. and L.Z.; investigation, E.M. and L.Z.; data curation, E.M. and L.Z.; writing—original draft preparation, E.M., L.Z. and P.G.; writing—review and editing, E.M., L.Z. and P.G.; visualization, E.M., L.Z. and B.V.; supervision, E.M. and P.G.; project administration, P.G.; funding acquisition, E.M. and P.G. All authors have read and agreed to the published version of the manuscript.

Funding: The research leading to these results has received funding from the European Social Fund (project No 09.3.3-LMT-K-712-19-0133) under a grant agreement with the Research Council of Lithuania (LMTLT).

Conflicts of Interest: The authors declare no conflict of interest.

References

1. Kahr, M.; Domke, M.; Steiner, H.; Hortschitz, W.; Stifter, M. Borosilicate Glass MEMS Lorentz Force Magnetometer. *Proceedings* **2018**, *2*, 788.
2. Okamoto, Y.; Miyamoto, I.; Cvecek, K.; Okada, A.; Takahashi, K.; Schmidt, M. Evaluation of Molten Zone in Micro-welding of Glass by Picosecond Pulsed Laser. *JLMN J. Laser Micro Nanoeng.* **2013**, *8*, 65–69. [CrossRef]
3. Plat, K.; von Witzendorff, P.; Suttmann, O.; Overmeyer, L. Process strategy for drilling of chemically strengthened glass with picosecond laser radiation. *J. Laser Appl.* **2016**, *28*, 022201. [CrossRef]
4. Liu, Y.; Zhang, C.; Li, S.; Guo, C.; Wei, Z. Experimental Study of Micro ElectrochemicalDischarge Machining of Ultra-Clear Glass witha Rotating Helical Tool. *Processes* **2019**, *7*, 195. [CrossRef]
5. Axinte, E. Glasses as engineering materials: A review. *Mater. Des.* **2011**, *32*, 1717–1732. [CrossRef]
6. Nisar, S.; Li, L.; Sheikh, M.A. Laser glass cutting techniques—A review. *J. Laser Appl.* **2013**, *25*, 042010. [CrossRef]
7. Sun, M.; Eppelt, U.; Russ, S.; Hartmann, C.; Siebert, C.; Zhu, J.; Schulz, W. Numerical analysis of laser ablation and damage in glass with multiple picosecond laser pulses. *Opt. Express* **2013**, *21*, 7858–7867. [CrossRef]
8. Yan, Y.; Ji, L.; Bao, Y.; Chen, X.; Jiang, Y. CO_2 laser high-speed crack-free cutting of thick-section alumina based on close-piercing lapping technique. *Int. J. Adv. Manuf. Technol.* **2013**, *64*, 1611–1624. [CrossRef]
9. Shin, H.; Kim, D. Strength of ultra-thin glass cut by internal scribing using a femtosecond Bessel beam. *Opt. Laser Technol.* **2020**, *129*, 106307. [CrossRef]
10. Kumkar, M.; Bauer, L.; Russ, S.; Wendel, M.; Kleiner, J.; Grossmann, D.; Bergner, K.; Nolte, S. *Comparison of Different Processes for Separation of Glass and Crystals Using Ultrashort Pulsed Lasers*; SPIE: Bellingham, WA, USA, 2014; Volume 8972.
11. Gečys, P.; Dudutis, J.; Račiukaitis, G. Nanosecond Laser Processing of Soda-Lime Glass. *J. Laser Micro Nanoeng.* **2015**, *10*, 254–258. [CrossRef]

12. Dudutis, J.; Stonys, R.; Račiukaitis, G.; Gečys, P. Glass dicing with elliptical Bessel beam. *Opt. Laser Technol.* **2019**, *111*, 331–337. [CrossRef]
13. Shin, J. Investigation of the surface morphology in glass scribing with a UV picosecond laser. *Opt. Laser Technol.* **2019**, *111*, 307–314. [CrossRef]
14. Tamura, A.; Kiyokawa, S.; Nakamura, Y.; Fushinobu, K. Picosecond laser ablation on glass using wavelength of 1064, 532, and 355 nm. *Opt. Eng.* **2020**, *59*, 075102. [CrossRef]
15. Sun, M.; Eppelt, U.; Hartmann, C.; Schulz, W.; Zhu, J.; Lin, Z. Damage morphology and mechanism in ablation cutting of thin glass sheets with picosecond pulsed lasers. *Opt. Laser Technol.* **2016**, *80*, 227–236. [CrossRef]
16. Markauskas, E.; Zubauskas, L.; Gečys, P. Efficient milling and cutting of borosilicate glasses through a thin flowing water film with a picosecond laser. *J. Manuf. Process.* **2021**, *68*, 898–909. [CrossRef]
17. Dudutis, J.; Zubauskas, L.; Daknys, E.; Markauskas, E.; Gvozdaitė, R.; Račiukaitis, G.; Gečys, P. Quality and flexural strength of laser-cut glass: Classical top-down ablation versus water-assisted and bottom-up machining. *Opt. Express* **2022**, *30*, 4564–4582. [CrossRef]
18. Markauskas, E.; Gečys, P. Thin water film assisted glass ablation with a picosecond laser. *Procedia CIRP* **2018**, *74*, 328–332. [CrossRef]
19. Tangwarodomnukun, V.; Wuttisarn, T. Evolution of milled cavity in the multiple laser scans of titanium alloy under a flowing water layer. *Int. J. Adv. Manuf. Technol.* **2017**, *92*, 293–302. [CrossRef]
20. Charee, W.; Tangwarodomnukun, V.; Dumkum, C. Laser ablation of silicon in water under different flow rates. *Int. J. Adv. Manuf. Technol.* **2015**, *78*, 19–29. [CrossRef]
21. Wee, L.M.; Ng, E.Y.K.; Prathama, A.H.; Zheng, H. Micro-machining of silicon wafer in air and under water. *Opt. Laser Technol.* **2011**, *43*, 62–71. [CrossRef]
22. Garcia-Giron, A.; Sola, D.; Peña, J.I. Liquid-assisted laser ablation of advanced ceramics and glass-ceramic materials. *Appl. Surf. Sci.* **2016**, *363*, 548–554. [CrossRef]
23. Kang, H.W.; Lee, H.; Chen, S.; Welch, A.J. Enhancement of bovine bone ablation assisted by a transparent liquid Layer on a target surface. *IEEE J. Quantum Electron.* **2006**, *42*, 633–642. [CrossRef]
24. Parmar, M.; James, S. Experimental and Modeling Study of Liquid-Assisted—Laser Beam Micromachining of Smart Ceramic Materials. *J. Manuf. Mater. Process.* **2018**, *2*, 28. [CrossRef]
25. Ma, Z.; Lu, M.; Wang, W.; Hong, Z.; Chen, Z.; Zhang, W.; Pan, S.; Shui, L.; Zhang, C. Sucrose solution assisted femtosecond laser ablation of aluminum film to induce nanospikes for efficient and stable oil-water separation. *Surf. Coat. Technol.* **2021**, *417*, 127182. [CrossRef]
26. Chen, Q.; Wang, H.J.; Lin, D.T.; Zuo, F.; Zhao, Z.X.; Lin, H.T. Characterization of hole taper in laser drilling of silicon nitride ceramic under water. *Ceram. Int.* **2018**, *44*, 13449–13452. [CrossRef]
27. Tsai, C.-H.; Li, C.-C. Investigation of underwater laser drilling for brittle substrates. *J. Mater. Process. Technol.* **2009**, *209*, 2838–2846. [CrossRef]
28. Zhou, J.; Huang, Y.X.; Zhao, Y.W.; Jiao, H.; Liu, Q.Y.; Long, Y.H. Study on water-assisted laser ablation mechanism based on water layer characteristics. *Opt. Commun.* **2019**, *450*, 112–121. [CrossRef]
29. Butkus, S.; Gaižauskas, E.; Mačernytė, L.; Jukna, V.; Paipulas, D.; Sirutkaitis, V. Femtosecond Beam Transformation Effects in Water, Enabling Increased Throughput Micromachining in Transparent Materials. *Appl. Sci.* **2019**, *9*, 2405. [CrossRef]
30. Butkus, S.; Alesenkov, A.; Paipulas, D.; Gaižauskas, E.; Melninkaitis, A.; Kaškelytė, D.; Barkauskas, M.; Sirutkaitis, V. Analysis of the Micromachining Process of Dielectric and Metallic Substrates Immersed in Water with Femtosecond Pulses. *Micromachines* **2015**, *6*, 2010–2022. [CrossRef]
31. Wee, L.M.; Khoong, L.E.; Tan, C.W.; Lim, G.C. Solvent-Assisted Laser Drilling of Silicon Carbide. *Int. J. Appl. Ceram. Technol.* **2011**, *8*, 1263–1276. [CrossRef]
32. Butkus, S.; Paipulas, D.; Sirutkaitis, R.; Gaizauskas, E.; Sirutkaitis, V. Rapid Cutting and Drilling of Transparent Materials via Femtosecond Laser Filamentation. *JLMN J. Laser Micro Nanoeng.* **2014**, *9*, 213–220. [CrossRef]
33. Sun, D.; Han, F.; Ying, W. The experimental investigation of water jet–guided laser cutting of CFRP. *Int. J. Adv. Manuf. Technol.* **2019**, *102*, 719–729. [CrossRef]
34. Mullick, S.; Madhukar, Y.K.; Roy, S.; Nath, A.K. Performance optimization of water-jet assisted underwater laser cutting of AISI 304 stainless steel sheet. *Opt. Lasers Eng.* **2016**, *83*, 32–47. [CrossRef]
35. Tangwarodomnukun, V.; Wang, J.; Mathew, P. A Comparison of Dry and Underwater Laser Micromachining of Silicon Substrates. *Key Eng. Mater.* **2010**, *443*, 693–698. [CrossRef]
36. Kruusing, A. Underwater and water-assisted laser processing: Part 1—General features, steam cleaning and shock processing. *Opt. Lasers Eng.* **2004**, *41*, 307–327. [CrossRef]
37. Liu, J.M. Simple technique for measurements of pulsed Gaussian-beam spot sizes. *Opt. Lett.* **1982**, *7*, 196–198. [CrossRef]
38. Zhao, L.; Maynadier, A.; Nelias, D. Stiffness and fracture analysis of photovoltaic grade silicon plates. *Int. J. Solids Struct.* **2016**, *97–98*, 355–369. [CrossRef]
39. Fuegl, M.; Mackh, G.; Meissner, E.; Frey, L. Analytical stress characterization after different chip separation methods. *Microelectron. Reliab.* **2014**, *54*, 1735–1740. [CrossRef]

40. Przybilla, C.; Fernández-Canteli, A.; Castillo, E. An iterative method to obtain the specimen-independent three-parameter Weibull distribution of strength from bending tests. *Procedia Eng.* **2011**, *10*, 1414–1419. [CrossRef]
41. Khalili, K.; Kromp, K. Statistical Properties of Weibull estimators. *J. Mater. Sci.* **1991**, *26*, 6741–6752. [CrossRef]
42. Bergman, B. On the estimation of the Weibull modulus. *J. Matter. Sci. Lett.* **1984**, *3*, 689–692. [CrossRef]
43. Martan, J.; Prokešová, L.; Moskal, D.; de Faria, B.F.; Honner, M.; Lang, V. Heat accumulation temperature measurement in ultrashort pulse laser micromachining. *Int. J. Heat Mass Transf.* **2021**, *168*, 120866. [CrossRef]
44. Guarino, S.; Ponticelli, G.S.; Giannini, O.; Genna, S.; Trovalusci, F. Laser milling of yttria-stabilized zirconia by using a Q-switched Yb:YAG fiber laser: Experimental analysis. *Int. J. Adv. Manuf. Technol.* **2018**, *94*, 1373–1385. [CrossRef]
45. Leone, C.; Genna, S.; Tagliaferri, F. Multiobjective optimisation of nanosecond fiber laser milling of 2024 T3 aluminium alloy. *J. Manuf. Process.* **2020**, *57*, 288–301. [CrossRef]
46. Žemaitis, A.; Gaidys, M.; Gečys, P.; Račiukaitis, G.; Gedvilas, M. Rapid high-quality 3D micro-machining by optimised efficient ultrashort laser ablation. *Opt. Lasers Eng.* **2019**, *114*, 83–89. [CrossRef]
47. Wu, B.; Liu, P.; Zhang, F.; Duan, J.; Wang, X.; Zeng, X. Effect of parameters on picosecond laser ablation of Cr12MoV cold work mold steel. *Appl. Phys. A* **2017**, *124*, 11. [CrossRef]
48. Wang, H.; Zhao, K.; Shen, H.; Yao, Z. Experimental study on direct fabrication of micro channel on fused silica by picosecond laser. *J. Manuf. Process.* **2020**, *55*, 87–95. [CrossRef]
49. Guo, Z.; Guo, B.; Zhao, Q.; Liu, W.; Zheng, Q. Optimisation of spray-mist-assisted laser machining of micro-structures on CVD diamond coating surfaces. *Ceram. Int.* **2021**, *47*, 22108–22120. [CrossRef]
50. Charee, W.; Tangwarodomnukun, V. Dynamic features of bubble induced by a nanosecond pulse laser in still and flowing water. *Opt. Laser Technol.* **2018**, *100*, 230–243. [CrossRef]
51. Supponen, O.; Obreschkow, D.; Tinguely, M.; Kobel, P.; Dorsaz, N.; Farhat, M. Scaling laws for jets of single cavitation bubbles. *J. Fluid Mech.* **2016**, *802*, 263–293. [CrossRef]
52. Adelmann, B.; Hellmann, R. Investigation on Flexural Strength Changes of Alumina Caused by Cutting using Fiber Laser. *JLMN J. Laser Micro Nanoeng.* **2014**, *9*, 153–160. [CrossRef]
53. Shin, H.; Kim, D. Cutting thin glass by femtosecond laser ablation. *Opt. Laser Technol.* **2018**, *102*, 1–11. [CrossRef]
54. Indrišiūnas, S.; Svirplys, E.; Jorudas, J.; Kašalynas, I. Laser Processing of Transparent Wafers with a AlGaN/GaN Heterostructures and High-Electron Mobility Devices on a Backside. *Micromachines* **2021**, *12*, 407. [CrossRef] [PubMed]
55. Sun, X.; Zheng, J.; Liang, C.; Hu, Y.; Zhong, H.; Duan, J. Improvement of rear damage of thin fused silica by liquid-assisted femtosecond laser cutting. *Appl. Phys. A* **2019**, *125*, 1–8. [CrossRef]
56. Collins, A.; Rostohar, D.; Prieto, C.; Chan, Y.K.; O'Connor, G.M. Laser scribing of thin dielectrics with polarised ultrashort pulses. *Opt. Lasers Eng.* **2014**, *60*, 18–24. [CrossRef]
57. Lu, J.; Xu, R.Q.; Chen, X.; Shen, Z.H.; Ni, X.W.; Zhang, S.Y.; Gao, C.M. Mechanisms of laser drilling of metal plates underwater. *J. Appl. Phys.* **2004**, *95*, 3890–3894. [CrossRef]
58. Yilbas, B.S.; Akhtar, S.S.; Karatas, C. Laser straight cutting of alumina tiles: Thermal stress analysis. *Int. J. Adv. Manuf. Technol.* **2012**, *58*, 1019–1030. [CrossRef]

micromachines

MDPI

Article

Experimental Study on Texture Coupling Mechanism and Antifriction Performance of Piston Rod Seal Pair

Jie Tang, Jie Zeng * and Xin Lu *

School of Aeronautical Engineering, Civil Aviation University of China, Tianjin 300300, China; jtang@cauc.edu.cn
* Correspondence: 2020011002@cauc.edu.cn (J.Z.); luzhougong@tju.edu.cn (X.L.)

Abstract: The effect of the coupling texture on the friction and wear of a piston rod-rubber seal pair under lubricating conditions is studied in this paper. Crescentiform textures with different area densities were fabricated on high carbon chromium bearing steel (GCr15) and ethylene propylene diene monomer (EPDM) materials by using a laser marking machine. We compare and analyze the effects of untextured, single-textured, and coupling-textured surfaces on the friction characteristics of the piston rod-rubber seal pair by conducting tests on the reciprocating module of the UMT-2 friction and wear testing machine. The results showed that the coupling-textured surface had the lowest coefficient of friction and wear compared to the untextured and single-textured surfaces. When the normal load was 10 N under the optimal coupling texture area density (6.4%), the friction and wear of the sealing pair decreased the most. Compared with the untextured surface, the friction coefficient was reduced by 27.9% and the wear amount was reduced by 30.0%; compared with the single-textured surface, the friction coefficient was reduced by 18.9%, and the wear amount was reduced by 23.8%. The coupling effect generated by the coupling texture effectively enhanced the formation and stabilization of the oil lubricant film and effectively captured wear debris, preventing it from continuously scratching the surface and reducing wear and roughness.

Keywords: surface texture; high carbon chromium bearing steel (GCr15); ethylene propylene diene monomer (EPDM); friction; wear morphology; coupling

Citation: Tang, J.; Zeng, J.; Lu, X. Experimental Study on Texture Coupling Mechanism and Antifriction Performance of Piston Rod Seal Pair. *Micromachines* **2022**, *13*, 722. https://doi.org/10.3390/mi13050722

Academic Editors: Jiang Guo, Chunjin Wang and Chengwei Kang

Received: 28 March 2022
Accepted: 29 April 2022
Published: 30 April 2022

1. Introduction

A hydraulic cylinder is the executive component of an aircraft hydraulic system, and its internal piston rod sealing pair is a metal-rubber sealing pair, which is prone to wear failure under the combined action of hydraulic oil pressure, temperature, and viscosity, resulting in leakage; this affects the servo of the main rudder surface of the aircraft and, thus, the reliability and safety of the hydraulic system [1]. Therefore, the problem of how to further improve the lubricating properties of the metal–rubber sealing pair to reduce the wear of the piston rod needs to be solved urgently.

As a technology that can effectively improve the surface friction performance of oil-lubricated friction pairs, surface texture can effectively improve the wear of piston rod seal pairs [2,3]. Nowadays, there are various ways to process micro-texture structures. According to different mechanism categories, there are two main categories of ways to process micro-texture structures: one is the micro-texture processing technique based on material removal, and the other is the dimple texture processing technology that plastically deforms the material. The techniques of micro-texture processing based on material removal include electrolytic processing techniques [4–7], micro-electro-discharge machining [8–11], abrasive air-jet technology [12–14], and laser surface micromachining technology [15–17]. Plastic deformation technology of materials refers to the processing of micro-texture structures by applying a load to the base material that exceeds the range of elastic deformation under the action of an external force. Such processing techniques include conventional vibration-impact processing techniques [18–20], ultrasonic vibration machining techniques [21,22],

embossing techniques [23], and laser shocking techniques [24–28]. Currently, laser surface micromachining techniques and electrolytic processing techniques are the mainstream texture processing techniques.

The mechanisms by which surface texture improves the tribological properties of materials include three main aspects: the ability to store lubricant under fluid lubrication conditions, improving lubrication conditions; the generation of hydrodynamic effect, increasing load-bearing capacity; and the storage of fine abrasive dust, reducing abrasive dust scratching. The morphology of the texture, geometrical parameters, and specific working conditions are the main parameters that influence the surface tribological properties [29]. Liao et al. [30,31] analyzed the influence mechanism of surface texture size parameters on the tribological properties of metal–rubber seal pairs by combining simulation and tribological experiments. The results showed that under the same conditions, the larger the working pressure and the larger the texture diameter, the greater the elastic deformation of the nitrile rubber and the better the tribological properties when the texture diameter was less than 300 μm. Wang's team [32–34] showed that a surface texture with reasonable size parameters and arrangement could effectively reduce the friction and wear of metal–rubber sealing pairs; some surface texture samples exhibited better parameter combinations, where the friction coefficient, temperature increase, and wear could be reduced by more than 30%. Jiang et al. [35] used a ball-disk friction tester to study the lubrication characteristics of micro-pit PDMS friction pairs made by photolithography-complex mold technology. The results showed that under low-speed conditions, a smaller-diameter texture in the mixed-lubrication region could reduce friction, and the larger the area ratio of the pits in the experimental range, the more obvious the effect. He et al. [36] analyzed the tribological properties of textured metal and rubber specimens through experiments and showed that a reasonable texture combination and distribution could effectively improve the tribological properties of metal–rubber sealing pairs. Li et al. [37] designed a crescentiform surface texture and compared the optimization of water film carrying capacity and friction-reducing property for different rotational speeds and loads and different texture sizes by simulation. The results showed that the crescentiform surface texture of model CC1006 had the best-integrated optimization of water film carrying capacity and friction reduction performance. Tang et al. [38] redesigned the crescentiform surface texture and investigated the tribological properties of ethylene propylene diene monomer (EPDM) rubber under different loading conditions, and the results showed that under low loading conditions, the crescentiform surface texture can effectively reduce the friction coefficient of the friction pair and reduce corrosive wear and adhesive wear. Miao et al. [39,40] compared the friction performance of cylinder liner and piston ring (metal–metal seal) with single texture and coupling texture. Compared with single texture, the friction performance of coupling texture is better; the surface of the texture is easier to generate a stable oil film, which can enhance the ability to collect abrasive chips to prevent abrasive chips from scratching the surface and play a role in reducing friction.

At this stage, only the coupling effect of simultaneous texture in metal–metal seals has been studied, However, most studies on the texture of metal–rubber seals have focused on both as separate objects, exploring the effect of texture on its overall surface properties, respectively. The research involving the coupling effect of the simultaneous texturing of the two is relatively lacking. Therefore, this paper uses the reciprocating module of a UMT-2 friction and wear testing machine to compare the friction performances of the coupling-textured, untextured, and single-textured surfaces of a piston rod–rubber seal pair and analyze the coupling mechanism.

2. Experiments

2.1. Specimen Design

Figure 1 shows a schematic diagram of the piston rod sealing system. Under the action of hydraulic pressure, the piston rod and the rubber ring undergo reciprocating relative sliding, thereby converting hydraulic energy into mechanical energy. In order to simulate

the reciprocating motion and working parameters of the piston rod and the rubber ring, the reciprocating module of a UMT-2 friction and wear testing machine was used. The upper sample was a pin that was made of high carbon chromium-bearing steel (GCr15), with a diameter of 3.6 mm and a height of 20 mm; the average surface roughness Ra measured after polishing is 0.2 μm. The lower sample was a disc made of EPDM material with a diameter of 24 mm, a thickness of 8 mm, and an elastic modulus of 7.8 MPa.

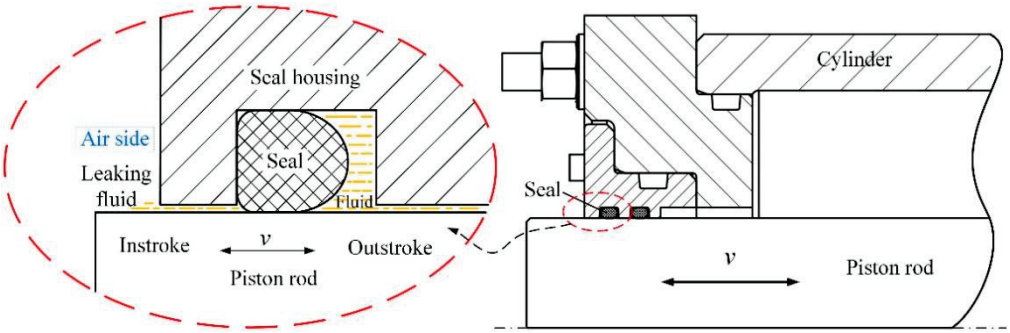

Figure 1. Schematic diagram of the piston rod sealing system.

The crescentiform texture possesses good tribological properties with the advantages of both groove-shaped texture and discrete pit texture (refer to [36,41]). Figure 2a shows the 3D morphology of the crescentiform texture prepared by Cui et al. [41]. It can be seen that the crescentiform texture is more complex in shape, more difficult to process, and more costly for practical applications. Therefore, Tang et al. [38] simplified the crescentiform texture; the newly designed crescentiform texture consists of two concentric arcs, as shown in Figure 2b. The three-dimensional map and size map of the crescentiform texture in this paper are shown in Figure 2c,d, with an outer diameter of 200 μm and an inner diameter of 120 μm. The opening angle of the crescentiform pattern is $\beta = 60°$, and the area is $S_t = 0.1675$ mm^2 [38]. In order to obtain coupling textures with different domain densities, the texture spacing was changed while keeping the texture size constant. The area density of the texture is defined as the ratio of the area covered by the crescentiform texture to the area covered by the dummy cells, which is calculated as follows:

$$\alpha = \frac{S_t}{S} = \frac{0.1675}{l^2} \tag{1}$$

where α is the area density of the texture, S_t is the area covered by the texture, S is the area covered by the cell, and l is the interval between the textures. To investigate the effect of coupling textures, texture patterns of different arrays were prepared by varying the texture area density of the GCr15 metal and EPDM rubber. The detailed texture pattern array parameters are shown in Table 1.

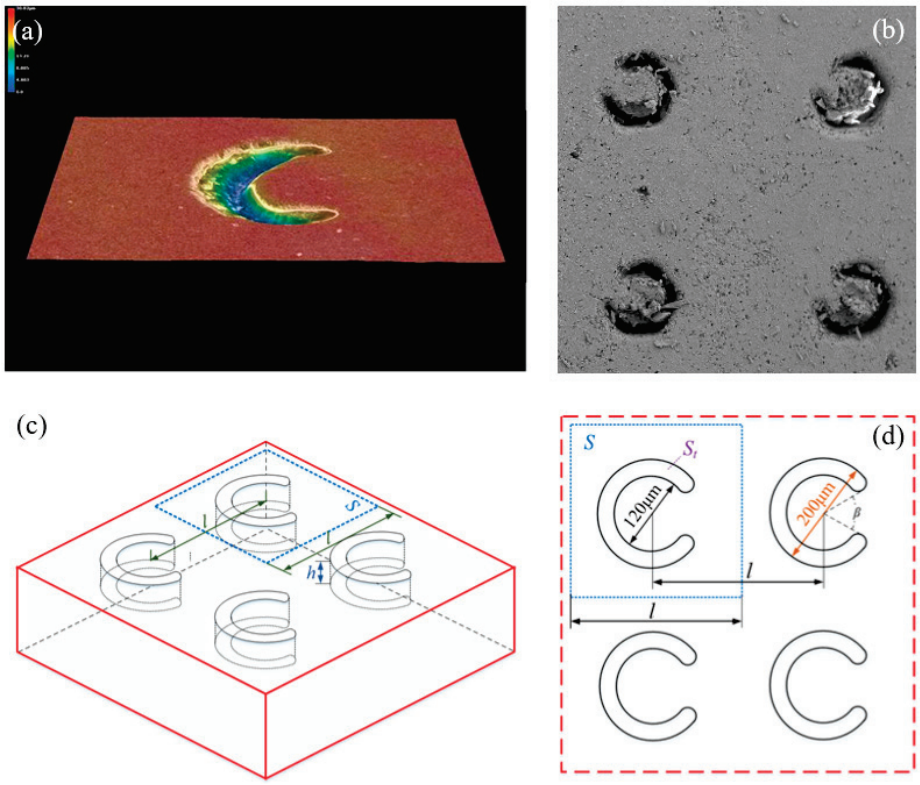

Figure 2. Schematic diagram of the crescentiform surface: (**a**) the crescentiform surface prepared by Cui et al., (**b**) the crescentiform surface prepared by Tang et al., (**c**) the three-dimensional schematic diagram of the crescentiform surface in this experiment, and (**d**) the crescentiform surface dimensions.

Table 1. Parameters for the array of textured pattern.

Parameters	Coupling Texture Area Density α	Texture Height h
for all samples	6.4%, 12.8%, 19.2%, 25.6%, 32.0%	5 μm

The coupling texture is a synergistic texture produced by the simultaneous texture of the two materials of the sealing pair. Therefore, a laser marker with a power of 75 W, a pulse frequency of 20 kHz, and a pulse width of 100 ns were used to process a crescentiform surface texture on the end face of the GCr15 pin; and a 50-W laser marker was used to process a crescentiform texture on the end face of the EPDM rubber. We washed and dried the test specimen with alcohol before texture processing. After processing, the texture heights at different positions were measured by a non-contact three-dimensional microscope, and the average value was calculated. Figure 3 shows the three-dimensional topography of the texture distribution on the surfaces of the GCr15 pin and the EPDM rubber.

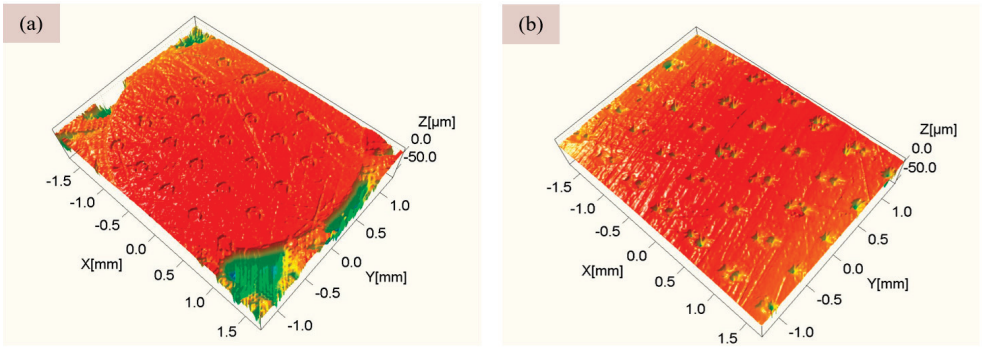

Figure 3. Three-dimensional topography of surface textures of the carbon chromium bearing steel (GCr15) pin and ethylene propylene diene monomer (EPDM) rubber: (**a**) GCr15 pin surface with a texture area density of 6.4%; (**b**) EPDM rubber surface with a texture area density of 6.4%.

2.2. Test Content

All tests were performed using the reciprocating module of a UMT-2 friction and wear testing machine, as shown in Figure 4. Before testing, the GCr15 metal material was lightly polished, and the GCr15 metal pins and EPDM rubber surfaces were cleaned with alcohol to remove dirt particles and then dried. The lower sample was fixed, and the upper sample moved back and forth via a motor. Test loads ranged from 10 to 40 N in 10 N increments. Since the normal movement speed of a hydraulic cylinder with rubber seals is 0.1–0.5 m/s [42], a movement speed of 0.4 m/s was selected. The movement amplitude was 10 mm, the frequency was 20 Hz, and the reciprocating friction test was carried out for 40 min [38]. All tests were carried out under lubricated conditions at room temperature (30 ± 2 °C). In order to provide sufficient lubricating conditions at the piston rod sealing interface, Castrol Magnetic Protection 0w-20 Oil was used; the lubricating oil was continuously supplied at a time interval of 5 s (12 drops per min) at the inlet area of the piston rod sealing contact. The normal load is set to 10, 20, 30, and 40 N (corresponding contact pressure is 1, 2, 3, and 4 MPa) [30]; the detailed test conditions are shown in Table 2.

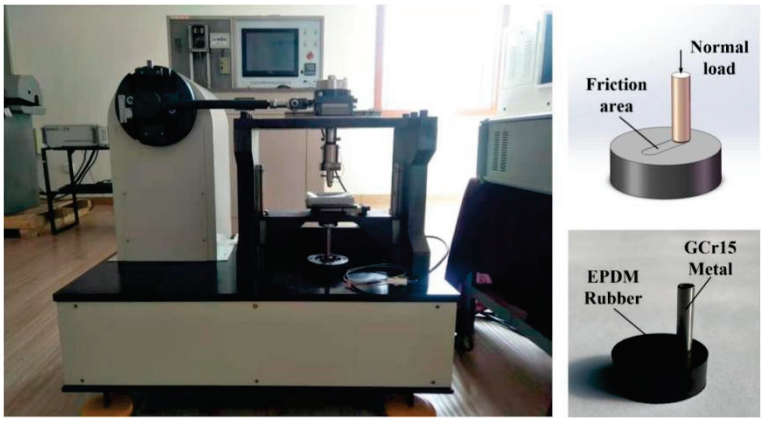

Figure 4. UMT-2 reciprocating test device.

Table 2. Friction test conditions.

Specification	Value
Normal load	10 N, 20 N, 30 N and 40 N
Speed	0.40 m/s
Lubricant	Castrol Magnetic Protection 0w-20 Oil
Displacement amplitude	10 mm
Room temperature	30 ± 2 °C

The normal load and friction force were measured by the *Z*-axis and *XY*-axis force sensors, respectively. After each test, the friction coefficient and wear amount of the EPDM sample were calculated using Equations (2) and (3). Each test was carried out three times, and the average values of the friction coefficient and wear amount were taken to ensure the accuracy of the test. The EPDM samples were sprayed with gold, and the sampling range was 0.8 × 0.8 mm. The wear scars and wear debris were observed by FE-SEM. The distribution of elements on the surface of the GCr15 metal after the test was measured by EDS.

$$Friction\ coefficient = \frac{F_f}{F_n} \tag{2}$$

$$Abrasion = W_b - W_a \tag{3}$$

where F_f is the friction force, F_n is the normal load, W_b is the weight of the EPDM sample before the test, and W_a is the weight of the EPDM sample after the test.

In order to verify the test method in this paper, single-textured specimens with a rubber surface texture area rate of 6.4% were selected for frictional wear tests under different contact pressure conditions, and the variation curve of friction coefficient with contact pressure was obtained and compared with the test data reported in the literature [38]; the comparison graph is shown in Figure 5. The "Single texture-Rubber" data in the figure is the test data of the textured sample only on the rubber. Under the same experimental conditions, the two sets of experimental data agreed well.

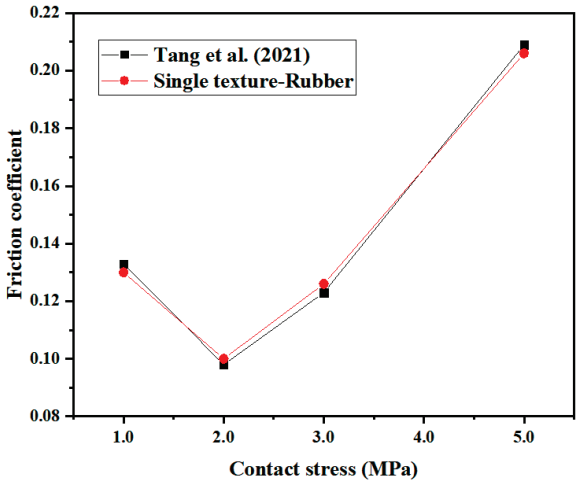

Figure 5. Comparison of the influence of the crescentiform texture on the friction coefficient under different contact pressures.

3. Results and Discussion

3.1. Effect of normal load

The effect of normal load on friction and wear behavior was investigated. Figure 6 shows the experimental results of the friction behavior of the piston rod seal specimens under different normal loads in the range of 10–40 N, a texture depth of 5 μm, and a sliding speed of 0.4 m/s. A textured area density of zero represents an untextured sample. As the normal load increased from 10 to 40 N, the friction coefficient of the coupling-textured sample increased gradually. This is because the larger the normal load is, the more the volume of rubber in the untextured area is pressed into the texture of the metal dimples. Then, the scraping and cutting effect is more obvious during the reciprocating motion of the rubber, and stress concentration occurs at the edge of the rubber texture, which leads to aggravated wear of the rubber texture edge, increases the surface roughness of the specimen, and then leads to an increase in the friction coefficient. The friction coefficient of the untextured specimen has a slowly decreasing trend, and the laser surface texture pattern in the literature [38] also has a similar trend. Compared with the untextured specimen,

when the normal load was less than 20 N, the friction coefficient of the coupling-textured specimen decreased significantly, while under a normal load greater than 20 N, it increased significantly. The minimum coefficient of friction was obtained on a textured array with a normal load of 10 N and a coupling texture area density of 6.4%. At lower normal loads (i.e., less than 20 N), the friction coefficient of the coupling texture sample decreased by 27.9% compared to the untextured specimen. Figure 7 shows the variation of the wear amount of samples with coupling texture area densities under different normal loads. It can be seen that when the area density of the coupling texture was in the range of 6.4–25.6%, the wear amount and friction coefficient of the sample had a similar trend with the normal load, and the wear amount increased with increasing normal load. When the normal load is 40 N, the wear amount is the largest. This is due to the increased wear caused by stress concentration at the edge of the texture; a large amount of wear debris is generated, which exceeds the wear debris capture ability of the coupling texture, causing the large wear debris to continue to damage the surface. This, in turn, leads to increased wear. The wear amount of the untextured specimen increased gradually with increasing normal load. Among all coupling textured arrays, the specimens under a normal load of 10 N had the lowest wear. When the coupling texture area density was 6.4% and the normal load was 10 N, the wear amount decreased by as much as 30.0% compared with the untextured specimen.

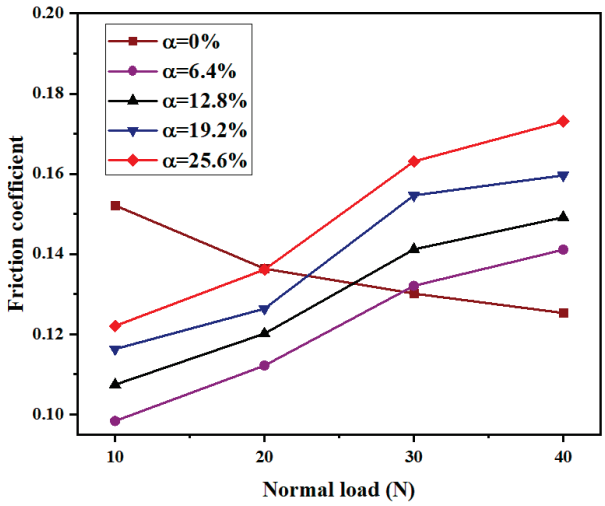

Figure 6. Variation of friction coefficient with normal load.

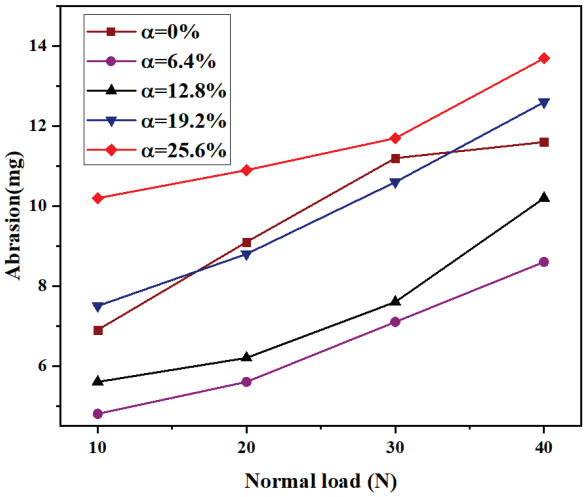

Figure 7. Variation of abrasion with normal load.

3.2. Effect of Coupling Texture Area Density

The effect of different texture area densities on the friction and wear properties of the coupling-textured and single-textured samples under a normal load of 10 N was investigated by changing the texture spacing without changing the texture size or height. Figure 8 shows the variation curves of friction coefficient vs. the area density of the samples under a normal load of 10 N and a texture depth of 5 μm. In the figure, "Single texture-Metal" indicates that the texture was only on the GCr15 metal (i.e., the upper sample). The results show that the friction coefficient of the experimental group textured only on the metal increased with area density, and the friction coefficient was lowest when the areal density of the textured array was 6.4%. The friction coefficient of the test group textured only on the rubber decreased first and then increased with increasing area density. When the area density of the textured array was 12.8%, the friction coefficient decreased significantly. When the area density of the textured array was greater than 12.8%, the friction coefficient decreased. The friction coefficients were all smaller than those of the experimental group textured only on the metal, which is consistent with the research in the literature [43]. Under a normal load of 20 N, the friction coefficient of the coupling-textured specimens increased with area density, and the friction coefficient was the smallest when the area density of the textured array was 6.4%. Compared with the single-textured samples, the friction coefficients of the coupling-textured samples were significantly reduced, with a maximum reduction of 18.9%. It can be seen that the coupling texture plays a positive role in the reduction of the friction coefficient, which is due to the coupling texture that enhances the replenishment of the oil film on the contact surface; the dynamic pressure effect is more obvious so that the friction coefficient is reduced. However, the increase of the area density of the coupling texture will reduce the bearing area, increase the specific pressure, and increase the friction coefficient, so that the friction coefficient increases with the increase of the area density. Figure 9 shows the variation curve of the wear amount vs. the area density of the sample with a texture depth of 5 μm under a normal load of 10 N. The variation trends of the wear amount and friction coefficient of the sample vs. texture area density were similar. The wear amount of the coupling texture increased with the increase in the area density of the textured array. When the normal load was 10 N, the area density was 6.4%, and the structural array experienced the least amount of wear. Compared with the single-textured samples, the wear of the coupling-textured samples all decreased, with a maximum decrease of 23.8%. This showed that under certain conditions, the effect of a coupling texture on wear reduction was more significant than that of a single texture.

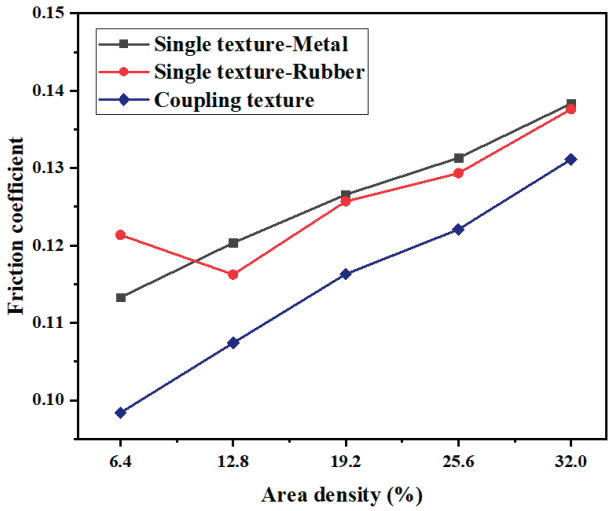

Figure 8. Variation of friction coefficient with area density.

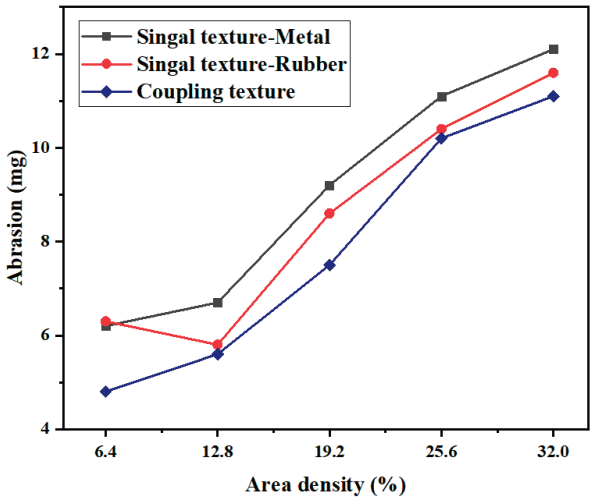

Figure 9. Variation of abrasion with area density.

3.3. Analysis of Wear Morphology

Figure 10 shows the typical morphologies of the worn surfaces of the EPDM materials under a normal load of 10 N. Figure 10a shows the worn surface of the EPDM material under the untextured condition, where rubber-specific pattern wear marks appeared on the surface of the sample. The overall pattern was relatively flat and regular. The wear debris adhered during the friction process acts as a solid lubricating layer in the friction pair and is discharged from the friction area during the subsequent friction process. Thus, uniform friction is achieved. Figure 10b shows the worn surface of the EPDM material is only on the surface of the GCr15 metal, and the texture area density is 6.4%. A large number of small corrosion pits were distributed on the surface of the material, mainly because the hydraulic oil eroded the surface of the EPDM material during the friction process, which is a typical manifestation of corrosion wear. The surface of the material had obvious flake peeling, indicating that adhesive wear had occurred during the friction process. There was a large amount of wear debris on the surface of the EPDM material, and there was a large amount of wear debris. This was because the texture on the surface of the GCr15 metal only collected part of the wear debris, indicating that the ability of the single texture to collect and store wear debris was limited. Figure 10c shows the worn surface of the EPDM material under the condition that only the EPDM rubber surface was textured, with a texture area density of 6.4%. There was wear on the textured edge, as well as crescent-shaped protrusions in the vertical direction, indicating that adhesive wear mainly occurred during the grinding process. Furthermore, there was more wear debris on the textured edge and the untextured area. Thus, the wear debris was not completely stored in the texture, and larger debris could further damage the surface. Figure 10d shows the worn surface of the EPDM material under the coupling texture treatment, with a texture area density of 6.4%. It can be seen that there was no obvious wear on the textured surface, and only a small amount of wear scars and small corrosion pits appeared in the untextured area. The wear mechanism was mainly corrosion wear. The wear debris was mainly concentrated in the texture, and there was basically no wear debris in the untextured area. This was because the coupling effect improved the ability of the texture to collect and store the wear debris, which effectively prevented large wear debris from damaging the surface.

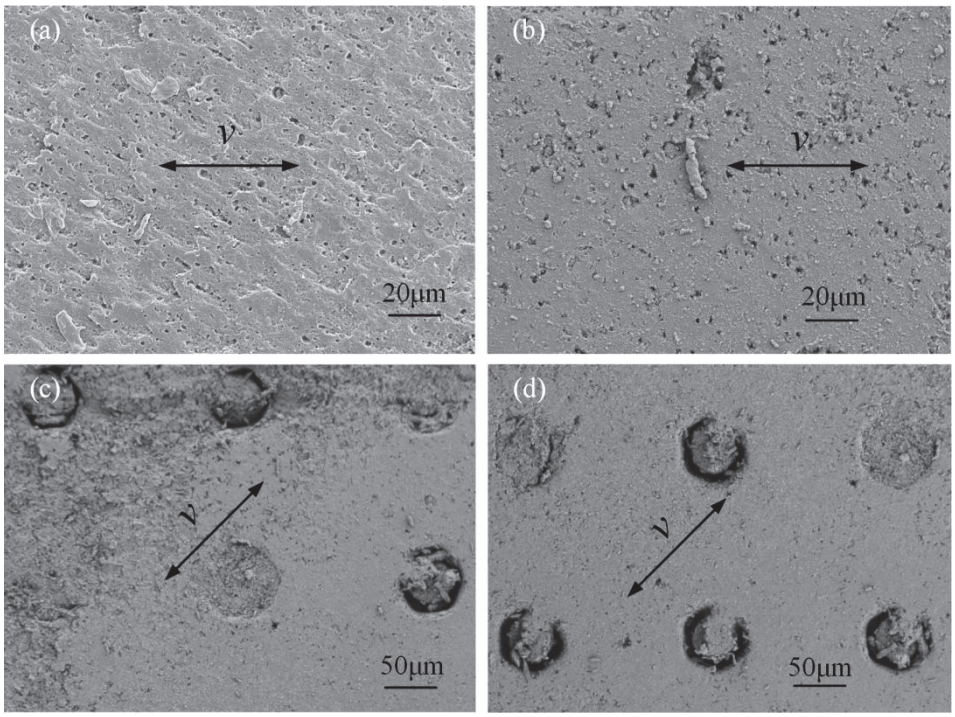

Figure 10. Surface topography of EPDM material after abrasion under conditions of (**a**) untextured, (**b**) single texture on GCr15 metal, (**c**) single texture on EPDM rubber, and (**d**) coupling texture parameters.

3.4. Morphology Analysis of Wear Debris

Wear debris can reflect the characteristics of the friction pair system and is an important information carrier. The analysis of wear debris can map the wear characteristics of a friction pair surface [44]. Figure 11a shows the wear debris morphology of the EPDM material of the untextured sample after wear under a normal load of 10 N. It can be seen that the main body of the wear debris was flake. It is generally believed that flake wear debris is the product of wear debris between friction pairs being rolled and ironed under the action of pressure, and its wear mechanism is mainly adhesive wear. Figure 11b shows the wear debris morphology of the EPDM material after wear under a coupling texture area density of 6.4% and a normal load of 10 N. Through observation, its overall size was slightly smaller than that of the other wear debris; it was peanut-shaped, and its surface was relatively smooth, which is typical of corrosion wear debris, where chemical reactions such as oxidative degradation and molecular bond breakage occur on the rubber surface. Under lower loads, the lubricating oil stored in the coupling texture could produce a good hydrodynamic pressure effect, and the oil film pressure and the normal load could be balanced, which could improve the formation and stability of the oil film. At the same time, the coupling texture had a good ability to collect and store wear debris, which avoided the continued damage from large wear debris, resulting in minimal surface wear. Figure 11c shows the wear debris morphology of the EPDM material after wear under a coupling texture area density of 32.0% and a normal load of 40 N. It can be seen that the wear debris under these conditions was strip-shaped, with obvious characteristics of cutting wear debris. Generally speaking, cutting wear particles are formed by the plowing of hard and sharp asperities on a softer wear surface [45]. Relevant studies [46] show that the introduction of surface texture will produce stress concentration at its edges, and when the normal load is large, significant bulges will occur, which may lead to the occurrence of micro-cutting. Here, the shape of the wear debris proved that under poor working conditions and coupling texture parameters, serious furrows and even cutting wear effects did indeed occur.

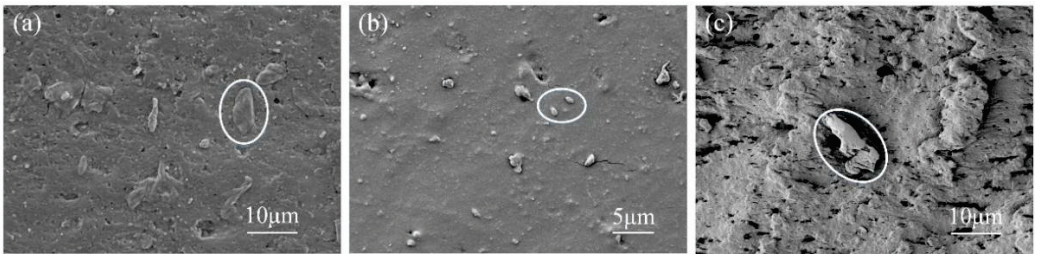

Figure 11. SEM images of wear debris of EPDM material: (**a**) morphology of wear debris of untextured samples; (**b**) wear debris topography with optimal coupling texture parameters; (**c**) wear debris topography with worst coupling texture parameters.

3.5. Energy Spectrum Analysis

Figure 12 presents electron microscope images and energy spectrum analyses of the GCr15 material under a normal load of 10 N for the untextured sample. Adhesive wear was indicated by dark flakes, and localized tears were featured along the sliding direction. From the energy spectra, it can be seen that the content of C and O elements on the surface of the GCr15 metal sample was relatively high, indicating that the polymer material had been transferred during the friction process. Figure 13 shows electron microscope images and energy spectrum analyses of the GCr15 material under a coupling texture area density of 6.4% and a normal load is 10 N. The wear surface around the dimples was smoother and less scratched. At this time, the content of C and O elements at the edge of the pit texture decreased compared with that of the untextured sample, indicating that the adhesion and transfer phenomenon of the polymer material was improved. Figure 14 shows electron microscope images and energy spectrum analyses of the GCr15 material under a coupling texture area density of 32.0% and a normal load of 40 N. There were many scratches on the surface of the sample, and serious wear occurred around the pit texture. The content of the C element at the edge of the pit texture was high, while that of O was low, indicating that during the grinding process, due to the stress concentration on the edge of the pit, the local high temperature made the EPDM material burn and degenerate, resulting in severe cutting wear, which was consistent with the results of the wear debris morphology analysis.

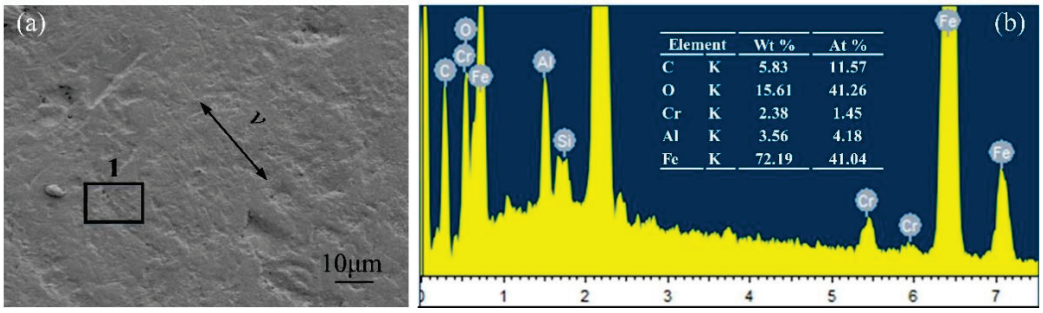

Figure 12. SEM images and EDS analysis of GCr15 metal surface after wear of untextured samples: (**a**) SEM image of untextured sample surface; (**b**) corresponding EDS analysis.

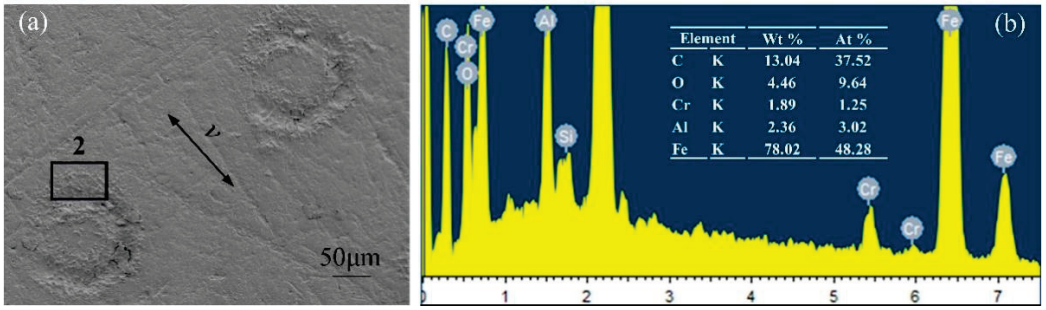

Figure 13. SEM images and EDS analysis of GCr15 metal surface under optimal coupling texture parameters: (**a**) SEM image of the sample surface with optimal coupling texture parameters; (**b**) corresponding EDS analysis.

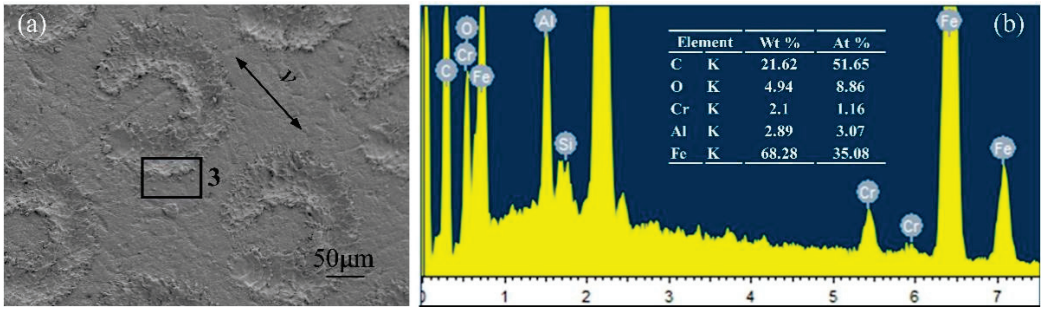

Figure 14. SEM images and EDS analysis of GCr15 metal surface under the worst coupling texture parameters: (**a**) SEM image of the sample surface with the worst coupling texture parameters; (**b**) corresponding EDS analysis.

3.6. Mechanism of Texture Coupling

The schematic diagram of the coupling texture mechanism (at the symmetry plane) is shown in Figure 15. Before the GCr15 metal dimple texture reached the EPDM rubber dimple texture, the lubricating oil stored in the EPDM rubber dimple texture formed an oil film on the untextured area. With the relative sliding of the friction pair, the GCr15 metal dimples collected the wear debris generated by part of the wear, which led to the weakening of the dynamic pressure effect in the dimple texture and a decrease in oil pressure. When the GCr15 metal dimple texture passed through the EPDM rubber dimple texture, the normal load extruded the lubricating oil from the EPDM rubber dimple, filling in the GCr15 metal dimple texture and replenishing the oil film. At the same time, the inside of the GCr15 metal dimple was pushed out. Part of the collected wear debris was flushed into the underlying rubber dimple texture, preventing the wear debris from continuing to damage the surface as the metal pin moved. When the GCr15 metal dimple texture left the EPDM rubber dimple texture, due to the lubricating oil supplemented by the EPDM rubber dimple texture, the lubricating oil in the GCr15 metal dimple texture enhanced the dynamic pressure effect and increased the maximum oil film bearing capacity. The reduction of wear debris in the metal pit texture also relatively enhanced its ability to capture new wear debris. Under the coupling effect of the metal dimple texture and the rubber dimple texture, the dynamic pressure effect inside the coupling texture increased, which increased the maximum pressure that the oil film could bear, forming a virtuous circle and improving the formation of the oil film on the contact surface during the entire friction process. After the coupling texture treatment discussed in Section 3.3, the distribution area of the wear debris on the worn surface of the EPDM material under an area density of 6.4% proved the wear debris capture mechanism of the coupling texture.

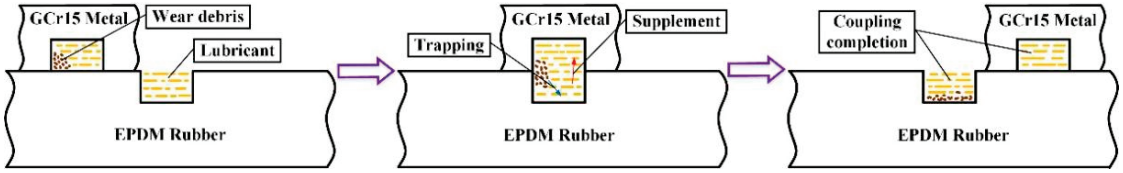

Figure 15. Action mechanism of coupling texture.

4. Conclusions

This paper presents the effects of coupling textures on the friction and wear of the piston rod–rubber seal pair under different normal loads; different texture area densities are introduced. We used a laser marker to create crescentiform textures on the surfaces of the two materials of the sealing pair and performed a reciprocating sliding test. The effects of untextured, single textured, and coupling textured surfaces on the friction characteristics of the piston rod–rubber seal pair were compared and analyzed. This study draws the following conclusions:

(1) The reduction in friction coefficient is inversely proportional to the normal load. Under lubricating conditions, the friction coefficient increases linearly with the increase of the normal load; under low normal load conditions, the magnitude of the friction coefficient is proportional to the area density of the coupling texture. The wear on the surface increases linearly.

(2) Under the condition of low normal load, the coupling texture array has a significant reduction effect on the friction coefficient and wear amount compared with the untextured and single textured surfaces. When the area density of the coupling texture is 6.4% and the normal load is 10 N, the friction and wear of the sealing pair decrease the most. Compared with the untextured surface, the friction coefficient decreased by 27.9% and the wear amount decreased by 30.0%; compared with the single-textured surface, the friction coefficient decreased by 18.9% and the wear amount decreased by 23.8%.

(3) The coupling effect generated by the coupling texture can effectively enhance the formation and stabilization of the oil film, produce a good dynamic pressure effect, and has a good ability to capture wear debris, prevent the wear debris from continuously scratching the surface, and reduce wear and roughness. The service life of the piston rod seal pair is improved.

Author Contributions: Conceptualization, J.T. and J.Z.; methodology, J.T. and X.L.; investigation, J.Z. and X.L.; original draft preparation, J.T. and J.Z.; writing, review, and editing, J.T., J.Z. and X.L. All authors have read and agreed to the published version of the manuscript.

Funding: This work was funded by the Tianjin Municipal Education Commission Scientific Research Program (no. 2020KJ019), Fundamental Research Fees for Central Universities (no. 3122020035), and the Graduate Research Innovation Project (no. 2021YJSS112).

Conflicts of Interest: The authors declare no conflict of interest.

References

1. Shen, M.X.; Zhang, J.P.; Meng, X.K.; Li, G.; Jiang, H.S.; Peng, X.D. Fretting Characteristics of Fluorine Rubber O-ring for Reciprocating Shaft Seal. *J. Mech. Eng.* **2015**, *51*, 39–45. [CrossRef]
2. Gu, C.X.; Meng, X.H.; Xie, Y.B.; Zhang, D. The influence of surface texturing on the transition of the lubrication regimes between a piston ring and a cylinder liner. *Int. J. Engine Res.* **2017**, *18*, 785–796. [CrossRef]
3. Li, Y.; Liu, X.J.; Zhang, Y.; Liu, K. Frictional Properties of Textured Surfaces under Plane Contact. *J. Mech. Eng.* **2012**, *48*, 109–115. [CrossRef]
4. Xia, D.P.; Lai, L.J.; Wu, J.G. Research on stainless steel surface micro-pit array processing technology based on constrained electrolysis. *Manuf. Technol. Mach. Tool* **2019**, *1*, 131–134.
5. Peng, C. Experimental Study of Electrolytic Transfer Processing of Micro Crater Arrays. Master's Thesis, Nanjing University of Aeronautics and Astronautics, Nanjing, China, 2016.
6. Zhen, L.; Xu, J.X.; Ao, S.S.; Liu, W.D.; Li, K.B.; Zhang, W. An Experimental Study on Solid-State Electrochemical Micromachining of Micro-Dimple Arrays. *J. Tianjin Univ. (Sci. Technol.)* **2019**, *3*, 236–241.

7. Mahata, S.; Kunar, S.; Bhattacharyya, B. Fabrication of Different Micro Patterned Arrays by Through Mask Electrochemical Micromachining. *J. Electrochem. Soc.* **2019**, *166*, 217–225. [CrossRef]
8. Xie, B.C. Research on Some Basic Problems of Micro-Hole and Array Hole Micro-Fine EDM. Master's Thesis, Harbin Institute of Technology, Haerbin, China, 2013.
9. Li, Y. Combined Micro-Milling/Micro-Electro-Discharge Machining Technology for Micro-Array Structures. Master's Thesis, Harbin Institute of Technology, Haerbin, China, 2016.
10. Koyano, T.; Hosokawa, A.; Takahashi, T.; Ueda, T. One-process surface texturing of a large area by electrochemical machining with short voltage pulses. *CIRP Annals* **2019**, *68*, 181–184. [CrossRef]
11. Wang, F.; Zhang, Y.B.; Liu, G.M.; Wang, Q. Improvement of processing quality based on VHF resonant micro-EDM pulse generator. *Int. J. Adv. Manuf. Technol.* **2019**, *104*, 3663–3677. [CrossRef]
12. Yan, Q.S. Principle and application of micro abrasive air jet processing. *New Technol. New Process* **2004**, *4*, 20–22.
13. Vanmore, V.V.; Dabade, U.A. Experimental and Parametric Optimization of Micro Holes on ANSI 304 Using Micro Abrasive Jet Machining (MAJM). *Procedia Comput. Sci.* **2018**, *133*, 620–626. [CrossRef]
14. Wakuda, M.; Yamauchi, Y.; Kanzaki, S.; Yoshiteru, Y. Effect of Surface Texturing on Friction Reduction between Ceramic and Steel Materials Under Lubricated Sliding Contact. *Wear* **2003**, *54*, 356–363. [CrossRef]
15. Wang, L.k.; Zhao, Y.; Yang, Z.X.; Zhao, Y.L.; Yang, X.W.; Gong, T.B.; Li, C. Femtosecond laser micromachining in combination with ICP etching for 4H-SiC pressure sensor membranes. *Ceram. Int.* **2021**, *47*, 6397–6408. [CrossRef]
16. Chen, L.; When, G.Q.; Guo, F.; Hu, T.; Liu, D. Fractal properties of nanosecond laser-induced superhydrophobic silicone rubber surface microstructures. *Chin. J. Lasers* **2021**, *48*, 260–268.
17. He, X.; Zeng, W.J.; Wang, G.R.; Zhong, L. Study on laser processing of surface weave of drill bit slide bearing. *Laser Infrared* **2020**, *50*, 1443–1449.
18. Li, W.S. Basic Research on the Application of Micro-Pit Machining Technology for Cylinder Liner. Master's Thesis, North University of China, Taiyuan, China, 2007.
19. Ke, M.; Zhu, X.J.; Wang, J.Q. Analysis of dynamic pressure lubrication performance of different shaped micro-pits. *Lubr. Eng.* **2013**, *11*, 60–63.
20. Zhang, Y.D.; Lin, J.Q.; FU, Q.L.; Hu, H.Y. Displacement detection and control of low-frequency vibration machining toolholder with surface micro-pits. *J. Zhejiang Univ. (Eng. Sci.)* **2008**, *8*, 1410–1414.
21. Zhang, Y. *Honeycomb Micro-Pit Design and Manufacturing Technology*; Science Press: Beijing, China, 2004.
22. Zhang, C.Y.; Zhao, B. Advances in ultrasonic vibration-assisted processing of surface microstructures and their properties. *Surf. Technol.* **2019**, *48*, 271–286.
23. Myint, S.M.; Minn, M.; Yaping, R.; Satyanarayana, N.; Sinha, S.K.; Bhatia, C.S. Friction and wear durability studies on the 3D negative fingerprint and honeycomb textured SU-8 surfaces. *Tribol. Int.* **2013**, *60*, 187–197. [CrossRef]
24. Wu, J.J.; Zhao, J.B.; Qiao, H.C.; Hu, X.L.; Yang, Y.Q. Research on the technical principle and typical applications of laser shock processing. *Mater. Today Proc.* **2021**, *44*, 722–731. [CrossRef]
25. Cao, Y.P.; Jiang, S.Z.; Shi, W.D.; Hua, G.R.; Feng, A.X.; Wang, Z.G. E690 Simulation and testing of laser impact micro-modeling of high-strength steel surfaces. *China Surf. Eng.* **2019**, *32*, 69–77.
26. Xiong, F. Forming Mechanism and its Performance of Controlled Surface Topography for Micro-Scale Laser Impact Processing. Master's Thesis, China University of Mining and Technology, Xuzhou, China, 2020.
27. Caslaru, R.; Sealy, M.P.; Guo, Y.B.; Wei, X.T. Fabrication and Tribological Functions of Micro Dent Arrays on Ti-6Al-4V Surface by Laser Shock Peening. *J. Manuf. Sci. Eng.* **2014**, *136*, 7925–7974. [CrossRef]
28. Dai, F.Z. Study of Metal Surface Morphology and Properties Based on Nanosecond Laser Shock Wave Effect. Master's Thesis, Jiangsu University, Zhenjiang, China, 2014.
29. Wang, H.T.; Zhu, H. Frictional properties of circular micro-pitted woven surfaces. *Lubr. Eng.* **2015**, *40*, 49–53.
30. Liao, W.L.; Chen, T.B. Influence of texture size on tribological performance of piston pump seal pair. *Ordnance Mater. Sci. Eng.* **2020**, *43*, 72–77.
31. Liao, W.L. Optimization of Texture Parameters of Fracturing Pump Plunger Seal Pair. Master's Thesis, Southwest Petroleum University, Chengdu, China, May 2018.
32. Wang, G.R.; Yang, C.H.; Li, R.; Zhong, L.; Jiang, L. Effect of Laser Textured Surfaces on Tribological Properties of Fracturing Pump Plungers. *Lubr. Eng.* **2015**, *40*, 17–20.
33. He, X.; Liao, W.L.; Wang, G.R.; Zhong, L.; Jiang, L. Influence of Edges Bulgeof Texture on Tribological Performances of Plunger-seal Pair in Fracturing Pump. *Lubr. Eng.* **2016**, *41*, 96–101.
34. Wang, G.R.; Liao, D.S.; Zhong, L.; Liao, W.L.; Li, M.Y.; Wei, G. Effect of Groove-like Surface Texture on Friction Performance of Plunger Seal Pair. *Surf. Technol.* **2019**, *48*, 165–173.
35. Jiang, L.; Ma, G.L.; Wang, X.L. Lubrication Properties of Surface Texture on PDMS. *Tribology* **2010**, *30*, 262–267.
36. He, X.; Zhong, L.; Wang, G.R.; Yang, C.H.; Jiang, L. Tribological Properties of Fracturing Seal with Textured Plunger. *Tribology* **2014**, *34*, 364–370.
37. Li, Y.K.; Wang, Y.S.; Jian, G.X.; Luo, H. Finite Element Analysis of Tribological Properties of Bionic Water-Lubricated Bearings with Nepenthes Alata Structures. *Tribology* **2021**, *41*, 344–356.

38. Tang, J.; Qi, K.; Zeng, J.; Li, Y.S.; Zeng, X.R.; Lu, X. Effect of Load on the Tribological Properties of Metal/Textured EPDM Seal Pair. *Surf. Technol.* **2021**, *50*, 243–249.
39. Miao, C.W.; Guo, Z.W.; Yuan, C.Q. Tribological behavior of co-textured cylinder liner-piston ring during running-in. *Friction* **2022**, *10*, 878–890. [CrossRef]
40. Miao, C.W.; Guo, Z.W.; Yuan, C.Q.; Xu, C.; Sheng, C.X. Coupling Mechanism and Friction Reduction Performance of Textured Cylinder Liner-Piston Ring. *Surf. Technol.* **2020**, *49*, 124–133.
41. Cui, X.B.; Yan, K.; Guo, J.X.; Wang, D. Biomimetic micro-textures, mechanical behaviors and intermittent turning performance of textured Al_2O_3/TiC micro-composite and micro-nano-composite ceramics. *Ceram. Int.* **2019**, *45*, 19934–19947. [CrossRef]
42. Liu, Y.S.; Li, Z.Y. *Hydraulic Components and Systems*, 4th ed.; Machinery Industry Press: Beijing, China, 2019.
43. Wang, H.J.; Liu, Z.L.; Zou, L. Influence of Surface Texture Layout on Friction and Wear of Polymer Materials. *Lubr. Eng.* **2018**, *43*, 6–11.
44. Yuan, C.Q.; Yan, X.P. Evaluation of Surface Features of Wear Components Based on Surface Characteristics of Wear Debris. *China Mech. Eng.* **2007**, *18*, 1588–1591.
45. Zhang, H.L.; Bu, Y.Y.; Qiu, X.Y. The Fractal Dimension of Profile of Spherical and Cutting Wear Debris. *Tribology* **2002**, *22*, 304–307.
46. Zhao, S.; Wang, X.L. The Effects of Surface Texture on the Wear Properties of Mechanical Seals Made of Metal and Polymers. *Tribology* **2015**, *35*, 761–767.

micromachines

Article

Deformation Analysis of Continuous Milling of Inconel718 Nickel-Based Superalloy

Xueguang Li [1,*], Yahui Wang [2], Liqin Miao [3] and Wang Zhang [1]

[1] College of Mechanical and Electrical Engineering, Changchun University of Science and Technology, Changchun 130022, China; zhangwang5434@sina.com
[2] Sinohydro Bureau 11 Co., Ltd., Zhengzhou 450000, China; 11wangyahui@sina.com
[3] Department of Numerical Design &Manufacturing, Changchun Research Institute of Equipment and Technology, Changchun 130012, China; mlq_1980@sina.com
* Correspondence: lixueguang@cust.edu.cn

Abstract: As a difficult-to-process material, Inconel718 nickel-based superalloy is more and more widely used in aerospace, ocean navigation, and large-scale machinery manufacturing. Based on ABAQUS simulation software, this paper takes the milling force and temperature in the milling process of the nickel-based superalloy as the research object, and establishes the empirical formula for the prediction model of cutting force and cutting temperature based on the method of multiple linear regression. The significance of the prediction model was verified by the residual analysis method. Through data analysis, it is obtained: within a certain experimental range, the influence degrees of each milling parameter on the cutting force and cutting temperature are $f_z > a_p > n$ and $f_z > a_p \approx n$, respectively. The actual orthogonal cutting test was carried out on the machine tool, and the reliability and accuracy of the prediction model of cutting force, cutting temperature and tool wear amount were verified. The model formulas of the shear velocity field, shear strain field and shear strain rate field of the main shear deformation zone are constructed by using mathematical analysis methods. The influence law of cutting speed and tool rake angle on the variables of main shear zone is calculated and analyzed. Through the combination of theory and experiment, the relationship between cutting force, chip shape and machined surface quality in milling process was analyzed. Finally, with the increase in the cutting force, the serration of the chip becomes more and more serious, and the roughness of the machined surface becomes greater and greater.

Keywords: milling force; milling temperature; multiple linear regression; range analysis; chip morphology; tool wear; surface quality

Citation: Li, X.; Wang, Y.; Miao, L.; Zhang, W. Deformation Analysis of Continuous Milling of Inconel718 Nickel-Based Superalloy. *Micromachines* **2022**, *13*, 683. https://doi.org/10.3390/mi13050683

Academic Editors: Bongchul Kang, Jiang Guo, Chunjin Wang and Chengwei Kang

Received: 21 March 2022
Accepted: 22 April 2022
Published: 27 April 2022

1. Introduction

High-temperature alloys, also known as heat-strength alloys, heat-resistant alloys or superalloy, are mainly based on iron, cobalt, and nickel; high-temperature alloys are those which can withstand complex stress and undergo high-temperature service in a very harsh environment. They are widely used in aviation, aerospace, ship, power and petrochemical industries, and are key materials in rocket engines and aviation jet engines [1,2]. Rare metals (molybdenum, niobium, tungsten, etc.) added to nickel-based superalloys give these materials high corrosion resistance and high temperature oxidation resistance. Furthermore, it increases the stability of the materials and creates hard spots inside the matrix, which makes the cutting efficiency of such materials low and causes severe tool wear. Therefore, using experimental methods to study cutting force and cutting heat is time-consuming, labor-intensive, and the cost is relatively high. At present, simulation processing and numerical simulation have been widely used in the research of cutting force, cutting temperature, chip morphology, tool wear, etc. [3–5].

Lu Xiaohong et al. [6] studied the thermal-mechanical coupling analysis of micro-milling of Inconel718 and proposed a modified three-dimensional analysis model of micro-milling force. In the model, the contact area is considered a moving finite-length heat source and an analytical cutting temperature model is proposed based on Fourier's law. The coupling calculation of the micro-milling force model and the temperature model are carried out through an iterative process. Yao Yang, et al. [7] established an empirical formula between cutting force and cutting process parameters through the linear regression method and orthogonal experiment design scheme, and verified the accuracy and reliability of the model by variance analysis. Shafiul Islam et al. [8] established a mathematical model of axial cutting force and verified it through the designed experimental group. The experimental results are in good agreement with the theoretical simulation results. In addition, response surface methodology was employed to optimize the cutting parameters. Xiaobin Cui et al. [9] found that the serration of chips became more and more obvious as the cutting speed increased. During the formation process of the separated sawtooth, the high temperature in the shear band had a substantial effect on the initiation of the crack in the chip. When the cutting speed increased, the formation frequency of sawteeth increased with a decreasing growth rate and the tool chip contact length exhibited a decreasing trend.

Linjiang He et al. [10] found some very small sawteeth on the free surface of chips under low cutting speeds, which transformed into irregular serrated chips with increasing cutting speeds and into serrated chip with an adiabatic shear band under high cutting speeds.Fulin Wang et al. [11] found stress concentration appears and shear slipping occurs along the shear plane in the process of serrated chip formation. The strain rate on the shear slipping surface is much greater than other places and the temperature gradient perpendicular to the shear plane is relatively higher. Chen Ertao et al. [12] used ABAQUS finite element software to study the influence of tool rake angle on chip formation and its morphology, cutting force change, etc., and concluded that the chip size is related to the tool angle.

Seyed Mohammad Ebrahimi et al. [13] has found that for low feed rates, the chip form will be changed from continuous to sawtooth form. Wenlong Song et al. [14] found that cutting speed had a profound effect on the cutting temperature. However, in high-speed cutting, there was not much difference in cutting performance owing to the high temperature caused by the elevated cutting speed. Grzesik et al. [15] studied the tool wear in Inconel718 superalloy turning from the perspective of improving process performance and productivity, and concluded that the main wear of the tool is abrasive, and there is groove wear at the cutting edge. Hao Pengfei [16] mainly carried out the cutting test of nickel-based superalloy under the condition of high-pressure cooling, and discussed the corresponding wear mechanism of the tool under different wear morphologies according to the experimental results. At the same time, the influence of different cutting speeds on the tool wear profile was systematically analyzed using a scanning electron microscope and energy spectrum analyzer.Xie Liming, Cheng Ge et al. [17] first designed the orthogonal milling test plan, and then used the MATLAB analysis software to calculate the empirical formula of the Cr12MoV milling temperature prediction model. Finally, the order of the influence of cutting process parameters on milling temperature and the optimal combination of cutting factor levels are obtained by means of range analysis. Hao Zhaopeng, Cui Ruirui, Fan Yihang et al. [18] found that there is a cutting temperature that can minimize tool wear during the cutting process. The research results can provide a more convenient and effective method to select reasonable process parameters.

However, as far as the current research situation is concerned, overall research is relatively lacking, the research aspect is not very comprehensive to a certain extent, and there is still relatively little research on the impact of actual cutting tests on the cutting process. This paper uses multiple linear regression methods to establish the empirical formulas of the cutting force and cutting temperature prediction models, and verifies the accuracy of the prediction models through actual orthogonal cutting tests and range analysis methods

to study the cutting mechanism of Inconel718 nickel-based superalloy. According to the cutting simulation model, the formation process of sawtooth chips in the cutting process of Inconel718 nickel-based superalloy is analyzed. Combined with actual cutting experiments, the general laws of chip shape, cutting force, machining surface quality and tool wear during the cutting process are analyzed, so as to provide a theoretical basis for the actual machining of superalloys.

2. Establishment of the Prediction Model of Cutting Force and Cutting Temperature

Research on cutting force and cutting temperature during machining is the basis for further research on cutting tools, workpiece material cutting performance, and tool wear. At the same time, cutting force and cutting temperature are also important physical quantities in machining and two of the key factors affecting the surface quality of the workpiece. In order to reasonably select the machining parameters during the high-speed cutting of Inconel718 nickel-based superalloy, it is necessary to effectively predict the cutting force and temperature during milling before machining.

In the actual machining process, the milling force and temperature are not only related to the milling parameters, but also affected by a series of factors such as tool wear and the clamping of the machining system. However, other factors are random and uncertain, so they cannot be summarized through experience or theory. In order to be able to obtain the prediction model formula of milling force and milling temperature, the following assumptions must be made about the machining process.

(1) In the milling process, it is necessary to ignore the influence of the machine tool itself, clamping conditions, workpiece shape, material, etc. on the cutting force and cutting temperature in the process, and set the machine tool as a rigid body without deformation.
(2) The tool will inevitably wear out during the machining process. This factor will affect the various parameters of the tool, which will lead to changes in the cutting force and cutting temperature. In the modeling process of cutting force and cutting temperature, it is assumed that the tool is always free of wear, and the size of the cutting force and cutting temperature are not affected by tool wear.
(3) It is assumed that the entire machining process has been orthogonal milling, ignoring the influence of possible milling angles on cutting force and cutting temperature.

Generally, J-C constitutive equations are used to simulate the behavior of workpiece materials during cutting [19]. Therefore, in this study, the J-C constitutive equation of plastic material, which includes the effect of temperature and strain rate strengthening, is used for establishing the workpiece model. This model can be expressed as follows:

$$\sigma = (A + B\varepsilon^n)[1 + c \ln \frac{\dot{\varepsilon}}{\dot{\varepsilon}_0}][1 - (\frac{T - T_r}{T_m - T_r})^m] \, (2-1) \quad (1)$$

where σ (MPa) is the flow stress; A (MPa) is the yield strength of the material under quasi-static conditions; B is the strain hardening coefficient of the material; n is the strain strengthening coefficient of the material; c is the strain rate sensitivity coefficient; m is the temperature sensitivity coefficient; T(K) is the material temperature; T_r(K) is the reference room temperature, K; T_m(K) is the melting temperature of the material; $\dot{\varepsilon}_0$ is the reference strain rate; ε is the strain of the material; $\dot{\varepsilon}$ is the strain rate. The J-C constitutive parameters of Inconel718 provided by Huichen and Xueren [20] are shown in Table 1.

Table 1. Johnson-Cook plasticity parameters of Inconel718.

A	450 MPa
B	1700
$C(\dot{\varepsilon}_0 = 0.001)$	0.017
n	0.65
m	1.3
Melting temperature	1570 °C
Excessive temperature	20 °C

2.1. Derivation of Empirical Formula

According to the principle of metal cutting, the index formula [21–24] for calculating cutting force and cutting temperature is:

$$\begin{array}{l} F = C_F \cdot a_p^{a_1} \cdot n^{a_2} \cdot {f_z}^{a_3} \\ T = C_T \cdot a_p^{b_1} \cdot n^{b_2} \cdot {f_z}^{b_3} \end{array} \tag{2}$$

where C_F and C_T are coefficients depending on the processing material and cutting conditions. The relationship among the feed speed v_f, the feed per tooth f_z, and the speed n can be expressed as:

$$v_f = f_z \cdot n \cdot z \tag{3}$$

where z is the number of milling cutter teeth, $z = 4$.

Take the logarithm of both sides of Equation (1) to get:

$$\lg F = \lg C_F + a_1 \cdot \lg a_p + a_2 \cdot \lg n + a_3 \cdot \lg f_z \tag{4}$$

Let $a_0 = \lg C_F, x_1 = \lg a_p, x_2 = \lg n, x_3 = \lg f_z, y = \lg F$, we can get:

$$y = a_0 + a_1 \cdot x_1 + a_2 \cdot x_2 + a_3 \cdot x_3 \tag{5}$$

This is a linear relationship between the dependent variable and the independent variable. y_i is used to represent the experimental result; the independent variables are x_{i1}, x_{i2}, x_{i3}, and the experimental error is ε_i, where $i = 1 \sim 16$. Then, the multiple linear regression equation is as follows:

$$\begin{cases} y_1 = \beta_0 + \beta_1 x_{11} + \beta_2 x_{12} + \beta_3 x_{13} + \varepsilon_1 \\ y_2 = \beta_0 + \beta_1 x_{21} + \beta_2 x_{22} + \beta_3 x_{23} + \varepsilon_2 \\ \cdots\cdots\cdots\cdots\cdots\cdots\cdots\cdots\cdots\cdots \\ y_i = \beta_0 + \beta_1 x_{161} + \beta_2 x_{162} + \beta_3 x_{163} + \varepsilon_{16} \end{cases} \tag{6}$$

Expressed as a matrix:

$$Y = X\beta + \varepsilon \tag{7}$$

Among them:

$$Y = \begin{bmatrix} y_1 \\ y_2 \\ \cdots \\ y_{16} \end{bmatrix} X = \begin{bmatrix} 1 & x_{11} & x_{12} & x_{13} \\ 1 & x_{21} & x_{22} & x_{23} \\ \cdots & \cdots & \cdots & \cdots \\ 1 & x_{161} & x_{162} & x_{163} \end{bmatrix} \beta = \begin{bmatrix} \beta_0 \\ \beta_1 \\ \beta_2 \\ \beta_3 \end{bmatrix} \varepsilon = \begin{bmatrix} \varepsilon_1 \\ \varepsilon_2 \\ \cdots \\ \varepsilon_{16} \end{bmatrix} \tag{8}$$

Y, X, β, and ε are corresponding matrices. The least-square method is used to estimate the parameter β, and the regression coefficient a_0, a_1, a_2, a_3 is the least square estimation of the parameter $\beta_0, \beta_1, \beta_2, \beta_3$ (including the influence of ε); then, the regression equation can be expressed as:

$$\hat{y} = a_0 + a_1 x_1 + a_2 x_2 + a_3 x_3 \tag{9}$$

where $\hat{y}$ is a statistical variable, where

$$a = \begin{bmatrix} a_0 \\ a_1 \\ a_2 \\ a_3 \end{bmatrix} \tag{10}$$

2.2. Orthogonal Simulation Experiment Design

In order to accurately calculate the empirical formula of the cutting force and cutting temperature prediction model, this article adopts the orthogonal experiment method. Orthogonal experimentation is a common method to study the influence of multiple factors. Compared with the comprehensive experiment, the orthogonal experiment selects some representative points from all combinations for experimenting. Through the experimental measurement values of these points, the influence of each factor on the results is analyzed. The advantage of the orthogonal experiment method is that the influence of cutting parameters on the object can be studied through fewer experiments.

In the research, the milling cutter is fixed, and it does not need to consider the influence of cutter parameters on the milling force. This paper designs 16 sets of orthogonal experiments with 3 factors and 4 levels. The experimental factors are axial cutting depth, spindle speed, and feed per tooth. Starting from reality, the value of each factor level is within the operating range of the machine tool. The range of experimental parameters is as follows:

(1) Spindle speed n: 3000 $\sim$ 4500 r/min;
(2) Axial depth of cut a_p: 0.2 $\sim$ 0.5 mm;
(3) Feed per tooth f_z: 0.1 $\sim$ 0.4 mm/r.

The orthogonal experiment and simulation data are shown in Table 2:

Table 2. Orthogonal simulation experiment data.

Numbering	Rotating Speed n(r/min)	Axial Depth of Cut a_p(mm)	Feed per Tooth f_z(mm/r)	F (N)	T (°C)
1	3000	0.2	0.1	184.58	292.61
2	3000	0.3	0.2	319.55	421.76
3	3000	0.4	0.3	647.19	493.56
4	3000	0.5	0.4	726.77	595.48
5	3500	0.2	0.2	420.43	408.73
6	3500	0.3	0.1	329.22	392.81
7	3500	0.4	0.4	749.23	605.54
8	3500	0.5	0.3	710.36	488.57
9	4000	0.2	0.3	646.95	542.46
10	4000	0.3	0.4	680.82	615.83
11	4000	0.4	0.1	314.51	404.08
12	4000	0.5	0.2	519.54	467.89
13	4500	0.2	0.4	401.83	422.37
14	4500	0.3	0.3	561.11	590.91
15	4500	0.4	0.2	545.96	559.71
16	4500	0.5	0.1	382.66	286.79

2.3. Data Processing and Determination of Model Coefficients

Taking the logarithm of the milling parameters in the table, the form of the matrix transformed by the multiple linear regression is:

$$Y_F = \begin{bmatrix} 2.2662 \\ 2.5045 \\ 2.8110 \\ 2.8614 \\ 2.6237 \\ 2.5175 \\ 2.8746 \\ 2.8515 \\ 2.8109 \\ 2.8330 \\ 2.4976 \\ 2.7156 \\ 2.6040 \\ 2.7490 \\ 2.7372 \\ 2.5828 \end{bmatrix} X = \begin{bmatrix} 1 & -0.6990 & 3.4771 & -1 \\ 1 & -0.5229 & 3.4771 & -0.6990 \\ 1 & -0.3979 & 3.4771 & -0.5229 \\ 1 & -0.3010 & 3.4771 & -0.3979 \\ 1 & -0.6990 & 3.5441 & -0.6990 \\ 1 & -0.5229 & 3.5441 & -1 \\ 1 & -0.3979 & 3.5441 & -0.3979 \\ 1 & -0.3010 & 3.5441 & -0.5229 \\ 1 & -0.6990 & 3.6021 & -0.5229 \\ 1 & -0.5229 & 3.6021 & -0.3979 \\ 1 & -0.3979 & 3.6021 & -1 \\ 1 & -0.3010 & 3.6021 & -0.6990 \\ 1 & -0.6990 & 3.6532 & -0.3979 \\ 1 & -0.5229 & 3.6532 & -0.5229 \\ 1 & -0.3979 & 3.6532 & -0.6990 \\ 1 & -0.3010 & 3.6532 & -1 \end{bmatrix} Y_T = \begin{bmatrix} 2.4663 \\ 2.6251 \\ 2.6933 \\ 2.7749 \\ 2.6114 \\ 2.5942 \\ 2.7821 \\ 2.6889 \\ 2.7344 \\ 2.7895 \\ 2.6065 \\ 2.6701 \\ 2.6257 \\ 2.7715 \\ 2.7480 \\ 2.4576 \end{bmatrix} \quad (11)$$

The M file is established by MATLAB software, and the cutting force value and each milling parameter in Formula (11) are calculated by multiple linear regression [25,26] to the numerical input program. The input program is:

y = [2.2662,2.5045,2.8110,2.8614,2.6237,2.5175,2.8746,2.8515,2.8109,2.8330,2.4976,2.7156, 2.6040,2.7490,2.7372,2.5828];

x1 = [−0.6990,−0.5229,−0.3979,−0.3010,−0.6990,−0.5229,−0.3979,−0.3010,−0.6990, −0.5229,−0.3979,−0.3010,−0.6990,−0.5229,−0.3979,−0.3010];

x2 = [3.4711,3.4711,3.4711,3.4711,3.5441,3.5441,3.5441,3.5441,3.6021,3.6021,3.6021, 3.6021,3.6532,3.6532,3.6532,3.6532];

x3 = [−1,−0.6990,−0.5229,−0.3979,−0.6990,−1,−0.3979,−0.5229,−0.5229,−0.3979,−1, −0.6990,−0.3979,−0.5229,−0.6990,−1]];

X = [ones(length(y),1),x1′,x2′ x3′];

Y = y′;

[b,bint,r,rint,stats] = regress(Y,X);

b,bint,stats

According to the results obtained by MATLAB:

$$a_0 = 2.1253;\ a_1 = 0.4642;\ a_2 = 0.3260;\ a_3 = 0.5919.$$

Therefore, the multiple regression model is:

$$y = 2.1253 + 0.4642x_1 + 0.3260x_2 + 0.5919x_3,$$

and the empirical formula of the cutting force prediction model available from above is:

$$F = 133.44 \cdot {a_p}^{0.4642} \cdot n^{0.3260} \cdot {f_z}^{0.5919}.$$

Furthermore, take the logarithm of T in the table, as shown in Formula (11). Type in MATLAB:

y = [2.4663,2.6251,2.6933,2.7749,2.6114,2.5942,2.7821,2.6889,2.7344,2.7895,2.6065,2.6701, 2.6257,2.7715,2.7480,2.4576];

According to the results obtained by MATLAB:

$$b_0 = 2.5139;\ b_1 = 0.1275;\ b_2 = 0.1258;\ b_3 = 0.3610.$$

Therefore, the multiple regression model is:

$$y = 2.5139 + 0.1275x_1 + 0.1258x_2 + 0.3610x_3,$$

and the empirical formula of the cutting force prediction model available from above is: $T = 326.51 \cdot {a_p}^{0.1275} \cdot n^{0.1258} \cdot {f_z}^{0.3610}$.

2.4. Significance Tests for Predictive Models

According to the results obtained by MATLAB:

(1) Cutting force regression coefficient group: $a_0 = 2.1253$, the confidence interval of a_0 is (−0.1699,4.4204), $a_1 = 0.4642$, the confidence interval of a_1 is (0.1722,0.7563), $a_2 = 0.3260$, the confidence interval of a_2 is (−0.3151,0.9670), $a_3 = 0.5919$, and the confidence interval of a_3 is (0.3998,0.7841). Statistics variable stats get: $r^2 = 0.8292$, $F = 19.4197$, $p = 0.0001$, obviously $p < \alpha = 0.05$. Perform residual analysis on the coefficient and enter in the MATLAB window: rcoplot(r,rint), the residual graph is shown in Figure 1a:

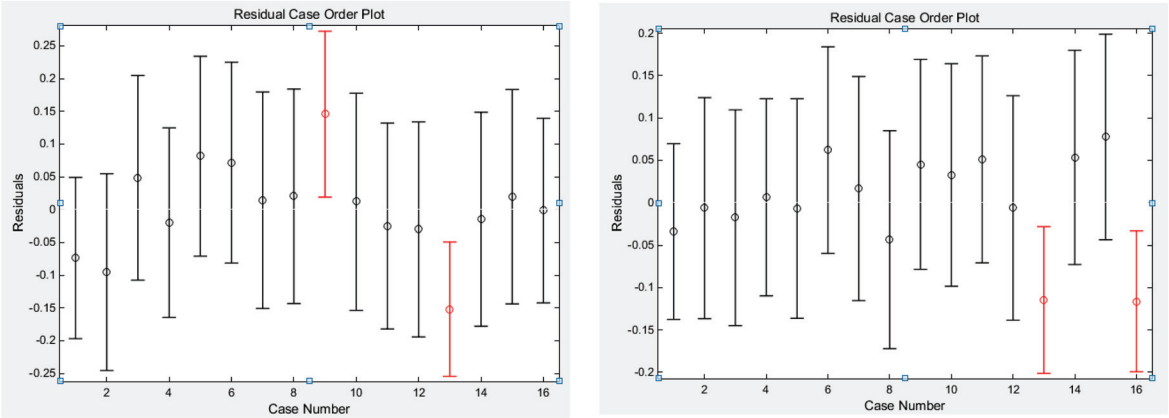

(**a**) (**b**)

Figure 1. Residual analysis graph. (**a**) Analysis of residual cutting force. (**b**) Analysis of residual cutting temperature.

It can be seen from the residual analysis graph that, except for the 9th and 13th entries, the residuals of the remaining data are close to the zero point and the confidence interval of the residuals all contain the zero point, which shows that the regression model can better conform to the original data. The 9th and 13th data can be regarded as abnormal points, and the regression model is considered credible [27]. From the above, the regression model $y = 2.1253 + 0.4642x_1 + 0.3260x_2 + 0.5919x_3$ is established, so the cutting force empirical formula $F = 133.44 \cdot {a_p}^{0.4642} \cdot n^{0.3260} \cdot {f_z}^{0.5919}$ is significant.

(2) Cutting temperature regression coefficient group: $b_0 = 2.5139$, the confidence interval of b_0 is (0.6733,4.3544), $b_1 = 0.1275$, the confidence interval of b_1 is (−0.1066,0.3617), $b_2 = 0.1258$, the confidence interval of b_2 is (−0.3883,0.6399), $b_3 = 0.3610$, and the confidence interval of b_3 is (0.2069,0.5152). Statistics variable stats get: $r^2 = 0.6981$, $F = 9.2480$, $p = 0.0019$, obviously $p < \alpha = 0.05$. Perform residual analysis on the coefficient and enter in the MATLAB window: rcoplot(r,rint), the residual graph is shown in Figure 1b.

It can be seen from the residual analysis graph that except for the 13th and 16th entries, the residuals of the remaining data are all close to the zero point, and the confidence interval of the residuals all contain the zero point, which shows that the regression model can better conform to the original data. The 13th and 16th data can be regarded as abnormal points, and the regression model is considered credible. From the above, the regression model $y = 2.5139 + 0.1275x_1 + 0.1258x_2 + 0.3610x_3$ is established, so the cutting force empirical formula $T = 326.51 \cdot {a_p}^{0.1275} \cdot n^{0.1258} \cdot {f_z}^{0.3610}$ is significant.

2.5. Influence Rule of Cutting Process Parameters

The range analysis method can be used to obtain the primary and secondary order of the degree of influence of each factor on the target parameter, the optimal combination scheme, and the influence law of the influencing factor on the target parameter in the analysis of the results of the orthogonal experiment. In order to obtain the order of the influence degree of each factor on the milling force and milling temperature, the range analysis method is used to analyze the simulation results, as shown in Tables 3 and 4:

Table 3. Cutting force (F) range analysis table.

Level	Rotating Speed n(r/min)	Axial Depth of Cut a_p(mm)	Feed per Tooth f_z(mm/r)
K_1	1878.09	1653.79	1210.97
K_2	2209.24	1890.70	1805.48
K_3	2161.82	2256.89	2565.61
K_4	1891.56	2339.33	2558.65
k_1	469.52	413.45	302.74
k_2	552.31	472.68	451.37
k_3	540.46	564.22	641.40
k_4	472.89	584.83	639.66
R_F	82.79	171.38	338.66
Primary and secondary order		$f_z > a_p > n$	

Table 4. Cutting temperature (T) range analysis table.

Level	Rotating Speed n(r/min)	Axial Depth of Cut a_p(mm)	Feed per Tooth f_z(mm/r)
K_1	1803.49	1666.17	1376.29
K_2	1895.65	2021.31	1858.09
K_3	2030.26	2062.89	2115.50
K_4	1859.78	1838.73	2239.22
k_1	450.87	416.54	344.07
k_2	473.91	505.33	464.52
k_3	507.57	515.72	528.88
k_4	464.95	459.68	559.81
R_T	56.7	99.18	215.74
Primary and secondary order		$f_z > a_p > n$	

Figure 2 is a trend graph showing the influence of spindle speed n, axial depth of cut a_p, and feed per tooth f_z on cutting force F and cutting temperature T. Based on this, the changes in milling temperature can be seen when various parameters are changed. Analyzing the range table and indicator factor trend chart shows that:

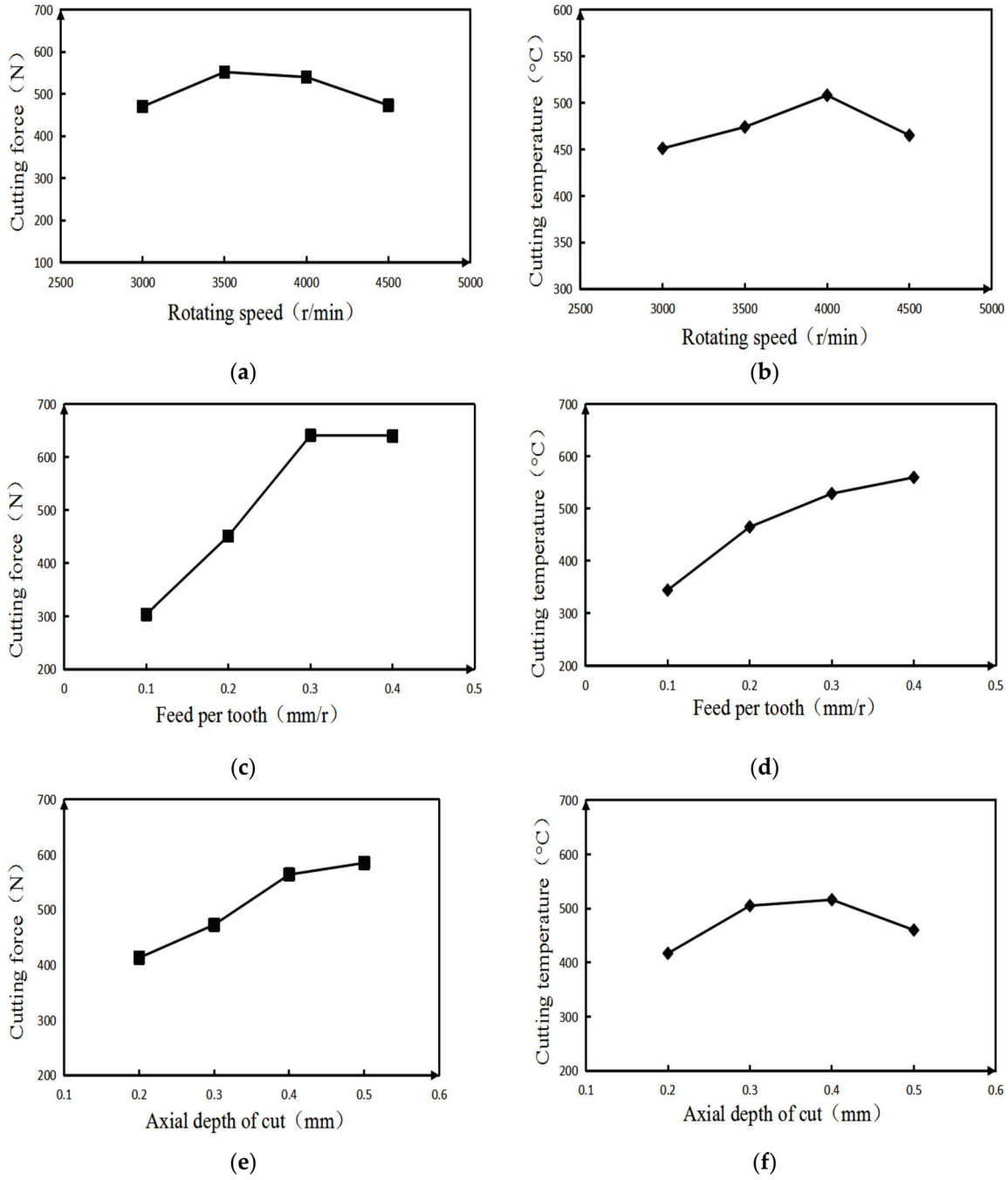

Figure 2. Trend chart of indicator factors. (**a**) The influence of spindle speed. (**b**) The influence of spindle speedon cutting forceon cutting temperature. (**c**) The influence of feed per tooth. (**d**) The influence of feed per tooth on cutting forceon cutting temperature. (**e**) Influence of axial depth of cut. (**f**) Influence of axial depth of cut on cutting forceon cutting temperature.

(1) The degree of influence of each milling parameter on the cutting force (F) is f_z, a_p, n in descending order, where f_z has a larger degree of influence, a_p has a medium influence on cutting force, and n has a smaller influence on cutting force. From the perspective of reducing the cutting force, the best combination of milling parameters is: $n = 4000$ r/min, $a_p = 0.4$ mm, $f_z = 0.1$ mm/r.

(2) The degree of influence of each milling parameter on the cutting temperature (T) is f_z, a_p, n in descending order, where f_z has a larger degree of influence, and the influence of a_p and n on cutting temperature is close. From the perspective of

reducing the cutting temperature, the best combination of milling parameters is: $n = 4500$ r/min, $a_p = 0.5$ mm, $f_z = 0.1$ mm/r.

(3) From Figure 2a,b, it can be seen that the milling force first increases and then decreases with the increase in the rotational speed. Since the shear angle increases with the increase in the rotational speed, the cutting deformation of the workpiece during the milling process gradually decreases, and the cutting force gradually decreases. When the rotation speed is lower than 4000 r/min, it can be seen that the change in cutting temperature shows an obvious upward trend, because during the machining process, severe friction occurs between the front and rear rake surfaces of the tool, the workpiece surface and the chip surface. These mutual frictions generate a lot of heat and gradually transfer it to other parts, so the temperature continues to increase. However, when the rotation speed continues to increase, the flow rate of the chips is also faster and more heat is taken away by the chip flow, so the temperature increases slowly.

(4) It can be seen from Figure 2c,d that after the increase in the feed per tooth, the thickness of the material to be cut from the workpiece increases with each turn of the milling cutter, so the cutting force gradually increases. However, at the same time, after the feed per tooth increases, the cutting deformation coefficient of the workpiece material will decrease to a certain extent due to the influence of temperature, so the change in cutting force will gradually become gentle. When the feed per tooth is increased, more material is removed per revolution of the tool, so the tool will generate more and more heat when cutting the workpiece, and the cutting temperature changes significantly.

(5) It can be seen from Figure 2e,f that with the gradual increase in the axial depth of cut, the area of the workpiece to be cut gradually increases, so the cutting force also increases. When the axial depth of cut is gradually increased, more heat needs to be generated to cut the workpiece material of the same path, so the change in cutting temperature will increase. However, in the actual machining process, as the axial depth of cut continues to increase, the contact length between the workpiece and the tool, the machining volume, etc. will increase significantly, and the machining environment at this time has changed significantly. Therefore, the cutting temperature does not increase in the same proportion.

3. Analysis of the Influence Law of Velocity Field, Strain Field and Strain Rate Field in the Main Shear Deformation Zone

According to the literature [28,29], the strain rate field $\dot{\gamma}$, strain field γ, and velocity field ν_x of the main shear deformation zone are as follows:

$$\dot{\gamma} = \begin{cases} \frac{\dot{\gamma}_m}{(\alpha h)^q} y^q \ y \in [0, \alpha h] \\ \frac{\dot{\gamma}_m}{(1-\alpha)^q h^q} (h-y)^q \ y \in [\alpha h, h] \end{cases}$$

$$\gamma = \begin{cases} \frac{\dot{\gamma}_m}{(q+1)V\sin(\Phi)(\alpha h)^q} y^{q+1} \ y \in [0, \alpha h] \\ -\frac{\dot{\gamma}_m}{(q+1)V\sin(\Phi)(1-\alpha)^q h^q} (h-y)^{q+1} + \frac{\cos(\gamma_o)}{\cos(\Phi-\gamma_o)\sin(\Phi)} \ y \in [\alpha h, h] \end{cases}$$

$$\nu_x = \begin{cases} \frac{\dot{\gamma}_m}{(q+1)(\alpha h)^q} y^{q+1} - V\cos(\Phi) \ y \in [0, \alpha h] \\ -\frac{\dot{\gamma}_m}{(q+1)(1-\alpha)^q h^q} (h-y)^{q+1} + V\sin(\Phi)\tan(\Phi-\gamma_o) \ y \in [\alpha h, h] \end{cases}$$

where α is the unequal coefficient, $\alpha = \frac{\cos\Phi\cos(\Phi-\gamma_o)}{\cos(\gamma_o)}$; h is the thickness of the main shear zone (mm), h = 0.025 mm; q is the exponent of the exponential function, which is 3 at low speed and 7 at high speed. V is cutting speed (m/min); Φ is shear angle (°); γ_o is tool rake angle (°); $\dot{\gamma}_m$ is the maximum shear strain rate (s-1).

According to the above analysis, cutting speed and tool rake angle are the two main factors affecting the main shear deformation zone. The following will analyze the influence of these two factors on the main shear zone.

3.1. The Influence Law of Cutting Speed

When analyzing the influence law of cutting speed, the rake angle of the tool used is 12°, and the cutting speed range is 30∼120 m/min. The curves of the influence of the calculated cutting speed on the velocity field, shear strain field, and shear strain rate field in the main shear deformation zone are shown in Figures 3 and 4.

It can be drawn from Figure 3a that: (1) In the main shear deformation zone, with the increase of the width of the main shear zone, the shear speed also increases. Furthermore, the size of the shear speed on the initial boundary (that is, the width of the main shear area on the figure is 0 mm) is affected by the initial cutting speed. (2) The tangential velocities on the final boundary (that is, the curves in the figure begin to stabilize) are all about 70 mm/s, and once the width of the main shear zone is greater than 0.02 mm, the change trend of the tangential velocity becomes gentle. (3) The main shear surface is defined as the plane where the tangential velocity component is equal to zero. It can be seen from Figure 3a that the lower the cutting speed is, the closer the location of the main shear surface (where the tangential velocity along the shear surface is 0) is to the starting boundary. That is to say, the lower the cutting speed, the smaller the width of the main cutting zone.

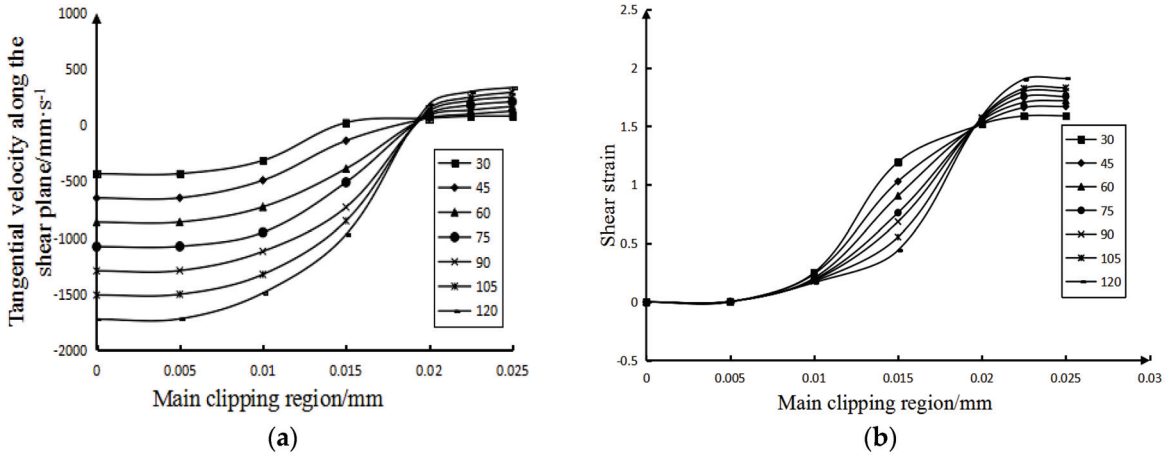

Figure 3. The influence of cutting speed. (**a**) The influence of cutting speed on the tangential velocity along the shear plane. (**b**) The influence of cutting speed on shear strain.

It can be concluded from Figure 3b: (1) Regardless of the cutting speed, the shear strain along the tangent direction of the shear plane at the beginning boundary of the main shear deformation zone is 0, because the material on the beginning boundary has not yet undergone any deformation. (2) Figure 3a shows the distance of the main shear zone corresponding to the main shear surface at each cutting speed. Therefore, it can be seen from Figure 3b that in the main shear deformation zone, the lower the cutting speed is, the closer the main shear surface is to the starting boundary. In fact, when the material crosses the final boundary of the main shear zone to form chips, its shear strain remains basically unchanged. Therefore, it can be seen that, the lower the cutting speed, the narrower the width of the main shear deformation zone. The analysis results are the same as above. (3) After crossing the main shear plane, the variation trend of the material shear strain gradually becomes gentle. This is because after the workpiece material crosses the main shear plane, the cut material forms chips and falls off the workpiece, and the tool no longer shears the chips, so the shear strain of the material tends to be stable.

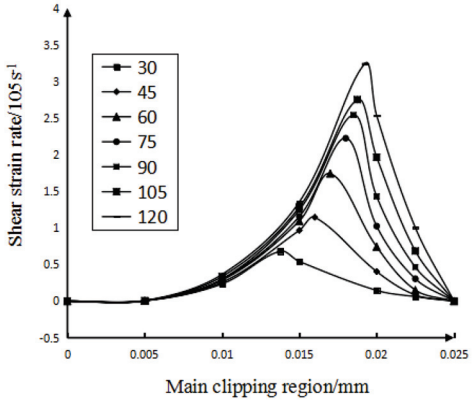

Figure 4. The influence of cutting speed on shear strain rate.

It can be concluded from Figure 4: (1) At the same cutting speed, with the gradual increase in the width of the main shear zone, the variation trend of the shear strain rate is to increase first and then decrease, and the greater the cutting speed, the greater the variation of the shear strain rate. (2) In the main shear zone, the shear strain rate on the main shear surface is the highest. It can also be seen from Figure 4 that the smaller the cutting speed, the closer the distance between the main shearing surface and the starting boundary. Furthermore, under each cutting speed condition, the shear surface in Figure 4 (the position with the highest shear strain rate) and the shear surface in Figure 3a are almost at the same position, which mutually confirms the correctness of the analysis results. (3) It can also be seen from Figure 4 that the lower the cutting speed, the smaller the maximum shear strain rate of the main shear deformation zone along the tangent direction of the shear plane; that is, the smaller the shear strain rate along the tangent direction of the main shear plane.

3.2. The Influence of Tool Rake Angle

When analyzing the influence law of the tool rake angle, the cutting speed adopted is 60 m/min and the range of tool rake angle is 0∼15°. Figures 5 and 6 show the curves of the influence of the calculated tool rake angle on the velocity field, shear strain field, and shear strain rate field in the main shear deformation zone.

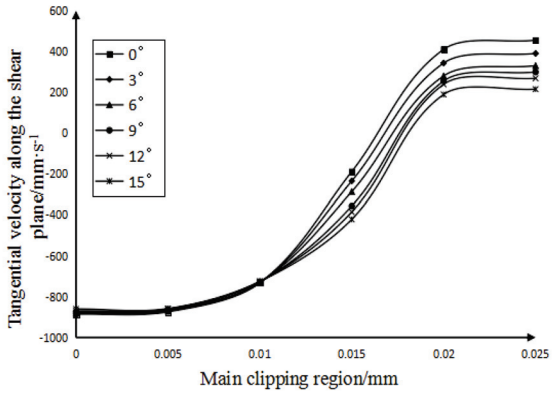

Figure 5. The influence of the tool rake angle on the tangential velocity along the shear plane.

It can be seen from Figure 5: (1) At the same tool angle, the magnitude of the tangential velocity along the shear plane increases with the increase in the width of the main shear zone. However, at the initial boundary of the main shearing area (that is, where the width of the main shearing area is 0 mm in the figure), the size of the tool rake angle has little effect on the shearing speed. (2) On the final boundary (that is, as the curves in the figure begin to stabilize), the smaller the tool rake angle, the greater the tangential velocity along

the shear plane. (3) It can be seen from the figure that the larger the degree of the rake angle of the tool, the farther the position of the main shear plane (that is, the tangential velocity along the shear plane in the figure is 0) is from the initial boundary. That is, the greater the degree of the tool rake angle, the greater the width of the main shearing area.

It can be seen from Figure 6a: (1) The rake angle of the tool has almost no effect on the shear strain of the starting boundary along the tangential direction of the shear plane. (2) The shear strain along the tangential direction of the shear surface at the final boundary of the main shear surface decreases with the increase in the rake angle of the tool. (3) When the tool rake angle is different, the position where the shear strain tends to be stable (where the curve tends to be stable) is not much different. It can be seen that the tool rake angle has little effect on the width of the main shear zone.

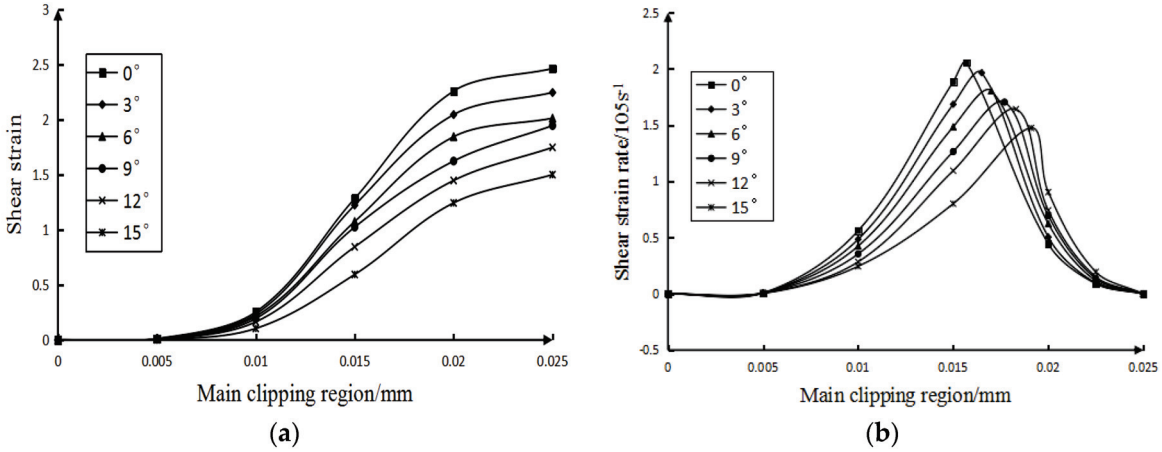

Figure 6. The influence of tool rake angle. (**a**) The influence of tool rake angle on shear strain (**b**) The influence of tool rake angle on shear strain rate.

It can be seen from Figure 6b: (1) The larger the rake angle of the tool, the smaller the tangential shear strain rate of the main shear deformation zone along the shear plane. (2) On the basis of the analysis, under the condition of each tool rake angle, the shear surface in Figure 6b (where the position with the highest shear strain rate) and the shear surface in Figure 4 are almost at the same position. the rake angle of the tool does not have a great influence on the position of the cutting surface.

4. Analysis of High Temperature Alloy Milling Process

4.1. Cutting Superalloy Test

In order to verify the accuracy of the predicted value of the theoretical model, it is necessary to conduct cutting tests on superalloys. In this paper, a CNC machining center is used to conduct continuous milling experiments on Inconel718 nickel-based superalloy, and the cutting force, chip shape, tool wear profile and the quality of the machined surface are analyzed in the cutting process. After the experiment, a stereo microscope was used to detect tool wear and chip morphology, and a surface roughness measuring instrument was used to detect the machined surface.

1. Test machine

This experiment uses the H330 CNC machining center for cutting experiments, as shown in Figure 7a,b:

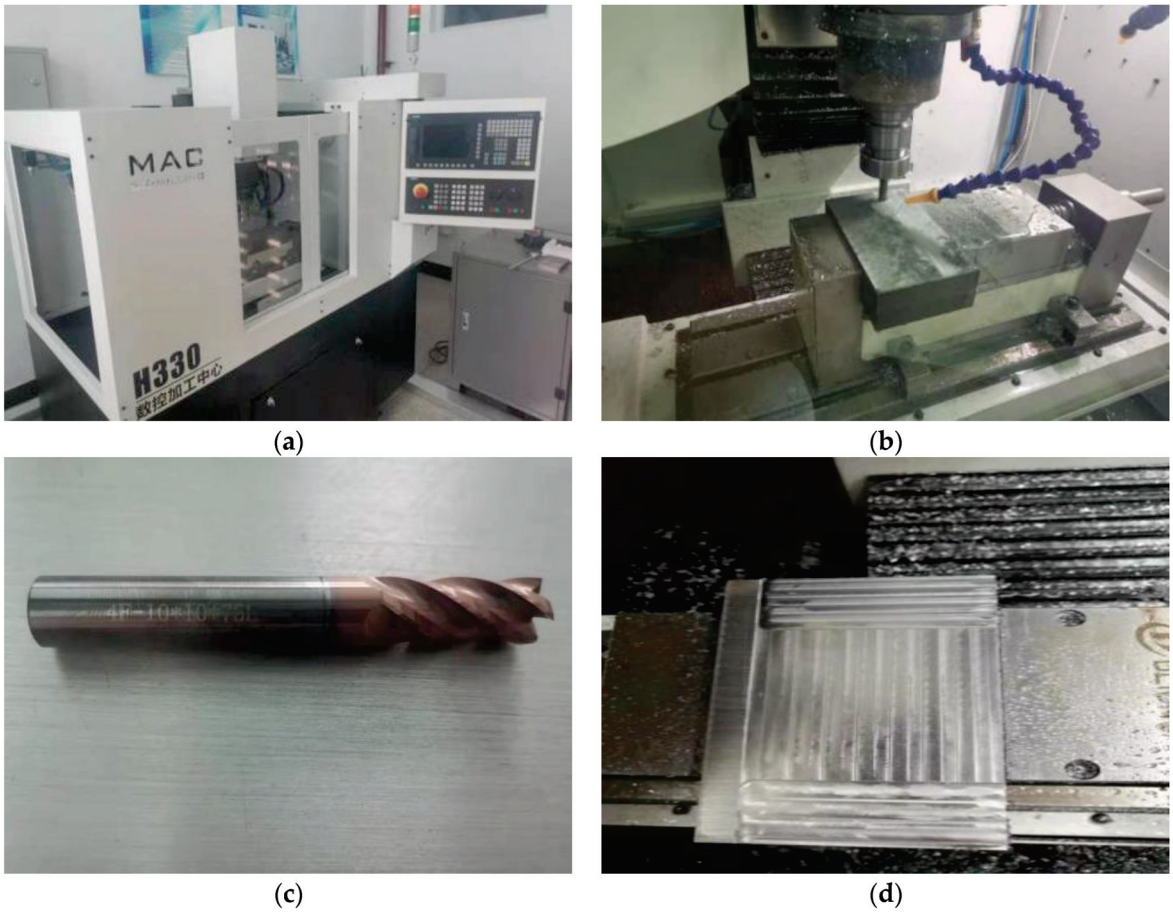

Figure 7. Experimental device. (**a**) CNC machining center. (**b**) The actual cutting test. (**c**) YG8 hard alloy spiral mill tool. (**d**) The finished part.

2. Cutting test materials

The milling cutter used was: YG8 hard alloy spiral mill tool, helix angle $\beta = 45^{\circ}$, tool diameter $D = 10$ mm, as shown in Figure 7c. The size of the test workpiece is: 100 mm × 100 mm × 20 mm, as shown in Figure 7d;

3. Experimental detection device

An Olympus SZ61 stereo microscope was used to observe the chip morphology. Its dimensions are 194 (W) × 253 (D) × 368 (H) mm, the handle stroke is 120 mm, the lens barrel tilt angle is 45° or 60°, the eyepiece is WHSZ15X-H FN 16*, and the objective lens is 110ALK0.4X 180–250. The NT1100 surface roughness measuring instrument is used to detect the surface quality of the processed workpiece. The longitudinal scanning range is 0.1−1 mm, the maximum scanning speed is 7.2 μm/s, and the sample stage size is 100 mm.The NT1100 surface roughness measuring instrument can perform fast, repeatable, and high-resolution three-dimensional measurement of the surface, and the measurement range can be from sub-nanometer roughness to millimeter step height.

4.2. Validation of the Prediction Model of Cutting Force and Cutting Temperature

Four groups of experiments were randomly conducted on the machining center to test the degree of agreement between the actual value of the data and the predicted value. Table 5 is as follows:

Table 5. Comparison of predicted and measured values.

Test Number	Rotating Speed (r/min)	Axial Depth of Cut (mm)	Feed per Tooth (mm/r)	*F* (N)			*T* (°C)		
				Predictive Value	Measured Value	Error (%)	Predictive Value	Measured Value	Error (%)
1	3000	0.4	0.4	689.55	730.00	5.95	571.39	533.79	6.58
2	3500	0.5	0.1	354.01	375.89	6.18	363.38	388.96	7.04
3	4000	0.3	0.3	558.91	526.55	5.79	514.77	554.61	7.74
4	4500	0.2	0.2	378.49	402.15	6.25	428.57	459.34	7.18
Average Error (%)					6.04			7.14	

It can be seen from Table 5 that the average error of the milling force is about 6.04%, the milling temperature is about 7.14%, and the error between the actual measured value and the predicted value is relatively small, which shows that the predicted value of the theoretical formula is more consistent with the actual measured data. So, the theoretical prediction model can be used to predict the magnitude of force and temperature within the range of selected milling parameters.

4.3. Analysis of the Formation Process of Sawtooth Chips

In this section, one tip of the mill tool was taken as a research object to analyze the cutting process. The cutting parameters are simulated with a cutting speed of 18 m/min, a cutting depth of 0.4 mm, a tool rake angle of 12°, and a tool cutting edge radius of 0.01 mm to systematically study the formation process of sawtooth chips.

Figure 8 shows the change trend of the workpiece cutting temperature field with the cutting time at the initial stage of the formation of sawtooth chips. At $t = 5 \times 10^{-4}$ s, the tool has just contacted the workpiece, the highest temperature of the workpiece cutting temperature field is directly in front of the tool tip, then it decreases along the shear surface to the free surface of the workpiece, and the cutting temperature of the free surface of the workpiece is the lowest. At the same time, the area with the highest temperature is the smallest. Along the shear plane, the smaller the temperature, the larger the area.

During the cutting process, the temperature of the main shear zone is distributed in the above-mentioned manner. However, as the cutting time goes by, the maximum temperature of the workpiece cutting temperature field continues to rise. For example, when $t = 5 \times 10^{-4}$ s, it is 202 °C, when $t = 8.8 \times 10^{-4}$ s, it is 446 °C, when $t = 1.2 \times 10^{-3}$ s is 507 °C, and when $t = 2.2 \times 10^{-3}$ s is 599 °C. At the same time, the minimum temperature of the free surface of the workpiece also increases with the passage of cutting time, from $t = 5 \times 10^{-4}$ s to $t = 2.2 \times 10^{-3}$ s, and the temperature changes from 80 °C to 135 °C. From the above data analysis, it can be seen that the closer the shear surface is to the free surface of the workpiece, the slower the temperature increase rate is. In fact, when the temperature of the free surface of the workpiece reaches the softening temperature of the material, all materials on the shear surface have been softened, thus creating conditions for the formation of jagged chips. The softening temperature of the free surface material of the workpiece is the critical temperature for the formation of sawtooth chips. Based on the research in this article, the critical temperature for the formation of sawtooth chips of Inconel718 nickel-based superalloy is about 500 °C.

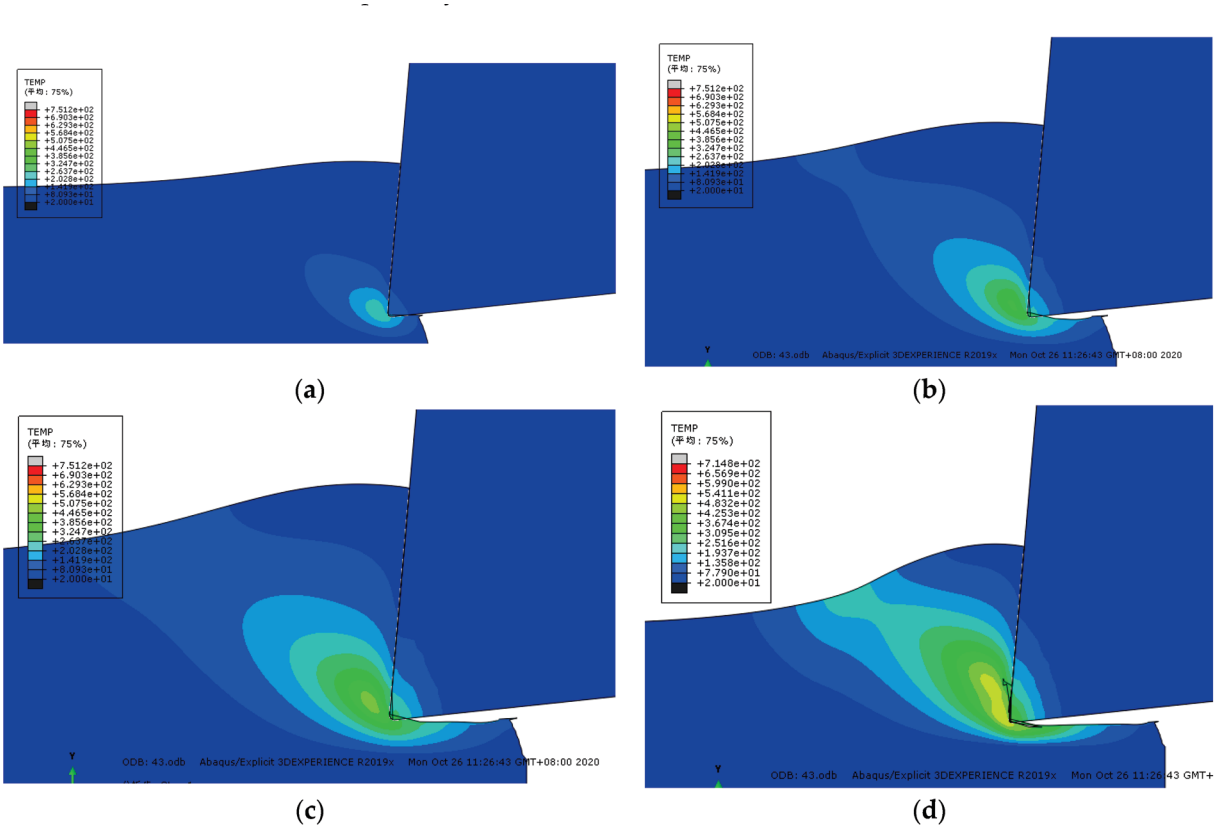

Figure 8. Changes in the cutting temperature field at the beginning of cutting (°C). (**a**) t = 5 × 10^{-4} s (**b**) t = 8.8 × 10^{-4} s. (**c**) t = 1.2 × 10^{-3} s (**d**) t = 2.2 × 10^{-3} s.

Figure 9 shows the simulation results of the formation of the second block of the sawtooth chip. When the tool moves to the moment of Figure 9a, the highest temperature of the cut area in front of the tool tip can reach 439 °C. However, the maximum temperature of the chip surface is above 668 °C, and the first segment of the saw-tooth chip is about to be completely formed. At the moment of Figure 9b, the first segment of the sawtooth chip has been completely formed, and the second segment has begun to form at the same time. At this time, the temperature in front of the tool tip reaches 501 °C. From the tool tip to the chip-free surface, the temperature decreases with the distance. As the cutting process progresses, the high temperature zone near the tool tip continuously spreads along the shear surface and covers the low-temperature zone near the chip-free surface. When the cutting proceeds to the moment in Figure 9c, the material in the first deformation zone continues to deform and the temperature continues to rise. In Figure 9e, the temperature of the material in the shear zone reaches about 682 °C. At this time, the thermal softening effect of the material is intensified, and the material on the shear surface undergoes concentrated slippage and plastic instability, so a convex surface is formed on the free surface of the workpiece. As the cutting progresses as shown in Figure 9f, the second block continues to slip due to the continued cutting of the tool. When proceeding to Figure 9g, the first deformation zone has been transferred to the second nodal block; so far, the second nodal block has been completely formed.

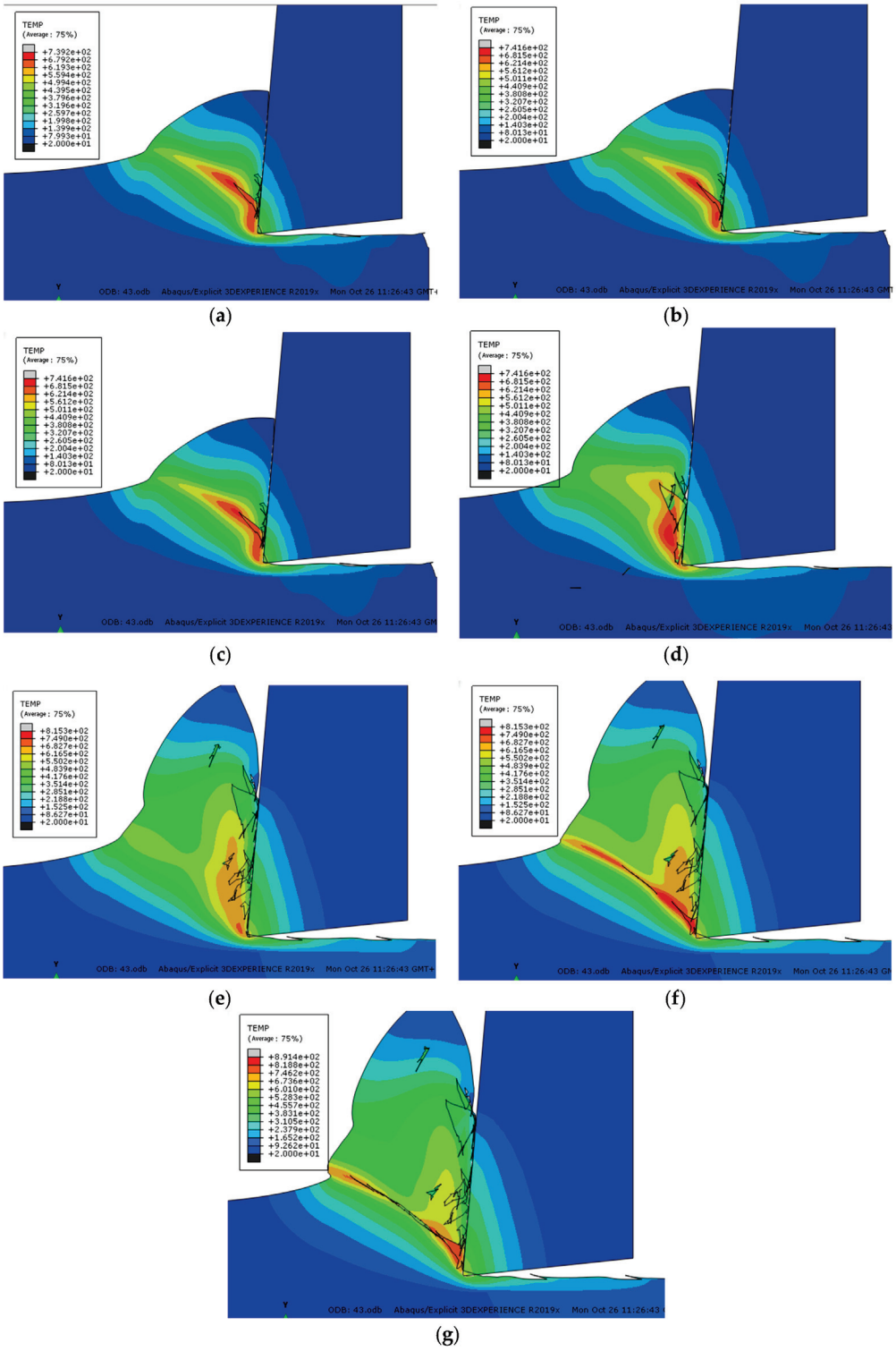

Figure 9. Changes in the cutting temperature field during the formation of serrated chips (°C). (**a**) The first section is aboutto be formed. (**b**) The first block isfully formed. (**c**) The second block begins to form. (**d**) The second nodal development process. (**e**) The second nodal mass starts to slip. (**f**) The second nodal slip process. (**g**) The second block is fully formed.

4.4. The Relationship between Cutting Force, Chip Morphology and Surface Quality

The actual cutting test is carried out to analyze the relationship between the cutting force, chip shape and the surface quality of the workpiece. By using Olympus SZ61 stereo

microscope to observe the chip morphology, the NT1100 surface roughness measuring instrument is used to measure the surface quality after processing. As shown in Figure 10:

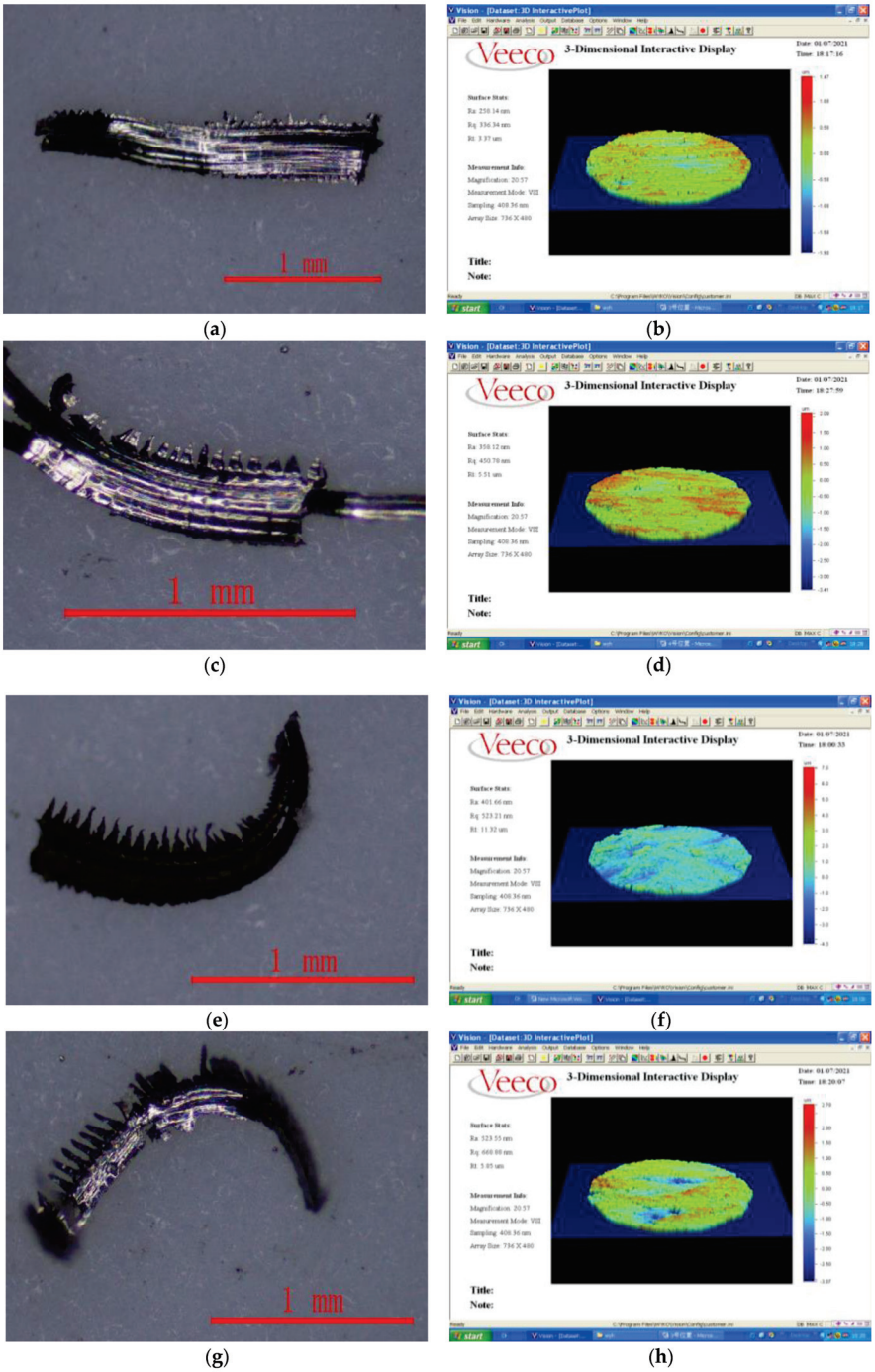

Figure 10. The shape of chips and roughness of surface. (**a**) Chip topography (Cutting force is 280 N). (**b**) Three-dimensional surface topography. (**c**) Chip topography (Cutting force is 400 N). (**d**) Three-dimensional surface topography. (**e**) Chip topography (Cutting force is 470 N). (**f**) Three-dimensional surface topography. (**g**) Chip topography (Cutting force is 620 N). (**h**) Three-dimensional surface topography.

In this chapter, the influence of cutting factors is ignored when the relationship between cutting force, chip morphology and surface quality is studied, and only cutting force is used as the influencing factor. It can be seen from Figure 10a–h that the degree of chip sawtooth generated during the cutting process becomes larger and larger with the gradual

increase in the cutting force, and the chip burr becomes sharper and sharper. In addition, the bottom part of the chip is relatively flat, and the other surface is sawtooth shape. It can be seen from Figure 10a that when the cutting force is low, the cutting speed at this time is relatively low, the shape of the chip is band-like, and the upper part of the chip has no clear saw teeth. However, when the machining speed increases, the serration of the chips becomes more and more serious, as shown in Figure 10c,e,g. This is because the shear force on the shear slip surface will increase sharply with the increase in the cutting speed, which will make the shear deformation on the shear slip surface more and more concentrated. Shear slip on the shear plane is also increasing, so chip serrations are also becoming more pronounced.

From Figure 10b, it can be seen that when the cutting force is low, the tool wear is not serious, so the processed surface quality is better at this time and the surface roughness is low. When the cutting force increases, as shown in Figure 10d,f,h, tool wear increases sharply, the degree of sawtooth chips deepens, and the scratches on the surface of the workpiece increase. At the same time, the increase in the cutting force increases the plastic deformation of the surface material of the workpiece, and the residual height of the processed surface increases, so the quality of the processed surface becomes worse and the surface roughness becomes larger and larger.

4.5. Research on the Wear Morphology of Cemented Carbide Tools

(1) Flank wear

Flank wear is the main wear form of carbide tools when milling high-temperature alloys. Flank wear is located at the tool flank near the main cutting edge. Flank wear is mainly caused by the friction between the tool's flank and the rebounding workpiece surface, as shown in Figure 11a. The wear of the blade face is relatively uniform; dense and uniform wear streaks appear on the wear surface. From the characteristic point of view, the form of wear is abrasive wear. At the same time, it can be seen that the closer the tool tip, the greater the cutting force the tool is subjected to, and the more serious the wear that occurs. This wear feature belongs to a kind of boundary wear, which is also consistent with the previous conclusion.

(2) Wear of rake face

When milling high-temperature alloys, the rake face wear occurs, and the manifestation is crater wear, as shown in Figure 11b. The surface wear is located on the rake surface near the main cutting edge. It is mainly caused by the chemical interaction between the rake face of the tool and the high-temperature chips. In the milling process, the chips and the rake face are in direct contact and friction, so the chemical activity is very high. When the milling speed is relatively high, higher temperature and higher pressure will be generated, and it is easy to form crescent wear in this contact area. That is to say, the higher the cutting temperature, the more serious the tool wear.

(3) Layers of flaking

As shown in Figure 11c, the tool also has lamellar spalling during the milling process. This wear phenomenon is mainly reflected in the vicinity of the cutting edge of the tool, where the cutting force and cutting temperature are the largest. The main reason is that when the tool cuts into and out of the workpiece, contact fatigue and thermal stress are generated. Under the action of this stress, the surface of the tool edge gradually develops cracks until it falls off the surface of the tool in layers.

(4) Tool chipping

The chipping phenomenon of the tool mainly occurs at the tip of the tool, as shown in Figure 11d.As the tool continues to cut the workpiece, the work hardening of the workpiece is gradually strengthened, and the tool is continuously weakened. When the cutting force during the milling process is greater than the yield strength of the tool, the tip of the tool will be chipped. After a tool is chipped, the tool is "blunted," and therefore, no longer capable of cutting the workpiece material.

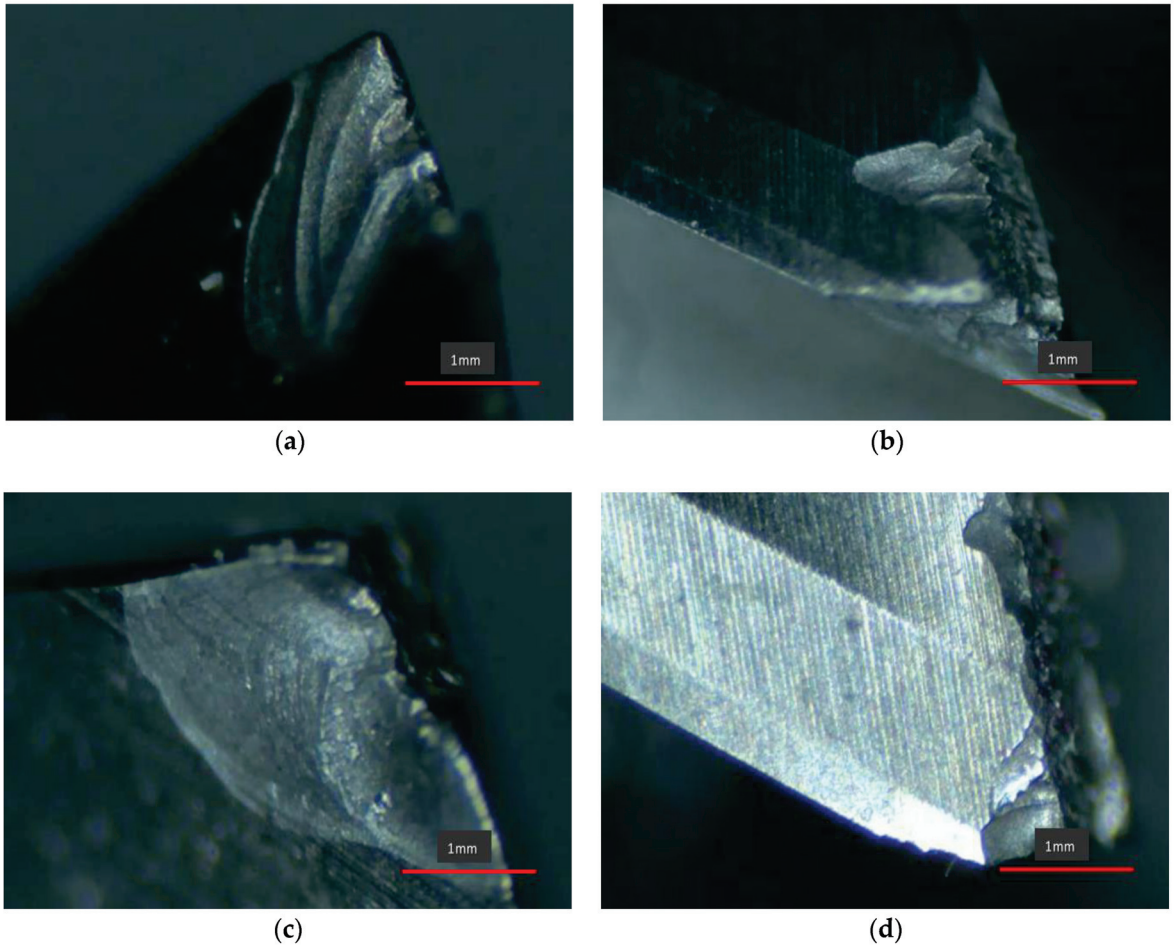

Figure 11. Wear morphology of tool. (n = 300 r/min, a_p = 0.4 mm, f_z = 0.4 mm/r). (**a**) Wear morphology of flank face. (**b**) Wear morphology of rake face. (**c**) Layered flaking. (**d**) Tool chipping.

5. Conclusions

Based on the simulation analysis and actual experiment, this paper describes an Inconel718 nickel-base superalloy milling orthogonal experiment, establishes the cutting force and cutting temperature prediction model empirical formulas in the milling process, and obtains the following conclusions:

(1) Through orthogonal experiment analysis, the empirical formula of the cutting force prediction model is established as: $F = 133.44 \cdot {a_p}^{0.4642} \cdot n^{0.3260} \cdot {f_z}^{0.5919}$; the empirical formula of the cutting temperature prediction model is:

$$T = 326.51 \cdot {a_p}^{0.1275} \cdot n^{0.1258} \cdot {f_z}^{0.3610}.$$

(2) Through the range analysis of the result data, it is concluded that from the perspective of reducing the cutting force, the combination of the best milling parameters is: $n = 4000$ r/min, $a_p = 0.4$ mm, $f_z = 0.1$ mm/r, from the perspective of

reducing the cutting temperature, the combination of the best milling parameters is: $n = 4500$ r/min, $a_p = 0.5$ mm, $f_z = 0.1$ mm/r.

(3) The actual orthogonal cutting test was carried out on the machine tool to verify the reliability and accuracy of the prediction model of cutting force and cutting temperature.

(4) With the velocity field, strain field and strain rate field model of the shear deformation zone, the influence curves of cutting speed and tool rake angle on shear speed, shear strain and shear strain rate are calculated and drawn. The influence of cutting speed and tool rake angle on shear speed, shear strain and shear strain rate are analyzed.

(5) The mechanism of the formation of sawtooth chips is analyzed, and the distribution of stress, strain and temperature and the causes of formation are analyzed in detail by means of distribution clouds. Through a combination of theory and experiment, the relationship among cutting force, chip shape and surface quality in the milling process is analyzed. Finally, as the cutting force increases, the sawtooth of the chips becomes more and more serious, and the roughness of the machined surface becomes larger and larger.

(6) The formation causes and formation processes of different tool wear morphologies are analyzed. In the high-efficiency milling of Inconel718 of cemented carbide end mills, the forms of tool wear are mainly blade spalling, tool chipping, tool surface pits and surface scratches. At the same time, tool front and flank wear will occur in high-speed cutting.

Author Contributions: Y.W. conducted most of the experiments and wrote the manuscript. X.L. directed the overall design and analysis of the experiment. L.M. and W.Z. helped collect and analyze some simulation and experimental data. All authors have read and agreed to the published version of the manuscript.

Funding: This work was financially supported by National Natural Science Foundation of Jilin Province, China (Grant No. 20200201065JC).

Institutional Review Board Statement: Not applicable.

Informed Consent Statement: Informed consent was obtained from all subjects involved in the study.

Data Availability Statement: Not applicable.

Acknowledgments: The authors wish to acknowledge support from the Virtual Simulation Laboratory of Changchun University of Science and Technology. The authors would also like to thank the anonymous reviewers for their helpful comments.

Conflicts of Interest: The authors declare that they have no conflict of interest.

References

1. Choudhury, I.A.; El-Baradie, M.A. Machinability of nickel-base super alloys: A general review. *J. Mater. Process. Tech.* **1998**, *77*, 278–284. [CrossRef]
2. Du, J.; Zhao, G.; Deng, Q.; Lu, X.; Zhang, B. Development of China's wrought superalloys. *J. Aeronaut. Mater.* **2016**, *36*, 27–39. [CrossRef]
3. Cheng, X.; Zha, X.; Jiang, F. Optimizing the geometric parameters of cutting edge for rough machining Fe-Cr-Ni stainless steel. *Int. J. Adv. Manuf. Technol.* **2016**, *85*, 683–693. [CrossRef]
4. Zong, W.J.; Cao, Z.M.; He, C.L.; Xue, C.X. Theoretical modeling and FE simulation on the oblique diamond turning of ZnS crystal. *Int. J. Mach. Tools Manuf.* **2016**, *100*, 55–71. [CrossRef]
5. Yiğit, M.; Arısoy, T. Prediction of machining induced microstructure in Ti–6Al–4V alloy using 3-D FE-based simulations: Effects of tool micro-geometry, coating and cutting conditions. *J. Mater. Process. Tech.* **2015**, *220*, 1–26. [CrossRef]
6. Lu, X.; Wang, H.; Jia, Z.; Feng, Y.; Liang, S.Y. Coupled thermal and mechanical analyses of micro-milling Inconel718. *Proc. Inst. Mech. Eng.* **2019**, *233*, 1112–1126. [CrossRef]
7. Yao, Y.; Shen, C.; Ma, D. Simulation of high-strength aluminum alloy cutting force in high-speed turning with PCD tool. *Tool Technol.* **2019**, *53*, 81–85.
8. Islam, S.; Yuan, S.; Li, Z. A Cutting Force Prediction Model, Experimental Studies, and Optimization of Cutting Parameters for Rotary Ultrasonic Face Milling of C/SiC Composites. *Appl. Compos. Mater.* **2020**, *27*, 407–431. [CrossRef]

9. Cui, X.; Zhao, B.; Jiao, F.; Zheng, J. Chip formation and its effects on cutting force, tool temperature, tool stress, and cutting edge wear in high- and ultra-high-speed milling. *Int. J. Adv. Manuf. Technol.* **2016**, *83*, 55–65. [CrossRef]
10. He, L.; Su, H.; Xu, J.; Zhang, L. Study on dynamic chip formation mechanisms of Ti_2AlNb intermetallic alloy. *Int. J. Adv. Manuf. Technol.* **2017**, *92*, 4415–4428. [CrossRef]
11. Wang, F.; Tao, Q.; Xiao, L.; Hu, J.; Xu, L. Simulation and analysis of serrated chip formation in cutting process of hardened steel considering ploughing-effect. *J. Mech. Sci. Technol.* **2018**, *32*, 2029–2037. [CrossRef]
12. Chen, E.; Wang, J.; Huang, S.; Dong, K.; Xu, L. Research on the influence of tool rake angle on chip formation and cutting force of SiC_p/Al composites. *Tool Technol.* **2018**, *52*, 90–93. [CrossRef]
13. Ebrahimi, S.M.; Araee, A.; Hadad, M. Investigation of the effects of constitutive law on numerical analysis of turning processes to predict the chip morphology, tool temperature, and cutting force. *Int. J. Adv. Manuf. Technol.* **2019**, *105*, 4245–4264. [CrossRef]
14. Song, W.; Wang, Z.; Deng, J.; Zhou, K.; Wang, S.; Guo, Z. Cutting temperature analysis and experiment of Ti–MoS_2/Zr-coated cemented carbide tool. *Int. J. Adv. Manuf. Technol.* **2017**, *93*, 799–809. [CrossRef]
15. Grzesik, W.; Niesłony, P.; Habrat, W.; Sieniawski, J.; Laskowski, P. Investigation of tool wear in the turning of Inconel718 superalloy in terms of process performance and productivity enhancement. *Tribol. Int.* **2018**, *118*, 337–346. [CrossRef]
16. Hao, P. Research on Tool Wear of PCBN Tool Cutting Nickel-Based Superalloy under High Pressure Cooling. Ph.D. Thesis, Harbin University of Science and Technology, Harbin, China, 2018.
17. Xie, L.; Cheng, G.; Jin, L. Research on Cr12MoV Cutting Temperature Prediction Model Based on Orthogonal Test. *Tool Technol.* **2016**, *50*, 30–33.
18. Hao, Z.; Cui, R.; Fan, Y. Research on Tool Wear Mechanism of Cutting Nickel-Based Superalloy GH4169. *J. Chang. Univ. Technol.* **2018**, *39*, 8–13+105. [CrossRef]
19. Rotella, G.; Dillon, O.W.; Umbrello, D.; Settineri, L.; Jawahir, I.S. Finite element modeling of microstructural changes in turning of AA7075-T651 Alloy. *J. Manuf. Process.* **2013**, *15*, 87–95. [CrossRef]
20. Yu, H.; Wu, X. *Material Data Manual for Aeroengine Design*; Aviation Industry Press: Beijing, China, 2010; pp. 91–105.
21. Chen, R. *Principles of Metal Cutting*; China Machine Press: Beijing, China, 2007.
22. Pálmai, Z.; Kundrák, J.; Makkai, T. The transient changing of forces in interrupted milling. *Int. J. Adv. Manuf. Technol.* **2019**, *104*, 3787–3801. [CrossRef]
23. Li, Q.; Yang, S.; Zhang, Y.; Zhou, Y.; Cui, J. Evaluation of the machinability of titanium alloy using a micro-textured ball end milling cutter. *Int. J. Adv. Manuf. Technol.* **2018**, *98*, 2083–2092. [CrossRef]
24. Peng, F.Y.; Dong, Q.; Yan, R.; Zhou, L.; Zhan, C. Analytical modeling and experimental validation of residual stress in micro-end-milling. *Int. J. Adv. Manuf. Technol.* **2016**, *87*, 3411–3424. [CrossRef]
25. Wang, Q. Research and Application of Functional Principal Component Analysis and Functional Linear Regression Model. Diploma Thesis, Chongqing Technology and Business University, Chongqing, China, 2020.
26. Ma, Y.; Yue, Y. Research on Surface Roughness Prediction Model of Titanium Alloy TC25 Milling. *Manuf. Technol. Mach. Tool* **2020**, *8*, 141–145. [CrossRef]
27. Liu, A. *SPSS Basic Analysis Tutorial*; Peking University Press: Beijing, China, 2014.
28. Liu, S.; Wan, X.; Dong, Z. Finite Element Analysis of the Influence of Chip Friction on Cutting Process. *Nonferrous Met.* **2007**, *42*, 33–36. [CrossRef]
29. Pu, X. Physical Simulation and Process Parameter Optimization of Nickel-Based Superalloy Machining. Diploma Thesis, Southwest Petroleum University, Chengdu, China, 2016.

MDPI
St. Alban-Anlage 66
4052 Basel
Switzerland
www.mdpi.com

Micromachines Editorial Office
E-mail: micromachines@mdpi.com
www.mdpi.com/journal/micromachines

Academic Open
Access Publishing

mdpi.com

ISBN 978-3-7258-1565-4